Universitat Autònoma de Barcelona

Plasma-magnetic field interaction in extreme astrophysical environments

Enrique Mestre Guillén

Plasma-magnetic field interaction in extreme astrophysical environments

Ph.D. Dissertation

Enrique Mestre Guillén

April 2021

supervised by

Emma de Oña Wilhelmi and Diego F. Torres

Tutor: Luis Font Guiteras

Departament de Física
Universitat Autònoma de Barcelona

Institute of Space Sciences (ICE, CSIC)
c. Can Magrans s/n, 08193 Bellaterra (Barcelona)

A mi padre, in memoriam

Contents

1 Introduction **6**

2 Galactic sources of gamma-rays **9**

2.1 Highly relativistic particles in astrophysical sources 9

2.1.1 Introduction 9

2.1.2 Cosmic rays 10

2.1.3 Observations in radio 13

2.1.4 Very-high-energy regime 14

2.2 Acceleration mechanisms 15

2.2.1 Fermi second-order acceleration 15

2.2.2 Acceleration in astrophysical relativistic shocks 16

2.2.3 Diffusive Shock Acceleration 17

2.2.4 Magnetic reconnection 18

2.3 Radiation mechanisms 20

2.3.1 Bremsstrahlung 20

2.3.2 Synchrotron and curvature radiation 21

2.3.3 Inverse Compton 23

2.3.4 Synchrotron–self-Compton 25

2.3.5 Pion decay 25

2.4 Galactic population of gamma-ray sources 27

2.4.1 Overview 27

2.4.2 Pulsars and pulsar wind nebulae 28

2.4.3 Supernova remnants 30

2.4.4 Stellar clusters 31

3 Observing the sky in the GeV and TeV regimes **33**

3.1 Detection techniques in the gamma-ray regime 33

3.1.1 Introduction 33

3.1.2 Pair detectors 34

3.1.3 Imaging Atmospheric Cherenkov Telescopes 36

3.1.4 Air-shower experiments . . . 39
3.2 Analysis Tools . . . 40
3.2.1 Introduction . . . 40
3.2.2 FERMIPY . . . 40
3.2.3 CTA Instrument Response Functions . . . 41
3.2.4 Tools for the simulation and analysis of CTA data: GAMMAPY and CTOOLS . . . 44
3.2.5 NAIMA and TEMPO2 . . . 45
3.3 Applications of the analysis tools . . . 46
3.3.1 Generating simulated 3D sky cubes . . . 46
3.3.2 Source confusion . . . 50
3.3.3 Other applications . . . 70

4 Prospects for the characterization of the very-high-energy emission from the Crab Nebula and pulsar 72
4.1 Introduction . . . 72
4.2 The Crab pulsar . . . 73
4.2.1 Simulations of the Crab pulsar phase curve . . . 74
4.2.2 Simulations of the Crab pulsar spectrum . . . 76
4.2.3 Generalization of the simulations to different phase curves at different flux levels . . . 78
4.3 The Crab pulsar wind nebula . . . 79
4.3.1 Simulations of the Crab Nebula spectral shape . . . 84
4.3.2 Simulations of the Crab Nebula morphology . . . 92
4.4 The flares in Crab . . . 95
4.4.1 Simulations of the Crab flares . . . 98
4.4.2 Application to the 2011 and 2013 flares . . . 104
4.4.3 Simulations of flares at different flux levels . . . 113
4.4.4 Hypotheses for the origin of the gamma-ray flares . . . 114

5 Hadronic acceleration of Galactic cosmic rays 122
5.1 Introduction . . . 122
5.2 SNR G39.2-0.3 . . . 124
5.2.1 Reanalysis of SNR G39.2-0.3 with LAT data and CO observations 125
5.2.2 Old dynamical age scenario . . . 129
5.3 The Carina arm region . . . 130
5.3.1 Westerlund 2 . . . 131
5.3.2 Fermi-LAT observations: Methodology. . . . 134
5.3.3 Fermi-LAT observations: Results. . . . 137

5.3.4 Modeling the high-energy spectrum of Westerlund 2 146

6 Conclusions **156**
6.1 General remarks 156
6.2 Plasma-magnetic field interaction: the Physics behind the sources under study 158
6.2.1 The Crab Nebula and pulsar 158
6.2.2 SNR G39.2-0.3 158
6.2.3 Westerlund 2 160
6.3 Prospects for future studies 161
6.3.1 Simulating CTA data 162
6.3.2 Future studies with CTA 163

Bibliography **170**

List of Figures **191**

List of Tables **201**

Appendices **207**

A Generation and analysis of 3D sky cubes **208**
A.1 Generator of 3D sky cubes 209
A.2 Analysis of 3D sky cubes 221
A.2.1 Detection significance 221
A.2.2 Spectral analysis 225
A.2.3 Morphological analysis 233

B Simulations of Crab flares **241**

C Particle spectrum fit with NAIMA **250**

D Publications **258**

Acknowledgements

En primer lugar, quiero agradecer a Emma de Oña Wilhelmi todo su esfuerzo por dirigir esta tesis y la oportunidad que me concedió de realizarla entre investigadores de enorme profesionalidad. Gracias por escuchar y resolver con paciencia la infinidad de dudas que te he planteado durante estos años, y por guiarme con tesón a la consecución del doctorado. Asimismo, agradezco profundamente a Diego F. Torres la codirección de la tesis, su asesoramiento (en todos los aspectos) a lo largo de la misma, su esfuerzo, y toda la ayuda que me ha prestado. Sin duda, esta tesis no hubiera podido llegar a buen puerto sin vosotros.

Envío también todo mi agradecimiento a Roberta Zanin, Luigi Tibaldo, Dmitry Khangulyan, Fabio Acero, Tim Lukas Holch, Ullrich Schwanke, Pablo Saz Parkinson, Felix Aharonian, Ruizhi Yang, Estrella Sánchez Ayaso, Jian Li, Iurii Sushch, Robert Brose, Yang Su, y a todos los que han colaborado conmigo para sacar adelante los artículos y resultados que sustentan esta tesis por su magnífico trabajo.

Por supuesto, guardo gratitud a los investigadores del ICE, en especial, a quienes me escucharon en las reuniones de grupo y me aportaron sus ideas. Debo dar las gracias también a todo el personal del centro, ya que hace que éste funcione.

Le dedico un agradecimiento especial a Mar Mezcua, que ha ejercido la figura de mentora, por dedicarme su tiempo, orientarme, y velar por mi bienestar como trabajador del centro.

Me acuerdo con cariño y gratitud de todos mis compañeros de doctorado (siendo tantos, disculpad que no os nombre expresamente) porque, habiéndome acompañado en mi paso por el ICE, han hecho de este camino una vivencia feliz que recordaré con afecto. Gracias a mis compañeros de despacho, por propiciar un ambiente tranquilo y beneficioso para el trabajo. De entre ellos mando un saludo especial a Axel, ya que compartimos juntos momentos de gran diversión.

Finalmente, quiero agradecer a mi madre y a mi hermana Irene todo el apoyo que me han dado siempre desde el hogar en los buenos y los malos momentos. Dedico con cariño esta tesis a mi padre, cuyo recuerdo siempre me acompaña, con admiración, además, de su valioso legado científico. Le doy las gracias a toda mi familia (no solo de sangre) y amigos que siempre me hacen sentir cerca de ellos. Por último, no tengo suficientes palabras para

agradecer a Vane todo lo que me ha dado en estos años, pero sé que, gracias a su amor, esta senda fue más hermosa y plena de lo que nunca pude imaginar.

Chapter 1

Introduction

For centuries, the optical light gathered by the naked eye, or by focusing optics with glass lenses and mirrors, was the only intermediary between the astronomical sources and our knowledge of the celestial bodies crowding the night sky. Only since the nineteenth century, the light at other wavelengths, firstly, in the infrared, converted into a tool to observe the astronomical objects, completing slowly more and more the picture of the night sky and pushing our understanding of the universe to the current knowledge achieved. Nowadays, our perception of the universe is mediated by many instruments gathering data along the entire electromagnetic spectrum and by other messengers than light.

The modern studies of astronomical objects at the highest energies of the electromagnetic spectrum (i.e., X-rays and gamma-rays) began in the 1960s. Formerly, the Sun had been detected in X-rays (in 1948), and different processes leading to gamma-ray emission in astrophysical environments had been proposed during the 1950s. The X-rays had been discovered, in fact, in 1895 by W. C. Röntgen, while P. Villard discovered gamma radiation only five years later (1900). However, since most of the X-rays and gamma-rays arriving at Earth are absorbed in the atmosphere, the X-ray and gamma-ray astronomy could not properly develop until the first instruments devoted to this field were ready to be launched to the upper atmosphere or space. During the 1970s, several satellites were launched to explore the X-ray sky, like *Uhuru*, *SAS-3*, or *OSO-8*, giving an unprecedented impulse to the field. The *Compton Gamma-Ray Observatory* (CGRO), launched in 1991, was the first major observatory for gamma-ray astronomy. Since then, several satellites, e.g., *Swift*, *INTEGRAL*, *AGILE*, or *Fermi*, have contributed to unveil a multitude of Galactic and extragalactic gamma-ray sources. In parallel, ground telescopes dedicated to detecting Cherenkov radiation, experimentally studied by P. A. Cherenkov and others since the 1930s, were developing. The first detection of this radiation (induced by cosmic rays in the atmosphere) was indeed achieved in 1952. Thirty-seven years later, the Whipple telescope detected the first TeV source pointing to the Crab Nebula.

The energetic gamma-ray radiation is known to be related to high-energy particles and

magnetic fields through various processes (e.g., synchrotron radiation, inverse Compton, or proton-proton interaction). The definitive evidence that such energetic particles of astrophysical origin exist was the association of cosmic rays with charged particles early in the 1930s. The cosmic rays, arriving on Earth from all directions, had been discovered in balloon flights by the Austrian physicist Victor Hess in 1912. Later, in 1948, the energy loss of cosmic-ray electrons scattering off the stellar photon fields was noted (Feinberg and Primakoff, 1948). Shortly after, in 1952, their interaction with the interstellar matter was proposed to be a source of gamma-rays in some astrophysical environments (following the neutral pion discovery in 1949, see Hayakawa, 1952). Similarly, in the same year, the gamma-ray flux from cosmic bremsstrahlung was estimated (Hutchinson, 1952). By 1958, the gamma-ray emission expected from astrophysical sources was far more optimistic (Morrison, 1958).

We developed this thesis in the context of understanding the interaction of high-energy particles and magnetic fields in extreme astrophysical environments, like pulsars and pulsar wind nebulae. We employed both simulations implemented with the tools currently in development for future gamma-ray data analysis and observations from the LAT instrument onboard the *Fermi* satellite. In particular, we focused on three sources, the Crab Nebula and pulsar, the supernova remnant SNR G39.2-0.3, and the Westerlund 2 stellar cluster. This work is structured as follows:

- Chapter 2 consists, firstly, of an introduction to the topic of relativistic particles in astrophysical environments (Section 2.1). We next address the most relevant mechanisms proposed to explain how these particles are accelerated and radiate (in Sections 2.2 and 2.3, respectively). Finally, we present several source classes (among the Galactic population of gamma-ray sources observed) investigated in this thesis, i.e., pulsars, pulsar wind nebulae, supernova remnants, and stellar clusters.

- Chapter 3 summarizes some of the detection techniques employed for the GeV and TeV regimes. In particular, we will treat pair-detectors (as *Fermi*-LAT), Imaging Atmospheric Cherenkov Telescopes (e.g., CTA), and air-shower detectors (Section 3.1). Then, we describe the different tools developed for this work (Section 3.2) and their applications on the astrophysical sources of our interest (Section 3.3).

- In Chapter 4, we present simulations regarding the prospects for detecting the Crab Nebula and pulsar (both in flaring and steady-state), in gamma-rays, with the future Cherenkov Telescope Array observatory, testing the main existing theories about the origin of the observed gamma-ray emission.

- In Chapter 5, we probe the hadronic acceleration of cosmic rays by means of analyzing the *Fermi*-LAT data (in the hundreds of MeV up to the GeV regime)

from two sources; the supernova remnant SNR G39.2-0.3 and the Westerlund 2 stellar cluster in the Carina arm region.

- To conclude, the last chapter, i.e., Chapter 6, is dedicated to conclusions.

Additionally, we included the principal tools employed to derive the results presented in this work in the appendices (for further details).

Chapter 2

Galactic sources of gamma-rays

2.1 Highly relativistic particles in astrophysical sources

2.1.1 Introduction

For decades, the astronomical observations carried out in multiple windows of the electromagnetic spectrum (see Figure 2.1), from radio to gamma-ray wavelengths, have gathered a large amount of evidence indicating the presence of highly relativistic particles in several types of astrophysical sources. It is nowadays clear that processes accelerating particles to very high energies are ubiquitous in the universe. On the one hand, direct evidence supporting this claim consists of observations of actual relativistic particles arriving on Earth, known as cosmic rays. On the other hand, the detection of secondary products originating in particle acceleration processes (e.g., high energy gamma-rays or neutrinos) can be considered indirect evidence of particles being accelerated to very high energies. The neutral particles, for instance, are not accelerated directly by electromagnetic fields. Consequently, these particles must be secondary products of either the collisions between particles or interactions between particles and magnetic fields.

A varied population of sources has been identified (or postulated) as particle accelerators (e.g., supernova remnants and pulsar wind nebulae). Then, collecting a large amount of data (with good quality) from multiple sources is crucial to understand the characteristics of this population of astrophysical accelerators. Different techniques are needed for this purpose. For example, it is known that cosmic rays prove the existence of protons and heavier ions being accelerated to extreme energies. However, since charged particles spiral around Galactic magnetic field lines, their path is deflected, retaining little information about the sites in which the acceleration took place. In contrast, light from any window of the electromagnetic spectrum carries this information and can provide or facilitate the source's identification. Unfortunately, although observations at different wavelengths can indicate the presence of an energetic electron population in the source,

in most cases, they do not provide evidence (for or against) of the presence of energetic baryons. Since neutrinos, like photons, are not deflected by the Galactic magnetic fields, a priori, neutrino data can simultaneously allow the identification of a source and prove the acceleration of baryons (in the same). However, current high-energy neutrino detection techniques suffer from limited statistics and low-angular resolution, and point sources of high-energy neutrinos are yet to be identified. Searching for electromagnetic counterparts of the high-energy neutrino events observed might help to identify these neutrino sources.

This chapter will summarize some of the main sources of information for the high-energy particle astrophysics domain. In particular, we will focus on: cosmic rays, which prove that acceleration of protons to energies of $\sim 10^{20}$ eV takes place in astrophysical environments; radio emission, because its non-thermal origin requires the presence of both relativistic electrons and magnetic fields; X-rays and soft gamma-ray photons, highly correlated with radio emission; and high-energy gamma-rays, which require either electrons with higher energy than those emitting in radio, or acceleration of baryons. Secondly, we will introduce the mechanisms involved in the acceleration of particles to very high energies and, next, the mechanisms originating the radiation observed from these particle populations. Lastly, we will provide an overview of the sources in which these processes occur, focusing on the types of sources relevant to the work we are presenting.

2.1.2 Cosmic rays

Cosmic rays were discovered by Victor Hess (Hess, V. F., 1912; 1913). In 1912 he demonstrated, carrying an electroscope in several flights with a hydrogen-filled balloon, that the amount of ionizing radiation increases with altitude. At that time, the Earth's crust was believed to be the source of the background flux of ionizing radiation. On the contrary, the results of Hess pointed to an extraterrestrial rather than terrestrial origin for the same (Friedlander, 2012). Furthermore, Hess concluded that the radiation was not originated either in the Sun since conducting a flight during the solar eclipse of 17 April 1912 observed no variation of the ionization rate. During the mid-20s, this radiation began to be known as cosmic rays. However, its physical nature was still not clear. Arthur Compton, in 1932, showed that the cosmic-ray flux varies as expected if consisting of charged particles being deflected by the Earth's magnetic field. Shortly after, different experiments showed that primary cosmic rays consist (mainly) of positively charged particles.

The spectral energy distribution of the cosmic rays spans over a huge range (Hillas, 2006), from 100 eV/nucleon to over 10^{20} eV/nucleon (Gaisser et al., 2013). This fact illustrates clearly the impossibility of observing cosmic rays over their entire energy range with a single type of detector or technique. Understanding the properties of cosmic rays,

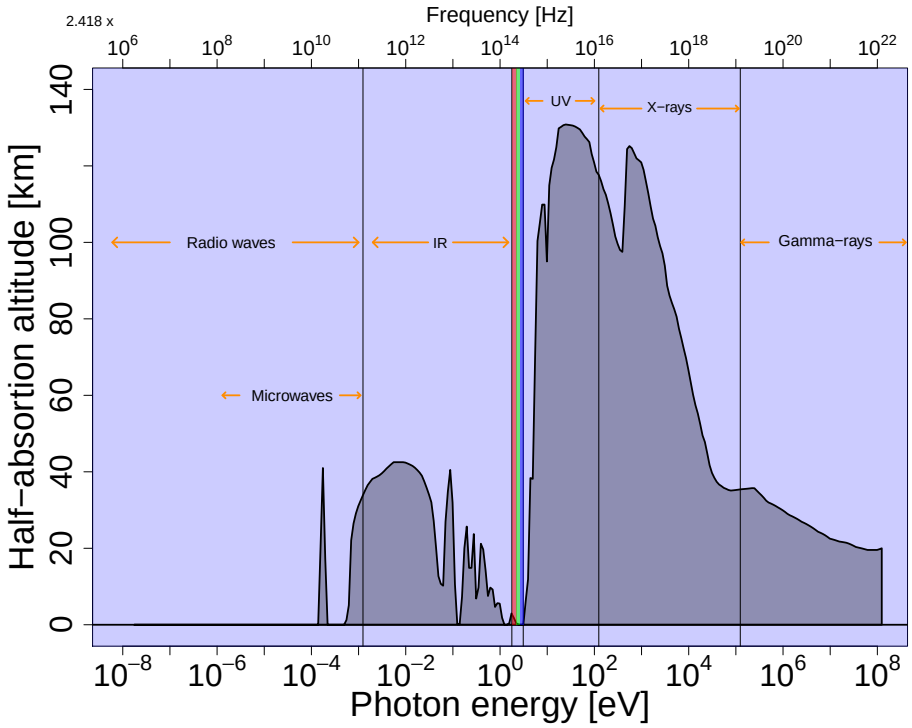

Figure 2.1: Half-absorption altitude with respect to photon energy. The data were taken from the *National Radio Astronomy Observatory* (NRAO).

then, has relied on the combination of results from many different instruments at different wavelengths (see, e.g., Figure 2.2). Cosmic rays at energies $E < 10^{15}$ eV are absorbed in the upper atmosphere. However, its relatively high flux (i.e., about one particle per square meter and second at energies of hundreds of GeV) facilitates its direct detection with balloon-borne or satellite experiments. Some instruments used in these experiments to measure the energy of (low-energy) cosmic rays are magnetic spectrometers (e.g., AMS-02, PAMELA) and calorimeters. The first ones track the curved path of the particle in a known magnetic field (given that primary cosmic rays have an electric charge), measuring the rigidity (i.e., $R = p/Z$, where p is the particle's incident momentum and Z the total charge magnitude) and the charge sign. The latter measure the energy deposited when the incident particle passes through matter. Since the cosmic-ray flux is decreasingly smaller with energy, the higher energy cosmic rays can not be directly studied from the upper atmosphere or space. However, their interaction with the atmosphere produces cascades of secondary products that are observable using ground-based techniques (i.e., Cherenkov light or air-shower detectors).

The spectral energy distribution of cosmic rays can be characterized (essentially) by a power-law distribution with an overall spectral index close to 2.7. It presents three main distinctive features: a leveling off at energies below a few GeV, a slight bend towards

a softer spectral index ($\alpha \approx -3.1$) called the "knee" (at about 5×10^{15} eV of energy), and a rather less prominent change of slope, known as the "ankle" at energies of about 5×10^{18} eV. The behavior of low-energy cosmic rays is reasonably well understood as a consequence of their interaction with the magnetic field carried by the solar wind rather than by the actual nature of the cosmic rays themselves (Fiandrini et al., 2020). However, the knee, ankle, and high-energy cutoff are more interesting from the point of view of the high-energy particle astrophysics domain.

The knee has been associated with a transition in the mass composition of cosmic rays towards heavier primaries at higher energies, with spectra of different nuclei cutting off at energies that are proportional to the nuclear charge ($E_{\text{cutoff}} \propto Z$, Hörandel et al., 2003), but also with propagation effects in the Galaxy (Ptuskin et al., 1993), and re-acceleration at shocks in the Galactic wind (Völk & Zirakashvili, 2004). The typical gyroradius ($R_g = p/qB$) for the knee protons is of the order of a few parsecs. Then, the protons should be confined in the Milky Way by the Galactic magnetic field. The dominant sources both below and above the knee energy should, therefore, be Galactic ones. In contrast, the gyroradius of protons with energies corresponding to the ankle is of the order of a few kiloparsecs. Since this is in order of magnitude comparable to the Galaxy dimensions, the ankle might indicate the point where extragalactic cosmic rays are dominant (Hillas, 2006). However, it is not fully clear how the transition from a parent population dominated by Galactic sources to one predominantly consisting of extragalactic ones occurs. Finally, the spectrum's last distinctive feature (located at the highest energies), i.e., the high-energy cutoff, matches an attractive explanation in the so-called GZK limit (Greisen, 1966; Zatsepin & Kuzmin, 1966). This limit is due to the interaction of extremely energetic protons ($E > 2.5 \times 10^{20}$ eV) with the cosmic microwave background (CMB) photon field, which gives origin, ultimately, to the production of a nucleon and a pion

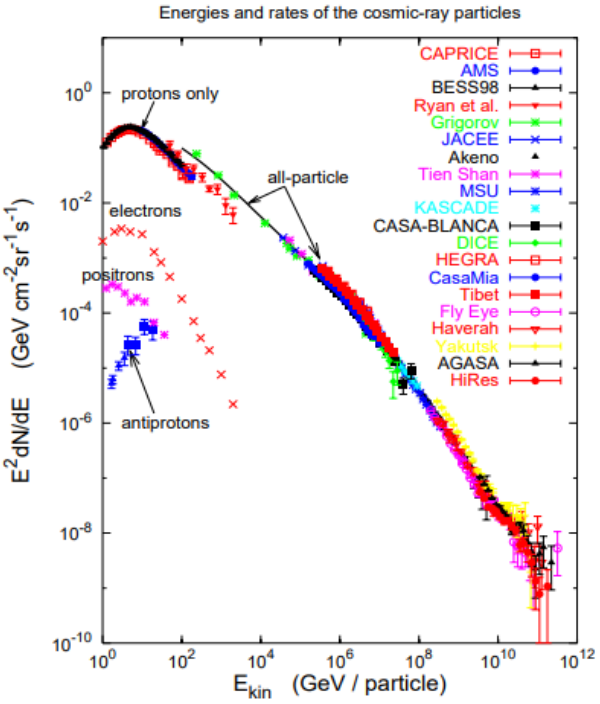

Figure 2.2: Spectral energy distribution of cosmic rays (taken from Hillas, 2006).

$(p + \gamma \rightarrow \Delta(1232) \rightarrow p + \pi^0(n + \pi^+))$.

The Galactic magnetic field plays a crucial role in transporting the charged particles through the interstellar medium as they diffuse away from the sources of cosmic rays (which have been associated with energetic Galactic phenomena, e.g., supernova remnants or powerful stellar winds, see Blasi, 2013). Random magnetic fields causing pitch-angle scattering can provide efficient confinement in the Galaxy and the spatial diffusion of cosmic rays with energies smaller than $10^{17}Z$ eV (Ptuskin, 2006). Additionally, the convective motion of interstellar gas (at large scales) with a frozen magnetic field leads to the convective transport of the energetic particles. In a rather simple approximation, the diffusive-convective transport of cosmic rays can be described by introducing their mean escape time from the Galaxy as a function only of particle energy, which is known as the "leaky box" model (Cowsik et al., 1967; Jones et al., 1990). However, Galactic cosmic rays can not always be treated as test particles moving in a given magnetic field since their energy density, i.e., ~ 1 eV/cm^3, is comparable to the one of the magnetic field (i.e., $B^2/2\mu_0$, with $B \sim 3$ μG) and to the energy density of turbulent motions of the interstellar gas ($\sim nkT$, with $n \sim 1$ and $T \sim 10^4$ K, see Ginzburg, 1965). Hence, cosmic rays also produce turbulence which self-consistently determines the cosmic-ray diffusion (Wentzel, 1974). Also, the cosmic-ray pressure is comparable to the other gas and field pressures determining the interstellar gas dynamics at large scales (Parker, 1969). In particular, the cosmic-ray pressure can drive a "Galactic wind" (Ipavich, 1975).

2.1.3 Observations in radio

The radio emission is the electromagnetic radiation of the longest wavelengths, extending the *radio window* from about $\lambda = 1$ millimeter to 10 meters. The Galactic disk, first detected at radio in the 1930s, is the dominant source of radio emission, as seen from Earth. On top of the same, a multitude of discrete sources, both Galactic and extragalactic, can be observed, as well as the isotropic 2.7 K thermal radiation of cosmological origin (i.e., the CMB). While optical emission is usually due to thermal radiation (i.e., Planck's law), non-thermal sources contribute the most to the total flux observed in the radio sky (especially at low frequencies). Most of the emission from discrete extragalactic sources is, indeed, of non-thermal origin. The last is simply an observation bias resulting from the fact that the most luminous radio emitters are non-thermal sources, which then can be observed at further distances than any dim thermal discrete source. The cosmic microwave background and the black-body emission from cold gas are the most obvious examples of thermal radio emission.

Several of the emission mechanisms producing the radio emission arriving at Earth (as synchrotron and bremsstrahlung radiation, which will be discussed in section 2.3) require the presence of relativistic electrons in the source and their acceleration to

relativistic energies. This fact illustrates the importance of radio astronomy for the particle astrophysics domain. The key ingredient of the non-thermal emission observed at radio wavelengths is the radiation emitted by an accelerated charged particle, which we will describe more deeply in Section 2.3. Its derivation can be found in Malcolm Longair's High Energy Astrophysics book (see Section 6.2). The total power radiated by a non-relativistic point charge as it accelerates is shown below. It is known as the *Larmor* formula, and it is valid in any frame of reference.

$$P_{rad} = \frac{q^2 a^2}{6\pi\epsilon_0 c^3} \tag{2.1}$$

Here, a is the proper acceleration of the particle with charge q (i.e., the acceleration measured in the particle's instantaneous rest frame). It is not difficult to derivate that it radiates as a dipole in the particle's rest frame. It is also well known that this radiation should be polarised (a characteristic imprint of synchrotron and cyclotron radiation). The resulting spectrum of the radiation is given by:

$$I(w)dw = \frac{q^2|\hat{a}(w)|^2}{3\pi\epsilon_0 c^3}dw \tag{2.2}$$

where $\hat{a}(w)$ is the Fourier transform of the particle acceleration.

2.1.4 Very-high-energy regime

The high-energy regime is (generally) defined by photons with energies above $\sim$ 100 eV. It includes, therefore, the X-rays (from about 100 eV to 100 keV) and gamma-rays (above $\sim$ 100 keV), which are often originated by mechanisms involving the acceleration of relativistic particles, usually (but not always) electrons. In this sense, the high-energy regime is far more related to the radio emission than to the intermediate windows of the electromagnetic spectrum as; near-infrared (NIR), optical, and ultraviolet (UV) wavelengths, which are dominated by thermal blackbody emission. Both bremsstrahlung (especially important in X-rays) and synchrotron radiation mechanisms (see section 2.3) produce high-energy photons as well as radio emission. Other non-thermal mechanisms involved in the emission of high-energy photons that we will discuss are inverse Compton scattering and neutral pion (π^0) decay. Both of these processes generate very-high-energy gamma-rays that can be observed with imaging air Cherenkov telescopes, as we will describe in Chapter 3. The inverse Compton (IC) scattering implies the presence of relativistic electrons in the source. However, it does not constitute evidence of the existence of relativistic hadrons. Contrary to IC, pion decay implies the presence of high-energy hadrons since pions are produced from interactions between energetic protons from a source and environmental matter (e.g., molecular clouds). Note that pion decay products are, therefore, important signatures of potential sources of cosmic rays.

2.2 Acceleration mechanisms

2.2.1 Fermi second-order acceleration

In 1949, E. Fermi described an early model of particle acceleration in an astrophysical environment, known nowadays as the Fermi second-order acceleration (or stochastic acceleration) mechanism. Fermi proposed that protons could be accelerated stochastically by reflections in inhomogeneities of the Galactic magnetic field (or wandering magnetic mirrors), which were later related with gas clouds in the interstellar medium.

The basic point of his argument was distinguishing between the observer's frame and the center-of-mass frame, in which the cloud is stationary. He showed that if these clouds move randomly with velocity V (in the observer's frame, i.e., particles reach the cloud from random directions), and particles remain for a characteristic time in the acceleration region, a power-law spectral energy distribution for the particles is obtained. The formalism is shown in Longair's book (see Section 17.3) and represented schematically in Figure 2.3. In the cited figure, the blue shaded area represents the moving interstellar gas cloud playing the role of a magnetic mirror, and the red lines are particle trajectories in head-on and following collisions.

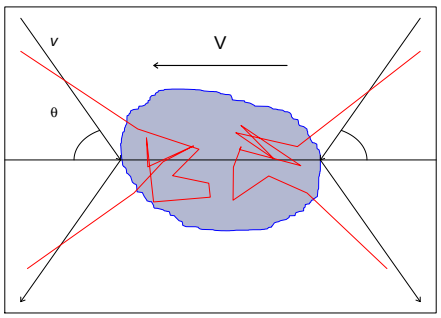

Figure 2.3: Schematic illustration of the Fermi second-order acceleration mechanism in an interstellar gas cloud.

The particle hits the cloud with velocity $v \approx c$ and at angle θ (in black lines). In this case, the probabilities of head-on and following collisions are proportional to $1 + (V/c)\cos(\theta)$, with $0 < \theta < \pi$.

In simplified terms, it can be seen that the energy obtained by collision is of second-order with respect to V/c:

$$\left\langle \frac{\Delta E}{E} \right\rangle = \frac{8}{3}\left(\frac{V}{c}\right)^2 \tag{2.3}$$

and the rate of energy increase results in:

$$\frac{\mathrm{dE}}{\mathrm{dt}} = \alpha E \tag{2.4}$$

where $\alpha = 4V^2/3cL$ and L is the mean free path between clouds. From this formalism, if the particle remains in the acceleration region for a time (τ_{esc}), a spectrum with exponential form; $dN/dE \propto E^{-x}$, where $x = 1 + (\alpha\tau_{esc})^{-1}$, can be derived.

This picture, however, presented unsolvable problems to explain the power-law spectrum of cosmic rays. Firstly, the typical random velocities of the interstellar clouds are very small compared to the speed of light ($V/c \leq 10^{-4}$). Secondly, the mean free path of cosmic rays in the interstellar medium is of the order of ~ 0.1 pc, which results in a few collisions per year and a very slow gain of energy (unless we restrict to turbulent regions at small scales, as young supernova remnants). Furthermore, there is no reason to expect a value of x close to 2.5, and besides, to overcome the ionization energy losses, either the particles are injected in the acceleration region with energy greater than that corresponding to the maximum energy loss rate or else the initial acceleration process is sufficiently rapid. The latter issue is known as the *injection problem*, and it is not exclusive to the Fermi second-order acceleration mechanism.

2.2.2 Acceleration in astrophysical relativistic shocks

Relativistic shocks are other astrophysical environments (aside from interstellar gas clouds) in which particle acceleration processes have been probed. In fact, shocks are common features in astrophysical sources and can originate in several ways; when a fast fluid flow is slowed down by a solid target or another fluid flow or if an initially super-sonic fluid flow decelerates to a sub-sonic speed. The shock implies, by definition, a discontinuity in the physical conditions (e.g., pressure, see Figure 2.4 for an example) of the medium that changes abruptly in the so-called shock front, which propagates not in a very different manner than ordinary waves.

If particle-particle collisions are not important in the gas dynamics, a fast particle population will remain out of thermodynamical equilibrium with respect to the bulk gas, interacting with the ambient magnetic field rather than with other particles. These shocks, called *collisionless shocks*, certainly exist in astrophysical environments and can support particle acceleration (in contrast to non-relativistic shocks).

The so-called shock jump conditions equate the gas's properties (fluid number density, energy density, and pressure) on either side of the shock. These equations are derived from the conservation laws of particle number, energy, and momentum. For relativistic fluids, the same can be expressed as follows:

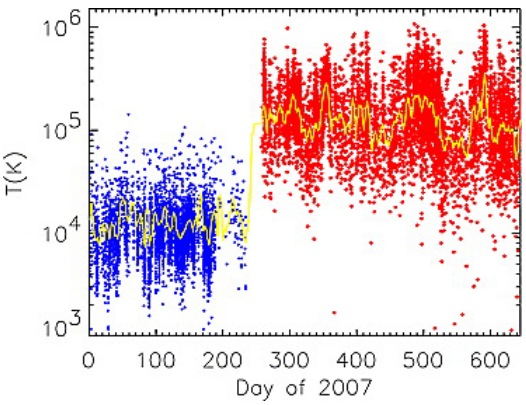

Figure 2.4: An example of shock. The temperature observed by the Voyager 2 spacecraft in the solar wind and heliosheath at crossing the termination shock in 2007 (taken from Richardson, 2008).

$$\Gamma_1 \beta_1 n_1 = \Gamma_2 \beta_2 n_2 \tag{2.5}$$

$$\Gamma_1^2 \beta_1 (\epsilon_1 + p_1) = \Gamma_2^2 \beta_2 (\epsilon_2 + p_2) \tag{2.6}$$

$$\Gamma_1^2 \beta_1^2 (\epsilon_1 + p_1) + p_1 = \Gamma_2^2 \beta_2^2 (\epsilon_2 + p_2) + p_2 \tag{2.7}$$

where subscripts 1 and 2 refer to downstream and upstream regions (corresponding to post- and pre-shock regions in the shock rest frame), respectively. The n, ϵ, and p parameters are the fluid number density, energy density, and pressure (measured in the local fluid rest frame), respectively. β is the fluid velocity (in the shock frame) in units of the speed of light (c). Finally, Γ corresponds to the Lorentz factor. In the easiest picture to work with, the shock is stationary in its frame of reference, and the velocity vectors lie both along with the shock normal.

Note that the presence of magnetic fields is crucial for particle acceleration mechanisms. However, it is not taken into account in the equations above, which are derived only for pressure forces. The shock jump conditions do not vary if the magnetic field is parallel to the shock velocity (because the magnetic field is, then, not affected by the shock), but it plays a major role if this is not the case (i.e., oblique shock, see Rankine-Hugoniot conditions).

2.2.3 Diffusive Shock Acceleration

The acceleration of fast particles diffusing through a shock front is called diffusive shock acceleration. The main characteristic of this process is that the acceleration is proportional to the shock velocity (V), resulting, in contrast to the Fermi second-order mechanism, in a power-law energy spectral index close to 2 ($x \sim 2$). The diffusive shock acceleration is, then, a Fermi first-order acceleration mechanism. Compared to the Fermi second-order process, the principal advantage is that the particles diffusing through a shock gain energy faster, encountering favorable collisions geometries. In the first approximation, we can consider that particles diffusing across a strong shock do not affect the gas dynamics. Hence, they can be treated as

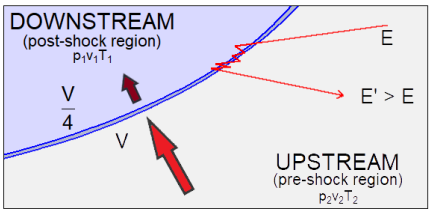

Figure 2.5: Schematic illustration of the diffusive shock acceleration mechanism in a shock front.

massless test particles. The conditions at the sides of the shock, as seen previously (see Equations 2.5, 2.6, and 2.7), are determined by the strong shock jump conditions. Note that the velocity distribution of a population of fast-moving particles in a volume of gas should quickly become isotropic in the gas rest frame because of the scattering.

It is convenient to describe the formalism in the frame of reference in which the shock front is at rest (Figure 2.5), flowing the upstream gas (pre-shock) into the shock with velocity v_2 and leaving the shock downstream (post-shock) with velocity v_1 (red arrows in Figure 2.5). The continuity equation, which requires the conservation of mass through the shock, then, is the following:

$$\rho_1 v_1 = \rho_2 v_2 \tag{2.8}$$

In the case of strong shocks (i.e., the shock velocity, V, is much larger than the speed of sound in the unshocked gas), and for a monoatomic or fully ionized gas, the following condition holds; $\rho_1/\rho_2 = 4$ (that is, $v_1 = v_2/4$). It means that the upstream (ideal) gas is compressed by a factor of four when it passes through the shock front. Then, in the shock rest frame, pre-shock and post-shock gas velocities are $v_2 = -V$ and $v_1 = -V/4$. As mentioned before, when a particle crosses the shock front obtains a small increase of energy proportional to the shock velocity, i.e., $\Delta E/E \propto V/c$. But note that if the particle crosses now the shock in the opposite direction, it will encounter gas moving towards the shock at velocity $\frac{3}{4}V$ and undergo the same process with the corresponding increase of energy. As already explained, if we consider particles ahead of the shock, the scattering ensures that the particle velocity distribution is isotropic in the frame of reference in which the gas is at rest ($< v_2 >= 0$). Samely, in the post-shock region, particles are scattered, and the velocity distribution becomes isotropic with respect to the shocked downstream flow. Therefore, in the pre-shock gas's rest frame, the post-shock region particles are approaching at an average velocity of $< v_1 >= \frac{3}{4}V$. The key point of the reasoning is that there are no crossings in which particles lose energy. In fact, it can be seen that in a cross back and forth of the shock, the gain of energy is:

$$\left\langle \frac{\Delta E}{E} \right\rangle = \frac{V}{c} \tag{2.9}$$

2.2.4 Magnetic reconnection

The diffusive shock acceleration scenario described in the previous section is the best-studied and most popular mechanism for efficiently accelerating cosmic rays. However, other possibilities have been hypothesized. One of them is *magnetic reconnection*, better attested in, for example, solar flares and coronal mass ejections, and extensively studied in particle-in-cell (PIC) simulations (Zenitani et al., 2009, and

references therein). The magnetic reconnection process occurs in short temporal and spatial scales, and its implications at large scales are not fully understood yet. Magnetic reconnection events are the consequence of magnetic field lines with opposite polarities that are forced to be close together. Eventually, the original field lines topology changes, and it is rearranged in a lower-energy configuration of the magnetic field. The energy released in the process has been postulated to be converted into particle acceleration and/or bulk flow of the plasma.

Different formalisms have been described in the literature to explain how magnetic reconnection can accelerate particles (Sweet, 1958; Parker, 1957; Petschek, 1964). For example, it is postulated that the geometry of the magnetic field lines reconnection can lead, in principle, to the formation of a *reconnection layer* in which multiple reconnection events occur, producing isolated "magnetic islands". This magnetic geometry provides a suitable environment for first-order Fermi acceleration, as the particles trapped in the reconnection layer repeatedly scatter off the surrounding magnetic fields. The reconnection events also induce a strong transient electric field, which would directly accelerate the particles. These particles can emit synchrotron radiation once they have escaped the reconnection region but should not produce synchrotron emission while they are in the same. They may generate, however, IC emission in the reconnection layer (see Figure 2.6).

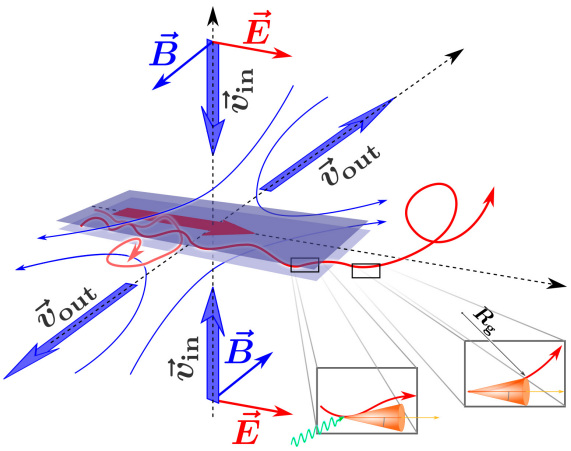

Figure 2.6: Sketch of a reconnection region. Two magnetized flows with oppositely directed magnetic field (B) converge with velocity v_{in} in the reconnection region, where the electric field (E) is co-directed in the converging flow (thick red arrow). The particles emit synchrotron and IC (in-figure boxes) along their trajectories (red lines). Credits: D. Khangulyan (taken from Mestre et al., 2020).

A key advantage of the acceleration by magnetic reconnection is that it can be generated in short timescales. The last property is important because some sources (e.g., the Crab Nebula) show sudden gamma-ray flares, pointing to a rapid acceleration of electrons, i.e., the flare might indicate the presence of a population of relativistic electrons that is presumably not present in the quiescent phase of the source. The electron energy spectrum produced by magnetic reconnection depends quite strongly on the following

parameter that describes the magnetization of the plasma (Sironi & Spitkovsky, 2014):

$$\sigma = \frac{\epsilon_0 B^2}{n m_e c^2} \tag{2.10}$$

where B is the magnetic field and n the electron number density. The magnetization parameter is indeed the ratio between the magnetic and plasma energy densities, meaning that σ can be much greater than the unity for relativistic flows (if Poynting-flux dominated). Those flows are believed to present a variety of flaring phenomena. Different works have pointed to the magnetic reconnection (in the relativistic regime) as an efficient mechanism in accelerating particles (Blackman & Field, 1994; Lyutikov, 2003; Lyubarsky, 2005; Takamoto, 2013; Guo et al., 2014, 2015; Liu et al., 2015). Interestingly, magnetic reconnection simulations have been able to produce non-thermal particle spectra resembling a power-law distribution (Guo et al., 2020; Matthews et al., 2020).

2.3 Radiation mechanisms

2.3.1 Bremsstrahlung

The bremsstrahlung radiation is emitted when an electron loses energy due to the interaction with an ion (or, in principle, in the interaction between any two charged particles, but electron-ion collisions are by far the most effective in producing radiation). Generally, in the astrophysical environment, this occurs in ionized gases and is also known as free-free emission since the electron is not bound to the ion either before or after the interaction (see the upper left panel in Figure 2.7). Most astrophysical bremsstrahlung involves highly energetic (but non-relativistic) electrons in a hot plasma, generating the emission known as thermal bremsstrahlung. Relativistic electrons interacting with ions also emit bremsstrahlung radiation, more likely to be observed in gamma-rays than at radio wavelengths because the photon energy scales with the energy of the electron. Since in relativistic bremsstrahlung, the radiated power (i.e., the electron energy loss rate) scales with the electron energy, as it travels through matter, the electron losses its energy exponentially. The distance in which the electron energy decreases by a factor of e is called *radiation length*.

The spectrum of bremsstrahlung for a single electron of fixed energy v is flat at low energies up to frequencies of $\omega \sim \gamma v/b$, where b is the impact parameter (i.e., the closest distance between the electron and ion, see Figure 2.7), and then falls off exponentially (e.g., green lines in Figure 2.9). In Longair's book, a more detailed description of bremsstrahlung is provided (see Chapter 6). An important result to consider is that energy losses by relativistic bremsstrahlung, for a power-law electron spectrum with a given spectral index (α), result in a photon spectrum with the same spectral index that particles.

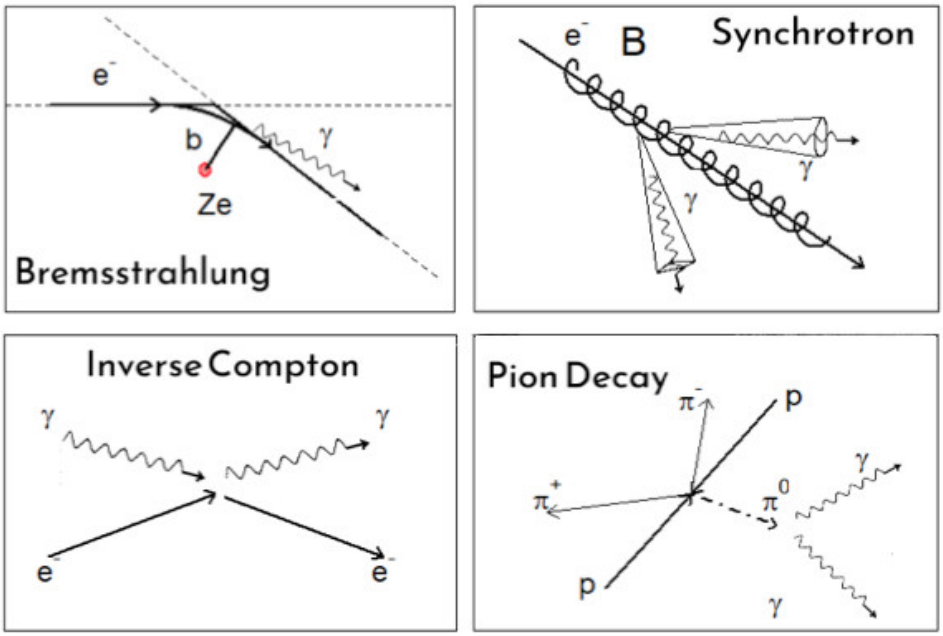

Figure 2.7: Sketch representing the geometries of different radiation mechanisms. See chapters 6, 8, and 9 of Longair's book for an in-depth discussion.

2.3.2 Synchrotron and curvature radiation

Synchrotron radiation is emitted by particles moving within a magnetic field. In a uniform static magnetic field (B), the electron moves in a spiral path with constant pitch angle θ and a radius (i.e., gyroradius, see Figure 2.7) given by the following expression:

$$r_g = \frac{\gamma m_0 v \sin(\theta)}{ZeB} \tag{2.11}$$

The corresponding angular gyrofrequency is, then:

$$w_g = \frac{ZeB}{\gamma m_0} \tag{2.12}$$

And the total energy loss from synchrotron radiation is:

$$-\frac{dE}{dt} = \frac{Z^4 e^4 B^2}{6\pi\epsilon_0 c}\frac{v^2}{c^2}\frac{\gamma^2}{m_0^2}\sin^2(\theta) \tag{2.13}$$

Provided $\gamma = E/m_0c^2$, the power radiated is proportional to m_0^{-4}. It necessarily implies that synchrotron emission from astrophysical sources is completely dominated by the one from electrons. Assuming electrons only, that the distribution of pitch angles is isotropic in $\cos(\theta)$, and averaging the equation before, it is derived:

$$-\frac{dE}{dt} = \frac{4}{3}c\sigma_T U_{mag}\beta^2\gamma^2 \tag{2.14}$$

where σ_T and U_{mag} are the Thomson cross-section and the energy density of the magnetic field, respectively. Note that for relativistic particles, $\beta \approx 1$. The magnetic field responsible for synchrotron emission is ordered over quite large distances, so synchrotron radiation typically has a high degree of polarization. In contrast, bremsstrahlung does not show a net polarization because the electrons encounter ions at random angles (i.e., the individual interactions produce polarized light, but there is no preferred direction overall).

For relativistic electrons, the polar diagram of the emission is distorted by aberration, and the leading lobe concentrates on a narrow beam of half-angle $1/\gamma$ (which is known as the *beaming* effect). As a consequence of beaming, the radiation from a relativistic electron is only visible for a fraction of $1/\pi\gamma$ of its gyratory period. Furthermore, the pulse's observed duration is much less than this because the electron itself is moving at $v \approx c$ and almost catches up with its own radiation.

$$\Delta t = \frac{1}{\gamma^2 w_g \sin(\theta)} \tag{2.15}$$

Therefore, synchrotron radiation from a single relativistic electron is emitted as a series of short pulses.

From a further derivation of the synchrotron spectrum (e.g., the blue lines in Figure 2.9), it can be seen that from cosmic-ray electrons with (power-law) spectral index $\Gamma = 3$ (Adriani et al., 2017), synchrotron radiation of spectral index $\frac{1}{2}(\Gamma - 1) = 1$ is expected. The last result can be compared, for example, with the Galactic synchrotron radiation spectrum above a few MHz, which shows a spectral index close to 0.7 (Peterson & Webber, 2002).

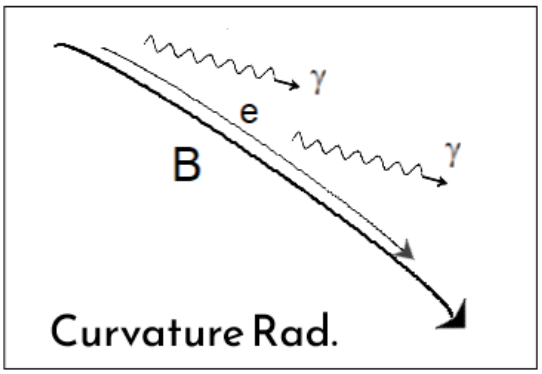

Figure 2.8: Sketch representing the geometry of curvature radiation.

The *curvature radiation* can be considered a variant of synchrotron radiation for charged particles moving along curved magnetic field lines. In this case, the radiation emitted is mainly due to the field line curvature instead of the gyro-acceleration. The curvature and synchrotron radiations share similar characteristics, but in the former, the radius of curvature of the field lines (ρ) plays the role of the gyroradius. The total emitted power results proportional to γ^4/ρ^2 at a characteristic frequency proportional to γ^3/ρ.

The *synchrotron* and *curvature* radiation frameworks describe with high precision the radiation emitted by a charged particle moving in a magnetic field, as long as the

same is primarily due to the gyro-acceleration of the particle or to the curvature of the magnetic field lines, respectively. However, both the charged particle spiral path along a magnetic field line and the curved *drift* motion (averaging over the fast oscillations) are present simultaneously. Hence, an intermediate regime, where both contributions are comparable, can occur. In this case, the emission from the particle, i.e., the so-called *synchro-curvature* emission, can significantly differ from that of the standard synchrotron or curvature regimes.

2.3.3 Inverse Compton

Both bremsstrahlung and synchrotron radiation mechanisms (discussed above) produce high-energy photons as well as radio emission. Additional non-thermal mechanisms involved in the emission of high-energy photons are inverse Compton scattering and neutral pion (π^0) decay. These mechanisms can produce very-high-energy gamma-rays, such as those observed by Imaging Air Cherenkov Telescopes (IACTs). Inverse Compton scattering implies, as previously commented, the presence of relativistic electrons in the source but does not require the presence of fast hadrons.

Inverse Compton (IC) is, more precisely, the scattering of a low-energy photon off a high-energy electron (Figure 2.7, as opposed to ordinary Compton scattering, where a high-energy photon, usually an X-ray, scatters off a low-energy electron). If we consider the case in which the energy of the photon (in the centre of momentum frame of reference) is much smaller than $m_e c^2$, the Thomson scattering cross-section can be employed to describe the probability of scattering. In this case, the total energy gained by the photon field due to the scattering of the (low-energy) photons is given by:

$$\frac{dE}{dt} = \frac{4}{3}\sigma_T c u_{rad} \beta^2 \gamma^2 \tag{2.16}$$

where u_{rad} is the energy density of radiation. For an electron population with a power-law spectral energy distribution of index p, the spectral index of the scattered radiation results in $a = (p+1)/2$. Note that the maximum energy which the photon can acquire corresponds to a head-on collision in which the photon is sent back along its original path. The maximum energy of the photon is then:

$$\hbar w_{max} = 4\gamma^2 \hbar w_0 \tag{2.17}$$

and, hence, the average energy of the scattered photons is

$$\hbar \bar{w} = \frac{4}{3}\gamma^2 \hbar w_0 \tag{2.18}$$

For example, a blue optical photon of 500 nm wavelength can be scattered to a gamma-ray of $\sim$ 2.5 MeV, for $\gamma = 1000$. Electrons with such Lorentz factor can

undoubtedly be found in some astrophysical sources.

If the photon's energy (in the centre of momentum frame of reference) is much larger than $m_e c^2$, we are in the so-called Klein-Nishina (K-N) regime. In general, in this case, the spectral index of the scattered radiation is $a \approx p + 1$ (for a power-law electron spectrum of index p). Furthermore, an exponential cutoff in the electron spectrum (at an energy E_c) of the form; $\exp[(-E_e/E_c)^{\beta_e}]$ (where E_e is the electron energy), will result in an exponential cutoff of the observed radiation ($\exp[(-E_\gamma/E_{\gamma,c})^{\beta_\gamma}]$) with same cutoff index (i.e., $\beta_e = \beta_\gamma$). The latest also occurs in the Thompson regime. However, in that case, with $\beta_e = \beta_\gamma/2$. It means that the emitted radiation's cutoff shape will always be harder in the K-N regime than in the Thompson one (for the same particle cutoff index). The shape of the up-scattered spectrum in the K-N regime will (basically) reflect the electron distribution (not depending strongly on the target photon field, see Lefa et al., 2012, for a detailed discussion). Figure 2.9 shows examples of the typical inverse Compton spectral shape (purple lines).

The ratio of the loss energy rates (for an ultra-relativistic electron) by synchrotron and inverse Compton radiation in a photon field of energy density u_{rad}, within a magnetic field of magnetic flux density u_{mag} is:

$$\eta = \frac{(dE/dt)_{IC}}{(dE/dt)_{syn}} = \frac{u_{rad}}{u_{mag}} \tag{2.19}$$

Thus, if both the synchrotron (radio) flux density and the X- and gamma-radiation from a source are observed, the source region's magnetic flux density can be estimated. Suppose $\eta > 1$ (in the equation above), low-energy radio photons produced by synchrotron radiation are scattered to X-ray energies by the same relativistic electrons. In this case, the X-ray (photon field) energy density is greater than that of the radio photons, so the electrons suffer even higher energy losses by scattering these X-rays to gamma-ray energies. In turn, these gamma-rays have a larger energy density than the X-rays and so on. It means that the energy of the electrons is lost at the very highest energies.

The timescales of electron energy losses (τ) corresponding to each of the emission mechanisms mentioned can be obtained as; $E/(dE/dt)$. For example, for synchrotron losses, the characteristic time (τ_{syn}) is proportional to $1/B^2\gamma$ (see Equation 2.14, provided that $U_{mag} = B^2/2\mu_0$), while for inverse Compton in Thompson regime (see Equation 2.16); $\tau_{\rm IC} \propto 1/\gamma U_{rad}$. The latter result contrasts with the Klein-Nishina regime, in which τ_{IC} increases with γ (through a not trivial function). In the case of bremsstrahlung, the energy loss timescale (for both electron-atom and electron-electron bremsstrahlung) decreases with the electron's energy (i.e., with γ), although more slowly than in the case of synchrotron and inverse Compton. For an electron confined within an expanding flow (e.g., in a pulsar wind nebula), adiabatic losses (i.e., due to the flow internal energy losses because of the expansion) are very significant. For instance, if assuming a uniformly

expanding sphere, the adiabatic cooling timescale is of the same order that the time electrons have been in the flow. Hence, if electrons have always been confined within the source (while expanding), adiabatic losses have always been significant (especially for low-energy electrons). For very-high-energy electrons instead, synchrotron losses dominate over the adiabatic ones (due to the $1/\gamma$ dependence we mentioned). The energy loss processes for high-energy electrons are summarized, e.g., in Section 16.2 of Longair's book.

2.3.4 Synchrotron–self-Compton

A special case of inverse Compton is when relativistic electrons, which are the source of low-energy photons, are also responsible for scattering these photons to X- and gamma-ray energies. This process is known as Synchrotron–self-Compton (SSC). In general, since the synchrotron photons are the ones scattered, the target photon field density (in SSC) depends on the (inverse square) radius of the volume in which the synchrotron photons are emitted. The models of SSC, however, are complex and depend strongly on the initial conditions assumed. The SSC flux at a given frequency comprises the contributions from electrons of different energies scattering off photons of varied frequencies. Thus, it is usual to treat the complex convolution of the electron energy distribution with the seed photon spectrum (emitted by synchrotron) with numerical methods, although some analytical approximations exist under certain conditions (especially for the Thompson regime, see, e.g., Gao et al., 2013).

2.3.5 Pion decay

The neutral pion π^0 has a very short lifetime of 1.78×10^{-16} seconds before decaying into two gamma-rays; $\pi^0 \rightarrow 2\gamma$, each of energy $m_{\pi^0}c^2/2$ in the pion rest frame. The pions are created in collisions between cosmic-ray protons and nuclei and the interstellar gas, roughly equal numbers of positive, negative, and neutral pions being created. Hence, in contrast with inverse Compton, pion decay is evidence for the presence of high-energy hadrons. The neutral pions decay into gamma-rays, while charged pions originate charged muons, electrons, positrons, and electron or muon neutrinos and antineutrinos.

As the neutral pion has zero spin, its decay is isotropic in its rest frame, so the energy distribution of the produced photons (for a pion velocity of β in units of c) is flat between:

$$E_{max,\gamma}, E_{min,\gamma} = \frac{1}{2} m_{\pi^0} c^2 \gamma (1 \pm \beta) \tag{2.20}$$

Consequently, an ultra-relativistic neutral pion ($\beta \approx 1$) will emit a flat spectrum (see, e.g., red lines in Figure 2.9) up to $m_{\pi^0}c^2$. If assuming the neutral pion is produced by a cosmic-ray proton of energy E_p hitting a stationary hydrogen nucleus, a minimum kinetic energy of 280 MeV required for neutral pion production is obtained, i.e., a little over twice

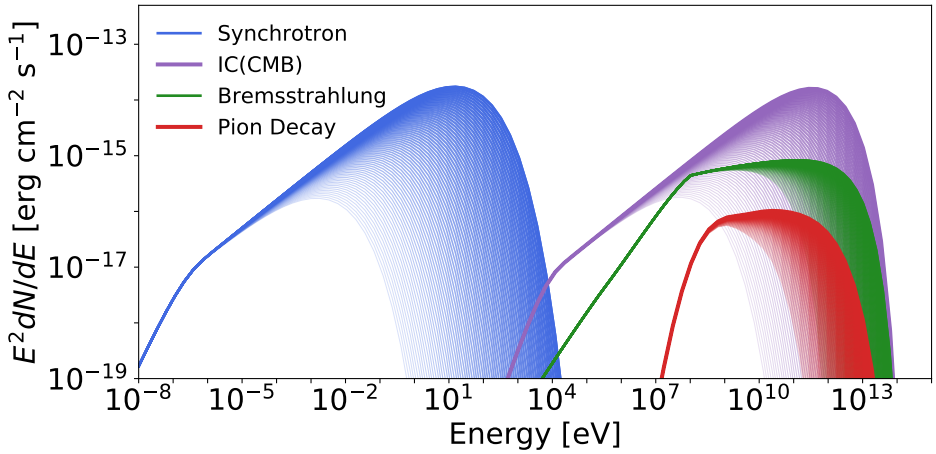

Figure 2.9: Spectral energy distribution of a particle population with index 2, cutoff energies ranging from 100 GeV to 10 TeV, and arbitrary amplitude, for different radiation mechanisms. The plot was produced with the NAIMA PYTHON package.

the mass of the π^0 itself. The diffuse gamma-ray emission from the Galaxy above 1 GeV is believed to be produced mostly by neutral pion decays.

In the pion rest frame, each gamma-ray originated from the neutral pion decay has an energy of approximately 67.5 MeV, corresponding to half the neutral pion mass. The last translates into a steep rise of the flux at energies above 70 MeV (up to $\sim$ 200 MeV) in the spectrum of hadronic sources (see the red lines in Figure 2.9). This feature, which is often called the "pion-decay bump", uniquely identifies pion-decay gamma-rays, indicating the presence of cosmic-ray protons (Ackermann et al., 2013).

It is noticeable that any environment producing neutral pions must also produce charged pions and, consequently, high-energy neutrinos. Note that the threshold energy for the charged pion production (i.e., $p + p \rightarrow p + n + \pi^+$) to occur, which is $\approx$ 292 MeV, is only slightly higher than the one corresponding to the neutral pion ($p+p \rightarrow p+p+\pi^0$). The reason is that the neutron and charged pion masses are only slightly larger than the proton and neutral pion ones. Although muon neutrinos (and antineutrinos) are the main product of the charged pions decays, neutrino oscillations result in a more homogeneous mix of neutrino flavors at astronomical distances from the source (see Kashti & Waxman, 2005, and references therein).

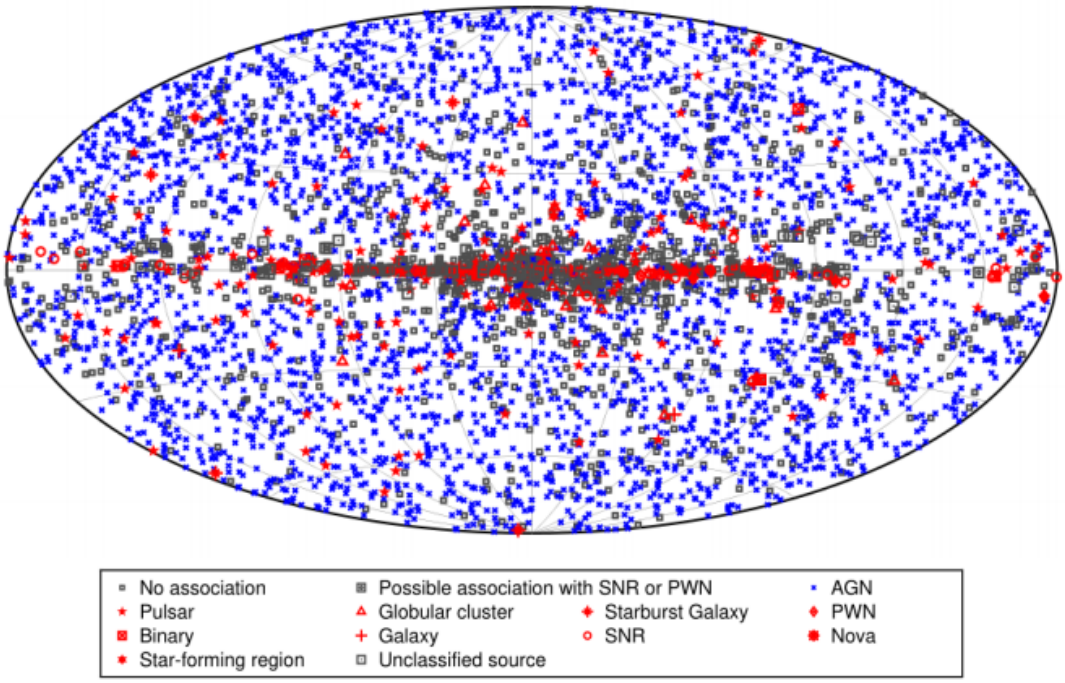

Figure 2.10: Full gamma-ray sky from the *Fermi Large Area Telescope Fourth Source Catalog* (4FGL, taken from Abdollahi and others, 2020).

2.4 Galactic population of gamma-ray sources

2.4.1 Overview

The sources observed in the gamma-ray sky (see Figure 2.10) are usually classified into two categories; Galactic and extragalactic sources. The extragalactic ones dominate, in fact, the point-like sources in the *Fermi Large Area Telescope Fourth Source Catalog* (4FGL) at GeV energies (Abdollahi, S. and others, 2020), with 3207 LAT sources (out of 5064) associated with Active Galactic Nuclei (AGNs, i.e., 3137 with blazars, 42 with radio galaxies, and 28 AGNs of other types). Furthermore, they are responsible for slightly less than half of the identified TeV sources[1]. The vast majority of continuous extragalactic gamma-ray sources are then blazars or closely related objects. It is generally accepted that blazars are active galactic nuclei that are looked at from a direction approximately aligned with the radio jet axis. As a result of relativistic beaming, the jet's emission is observed amplified with respect to the unbeamed emission coming from other parts of the AGN. Typically, less than 20% of optically selected (type I) AGNs are radio-loud (Harrison et al., 2015), and only properly aligned radio-loud AGNs will be observed as blazars. It follows then that blazars must represent, actually, a small minority of the AGNs. Consequently,

[1]See `http://tevcat.uchicago.edu/`.

the fact that blazars constitute the vast majority of the AGNs detected in gamma-rays (see, e.g., the 4FGL catalogue) must be an observational bias largely due to the beaming effect. Among the gamma-ray sources in the LAT 4FGL catalogue, a few are associated with starburst galaxies, with two of them, i.e., NGC 253 and M82, detected at TeV energies (Acero et al., 2009; Acciari et al., 2009). It is, in principle, not a surprising result. The high rate of star formation should imply a proportion of massive stars larger than the one in typical galaxies, and supersonic stellar winds, which have been related with cosmic-ray acceleration, are common among young and massive stars (see, e.g., Casse & Paul, 1980). As we have seen, cosmic-ray protons produce gamma-rays when interacting with ambient gas. Furthermore, massive stars evolve faster, and then also a larger rate of supernovae explosions is expected. The Galactic plane surveys carried out by different instruments (e.g., Aharonian et al., 2002; Abdo et al., 2007a; Abeysekara et al., 2016; H.E.S.S. collaboration, 2018; Abeysekara et al., 2018; Bulgarelli et al., 2019; Abdollahi et al., 2020) at gamma-ray energies have identified young and mid-age supernova remnants as important sources of gamma-rays, and probably also of cosmic rays, in the Milky Way. In any case, given that it is expected a larger amount of cosmic-ray accelerators in starburst galaxies, detecting gamma-ray emission from the same is reasonably foreseen.

We will center this section, from here, in the Galactic sources (excluding the transient ones), which are the most relevant sources for the work that we present. From the gamma-ray source catalogues, most of the (associated) Galactic sources are related to either compact objects (i.e., pulsars), pulsar wind nebulae (PWNe), supernova remnants (SNRs), or stellar clusters.

2.4.2 Pulsars and pulsar wind nebulae

Pulsars are fast rotating neutron stars and represent the last stage of the life of a massive star. The death of a massive star is an event associated with its core collapse, and it is followed by a violent and luminous explosion that releases huge amounts of energy and enriches the interstellar medium with the matter from its ejected outer layers. They are usually observed in radio wavelengths by a beam (or "lighthouse") emission that, according to the canonical picture, arises in the form of collimated jets (from the pulsar's magnetic poles) that regularly sweep the direction towards Earth. However, the detailed properties of the jets are not fully understood. In any case, their emission arrives at us in the form of periodic pulses that slow down over time (due to the losses in the pulsar's rotational kinematic energy). The latest is believed to occur through a relativistic wind composed mainly of electrons and positrons (and possibly ions) accelerated to very high energies. The presence of fast electrons and a magnetic field (as explained in Section 2.3.2) imply, in principle, the existence of appropriate conditions for the generation of synchrotron radiation.

From the observational point of view, pulsars dominate the Galactic sources in the most recent *Fermi*-LAT point source catalogue, with 239 pulsars identified. They constitute, indeed, the largest population of identified sources in the 4FGL catalogue. The whole population of pulsars observed shows a variety of light curves both in gamma-rays and radio (i.e., displaying a single peak, two close peaks, two peaks well separated, or more than two peaks). Their spectra are generally well described with a power-law (of about 1.5 spectral index, on average) extending up to an exponential cutoff at GeV energies. This cutoff has been measured with the *Fermi*-LAT instrument indeed for multiple sources (see Abdo et al., 2013). *Fermi*-LAT was actually the first instrument to discover pulsars through their gamma-ray pulsations alone (Abdo et al., 2008), although the conversion efficiency of the rotational energy loss rate to gamma-rays is not clearly established. Pulsars are found either isolated, although powering the surrounding medium, in binary or multiple systems, or within larger concentrations of matter (i.e., in globular and open stellar clusters). The isolated pulsars period can be characterized with precision due to its regularity, allowing to estimate other physical quantities in terms of the rotating dipole model (e.g., surface magnetic field and rotational energy loss rate) and giving birth to a multitude of not well-separated classes of pulsars: classical pulsars, milliseconds pulsars, anomalous X-ray pulsars, and soft gamma-ray repeaters. A review of the basics of pulsar physics can be found in Chapter 13 of Longair's book.

When the cold pulsar wind is confined by a more slowly expanding gas shell, i.e., the remnant of the progenitor core-collapse supernova, or by the interstellar medium, the result is a pulsar wind nebula (PWN). The properties and evolution of this type of object are complex and, as expected, linked with the properties of both the progenitor supernova and the environment in which the remnant gas shell is expanding. Observationally, tens of pulsar wind nebulae have been detected in X-rays and gamma-rays (Kargaltsev et al., 2013), representing an important part of the Galactic TeV sources. The Crab Nebula, which is a pulsar wind nebula, was the first TeV source discovered (in 1989 by the *Whipple* 10 meters telescope, Weekes et al., 1989) and is still commonly used as a test target for Cherenkov telescopes[2]. Some PWNe can be observed associated with young supernova remnants, while ancient PWNe might account for a significant part of the unidentified Galactic (TeV) gamma-ray sources (Kaufmann & Tibolla, 2018). Also, pulsars traveling with high space velocities can create PNWe with bow shock morphologies, as they interact with the interstellar medium at supersonic speeds (Gaensler & Slane, 2006).

The means by which PWNe accelerate electrons to very high energies are still not well understood. The pulsar's cold wind can not be, in principle, directly observed, i.e., it is not detected until its termination, and therefore, its properties must be derived from the observations of the synchrotron nebula. The presence of magnetic fields and a termination

[2]See `https://www.cta-observatory.org/lst1-detects-vhe-emission-from-crab-pulsar/`

shock front would initially suggest that diffusive shock acceleration can occur. However, from a theoretical point of view, it is easier to achieve significant non-thermal acceleration of electrons in weakly magnetized shocks (Sironi & Spitkovsky, 2011), and the problem is still under study. Besides, it is also unclear whether, or to what extent, protons and positive ions can be accelerated together with the electron and positrons. Alternatively, the turbulent magnetic fields downstream of the shock may trigger the magnetic reconnection mechanism (Lyubarsky, 2003).

2.4.3 Supernova remnants

Several shell-type supernova remnants (SNRs) have been identified as sources of very-high-energy gamma-rays with space- and ground-based instruments (see Aharonian, 2013). An example to illustrate it is Cassiopeia A (Aharonian et al., 2001a; Albert et al., 2007; Acciari et al., 2010; Abdo et al., 2010a), identified as a young (type IIb) core-collapse supernova (Krause et al., 2008a). Another historical SNR, i.e., Tycho's, was securely identified as a type Ia supernova (Krause et al., 2008b). Unlike the core-collapse ones, Type Ia supernovae do not leave a compact remnant (since the explosion disrupts the entire star), but both Cas A and Tycho's remnants are gamma-ray sources detected at TeV energies (Acciari et al., 2010; 2011). Tycho's multi-wavelength spectrum suggests that the origin of its gamma-ray emission is an accelerated population of protons producing gamma-ray radiation by the pion production and decay mechanism (Giordano, 2012). However, the GeV-TeV emission of other SNRs (like RX J1713.7–3946) might be produced by inverse Compton mechanism instead (e.g., from trapped cosmic-ray electrons, see Ellison et al., 2012).

The supernova remnants have long been postulated as the main sites for the acceleration of Galactic cosmic rays (see Bell, 1978; Lagage & Cesarsky, 1983), at least up to energies of $\sim$ 1 PeV, and the diffuse shock acceleration is the mechanism usually assumed to be at play behind the acceleration of the particles. A simple argument that explains why supernovae are often considered the main sources of Galactic cosmic rays arises from energetic arguments. On the one hand, considering the rate of supernovae in our galaxy (of 2.8 ± 0.6, see Li et al., 2011) per century, that about $\sim 80\%$ of the same are core-collapse supernovae, and that the energy released by each one is about $\sim 10^{51}$ ergs, the expected power released by core-collapse supernovae results to be $\sim 10^{42}$ erg/s. On the other hand, the energy density of the cosmic rays in the interstellar medium has been estimated in the order of 1 eV/cm^{-3}, which implies approximately the sustaining power of 10^{41} erg (for a total matter transversed by cosmic rays of $\sim$ 5 g/cm^2). Comparing both results, and if the conversion efficiency of supernova remnants is $\sim 10\%$, the energy density of cosmic rays observed up to the "knee" of the spectrum could be explained (see Lingenfelter, 2019, and references therein for a more detailed discussion). Furthermore, the

amplitude of the observed anisotropy in the distribution of Galactic cosmic rays could be consistent with the expected from the stochasticity in the spatial and temporal distribution of supernova explosions (Blasi & Amato, 2012).

2.4.4 Stellar clusters

Stellar clusters are another class of sources that have been identified as potential sites of particles acceleration to very high energies (see Aharonian et al., 2019, and references therein). It could be expected for several reasons. On the one hand, stellar clusters can host supernova remnants and pulsar wind nebulae, which are (as seen before) particle acceleration sites. On the other hand, they are known to host different astrophysical environments in which particles acceleration may take place, e.g., at the boundaries of wind-blown bubbles, in colliding wind zones around massive binary systems, within the interaction of collective stellar winds, or within the interaction between stellar winds and supernova remnants (Cesarsky & Montmerle, 1983; Eichler & Usov, 1993; Bykov, 2001; Binns et al., 2005; Bykov, 2014; Aharonian et al., 2019).

It is widely accepted that massive stars are not born isolated but in groups within giant molecular clouds, collapsing and fragmenting in clumps of condensed gas (Shu et al., 1987). The accretion of the molecular cloud material, gravitationally attracted by the massive stars, is interrupted by the progenitor molecular cloud's dissipation, caused by the stellar winds, outflows, and UV photodissociation. The stars newly formed can either lose their association with time or keep their gravitational bound, ending as dense stellar clusters. However, ultimately, a large fraction of massive stars are located in systems with multiple stars. In the regions where their strong supersonic winds, reaching terminal velocities of thousands of kilometers per second, collide, strong shocks are formed. In these shocks, electrons and protons can be accelerated to high energies, as we have seen, by the diffusive shock acceleration process. In the wind-wind collision zone, relativistic electrons also are scattering off (by the inverse Compton mechanism) the dense photospheric stellar radiation field, setting the appropriate conditions for the generation of gamma-rays. Also, the inelastic scattering of relativistic nucleons on particles in the dense stellar wind produces a significant amount of neutral pions, which decay into very-high-energy gamma-rays, as mentioned in the previous section (White & Chen, 1992; 1995).

Finally, the collective effect of the strong supersonic winds from young massive stars and supernovae can lead to the formation of large (> 50 pc) galactic bubbles, also called superbubbles (SBs, see Bykov et al. 2020; Gabici et al. 2019, and references therein). These latest are filled with a hot and tenuous plasma, where cosmic rays may be re-energized. In the superbubbles, the spectrum of accelerated particles may even extend beyond the "knee" energy. These particles are scattered where the interaction of wind material forms regions of strong small-scale turbulence and magneto-hydrodynamic

(MHD) waves.

Chapter 3

Observing the sky in the GeV and TeV regimes

3.1 Detection techniques in the gamma-ray regime

3.1.1 Introduction

In the previous chapter, we presented an overview of the observations that evidence the existence of relativistic particles in astrophysical environments. We also discussed how these particles can be accelerated to very high energies, how the accelerated particles radiate, and in which type of sources these acceleration processes may occur. In this chapter, we will summarize, firstly, some detection techniques behind the observations (at GeV and TeV energies) of the gamma-ray emission radiated by these accelerated particles (Section 2.2). In particular, we will provide an overview of pair detectors (Section 3.1.2) and Cherenkov light detection technique (in Section 3.1.3), with special attention to the observatories that made possible our research work, i.e., *Fermi*-LAT and CTA. Next, we will introduce the analytical tools employed in our research (Section 3.2) and, finally, some applications of the same (Section 3.3).

X-rays can be, in principle, observed with focusing optics, although with the peculiarity that X-rays can be reflected only in grazing-incidence mirrors, i.e., at very shallow angles (Aschenbach, 1985). As a result of this, X-ray telescopes can consist of tens of nested grazing-incidence mirrors in a co-focal configuration, allowing the incoming X-ray beam to be focused far behind the mirrors (e.g., *XMM–Newton*, see Jansen et al., 2001). In contrast to X-rays, the observation of gamma-rays can not be afforded by *conventional* astronomy (i.e., with focusing optics) due to the very-high-energy of gamma-ray photons. In addition, gamma-rays are absorbed in the upper atmosphere (see Figure 2.1). Therefore, in principle, there are only two ways to observe them; either detect them directly in space (e.g., pair detectors); or look for the secondary products arising from the absorption

of gamma-rays in the upper atmosphere (i.e., indirect detection, from Earth, through secondary particle cascades or Cherenkov light). For the softer gamma-rays, the first approach can be achieved (e.g., *Fermi*-LAT, Atwood et al., 2009; *AGILE*, Tavani et al., 2009), while the most energetic gamma-rays can be only observed, in practice, following the second approach (e.g., MAGIC, Aleksić et al., 2016; H.E.S.S., Bernlöhr et al., 2003; VERITAS, Holder et al., 2006; HAWC, Abeysekara et al., 2013; MILAGRO, Atkins et al., 2001; TIBET, Amenomori et al., 2001; LHAASO, Bai et al., 2019).

Observing soft gamma-rays ($\sim$ 100 keV - 10 MeV), however, is challenging. Aside from being too energetic to focusing optics techniques (including grazing-incidence mirrors), they are not energetic enough for electron-positron (e^+e^-) pair production in tracking calorimeters (used for harder gamma-rays). Some techniques applied in this energy regime were scanning collimators and coded mask aperture (e.g., *Suzaku*, Serlemitsos et al., 2007; and *INTEGRAL*, Winkler et al., 2003). Suppose the collimator axis sweeps a region around the position of an X-ray point-like source. In that case, the number of counts per second detected varies as a function of time during the source's transit through the collimator's field of view. Hence, the source's position and flux can be derived. The intermediate-energy gamma-rays (30 MeV - 300 GeV) are energetic enough for e^+e^- pair detectors (e.g., *Fermi* and *AGILE*). Finally, the high-energy gamma-rays can not be detected directly, either by spaceborne or ground-based instruments, and are only observed indirectly by ground-based air-shower or Cherenkov light detectors.

3.1.2 Pair detectors

The instrumentation employed to detect gamma-rays directly in space-borne experiments usually relies on pair detectors. The detection principle underlying this type of detectors, used in different gamma-ray telescopes, is pair conversion, i.e., the conversion of incoming gamma-rays into electron-positron pairs within the electric field of an atom (i.e., two-photon pair production, $\gamma\gamma \rightarrow e^+e^-$, with the second, very-low-energy photon coming from the electromagnetic field). For the pair conversion to occur, the incident photon energy must be larger than $\sim$ 1 MeV since the production of an electron-positron pair requires an energy at least equal to its mass (i.e., about $2\times m_e$, where $m_e = 0.511\mathrm{MeV/c^2}$). The main advantage of facilitating this conversion inside the instrument is tracking the outgoing electron and positron trajectories to reconstruct the arrival direction of the incoming photon. Ultimately, the photon's energy can be measured with a calorimeter through its absorption. A calorimeter is a material (e.g., Sodium Iodide, or NaI) with the appropriate properties to intercept a primary particle and absorb its energy inside the detector's volume (in a subsequent cascade of decreasingly energetic particles). Then, it transforms some fraction, usually small, of the deposited energy into another type of measurable signal, proportional, in intensity, to the primary particle energy

(e.g., scintillation light, Cherenkov light, or ionization charge, see Fabjan and Ludlam, 1982). Therefore, the pair-conversion tracking calorimeters may follow, for example, the next scheme: (1) thin plates of some high-Z material to facilitate the gamma-rays pair conversion (2) some tracking elements to follow the trajectories of secondary particles (3) a calorimeter to absorb the initial photon energy and convert it to some physical signal (4) and further instrumentation to collect and process this signal.

In practice, spaceborne experiments of this type are limited to energies below a few hundreds of GeV. Higher energy events are rare enough to require too large collecting areas, and calorimeters capable of containing the high-energy showers induced by these events would be too heavy to be carried out to space. The performance of pair-conversion instruments strongly depends on the energy range. Some difficulties related to these techniques are, for example, that at too low energies, the electron-positron pairs may scatter in the tracker device, limiting the angular resolution. Likewise, the calorimeter's energy losses may be substantial at high energies, resulting in a degradation of the energy resolution. The performance (of these kinds of instruments) also depends on the angle of incidence of the primary photon since a vertically incident photon can pass through the whole detector, but another coming from a different direction may escape from the instrument before passing through the entire system.

3.1.2.1 Fermi-LAT

The Large Area Telescope (LAT, see Atwood et al., 2009) is the primary instrument onboard the *Fermi Gamma-ray Space Telescope*, launched on 11 June 2008 from Cape Canaveral. It is an imaging wide field-of-view telescope for gamma-ray astronomy, consisting of a pair-conversion precision tracker and calorimeter. Both consist of a 4×4 array (16 modules with 18 tracking planes each), a segmented anti-coincidence detector covering the tracker array, and a programmable trigger and data acquisition system. The 18 tracking planes include two layers of single-sided silicon strip detectors and 16 planes above inserted between a high-Z converter material (i.e., tungsten), in which the gamma-rays reaching the LAT instrument are converted into electron-positron pairs (Section 3.1.2). With the LAT instrument, *Fermi* surveys the gamma-ray sky in the 20 MeV to greater than 300 GeV energy range, completing a scan of the whole sky every three hours. The data recorded by LAT during the last decade are compiled in different catalogues of gamma-ray sources. The *Fourth Large Area Telescope* catalog (4FGL, see Abdollahi et al., 2020), for instance, has recently been released. It is based on eight years of LAT data (covering from 50 MeV to 1 TeV in energy) and includes 5064 gamma-ray sources, from which more than a thousand have yet to be identified.

During the last decade, the *Fermi* observatory has meant a significant boost in the field of gamma-ray astronomy, providing important contributions regarding different types of

sources, like pulsars, gamma-ray bursts, active galactic nuclei, supernova remnants, and cosmic rays. Some relevant contributions of *Fermi*-LAT in the context of this thesis are, e.g., the detection of the "pion-decay bump" in the gamma-ray spectrum of supernova remnants (Ackermann et al., 2013), the detection of flares in the Crab Nebula (Abdo et al., 2011a; Buehler et al., 2012; Mayer et al., 2013; Arakawa et al., 2020), the LAT observations towards star-forming regions in massive stellar clusters (Ackermann et al., 2011a; Lemoine-Goumard et al., 2011; Tibaldo et al., 2013; Yang et al., 2018; Aharonian et al., 2019; Saha et al., 2020; Sun et al., 2020a;b), and the characterization of a large population of Galactic gamma-ray pulsars (Abdo et al., 2009; 2010b; 2013; Saz Parkinson et al., 2010).

3.1.3 Imaging Atmospheric Cherenkov Telescopes

3.1.3.1 Cherenkov atmospheric radiation

The interaction of primary gamma-rays with the upper atmosphere allows us to observe cosmic gamma-rays with ground-based techniques by detecting the subsequent cascade of hadronic and leptonic secondary products (i.e., electrons, protons, nuclei, and gamma-rays) or the electromagnetic radiation they emit. Its direct detection is possible at TeV energies (and higher energies). Still, the detection of Cherenkov light emitted by the secondary electrons, makes accessible lower energies, down to the GeV regime (Aharonian et al., 2001b; 2004).

The Cherenkov light is emitted as a rapid flash (lasting a few nanoseconds) when a charged particle travels faster than c/n, where n is the propagation medium's refractive index. Its detection allows us to estimate the length, width, and alignment of the parent shower with respect to the primary photon's arrival direction. The light is emitted in a cone of aperture half-angle $\theta = \arccos(1/\mathrm{n}\beta)$, where for fast electrons β is very closed to 1. For a typical refractive index of $n = 1.0001$ at 10 km altitude; $\theta \sim 1°$. Note that the refractive index depends on atmospheric variables like temperature, pressure, and water vapor content, and therefore,

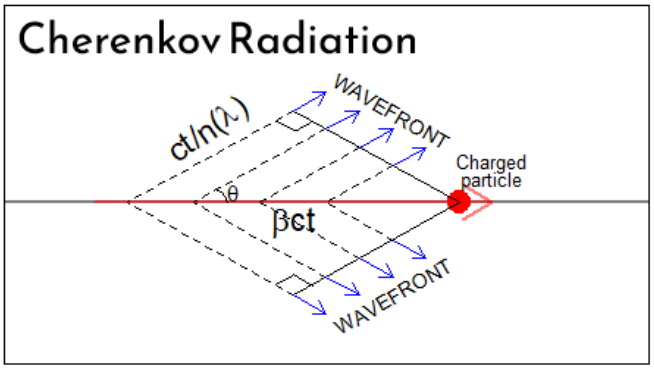

Figure 3.1: Sketch of the geometry of Cherenkov radiation.

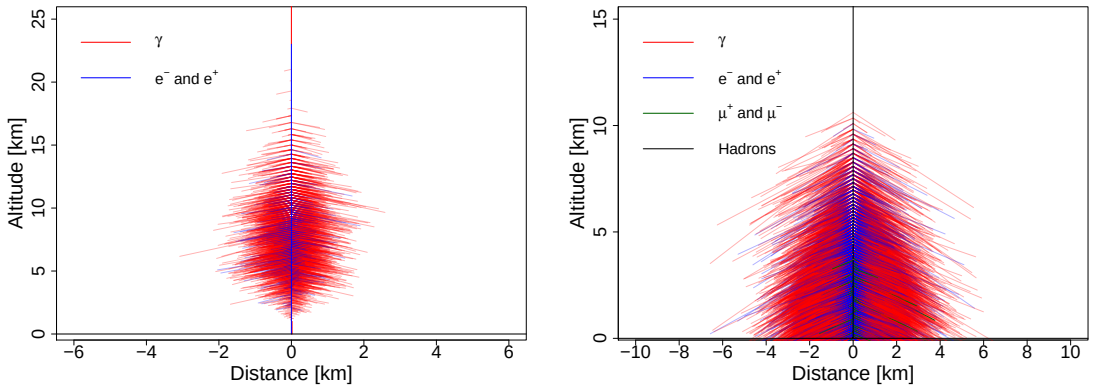

Figure 3.2: The panels (above) illustrate an electromagnetic (in the left) and proton-induced (in the right) atmospheric shower. We based the illustrations on Sajjad and Falvard (2020) and Engel et al.'s (2011) papers for the electromagnetic- and hadronic-cases.

it depends on the altitude. For example, Cherenkov light hits the ground at about ~ 120 meters from the shower axis if emitted at an altitude of 10 km to 20 km, while light emitted closer to the ground deviates less from the shower axis. The median altitude of emission of a 1 TeV shower is about 8 km over the sea level for a vertical incident direction of the primary gamma-ray (Hillas, 1996).

The spectrum of Cherenkov radiation emitted by a charge q, along a unit of length traveled dx in a medium of permeability μ, is given by the Frank-Tamm formula (Frank & Tamm, 1937):

$$\frac{d^2E}{dxdw} = \frac{q^2}{4\pi}\mu(w)(1 - 1/\beta^2 n^2(w))w \tag{3.1}$$

3.1.3.2 The Cherenkov Telescope Array

The Cherenkov Telescope Array (CTA, Acharya et al., 2013) is a new ground-based observatory in construction for the very-high-energy gamma-ray astronomy and represents a new generation of Imaging Air Cherenkov Telescopes (IACTs). It is located in two sites, a northern location in La Palma (Spain) and a southern one in Paranal (Chile). CTA consists of an array with small-, medium- and large-size telescopes (SSTs, MSTs, and LSTs, respectively), sensitive to different energy ranges (from; 20 GeV to 3 TeV for the LSTs, 80 GeV to 50 TeV for the MSTs, and 1 TeV to 300 TeV for the SSTs). The southern site, with approximately 4 square kilometers, is planned to host 4 LSTs, 25 MSTs, and 70 SSTs, while the northern array, with a smaller size and consisting of 4 LSTs and 15 MSTs, will be focused on the low- and mid- energy range (20 GeV to 20 TeV).

The CTA observatory aims at significantly improving the current knowledge in multiple topics in the core of modern astronomy, including cosmic rays, extreme astrophysical environments, and dark matter. Therefore, achieving the CTA science goals requires studying varied sources, as active galactic nuclei, pulsars with their pulsar wind nebulae, supernova remnants, and transient phenomena. The CTA ambitious concept is supported in: full-sky coverage, the large energy regime covered (from tens of GeV up to more than 300 TeV), its large detection area, an unprecedented angular, energy, and timing resolution (improving the sensitivity of the existing very-high-energy instruments by a factor of five to ten depending on the energy range), the synergies with other current observatories, the capacity of fast response to external multi-wavelength alerts, and telescopes designs optimized for rapid movement. For instance, the angular resolution of both arrays will be equal to or better than 0.1° at 0.1 TeV and 0.05° at energies above 1 TeV, while the energy resolution will be equal to or better than 30% at 50 GeV and 10% at all energies above 1 TeV (Hassan et al., 2015). With its improved sensitivity, CTA will detect (likely) more than 1000 new sources of gamma-rays over the whole sky, shedding light on multiple fundamental questions regarding, for example, the origin and role of relativistic cosmic particles or the non-thermal phenomena in the universe.

The core of the CTA project is summarized in individual Key Science Projects (KSPs), which comprise the different key targets (i.e., the Galactic Centre, the Large Magellanic Cloud, Transients, Galaxy Clusters, Active Galactic Nuclei, Star-forming Regions, Cosmic-Ray PeVatrons) and surveys (i.e., Galactic Plane Survey and Extragalactic Survey) for the future CTA operations. The most relevant KSPs in the context of this thesis are the Galactic Plane Survey (GPS) and the Transients and Star-forming Regions ones. Cherenkov Telescope Array Consortium et al. (2019) provides a detailed review of the different KSPs.

The GPS (Dubus et al., 2013) will cover the full Galactic plane (especially the inner region, i.e., $|l| < 60°$) using both the northern and southern observatories at a sensitivity level of a few mCrab (where 1mCrab $= 5.07 \times 10^{-13}$ ph cm^2 s^{-1} for 125 GeV of minimum threshold energy). Its main goal is to provide a census of Galactic very-high-energy gamma-ray sources (e.g., SNRs, PWNe, or binary systems), identifying promising targets for follow-up observations and also determining the properties of the Galactic plane diffuse emission. The source confusion problem (discussed in Section 3.3.2) will be a significant issue to address in the GPS. In particular, the inner region of the Galaxy will be the most affected. Initial studies led to an approximate lower limit to the amount of source confusion of 13 – 24% at 100 GeV and 9 – 18% at 1 TeV (in the region $|l| < 30°$ and $|b| < 2°$, see Cherenkov Telescope Array Consortium et al., 2019).

The transient phenomena observations aim to discover new transient events and follow-up transient alerts raised by other instruments. Several classes of targets, e.g.,

gamma-ray bursts (Inoue et al., 2013; Mazin et al., 2013), flares from compact objects (Bednarek, 2013; de Oña Wilhelmi et al., 2013), jet ejection events (Paredes et al., 2013), or novae (Dubus, 2015), are considered for triggering these follow-up observations. The observing strategy for transients (e.g., trigger criteria or observation time) will depend on the type of object and the operations phase (Bartos et al., 2014; Szanecki et al., 2015; Gerard et al., 2015).

So far, only very few star-forming systems have been detected at TeV energies. Hence, CTA observations of star-forming regions could significantly expand our knowledge of cosmic-ray accelerators in the Milky Way and nearby galaxies and may allow us further to examine the relation between particle acceleration and star formation. Different star-forming regions, e.g., Carina (Preibisch et al., 2011), Cygnus (Popkow et al., 2015), and Westerlund 1 (Abramowski et al., 2012a), together with star-forming and starburst galaxies, e.g., M31 or NGC 253 (Abdo et al., 2010c,d), have been proposed for detailed study.

3.1.4 Air-shower experiments

Alternatively to Cherenkov telescopes, as previously commented, another possibility is to directly look for the secondary particles produced in the interaction of the primary gamma-ray with the atmosphere, i.e., to detect the particle showers on the ground (e.g., Pierre Auger Observatory, The Pierre Auger Observatory collaboration, 2013; HAWC, Abeysekara et al., 2013; MILAGRO, Atkins et al., 2001; Tibet, Amenomori et al., 2001; LHAASO, Bai et al., 2019). These are called air-shower detectors. Some of them are hybrid detectors, e.g., the Pierre Auger Observatory (see The Pierre Auger Observatory collaboration, 2013), meaning that measure both the particle showers on the ground and radiation from the cascade emitted by the secondary particles, i.e., the fluorescence of atmospheric nitrogen excited by electrons and positrons. The atmosphere's nitrogen molecules de-excite by emitting several emission lines in the near-ultraviolet (collected on the ground with focusing optics). The total fluorescence is proportional to the number of particles in the cascade, and therefore, to the shower energy (Nečesal et al., 2011).

Most of these observatories consist of water detector tanks spread over a large area. The charged particles arriving at the tanks are much faster than c/n if n is the refractive index of water, i.e., $n \approx 1.33$. Therefore, water is an efficient medium (more efficient than air) in generating Cherenkov radiation, being the cone aperture half-angle of about $\theta \sim 40^\circ$ (see the previous section). The Cherenkov radiation originated in the water tanks is collected with photomultipliers at the bottom of the same. Also, due to the water density, gamma-rays can undergo the pair-production process inside the tanks, i.e., emitting the resulting electron and positron Cherenkov radiation. Hence, these experiments can measure both charged particles and gamma-rays from the cascade.

Both imaging atmospheric and water Cherenkov telescopes take advantage of their vast (effective) collecting areas ($> 10^4$ m^2, see, e.g., Atkins et al., 2001; Holder et al., 2006; Bernlöhr et al., 2013; Aleksić et al., 2016; Bai et al., 2019). However, water Cherenkov detectors have relatively high energy thresholds, given that high-energy showers are more penetrating, i.e., produce more charged particles at lower altitudes than lower energy showers (Hillas, 1996). Also, the discrimination of showers induced by gamma-rays, protons, and heavy nuclei is typically more difficult than for IACTs since air-shower detectors only observe the tails of these showers (Naurois & Mazin, 2015). The multiple views of the same shower with stereoscopic IACTs facilitate a more accurate reconstruction of the shower direction and better localization of the shower core (Aharonian et al., 1997a), providing better angular and energy resolution than water Cherenkov telescopes. In contrast, the latest have much larger duty cycles, i.e., close to 100% (also observing during daytime), and can also achieve high integrated sensitivity (in years) but with a very wide field-of-view (~ 2 sr aperture), which is convenient for performing unbiased surveys (see, e.g., Bai et al., 2019).

3.2 Analysis Tools

3.2.1 Introduction

In this section, we will introduce some tools available for the analysis of gamma-ray data. In particular, the tools employed for our research work, i.e., FERMIPY, GAMMAPY, CTOOLS, and the CTA instrument response functions. First, we will describe the FERMIPY python package, which facilitates the reduction and analysis of *Fermi*-LAT (see Section 3.1.2.1) data. Next, we will introduce the CTA instrument response functions, which are needed to simulate CTA observations and data. Finally, we will conclude by presenting an overview of GAMMAPY and CTOOLS software, currently in development for future CTA data analysis.

3.2.2 FERMIPY

FERMIPY (Wood et al., 2017) is an open-source software in PYTHON based on the *ScienceTools* (which are mostly written in the C++ programming language) for the reduction and analysis of LAT data. FERMIPY also relies on a number of PYTHON (open-source) libraries, including NumPy (Harris et al., 2020), SCIPY (Virtanen et al., 2020), and ASTROPY (Price-Whelan et al., 2018).

FERMIPY provides a high-level interface for LAT data selection and multiple methods for data analysis. The data selection defines the input data set, for which many configuration options, related for example, to the data binning (e.g., bin and ROI size),

the data selection parameters (e.g., maximum and minimum energy, starting and ending time, maximum zenith angle, or event class and type), or data modeling (i.e., isotropic and Galactic diffuse emission models and source catalogues), can be applied. FERMIPY has implemented advanced methods for, among others, computation tools, generating test statistic (TS) and residual maps, finding new sources, extracting the spectral energy distribution, light curve, best-fit position, and extension of the source, or performing phase-selected analyses. We will describe here only the most relevant methods used in our research work[1].

To spatially localize a source in LAT data, FERMIPY provides a localization method based on scanning the likelihood surface in a local patch around the nominal source position. Firstly, it generates a likelihood map in the region (with the TS map generation method), fixing all background parameters to a fiducial value, and computes a first estimation of the source's position (e.g., see the left panel of Figure 3.3). Then performs a scan of the likelihood surface around the best-fit position obtained in the first step, fitting all the model parameters (e.g., see the right panel in the cited figure). It generates the TS maps using a simplified likelihood fitting implementation to adjust the test source's normalization. Also, it performs the computation of the spectral energy distribution by independent fits of the source's flux (normalization) in energy bins. In each bin, the source's normalization is fitted with a power-law parametrization (with fixed index). When fitting the source's normalization, the background component parameters can be either fixed or fitted under constraints derived from the global fit (to minimize over-fitting). The spatial analysis of the source can be performed with an extension computation method, based on the likelihood ratio test applied to a best-fit model for the extension (compared to the point-like source hypothesis). The best-fit extension is computed by performing a likelihood profile scan over the source's width (68% containment radius) and maximizing the model's likelihood.

3.2.3 CTA Instrument Response Functions

The Instrument Response Function (IRF, Hassan et al., 2015) comprises the mathematical description necessary to model the expected number of events that the observation of a gamma-ray source would produce on a detector. This formalism relates the properties of the events measured by an instrument (i.e., measured energy E', incident direction p', and arrival time t') with the incident photon's physical quantities (i.e., true energy E, true incident direction p, and true arrival time t). In general, we can factorize the instrument response function in three independent terms (or response functions): the effective collection area of the detector (A_{eff}), the point spread function (PSF), and the energy dispersion (E_{disp}). The effective area (i.e.,

[1] See https://fermipy.readthedocs.io/en/latest for more details

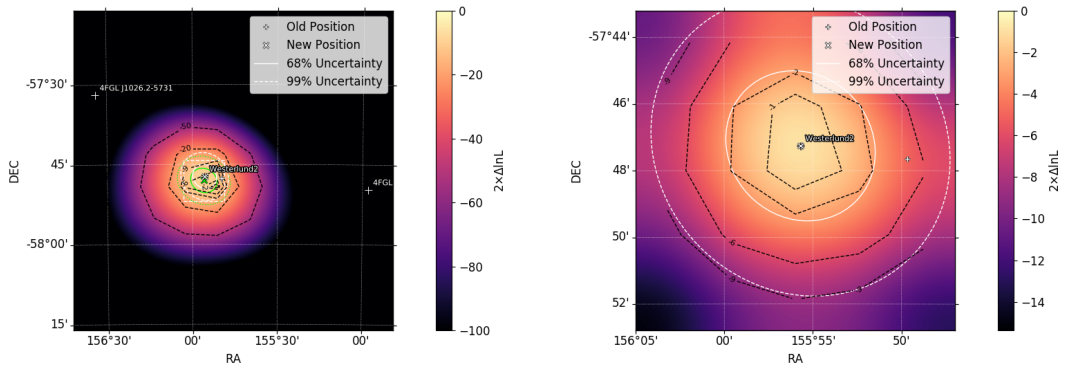

Figure 3.3: First (at the left) and second (at the right) iterations of the FERMIPY localization method applied to Westerlund 2.

$A_{eff}(E, p, t)$, which has units of area) is the product of the detector's collection area and the detection efficiency at true energy and position (given a true arrival time; t). The point spread function determines the probability of measuring a particular incident direction given its true direction and energy $(PSF(p'|p, E, t))$ and is expressed in units of the inverse of solid angle. Then, we can consider $p - p'$ as the probability density of the angular separation between the true and reconstructed directions for the gamma-ray instrument. Finally, the energy dispersion (in units of the inverse of energy) gives the probability to reconstruct the photon at certain energy given its true energy and position $(E_{disp}(E'|E, p, t))$, being E'/E the dubbed probability density of the migration. Note that the implicit assumption that energy dispersion and PSF are completely independent is, however, not valid in general. Nevertheless, note that none of the instrument response functions depends on the gamma-ray source's (being observed) spectral shape. The factorization of the instrument response is given, then, by the following expression:

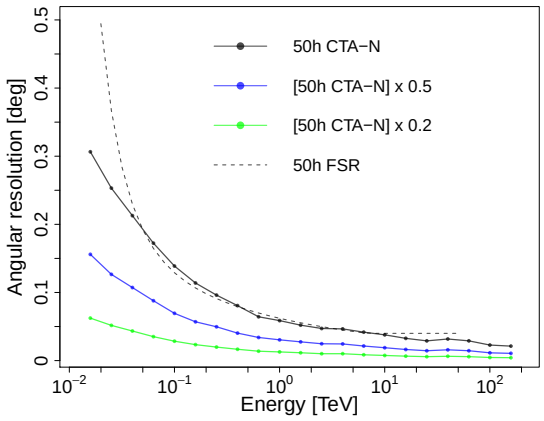

Figure 3.4: The solid lines depict the CTA-N angular resolution (in black), and the same improved by a factor 2 (in blue) and 5 (in green). The black dashed line depicts the CTA-N system requirements.

$$\mathrm{R(p', E', t' \ |p, E, t) = A_{eff}(p, E, t) \times PSF(p' \ |p, E, t) \times E_{disp}(E' \ |p, E, t)} \qquad (3.2)$$

and the expected number of detected events can be approximated as:

$$N(p,E) = t_{obs} \times \int_E dE \int_p dp \mathrm{R(p', E' \ |p, E)} \times \phi(\mathrm{E, p}) \tag{3.3}$$

where $\phi(E,p)[\mathrm{m^{-2}s^{-1}TeV^{-1}sr^{-1}}]$ is the sky flux model.

The CTA instrument's performance has been extensively studied through Monte Carlo simulations (Bernlöhr et al., 2013; Hassan et al., 2015; 2017) based on the CORSIKA air shower code[2] and the telescope simulation tool SIM_TELARRAY (Bernlöhr, 2008). The background cosmic-ray spectra of proton and electron/positron particle types are taken into account to compute the IRFs and modeled according to recent measurements from cosmic-ray instruments. The most recent version of the resulting (i.e., predicted) CTA IRFs is public and available[3]. The Hassan et al. (2015) paper provides further details of the CTA IRFs (and explains how the same were obtained). The response functions available (e.g., version prod3b) have been optimized for the detection of isolated point-like sources against the residual cosmic-ray background, being computed for exposure times of 0.5, 5, and 50 hours and at different zenith angles, i.e., 20°, 40°, and 60°.

In this thesis, we also performed simulations with artificially altered versions of the response functions previously described. Modifying the IRFs allows us to evaluate, in a general approach, scenarios beyond the response functions currently available. In Chapter 4, for example, we employed IRFs with the point spread function (68% containment radius for the simple Gaussian assumption) improved by a factor 2 (or 5), as represented in Figure 3.4. The modified IRFs account for future (i.e., more advanced) versions (of the IRFs) that may significantly adjust critical parameters of the simulations we carried out, as the angular and energy resolutions.

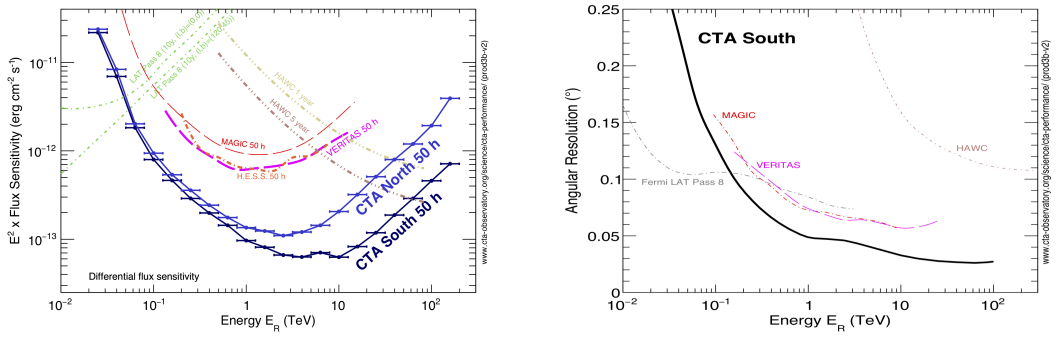

Figure 3.5: The different lines depict the sensitivity and angular resolution of the CTA observatory compared to other instruments. The plots were taken from `https://www.cta-observatory.org/science/cta-performance`.

[2]See https://www.ikp.kit.edu/corsika/

[3]See https://www.cta-observatory.org/science/cta-performance/

3.2.3.1 CTA science performance requirements and systematic errors

The system-level performance requirements for CTA are public and available. The documentation released describes the required performance of the telescope arrays at the CTA northern and southern observing locations, including sub-arrays formed of all telescopes of a specific type (at a given site). These requirements will be verified for the system as-built during the science verification phase, using both selected gamma-ray targets and Monte Carlo simulations.

A major difficulty in exploring the capabilities (and prospects) of CTA regarding the observation of different sources, through simulations, like those we will present throughout this work, is the uncertainty on the systematic errors. The systematics, indeed, are the dominant source of uncertainty when studying in detail a bright source (as the Crab). For this reason, we will need to take them into account, when possible, at some point in the simulations performed, as we will see, to guarantee a better assessment of the CTA capabilities. The reconstruction of events, the Monte Carlo determination of the effective area, and the uncertainty in the atmospheric conditions and background, are some of the many sources of systematic errors in air Cherenkov telescope measurements.

We will use in this work some of the requirements summarized in the cited documentation. For example, the systematic error in the energy scale (E_0), according to the system requirements, will be requested to be less than 4%. It constitutes an improvement of at least a factor 2 over the current measurements with IACTs (Aharonian et al., 2004, 2006; Aleksić et al., 2015; Holler et al., 2015). We have also considered that the systematic error of the flux (at a given apparent energy) must be less than 10% between 50 GeV and 300 TeV.

3.2.4 Tools for the simulation and analysis of CTA data: GAMMAPY and CTOOLS

GAMMAPY (Deil et al., 2017; Nigro et al., 2019) and CTOOLS (Knoedlseder et al., 2016) are open-source packages in development for gamma-ray astronomy. GAMMAPY is built on NUMPY (Harris et al., 2020) and ASTROPY (Astropy Collaboration, 2013; 2018) PYTHON libraries, and with CTOOLS has been developed as a prototype for the Cherenkov Telescope Array science tools, being both also useful for the data analysis of existing IACTs. The CTOOLS software package is based on GAMMALIB (that contains a C++ library, see Knoedlseder et al., 2016) and includes a PYTHON module to provide support for the scientific analysis of astronomical gamma-ray data. GAMMAPY and CTOOLS constitute the architecture used in the research work we present for the simulation of CTA data and our subsequent analyses.

Both GAMMAPY and CTOOLS provide a multitude of tools for gamma-ray data analysis

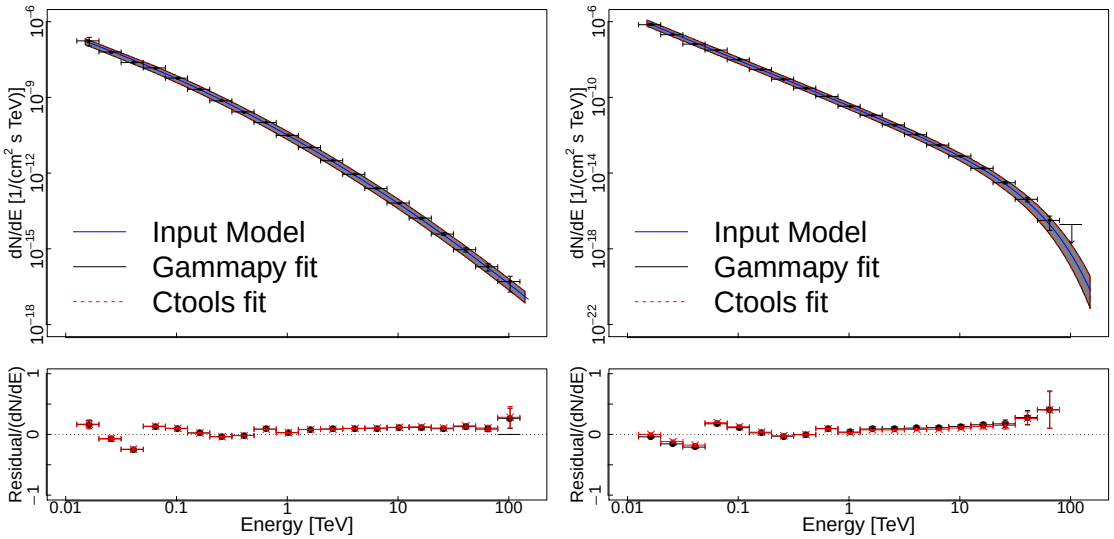

Figure 3.6: Comparison between GAMMAPY and CTOOLS simulations.

and CTA performance simulations, including tools for, e.g., imaging, spectral, timing, and likelihood analysis, among other utilities. In the following sections, we describe the application of both software to our research work. We classified them in either the simulation of sources of particular interest or observation simulations dedicated to the study of source confusion in CTA data.

In Figure 3.6, we show a simulation of the Crab Nebula spectrum both for a log-parabola (left panel) and exponential cutoff power-law (right panel) model with GAMMAPY (in black points and shaded area, the latter representing the 3σ error region) and CTOOLS (in red). The blue line represents the input model, and we show the residuals below the main panels. We performed these simulations for 50 hours of observation time with the CTA northern array. Note that the results of the simulations for both software are in very close agreement.

3.2.5 NAIMA and TEMPO2

The NAIMA PYTHON package (Zabalza, 2015) is another relevant tool used for this thesis. It is an ASTROPY (Astropy Collaboration, 2013; 2018) affiliated package for the computation of non-thermal radiation emitted by relativistic particle populations. NAIMA's principal utilities are; a set of non-thermal radiative models (i.e., including synchrotron, inverse Compton, Synchrotron-self-Compton, bremsstrahlung, and neutral pion decay emission processes, discussed in the previous chapter) and tools to perform Markov Chain Monte Carlo (MCMC) fitting of spectral data (MacKay, 2003; Foreman-Mackey et al., 2013).

Finally, TEMPO2 is a software package (primarily written in C but compiled using a C++ compiler) for pulsar timing developed at the Australia Telescope National Facility,

mainly by George Hobbs and Russell Edwards (Edwards & Hobbs, 2006a;b). It is based on the previous package TEMPO, significantly improving its capabilities. Lorimer and Kramer's book (2004) provides, e.g., an overview of pulsar timing.

3.3 Applications of the analysis tools

3.3.1 Generating simulated 3D sky cubes

The tools presented above allowed us to perform a collection of CTA data simulations, which we later applied to different purposes. Firstly, we were interested in simulating observations of the system formed by the Crab Nebula and pulsar with CTA, provided that it is the most studied source at gamma-ray energies (and still the most classical target for new Cherenkov telescopes, as currently, the CTA large-, medium-, and small-size telescopes prototypes[4]). We will dedicate Chapter 4 to this problem. We also aim at applying the tools developed to other sources of interest that may constitute possible candidates for future detection at very high energies, as stellar bowshocks (e.g., LS2355, Sánchez-Ayaso et al., 2018, discussed in Section 3.3.3). Finally, the confusion of sources (in CTA data) is another topic of our interest, and we will examine it in Section 3.3.2.

The problem of source confusion, i.e., the difficulty of distinguishing sources (and deriving their properties) that overlap in crowded regions, will (certainly) have to be addressed by the CTA observatory soon, given the large extension of some gamma-ray sources as pulsar wind nebulae, which can extend even more than 1° (depending on the age and distance), or the so-called "halos" (Linden et al., 2017). These halos have been recently observed, for example, by HAWC around the pulsars Geminga and PSR B0656+14 at TeV energies (Abeysekara et al., 2017). The TeV emission might be originated by electrons and positrons diffusing away from the pulsars and up-scattering the CMB photon field (see the cited paper). We will first describe the simulation scheme that allowed us to address the goals described above and its application to the source confusion problem.

To simulate CTA data of gamma-ray sources, we have implemented a generator of simulated 3D sky cubes, with two spatial dimensions corresponding to the direction in the sky plus an energy axis discretized in bins (see Figure 3.7). The simulator is implemented in GAMMAPY (version 0.7) and is public and available[5]. Our simulation scheme allows simulating CTA observations of a gamma-ray source or two sources at any position in the sky. Furthermore, the sources can be placed on top of each other but with different morphology and spectra. Therefore, it facilitates, for example, simulating a system with a pulsar and its pulsar wind nebula or studying the source confusion problem.

To run the generator, we must first provide a spectral and spatial model of the

[4] `https://www.cta-observatory.org/about/how-cta-works/`

[5] In https://github.com/emestregui/The-CTA-Crab-Nebula-and-Pulsar/tree/master/3D_cubes_simulator_archive

sources with two configuration YAML files. The configuration options that we must supply include the binning for the output sky cubes (i.e., bin size, coordinates system, number of bins, number of pixels in each spatial dimension, and projection method), the spectrum, position, and spatial model of the source, the pointing parameters of the observation (i.e., pointing position and observation time), and the data selection options (i.e., ROI, maximum and minimum energy, and offset from the center of the FoV). We can model the source with the radiative and morphological models implemented within GAMMAPY (version 0.7), including power-law, exponential cutoff power-law, and log-parabola characterizations of the spectral shape and 2D Gaussian-, sphere- or shell-like spatial models.

The resulting sky cubes contain the expected events (from here *counts*) arising in the detector from an observation of the simulated sources. The output of a complete run of the cubes generator comprises the predicted counts from the two sources (without background, in the dubbed flux cube), an observation simulation with an 'ON' and 'OFF' cube, a cube of excess (i.e., 'ON' minus 'OFF'), and secondary products (also in the form of 3D sky cubes) such as an exposure cube (i.e., effective area times observation time) or a sky cube with the total flux from the sources. The 'ON', 'OFF', and excess cubes can be written both convoluted with the point spread function or not.

The 'ON' cube, comprising the predicted counts of both sources and background counts (being the three components smeared by Poisson noise), is the sky cube to be analyzed to examine the prospects of CTA for the characterization of the simulated sources (given a certain realization of the generator of cubes). The 'OFF' cube contains only predicted background counts smeared by Poisson noise and is interpreted as an observation simulation of a region in the sky with no gamma-ray sources (significantly) detected. We computed the predicted background from the cosmic-ray background rates. The CTA IRFs provide these rates for each particular offset (i.e., distance to the center of the field of view) and energy bin. Therefore, the simulations account for the full CTA IRFs (i.e., effective area, energy dispersion, and energy-dependent point spread function) and the offset. The cubes generated can account for the whole energy range covered by the IRFs, i.e., from about 20 GeV to 300 TeV, and observation times ranging from seconds to hundreds of hours.

Figure 3.7, for example, represents both an 'ON' and 'OFF' cube resulting from a realization of the generator of cubes previously described. In the left panel, the 'ON' cube is generated for the observation simulation of an extended source on top of a point-like one, for 50 hours of observation time with the CTA northern array, at 40° zenith angle. We characterized the extended source's spectrum with a log-parabola spectral shape, with the parameters corresponding to the Crab Nebula best-fit spectrum with the MAGIC telescope (see Aleksić et al., 2015). The simulated extended source has a 2D sphere-like

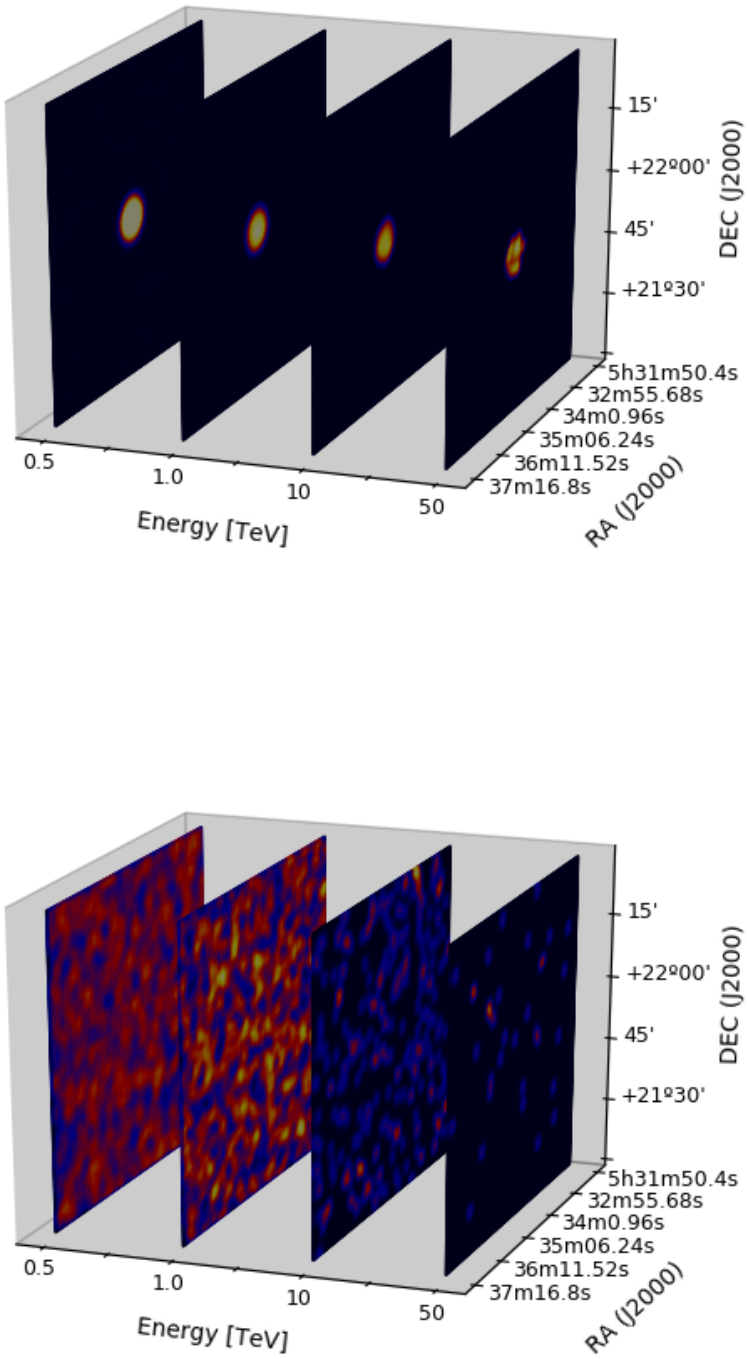

Figure 3.7: We show an example of simulated 3D sky cubes. In particular, we display four energy bins taken from an 'ON' (in the upper panel) and 'OFF' (below) cube. We smoothed the plots (in counts units) by applying a small Gaussian kernel convolution.

morphology of 0.1° of radius. The point-like source was placed in a position coincident with that of the Crab pulsar (RA = 83.63° and DEC = 22.01°). Its power-law spectrum corresponds to the spectral energy distribution measured for the Crab pulsar (as published by the MAGIC collaboration in Ansoldi et al., 2016). The plot corresponds to an energy of ~ 10 TeV. In the right panel, we took the 'OFF' cube from the same simulation shown in the left panel but at different energy (i.e., from 700 GeV to 1 TeV). In both panels, the field of view is $1.25° \times 1.25°$ in 250×250 bins.

Additionally, several analysis tools used are available and public, along with the cubes generator. These allow us to perform 1D spectral analysis (by projecting the cubes along the energy axis) and 2D morphological analysis using the SHERPA software (Freeman et al., 2001; Refsdal et al., 2009) for each energy bin of the sky cube. The source's detection significance, computed as suggested in Li & Ma (1983), can also be obtained with the analysis tools made public. The tools developed also allow us to analyze the source's spectral energy distribution. For this purpose, GAMMAPY provides a 1D SHERPA spectral fitting method, with maximum likelihood functions (Cash or Wstat, see Cash 1979) statistics and Nelder-Mead Simplex optimization method (Wright 1996; Lagarias et al., 1998) based on a forward-folding technique (Piron et al., 2001). However, we developed the spectral analysis tool for the particular case of a point-like source and an extended source on top of each other (e.g., the system formed of a pulsar and its pulsar wind nebula). In this case, we can obtain the spectral energy distribution of both sources simultaneously. Nevertheless, we recommend extracting the spectral energy of each one separately. For this purpose, to improve the spectral analysis of one of the sources, firstly, we must simulate the source of no interest isolated. Then, the 'ON' sky cube resulting from the simulation (with only the source of no interest and background) can be used as an 'OFF' cube regarding the simulation of both sources together (i.e., we treat the source of no interest as background underlying the source to study).

We can fit the spectral energy distribution of a source to either power-law, exponential cutoff power-law, or log-parabola spectral models. It is also possible to fit the same observation simulation sequentially to a list of models, with any combination of those mentioned, to compare them. In the morphological analysis tool that we released, we assumed the point spread function employed to be a simple Gaussian, with the Gaussian width (σ) taken from the CTA IRFs. For the spatial analysis, the SHERPA fitting is only applied to the energy bins with a Li & Ma significance greater (or equal) than three, with an excess greater (or equal) than seven counts, to avoid possible problems arising from the lack of data.

The generator of cubes described above can provide, for instance, the minimum size necessary to resolve a source given the predicted CTA point spread function (as we demonstrate in the next chapter). We can compute it by performing simulations of a

test source with each time a larger extension. We can also find the maximum PSF that would allow us to resolve a source of a given (i.e., fix) extension with artificially modified IRFs (as described in the previous section).

3.3.2 Source confusion

The difficulty in the discrimination of sources overlapping in crowded regions (i.e., source confusion) is one of the main problems that will arise in the analysis of CTA data and can be addressed, through simulations, with the tools described in this chapter. For instance, we can probe several questions with a relatively simple approach, such as; can we distinguish using CTA data between the case of two sources on top of each other and a single one? If this is the case, can CTA retrieve the spectrum and morphology of each source? Or, can we compare a combination of morphological templates (for different sources) on top of each other directly with CTA data?

To probe the source confusion problem in CTA data, we performed observation simulations of several sources with CTOOLS (see Section 3.2.4), both isolated and confused in pairs. We carried out the simulations using the data available from the H.E.S.S. Galactic Plane Survey (HGPS[6], published in 2018), i.e., the most exhaustive survey of our galaxy at very-high-energy gamma-rays. In particular, we employed these observations as morphological templates of the sources of interest at TeV energies. Any sky map describing the intensity distribution of the source (in arbitrary units) can be used as a morphological template for the same in our simulations.

To simulate the source confusion problem in some arbitrary regions, we placed the sources on top of each other artificially, with a small separation in between (i.e., 0.2° and 0.3°). In particular, we define that two sources are confused if their separation (d) is smaller than the sum of their best-fit Gaussian widths (i.e., $d < \sigma_1 + \sigma_2$, where the Gaussian widths are fitted for each source individually). This condition is satisfied, indeed, in all the simulations of confused sources that we will present in this chapter, in which $(\sigma_1 + \sigma_2)/d$ is about $[2 - 4]$. We performed simulations of the following sources: Vela X, G327.1-01.1, MSH 15-52, and HESS J1303-631 (accounting for a luminous and very extended source, i.e., Vela X, a much fainter and smaller source than Vela X as G327.1-01.1, and intermediate sources in extension and flux; MSH 15-52, and HESS J1303-631). First, we will describe each source's simulations (individually performed), and then, we will summarize the results for some cases of the previous sources artificially confused. To probe the source confusion problem (in CTA data) with both the northern and southern arrays, we carried out all the simulations (of isolated and overlapping sources) with the IRFs of both the CTA-North and CTA-South observatories. We will present the results referenced to 25 hours of observation time, except for the case of G327.1-01.1 (which is

[6]Data are available in `https://www.mpi-hd.mpg.de/hfm/HESS/hgps/`

the faintest source) when individually simulated (in this case, referenced to 50 hours of observation time).

3.3.2.1 Vela X

Vela X, in the western part of the Vela constellation (RA $\approx 128.88°$ and DEC $\approx -45.66°$), is one of the nearest pulsar wind nebulae (with an estimated distance of ~ 290 pc) and has been associated with the energetic and middle-aged ($\tau_c \sim 11$ kyr) Vela pulsar (dubbed PSR B0833-45, with a spin-down luminosity of 7×10^{36} erg s^{-1}). Vela X was first detected in radio wavelengths (in 1958, Rishbeth, 1958). Since its discovery, the nebula has been detected by numerous instruments at different wavelengths (Thompson, 1975; Wallace et al., 1977; Ögelman et al., 1993; Kanbach et al., 1994; Markwardt & Ögelman, 1995; Helfand et al., 2001; Aharonian et al., 2006b). In the mid-90s, the X-ray emission from the PWN was characterized by the *ROSAT* satellite, revealing a collimated X-ray filament (known as the Vela X "cocoon", Markwardt & Ögelman, 1995) from the pulsar towards the center of Vela X. In 2004, the H.E.S.S. experiment detected the extended emission of Vela X at very-high-energy gamma-rays (Aharonian et al., 2006b; Abramowski et al., 2012b).

The spectrum of the nebula at TeV energies is well represented by a power-law with an exponential cutoff shape, being the cutoff located at an energy of ≈ 14 TeV, an index similar to 1.36, and differential flux of about 1.16×10^{-11} cm^{2}s^{-1}TeV^{-1} (referenced at 1 TeV, see Abramowski et al., 2012b). The morphology of the pulsar wind nebula at the energies of H.E.S.S. observations (see panel a in Figure 3.8) can be described with a Gaussian profile along its major axis, with an intrinsic size of $\sigma = 0.52°$. Along its minor axis, the TeV source is better described with the sum of two Gaussian components. The former is a narrow component of $\sigma = 0.12°$ width, while the latter is a more extended one of Gaussian size $\sigma = 0.60°$.

In Figure 3.8, we plotted the observation simulations of Vela X for 25 hours with the CTA northern (panel b) and southern (panel c) arrays (from 1 TeV to 180 TeV of energy). The simulated sky maps can be compared to the template used to describe the source's morphology (obtained from the H.E.S.S. Galactic plane survey), shown in panel (a) of the cited figure. The color bar plotted at the template's side is in units of integral flux over 1 TeV ($\times 10^{14}$ cm^{-2}s^{-1}). However, the color bars plotted at the side of the simulated CTA sky maps depict the number of events obtained (after background subtraction, i.e., the excess in counts). We smoothed the plots by applying a small Gaussian kernel (of $0.06°$ width) convolution. For comparison, note that the angular resolution expected for the CTA northern and southern arrays is about $3'$-$2'$ at 1 TeV of energy. The color-map employed for the plots has been often used in H.E.S.S. collaboration publications. The effect it aims to achieve is showing in black and blue tonalities the non-significant features

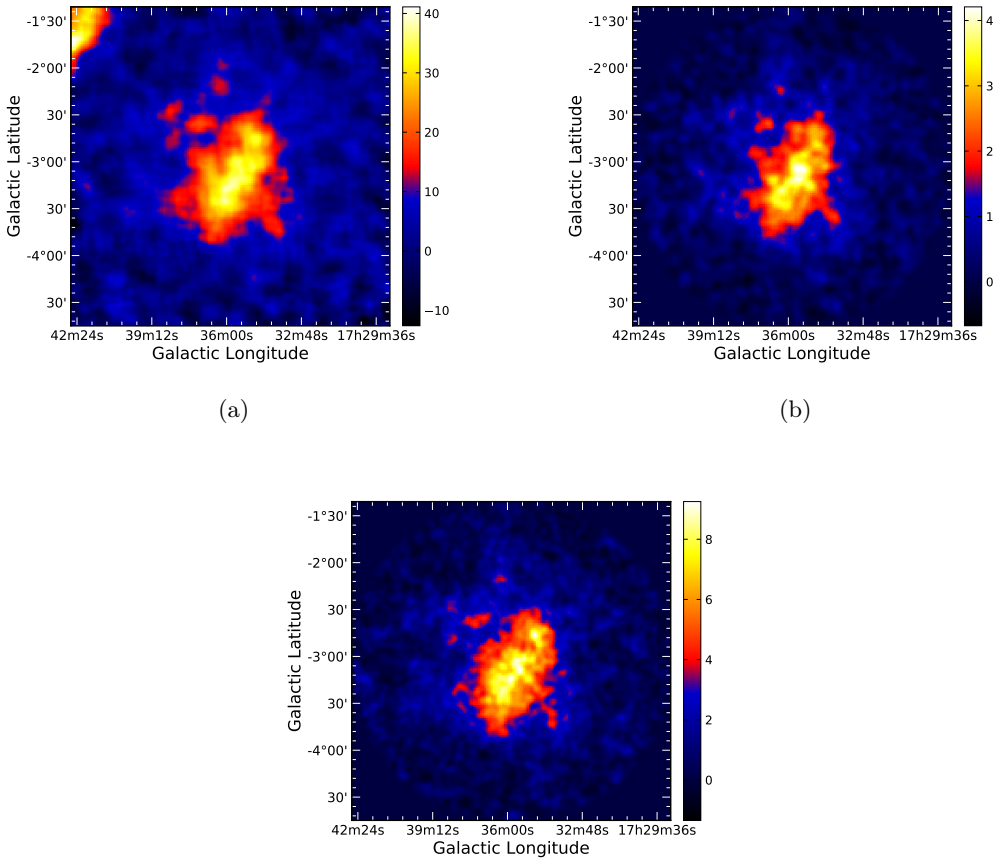

(a) (b)

(c)

Figure 3.8: (a) Vela X template employed in the simulations. (b) Observation simulation of Vela X with the CTA northern array and 25 hours of observation time. (c) Same as (b) but with the CTA southern array instead. The sky region plotted is a square of 3.4° of side.

(i.e., not well visible features), in red, the features at the detection threshold (i.e., the "transition" region), and in yellow and white tonalities the significant features (i.e., those very well visible).

In table 3.1, we summarized the results (accounting only for statistical errors) from the simulations plotted in the (b) and (c) panels of Figure 3.8. Note that the input spectral shape was successfully retrieved at 95% CL, while the best-fit Gaussian model corresponds to an extension in agreement with the one reported by the H.E.S.S Galactic Plane Survey (see Table 10 in H.E.S.S. collaboration., 2018, i.e., $\sigma = 0.58^\circ \pm 0.05^\circ$). The source is very significantly detected both with the northern and southern arrays, and the results of the simulations are best-fitted to the input model, i.e., to the template in Figure 3.8 (first panel), compared to a Gaussian shape (as expected, given the large flux and extension of the source). We also fitted the simulations to an elliptical morphology, obtaining a position angle (counted counterclockwise from North) of $44.7^\circ \pm 4.7^\circ$ ($70^\circ \pm 3.0^\circ$), a minor axis of $0.593^\circ \pm 0.006^\circ$ ($0.598^\circ \pm 0.004^\circ$) radius, a major axis radius of $0.651^\circ \pm 0.007^\circ$ ($0.648^\circ \pm 0.004^\circ$), and a detection significance of $\sqrt{TS} = 87.1$ ($\sqrt{TS} = 141.3$), in 25 hours with the CTA northern (southern) array (accounting only for statistical errors). The elliptical morphology, therefore, describes the results of the simulations better than the Gaussian model. Note that the detection significance is $\sqrt{TS} = 39.4$ in the H.E.S.S. Galactic plane survey (see Table 10 in H.E.S.S. collaboration. 2018), although we can not directly compare it to the observations simulations presented above (due to the different observation times between both cases). The observation time of the sources in the HGPS, for instance, depends on their position.

The number of degrees of freedom corresponding with the simulations described in Table 3.1 can be computed as the addition of the following three quantities: (1) the number of free spectral parameters, i.e., three for the exponential cutoff power-law model and two for the simple power-law characterization; (2) the number of free parameters of the morphological model, i.e., three for a Gaussian shape (two from the source's position plus the Gaussian width), and zero for the morphological template (with a fixed normalization and position of reference); (3) and two additional free parameters from the null hypothesis (H_0), i.e., the observation can be explained with only a background component with a power-law type spectrum. Note that this would not be the case if the templates were taken from a library of (empirical or simulated) spatial models and compared with authentic images of PWNe (observed by CTA). On the one hand, the difference is that it will not exist a fixed reference position known to compare the models (from the library) and the real CTA data. On the other hand, the best morphological model in the library matching a PWN detected by CTA can happen to be rotated (at an arbitrary angle) with respect to the CTA data. Therefore, although in Table 3.1, the Gaussian fit involves three degrees of freedom more than the fit to an arbitrary (morphological) template, we will not deal

Parameter	Fixed?	Model	CTA-N result	CTA-S result
Spectrum results				
$N_0[10^{-11}\mathrm{cm}^{-2}\mathrm{s}^{-1}\mathrm{TeV}^{-1}]$	No	1.16	1.163 ± 0.036	1.121 ± 0.024
E_{ref}[TeV]	Yes	1	1	1
Index	No	1.36	1.354 ± 0.029	1.355 ± 0.019
E_{cutoff}[TeV]	No	13.9	13.87 ± 0.66	14.33 ± 0.43
Fit to gaussian shape				
Ra	No	128.8839	128.830 ± 0.011	128.8451 ± 0.0073
Dec	No	-45.6601	-45.6916 ± 0.0079	-45.6865 ± 0.0052
Size (Gaussian)	No		0.6217 ± 0.0046	0.6305 ± 0.0030
$\sqrt{TS}$ (Gaussian)			86.5	140.0
Fit to templates				
$\sqrt{TS}$ (Input template)			95.4	155.2

Table 3.1: Vela X input model and best-fit parameters to the CTA observations simulations depicted in (b) and (c) panels of Figure 3.8. We fitted the simulations using the Vela X template morphology, i.e., the panel (a) in the cited figure and a Gaussian model.

with this problem when using real CTA images.

3.3.2.2 SNR G327.1-1.1

SNR G327.1-1.1, located at the position RA = 238.65° and DEC = −55.08°, is a composite supernova remnant, i.e., exhibits both a faint and rather small ($\sim 0.15°$ in angular size) shell and a brighter pulsar wind nebula (slightly off-center with respect to the SNR). It is seen both in radio wavelengths (Whiteoak et al., 1996) and X-rays (Temim et al., 2009). The nebula is also a TeV source (Acero et al., 2011; H.E.S.S. Collaboration, 2018), detected by H.E.S.S. (see Figure 3.9), which in the most conservative H.E.S.S. analysis, contrary to the case of the very extended Vela X, was determined to be compatible with being a point-like source. However, the H.E.S.S. Galactic Plane Survey lists a source's extension of $0.02° \pm 0.009°$ (H.E.S.S. collaboration, 2018). Its spectrum (at TeV energies) is well represented by a power-law of index 2.1 and differential flux of about 1.7×10^{-13} $\mathrm{cm}^2\mathrm{s}^{-1}\mathrm{TeV}^{-1}$, referenced at an energy of 1.39 TeV (Acero et al., 2011; H.E.S.S. Collaboration, 2018).

Given that it is the faintest source examined (e.g., its integral flux from 1 TeV to 10

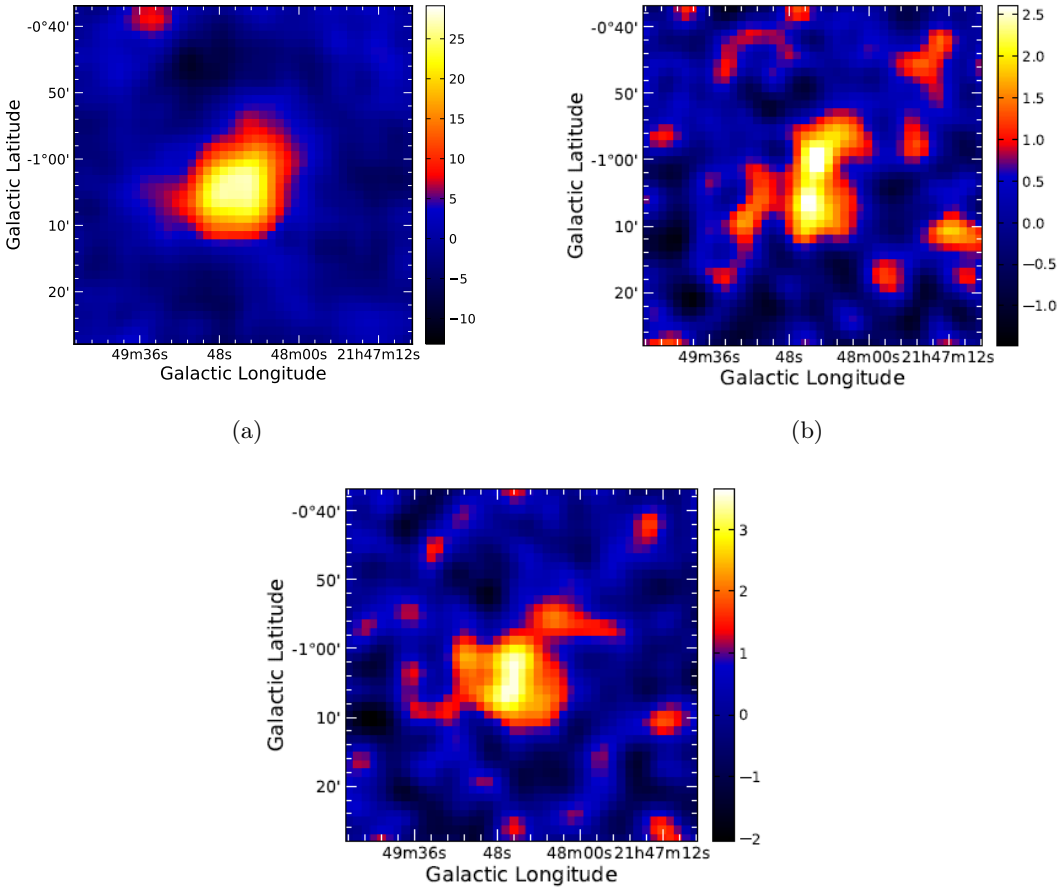

(a) (b)

(c)

Figure 3.9: (a) G327.1-01.1 template used for the simulations. (b) Observation simulation of G327.1-01.1 for 50 hours with the CTA northern array. (c) Same as (b) but with the CTA southern array instead. The sky region plotted is a square of 0.85° of side.

Parameter	Fixed	Model	CTA-N result	CTA-S result
Spectrum results				
$N_0[10^{-13}cm^{-2}s^{-1}TeV^{-1}]$	No	1.7	1.56 ± 0.24	1.28 ± 0.16
E_{ref}[TeV]	Yes	1.39	1.39	1.39
Index	No	2.1	2.01 ± 0.07	1.97 ± 0.06
Fit to gaussian shape				
Ra	No	238.65	238.618 ± 0.024	238.673 ± 0.020
Dec	No	-55.08	-55.075 ± 0.013	-55.064 ± 0.012
Size (Gaussian)	No		0.036 ± 0.010	0.042 ± 0.077
$\sqrt{TS}$ (Gaussian)			8.2	11.5
Fit to templates				
$\sqrt{TS}$ (Input template)			10.6	14.0
$\sqrt{TS}$ (Template 2)			4.9	7.1
$\sqrt{TS}$ (Template 3)			7.1	9.8

Table 3.2: G327.1-01.1 input model and best-fit parameters to the CTA observations simulations in (b) and (c) panels of Figure 3.9. We fitted the simulations both to a source with the template morphology shown in panel (a) (of the cited figure) and a Gaussian model.

TeV of energy represents about 1.5% of the Crab Nebula's flux in the same band), in the case of G327.1-01.1, we performed the simulations for 50 hours of observation time, both with the CTA northern and southern arrays (above 400 GeV of energy, see Figure 3.9 and Table 3.2). Besides performing a simple Gaussian fit, we fitted the observation simulations to the morphological templates of all the sources listed, except that of Vela X, i.e., HESS J1303-631 (named Template 2 in Table 3.2) and MSH 15-52 (i.e., Template 3 in the cited table). The observation simulations of Vela X, summarized previously (see Table 3.1), are the only ones that we could not fit employing the other templates (as the morphological input model). This problem is due to the Vela X template extension, which is larger (by a factor of two) than the rest of the templates used. Note that, despite being the faintest source considered, the Test Statistic resulting for each fit favors the input model compared to the morphologies of MSH 15-52 and HESS J1303-631. The input template is also significantly best-fitted than a Gaussian shape. However, the detection significance, as expected, is much smaller than in the case of Vela X, due to its smaller extension and flux, being the fit to the input template, the only model with $\sqrt{\mathrm{TS}} > 10$ for the simulations with the northern array.

For comparison, we fitted the simulations of G327.1-01.1 to a point-like source. However, it does not improve the detection significance compared to the Gaussian fit, with $\sqrt{TS} = 7.2$ and $\sqrt{TS} = 7.9$ for 50 hours of observation time (with the CTA northern and southern arrays).

3.3.2.3 MSH 15-52

MSH 15-52 is an asymmetric supernova remnant of complex morphology. It is located at an estimated distance of $\sim$ 4 kpc (Aharonian et al., 2005a; Tsirou et al., 2017) and has been related to the pulsar PSR B1509-58 (Seward and Harnden, 1982). In radio wavelengths, the SNR is seen roughly circular with $\sim 0.5^\circ$ of diameter (Caswell et al., 1981). The existence of a pulsar wind nebula surrounding PSR B1509-58, detected as an elongated structure approximately centered on the pulsar (with two arms extending several arcminutes along with the NW and SE directions and power-law photon index of ~ 2), was confirmed by *ROSAT* (Trussoni et al., 1996; Brazier & Becker, 1997) and ASCA (Tamura et al., 1996). The source's observations with H.E.S.S. (Aharonian et al., 2005a, see also panel a of Figure 3.10) showed a spectral energy distribution at TeV energies, consistent with a power-law of differential flux 5.7×10^{-12} cm^{2}s^{-1}TeV^{-1} (referenced at 1 TeV) and index $\Gamma \approx 2.05$. The morphology of the H.E.S.S. counterpart of MSH 15-52 (i.e., HESS J1514-591, Aharonian et al., 2005a), centered at RA = 228.53° and DEC = -59.16°, was characterized (in the H.E.S.S. Galactic plane survey, H.E.S.S. Collaboration, 2018) with an extension of $\sigma = 0.14^\circ$ for a Gaussian fit.

We carried out the simulations performed for MSH 15-52 (summarized in Figure 3.10

Parameter	Fixed	Model	CTA-N result	CTA-S result
Spectrum results				
$N_0[10^{-12}cm^{-2}s^{-1}TeV^{-1}]$	No	7.18	7.16 ± 0.21	7.14 ± 0.11
E_{ref}[TeV]	Yes	1	1	1
Index	No	2.05	2.076 ± 0.042	2.047 ± 0.020
E_{cutoff}[TeV]	No	20	21.0 ± 3.0	19.9 ± 1.3
Fit to gaussian shape				
Ra	No	228.53	228.4854 ± 0.0053	228.4843 ± 0.0025
Dec	No	-59.16	59.1606 ± 0.0028	-59.1603 ± 0.0014
Size (Gaussian)	No		0.1429 ± 0.0016	0.14524 ± 0.00077
$\sqrt{TS}$ (Gaussian)			89.9	192.6
Fit to templates				
$\sqrt{TS}$ (Input template)			91.9	196.6
$\sqrt{TS}$ (Template 2)			62.6	95.4
$\sqrt{TS}$ (Template 3)			82.5	125.6

Table 3.3: MSH 15-52 input model and best-fit parameters to the CTA observations simulations in (b) and (c) panels of Figure 3.10. We fitted the simulations both to a source with the MSH 15-52 template morphology, i.e., in panel (a) of the cited figure and a Gaussian model.

and Table 3.3) for 25 hours of observation time. In this case, we referred to the G327.1-01.1 template as Template 2, while Template 3 refers to the one of HESS J1303-631. Again, the input template was the model best representing the observation simulations (with a large detection significance). The best-fit Gaussian shape resulted in an intrinsic extension compatible with the one reported by the H.E.S.S. Galactic plane survey (i.e., $0.14^\circ \pm 0.03^\circ$, note that $\sqrt{TS} = 42$ in the same).

Finally, we fitted the simulations described above to an elliptical morphological model for comparison. The best-fitted model presented a position angle of $-64.4^\circ \pm 4.9^\circ$ ($-66.6^\circ \pm 2.7^\circ$), a minor axis radius of $0.135^\circ \pm 0.002^\circ$ ($0.133^\circ \pm 0.001^\circ$), a major axis radius of $0.154^\circ \pm 0.002^\circ$ ($0.155^\circ \pm 0.002^\circ$), and a detection significance of $\sqrt{TS} = 90.5$ ($\sqrt{TS} = 138.0$) with the CTA northern and southern arrays. In addition, we retrieved the input spectral model (taken from H.E.S.S. collaboration, 2018) in all the cases with small statistical errors.

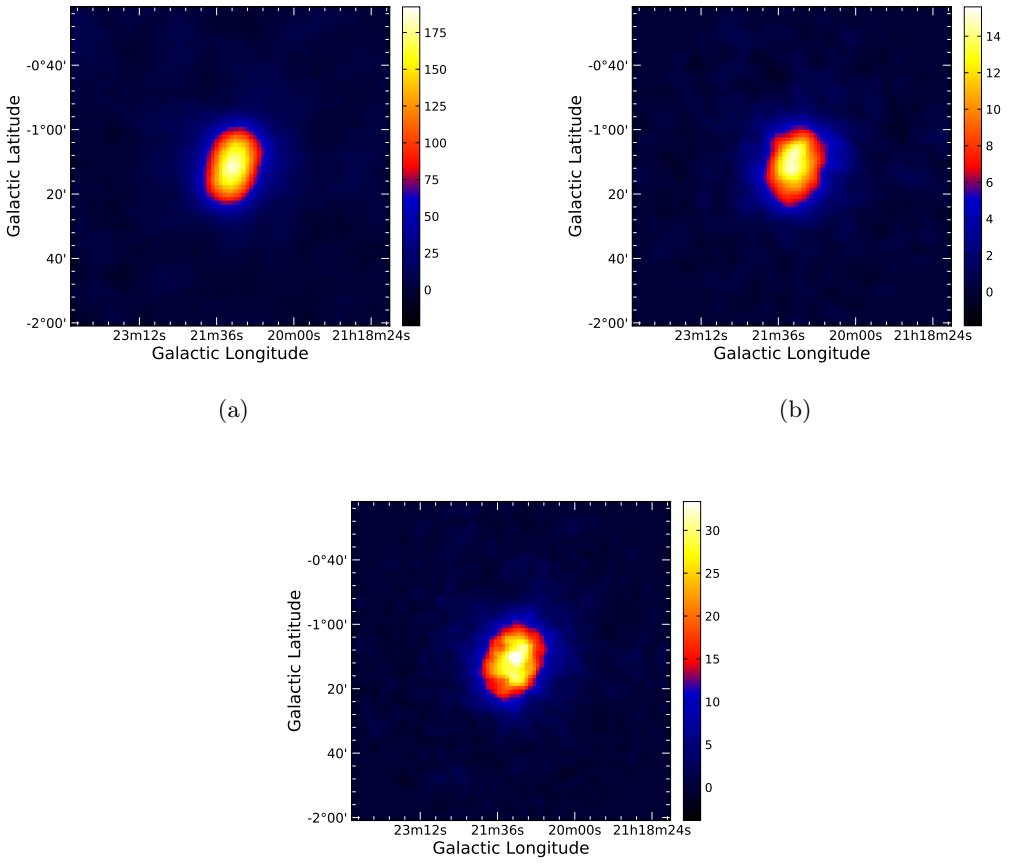

(a)

(b)

(c)

Figure 3.10: (a) MSH 15-52 template used for the simulations. (b) Observation simulation of MSH 15-52 for 25 hours with the CTA northern array. (c) The same as (b) but with the CTA southern array instead. The sky region plotted is a square of 1.6° of side.

3.3.2.4 HESS J1303-631

HESS J1303-631 was initially classified as one of the gamma-ray "dark" sources since, aside from being detected at very high energies, it had no known extended counterparts at different energy windows (H.E.S.S. Collaboration et al., 2012a; Sushch et al., 2017). It was discovered with H.E.S.S. in 2005 (Aharonian et al., 2005b) at TeV energies. Later, the TeV source was related to the pulsar PSR J1301-6305 and interpreted as an evolved PWN through its energy-dependent morphology and the identification of an associated X-ray PWN in *XMM-Newton* data (H.E.S.S. Collaboration et al., 2012a). A radio counterpart of HESS J1303-631 has been recently searched with ATCA, detecting no significant extended emission related to PSR J1301-6305 (Sushch et al., 2017).

The source, as previously commented, is known to have energy-dependent morphology. The extended emission shrinks towards the pulsar at energies above 10 TeV, whereas at lower energies, the emission region's peak position is (significantly) shifted with respect to the PSR J1301-6305 position. This scenario is expected for ancient pulsar wind nebulae since young and energetic electrons are expected to be close to the pulsar (off-scattering soft background photons by inverse Compton), while older and cooled down (lower energy) electrons might extend further from the same, e.g., being left behind by the pulsar's proper motion (Sushch et al., 2017). These electrons can still off-scatter CMB photons. However, they can only generate lower energy gamma-rays (H.E.S.S. Collaboration et al., 2012a, and references therein).

Figure 3.11 and Table 3.4 summarize the simulations of HESS J1303-63. Note that the H.E.S.S. Galactic plane survey reported a Gaussian size for the source of about $0.18^\circ \pm 0.02^\circ$ (with a detection significance of $\sqrt{TS} = 54.5$). It is, then, an extension significantly smaller than the one fitted from the simulations ($\sigma \approx 0.26^\circ$). The elliptical morphological model that best-fit the observation simulations presents a minor axis radius of $0.204^\circ \pm 0.004^\circ$ ($0.207^\circ \pm 0.003^\circ$), a major axis radius of $0.345^\circ \pm 0.006^\circ$ ($0.339^\circ \pm 0.004^\circ$), and a position angle of $4.5^\circ \pm 1.6^\circ$ ($2.2^\circ \pm 1.0^\circ$) for 25 hours of observation time with the CTA northern (southern) array. It implies, therefore, an asymmetry of $\sigma_{\rm major}/\sigma_{\rm minor} = 1.66 \pm 0.05$ (1.64 ± 0.03) with CTA-North (South). Indeed, the elliptical model represents the observation simulations better than the Gaussian model, with $\sqrt{TS} = 55.2$ and $\sqrt{TS} = 85.5$ for the northern and southern arrays, respectively.

The results of the simulations presented in this section for Vela X, MSH 15-52, G327.1-01.1, and HESS J1303-631, summarized in Tables 3.1, 3.2, 3.3, and 3.4, show that it is possible to associate a morphological template, among various ones, to a CTA observation simulation. In all the cases examined, we detected the simulated source at high significance ($\sqrt{TS} > 5$) within a modest observation time (i.e., $\lesssim 50$ hours). At the same time, we showed it is possible to retrieve the source's position and spectrum with minor statistical errors, down to an integrated flux level (above 1 TeV) of $\sim 3.6 \times 10^{-13}$ cm^{2}s^{-1}

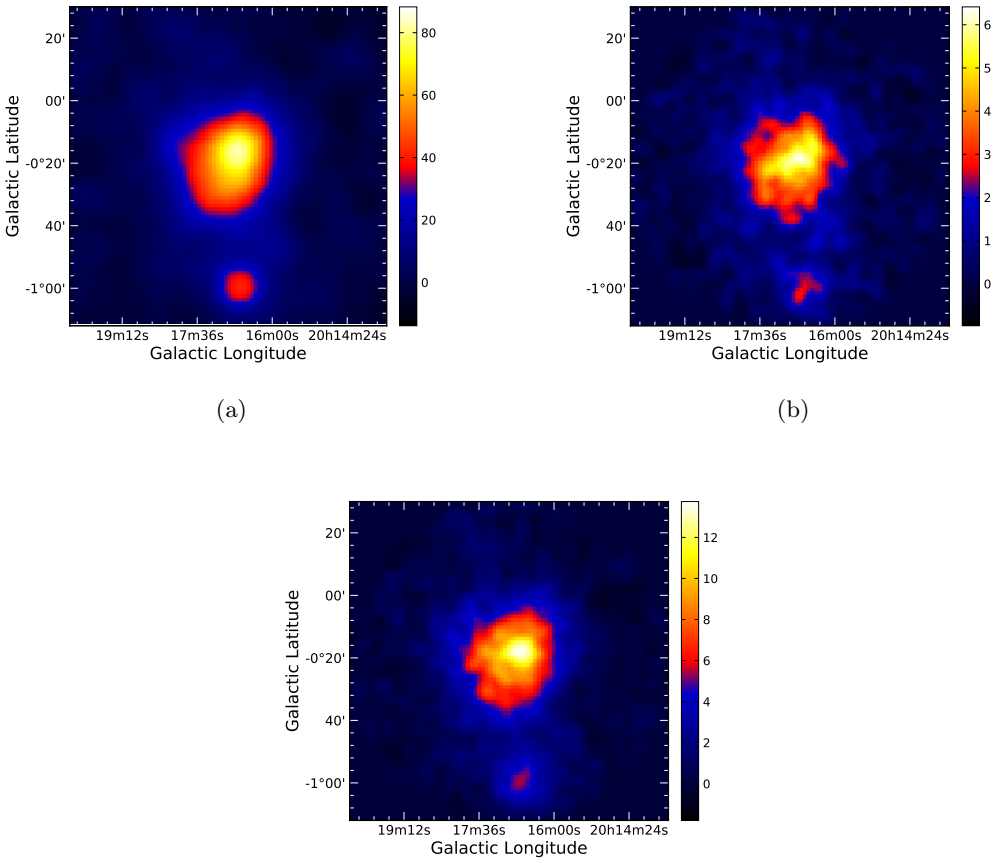

(a)

(b)

(c)

Figure 3.11: (a) HESS J1303-631 template used for the simulations. (b) Observation simulation of HESS J1303-631 for 25 hours with the CTA northern array. (c) The same as (b) but with the CTA southern array instead. The sky region plotted is a square of 1.7° of side.

Parameter	Fixed	Model	CTA-N result	CTA-S result
Spectrum results				
$N_0[10^{-12}cm^{-2}s^{-1}TeV^{-1}]$	No	6.86	6.63 ± 0.25	6.82 ± 0.18
E_{ref}[TeV]	Yes	1	1	1
Index	No	2.04	2.041 ± 0.058	2.046 ± 0.040
E_{cutoff}[TeV]	No	14.3	14.1 ± 2.1	13.3 ± 1.3
Fit to gaussian shape				
Ra	No	195.76	195.763 ± 0.014	195.7617 ± 0.0093
Dec	No	-63.19	-63.2104 ± 0.0058	-63.2075 ± 0.0038
Size (Gaussian)	No		0.2605 ± 0.0035	0.2554 ± 0.0023
$\sqrt{TS}$ (Gaussian)			52.8	81.2
Fit to templates				
$\sqrt{TS}$ (Input template)			58.8	89.9
$\sqrt{TS}$ (Template 2)			28.1	39.6
$\sqrt{TS}$ (Template 3)			51.0	77.6

Table 3.4: HESS J1303-631 input model and best-fit parameters to the CTA observations simulations in the (b) and (c) panels of Figure 3.11. We fitted the simulations both to a source with the HESS J1303-631 template morphology, i.e., in (a) panel of the cited figure and Gaussian model.

(corresponding to approximately 1.5% of the Crab's integrated flux in the same energy regime). Also, we recovered the input extension of the sources (for a Gaussian fit) even for the smallest source ($\sigma \approx 0.02^\circ$) considered. Interestingly, the best-fitted (morphological) model favored the input template hypothesis for all the simulations (compared to the rest of the templates and Gaussian assumptions).

3.3.2.5 Confused sources

The simulations performed for individual sources in previous sections allowed us to conduct simulations of confused sources in a general approach. To simulate the source confusion in CTA data, we artificially overlapped the morphological templates used for individual sources separating them only by 0.2° and 0.3°. In particular, we probed the following cases: (1) The position of MSH 15-52 was made coincident with the one of HESS J1303-631 and then shifted by $+0.2^\circ$ and $+0.3^\circ$ in Galactic longitude. (2) We located Vela X at the position of MSH 15-52, and then we introduced the same separation between the templates (in Galactic longitude, as in the first case). (3) We shifted the HESS J1303-631 position to be coincident with the one of G327.1-01.1 and then introduced a separation of -0.2° and -0.3° (also in Galactic longitude). We did not rotate the templates in any of the cases mentioned. Tables 3.5, 3.6, and 3.7 summarize the results for the simulations (of the cases above) with 25 hours of observation time.

To analyze the observation simulations performed, we fitted them to different hypotheses both with the CTA northern and southern arrays, retrieving the detection significance (i.e., $\sqrt{TS}$) in each case (see Tables 3.5, 3.6, and 3.7). (1) Firstly, we fitted the simulations to the morphological templates of (each of) the confused sources separately (third and fourth columns of the cited tables). (2) Then, we looked for the best-fit Gaussian model (fifth column of the tables mentioned). (3) Finally, we fitted the simulations to both source templates superposed (i.e., artificially confused) in the same configuration used, in the first place, as the input morphological model (last column of the tables). Note that the confused sources are fitted, in fact, as a single source, i.e., with an arbitrary spectrum (the SED of one of the sources) and a single morphological template. Although the template is the superposition of two templates, at this step, we still treat it as the morphological template of a single source. It explains why the detection significance (of the fit to the confused sources templates) does not increase with the separation in Tables 3.5, 3.6, and 3.7 (see the last column). However, our ultimate goal is not to fit the observation simulations of confused sources to a superposition of templates but to fit each of the confused sources to a particular (morphological) template. Therefore, the mentioned tables only represent a hint to decide whether we should treat the observation simulation as a single source or not. The results show that, in general, it is possible to associate a CTA observation simulation with two templates (from individual sources) on top of each other

Parameter	CTA Array	HESS J1303-631 type	MSH 15-52 type	Gaussian	Two sources
0.2° *offset.*					
$\sqrt{TS}$	North	98.4	105.8	110.0	112.4
$\sqrt{TS}$	South	149.5	157.8	164.3	168.6
0.3° *offset.*					
$\sqrt{TS}$	North	82.4	94.1	101.6	105.5
$\sqrt{TS}$	South	126.0	143.34	153.4	160.9

Table 3.5: The TS obtained from fitting the CTA observations simulations of MSH 15-52 and HESS J1303-631 (artificially confused) to; (1) The MSH 15-52 template morphology. (2) The HESS J1303-631 template morphology. (3) A Gaussian model. (4) A source with the morphology of the MSH 15-52 plus HESS J1303-631 templates.

if the sources do not differ strongly in extension and/or flux. The latter is, for example, the case of the faint G327.1-01.1 source and the more luminous one HESS J1303-631 (in Table 3.7). The best-fitted model was a single source with the morphological template of the brighter and more extended of the two sources (but with a different spectrum than HESS J1303-631). This confusion probably occurs because G327.1-01.1 is too dim (e.g., its integral flux above 1 TeV is about 15 times smaller than for HESS J1303-631) and small (by almost a factor of ten in size) in comparison with HESS J1303-631.

Once we assume an observation simulation comes from the superposition of two sources, we are interested in fitting (from the simulation) each source's spectrum and morphology (simultaneously). Hence, in the first two cases described above, we fitted the observation simulations to two different sources located at different positions and with different spectra (each with its corresponding morphological template). Both in the case of HESS J1303-631 confused with MSH 15-52 and MSH 15-52 confused with Vela X, we could retrieve the sources spectra with a similar statistical error than in the case of the sources individually simulated (both for 0.2° and 0.3° of separation). In addition, each source's detection significance increases with the separation (as expected). For example, the HESS J1303-631 and MSH 15-52 detection significances were $\sqrt{TS} = 39.1$ and $\sqrt{TS} = 55.1$ ($\sqrt{TS} = 48.8$ and $\sqrt{TS} = 66.8$), respectively, for a separation of 0.2° (0.3°).

In the simulations described above, we did not consider the orientation of the templates. However, we can extend the procedure explained to compare CTA data with a morphological template rotated by different arbitrary angles. In this case, we would treat each rotated template as a different template from the rest. Since considering different orientations for each template can increase the number of simulations required

Parameter	CTA Array	MSH 15-52 type	Vela-X type	Gaussian	Two sources
0.2° *offset.*					
$\sqrt{TS}$	North	129.7	137.1	135.8	147.8
$\sqrt{TS}$	South	196.1	215.5	209.6	228.8
0.3° *offset.*					
$\sqrt{TS}$	North	122.6	131.2	131.4	144.1
$\sqrt{TS}$	South	188.12	209.4	206.8	226.4

Table 3.6: The TS obtained from fitting the CTA observations simulations of MSH 15-52 and Vela X (artificially confused) to; (1) The MSH 15-52 template morphology. (2) The Vela X template morphology. (3) A Gaussian model. (4) A source with the morphology of the MSH 15-52 plus Vela X templates.

Parameter	CTA Array	G327.1-01.1 type	HESS J1303-631 type	Gaussian	Two sources
0.2° *offset.*					
$\sqrt{TS}$	North	12.1	59.1	55.2	56.6
$\sqrt{TS}$	South	19.4	91.1	84.0	87.9
0.3° *offset.*					
$\sqrt{TS}$	North	5.83	57.7	53.8	56.0
$\sqrt{TS}$	South	7.0	90.6	83.5	87.5

Table 3.7: The TS obtained from fitting the CTA observations simulations of G327.1-01.1 and HESS J1303-631 (artificially confused) to; (1) The G327.1-01.1 template morphology. (2) The HESS J1303-631 template morphology. (3) A Gaussian model. (4) A source with the morphology of the G327.1-01.1 plus HESS J1303-631 templates.

	Radius (FoV) [deg]			$t_{\rm obs}$ [h]		
	0.2	10	20	2	10	100
$t_{\rm simul}$ [s]	2.244 ± 0.014	2.230 ± 0.012	2.273 ± 0.035	2.246 ± 0.017	2.383 ± 0.015	3.95 ± 0.050

	$E_{\rm th}$ [TeV]			$\rm F_{1TeV}$ [$\rm cm^{-2}s^{-1}$]		
	0.5	0.1	0.03	2×10^{-12}	10^{-11}	10^{-10}
$t_{\rm simul}$ [s]	2.270 ± 0.014	2.687 ± 0.018	3.601 ± 0.069	2.257 ± 0.042	2.245 ± 0.097	2.263 ± 0.047

	$E_{\rm th}$ [TeV]		
	0.5	0.1	0.03
$t_{\rm simul}$ [s]	3.453 ± 0.033	14.24 ± 0.47	34.56 ± 0.91

Table 3.8: We summarize (above) the computation time ($t_{\rm simul}$) required for the simulation of two (confused) sources (from a morphological spatial template, with CTOOLS) for different input parameters. The input parameters varied are the radius of the field-of-view, observation time ($t_{\rm obs}$), energy threshold ($E_{\rm th}$), and total flux of the (confused) sources above 1 TeV of energy ($\rm F_{1TeV}$). The first two parts of the table are referenced to a simulation with a (FoV) radius of 0.1°, $t_{\rm obs} = 1$ hour, $E_{\rm th} = 1$ TeV, and $\rm F_{1TeV} = 10^{-12}$ $\rm cm^{-2}s^{-1}$ (lasting $t_{\rm simul} = 2.236 \pm 0.011$ s). We indicate in each column of the table the parameter that changed compared to the cited ones. The third and bottom part of the table is referenced to a simulation with (FoV) radius of 10°, $t_{\rm obs} = 25$ hours, and $\rm F_{1TeV} = 2 \times 10^{-12}$ $\rm cm^{-2}s^{-1}$, indicating that the combination of increasing observation times and lower energy thresholds boosts the computation time needed per simulation.

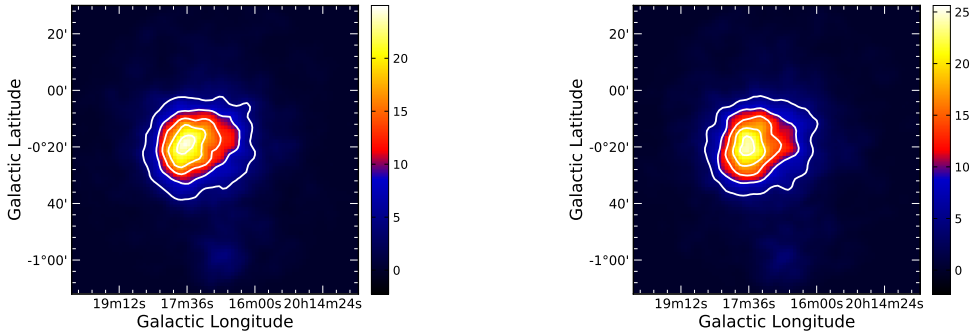

Figure 3.12: Simulation observation of HESS J1303-631 and MSH 15-52 sources with a separation of 0.2° (without background). The simulations correspond to 25 hours with the CTA southern array.

by a large factor, each simulation's computation time becomes an important issue. The computation time per template was typically $\sim 2-4$ seconds (see Table 3.8). However, the computation time required for a simulation could increase dramatically (by more than a factor of ten) along with the observation time (i.e., for $t > 25$ hours) for simulations with a low energy threshold (i.e., ~ 30 GeV). This difficulty limits carrying out a large number of simulations to either relatively high energy thresholds (i.e., $\gtrsim 0.5$ TeV) for large observation times (more than 25 hours) or short (i.e., $\lesssim 10$ hours) observation times (per simulation) when considering very low energy thresholds (at tens of GeV). Table 3.8 summarizes the computation time required (per simulation) according to various choices for the input parameters. It is noticeable that the boost of the required observation time only occurs in rather exceptional cases.

To conclude, we tested if the computation of the observation simulations with two sources (without background) can be considered a linear operation (or nearly linear), i.e., if the result of carrying out an observation simulation with two sources without background is similar to perform an observation simulation for each source (without background) and adding them later. Figure 3.12 shows an example of both operations with MSH 15-52 and HESS J1303-631 sources. In the left panel of the same, the simulation is carried out for the two sources together, while in the right one, we simulated the sources alone, and the resulting observation simulations were ultimately added. Figure 3.12 shows, indeed, that the observation simulations performed are nearly a linear operation (if not accounting for the background). The similar statistics of both simulations in Figure 3.12, e.g., the total number of events (12587 and 12592 for the left and right panels, respectively), the maximum number of events in a bin (32 and 35), or the mean residual of both simulations subtraction (≈ 0), proves further the last statement.

3.3.2.6 Conclusions and caveats

In light of the simulations and results described above, we reached several conclusions: (1) It is possible to compare, with a simple approach, a morphological template or a combination of them directly with CTA (simulated) data. The templates must depict the intensity distribution of the source (or sources) along the sky spatial dimensions but are valid in any arbitrary flux units. (2) It is possible, in principle, to distinguish between the case of two confused sources and the single source assumption in a modest observation time (i.e., in less than 50 hours). In some cases, we achieved the discrimination with high confidence (see Table 3.6). However, it depends on the separation between the sources and their relative (and total) flux and extension. Considerable differences between both sources extension and/or flux level (e.g., by a factor larger than ten) complicate the discrimination of the different hypotheses. (3) Once we identify the source confusion problem, we can retrieve the extension and spectrum of each source with similar statistical errors than if isolated (when using the input template as the best-fit morphological model). (4) The simulation time required per simulation is, generally, in the order of a few seconds. However, it can significantly increase in some particular configurations with more than 25 hours of observation time and low energy thresholds (i.e., tens of GeV).

Our study, nonetheless, is limited in some respects. (1) Firstly, to apply this approach to the source confusion problem, we need a library of morphological templates (either simulated or based on observational data). How to achieve such a comprehensive library of extended TeV sources is a topic beyond the scope of this thesis. (2) Also, we did not rotate the templates nor considered the uncertainty in the distance to the source. In principle, rotating a template or placing it at a different distance could be interpreted as creating a new template. Hence, we can easily include it in the simulations described. However, these operations over the templates multiply their number, complicating the comparison of the library to the data. The procedure's cost in computation time will limit its application to some extent. To place a template at a distance other than that of reference, we can rescale its flux and spatial axes. The flux should scale with the distance to the source (r) as $1/r^2$, while the spatial axes as $1/r$. The precision of the latter operation (from trigonometric arguments) is $< 0.01\%$ if $2r/D > 50$, where D is the template's physical diameter. For example, Figure 3.13 (b) and (c) panels depict the simulations of HESS J1303-631 for 25 hours of observation time with the CTA southern array rescaled at twice and four times the distance of the reference template, respectively. (3) Finally, we did not consider a source with energy-dependent morphology, i.e., we assume the templates describe the source's morphology in all the energy range simulated. Further studies on this case are still pending.

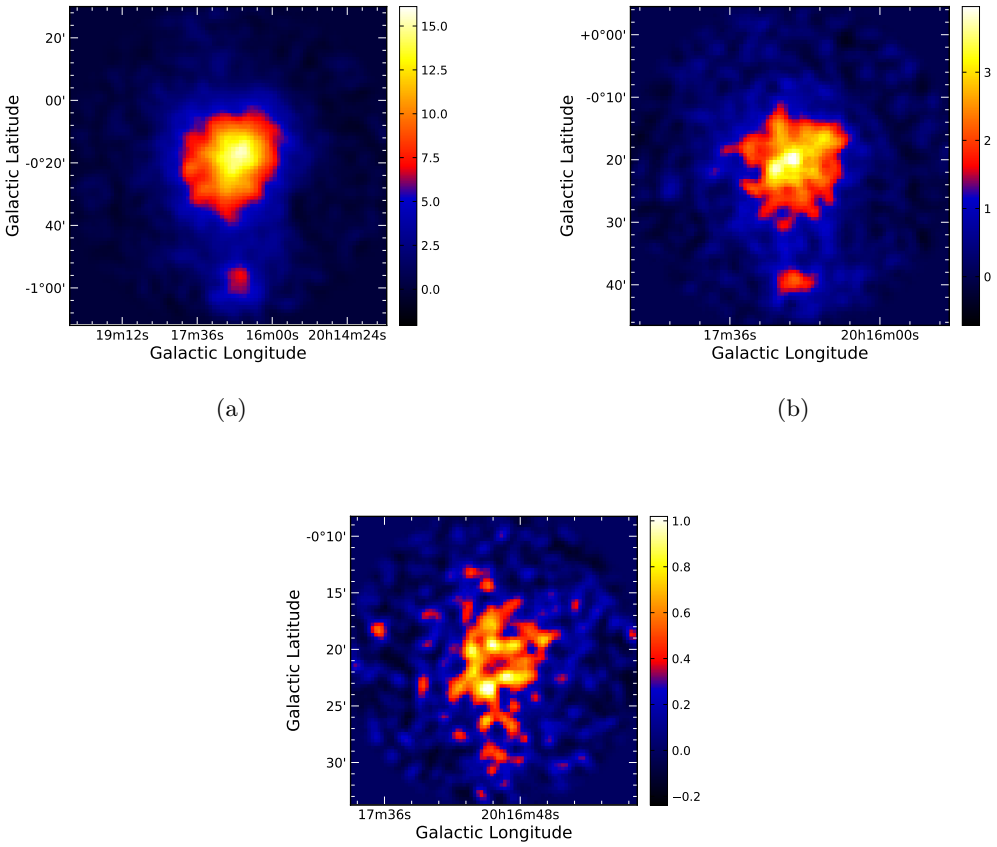

Figure 3.13: (a) Simulation observation of HESS J1303-631 for 25 hours of observation time with the CTA southern array (b) Same as (a) but rescaling the HESS J1303-631 template at twice its distance (c) The same rescaled at fourth times the distance of (a).

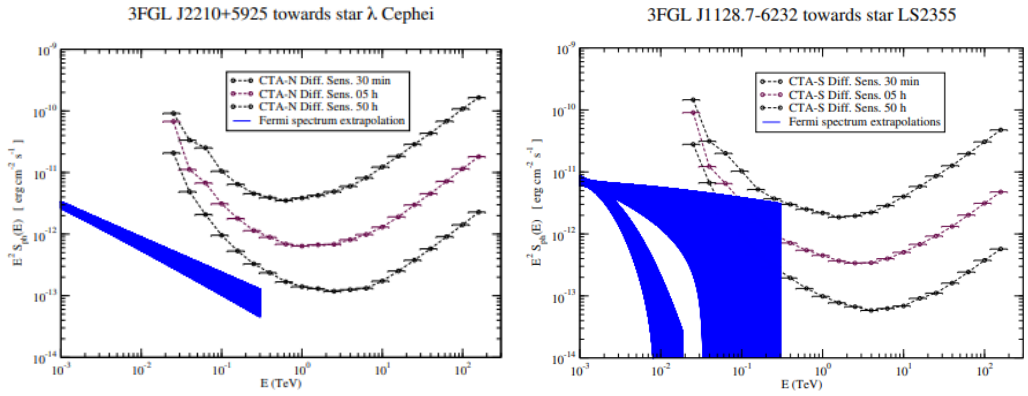

Figure 3.14: Expected gamma-ray emission from two stellar bowshocks compared with the predicted CTA sensitivity. Credits: Estrella Sánchez-Ayaso

.

3.3.3 Other applications

An interesting application of the tools presented above is to explore the prospects (with CTA) for more exotic types of sources (expected to emit at very high energies). For instance, among these less explored gamma-ray emitters are bowshocks of massive runaway stars. Del Valle & Romero (2012; 2014) argued these bowshocks could be indeed sites of particle acceleration and very-high-energy gamma-rays production via inverse Compton of relativistic electrons with background thermal photons (and to lesser extents, via proton-proton interactions). However, the (expected) luminosities of these sources (at GeVs, $\sim 10^{31} - 10^{33}$ erg s^{-1}) are rather moderate or dim for current gamma-ray instruments. Despite this limitation, some associations between stellar bowshocks (like λ Cep and LS 2355) and unidentified *Fermi* sources (Sánchez-Ayaso et al., 2018) have been proposed. CTA may detect some of these sources in upcoming years (see Figure 3.14). Preliminary simulations (with GAMMAPY) of several bowshocks (i.e., those associated with the LAT sources 3FGL J2210+5925, FL8Y J0004.8+6623, 3FGL J1128.7-6232, and FL8Y J1908.7+0811) using the Instruments Response Functions described in Section 3.2.3 did not result in the detection of the sources with CTA (in less than 50 hours). Nevertheless, the uncertain spectral shape of the sources in the CTA band prevented us from excluding this possibility.

The stellar bowshock with the highest flux among those examined is 3FGL J1128.7-6232 (towards LS 2355, Sánchez-Ayaso et al., 2018). Figure 3.15 (taken from the cited paper) shows the source's multi-wavelength spectrum. The authors provided the LAT data depicted in the cited figure in Table 4 of Sánchez-Ayaso et al. (2018). To study the capabilities of CTA for detecting this source, we first fitted the mentioned spectral shape (from 500 MeV to 100 GeV), in an optimistic approach, to a simple power-law (i.e., $N_0 \times (E/E_0)^{-\Gamma}$).

Then, we convolved the resulting model with the CTA IRFs (using the ones corresponding to 50 hours with the southern array, i.e., the most sensitive response available). In this case, we derived an integral flux upper limit for the source of 1.5×10^{-13} cm^{-2} s^{-1} (at 95% CL) in the CTA energy band (i.e., above 20 GeV of energy). The best-fit (power-law) model cited implies a differential flux of $N_0 = (2.2 \pm 0.3) \times 10^{-12}$ cm^{-2} s^{-1} MeV^{-1} (referenced to an energy E_0 of 1 GeV) and an index of $\Gamma = 2.94 \pm 0.08$, with $\chi^2 = 2.4$ for 3 degrees of freedom. Despite the optimistic scenario considered for the projected spectrum of the source (in the CTA energy window), the convolution of the radiation model obtained did not result in the source's detection (with the CTA southern array) within a maximum of 300 hours of observation time.

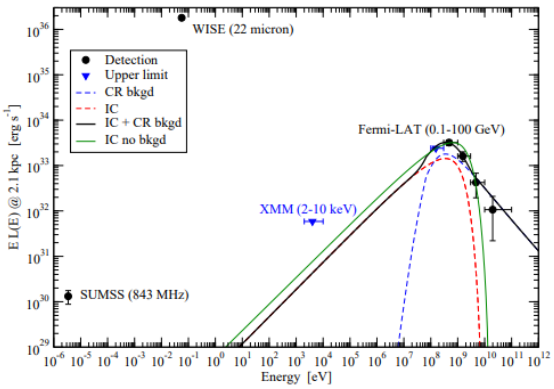

Figure 3.15: The SED of the LS 2355 bowshock at an assumed distance of 2.1 kpc. The plot was taken from Sánchez-Ayaso et al. (2018).

Chapter 4

Prospects for the characterization of the very-high-energy emission from the Crab Nebula and pulsar

4.1 Introduction

The Crab Nebula and pulsar (hereafter, the Crab, see Section 2.4.2) are, without a doubt, the most studied sources in the very-high-energy (VHE) regime. Its importance in the field (of HE and VHE astronomy) is so notorious that Crab was used as a standard candle, for long, in X-ray and gamma-ray studies since its first detection (at VHEs) in 1989 with the Whipple telescope. Its long-term flux stability and luminosity propitiated this treatment. Furthermore, the Crab has been a reference source to probe multiple hypotheses on how relativistic particles are accelerated to extreme energies in astrophysical environments and how they emit the radiation observed at very high energies. Also, the Crab has been multiple times used as a test target for characterizing the performance of IACTs (see Section 3.1.3) since these began to operate decades ago.

These attributes (summarized above) justify and highlight the importance of analyzing the prospects for CTA, representing the new generation of IACTs, regarding the Crab Nebula and pulsar observation. The performance of CTA regarding the Crab can be studied indeed, through simulations, with the tools presented in Chapter 3. The present chapter will describe the Crab Nebula and pulsar detection, spectrum, morphology, and variability, as expected from the Instrument Response Functions (see Section 3.2.3) predicted for the future CTA observatory. Firstly, we will focus on the Crab in steady-state, i.e., as it is usually observed. Next, we will explore the Crab Nebula variability in short timescales (i.e., the dubbed Crab flares) at GeV and TeV energies.

4.2 The Crab pulsar

The Crab pulsar is one of the few pulsars to date that could be detected and characterized across the entire electromagnetic spectrum, i.e., from radio frequencies to gamma-rays. It spins with a period of P = 33 ms and exhibits a spin-down rate of $\dot{P} = 4.21 \times 10^{-13}$, corresponding with a spin-down luminosity of $L_{spin} = 3.8 \times 10^{38}$ erg s^{-1}. It is also the pulsar whose age is known with the best precision since it constitutes a remnant of the historical supernova explosion observed in 1054 AD by Chinese astronomers.

At energies of hundreds of MeV, the LAT instrument onboard the *Fermi* satellite (see Section 3.1.2.1) has performed the pulsar's most precise observations. The pulsed emission (in this energy regime) is believed to be due to synchro-curvature radiation (see Section 2.3.2) up to (at least) energies of $\sim$ 10 GeV. The phase-averaged spectrum, at these energies, could be well described by a 1.97 power-law index with an exponential cutoff at $(5.8 \pm 0.5 \pm 1.2)$ GeV (see Abdo et al., 2010e). This cutoff energy is actually in agreement with the expected from the synchro-curvature radiation theory (Viganó & Torres, 2015), where the maximum energy of the emitted radiation is limited by either magnetic and gamma pair absorption or radiation losses. In particular, the *Fermi*-LAT observations, together with the pulsar's detection (with MAGIC) at $\sim$25 GeV (Aliu et al., 2008), favored the so-called *outer gap* models (Cheng et al., 1986), which locate the emission origin at high altitudes within the magnetosphere.

Surprisingly, the picture described above was challenged drastically in 2011, when a new spectral component emerging above the cutoff energy (i.e., at $\sim$ 6 GeV and extending towards $[0.5 - 1]$ TeV) was detected. The discovery of such energetic pulsed emission from the Crab opened a new window in pulsar physics. This component was first seen by VERITAS (Aliu et al., 2011) and later confirmed by MAGIC (Aleksić et al., 2011; 2012) and points to the existence of relativistic particles close to or beyond the light cylinder (i.e., limiting surface where co-rotation with the pulsar is no longer possible), where absorption is negligible. An alternative emission mechanism to those invoked so far to explain the pulsed emission may be necessary to account for this new component, for example, inverse Compton radiation from synchrotron pulsed photons of lower energy. Different studies have proposed different locations for the origin of the emission, which is still unknown, e.g., the pulsar magnetosphere (Aleksić et al., 2011; Lyutikov et al., 2012), the pulsar wind region (Aharonian et al., 2012), or current sheets (Contopoulos et al., 1999; Cerutti et al., 2016) extending beyond the light cylinder (Mochol & Pétri, 2015). Normal synchro-curvature emission could still be playing a role, as is usual in the case of other pulsars (see Viganó & Torres, 2015). Interestingly, the presence of two different mechanisms behind the HE and the VHE components suggests that some distinctive spectral features may appear in this part of the spectrum. If this is the case,

its detection could shed some light on the emission mechanisms at work.

4.2.1 Simulations of the Crab pulsar phase curve

The Crab pulsar observations at VHEs show a light curve with two distinctive peaks (i.e., the main pulse, or P1, and the inter-pulse, or P2) and an additional component between P1 and P2 (usually dubbed *Bridge* emission). P1 is the main pulse at GHz frequencies and is used to define the phase equal 0, whereas P2 is shifted by ~ 0.4 (in phase) compared to P1. The pulses widths, relative intensity, and the *Bridge* emission's flux level depend on energy (Kuiper et al., 2001). For instance, in gamma-rays, P2 replaces P1 as the dominant component of the phase curve, and both pulses are much narrower than in the energy window covered by *Fermi*-LAT. The *Bridge* emission, which at the energies accessible by *Fermi*-LAT is prominent and well-characterized by a 3.35 power-law photon index (above 50 GeV), fades away at an energy of about 150 GeV (Aleksić et al., 2014).

Figure 4.1 presents an example of simulation (performed with CTOOLS) of the Crab's phase curve detection with the CTA northern array (for an observation time of 100 hours). For this work, we adopted the location of P1 and P2 described in Ansoldi et al. (2016). P1 is located in the -0.017 to 0.026 interval and P2 in the 0.377 to 0.422 one (in phase). Concretely, P1 is centered at the position $0.9968 \pm 0.0020_{stat} + 0.0055_{sys} - 0.0048_{sys}$ and P2 at $0.4046 \pm 0.0035_{stat} + 0.0047_{sys} - 0.0074_{sys}$, with a full width at half maximum (FWHM) of $0.01 \pm 0.003_{stat} + 0.003_{sys} - 0.01_{sys}$ and $0.04 \pm 0.009_{stat} + 0.005_{sys} - 0.008_{sys}$ in phase for P1 and P2 (according to the cited work), respectively. The phase curve model used for the simulations consists of two Gaussian peaks placed at the locations described above and with the same widths (note that FWHM $\approx 2.335\sigma$ for a Gaussian peak). We forced the relation of events contained in both peaks (of the template) to agree with the one summarized in Ansoldi et al. (2016) above 400 GeV, i.e., P2/P1 $= 2.9 \pm 1.4$.

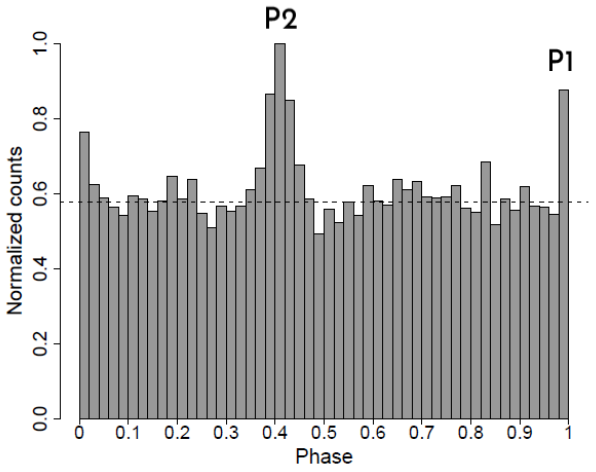

Figure 4.1: We obtained the phase curve depicted from a simulation (carried out with CTOOLS) of the Crab pulsar above 400 GeV of energy with the CTA northern array (for 100 h of observation time).

We simulated the pulsar at the Crab's radio position (RA = 05:34:31.992 and DEC =

+22:00:51.84, Lobanov et al., 2011) for energies ranging from 20 GeV and 180 TeV, with a power-law spectrum of 2.9 photon index and 2×10^{-11} cm^{-2}s^{-1}TeV^{-1} at 150 GeV (i.e., the spectrum of the P2 component according to Ansoldi et al., 2016, see the blue shaded area in Figure 4.2). The spectrum for each peak of the Crab pulsar phase curve is shown in Figure 4.2 with Fermi-LAT and MAGIC data. The data used for representing the Crab P1 and P2 spectra were taken from Ansoldi et al. (2016), while the steady nebula spectrum plotted, for comparison, was compiled from Meyer et al. (2010) and Buehler et al. (2012). We extracted the Crab's phase curve (from the simulations performed) in a region with 0.3° of radius around the pulsar's position. Note that the spectrum of P2 considered (from hereafter) for the Crab pulsar simulations is harder than the one of P1 (see the red shaded area in Figure 4.2, with a fitted photon index of ≈ 3.5). Hence, this approach for the simulations of the Crab pulsar can be considered a somewhat optimistic case. Figure 4.3 shows the statistical error in the positions and widths of P1 and P2 peaks (retrieved from the Crab pulsar's simulated phase curves described above, for a Gaussian fit) versus the observation time. In particular, the values of observation time represented are 20 (black point), 50 (violet triangle), 150 (yellow square), 200 (blue diamond), 250 (red crossed-diamond), and 300 (green crossed-square) hours. The statistical error of the P1 position and width is smaller than for P2, as we expected since it follows the statistics used to generate the phase curve template (i.e., the statistics in Ansoldi et al., 2016). Note, however, that the detection significance should be smaller for P1 (as in the cited paper), which is indeed satisfied. The P2 and P1 detection significances (above 400 GeV, computed with the H-test statistic, De Jager et al., 1989) are 11.2σ and 8.4σ, respectively (in 300 hours). The relation of (excess) events retrieved is compatible with that of the template, i.e., P2/P1 $= 2.86 \pm 0.17$, with ~ 1150 (excess) events above 400 GeV in 300 hours for P2 and ~ 400 (excess events) for P1. These are slightly above twice the excesses observed with MAGIC (in ~ 320 hours, see Ansoldi et al., 2016). The improvement in the measured statistical error both of the peaks positions and Gaussian widths is about a factor $[2-3]$ (in 300 hours above 400 GeV) compared to the precision used for the Crab phase curve

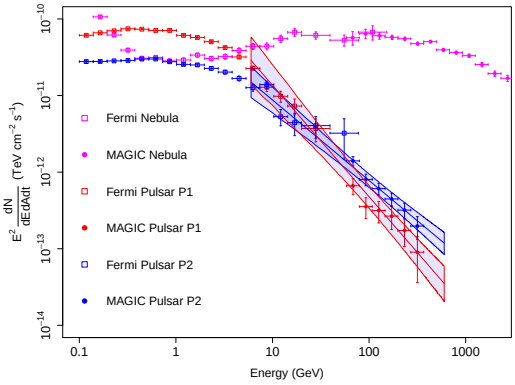

Figure 4.2: The Crab Nebula and pulsar spectra are depicted with data taken from Ansoldi et al. (2016) and Buehler et al. (2012).

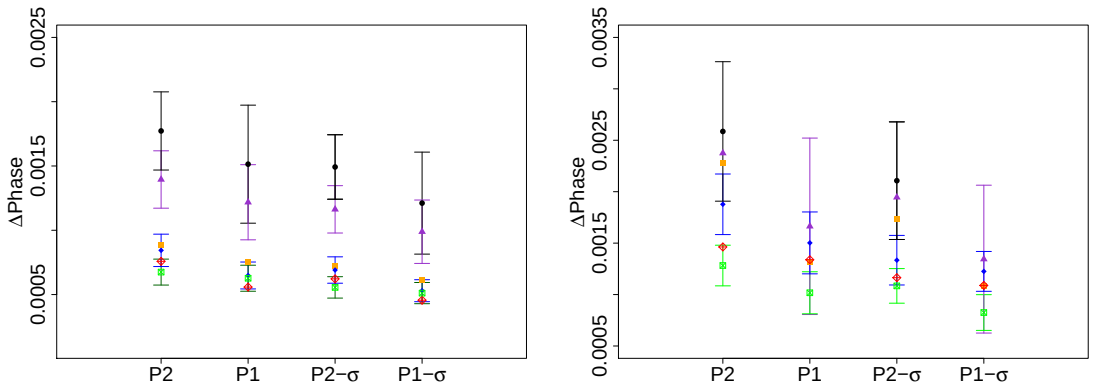

Figure 4.3: Panel (a) depicts the statistical error retrieved from the Crab pulsar simulations for the positions and Gaussian σ of P1 and P2 peaks above 40 GeV, with different observation times. The panel (b) corresponds to the same but above 400 GeV.

template (from $\sim$ 320 hours of MAGIC above 400 GeV, as described above). The error in the measured separation between the peaks (i.e., 0.4127 ± 0.0017 for 300 hours of observation time with the CTA northern array) also implies this improvement compared to the MAGIC measurements. Burtovoi and Zampieri's (2016) paper provides more detailed simulations of the Crab pulsar phase curve with CTA. Note also that the simulations we present do not include the *Bridge* component since it is only relevant at the lowest energies, i.e., at the energies in which the noise is more prominent, and CTA is less sensitive.

4.2.2 Simulations of the Crab pulsar spectrum

To investigate the capabilities of CTA to explore the physics behind the Crab pulsed emission, we performed simulations of the Crab pulsar with the CTA northern array, using the 3D sky cubes simulator and the Instrument Response Functions described in Sections 3.3.1 and 3.2.3, respectively. We aim at probing, through these simulations, the maximum energy at which the detection is feasible, the significance of the periodicity detection, and the capabilities of CTA to detect features in the Crab pulsar spectrum. The analysis of the simulations performed includes, as a component of the background model, the steady emission from the Crab Nebula, simulated as an extended source with the log-parabola spectral shape measured by MAGIC (see Aleksić et al., 2015). However, we will describe the simulations of the nebula in more detail in the next section.

The Crab pulsar was simulated, in this case, as a point-like source at the position and with the spectral parameters described previously for the simulations of the Crab's

phase curve. The analysis of the resulting sky cubes extended the pulsar spectrum up to TeV energies. In particular, the maximum energies at which we still detect the pulsar (in 300 hours of observation time) corresponded to the energy bin (of the simulated 3D sky cubes) spanning from 3 TeV to 7 TeV at 3σ (or 1 TeV to 3 TeV at 5σ). We successfully retrieved the pulsar spectrum assumed for the simulations from the analysis of the 3D sky cubes, with a best-fit spectral index (for 300 hours of observation time) of $\Gamma = 3.0 \pm 0.18$ and $(2.1 \pm 0.26) \times 10^{-11}$ cm^{-2}s^{-1}TeV^{-1} of flux at an energy of 150 GeV, measured from 80 GeV to 680 GeV, and taking into account the emission of the nebula as part of the background for the pulsar spectrum analysis.

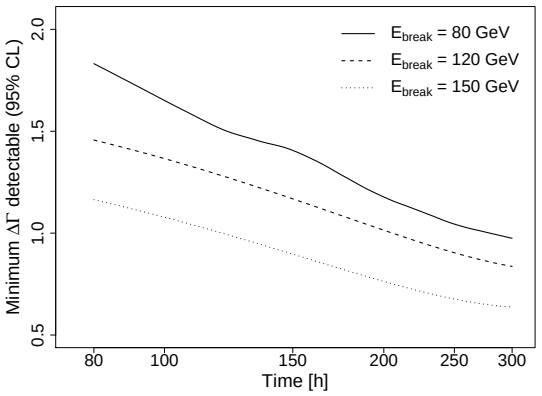

Figure 4.4: Minimum index variation detected (at 95% CL) resulting from fitting the pulsar spectrum to a smoothed broken power-law at different observation times. The legend shows the different (fixed) energy breaks employed. The plot was taken from Mestre et al. (2020).

CTA will characterize the spectrum of the Crab pulsar at VHEs with unprecedented sensitivity. Therefore, the possibility of finding new spectral features at hundreds of GeV, reflecting a transition between different dominant emission mechanisms (as previously discussed), should be considered. From an empirical point of view, the transition between two different spectral components can translate into a "kink" of the spectral shape, characterized by a noticeable change of the slope below and above this spectral feature.

To explore the presence of this kind of features in the Crab pulsar spectrum, in particular, of a "kink" at energies of $\sim$ 100 GeV, we fitted the simulations performed to a smooth broken power-law spectrum, fixing the energy break (E_{break}) to different values ranging from 80 GeV to 150 GeV. The smooth broken power-law function is suitable for our purpose since it is characterized by asymptotically approaching a power-law characterization of index Γ_1 below the energy break (i.e., $E << E_b$) and to a power-law of a steeper index (Γ_2) in the opposite case, i.e., $E >> E_b$. We then retrieved (from the fitted models) the precision on the best-fit spectral indices (Γ_1 and Γ_2) below and above the break energy assumed. For comparison, the best-fit (power-law) index obtained from the *Fermi*-LAT and MAGIC joint data analysis is 3.05 ± 0.05 for P2 (see the solid blue line and shaded area in Figure 4.2), whereas, for the case of P1 is 3.46 ± 0.07 (shown in red in

the cited figure). Also, we could best represent the P2 measurements (with MAGIC) from 68 GeV to 316 GeV with a 2.94 ± 0.03 (power-law) index (in all the cases accounting only for statistical errors). We now can define the minimum index variation detectable as the minimum difference between the two indices ($\Delta\Gamma = \Gamma_1 - \Gamma_2$) for which the total spectrum is no longer compatible with the simple power-law input model at 95% CL. Applying the procedure explained above resulted in a minimum index variation detectable of $\Delta\Gamma \sim 0.6$ at 95% CL in 300 hours with the break energy located at 150 GeV (see Figure 4.4).

Figure 4.4 shows that the minimum index variation detectable improves as we locate the break at higher energies. In part, it is due to the improvement of the CTA sensitivity around the break energy as the same approaches to TeV energies (where the performance of CTA is better). Also, to the reduction of noise towards higher energies. However, it is due mainly to the spectrum fit below the break energy (down to 20 GeV), which rapidly improves if we locate the break at higher energies. The reason is that if we expand the lower energy range, we simply include a larger amount of energy bins to fit. The spectral fit above the break energy is less sensitive to its location since we could expand the (fitted) energy range up to a few TeVs of energy. Note that we could better constrain the spectral index below the break energy (Γ_1) by combining the CTA measurements with those available from other instruments at lower energies (e.g., MAGIC and/or VERITAS). For example, if we compare the best-fit indices (for the smooth broken power-law case) with the input model index (i.e., 2.9), the minimum index variation detectable above the break energy would result (approximately) the one showed in Figure 4.4 but improved by a factor $[0.5 - 0.7]$ (depending on the break location and observation time).

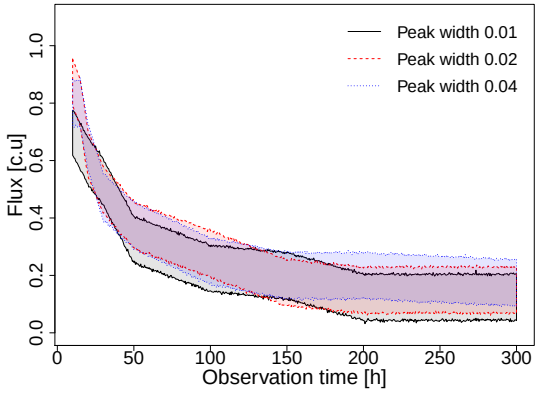

Figure 4.5: Minimum source flux (in Crab units) necessary to detect a periodicity at a 5σ-level as a function of the observation time (for the Gaussian peak templates described). The shadowed regions depict the 3σ error. The plot was taken from Mestre et al. (2020).

4.2.3 Generalization of the simulations to different phase curves at different flux levels

Additionally to the Crab pulsar simulations presented in this chapter, and to provide a more general picture of the CTA performance regarding the observation of pulsed emission

from different sources, we generalized the simulations described above considering both different light curve shapes and various flux levels. For that purpose, we applied the simulations introduced in section 4.2.1 (performed with CTOOLS) to different templates consisting of a single Gaussian peak (discretized in bins of 0.01 of width in phase). We located the Gaussian peaks at the P2 position with Gaussian σ of 0.01, 0.02, and 0.04 (in phase), corresponding (approximately) to 0.5, 1, and 2 times the P2 width. The different flux levels considered were 0.2, 0.5, 1, and 2 times the Crab flux (i.e., in Crab units). We rescaled the Crab spectrum (particularly the one for P2, above 20 GeV of energy) by this factor, with no change in the spectral index. Burtovoi et al. (2017) provides more detailed prospects for detecting the most energetic *Fermi* pulsars.

The periodicity was probed, as in Section 4.2.1, with the H-test statistic for the events with folded phases (De Jager et al., 1989), and the probability associated with an H-test statistic for the best number of harmonics was taken from De Jager & Büsching's (2010) result and converted into a Gaussian sigma (with the area under the Gaussian probability density function integrated from σ to infinity). Figure 4.6 shows the results obtained. The simulations of smaller widths showed an intrinsic spread-out of 4.7×10^{-3} in phase, which is constant with the observation time (by construction), i.e., one should limit the simulations of the phase curve for a Gaussian peak template with $\sigma > 0.005$ in phase.

To explore the performance of CTA regarding the pulsed emission of sources dimmer than Crab, we also tested (with the tools described above) the minimum flux necessary to detect the periodicity (at 5σ) for a fixed observation time. We summarize the results in Figure 4.5, which represents, together with Figure 4.6, the sensitivity of CTA to detect pulsars displaying different light curves and flux levels (at energies above 80 GeV). The prospects derived could be helpful for future pulsar population studies with the CTA observatory.

Figure 4.5 shows that we could detect periodicity (at 5σ significance) from pulsars down to a flux level of 0.1 (in Crab units). Note, however, that we could not establish the dependence of the periodicity detection's significance as a function of the peak width (Figure 4.6) because of the large dispersion of the measurements. We expected, as previously discussed, to detect the narrower peaks at a smaller significance.

4.3 The Crab pulsar wind nebula

The Crab pulsar wind nebula is located in the Perseus Arm of the Milky Way, at a distance of ≈ 2.2 kpc. It presents an energy-dependent morphology with decreasing size in energy that is seen approximately ellipsoidal in optical, with major and minor semi-axes of ~ 7 and 4.6 arcminutes, corresponding to ~ 4.1 and ~ 2.7 parsecs of physical size, respectively. At higher energies, an inner structure with the shape of a torus and perpendicular jets

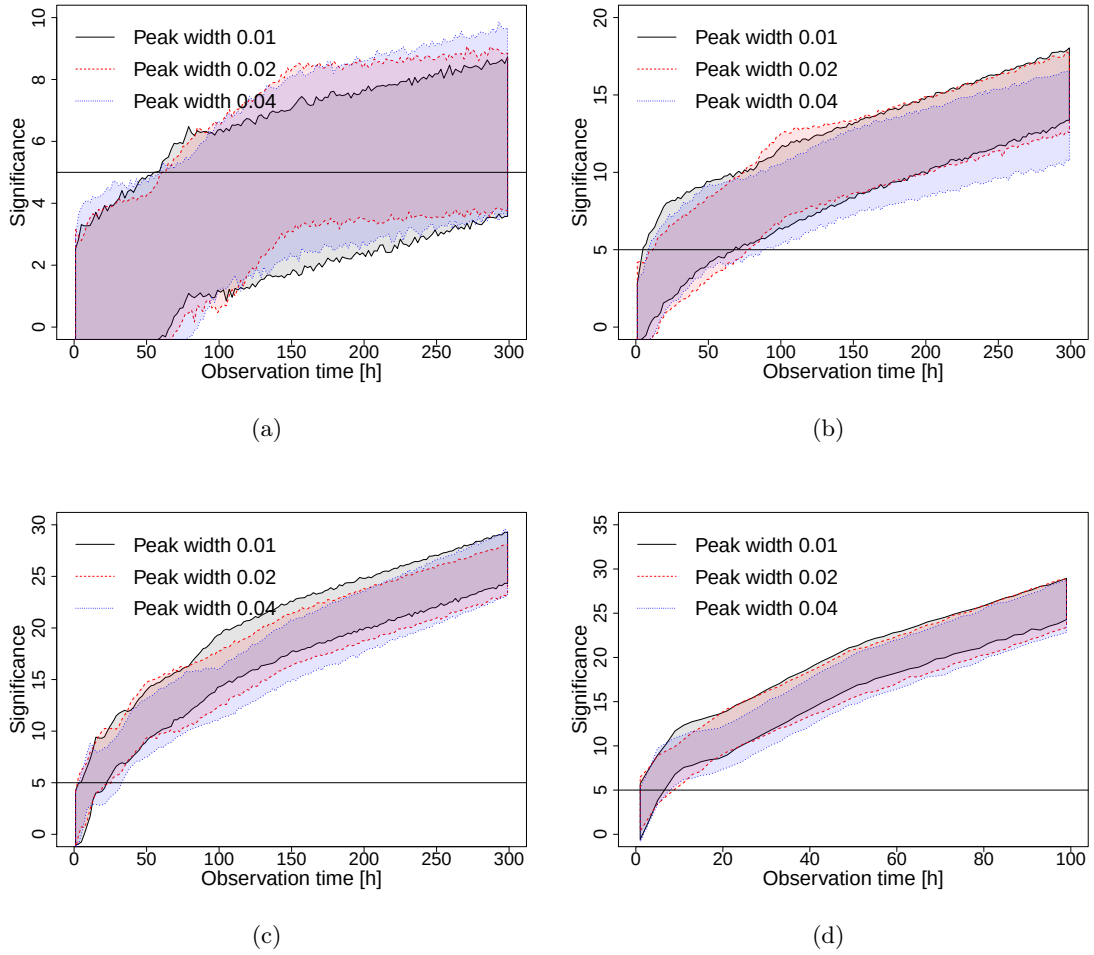

Figure 4.6: The different panels depict the evolution in time of the periodicity detection's significance (3σ region). The source's flux is (a) 0.2, (b) 0.5, (c) 1, (d) and 2, in Crab units. We smoothed the curves through the interpolation method, and the 3σ region was computed by bootstrapping (Efron, 1979) of the H-statistic and simulations. The plots were taken from Mestre et al. (2020).

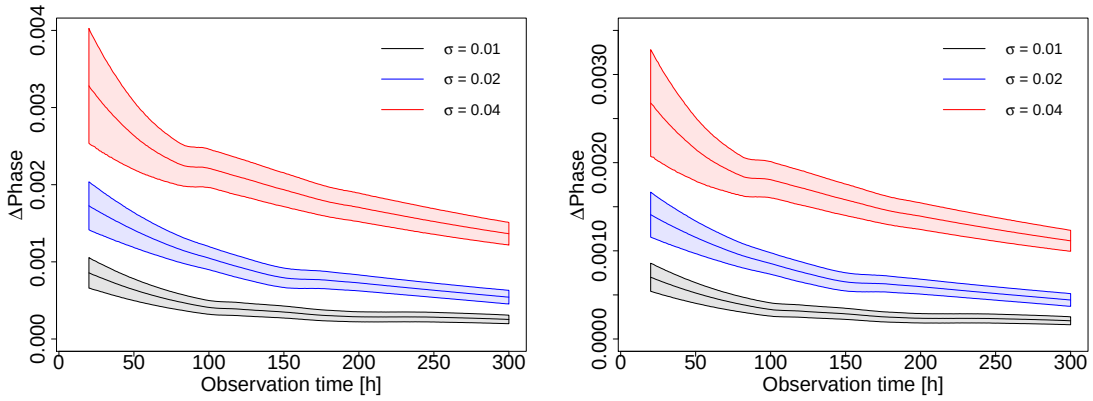

(a) (b)

Figure 4.7: In panel (a), the statistical error in the peak's best-fit position (for different Gaussian peak widths, with the 1σ error region noted). In panel (b), the same for the Gaussian sigma. We smoothed the curves through the interpolation method and computed the 1σ error region by bootstrapping (Efron, 1979) the (simulated) events phases.

becomes visible. The nebula spectrum (of non-thermal origin) has been measured along the entire electromagnetic spectrum, from radio to gamma-rays, and can be described by two components. The former is attributed to synchrotron radiation (see Section 2.3.2) and extends from radio to high-energy gamma-rays. The latter emerges above $\sim$ 1 GeV of energy. It has been interpreted as inverse Compton scattering (see Section 2.3.3) of the same particles against soft background photons (i.e., cosmic microwave background, far-infrared and near-infrared backgrounds, and the synchrotron photons of the nebula itself or Synchrotron-self-Compton, see Section 2.3.4). For a more extensive review of the Crab Nebula, see Bühler and Blandford (2014).

The recent measurements performed by the last generation of IACTs, despite having achieved statistical uncertainties of $\sim$ 5% below 100 GeV (Aleksić et al., 2015), have still not firmly established the spectral shape of the inverse Compton component of the nebula. The more considerable uncertainties arise at the highest energies, above tens of TeV, mainly because of the relatively poor photon statistics and the large systematic uncertainties that the imaging Cherenkov technique suffers at these energies. Nonetheless, the energy interval spanning above few tens of TeV is particularly interesting and still poorly explored. The so-called cutoff region can be related to the maximum energy of the emitting particles and the energy losses and contains essential information on particle acceleration and evolution in the nebula. In the Crab's specific case, the high magnetic field of $\sim$ 100 μG (Kennel & Coroniti, 1984; Meyer et al., 2010; Martín et al., 2012) estimated for the nebula implies that the most energetic parent particles dissipate their energies by

synchrotron radiation losses (see Section 2.3.3). On the one hand, the spectrum steepens at VHEs due to the transition of the inverse Compton mechanism from the Thomson (i.e., $\sqrt{4\epsilon_0 E_e} << m_e c^2$, where E_e is the energy of the electrons and ϵ_0 the one of the photons) to the Klein-Nishina (KN, i.e., $\sqrt{4\epsilon_0 E_e} >> m_e c^2$) regime, which occurs at different energies for the three dominant target photon fields, i.e., the Synchrotron-self-Compton, the far-infrared, and the CMB (Atoyan & Aharonian, 1996). The overall spectral shape is, therefore, determined by the superposition of the three contributions. On the other hand, the energy dependence of the particle diffusion mechanism can also generate possible spectral breaks (Lefa et al., 2012).

At lower energies, i.e., from a few up to hundreds of GeV, the joint analysis of *Fermi*-LAT and MAGIC data from the nebula revealed a rather flat IC peak. These measurements closed the previously existing gap between the observations from space- and ground-based instruments and provided for the first time a complete coverage of the Crab's IC peak. Due to the small uncertainties achieved with the combination of data from both instruments, the peak does not result trivial to reproduce in this energy regime (see Aleksić et al., 2015, for an in-depth discussion). So far, any of the theoretical models proposed fully describe the spectral shape and the morphology observed with high precision, despite the varied prescriptions of the time evolution of the system and particle populations that have been applied (see, e.g., Pacini & Salvati, 1973; Hillas et al., 1998; Aharonian et al., 2004; Meyer et al., 2010; Tanaka & Takahara, 2010; Bucciantini et al., 2010; Torres et al., 2014, and references therein). More detailed studies of the spectral shape of the VHE emission should allow us to finally disentangle both the strength and structure of the magnetic field and the properties of the particle distribution function in the nebula. The characterization of the IC peak for a young (less than a few kyr old) and energetic particle dominated nebula (as Crab) is especially interesting, taking into account that SSC scattering becomes only relevant in these type of nebulae if located within a far-infrared background field with relatively low energy density (Torres et al., 2013).

From an empirical point of view, several analytical models have been proposed to describe the VHE emission from the nebula. Despite currently, it is already clear that there is no trivial mathematical function that can satisfactorily reproduce the whole IC component, from $\sim$ 1 GeV to tens of TeV, there are different approximations that can describe it in reduced intervals of energy. At energies larger than a few hundreds of GeV, i.e., above the IC peak, the emission was fitted first by HEGRA to a simple power-law up to 80 TeV (PL: Aharonian et al., 2004):

$$\frac{dN}{dE} = N_0 \left(\frac{E}{E_0} \right)^{-\alpha} \tag{4.1}$$

More recent descriptions have proposed other characterizations, such as; a power-law with

an exponential cutoff at 14.3 TeV (PLEC-HESS, Aharonian et al., 2006a);

$$\frac{dN}{dE} = N_0 \left(\frac{E}{E_0} \right)^{-\alpha} \exp \left[\left(- \frac{E}{E_{\rm cutoff}} \right) \right] \tag{4.2}$$

or a log-parabola (LP-MAGIC: Aleksić et al., 2015; LP-HESS: Holler et al., 2015, see also Meagher & VERITAS Collaboration, 2015) that (more recently) has been extended up to 100 TeV (HAWC Collaboration et al., 2019).

$$\frac{dN}{dE} = N_0 \left(\frac{E}{E_0} \right)^{-\alpha - \beta \log (E/E_0)} \tag{4.3}$$

It is commonly accepted that the Crab Nebula spectrum exhibits some curvature above 10 TeV. However, the exact position and shape of this spectral break are still under debate.

The nebula's morphology is another aspect of the Crab extensively studied along the entire electromagnetic spectrum. Its extension reflects the interplay between radiation losses and particle transport mechanisms, depending ultimately on the underlying particle population's energy. For an extensive review of the synchrotron component's morphology at different wavelengths, see Hester (2008) and references therein. The morphology of this component shows a clear dependence on the energy window observed. At X-rays, the Crab exhibits a complex structure consisting of a torus and two narrow jets emerging from the direction perpendicular to the torus plane. The nebula's size is energy-dependent as a consequence of the energy losses due to synchrotron burn-off, which limits the particle energy as a function of the distance from the shock, and therefore the size of the nebula.

Contrary to the morphological characteristics of the synchrotron nebula, the IC nebula's morphology is poorly known. The low angular resolution of the gamma-ray telescopes, which is, e.g., of the order of 0.5° for the *Fermi*-LAT detector (at few GeVs) and a few arcminutes for the current generation of IACTs, always limited its study intensely. We expect its extension to be related to the synchrotron nebula's size (since it depends on the same population of synchrotron electrons) and to the photon field's spatial distribution. At energies above 1 GeV, an extension of 0.03° (*Fermi*-LAT Collaboration & Biteau, 2018; Yeung & Horns, 2019) was derived using *Fermi*-LAT data. At higher energies, the nebular shrinking due to synchrotron burn-off (Atoyan & Aharonian, 1996) was finally established by the H.E.S.S. collaboration thanks to advanced analysis techniques, which improved the angular resolution down to 0.05° above 700 GeV. The size (i.e., σ) of the measured Gaussian morphology is $52.2'' \pm 2.9''_{stat} \pm 7.8''_{sys}$ (H.E.S.S. Collaboration, 2020). Such extension is in good agreement with the theoretical expectations, probing for the first time electron energies in the 1-10 TeV range. This electron population is, in fact, responsible for the 0.1 keV synchrotron emission that is inaccessible because of its absorption with the interstellar medium.

Table 4.1: The table below summarizes the spectral models (taken from the literature) used for the Crab Nebula's IC component. The corresponding references, in order of appearance, are Aharonian et al. (2004); Aleksić et al. (2015); Holler et al. (2015); Aharonian et al. (2006a); HAWC Collaboration et al. (2019).

	N_0 $[cm^{-2}s^{-1}TeV^{-1}]$	E_{ref} [TeV]	α	β	E_{cutoff} [TeV]
PL	2.83×10^{-11}	1	2.62	-	-
LP-MAGIC	3.23×10^{-11}	1	2.47	0.104[1]	-
LP-HESS	17.9×10^{-11}	0.521	2.1	0.24	-
PLEC-HESS	3.76×10^{-11}	1.0	2.39	-	14.3
LP-HAWC	2.35×10^{-13}	7.0	2.79	0.1	-

[1] In Alecksić et al. (2015), the log-parabola formula is written with a decimal logarithm. In this work, we used the natural logarithm instead.

4.3.1 Simulations of the Crab Nebula spectral shape

We carried out the nebula simulations with the 3D sky cubes described in Section 3.3.1, centered around the Crab's pulsar position (see the previous section) and using different models to characterize its spectrum and morphology. In particular, Table 4.1 summarizes the spectral models employed to describe the emission from the nebula. These models have been reported by different instruments (i.e., HEGRA, MAGIC, H.E.S.S., and HAWC) and techniques and rely on different functions for the spectral shape's parametrization (i.e., power-law, exponential cutoff power-law, and log-parabola, see Equations 4.1, 4.2, and 4.3, respectively). We next simulated the nebula's morphology following two different approaches. Firstly, a simple 2D Gaussian model sampling different widths to test (in a general approach) the CTA capabilities regarding morphological studies of extended sources. Secondly, a more realistic model depicting the torus-plus-jets structure. We obtained the model from the 2-dimensional MHD simulations of the Crab performed in Volpi et al. (2008), which were kindly provided to us by the authors.

4.3.1.1 Detection significance versus observation time and maximum energy detected

We applied the simulations performed to compute the minimum observation time needed to detect the Crab Nebula (at 5σ significance) in different energy regimes. In particular, it is interesting to look at the highest energy bins ($E > 50$ TeV) considered since these bins span over the energy interval that will allow the definitive discrimination between the different spectral models cited in Table 4.1. For this purpose, we simulated the Crab

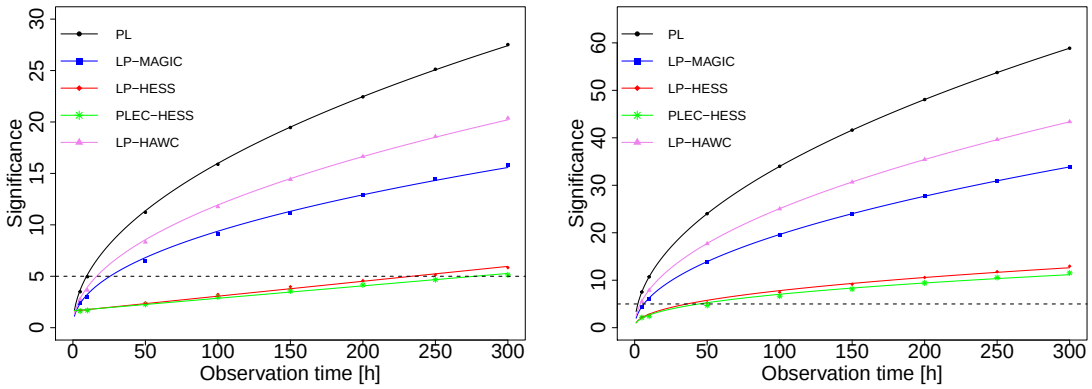

Figure 4.8: The different lines depict the detection significance of the Crab Nebula with the CTA northern (in the left panel) and southern (in right panel) arrays as a function of the observation time for the different assumptions on the spectral shape listed in Table 4.1 (at energies above 50 TeV). The plots correspond to observation times larger than one hour.

Nebula spectrum from 20 GeV up to 300 TeV under the various spectral assumptions listed in Table 4.1. The simulations were performed with GAMMAPY over equally spaced moving intervals of observation time spanning between 3.6 seconds and 300 hours, in steps of increasing width from 10^{-4} to 0.1 hours. We then computed the detection significance for each observation simulation using equation 17 of Li & Ma (1983). We present in Figure 4.8 the results for energies above 50 TeV (in colored points). These are based on 5000 realizations performed for each spectral model and observation time considered and were fitted to a power-law shape (see the colored lines in the cited figure), i.e., $\sigma = \alpha \times t^{\beta}$ (where $\beta \approx 0.5$). Note that the results for the LP-HESS and PLEC-HESS models with the CTA northern array are best-fitted by a simple linear model, possibly, because of their poor statistics in this energy regime.

In Table 4.2, we also show the minimum observation time needed to achieve a mean significance of 5σ (in the observation simulations) for different energy intervals, both with the CTA northern and southern arrays. The results indicate that the Crab Nebula can be detected (at 5σ) in less than 25 seconds for either model from Table 4.1 in the most sensitive among the computed bins $[0.1 - 1]$ TeV. Note also that at the highest energies ($E > 50$ TeV) explored, the results are strongly model-dependent, reflecting the poor knowledge we have on the nebula spectrum in this energy regime. However, note that the emission from the Crab was detected with the CTA northern array at energies above 50 TeV (at 5σ) within the observation time range considered for all the models, even though this energy regime is far from the CTA best performance energy range (i.e., approximately from 2 TeV to 10 TeV). CTA, then, is expected to set strong constraints on the nebula's

Table 4.2: In the tables below, we summarize the minimum observation time (in hours) needed to detect the Crab Nebula (at 5σ) in various energy ranges and under different assumptions for the spectral model. We considered the spectral models listed in Table 4.1. The upper part of the table corresponds to the CTA northern array, whereas the bottom part is for the southern one.

Energy [TeV]	PL	LP-HAWC	LP-MAGIC	LP-HESS	PLEC-HESS
E < 0.1	0.027	0.40	0.37	3.8	0.059
0.1 < E < 1	0.0053	0.0037	0.0056	0.007	0.0046
E > 5	0.16	0.13	0.17	0.22	0.15
E > 50	10.1	18.4	30.3	233	298

Energy [TeV]	PL	LP-HAWC	LP-MAGIC	LP-HESS	PLEC-HESS
E < 0.1	0.0046	0.061	0.056	0.57	0.01
0.1 < E < 1	0.0014	0.0023	0.0024	0.0028	0.0016
E > 5	0.046	0.037	0.05	0.064	0.042
E > 50	2.2	4.1	6.8	46	57

emission at the highest energies currently observed in the Crab. The observations from the southern array imply large zenith angles. On the contrary, the Crab culminates almost at the zenith for the northern site, thus being observable at small zenith angles, which guarantees the lowest energy threshold possible. For this reason, we have considered the IRFs for the northern and southern sites at 20° and 60° zenith angle, respectively.

The highest energy bin containing a 5σ signal in 300 hours extends up to $E \approx 60$ TeV for the PLEC-HESS and $E \approx 100$ TeV for the LP-MAGIC and the LP-HAWC assumptions. To further explore our simulation scheme performance, we tried observational times greater than 300 hours, i.e., up to 500 hours in steps of 100 hours. Still, we did not reach a 5σ detection above 115 TeV for any observation time considered.

4.3.1.2 Characterization of the spectral shape

An interesting result arising from the analysis of the simulations performed is whether CTA can disentangle the different mathematical approximations listed in Table 4.1 or not. To estimate the capabilities of CTA to distinguish the various assumptions on the nebula spectral shape, we computed the expected distribution of the excess events in energy bins for each of the considered spectral models and 50 hours of observations (see Figure 4.9). To evaluate the statistical uncertainties in the excess calculation, we simulated each of the spectral models 5×10^3 times, and from these distributions, the mean and deviance were obtained. We then compared the distributions in pairs using a chi-square

test ($\chi^2 = \sum_i (M_i - m_i)^2/m_i$, where M_i and m_i are the numbers of events observed for each of the models being compared in the i^{th} energy bin). When we compare the distributions obtained in the whole energy range, the supposition that two distributions resulting from two different hypotheses can be compatible is rejected in all cases (with the chi-square test at 95% CL). It is mainly due to the differences of the hypotheses in the lower energy range. Still, even when considering only the cutoff region, i.e., above 8 TeV, it is possible to discriminate between LP-MAGIC and PLEC-HESS at 95% CL in 50 hours of observation time. The LP-MAGIC, LP-HAWC, and LP-HESS models were also differentiated among them above 8 TeV of energy. Furthermore, at energies above 50 TeV, the HESS-PLEC model was distinguished from both MAGIC and HAWC log-parabolas (and vice versa) because of the distinctive suppression of the emission of the HESS-PLEC model above the cutoff energy.

We also applied to the (simulated) sky cubes a different approach to probe the discrimination between the various characterizations of the spectral shape described above. It consisted of fitting the data obtained for the LP-MAGIC assumption with 50 hours of observation time to each of the spectral models listed in Table 4.1 (i.e., log-parabola, simple power-law, and power-law with an exponential cutoff). The model's free parameters (for each spectral shape fitted to the data) are all except for the energy of reference (fixed to 1 TeV). The most energetic bin of the simulated sky cubes at which we still detect the source spanned from 50 TeV to 80 TeV (at 5σ significance, or from 80 TeV to 125 TeV at 3σ). For instance, the best-fit log-parabola model corresponded to a differential flux (at the reference energy) of $\mathrm{N_0} = (3.216 \pm 0.016) \times 10^{-11} \mathrm{cm^{-2} s^{-1} TeV^{-1}}$, with $\alpha = 2.471 \pm 0.004$ and $\beta = 0.1038 \pm 0.0019$ (accounting only for statistical errors). We can compare the values obtained with those of $\mathrm{LP-MAGIC}$ in Table 4.1 to verify the noticeable agreement between the spectral fitting and the input model. Performing the same kind of simulations for the rest of the assumptions regarding the nebula spectral shape, we obtained similar statistical errors, i.e., $0.5\% - 1\%$ for $\mathrm{N_0}$, $0.1\% - 0.5\%$ for α, $1\% - 2\%$ for β, and $\sim 5\%$ for E_{cutoff}. Then, as we expected for such a bright source, the principal source of uncertainties should actually come from systematic errors. Hence, to take this into account, we added fiducial systematic uncertainties for the energy scale and flux (in quadrature to the statistical error, see Section 3.2.3).

To include the systematic errors in the Crab Nebula studies (given the spectral models considered), we first simulate the spectrum taking into account only statistical errors by performing 1D analysis fitting over the simulated data, i.e., after the convolution of the analytical models with the CTA IRFs. Then, we compute the expected flux for each bin of energy simulated (with GAMMAPY) and smear it by adding (quadratically) the systematic errors to the statistical ones. We already accounted for the systematic error on the energy scale (see Section 3.2.3.1) before smearing the expected flux in each energy bin. To include

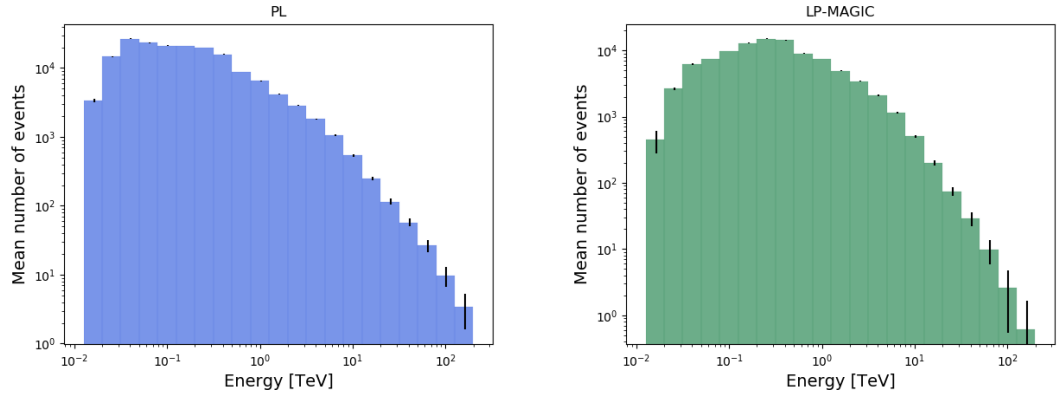

(a)

(b)

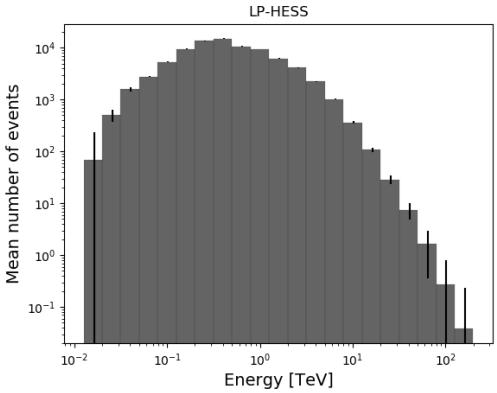

(c)

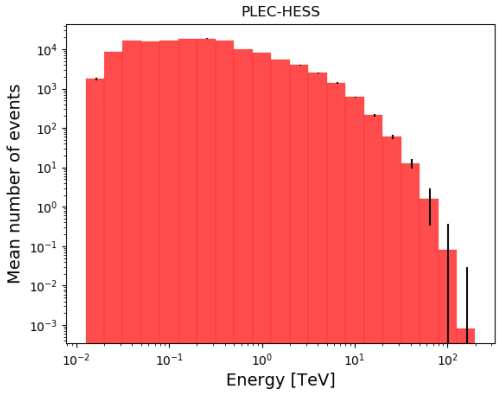

(d)

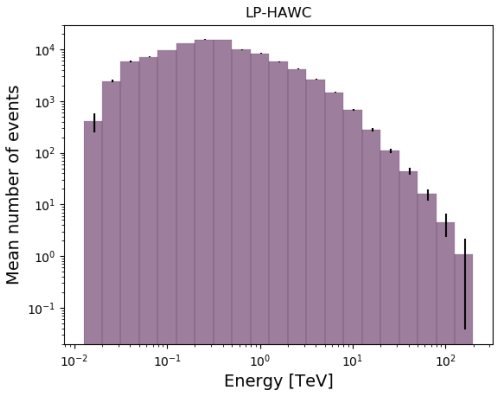

(e)

Figure 4.9: The different histograms above depict the average number of (excess) events obtained in discrete energy bins for the Crab Nebula simulations (according to the different assumptions for the spectral shape in Table 4.1) with the CTA northern array and 50 hours of observation time.

Table 4.3: On the left, a summary of the systematic errors applied. On the right, resulting AIC values for the different characterizations fitted to the LP-MAGIC model simulations.

	Syst. (%)	0.5 × Syst.	AIC	LP	PL	PLEC
Flux	10	5	Syst.	33.7	84.4	190.2
E_0	4	2	0.5 × Syst.	33.0	126.2	461.2

it, we allowed the energy scale to fluctuate according to a 4% of systematic error, as discussed in the cited section. Finally, we refit the new spectral points, in which both the statistical error and the systematic ones are included, and we use these results as input for the discrimination tests. Additionally, we have considered a factor 2 improvement over the fiducial requirements for the systematic errors to explore the optimal capabilities of CTA in more detail. The left part of Table 4.3 summarizes the systematic errors employed.

To compare the different characterizations fitted to the LP-MAGIC model simulations, we used the Akaike's Information Criterion (AIC, see Burnham & Anderson, 2004). The AIC statistic for each of the fitted models is given by $AIC = 2k - 2\log(L)$, where k is the number of (free) parameters of the model and $\log(L)$ is its log-likelihood. Note that the exact value of the AIC statistic does not evaluate (by itself) the goodness of the fitted model. However, by comparing the different AIC values, we can rank the models by the goodness of fit, being the model with the lowest AIC, which best represents the data. This test is applied to compare non-nested models, which is our case given the varied spectral shapes considered.

The right part of Table 4.3 lists the resulting AIC values for the log-parabola (LP, which best represents the data), power-law (PL), and power-law with an exponential cutoff (PLEC) best-fit models (taking into account the systematical errors and the mentioned improvement for the same). To obtain an equal value of the systematic and statistical error for a source like the Crab Nebula, we had indeed to tighten the systematic errors requirements to be smaller than $\approx 0.2\%$ in the energy scale and flux (reaching $\approx 1.5 \times 10^{-13}$ cm^{-2} s^{-1} TeV^{-1} of systematic uncertainty for the differential flux at 1 TeV), which is unlikely to happen.

4.3.1.3 Cutoff energy

Another interesting result from the analysis of the simulations performed is the lower limit on the cutoff energy computed as a function of the observation time. We could estimate it from the simulations of a power-law input spectral model. We used the same index (α) and differential flux (N_0) of the LP-MAGIC assumption for different observation times, spanning from 8 to 300 hours, and performing 10^5 realizations for each observation time.

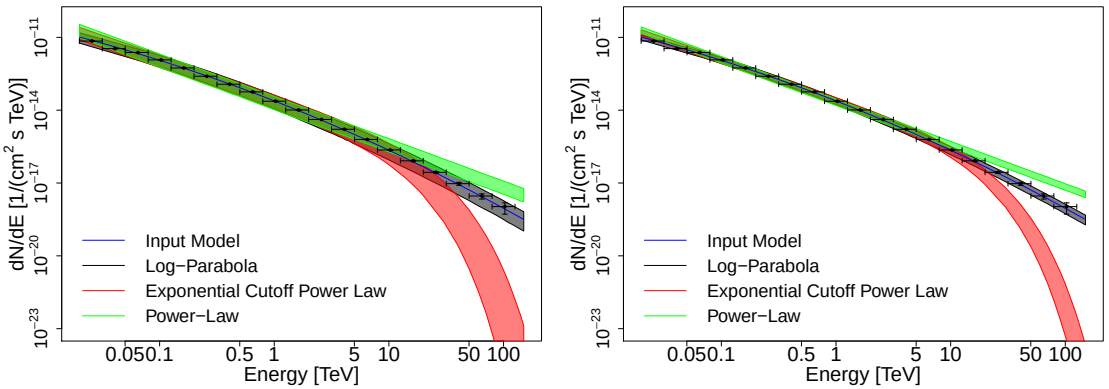

Figure 4.10: Result of fitting all the spectral shapes considered to the nebula simulations with the LP-MAGIC model (see Table 4.1), with the 3σ error region noted. On the left, the results under the assumption of the systematic error requirements in Section 3.2.3. On the right, we improved the systematic uncertainty by a factor 2. The plots were taken from Mestre et al. (2020).

Then, we fitted a power-law with an exponential cutoff function to the simulations and computed the lower limit of the cutoff energy (at 95% CL).

Figure 4.11 illustrates the results. Note that, according to the simulations performed, CTA will probe the presence of a feature like an energy cutoff in the nebula spectrum, at energies of tens of TeV, in a modest observation time (i.e., in less than 50 hours). The Crab Nebula spectrum, measured by LHAASO-KM2A (Aharonian et al., 2021), HAWC (Abeysekara et al., 2019), and Tibet (Amenomori et al., 2019) air-shower detectors up to more than 100 TeV, does not show evidence of an exponential cutoff below the mentioned energy. Hence, in light of the previous result, it will be possible to compare these air-shower detectors observations with CTA measurements even in an early stage of the CTA operations.

4.3.1.4 Shape of the cutoff region

Let's suppose now, however, that using CTA data, a power-law with an exponential cutoff could finally describe the nebula spectrum, rejecting the rest of the cited characterizations. The most relevant question that would arise, in this case, is whether the shape of the cutoff region can be well established. For this reason, we are also interested in probing the CTA capabilities to discern the cutoff shape (once we assumed that an energy cutoff exists). We considered, then, the following modified power-law with exponential cutoff function:

$$\frac{dN}{dE} = N_0 \left(\frac{E}{E_0}\right)^{-\alpha} \exp\left[-\left(\frac{E}{E_{\text{cutoff}}}\right)^{k}\right] \tag{4.4}$$

In the equation above, different values of k can reflect either the energy-dependence of

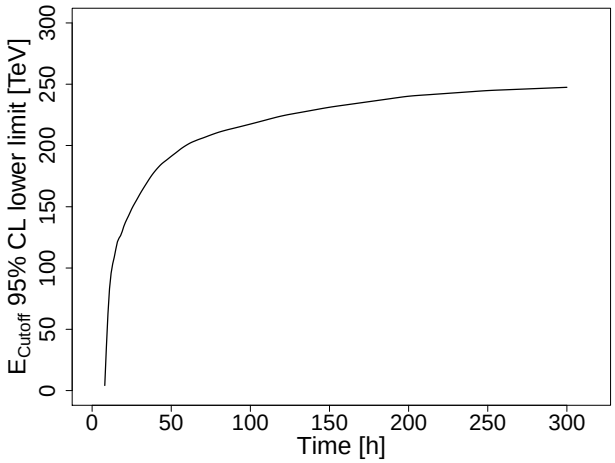

Figure 4.11: The black line depicts the energy cutoff lower limit at 95% CL for different observation times. The plot was taken from Mestre et al. (2020).

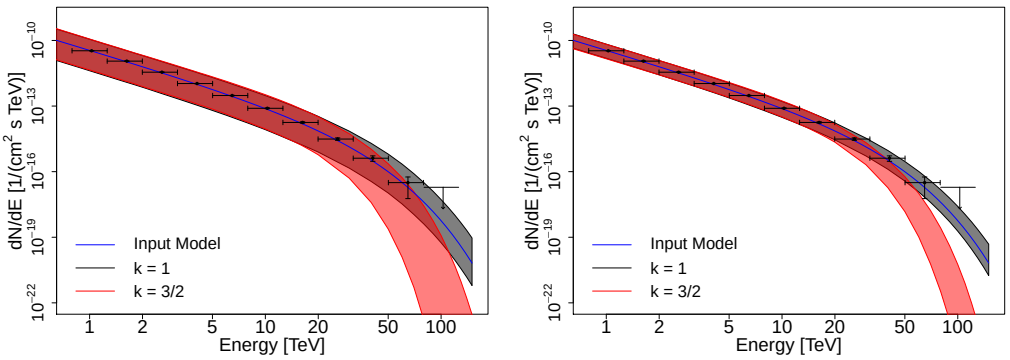

Figure 4.12: The panels represent the CTA capabilities to disentangle between different shapes of an exponential spectral cutoff, i.e., different values of k, as defined in Equation 4.4. In particular, we show the cases $k = 1$ and $k = 3/2$. The shaded area represents the systematical and statistical errors, quadratically added. On the left, we calculated the errors using the systematic error requirements, whereas, on the right, we used the systematic errors reduced by a factor 2. The plots were taken from Mestre et al. (2020).

the particle propagation mechanisms with, e.g., $k = 1/3$, $3/11$, $1/4$, and $1/5$ corresponding with the Bohm, Kraichnan, Kolmogorov, and hard-sphere turbulence spectral models (in Thomson regime), respectively (as explained in Romoli et al., 2017), or the transition from the Thomson to the Klein-Nishina region of the inverse Compton mechanism. In the specific case of IC scattering of synchrotron photons in the KN regime, which is the dominant regime in the Crab Nebula, Lefa et al. (2012) computed the following possibilities: $k = 3/2$, $5/3$, 2, 3 (corresponding, in this regime, to the same electron cutoff shape, i.e., $k = \beta_e$, see Table 1 of the cited paper).

We now suppose, as a primary hypothesis for the simulations, the PLEC-HESS spectral model, i.e., the $k = 1$ specific case in Equation 4.4 (with the PLEC-HESS parameters listed in Table 4.1). Note that we can consider it as a somewhat optimistic case since recent results by MAGIC (Aleksić et al., 2015), H.E.S.S. (Holler et al., 2015), and HAWC (HAWC Collaboration et al., 2019) indicate that the spectral break should occur at higher energies, where the statistics become more and more an issue. Then, we simulated a power-law with an exponential cutoff spectrum following the mentioned assumption (for 50 hours of observation time) and fitted the results with Equation 4.4 and $k = 1$, $3/2$, $5/3$, 2, 3. We ranked the fitted models through the AIC statistic computed for each fitting function, as in the previous case. The different cutoff shapes were compared to the $k = 1$ case, taking the AIC the values of 34.6, 52.7, 79.6, and 196.31, with $k = 1$, $3/2$, $5/3$, and 2, respectively (while for $k = 3$, the AIC resulted in more than 200). The AICs computed were always positive and indicate that it is possible to disentangle between an exponential and a super-exponential cutoff shape with a minimum k value of $3/2$ (see Figure 4.12). We also simulated the various models previously compared to the $k = 1$ case (Equation 4.4), comparing them later against each other. The results show that it would be possible to discriminate within the super-exponential cutoffs considered, even when including systematic uncertainties. Concretely, the smallest difference in the β parameter that could be distinguished (at 95% CL) from the $\beta = 1$ model, with the observation time and systematic error improvement considered, was $\Delta\beta \approx 0.2$.

4.3.2 Simulations of the Crab Nebula morphology

The size of the nebula, as previously discussed, depends on the energy window considered. Empirically, Ku et al. (1976) suggested the energy-dependent size (from optical to X-rays) along the NW-SE direction of the Crab Nebula to be proportional to $\mathrm{E}^{-0.148}$. For instance, the size at energies of 0.5 - 8 keV measured by Chandra observatory is about $2'$ (Dubner et al., 2017). Although the current spatial resolution of the IACTs at VHEs is limited to a few arcminutes, the Crab Nebula's extension was measured for the first time above $\mathrm{E} > 0.7$ TeV, and a radius of $\approx 0.015°$, assuming a Gaussian source shape, was established with advanced techniques based on a very precise knowledge of the instrument point spread

function (H.E.S.S. Collaboration, 2020).

This section will present our studies regarding the prospects to measure the nebular shrinking at increasing energies with CTA. In particular, we are first interested in determining the maximum energy at which CTA can significantly resolve the Crab. We will also discuss the capabilities of CTA to detect a possible asymmetry in the morphology of the Crab. We expect the Crab Nebula to exhibit (at TeV energies) the jet-torus structure revealed by *Chandra* (see Volpi et al., 2008), and despite the arcsecond resolution of the X-ray detectors is undoubtedly beyond the CTA performance, such a complex structure can translate on a measurable asymmetry in the two spatial dimensions.

4.3.2.1 Minimum size resolvable versus energy

For all simulations performed in this section, we accounted for 50 hours of observation time, and we assumed a spectral shape following the prescription of the LP-MAGIC model. We studied the capabilities of CTA to resolve the extension of the Crab Nebula through GAMMAPY 3D sky cubes simulations, assuming a 2D projected spherical source and the LP-MAGIC spectral model. We varied the sphere radius from 0.004° (being the smallest value of size per bin considered in the simulated sky cubes of 0.002°/bin) to 0.03° in steps of 0.002° for fourteen different integral energy bins of lower energy bounds equally spaced in a log-scale spanning from 50 GeV to 50 TeV and a fixed upper bound of 300 TeV. The PSF was assumed to be Gaussian-shaped with a 68% containment radius taken from the CTA IRFs. After the convolution of the energy-binned sky cubes with the corresponding PSF, we fit the resulting (stacked 2D) data with a projected 2D sphere convolved with the PSF, using the SHERPA tool. Then, we called the minimum resolvable radius at a given energy bin to the smallest radius of the source for which the fitted size is significantly larger than zero (at 3σ significance) and compatible with the input radius (at 95% CL). We show the minimum resolvable radius in Figure 4.13 (see the left panel), reflecting both the effect of the PSF and the spectral shape. The cross and dot mark, respectively, the Crab Nebula's extension as measured with *Fermi*-LAT and H.E.S.S. The results show that CTA will resolve the Crab Nebula at a large energy range, from tens of GeV to TeV energies. The right panel of Figure 4.13 depicts the retrieved size for the simulated sky cubes against the model's input size. Hence, the plot represents the goodness of the extension fitting method followed in this work.

4.3.2.2 Morphological studies using a realistic template from a MHD simulation

To prove the CTA capabilities to detect asymmetries in the Crab Nebula's morphology at different energies, we needed a more realistic approach to the nebula's morphological properties at VHEs than the 2D Gaussian model described above. Therefore, we used

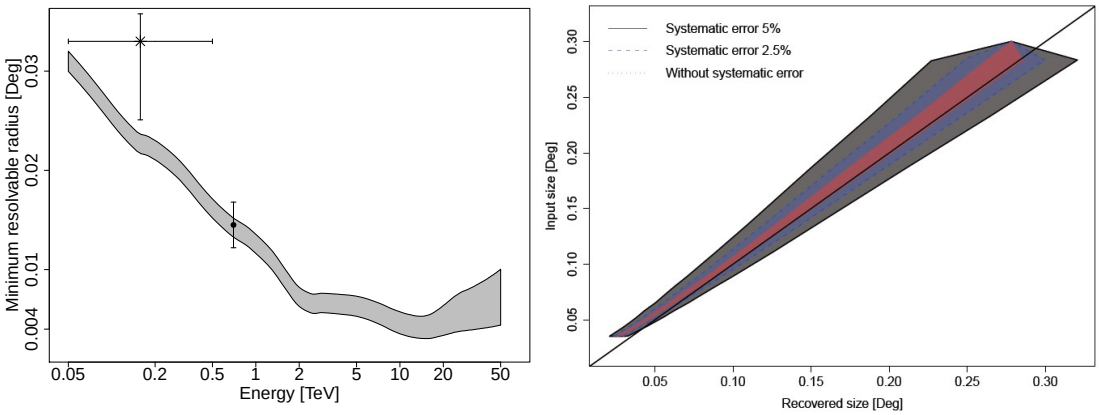

Figure 4.13: On the left, we represent the minimum size resolvable (in the simulations) versus the lower energy bound of the energy interval simulated (we permanently fixed the upper bound to 300 TeV), using the CTA IRFs, with the 1σ error region noted. We added the Crab Nebula's measured size with H.E.S.S. for energies above 0.7 TeV (black dot) and the one measured from 5 GeV to 500 GeV with *Fermi* (black star) with the 1σ error bars for comparison. On the right, the measured extension versus the input size for the simulations. The plot on the left was taken from Mestre et al. (2020).

a spatial template for simulating the Crab at TeV energies. In particular, we employed the synthetic surface brightness map at 1 TeV resulting from the 2-dimensional MHD simulations of the Crab described in Volpi et al. (2008), see Figure 4.14a. The simulations were carried out with CTOOLS, importing the 2D fits image provided by the authors of the cited work and the CTA northern array full system requirements for the angular resolution, which are in good agreement with the angular resolution provided by the version of the IRFs used in the previous analysis.

Figure 4.14b shows the resulting sky map for 100 h of observation time and an energy range spanning from 0.7 TeV to 100 TeV. To test the (simulated) events map's asymmetry, we performed 2D SHERPA morphological fittings, comparing the results obtained using both symmetric and asymmetric 2D Gaussian models. In the first case, we obtained a reconstructed size of $(0.017(8) \pm 0.0002)^\circ$ (accounting only for statistical errors), which is in agreement (at 95% CL) with the extension reported by H.E.S.S. (if taking into account the systematical error of the same, $0.0145^\circ \pm 0.0008^\circ_{stat} \pm 0.0022^\circ_{sys}$). The Test Statistic favors the asymmetric function ($\sqrt{\mathrm{TS}} \simeq 21$), with a σ_x of $(0.021(1) \pm 0.0002)^\circ$ and a σ_y of $(0.013(8) \pm 0.0003)^\circ$ along the major and minor semi-axes. The result implies that a significant (at 95% CL) asymmetry of $\sigma_x/\sigma_y \sim 1.53 \pm 0.18$ is observed.

To conclude, for illustrative purposes, we artificially improved the angular resolution by a factor of five to show that, in this case, the jet-torus structure can be easily established (see Figure 4.14c). A hint of the torus shape is indeed already visible with a factor

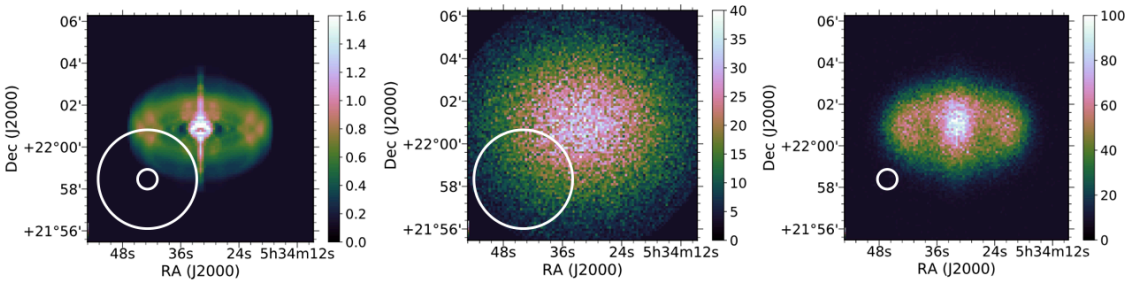

Figure 4.14: (a) Morphological template used for the jet-torus scenario. The white circles represent the PSF one sigma for the full system requirements (of approximately 0.04° for the energy bin spanning from 0.8 TeV to 1.25 TeV), and the same improved by a factor of five (i.e., 0.008° referred to the same energy bin). It is a surface-brightness map in units of erg $\mathrm{cm}^{-2}\mathrm{sr}^{-1}\mathrm{s}^{-1}\mathrm{Hz}^{-1}$. (b) Observation simulation of 100 hours with the CTA full system requirements for the angular resolution plotted with the corresponding PSF (white circle) in counts (after background subtraction). (c) Observation simulation as in (b), but with the angular resolution improved by a factor of five (exceeding by far the current CTA system requirements), again with the corresponding PSF depicted. The plots were taken from Mestre et al. (2020).

four of improvement. However, the spatial resolution implied in both cases is surely not achievable with CTA. In any case, this unrealistic improvement of the CTA expected spatial resolution would improve the error in the reconstructed major and minor semi-axis (σ_{x} and σ_{y}, for an asymmetric Gaussian fit) by a factor of ~ 6, retrieving an asymmetry of $\sigma_x/\sigma_y \sim 1.31 \pm 0.03$.

4.4 The flares in Crab

The apparent (long-term) stability of the flux from the Crab has motivated current and future IACTs, as CTA, to use observations from the bright nebula to characterize their instrument's performance within the science verification period. However, spaceborne gamma-ray instruments detected several flares of different magnitude during the last decade. In particular, *Fermi*-LAT and AGILE (Abdo et al., 2011a; Tavani et al., 2011; Buehler et al., 2012; Ojha et al., 2013; Mayer et al., 2013; Striani et al., 2013; Arakawa et al., 2020) detected the flares in the high-energy regime (HE, i.e., $\geq$ 100 MeV) with variability timescales of hours (Abdo et al., 2011a; Tavani et al., 2011; Balbo et al., 2011). The flaring activity observed is characterized by rapid flux variations from the nebula and vast amounts of energy released. For instance, during the April 2011 flare, first detected by *Fermi*-LAT (Buehler et al., 2011; 2012) and later confirmed by AGILE (Striani et

al., 2011), the nebula doubled its high-energy flux level (compared to the usual one or steady-state) in less than 8 hours.

The most luminous gamma-ray flare detected so far in the Crab Nebula occurred in April 2011 (Striani et al., 2011; Buehler et al., 2012) and lasted nine days. The photon flux of the nebula reached a peak during the flare of $(186 \pm 6) \times 10^{-7}$ cm^{-2}s^{-1} above 100 MeV. The latter implies an enhancement of approximately a factor 30 (in flux) over the nebula's average emission. At short timescales, the gamma-ray flares from the Crab have shown complex substructures, particularly sub-flares lasting only a few hours. For instance, during the April 2011 flare, two sub-peaks centered around the dates 55665 and 55667 (in MJD) were detected, both with a doubling timescale (t_{var}) smaller than 8 hours. It means, applying causality arguments, that the emission region must be compact (i.e., smaller than $c \times t_{var} \sim 2.8 \times 10^{-4}$ pc in size). The flare spectral energy distribution had a distinctive narrow shape, peaking at an energy of $E_{peak} \simeq 400$ MeV.

Fermi-LAT (Ojha et al., 2013; Mayer et al., 2013) and AGILE (Striani et al., 2013) reported a more moderated-flux flare in the Crab in March 4, 2013. In this case, the peak photon flux of the synchrotron emission for energies above 100 MeV was $(103.4 \pm 0.8) \times 10^{-7}$ cm^{-2}s^{-1}, i.e., about 17 times above the steady component's level. The flare lasted for approximately two weeks, and the observations indicated variability on timescales of ~ 5 hours, which results in an emission region size $\lesssim 1.7 \times 10^{-4}$ pc (Mayer et al., 2013). Interestingly, the spectrum peaked at $\sim$ 400 MeV at the time of the highest flux, as in the April 2011 flare. A multi-wavelength observing campaign was carried out with different instruments, providing the opportunity to study the emission during the flaring state at multiple energy windows, from infrared to X-rays (Mayer et al., 2013), and in the VHE regime (Aliu et al., 2014; H.E.S.S. Collaboration et al., 2014). Furthermore, blind searches of flares in Crab have been performed, e.g., by the ARGO-YBJ air-shower detector, reporting no significant excess of events during the 2011 and 2013 flares (Bartoli et al., 2015). The observations conducted with VERITAS and H.E.S.S. the following days after the 2013 flare reported no significant changes in the nebula's steady flux (at energies above 1 TeV). Both observations result in similar upper limits to the integral flux variability when considering systematical and statistical errors, i.e., $\sim 55-65\%$ of integral flux enhancement (at 95% CL). Table 4.4 summarizes the properties of the 2011 and 2013 flares. Buhler and Blandford (2014) presented an excellent review of the different flares detected up to September 2013.

The characteristics of the flares previously highlighted, i.e., the rapid variability observed and the energy range in which the flares are detected, suggest that the flaring activity is a phenomenon associated with fast variation of magnetic fields and/or compact regions. However, note that these two ingredients do not promote a rapid variation in the inverse Compton component that should emerge at TeV energies (Horns &

Table 4.4: We summarize below the properties of the 2011 and 2013 flares, obtained from Buehler et al. (2012), Mayer et al. (2013), and H.E.S.S. Collaboration et al. (2014).

Flare	Duration [days]	Flux ($E > 100$ MeV) [$\times 10^{-7}$ cm^{-2} s^{-1}]	t_{var} [h]	E_{peak} [MeV]
2011	~ 9	186 ± 6	$\lesssim 8$	375 ± 26
2013	~ 14	103.4 ± 0.8	~ 5	484^{+409}_{-166}

Aharonian, 2004), at least at a detectable level with the current generation of Cherenkov telescope arrays. Despite the considerable effort done to follow those flares in several multi-wavelength campaigns (Weisskopf et al., 2013; H.E.S.S. Collaboration et al., 2014), no significant correlation between spectral and/or morphological variations of the nebula and the flares observed at hundreds of MeV has been found. Further hints that could shed light on the mechanisms underlying the flares observed remain still elusive.

On the one hand, the GeV regime can be explored by current and future IACTs, as CTA, with great sensitivity. On the other hand, the detection of transients, like the Crab flares, is included in one of the known as Key Science Programs (KSPs) of the Cherenkov Telescope Array (Acharya et al., 2013), which comprises both fast response to external alerts (i.e., sent by other observatories at different wavelengths) and a design of the telescopes optimized for rapid movement. However, the different theoretical models put forward (so far) to explain the characteristics of the flaring emission led to different flux level predictions in the different energy regimes. Hence, we might consider in this work a broad range in flux for possible counterparts of the Crab flares at tens of GeV and TeV energies.

In this section, we will discuss the capabilities of CTA to constrain the contribution of the flares in the GeV and TeV regimes. For that purpose, we carried out (a large number of) simulations to reproduce the ~ 400 MeV emission of the flares detected by gamma-ray satellites and derive the expected emission in the VHE regime. We computed the simulations under different assumptions regarding the magnetic and photon fields (in the nebula) and the parent particle population's spectral energy distribution. The comparison between the CTA simulated data and previous IACTs observations from H.E.S.S. (H.E.S.S. Collaboration et al., 2014) resulted in constraints on the physical parameters ruling the flare emission. We will discuss these results in the present Chapter.

4.4.1 Simulations of the Crab flares

4.4.1.1 Setup of the simulations

As we have discussed, the nebula's broad-band spectrum consists of a wide synchrotron component and a narrow inverse Compton peak, and we expect synchrotron radiation to be the dominant channel in which particles cool down. Therefore, the radiation observed critically depends on the magnetic field's strength, which on average is well-constrained through the nebula's multi-wavelength properties ($\bar{B} \sim 120$ μG, see, e.g., Atoyan & Aharonian, 1996; Hillas et al., 1998; Martín et al., 2012; Khangulyan et al., 2020b). However, the flares might originate in some locations of the nebula where the magnetic field can deviate strongly from the average one (see, e.g., Kennel & Coroniti, 1984; Hester et al., 1995; Lyubarsky, 2012; Porth et al., 2014) and by parent particle populations of very different spectral indices. The spectral indices observed in the Crab flares, showing a large variability from flare to flare, support the last statement (Buhler & Blandford, 2014; Arakawa et al., 2020) indeed.

The inverse Compton component emerges from high-energy electrons upscattering several photon targets, i.e., the cosmic microwave background, far-infrared, near-infrared photon background fields, and the synchrotron emission, which is believed to dominate the total gamma-ray emission of the nebula. Hence, to simulate this component, the mentioned photon fields must be characterized. The FIR background is (typically) attributed to an isotropic photon field emitted by dust at a temperature of 70 K with an energy density of 0.5 eV/cm^3 (Marsden et al., 1984). The NIR background photon field is described for starlight with a temperature of 5000 K and an energy density of 1 eV/cm^3 instead (Atoyan & Aharonian, 1996). These background fields can be approximated as diluted Planckian distributions, and the corresponding emission spectra can be obtained based on an approximate treatment (see Khangulyan et al., 2014). The Synchrotron-self-Compton component, however, depends on the emission region's size. For the entire nebula, with a radius of $R_{syn} \sim 1.5$ pc, the total energy density provided by the synchrotron photons amounts to $\omega_{SSC} \simeq 2$ eV/cm^3 (see Mestre et al., 2021) for a total luminosity (of the nebula) in the synchrotron regime of $\mathrm{L_{syn}} \sim 10^{37}$ erg s^{-1} (see Table 1 in Aharonian et al., 1997b). Nonetheless, the fast variability observed on the flares limits the emission region's size (due to causality arguments, as we have already seen) to $c \times t_{var}$, where t_{var} is the flare duration.

The main goals behind the analysis of the simulations that we will present (in this section) are to evaluate the prospects of CTA for the detection of (short timescale) variability in the Crab Nebula and to explore the constraints that CTA can impose on the properties of the population of electrons behind the Crab flares. For this purpose, we first fitted the 2011 and 2013 flares spectra assuming the classical synchrotron emission

(see Section 2.3.2) as coded in the NAIMA PYTHON package (Zabalza, 2015) and computed the corresponding inverse Compton emission (Section 2.3.3) for different realizations of the magnetic field strength. Then, we convolved the synchrotron tail and IC components with the CTA response, including the expected emission from the nebula, and derived the sensitivity of CTA for the different electron populations compatible with the flare emission observed.

To account for the uncertainties discussed above on the particle population originating the flares, we performed the simulations considering a broad range of indices for the particle spectrum, i.e., $\Gamma_{\rm e} = [1 - 3]$. These have been associated with non-thermal acceleration processes, see, e.g., Longair's book (1981). Also, to calculate the corresponding synchrotron emission, we probed magnetic field intensities ranging from a few μG to mG. We aim at covering any particular region of the nebula in which the flares might occur. Likewise, we calculated the IC part using the CMB and IR photon targets. Similarly, we obtained the SSC contribution in a region of a size $c \times t_{var}$, i.e., related, by causality arguments, with the variability timescale of each particular flare considered. Note that the space of parameters is also, a priori, limited by the total energy budget stored in the nebula. We estimated it as the product of the nebula luminosity in gamma-rays ($L_\gamma \sim 2 \times 10^{35}$ erg s^{-1}, see Rudak & Dyks, 1998) and the synchrotron cooling time (τ_{syn}) for the electrons (with energy E_e) in the nebula:

$$\tau_{syn} L_\gamma = \frac{3 m_e^4 c^7}{2e^4} E_{\rm e}^{-1} B^{-2} \sim 5 \times 10^{43} (B/100\,\mu{\rm G})^{-2} \text{ erg} \tag{4.5}$$

Note, however, that this energy limit does not account for processes that may re-accelerate the particles in the emission region, resulting in additional boosts of energy. We particularized the simulations for two types of flares with different characteristics, i.e., very bright flares similar, at hundreds of MeV, to the one observed by *Fermi*-LAT in April 2011, and flares of more moderated-flux resembling (at LAT energies) the one detected in March 2013.

We assumed for this work that the electron particle distribution generating the observed flares can be well characterized by a power-law with an exponential cutoff distribution (see Equation 4.2). The magnetic field (B) and the particle index ($\Gamma_{\rm e}$) are the only free parameters considered to derive the resulting spectral energy distribution of synchrotron radiation from the electron population. The rest of the relevant parameters, i.e., the maximum energy reached, the amplitude of the gamma-ray spectrum (determined by the amplitude of the electron particle distribution, N_0), and the particle spectrum cutoff energy, are obtained from fitting the spectrum at hundreds of MeV to the different data sets employed, in particular, the LAT measurements of the April 2011 and March 2013 flares. We obtained the best-fit amplitude ($\rm N_0$) and cutoff energy (E_p), for a given electron index and magnetic field, through a log-likelihood optimization method implemented using

the open-source software NAIMA (Zabalza, 2015).

We considered Γ_e ranging from 1 to 3 (as discussed above) with linearly spaced steps of 0.1 and 14 bins of magnetic field ranging from 10 μG to 5 mG. Concretely, we consider the following values of B, 10 μG, 100 μG, and 1 mG, plus 11 values logarithmically spaced from 50 μG to 5 mG. Note that both very low (10 μG) and very large (few mG) magnetic fields are difficult to justify in standard pulsar wind nebula theory. However, on the one hand, we are interested in probing the performance of the simulations over the largest space of parameters possible. On the other hand, it guarantees that all possible hypotheses on the emission location can, in principle, be compared with the results. Note that, e.g., magnetic fields of the order of $[1-5]$ mG have been obtained for small-scale structures near the termination shock if considering equipartition between the magnetic and particle energy densities (see Hester et al., 1995). However, we will mainly focus on discussing the results with $B > 50$ μG.

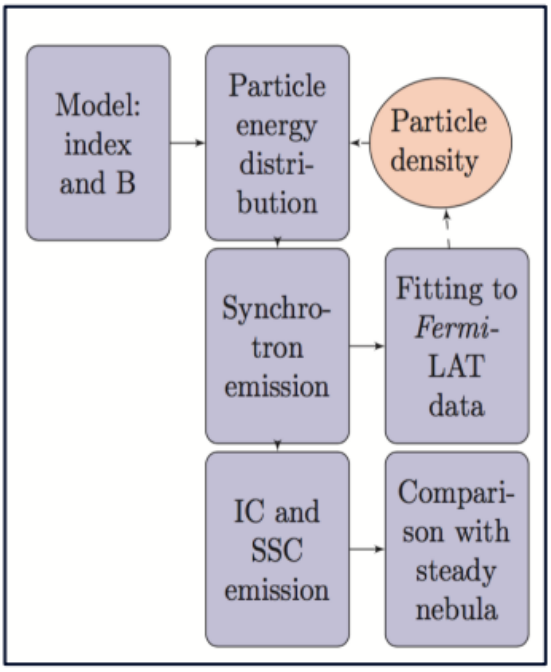

Figure 4.15: Schematic summary of the flare simulations workflow.

We compute the synchrotron emission using the NAIMA PYTHON package, according to the approximation of the synchrotron emissivity in a random magnetic field in Aharonian et al. (2010), and choosing an electron energy threshold of 50 GeV. Once we calculate the amplitude and cutoff energy of the particle energy distribution from LAT data, we obtain the total density of electrons (N_0) and determine the corresponding inverse Compton component on all relevant photon targets.

Figure 4.15 shows a schematic summary of the simulation workflow. To illustrate the effect of the different parameters on the simulation, we also plotted in Figure 4.16 the obtained amplitude (N_0, in the left panel) and integrated energy in electrons (W_e, in the right one) as a function of the fitted cutoff energy (E_p), for different values of the index (Γ_e) and magnetic field (B).

The total SED of the flare (see Figure 4.17 as an example) consists of the sum of the different contributions. We obtained the synchrotron and inverse Compton components for 100 energy bins logarithmically spaced from 10^{-7} eV to 1 PeV. We then retrieve the

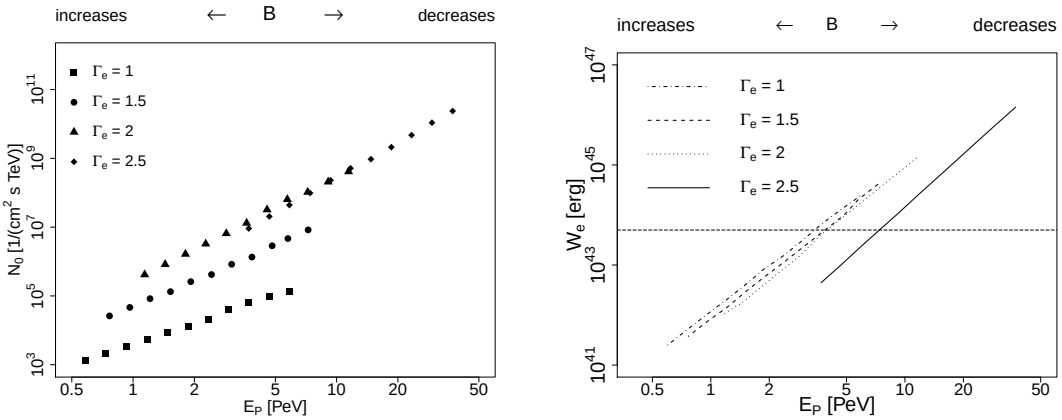

Figure 4.16: In the left panel (taken from Mestre et al., 2021), we represented the fitted amplitude of the electron energy distribution (N_e) as a function of Γ_e, E_p, and B for the April 2011 flare. For each value of Γ_e, the points correspond from left to right to 11 values of magnetic field logarithmically spaced from 5 mG to 50 μG. The right panel depicts the integrated energy in electrons above 1 TeV (W_e) in the same manner of the left panel.

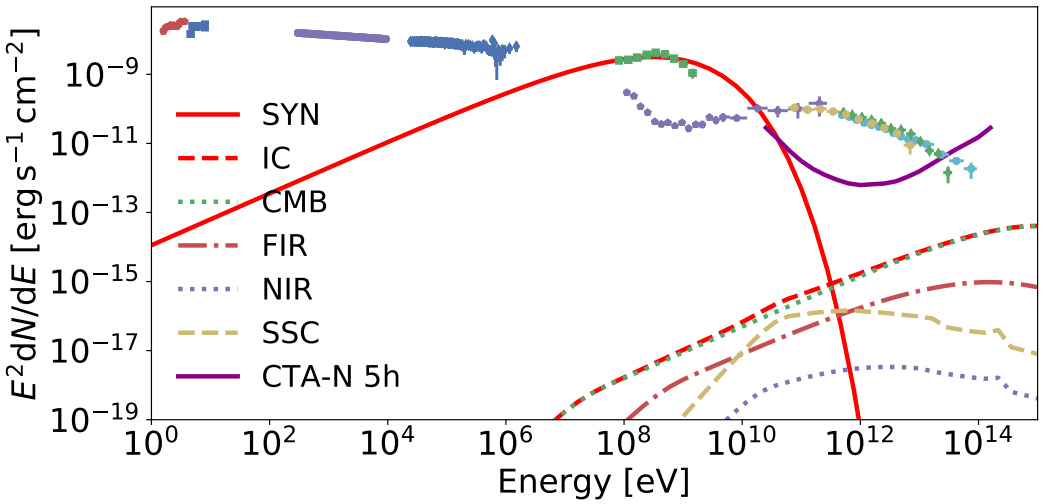

Figure 4.17: The different lines depict the synchrotron and IC emission of a simulated flare (fitted to the 2011 April flare spectrum) with B = 100 μG and Γ_e = 1.5. The green squares correspond to the nebula spectrum during the 2011 April flare (as seen by *Fermi*-LAT). The rest of the data correspond to the steady nebula emission (the compilation was taken from Meyer et al., 2010, and Buehler et al., 2012). The plot was taken from Mestre et al. (2021).

total energy in electrons above 1 TeV ($W_{\rm e}$) from the (IC component) integration of the different flare models. Also, we can directly compare the nebula's integral flux (in the flaring state) above 1 TeV with the upper limit established by H.E.S.S. and VERITAS in the case of the March 2013 flare. It should be clear that our primary interest is not to find the best-fit particle index (Γ_e) and magnetic field (B) for the Fermi-LAT data of the 2011 (or 2013) flare (in particular, see Figure 4.17). Principally, we aim at exploring multiple models of flares in a broad space of parameters (Γ_e and B) while ensuring that the same present a similar flux level than the past (2011 and 2013) bright flares detected in the LAT energy window.

Additionally, we considered an alternative approximation for the flare emission at GeV energies. For the same, we assumed a power-law decay for the synchrotron radiation model instead of an exponential one (as expected for Jitter radiation, see Kelner et al., 2013). In particular, to probe this scenario, we fitted the *Fermi*-LAT data above 400 MeV with simple power-law models of a fixed index ($\Gamma_{\rm Jit}$), ranging from 2.5 to 3.5 in steps of 0.1, with the amplitude (of the emission) normalized to 0.85 GeV.

4.4.1.2 Convolution of simulated flares with the CTA response functions

We carried out the observation simulations folding the resulting radiation model with the CTA Instrument Response Functions (version prod3b, see Section 3.2.3). For this purpose, we used the CTA GAMMAPY PYTHON tool (version 0.7, see Section 3.2.4). We will focus the discussion of the results for the IRFs corresponding to observations at low zenith angle (i.e., 20°) from the northern array, as in the simulations of the steady nebula, aiming to guarantee the lowest energy threshold possible (and optimized for an exposure time of five hours). However, the simulations were carried out also with the IRFs of the southern array at a large zenith angle (i.e., 60°). The results obtained are presented here for a fiducial observation time of ten hours, assuming that the nebula is flaring during the entire observation time.

We reconstructed the photon spectrum resulting from the simulated particle population through a fitting process, using maximum likelihood (implemented in SHERPA, see Cash, 1979) and the Nelder-Mead Simplex optimization method (Wright, 1996; Lagarias et al., 1998) based on a forward-folding technique (Piron et al., 2001). The forward-folding technique relies (in general) on a spectral shape assumption and the comparison between the number of expected events from a source (i.e., of counts in the 'ON' region) and the ones expected from the background (i.e., in one or several 'OFF' regions). To avoid possible problems associated with the radiation model's discretization in energy bins, we parametrized our model's spectrum using an exponential power-law function from 20 GeV to 200 GeV and a power-law one from 1.25 TeV to 50 TeV. These components account for the MeV and GeV synchrotron contribution and the IC one at TeVs, respectively. The

detection of flares at intermediate energies of the CTA band, e.g., from 200 GeV to 1 TeV, is considerably more challenging due to both the synchrotron and IC emissions from the flares are, in principle, several orders of magnitude dimmer than at tens of GeVs and TeVs, respectively (or at least we expect it, see Figure 4.17).

In our simulations, the background is dominated by the nebula's emission, especially in the TeV regime. We used the steady nebula simulations (in the previous section of this chapter) to account for this issue. In particular, we used the log-parabola spectral shape fitted to the nebula in Aleksić et al., 2015 (i.e., LP-MAGIC in the notation of previous sections). The CTA IRFs provide the cosmic-ray background, computed within the nebula simulations both in the flaring and steady-state. To evaluate the capabilities of CTA to disentangle variations on the large Crab Nebula steady emission, we followed the next steps; (1) firstly, we fitted the simulated spectrum (i.e., the flare plus steady emission) in the GeV (from 20 GeV to 200 GeV) and TeV (from 1.25 TeV to 50 TeV) regimes to simple power-laws. (2) Secondly, we computed the integral flux in both the GeV and TeV regimes, using the best-fitted models previously obtained. (3) Then, we estimated the mean total expected excess (i.e., the expected counts from the source, with background subtraction) and its standard deviation by iterating over 10^4 realizations for each flare model (and ten hours of observation time). We also computed the integral flux and average expected excess in both the GeV and TeV regimes for the flare and steady components individually (to use them as reference). (4) To compare the non-flaring and flaring SED, we carried out a Pearson's chi-squared test, with the (flaring) excess distribution as the observed data (H_1) and the steady-state as expected data (null hypothesis, or H_0). These are analogous to the tests performed to the excess distributions (depicted in Figure 4.9) of the steady nebula. We carried out the tests for each of the 10^4 realizations, considering that a flare is detectable when we can reject the null hypothesis at 99% CL. (5) Finally, we computed the enhancement of integral flux above 1 TeV (compared to the nebula simulations in steady-state) expected for the different flare models. It is defined as:

$$\mathrm{Z} = \frac{\int_{1\mathrm{TeV}}^{300\mathrm{TeV}} \mathtt{F}_{\mathtt{flare,E}}\,\mathrm{d}E + \int_{1\mathrm{TeV}}^{300\mathrm{TeV}} \mathtt{F}_{\mathtt{steady,E}}\,\mathrm{d}E}{\int_{1\mathrm{TeV}}^{300\mathrm{TeV}} \mathtt{F}_{\mathtt{steady,E}}\,\mathrm{d}E}\,. \tag{4.6}$$

Note that models representing flares with very different spectral shapes can result in similar flux enhancements in Equation 4.6. The flares with integral fluxes comparable to the MAGIC nebula correspond to $Z \approx 2$.

Furthermore, to test the capability of CTA to detect flares of different duration from those described above, we computed the minimum flare duration (using as a fiducial flux level the one of the 2011 flare) that the CTA northern and southern arrays could detect (for different values of B and Γ_e). For each of those, we performed 5000 observation simulations of the nebula in both steady and flaring states and applied chi-square tests

Γ_e	1.0	1.5	2.0	2.5	Γ_e	1.0	1.5	2.0	2.5
Time [h]	0.35	0.14	0.02	$<< 1$	Time [h]	0.11	0.05	$<< 1$	$<< 1$

Table 4.5: We provide (above) the observation time (in hours) necessary to detect different models of flares (fitted to the LAT 2011 April flare data) at energies from 20 GeV to 120 GeV with the chi-square test applied to the excess distributions (at 99% CL). Note that we assume that Crab is flaring during the entire time of observation.

between the excess distributions (as explained above). Instead of the ten hours considered above, we used different observation times, ranging from 0.01 to 500 hours (in adaptative bins varying from 0.01 to one hour in size), and calculated the minimum time to detect a significant variation over the steady-state. To consider the varying observation time properly, we used the IRFs optimized for an exposure time of 50, 5, and 0.5 hours and re-scaled the total energy in electrons above 1 TeV ($W_{\rm e}$) from the one obtained in ten hours.

To conclude, we have not yet considered the effect of the systematic errors in our simulations, which should be, in principle, the main limitation to measure variability over the nebula's baseline flux. The many uncertainties on the CTA systematics prevent us from estimating its quantitative effect on the simulations. Therefore, one should consider the results of this work as an optimistic scenario.

4.4.2 Application to the 2011 and 2013 flares

We will now summarize the results of applying the method to simulate flares in the Crab Nebula (described in the last section) to the 2011 and 2013 flares LAT data (compiled from Bühler & Blandford, 2014). Figures 4.18 and 4.19 illustrate (for the synchrotron and inverse Compton components, respectively) the qualitative relationship between the magnetic field and particle index parameters and the expected gamma-ray emission from the resulting flares.

4.4.2.1 Results in the sub-100 GeV region

The first figure cited, in particular, focuses on the sub-100 GeV region. It is noticeable that the synchrotron spectrum in the energy window depicted in the figure depends very weakly on the magnetic field. However, this effect is a consequence of fitting the synchrotron emission to the LAT data, which sets strong constraints on the synchrotron flux level above hundreds of MeV given a certain index for the parent particle population. The simulations of the synchrotron component of the flares emission show, in all the tested cases, that CTA should be able to detect a flare with similar flux to the one observed in 2011, as seen in Table 4.5 and Figure 4.18. The simulations performed indicate that

the detection should be possible in less than one hour for $\Gamma_e > 1.0$ below 200 GeV. In this energy regime, the flare models represent an integral flux variation above 20% of the steady nebula flux.

Furthermore, for stepper spectra, i.e., $\Gamma_e > 2.0$, we could detect the flares (in less than an hour) even at higher energies, up to a maximum energy of about 300 GeV (with $2 < \Gamma_e \leq 3$). It was possible because of the large flux expected in the GeV regime if the threshold energy is low enough. For instance, the predicted excess (in counts) for the steady nebula (in ten hours from the CTA northern site) from 20 GeV to 120 GeV is (approximately) twice the excess predicted in the 1.25 TeV to 50 TeV band. The capabilities of CTA regarding the detection of the synchrotron emission from the Crab flares result even more emphasized (given the large flux expected as the energy threshold decreases) when comparing the simulations with the sensitivity of an array with only 4 Large Size Telescopes (in the North site). We also show it in Figure 4.18, in which the MAGIC sensitivity (Aleksić et al., 2016) was added too, for comparison.

For bright flares, then, the large CTA-LST sub-array should be sufficient to set strong constraints on the Crab flares synchrotron tail. Even for current instruments like MAGIC (see the magenta dot-dashed line in Figure 4.18), prospects are optimistic, allowing a good determination of the particle spectrum if the right observation conditions are met. For a flux level similar to the one observed in the April 2011 flare, enough time of observations at a low zenith angle (E < 300 GeV) may have resulted in a detectable enhancement of flux for a soft particle index ($\Gamma > 2$). Unfortunately, MAGIC performed the Crab Nebula's observations during the (April 2011) flare under strong moonlight, which increased both the analysis energy threshold and the systematic uncertainties (see Ahnen et al., 2017a). Hence, we can not compare these observations with the mentioned result.

4.4.2.2 Results in the TeV regime

In contrast to the synchrotron emission at GeVs, the magnetic field strongly affects the TeV IC component, suppressing the flare contribution for very large intensities. Table 4.6 and Figure 4.19 summarizes the simulations in this energy regime. Opposite to the sub-100 GeV regime, soft electron spectra favor the production of GeV and TeV photons by promoting lower-energy electrons, which provide a larger SSC target photon field. From these simulations, we derived that only certain combinations of parameters (B and Γ_e) characterizing the flare emission result in a detectable variability over the nebula's steady flux. Supposing the parent particle population of the flare presents a hard (power-law) index, i.e., $\Gamma_e < 2.2$, we would achieve the inverse Compton component detection only for very weak magnetic fields, i.e., $\lesssim 50$ μG, whereas for softer electron distributions, i.e., $\Gamma_e > 2.5$, realizations with magnetic fields as large as one mG result in detectable levels of flux.

Γ_e / B[μG]	1.5	1.8	2.1	2.5
1000	> 500	> 500	> 500	8.0
500	> 500	> 500	> 500	0.8
100	> 500	> 500	160^*	0.02
50	> 500	> 500	40^*	$<< 1$
10	> 500	93^*	0.3^*	$<< 1$

Γ_e / B[μG]	1.5	1.8	2.1	2.5
1000	> 500	> 500	> 500	2.7
500	> 500	> 500	> 500	0.3
100	> 500	> 500	130^*	$<< 1$
50	> 500	> 500	15^*	$<< 1$
10	> 500	27^*	$<< 1^*$	$<< 1$

Table 4.6: We summarize (above) the observation time (in hours) necessary to detect different models of flares (fitted to the LAT 2011 April flare data) at energies from 1.25 TeV to 50 TeV, obtained as Table 4.5. The table's left part corresponds to the CTA northern array, whereas the right part corresponds to the southern one. We assume that Crab is flaring during the entire time of observation. The models indicated with asterisks imply $W_e > 5 \times 10^{43}$ erg if the flare duration is the one noted.

Tables 4.5 and 4.6 list (in more detail) the observation time needed to detect the flare models in different energy regimes, obtained by evaluating the excess observed over the contribution of the steady nebula, both for the northern and southern arrays. For comparison, note that we detected the Crab steady nebula at 5σ in less than one hour both from the CTA northern and southern sites, for an energy range from 1.25 TeV to 50 TeV. Hence, the steady emission is detectable in ten hours at large significance.

4.4.2.3 Variations in the nebula spectral shape

Besides probing if the flare models considered are detectable and in which observation time, we attempted to reconstruct, from the simulations, the flare contribution to the steady nebula spectral shape. For the GeV regime, we fitted the observations simulations of the nebula in flaring state (up to 200 GeV) to three different models, a simple power-law, a smooth broken power-law with the energy break located between 50 GeV and 300 GeV (and the higher energy component extending up to 1 TeV), and to a power-law with an exponential cutoff model. Instead, we only fitted the TeV regime to a simple power-law model from 1.25 TeV to 50 TeV of energy. The specific treatment described in each energy band is related to the spectral shape of both the synchrotron and IC components of the flare emission. The power-law with an exponential cutoff characterization best describes the synchrotron spectrum in the GeV regime. The IC part (at TeV energies), however, is best characterized by a power-law shape. The addition of the flaring and steady (spectral shape) components at tens/hundreds of GeV can then resemble any of the three models exposed before in this band. Simultaneously, at TeV energies, we expect the flare emission (at least in our simulations), only to cause a steepening of the photon (power-law) index of the nebula's SED (if compared to the steady case, see Figures 4.18 and 4.19).

The results showed that only in a handful of cases a clear deviation from the steady nebula spectrum was observed. For example, for $\Gamma_e = 2.5$ and B = 100 μG, we measured a significant difference of spectral (power-law) indices of 0.66 ± 0.03 below 300 GeV, compared to the (photon power-law) index measured in steady-state for the GeV regime (i.e., 2.33 ± 0.03). We could represent the emission from the nebula below 1 TeV, in this case, by a smooth broken power-law with the break located at $\sim$ 300 GeV and a difference between the higher and lower energy indices similar to the one mentioned (i.e., 0.69 ± 0.02). This effect is also present in the TeV regime (at a 3σ level), in which we observe a significant variation in the spectral index (i.e., 0.46 ± 0.03, compared to 2.75 ± 0.03). The exponential cutoff power-law model could not properly describe the flaring nebula simulations in the GeV regime in any case (as expected), meaning that, in this band, any of the simulated flares models overcome the emission of the steady nebula (in flux) by a very large factor. In Figure 4.20, we show, for completeness, the enhancement of flux above 1 TeV as defined in Equation 4.6, applied to the simulations (fitted to the 2011 flare) as a function of the

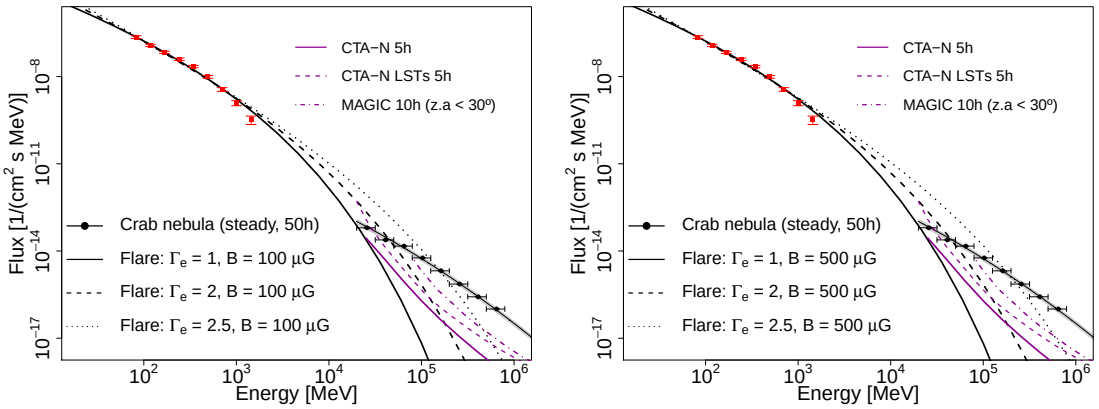

Figure 4.18: The different black lines depict the synchrotron emission for flares (fitted to the LAT 2011 April flare data) of various indices ($\Gamma_e = 1, 2, 2.5$) and magnetic fields ($B = 100$ μG in the left panel, and 500 μG in the right one) together with the simulations of the Crab Nebula steady spectrum (in black line with dots), with the (3σ) error region noted (see the black shaded area, accounting only for statistical errors). The data recorded by LAT of the 2011 flare is shown in red squares. The magenta solid (and dashed) lines correspond to the CTA northern array's sensitivity (when considering only its four Large Size Telescopes) for five hours of observation time. The magenta dot-dashed line corresponds to the MAGIC's sensitivity at a low zenith angle, i.e., $z < 30°$ (see Tables A.5 and A.6 in Alecsić et al., 2016). The plot was taken from Mestre et al. (2021).

magnetic field and particle index. It is also interesting to note that none of the performed simulations results on a flux level above the nebula at energies below 1 MeV, preventing the detection of counterparts with low spatial resolution (i.e., of scales above the arcminute) instruments at lower energies, which can not resolve the nebula's morphology (see Figure 4.17). However, this may not be the case if a power-law spectral shape cannot characterize the particle spectrum.

4.4.2.4 Constraints from the energy available in the nebula

For the moment, we have not yet discussed any restrictions regarding the total energy available in the system, which is limited, in principle, to about $\sim 5 \times 10^{43}$ erg. Suppose some process re-accelerating the particles is not taking place, or any other way to provide a larger energy budget is involved. In that case, only some combinations of the magnetic fields and spectral indices should be possible. For $\Gamma_e > 2.2$, for instance, the models with a magnetic field below B ~ 500 μG would be ruled out according to the upper limit established, i.e., $W_e > 5 \times 10^{43}$ erg. However, the magnetic field's intensity has to be increased to one milligauss when considering softer indices, $\Gamma_e > 2.5$. For the range of particle indices considered, i.e., $\Gamma_e > 1$, only magnetic fields stronger than ~ 150 μG keep

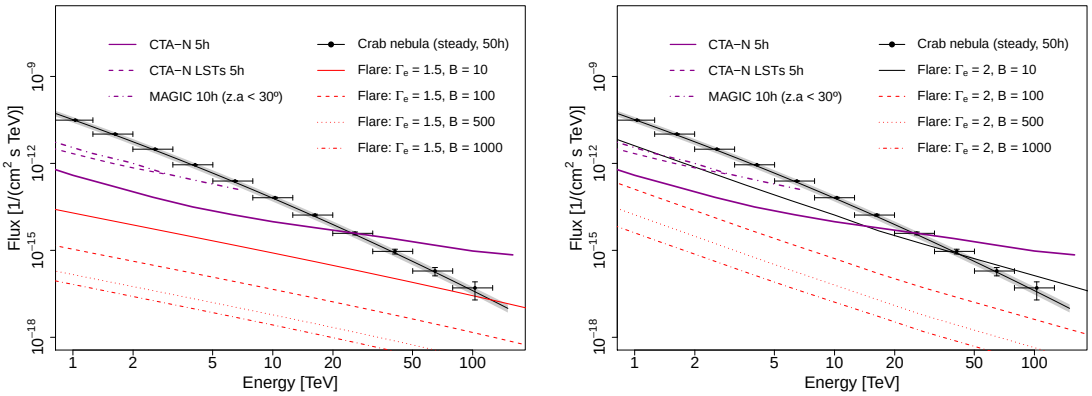

Figure 4.19: The different lines depict the IC emission for different flares models (fitted to the LAT 2011 April flare data, in black if the flare is detected in the TeV regime and in red otherwise). In these cases, $\Gamma_e = 1.5$ (left) and $\Gamma_e = 2$ (right). On top is the (simulated) Crab steady nebula spectrum (in black line with dots) with the (3σ) error region noted (in a black shaded area, accounting only for statistical errors). We accounted for the SSC emission in a region of 2.8×10^{-4} pc in size. The sensitivity curves (in magenta) were defined in Figure 4.18. The plot was taken from Mestre et al. (2021).

the total energy in electrons (above 1 TeV) below the mentioned upper limit. It can be seen (in more detail) in Figure 4.21 (computed for the 2011 flare), in which the red shaded area marks the, in principle, forbidden values of B and Γ_e, given the maximum energy in electrons allowed.

4.4.2.5 Results for the March 2013 flare

We also applied the simulating scheme presented (up to now) to fit the 2013 flare LAT data from 80 MeV to 1 GeV. We considered the same parameters space of the 2011 case, with the magnetic field strength in the range of 10 μG to 5 mG and Γ_e ranging from 1 to 3. For each model of flare simulated, we computed, as in the previous case, the integral flux above 1 TeV by fitting the total inverse Compton (with the CMB, NIR, and FIR photon fields) component and accounting for the SSC, in this case, in a region of 1.7×10^{-4} pc in size. Contrary to the 2011 case, the observations with H.E.S.S. and VERITAS resulted, as commented, in constraints to the 2013 flare emission (i.e., $Z \lesssim 1.6$). The flux enhancement obtained (see Equation 4.6) for the different flares models was (directly) compared to the upper limit reported by H.E.S.S. and VERITAS, imposing constraints on the accelerating magnetic field and the electron population's particle index.

The simulations showed that the flares are detectable in the GeV regime for $\Gamma_e > 1.4$, in ten hours of observation time, implying an enhancement of flux (and counts, in the GeV regime) above 4% compared to the steady nebula. Figure 4.22 summarizes the results in

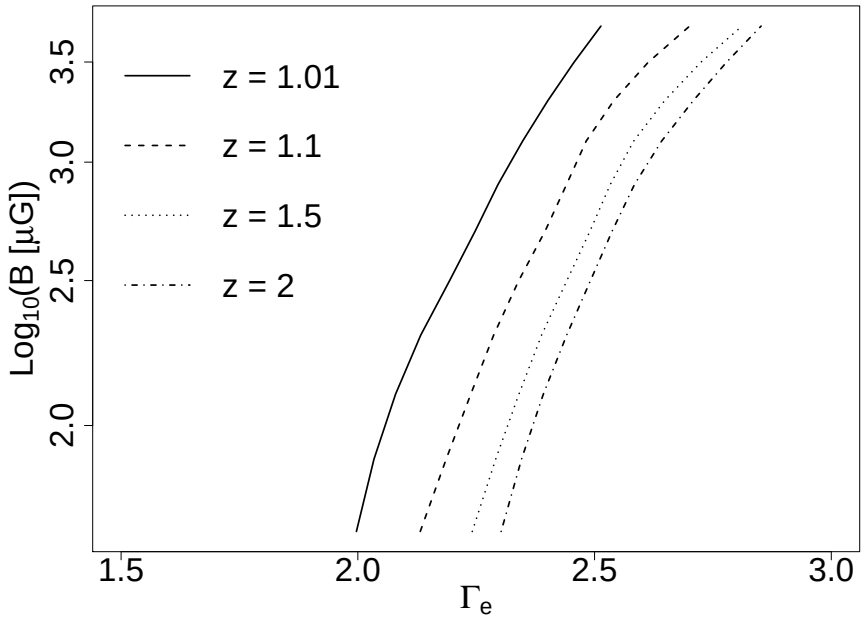

Figure 4.20: The different lines show the enhancement of integral flux above 1 TeV (in Equation 4.6) for various flare models (fitted to the LAT 2011 April flare data and accounting for the SSC). The plot was taken from Mestre et al. (2021).

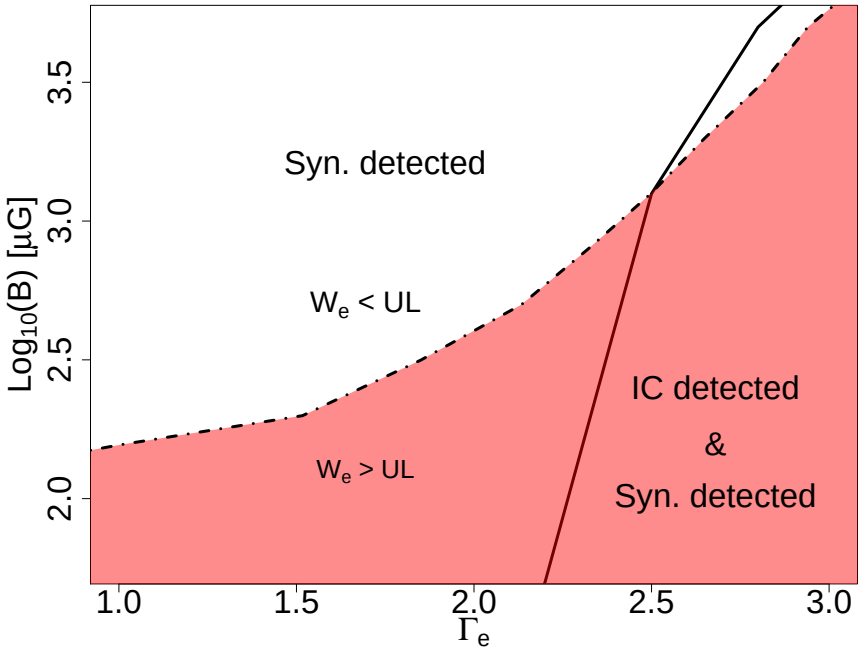

Figure 4.21: The plot summarizes the flaring nebula observation simulations for the different models fitted to the LAT data of the April 2011 flare. The models below the solid line are detectable in the TeV and GeV regimes (i.e., from 1.25 TeV to 50 TeV of energy, and below 200 MeV) if observed with CTA. In contrast, we only detected the models above the solid line in the GeV regime. However, the models below the dash-dotted line (red shaded area) require an energy in electrons $W_{\rm e} > 5 \times 10^{43}$ erg. The plot was taken from Mestre et al. (2021).

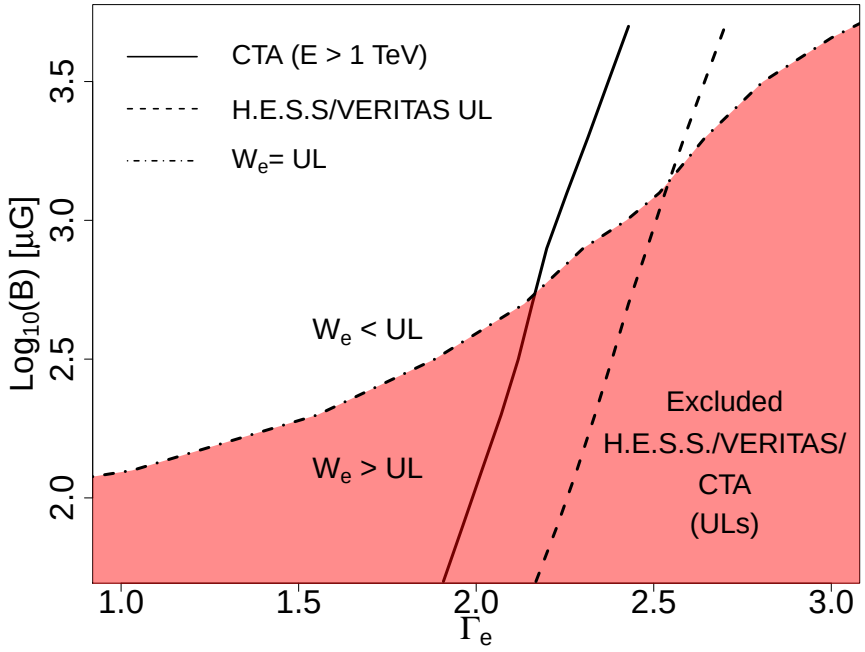

Figure 4.22: The plot summarizes the flaring nebula observation simulations for the different models fitted to the LAT data of the March 2013 flare, compared to the upper limits established by H.E.S.S. and VERITAS observations. The models located below the dashed line imply an enhancement of integral flux above 1 TeV larger than 60% (i.e., $Z > 1.6$ in Equation 4.6). Therefore, these models violate the upper limits established by the H.E.S.S. and VERITAS observations of the 2013 flare. The exclusion region (for the integral flux upper limit above 1 TeV) extends up to the solid line ($Z > 1.01$, with only statistical errors), supposing the flare is not detectable in 50 hours with the CTA northern array. The models below the dashed-dotted line (red shaded area) violate the upper limit estimated for the (TeV electrons) total energy. The plot was taken from Mestre et al. (2021).

B[μG]/Flux	F_{2011}	$0.5 \times F_{2011}$	$0.1 \times F_{2011}$	B[μG]/Flux	F_{2011}	$0.5 \times F_{2011}$	$0.1 \times F_{2011}$
1000	8.0	166^*	$> 500^*$	1000	2.7	65^*	$> 500^*$
500	0.8	6.0^*	$> 500^*$	500	0.3	1.9^*	$> 500^*$
100	0.02	0.07	32^*	100	$<< 1$	$<< 1$	13^*

Table 4.7: We summarize (above) the observation time (in hours) necessary to detect different models of flares from 1.25 TeV to 50 TeV with the CTA northern (left) and southern (right) arrays. The first column (F_{2011}) corresponds to flare models fitted to the LAT data of the April 2011 flare. The models with an asterisk imply that the energy in electrons (above 1 TeV) is larger than 5×10^{43} erg. We assume the Crab is flaring during the entire observation time.

the TeV regime. The red shaded area shows the exclusion region (like in Figure 4.21) due to the nebula's energy budget. Note that the CTA exclusion region (solid line) improves the constraints imposed by the H.E.S.S. and VERITAS observations (dashed line). It is also interesting to note that if the energy available is the one provided by Equation 4.5, only a few combinations of B and Γ_e imply both a detectable flux and energy in electrons below the nebula's reservoir, being the combination of both criteria the most constraining argument.

4.4.3 Simulations of flares at different flux levels

To evaluate the capabilities of CTA for the detection of flares at different flux levels, we repeated the simulations of the 2011 April flare but now re-scaling the *Fermi*-LAT data by two factors: 0.5 and 0.1. In this case, we fixed the electron population index (Γ_e) to 2.5 to guarantee the detection in the TeV regime (i.e., from 1.25 TeV to 50 TeV) of the brightest model of flare (at least, see Figure 4.21) in less than ten hours (see Table 4.7). We then focused on the different flare models with magnetic fields between 100 μG and one mG. The simulation tools and the analysis methods employed are the same as explained in the previous cases.

As expected from the simulations presented before, we best detect the different flare models in the GeV regime. For instance, all the models of flare considered would be detectable in less than an hour at energies below 200 GeV (at 95% CL) with the CTA northern and southern arrays, supposing in all the cases an enhancement of flux (in counts) of more than 30% (below 200 GeV) compared to the steady nebula. Also, in the TeV regime, we would detect flares dimmer than April 2011 flare by a factor of 0.5 (at hundreds of MeV) in less than 10 hours for B < 500 μG (see Table 4.7), with an enhancement of flux (from 1.25 TeV to 50 TeV) larger (or similar) than 10% (in counts). As previous results, some of the models imply that the energy in electrons (above 1 TeV) is larger than the upper limit discussed (5×10^{43} erg, with no re-acceleration of particle processes

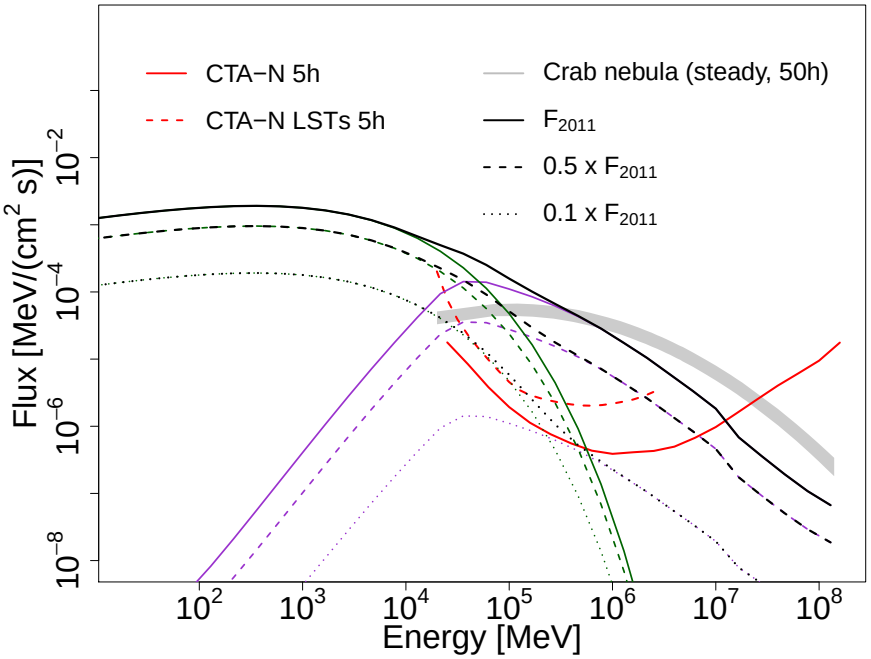

Figure 4.23: We depict the synchrotron (green lines), IC (purple lines), and total (black lines) emissions for different flare models. We fitted the flare depicted in solid line to the LAT 2011 flare data (above 80 MeV) for a 2.5 index. The dashed (dotted) lines correspond to the same model re-scaled by a factor of 0.5 (0.1). All models assume $B = 500$ μG. The red solid (dashed) line indicates the sensitivity of CTA-N (accounting only for five hours with its four LSTs). We noted the simulated steady spectrum (for 50 h of CTA-N) in a gray shaded area (3σ region).

considered). However, this upper limit is not problematic when considering magnetic fields similar to the (expected) average magnetic field of the nebula, i.e., $B \sim 100$ μG. In contrast, the flare models ten times dimmer than the 2011 April flare, challenging the upper limit established for the TeV electrons energy, were not detected (in less than 10 hours) for magnetic fields stronger than 100 μG.

4.4.4 Hypotheses for the origin of the gamma-ray flares

The rapid variability in the Crab Nebula during the (MeV-GeV) flares observed is not explained straightforwardly with PWN theory in a standard approach. According to the same, the dominant contribution to the emission below a few tens of GeV is believed to be provided by synchrotron emitting leptons in the shocked pulsar wind. In contrast, the inverse Compton emission from this population can be registered at TeV energies. In particular, the emission below a few tens of GeV is associated with the high-energy tail of such synchrotron emission. However, the same is limited, in

an ideal magneto-hydrodynamic outflow, by the synchrotron burn-off limit, which in the plasma-comoving frame constraints the peak of the synchrotron spectral energy distribution to $\bar{h}\omega_{max} < 200$ MeV of energy, assuming that the acceleration and radiation sites are co-located, see, e.g., Guilbert et al. (1983). The spectrum measured for the Crab Nebula (in steady-state) seems to agree with this limit. Therefore, to explain the variable emission emerging at a few hundred MeVs with a flux level exceeding the steady nebula emission and peaking at higher energies than $\sim$ 200 MeV, a second component has to be invoked. It is not clear, however, the origin of this second component. Furthermore, the gamma-ray emission seems to be inconsistent with the usual synchrotron or inverse Compton mechanism. For instance, the IC scenario can be robustly ruled out, given the short variability timescales. Simultaneously, the large energy at which the peak is located excludes the synchrotron mechanism in the ideal MHD setup.

The discovery of the flares in Crab motivated numerous interpretations about the origin of the emission observed, e.g., within the limits of an ideal MHD outflow, a relativistic-moving acceleration site (see, e.g., Bednarek & Idec, 2011; Lyubarsky, 2012; Lyutikov et al., 2018), and/or a radiation mechanism other than synchrotron (i.e., Jitter radiation as in Teraki & Takahara, 2013), could in principle account for the observed radiation. Alternatively, supposing that the MHD assumptions are violated in some region, for example, due to reconnection of the magnetic field (see Section 2.2.4), an electric field component parallel to the magnetic field can be generated, resulting in a beam of high energy particles moving along the unscreened electric field. These accelerated particles eventually escape from the acceleration region and can be deflected by the average magnetic field, emitting synchrotron and inverse Compton radiation along their trajectories. Furthermore, suppose the linear size of the reconnection region is large. In that case, the particles in the current sheet can achieve significant energies, producing, once they escape from the reconnection region, synchrotron-like emission in the super-critical regime (see, e.g., Cerutti et al., 2012). Hence, they should emit a substantial part of their energy over a short time (compared to the gyrorotation) in a highly anisotropic regime.

In the present section, we will compare some of the scenarios proposed previously with the flaring nebula simulations described in this chapter, deriving from the same, when possible, quantitative constraints to the different approaches. In the following, we aim to discuss further possibilities and prospects for detecting the Crab flares with CTA.

4.4.4.1 Relativistically moving MHD outflow

The first class of the scenarios mentioned is the one that invokes relativistic MHD outflows. In these models, we can describe the emission site as a region of size R', moving with a significant bulk Lorentz factor Γ, such that the Doppler boosting factor is $\delta_{10} \sim 1$ (here $\delta_{10} = 0.1/(\Gamma(1-\beta\cos\theta))$). In such a case, the strength of the comoving magnetic field (B')

should be high enough to satisfy the Hillas criterion, which demands, in general terms, that the particle's Larmor radius should be smaller than the accelerating region's size. It can be expressed as follows:

$$R' > 3 \times 10^{15} E'_{\rm PeV} B'^{-1}_{\rm mG}\,{\rm cm} \tag{4.7}$$

where $E'_{\rm PeV}$ is the maximum comoving electron energy (in PeVs). Since the Doppler boosting factor relates the observables in the comoving and laboratory frames (i.e., $\nu = \delta \times \nu^{'}$), the peak photon energy observed can be obtained from the synchrotron spectrum (in an approximate treatment) as:

$$E_{peak} = 600 E'^{2}_{\rm PeV} B'_{\rm mG}\ \delta_{10}\,{\rm MeV} \tag{4.8}$$

To derive the previous result, see, e.g., the Equation 8.127 of Longair's book (1981), multiplied by the Plank's constant. Also, note that taking into account the fulfillment of the light crossing criterion ($R^{'} < c\delta t_{var}$, with a variability time observed; $t_{var} < 10^5$ s) and that the synchrotron cooling time, i.e., $t_{syn} = 3m_e^4 B^{'-2} E^{'-1}/2e^4$, is responsible for the variability:

$$t_{syn} = 4 \times 10^4 E'^{-1}_{\rm PeV} B'^{-2}_{\rm mG}\ \delta_{10}^{-1}\,{\rm s} \tag{4.9}$$

$$R^{'} < 3 \times 10^{16} \delta_{10}\ {\rm cm} \tag{4.10}$$

Then, assuming the variability time should be larger than the synchrotron cooling time ($t_{var} > t_{syn}$) and combining the expressions above, we obtain:

$$E'_{\rm PeV} > \left(\frac{E_{peak}}{600\,{\rm MeV}}\right)^{2/3} \left(\frac{t_{\rm var}}{4 \times 10^4\,{\rm s}}\right)^{1/3} \delta_{10}^{-1/3} \tag{4.11}$$

and

$$B'_{\rm mG} < \left(\frac{E_{peak}}{600\,{\rm MeV}}\right)^{-1/3} \left(\frac{t_{\rm var}}{4 \times 10^4\,{\rm s}}\right)^{-2/3} \delta_{10}^{-1/3} \tag{4.12}$$

Finally, using Equations (4.11) and (4.12) in Equation (4.7), we can retrieve the blob size in terms of the peak photon energy E_{peak} and variability time t_{var}:

$$R' > 3 \times 10^{15} \left(\frac{E_{peak}}{600\,{\rm MeV}}\right) \left(\frac{t_{\rm var}}{4 \times 10^4\,{\rm s}}\right)\ {\rm cm} \tag{4.13}$$

Furthermore, note that the nebula's size (i.e., $\sim 3.4 \times 10^{18}$ cm) also limits the maximum size of the blob physically.

We will show now that, with a simple approach, one can compare the formalism described above with the Crab flares simulations. For instance, we can easily estimate the Doppler boosting factor's values (δ_{10}), according to the approximations equated, that

are coherent with our simulations. Firstly, for the different magnetic field intensities sampled in the simulations (i.e., $B^{'}$ in this formalism), we can obtain an upper limit for the Doppler boosting factor using Equation 4.12. Note that in the same equation, the peak photon energy (E_{peak}) and variability time (t_{var}) are magnitudes derived directly from the observations of the flares. Hence, we can use fiducial values from the (2011 or 2013 flare) data available. Besides, we retrieved the comoving energy of the electrons ($\mathrm{E}'_{\mathrm{PeV}}$) straightforwardly from the simulations since these compute the electron energy distribution (see in Section 4.4.1). Hence, Equation 4.11 establishes a lower limit for the Doppler boosting factor. Using Equations 4.7 and 4.13, we can determine the minimum size of the blob and compare it both to the nebula's size and Equation 4.10. An alternative approach to check the consistency between the formalism and our simulations is to compare the simulation parameters (E'_{PeV} and $R^{'}$, from Equation 4.7) with those obtained from Equations 4.11 and 4.13.

We concluded that the energy of the electrons, computed within the simulations (E'_{PeV}), is consistent with the relativistic moving outflow scenario in most cases. Concretely, when $\Gamma_e > 1.5$ (within a 10% of error), allowing the Doppler boosting factor to take a value within a specific range, being the upper and lower limit of that interval determinate by Equations 4.11 and 4.12. Figure 4.24 (left panel) shows these constraints derived for the Doppler boosting factor as a function of the magnetic field and particle index employed in the simulations. Combining the last result and the convolution of the flare models with the CTA IRFs (in Figure 4.21), we showed that the detection of a flare in the TeV regime could constrain (given this scenario for the origin of the emission) the Doppler boosting factor to a very limited range. For instance, the flare models detected in the TeV regime with integrated energy in electrons (above 1 TeV) smaller than 5×10^{43} erg, implying milligauss magnetic fields, are only feasible for Doppler factors ranging from 0.026 to 51.9 (although, if the emission region is moving towards the Earth along the line-of-sight, $\delta > 1$ must be satisfied).

Similarly, the minimum size of the blob computed from simulations is consistent with Equation 4.13 ($R' > 4.5 \times 10^{14}$ cm), for $\Gamma_e > 1.5$, resulting in 1.8×10^{15} cm at most for $\Gamma_e = 3$, still ~ 2000 times smaller than the nebula's size. Equation 4.10, on the other hand, takes an upper limit for the blob size larger than 2.5×10^{15} cm in all the simulations performed. The right panel of Figure 4.24 depicts it. We represented the lower limit obtained for the blob's size, from Equation 4.7, in black lines. The red line corresponds to the lower limit obtained from Equation 4.13 with $E_{peak} = 200$ MeV and $t_{var} = 5$ hours.

4.4.4.2 Jitter radiation

Another possible origin of the flares that has been hypothesized is that the flare emission can be generated in an ideal MHD outflow if the radiation mechanism is distinct from

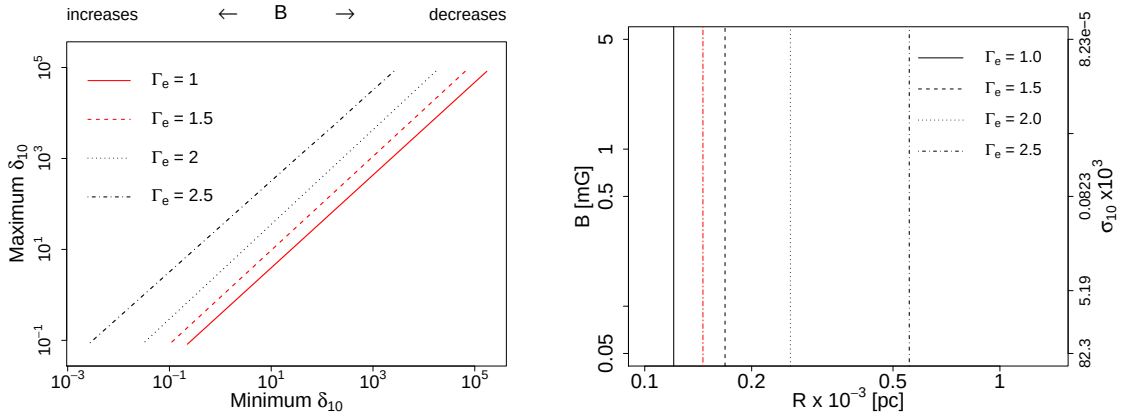

Figure 4.24: In the left panel (taken from Mestre et al., 2021), we represent the Doppler boosting factor lower and upper limits from Equations 4.11 and 4.12. The simulations plotted in red are not consistent with the relativistic moving outflow scenario for any Doppler factor since the particle spectrum's cutoff energy (E'_{PeV}) fitted in these cases is too small compared to the Doppler boosting factor upper limit derived with Equation 4.12. In the right panel, we plotted the different lower limits for the blob size obtained with Equations 4.7 (in black) and 4.13 (in red), as a function of the particle index and magnetic field assumed. We derived the Doppler boosting factor depicted in the right axis from the simulations.

the typical synchrotron. In particular, Jitter radiation, i.e., a modification of the classical synchrotron radiation for the case of turbulent magnetic fields (see Kelner et al., 2013, and references therein), was suggested to explain the flares (Bykov et al., 2012; Teraki & Takahara, 2013). The theory of Jitter radiation states that the mechanism is characterized by the same cooling time that synchrotron for the same mean magnetic field strength. However, the peak energy is boosted by a factor $R_g/(\gamma\lambda_{turb})$, where R_g, γ, and λ_{turb} are the giro-radius for the average magnetic field, the particle's Lorentz factor, and the turbulent field correlation length, respectively.

If the correlation length is small enough (i.e., smaller than the photon formation length), it is expected, additionally, to observe a shift of the total spectral energy distribution towards higher energies. The latter would, a priori, promote the detection of the flare at the lower energies of the CTA band. In this case, the resulting spectrum can be very different than in classical synchrotron. The peak photon energy would be shifted to larger energies, but also the shape of the SED above the peak would resemble a power-law distribution (Fleishman, 2006; Kelner et al., 2013), being the emerging index related to that of the spectrum of the particle distribution and the magnetic turbulence. We would also expect a power-law high-energy tail if the magnetic field's correlation length is comparable to the giro-radius (however, in this case, the peak maximum would remain

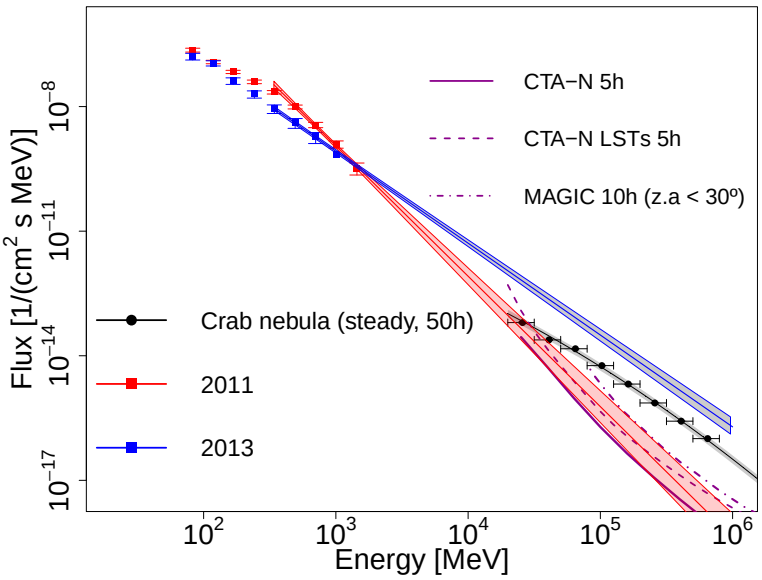

Figure 4.25: We represent the LAT data of the 2011 and 2013 flares fitted to a power-law model above 400 GeV (with the 1σ error region noted) and compared to the nebula steady emission and the CTA/MAGIC sensitivity.

unchanged, see Kelner et al., 2013).

In summary, in this theoretical approach, the resulting emission beyond the maximum of the radiation might follow a power-law extending to high energies instead of the standard exponential cutoff considered to this moment. To evaluate this possibility, we fitted the *Fermi*-LAT data (above 400 MeV) of the April 2011 (and March 2013) flare with several power-law photon spectra of fixed indices. Then, we investigated the detectability of the flare models in the GeV regime using the approach described in this chapter. To compare with the simulations that we will describe next, note that the best-fit power-law to the LAT (2011 flare) data results in a spectral photon index of 3.14 ± 0.13 (at 1σ) and a flux at 850 MeV of $(1.89 \pm 0.07) \times 10^{-9}$ cm^{-2} s^{-1} MeV^{-1} (with a reduced $\chi^2 = 1.4$ for two degrees of freedom). Similarly, the best-fit (power-law) model to the 2013 flare data resulted in a harder photon index of 2.21 ± 0.05 and $(1.20 \pm 0.05) \times 10^{-9}$ cm^{-2} s^{-1} MeV^{-1} of differential flux at 850 MeV (with a reduced chi-square of $\chi^2 = 0.29$ for two degrees of freedom). We depicted both models in Figure 4.25. As explained in Section 4.4.1, we considered a power-law decay for the synchrotron radiation by simulating the *Fermi*-LAT data above 400 MeV with simple power-law models of (fixed) indices ranging from 2.5 to 3.5 in steps of 0.1. We will now present the results from these simulations.

The simulations fitted to the 2011 data with $\Gamma_{\rm Jit} = 3$ showed that the flare is always detectable below 500 GeV (in 10 hours), with the chi-square tests applied to the excess

distribution. The model indeed corresponded to an increase of integral flux of $\sim 70\%$ in the GeV regime, i.e., from 20 GeV to 200 GeV. We also tested a softer model with $\Gamma_{\rm Jit} = 3.5$, resulting in a detectable emission (at the same time) below 200 GeV of energy. In this case, the increase of integral flux (and excess counts) was $\sim 9\%$ in the GeV regime. The scenario is optimal for the harder spectrum considered. Using $\Gamma_{\rm Jit} = 2.5$, the flare emission above the nebula can be observed up to TeV energies (in 10 hours). The integral flux is up to ~ 6 (~ 2) times larger than in steady-state in the GeV (TeV) regime. The enhancement of integral flux (above 1 TeV), in this case, is therefore above the upper limit established by H.E.S.S. and VERITAS for the 2013 flare. Since the best-fit power-law model to the 2013 data flare resulted in a harder photon index, despite having smaller flux at hundreds of MeV, we expect the flux projected at tens of TeV to be larger than for the 2011 case, implying then even better results than those explained.

We concluded, therefore, that if the Jitter mechanism is behind the origin of the Crab flares, the large excess expected below a few hundreds of GeV could result in a significant detection with CTA of bright but also moderated flares. Furthermore, it could be possible to achieve even in the early stages of the construction phase (see Figure 4.25).

It is important to remember at this point that the photon spectrum of the flare in the GeV regime is not derived (in this scenario) from fitting the spectrum of an electron particle population. In contrast, the simulations of the inverse Compton component of the flares, as explained in Section 4.4.1, depend on the synchrotron emission of a fitted particle population characterized by an exponential cutoff power-law spectrum. This characterization of the particle spectrum can not reproduce in any case a power-law spectrum emission above 400 MeV, as expected from the Jitter radiation hypothesis. Therefore, the simulations do not allow us to compute the inverse Compton component or the particles energy distribution in this case, and as a result, the energy integrated energy in electrons (W_e) either.

4.4.4.3 Magnetic reconnection

The third possibility discussed in the literature refers to an alternative mechanism, in which in certain regions of the nebula, magnetic field lines of different orientations draw near each other and create a reconnection layer (see Section 2.2.4). Magnetic reconnection activates several processes. First of all, the flow configuration is such that the initially highly magnetized flow that reaches the reconnection layer (this motion is vertical in Figure 2.6) gets ejected from the same. Since the outlet MHD flow has large internal energy, it might propagate with large bulk Lorentz factors, as occurs in, e.g., the case of Petchek-type relativistic reconnection (see Zenitani et al., 2009). The non-thermal processes that operate in such outflow work in the same way as discussed in Chapter 2. If, in addition, the guiding magnetic field is weak, the magnetization of the flow should

be small, favoring higher inverse Compton fluxes. However, the last scenario requires an almost perfect alignment of the reconnecting magnetic field, which seems to be a significantly less probable realization than one with not a strictly anti-parallel magnetic field. In contrast, if the guiding magnetic field is comparable to the reconnecting field, the flow remains highly magnetized. In this case, the IC emission results significantly suppressed. Typically, the magnetic fields adopted in reconnection scenarios are of the order of the milligauss (see, e.g., Cerutti et al., 2012), which makes very hard the detection of the counterpart IC emission.

Suppose particles are directly accelerated by the magnetic field in the reconnection layer (along the thick red arrow in Figure 2.6), then, during the acceleration process, they effectively reside in a region with a weaker magnetic field. It implies that synchrotron cooling is suppressed, but the particles still produce some IC emission. The acceleration time in the reconnection layer, $t_{\rm rl,acc} \simeq E_e/ev_{\rm in}B$, is longer by a factor of approximately $c/v_{\rm in}$ than the synchrotron cooling time in a magnetic field B (which, given the location of the synchrotron peak at a few hundreds of MeV, should be about $t_{\rm syn} \simeq E/eBc$). Thus, if the reconnection operates in a non-relativistic regime, $v_{\rm in} \ll c$, then the reconnection layer's emission may provide the dominant IC contribution. As, in this case, the particles produce IC and synchrotron emission at very different parts of their trajectories, the two components may have quite different beaming patterns. It is interesting to note that, in principle, one could expect *orphan* flares in the TeV regime. That opens exciting prospects when observing bright PWNe in which the spectrum can be measured with good statistics. However, the many uncertainties on these models prevent us from making further quantitative estimations of the expected radiation, impeding us to compare them with our simulations.

Chapter 5

Hadronic acceleration of Galactic cosmic rays

5.1 Introduction

As we introduced in Section 2.4.3, the non-thermal emission observed from supernova remnants with gamma-ray satellites has established these sources as sites where the hadronic acceleration of cosmic rays to a few hundreds of GeV (at least) takes place. In particular, SNR shocks have been stipulated as the sites where acceleration up to the cosmic-ray "knee" occurs (see Section 2.2.3). These accelerated CRs are known later to interact with particles from interstellar gas clouds in their surroundings. Moreover, the enriched medium in which core-collapse supernova remnants evolve provides a large density of target material where the hadronic production of gamma-rays is enhanced (see Section 2.3.5).

The deep survey carried out by the LAT instrument onboard the *Fermi* satellite revealed tens of sources (very likely) associated with gamma-ray (GeV) supernova remnants. These are listed, e.g., in the first *Fermi*-LAT supernova remnant catalog (Acero et al., 2016). Out of these SNRs, most could be classified, through tracers of age and environment, within the previously observed trends of this Galactic population, i.e., one consisting of young and hard-spectrum SNRs fainter at GeV energies, and the second one of brighter and older (often interacting with dense molecular clouds) SNRs. These old and evolved ones have lost much of their energy budget. However, the dense surrounding media boosts the gamma-ray production via proton-proton interaction.

The main characteristics of the spectral energy distribution resulting from this emission process (see the red lines in Figure 2.9) are, first, a sharp rise in the $\sim 70 - 200$ MeV range due to the energy threshold required for neutral pion production, and second, a flat emission up to the energy determined by the interplay between the maximum energy to which the CRs are accelerated and the escape rate of high energy protons

into the interstellar medium. However, detecting these distinctive features has only been possible, from a detailed analysis of the spectrum, for a handful of interacting SNRs (Ackermann et al., 2013; Giuliani et al., 2014; Jogler & Funk, 2016; Ambrogi et al., 2019). The bremsstrahlung radiation mechanism is another possibility to explain the observed gamma-ray spectrum at energies above $\sim$ 100 MeV. It also originates a hard spectral energy distribution in this regime (e.g., see Figure 2.9), but in this scenario, the electrons (instead of protons) interact with the surrounding media. The main difficulty arising from this model, in general, is to explain the sharp drop at lower energies, i.e., at tens of MeV, which typically results in invoking an artificial lower cutoff in the spectrum of electrons (Ambrogi et al., 2019).

The emission mechanisms that ultimately dominate the gamma-ray emission from supernova remnants depend on many different aspects. Since a fast shock velocity promotes, in principle, both the acceleration of hadronic and leptonic cosmic rays, it is still not clear if the gamma-ray emission of the brightest sources observed is originated from proton-proton interactions, by electrons off-scattering soft photon fields through inverse Compton mechanism, or via bremsstrahlung. Competing gamma-ray processes, in principle, should have different imprints on the spectral shape. For example, those related to leptonic emission might show a broad peak at hundreds of GeV. For this reason, sampling the spectrum from a few hundreds of MeV to tens of TeV should result in a strong lead to the origin of the observed radiation. The shape of the bright and young SNRs spectra seems to favor, in general terms, a leptonic origin (see, e.g., Abdo et al., 2011b). However, the hadronic interpretation can not be completely ruled out. In contrast, the spectral shape of other young but much fainter remnants (e.g., Cassiopeia A or Tycho, see Ahnen et al., 2017b) seem to be better explained by hadronic interaction.

Other types of sources identified as accelerators of Galactic cosmic rays to VHEs (since the 1980s, see, e.g., Casse & Paul, 1980; Voelk & Forman, 1982; Cesarsky & Montmerle, 1983; White, 1985) are star-forming regions (SFRs) within massive star clusters (Ackermann et al., 2011a; H.E.S.S. Collaboration et al., 2011; Abramowski et al., 2012a; H.E.S.S. Collaboration et al., 2015a; Yang et al., 2018; Aharonian et al., 2019; Saha et al., 2020 Yang & Wang, 2020; Sun et al., 2020a;b). In particular, several locations in SFRs have been proposed as acceleration sites, such as the vicinity of OB and Wolf-Rayet stars, at the interaction of their fast winds with supernova shocks, or in so-called super-bubbles (see Bykov et al., 2020, and references therein). At the moment, several star-forming regions as, e.g., Cygnus OB (Abdo et al., 2007b; Ackermann et al., 2011a; 2012) or 30 Doradus (in the Large Magellanic Cloud, Bamba et al., 2004; Smith & Wang, 2004; Yamaguchi et al., 2009; H.E.S.S. Collaboration et al., 2015a), have been established as likely accelerators of Galactic cosmic rays through observations at GeV and TeV energies. However, a firm identification remains elusive, given the large extension of

the sources and/or other efficient accelerators in the region, such as pulsars and pulsar wind nebulae, are present. This chapter will examine the gamma-ray emission of the SNR G39.2-0.3 and the VHE emission towards the Westerlund 2 massive stellar cluster.

5.2 SNR G39.2-0.3

SNR G39.2-0.3 (also dubbed 3C 396) is a core-collapse (Type IIL/b) supernova (Lee et al., 2009). The progenitor stars of this class of supernovae go through a phase of red supergiant (RSG). In this phase, the star enriches the circumstellar medium (where the remnant will expand) with its in-homogeneous, cool, dense outflows. The source presents a bright near-infrared [Fe II] and H_2 emission (attributed to shocked molecular gas), as in a few other cases known, i.e., G11.2–0.2, RCW103, W44, and W49B (see Lee et al., 2009, and references therein). The X-ray spectral analysis of the remnant points to age, still presenting a large uncertainty, ranging between ~ 3 kyr (Su et al., 2011) and ~ 7 kyr (Harrus & Slane, 1999). SNR G39.2–0.3 is an asymmetric composite supernova remnant, i.e., identified both by the SNR shell and a pulsar wind nebula. The non-thermal emission likely associated with the pulsar wind nebula arises from the central part of the remnant. In contrast, the western part of the shell, brighter in radio and X-rays, is believed to interact with a molecular cloud. The remnant's radio emission also shows a faint tail extending from the prominent western shell toward the east (Olbert et al., 2003; Sezer et al., 2020).

The source has been extensively observed using millimeter molecular tracers (see the cited papers), revealing a remarked cavity-like structure at $V_{LSR} \sim 69$ km s^{-1} around the remnant. A different association with a region located at $V_{LSR} \sim 88$ km s^{-1}, which seems to be perfectly confined by the western molecular wall, was also proposed (Su et al., 2011) from CO millimeter observations. On the eastern side, the fading material matches the X-ray and radio emissions. At microwave frequencies, the spectral energy distribution was described by two components (Cruciani et al., 2016). In the 1-30 GHz range, the first corresponds to a synchrotron spectrum with (power-law) index $\alpha = 0.36$. The second is a thermal (black body) emission from dust at a temperature of 25 K and optical depth (at 100 μm) of 3.6×10^{-4}. The bright infrared emission was also detected by *Spitzer* (Reach et al., 2006), as both filamentary emission in the western and eastern parts and (faint) diffuse emission around the entire shell.

In the high-energy regime, the *Fermi* source 4FGL J1903.8+0531 (listed in the *Fourth Source Catalog*), lying at a distance smaller than 0.1° from the SNR G39.2–0.3 radio position, seems to be associated with the remnant. A log-parabola function with indices $\alpha = 2.72 \pm 0.16$ and $\beta = 0.26 \pm 0.08$ (The *Fermi*-LAT collaboration, 2019), represents well its gamma-ray spectrum. Finally, there is no counterpart of the source reported at TeV

energies. In this regime, observations carried out by H.E.S.S. established an upper limit for the source's flux of about 6×10^{-13} erg/cm^{2}s (see H.E.S.S. Collaboration et al., 2018).

5.2.1 Reanalysis of SNR G39.2-0.3 with LAT data and CO observations

5.2.1.1 Data selection

The source was recently reanalyzed in the high-energy regime with $\sim$ 11 years of LAT data (i.e., from 2008 August 4, 2008, to 2019 June 19) at energies between 100 MeV and 100 GeV (see de Oña Wilhelmi et al., 2020). The analysis located the point-like source at the position RA(J2000) = $(286.01^\circ \pm 0.02^\circ)$ and DEC(J2000) = $(5.47^\circ \pm 0.02^\circ)$ with 0.066° error at 99% CL, pointing strongly to a physical association between the remnant and the LAT gamma-ray source. Figure 5.1 shows the localization of the source (with a red line) superposed to a (large-scale) CO map derived from the MWISP survey (see Su et al., 2019, for more detailed information). The MWISP survey of the Galactic plane is carried out with the 13.7 m telescope of the Purple Mountain Observatory, observing the ^{12}CO(J=1–0), ^{13}CO(J=1–0), and C^{18}O(J=1–0) lines simultaneously. It covers the region of $l = -10^\circ$ to $l = +250^\circ$ and $|b| \lesssim 5^\circ$. The data presents moderate resolution (with a half-power beamwidth of $\sim 50''$ at the frequency of $\sim 110 - 115$ GHz) and a typical RMS noise level of ~ 0.5 K for ^{12}CO and ~ 0.3 K for ^{13}CO and C^{18}O, at a velocity resolution of 0.17 km s^{-1} with a uniform grid spacing of $30''$. The region surrounding the source depicted is obtained integrating between 67 km s^{-1} and 74 km s^{-1} (as in Lee et al., 2009) and between 80 km s^{-1} and 88 km s^{-1} (Su et al., 2011). The integrated mass density derived, computed assuming a linear relationship between the velocity and the integrated CO intensity, is similar for the two velocity ranges, with 440 cm^{-3} (326 cm^{-3}) for the 69 km s^{-1} (88 km s^{-1}) range at a fiducial distance of 6.2 kpc (and a conversion factor $X_{CO} = 2.0 \times 10^{20}$ cm^2 (K km s)). The two molecular clouds mentioned are (clearly) visible on both maps, with a slight offset between the first one (towards the North in the panel a) and the Fermi source and the radio shell position.

Figure 5.2 shows the spectrum obtained at LAT energies (for a point-like source). The best-fitted log-parabola model corresponds to indices of $\alpha = 2.6 \pm 0.1$ and $\beta = 0.20 \pm 0.03$ with $(8.0 \pm 0.7) \times 10^{-13}$ MeV^{-1}/cm^2 s of differential flux at an energy of 2.3 GeV, in good agreement with previous measurements (Sezer et al., 2020; The Fermi-LAT collaboration, 2019).

5.2.1.2 Modeling of the SNR G39.2-0 multiwavelength spectrum

As discussed in de Oña Wilhelmi et al. (2020), the good spectral and morphological agreement between 4FGL J1903.8+0531 and SNR G39.2–0.3 indicates a clear association of the two sources, while the molecular content in the region surrounding the source

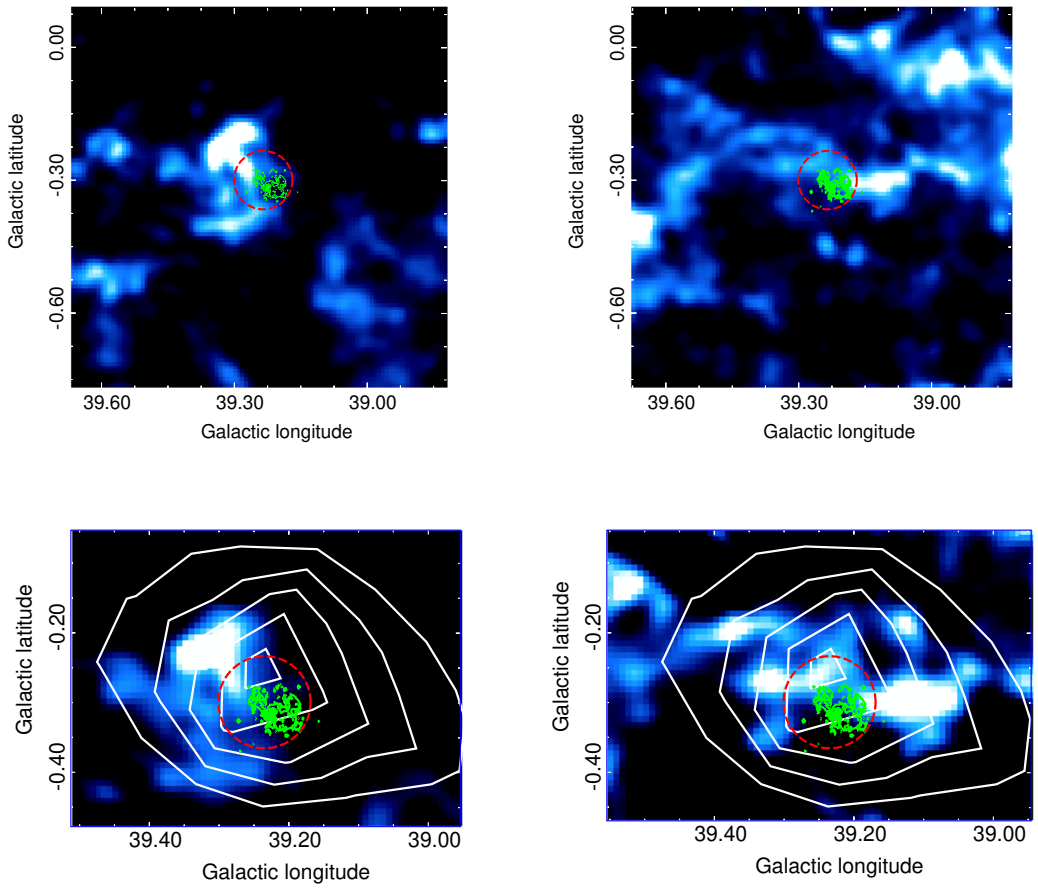

Figure 5.1: On the top left, (a) depicts the ^{13}CO large-scale intensity map integrated between 67 km s^{-1} and 74 km s^{-1} obtained from the MWISP survey. On the top right, (b) shows the intensity map integrated between 80 and 88 km s^{-1}. The red dashed-line circle marks the 99% localization error of the *Fermi* reanalysis. The green contours correspond to the radio shell, derived from the image compiled by Ferrand & Safi-Harb (2012). The bottom panels show the ^{12}CO channel (MWISP survey), centered on the position of SNR G39.2-0.3. The left one (c) for the 69 km s^{-1} map and the right one (d) for the 88 km s^{-1} one. White contours are obtained from the LAT significance map above 3 GeV, starting on TS=25 (or $\sim 5\sigma$ significance in steps of 10). The plot was taken from de Oña Wilhelmi et al. (2020).

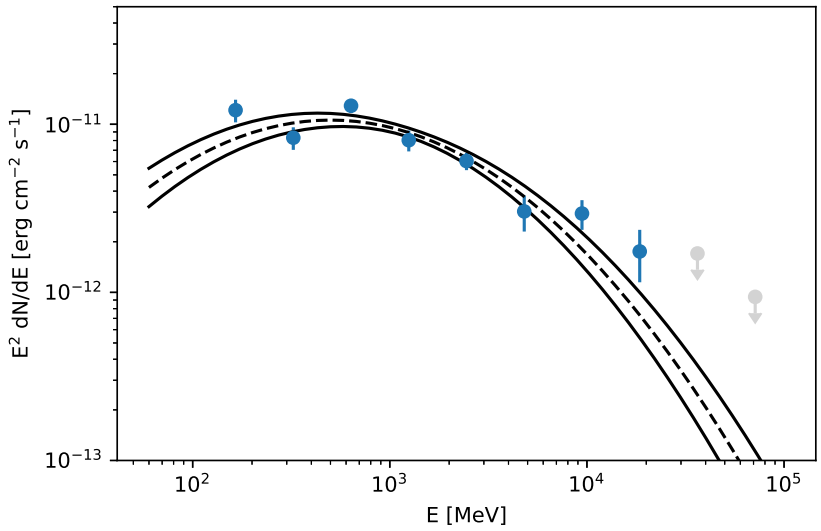

Figure 5.2: Spectral energy distribution of 4FGL J1903.8+0531, associated with SNR G39.2–0. The black lines represent the best-fitting shape, and the 1σ error derived for the energy range between 100 MeV and 100 GeV. The plot was taken from de Oña Wilhelmi et al. (2020).

suggests a scenario in which the remnant is accelerating cosmic rays, electrons or hadrons, which ultimately interact with the ambient material. The modeling of the multi-wavelength spectrum of the source supports this scenario. Note that the X-ray (non-thermal) emission detected by *Chandra* is likely associated with the central pulsar wind nebula rather than with the SNR shell. The synchrotron and inverse Compton emission mechanisms do not appropriately explain the spectral shape observed unless an unrealistic energy density of the FIR photon field, i.e., a few hundred eV/cm^3, contrary to the ~ 2 eV/cm^3 measured, is invoked (to boost the IC flux). The bremsstrahlung emission corresponding with the low-energy part of the electron population that best describes the data, well constrained by fitting the radio emission, does not reproduce either the source's LAT spectrum. However, it constrains the electron population's amplitude to be smaller than 3×10^{34} eV^{-1} for a density of ~ 400 cm^{-3} (as discussed above). The (joint) radio and GeV data analysis also limits the remnant's magnetic field to a lower value of ~ 150 μG and the maximum electron energy to $E_{cut} \leq 100$ GeV (for a power-law with an exponential cutoff electron energy distribution). It is, in principle, a large magnetic field for an evolved SNR. However, it is still reasonable for SNRs of a few thousand years interacting with a dense cloud. For instance, molecular clouds with densities $\lesssim 300$ cm^{-3} are expected to present (approximately) a constant magnetic field of about 10 μG (Crutcher et al., 2010), which can then be further compressed by the SNR shock, under certain conditions,

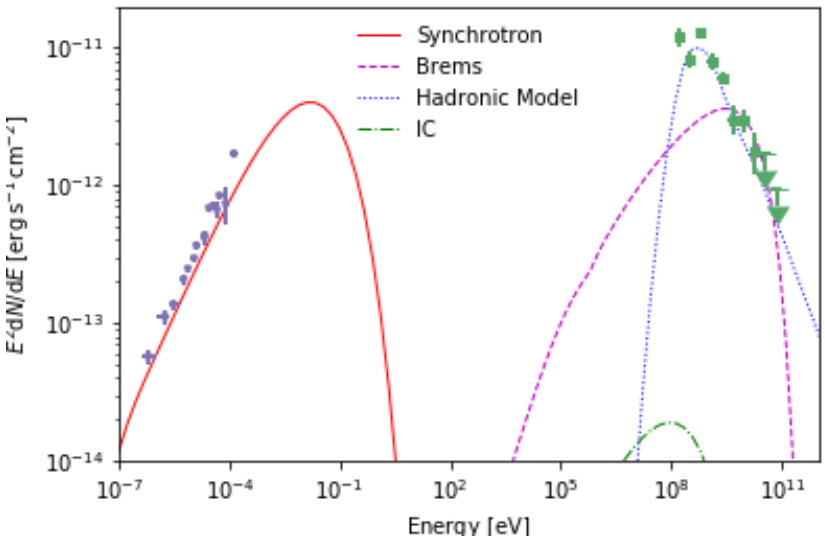

Figure 5.3: Multiwavelength spectral energy distribution of the SNR G39.2–0.3. The lines indicate the best-fitting models for both leptonic and hadronic interpretations of the high-energy emission. The plot was taken from de Oña Wilhelmi et al., (2020).

to similar values than the one obtained. See de Oña Wilhelmi et al. (2020) for a more detailed discussion and other alternative explanations.

In contrast with the leptonic models, the best-fitted hadronic model can reproduce the spectral shape observed for the SNR (see Figure 5.3). This model assumes the injected protons population to follow a broken power-law energy distribution. The last would naturally account for a superposition of different cutoff energies during the evolution of the remnant and subsequent particle escape at later times, or intrinsic properties of the cosmic-ray acceleration in the shock, i.e., the finite size of the emission region or evolution of the shock in a partially ionized medium (see de Oña Wilhelmi et al., 2020, and references therein).

The energy in electrons (E_p) obtained above 100 MeV of energy is $\mathrm{W_p} = 3.2^{+1.1}_{-0.8}10^{49}$ erg (at 6.2 kpc distance), representing only a few percent of the total energy estimated for the SNR explosion, i.e., $[3.5 - 7] \times 10^{50}$ erg according to Harrus & Slane (1999). The spectral indices of protons were fitted to $s_1 = 2.0 \pm 1.5$ and $s_2 = 2.78 \pm 0.06$, with the break energy located at $\mathrm{E_b} = 220 \pm 70$ MeV. s_1 is poorly constrained because of this low break energy. A simple power-law proton distribution results in an index of $s = 2.75^{+0.04}_{-0.06}$ and similar total energy in protons (above 100 MeV) than the previous case. The low-energy break measured, given the large magnetic field obtained, makes SNR G39.2–0.3 an extremely inefficient particle accelerator. For a type II supernova remnant of several kyr of age, shock velocities of the order of 10^3 km/s are still expected (see Gabici et al., 2016). Thus,

for a large magnetic field, protons could, in principle, be accelerated up to TeV energies. The low cutoff energy could arise from either a slow shock or a large escape rate of TeV protons. The gamma-ray source's point-like morphology is centered on the SNR rather than on the peak of the radio emission integrated between 67 and 74 km s^{-1}, pointing to an association with the second velocity range proposed ($[80 - 88]$ km s^{-1}). But Su et al. (2011) revealed a thick molecular wall at this velocity (coincident with the bright X-ray, IR, and radio emission from the west part of the remnant). This wall tentatively suggests a natural hampering of the remnant expansion (limiting its acceleration efficiency to VHEs) and, at the same time, an explanation for the large magnetic field needed to account for the radio emission.

Since the acceleration of protons and electrons should occur in a comparable way, the spectral shape of both particle populations should, in principle, be similar. At least, at low energies in which electrons are not significantly affected by synchrotron cooling. It implies the electron spectrum should reflect the spectral break obtained for the proton energy distribution. Taking into account that the characteristic energy of the emitted synchrotron photon can be approximated by:

$$\nu_{\rm ch} \simeq 0.8 \left(\frac{E}{1\,\mathrm{GeV}}\right)^2 \left(\frac{B}{150\,\mu\mathrm{G}}\right)\ \mathrm{GHz}, \tag{5.1}$$

and that the observations in radio do not show a break in the spectrum below ~ 31 GHz (Cruciani et al., 2016), the spectral break, a priori, can only occur at energies of hundreds of MeV for extremely high magnetic fields. Nonetheless, the estimate of the break energy is rather uncertain, given that a simple (~ 2.75 index) power-law particle spectrum has not actually been ruled out.

5.2.2 Old dynamical age scenario

The gamma-ray spectrum derived for SNR G39.2-0.3 (see Figure 5.2), with a turn-over at GeV energies ($\sim$ 2.3 GeV from the log-parabola fit), suggests a remnant in the post-adiabatic stage, i.e., characterized by a low shock velocity and substantial escape of cosmic rays. Detailed modeling of the time evolution of the cosmic-ray spectrum in this phase, see, e.g., Brose et al. (2020), showed that the inefficient confinement of high-energy particles could lead to the formation of a spectral break at 10 - 100 GeV. However, numerical simulations of the expected gamma-ray emission from particle acceleration in SNRs performed in de Oña Wilhelmi et al. (2020), compared to the gamma-ray spectrum observed, ruled out a break energy above ~ 3 GeV of energy (if the particle acceleration at the shock produces the usual 2 index power-law spectrum). Hence, the remnant's dynamical age is likely very old, i.e., the remnant is far into the post-adiabatic phase.

As discussed in the cited paper, a softer particle spectrum than expected from diffusive shock acceleration (i.e., 2) is, in principle, possible and can explain the gamma-ray

spectrum of the remnant. In particular, a lower index close to $s_1 = 2.75$ represents well the *Fermi* data, being in this case, the break energy less important. However, it disagrees with the radio observations, which indicate a featureless 1.8 (power-law) index electron spectrum. Besides, there is no obvious reason to expect a proton spectral shape significantly different from the one of electrons.

As we saw, any of the two approaches presented, i.e., low break energy or soft particle spectrum, entirely agree with time evolution models and the synchrotron spectrum observed (up to tens of GHz). A tentative approach to reconcile the discrepancies is to consider the elemental composition of the surrounding medium. The presence of heavy elements, both as cosmic rays and/or as target material, would result in a shift of the gamma-ray peak towards lower energies (Bhatt et al., 2020). Figure 6 of de Oña Wilhelmi et al. (2020) shows the gamma-ray spectrum expected (from numerical calculations) with different heavy nuclei compositions of cosmic rays (being accelerated at the shock). The cited paper proved that a typical carbon-loaded Wolf-Rayet wind model, with a mixed 55% He and 45% C composition, reproduces the observed spectral shape, implying peak energy of 0.8 GeV. With a composition close to the usual one of the interstellar medium, the main sequence stellar wind should dominate the stellar wind bubble's total mass. However, the main-sequence wind may be pushed to the bubble's edge by the WR winds. Hence, it is not unrealistic to assume that the particles injected at the shock are precisely those that originated from a heavier composition. The low-energy turn-over observed in the G39.2-0.3 gamma-ray spectrum (and in a few others SNRs) might be then taken as a possible hint of gamma-rays produced in heavy nuclei interactions. More precise measurements of gamma-ray spectra are needed to probe the composition of the media surrounding supernova remnants.

5.3 The Carina arm region

The Carina arm region, towards the stellar cluster Westerlund 2, has been of notorious interest for the VHE astronomy in the last decade. For instance, the Galactic survey carried out by the H.E.S.S. observatory (H.E.S.S. Collaboration, 2018) has revealed several prominent TeV sources in this direction, where *Fermi*-LAT has also observed different gamma-ray pulsars and supernova remnants (Abdo et al., 2009; Saz Parkinson et al., 2010; The Fermi-LAT Collaboration, 2012; Acero et al., 2013; Ackermann M., et al., 2017; Yang et al., 2018). In particular, HESS J1023-575, HESS J1026-582, and HESS J1018-589 (later split into two sources HESS J1018-589 A and HESS J1018-589 B) have been the object of numerous recent studies (H.E.S.S. collaboration, 2011; H.E.S.S. collaboration, 2012b; H.E.S.S. collaboration, 2015). The gamma-ray emission from HESS J1023–575 (H.E.S.S. collaboration, 2011) is coincident in direction with the position of Westerlund

2, while HESS J1026-582 lies $\sim 0.6^\circ$ apart. Westerlund 2 hosts a large number of hot and massive stars, including two remarkable Wolf-Rayet stars (WR 20a and WR 20b) detected by *Chandra* in X-rays (Nazé et al., 2008). The nearby gamma-ray pulsar PSR J1023–5746, with a period of 111.5 milliseconds, was suggested to be associated with the extended HESS J1023–575 TeV emission (H.E.S.S. collaboration, 2011). However, there is no corresponding pulsar wind nebula (firmly) identified. In contrast, PSR J1028–5819 (with 91.4 milliseconds period, Abdo et al., 2009) has been related with HESS J1026-582, located at the south-east of the pulsar. As in the case of PSR J1023–5746, no associated pulsar wind nebula has been found so far at X-rays.

The other prominent region with various gamma-ray sources detected is HESS J1018-589 (H.E.S.S. collaboration, 2015). The region includes three main potential emitters of VHE gamma-rays; a supernova remnant, i.e., SNR G284.3–1.8 (also dubbed MSH 10-53), the pulsar PSR J1016–5857, and the LAT gamma-ray binary 1FGL J1018.6–5856. The former, i.e., SNR G284.3–1.8, appears in radio as an incomplete and poorly defined shell. On the one hand, PSR J1016-5857 is a young and energetic (107 milliseconds) pulsar near SNR G284.3–1.8 that may be associated with the remnant (Camilo et al., 2001). It is also believed to be powering a pulsar wind nebula associated with the extended TeV emission named HESS J1018–589 B. On the other hand, the binary system 1FGL J1018.6–5856 gamma-ray emission is coincident with the point-like source HESS J1018–589 A, while observations in the optical showed that the non-thermal source is also positionally coincident with a massive O-type star proposed to be the neutron star companion.

5.3.1 Westerlund 2

Westerlund 2 is one of the best-studied massive stellar clusters in our Galaxy. It is centered in one of the most luminous and massive HII regions in the Galaxy dubbed RCW 49, which is ionized by the Westerlund 2 cluster. RCW 49 is a prominent optical source (NGC 3247 or G29, Rodgers et al., 1960), centered at the position $l = 284.3$ and $b = -0.3$, with a dimension of 90×35 arcminutes. High-resolution observations of the RCW 49 region in the radio continuum (at 1.38 and 2.38 GHz) with ATCA revealed two wind-blown shells (see Figure 5.4). The more massive one surrounds Westerlund 2 (with $\sim 7'$ diameter) and exhibits a distinctive blister structure on the western side. In contrast, the other shell (with a diameter of $\sim 4'$) is centered in the position of the Wolf-Rayet star WR 20b (Whiteoak & Uchida, 1997). The region was also observed by *Spitzer* in infrared wavelengths, concluding that, in the same, star formation is still ongoing (Whitney et al., 2004).

At TeV energies, an extended source discovered by the H.E.S.S. observatory (HESS J1023-575, Aharonian et al., 2007), is coincident with Westerlund 2 and the wind-blown

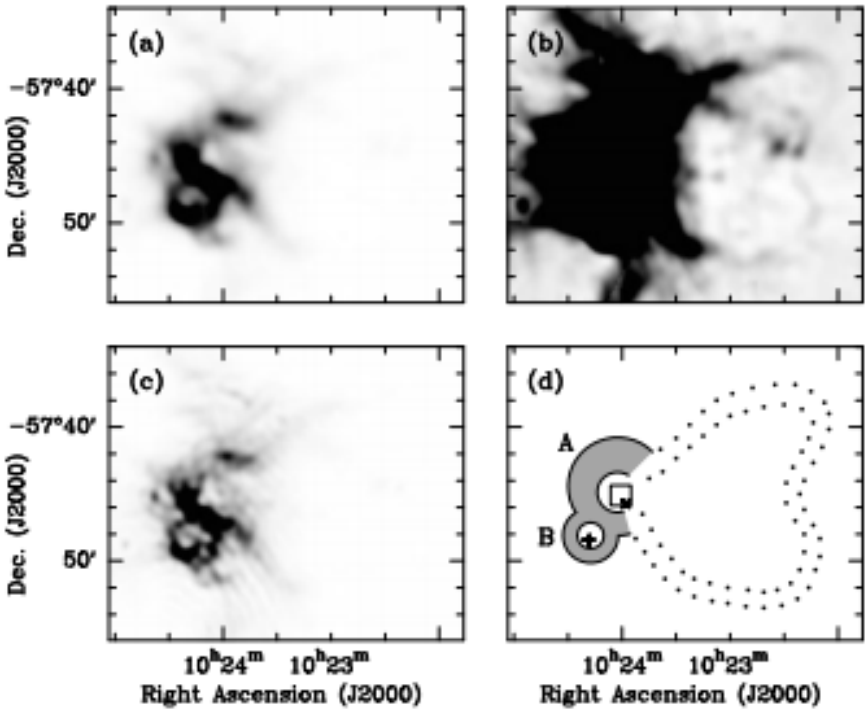

Figure 5.4: The panels above correspond to images of the core of RCW 49 at 0.843 GHz (taken from Whiteoak & Uchida, 1997). In (a) with a resolution of 43″, in (b) with a greyscale that enhances fainter structure, in (c) at a resolution of 25″, and in (d) a sketch of the wind-blown shells (A and B) with the blister outlined by a dotted curve. WR 20a and b are indicated by the cross-mark and plus sign, respectively. The box encloses the Westerlund 2 cluster location.

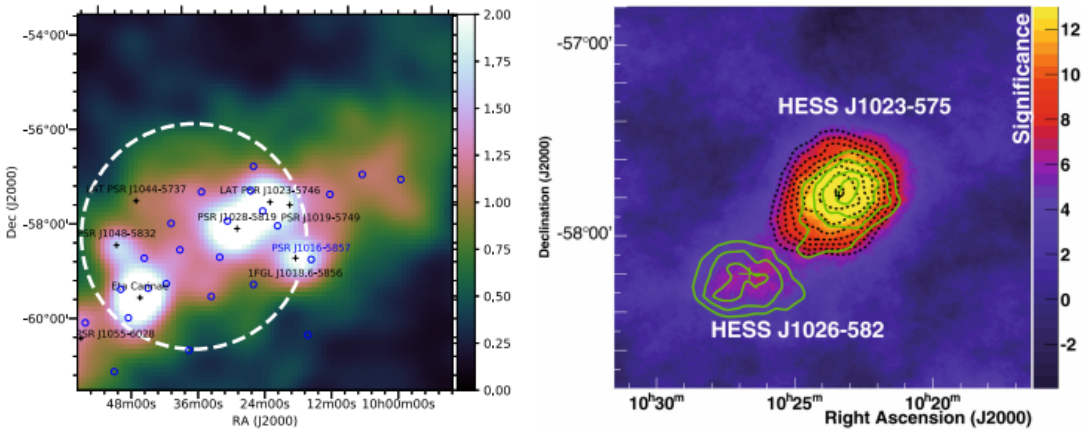

Figure 5.5: The left panel, taken from Yang et al. (2018), shows the gamma-ray emission (in counts) above 10 GeV for a ($8° \times 8°$) region around Westerlund 2. The black crosses and blue circles represent identified and unassociated sources from the 3FGL catalogue. The white dashed line shows the extended emission of FGES J1036.4–5834. At the right, the Westerlund 2 field in H.E.S.S. data showing the significance of the VHE gamma-ray emission. The black (dashed) and green (solid) contours correspond to $0.7 < E < 2.5$ TeV and $E > 2.5$ TeV, respectively. The right panel is taken from HESS Collaboration (2011).

shell. The TeV source is located at $\alpha = 10^h23^m24^s \pm 7.2^s_{stat}$ and $\delta = \breve{}57°47'24'' \pm 1' 12_{stat}''$ (J2000). It has an extension of $\sim 0.2°$, and a power-law 2.58 photon index accounts well for its spectrum (H.E.S.S. Collaboration et al., 2011). In the GeV regime, a young (characteristic age of $\sim$ 4.6 kyr) and energetic ($\sim 10^{37}$ erg/s of spin-down luminosity) pulsar known as PSR J1023–5746 lies $8'$ away from the cluster (i.e., at the position $\alpha = 10^h23^m02.9^s$ and $\delta = \breve{}57°46'05''$, Saz Parkinson et al., 2010).

A PWN associated with PSR J1023–5746 was suggested as the possible counterpart of the TeV source and searched in the *Fermi*-LAT data (Ackermann et al., 2011b; Acero et al., 2013). Two GeV Fermi Galactic Extended Sources (FGES, Ackermann et al., 2017), FGES J1023.3–5747 and FGES J1036.4–5834, were also detected within the region. FGES J1023.3–5747, with $\sim 0.28°$ of extension (for a 2D disk model), is spatially coincident with the TeV source HESS J1023–575, while the second source, FGES J1036.4–5834, is very extended (with more than 2° of radius) and presents a hard spectrum with a power-law 2 photon index (The Fermi-LAT Collaboration, 2017; Yang et al., 2018).

Besides the PWN scenario, several accelerators have been proposed to power the TeV emission. Westerlund 2 contains an extraordinary ensemble of hot and massive OB stars, with many early-type stars and twelve very hot O-stars with spectral types earlier than O7 (Rauw et al., 2007). The total energy release for the collective winds was estimated to be $\sim 5.7 \times 10^{37}$ erg s^{-1} (see the cited paper). Westerlund 2 also hosts one of the most massive binary systems, composed of two WN6ha stars (Rauw et al., 2004), dubbed WR

20a. Their orbital period is $\sim$ 3.6 days, and the estimated kinetic energy loss rate is 10^{37} erg s^{-1} (Bonanos et al., 2004). The medium surrounding Westerlund 2 is rich and complex, and several massive molecular clouds overlap with the GeV and TeV gamma-ray sources (coincident with the stellar cluster, see Dame, 2007; Furukawa et al., 2009).

The attempts to determine the distance accurately to Westerlund 2 led to a persistent uncertainty since its discovery, resulting in different estimates ranging in a broad interval between 2 kpc and 8 kpc (see, e.g., Salpeter, 1955; Moffat et al., 1991; Piatti et al., 1997; Carraro & Munari, 2004; Uzpen et al., 2005; Rauw et al., 2005; Dame, 2007; Tsujimoto et al., 2007; Rauw et al., 2007; Ascenso et al., 2007; Furukawa et al., 2009; Vargas Álvarez et al., 2013a). We will consider this uncertainty for the analysis we present in this Chapter, although adopting a reference value of 5 kpc, roughly in the mid-range of the recent optical photometric work (Vargas Álvarez et al., 2013a; Drew et al., 2018) and at the bottom end of the interstellar medium (ISM) estimates (Dame, 2007; Furukawa et al., 2014).

In the following sections, we will describe first the LAT data used to reanalyzed the region at VHEs. Then, we will explain how we modeled the gamma-ray emission, and finally, we will discuss different hypotheses for the origin of the observed radiation.

5.3.2 Fermi-LAT observations: Methodology.

We have investigated the gamma-ray emission characteristics from FGES J1023.3–5747 and PSR J1023–5746 (in the region described above). For this purpose, we used $\sim$ 11 years of Fermi-LAT data spanning from 4 August 2008 to 24 April 2019 (or 239557417 - 577782027 seconds in Fermi Mission Elapsed Time), exploring the energy range from 200 MeV to 500 GeV. The region of interest (ROI) examined was defined by a radius of 20° around the radio position of PSR J1023–5746, i.e., RA = 155.76° and DEC = −57.77° (Kerr et al., 2015).

We carried out the analysis following the prescriptions recommended by the *Fermi*-LAT collaboration[1]. Hence, we analyzed only the dubbed SOURCE class events selecting the FRONT+BACK events types, with a maximum zenith angle of 90° to eliminate Earth limb events. As previously commented, we selected the events with a minimum energy of 200 MeV. The *Fermi*-LAT band extends to lower energies. However, we are interested in avoiding poorly reconstructed events due to the large angular resolution and the large crowding of sources in the region. Note that, as seen before, the analysis of the source spectrum below 200 MeV is crucial to characterize hadronic-originated gamma-rays sources due to the neutral pion decay spectrum rises steeply below this energy, originating the feature often referred to as the pion-decay bump (see Figure 2.9). However, this particular source is not a promising candidate for this analysis, given the source's moderate flux limits the photons flux at very low energies. Furthermore, the extended morphology complicates

[1]See in `https://fermi.gsfc.nasa.gov/ssc/data/analysis/`

the study compared to the point-like case. The presence of several sources in the region (as PSR J1023–5746) may further contaminate the spectrum, especially at tens of MeV, preventing an accurate characterization in this energy regime. For the moment, we will focus on studying the general GeV to TeV spectral shape, leaving the analysis of the pion decay bump region to further studies.

To properly characterize the spectrum and morphology of FGES J1023.3-5747, we first need to disentangle its diffuse gamma-ray emission from the radiation coming from the pulsar PSR J1023–5746 and other nearby sources. Thus, we first derived the spectral energy distribution of all the sources in the field of view (i.e., a radius of 20° around the position of FGES J1023.3–5747). We built a comprehensive model describing the gamma-ray sources in the region by including all the LAT sources (located within the same) listed in the *Fermi*-LAT Fourth Source Catalog (4FGL, Abdollahi, et al., 2020). Also, to account for the significant contribution to LAT data from Galactic and extragalactic diffuse gamma-rays, we employed (public and available) Galactic (in version gll_iem_v07) and isotropic (iso_P8R3_SOURCE_V2_v1) diffuse emission models. The model's free parameters correspond to the spectral parameters of the sources within 3° around the position of PSR J1023–5746 (except for the energy scale). Beyond this radius, the normalization of all the sources spectra with Test Statistic greater than ten (TS > 10) is also free. The Test Statistic mentioned is defined as TS = 2log(L/L$_0$), where L is the maximum value of the likelihood function over the ROI including the source in the model, and L_0 is the same without the source (Mattox et al., 1996). The detection significance is usually approximated as; $\sqrt{TS}$.

We analyzed the (P8R3, Atwood et al., 2013; Bruel et al., 2018) data using the FERMIPY PYTHON package (version 0.18.0, Wood et al., 2017), described in more detail in Section 3.2.2. The data were binned in 8 energy bins per decade and spatial bins of 0.1° of size. The response of the LAT instrument was evaluated with the version P8R3_SOURCE_V2 of the Instrument Response Functions. We applied the energy dispersion correction to the sources in the model employed, except (as usual) for the isotropic diffuse emission model.

The current version of LAT data (i.e., PASS 8) classifies the events into quartiles based on the varying quality of the direction reconstruction (PSF events types). Our analysis considered the four Point Spread Function (PSF) event types available (dubbed PSF0, PSF1, PSF2, and PSF3). We applied the appropriate IRF and isotropic background models according to the quality of the reconstructed event directions. We thus are preventing the loss of possibly useful information in the analysis by treating separately high-quality events and poorly localized ones.

A method (known as pulsar gating) to enable the analysis of the gamma-ray emission from a source, while discriminating the same from a nearby pulsar emission, is to perform

a timing analysis of the pulsed radiation and remove the intervals of time in which the pulsar is switched on. We applied this method to the LAT data described above to facilitate the diffuse gamma-ray emission analysis (from FGES J1023.3–5747) underlying the PSR J1023–5746 radiation. We performed the timing analysis of the pulsar employing the analysis package TEMPO2 (Hobbs et al., 2006) and computed the phase curve of PSR J1023–5746 by assigning the corresponding phases to the gamma-ray events located within 0.6° of radius around the pulsar's position (i.e., RA = 155.76°, DEC = -57.77°). The events phases were calculated using the updated ephemeris of PSR J1023–5746 at epoch 55635 MJD, which allows us to enlarge the data set to the time interval cited (i.e., more than eleven years). This ephemeris was kindly provided to us by the *Fermi*-LAT collaboration. Then, we applied the Bayesian Blocks method (Scargle et al., 2013) to the PSR J1023–5746 light curve and obtained different components, defined as ON, OFF, and *Bridge* emission. Bayesian Blocks is a time-domain algorithm to find the optimal step-function model of time series data. For comparison, we also computed the contribution to the phase curve of each of the sources in the model. To calculate it, we used the *Fermi* tool *gtsrcprob*, assigning every event the probability of belonging to each of the sources in the model.

The spectral energy distributions of the sources were obtained with the *sed()* method of FERMIPY for twelve bins of energy (spanning from 200 MeV to 500 GeV), using the whole ROI, and being the FGES J1023.3–5747 and PSR J1023–5746 spectra characterized by exponential cutoff power-law and simple power-law models, respectively. We applied this method cutting the events in phase to obtain the sources spectra in the different components of the phase curve. Finally, we probed the consistency of the spectral analysis by exploring the systematic uncertainties on the spectra computation method. The systematics are mainly due to the LAT effective area (A_{eff}) and the Galactic diffuse emission model. Those due to the LAT effective area can be evaluated with the bracketing A_{eff} method (see https://fermi.gsfc.nasa.gov/ssc/data/analysis/scitools/Aeff_Systematics.html), while the systematic errors due to the diffuse Galactic model were tested by artificially changing its normalization by ±6% compared to the best-fitted value (as in Ajello et al., 2011, and Li et al., 2018).

We analyzed the FGES J1023.3–5747 size with the FERMIPY extension method, based on a likelihood ratio test with respect to the point-source hypothesis. We tested both 2D symmetric Gaussian and 2D radial disk models for the extended source's morphology. The best-fit extension in each case is computed by performing a likelihood profile scan over the source width (68% containment) and maximizing the model's likelihood.

To conclude the analysis, we imposed different additional cuts of energy on the LAT data, particularly with breakpoints at: 700 MeV, 3 GeV, 10 GeV, 40 GeV, 70 GeV, and 135 GeV. Next, we re-analyzed the data in each (differential) energy bin, studying the

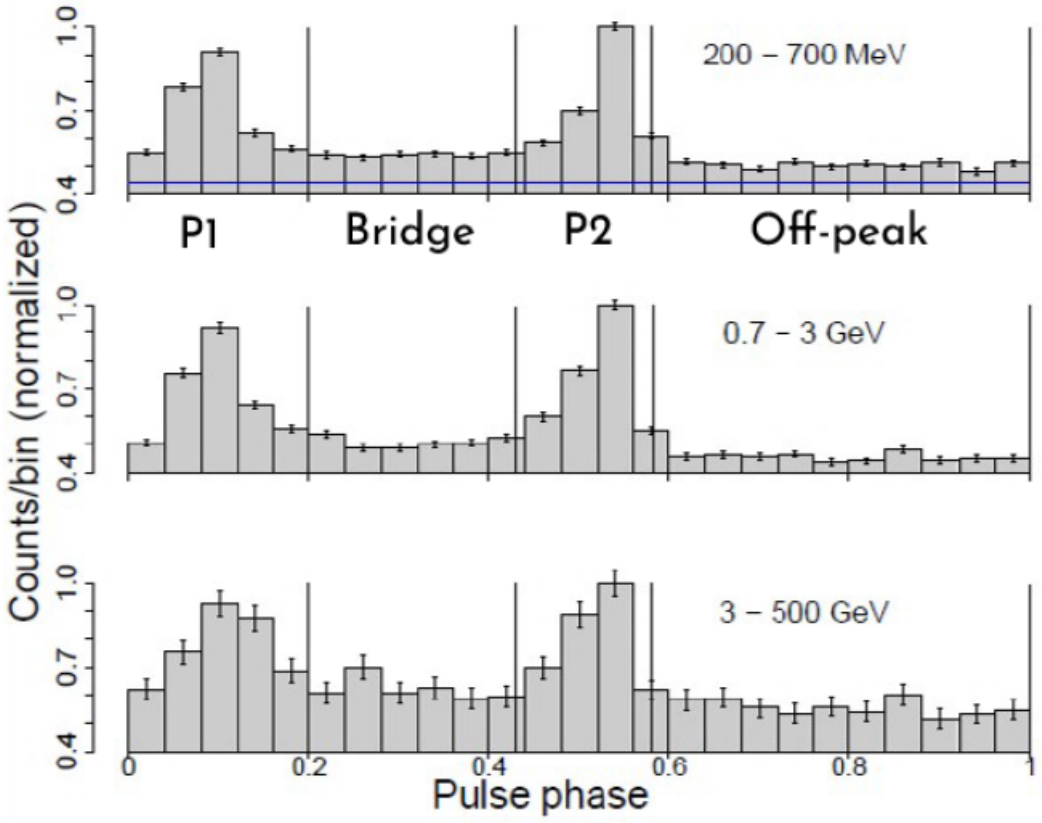

Figure 5.6: Phase curve of PSR J1023.1-5745 obtained at different energies in a region of 0.6° around the pulsar's position (normalized by the height of P2) with the various components of the phase curve noted. The horizontal blue line corresponds to the expected contribution in the phase curve of background sources (i.e., all the sources in the field of view except FGES J1023.3–5747 and PSR J1023.1-5745).

morphological characteristics of FGES J1023.3–5747 (see Figure 5.10). Furthermore, we obtained the source's radial profile by fitting its extended emission to several normalized templates (simultaneously). These templates consist of uniform concentric circular rings with 0.1° of width, spanning to an outer radius of 0.4° from the source. To obtain the flux in each region, we integrated the best-fit model (for each template) from 3 GeV to 500 GeV of energy.

5.3.3 Fermi-LAT observations: Results.

5.3.3.1 Timing analysis of PSR J1023–5746

The timing analysis of the bright pulsar PSR J1023–5746, which dominates the gamma-ray emission in the region below a few GeV, with TEMPO2 and the Bayesian Blocks method, showed a phase curve displaying two peaks. The former (hereafter P1) spans from 0 to 0.2 in phase, while the latter (or P2) comprises the 0.43 to 0.58 interval. A *Bridge* emission is

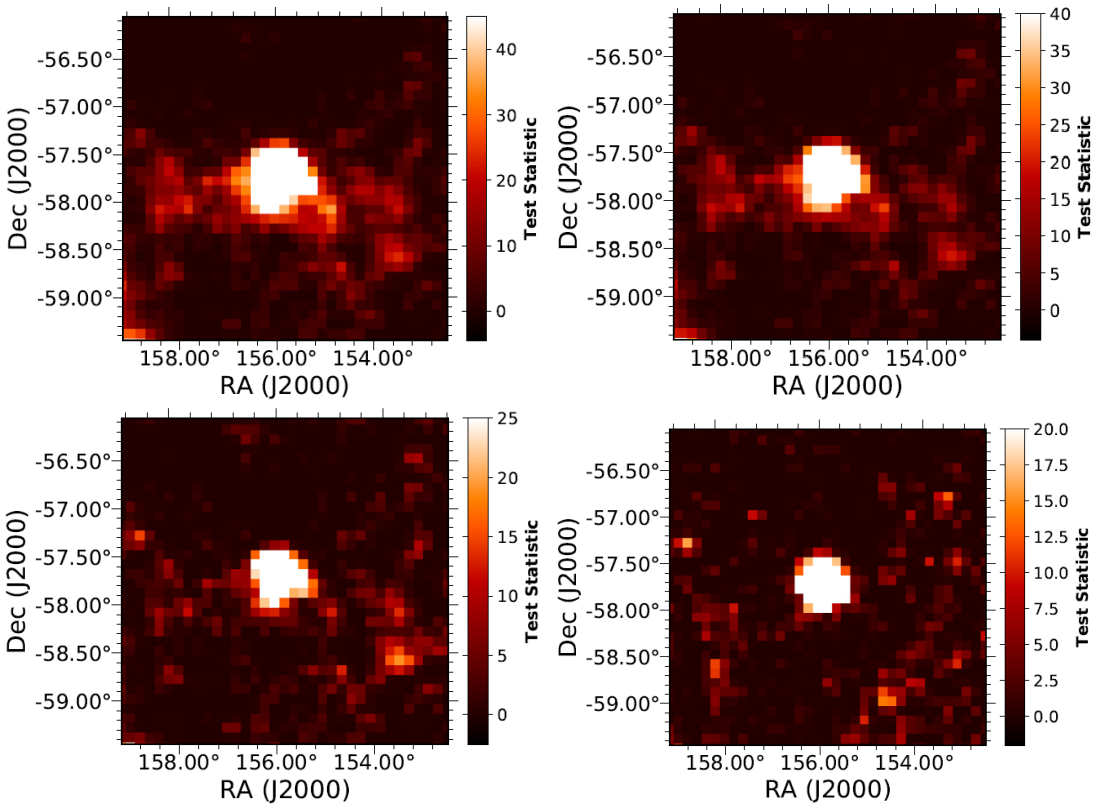

Figure 5.7: Test statistic map centered on the position of FGES J1023.3–5747 at energies above: 200 MeV (upper left), 700 MeV (upper right), and 3 GeV (below left), cut in phase from 0.58 to 1, and above 10 GeV without cutting in phase. It was computed for a point-like test source with an index 2 power-law spectrum.

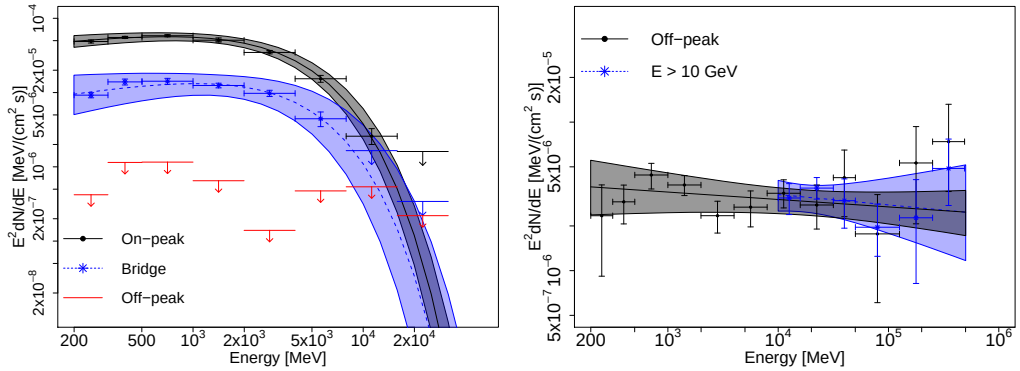

Figure 5.8: On the left, a) Spectral energy distribution (with only statistical errors) of PSR J1023–5746 derived from the on-peak (in black, with dot markers), the *Bridge* (in blue, with star markers), and off-peak-region (red upper limits). On the right, b) The SED (only statistical errors) derived from FGES J1023.3–5747 after gating the pulsed emission (in black) and analyzing only the gamma-ray emission above 10 GeV (without cutting in phase, in blue). The shaded area marks the 1σ error on the fitted spectral model.

apparent between the peaks, with a flux level slightly above the one of the off-peak region (i.e., the [0.58 - 1] interval). A Gaussian fit of both P1 and P2 locates the center of the peaks at the positions 0.085 ± 0.002 and 0.0539 ± 0.002 in phase, respectively. Also, the peaks presented a similar width, i.e., $\sigma = 0.017 \pm 0.001$ for P1 and $\sigma = 0.021 \pm 0.002$ for P2. We analyzed the pulsed emission in three energy bins; from 200 MeV to 700 MeV, from 700 MeV to 3 GeV, and from 3 GeV to 500 GeV. Figure 5.6 shows the results for each energy bin (in normalized counts per bin). Note that, contrary to other pulsars such as Crab or Vela, the light curve remains similar in different energy ranges (within the current statistics), i.e., there is no significant shift observed between the peaks at different energies. The relation between the height of the peaks and the number of events in each peak, i.e., P1/P2 ≈ 0.8, does not differ significantly for the different energy bins. The second peak is the most prominent in the three energy intervals. Besides, the number of events in the *Bridge* component for each energy bin is not more than $\sim 10\%$ larger than expected from the extrapolation of the off-peak statistics. The Galactic diffuse emission, which is the main contribution to the background events (represented as a blue line in Figure 5.6), is dominant both in the *Bridge* and off-peak regions if compared to the PSR J1023.1-5745 and FGES J1023.3–5747 emissions, especially at lower energies. Thus, it explains the similar level (in counts per bin) observed in Figure 5.6 for both components. The contribution from FGES J1023.3–5747 is expected to be alike in each interval of the phase curve, given that the extended source should not vary in synchrony with the pulsed emission.

5.3.3.2 PSR J1023–5746: Position, detection significance and spectrum

We performed the PSR J1023–5746 emission analysis describing the pulsar as a point-like source with an exponential cutoff power-law spectrum. The position fitting method located the source at RA = $155.772^\circ \pm 0.005^\circ$ and DEC = $-57.764^\circ \pm 0.005^\circ$. Table 5.1 summarizes the position fitted for the pulsar (and extended source) in each component of the phase curve. The pulsar is well-detected both in the on-peak and *Bridge* regions, with $\sqrt{TS} \gtrsim 80$ in both cases. Table 5.2, together with the left panel of Figure 5.8, presents the spectral analysis performed. The pulsar SED showed an exponential cutoff located at an energy of ~ 3 GeV. Both the pulsar position and spectrum obtained (in the on-peak region) are in good agreement with the analysis reported in the *Second Fermi Large Area Telescope Catalog of Gamma-ray Pulsars* (2PC, Abdo et al., 2013). The cutoff energy obtained in the on-peak region agrees with the best-fitted one for the *Bridge* component. Furthermore, the spectral indices in both analyses are compatible, within the uncertainties (at 95% CL, see Table 5.2), indicating possibly a common location of the radiation zone (most likely within the pulsar magnetosphere). The positions fitted for PSR J1023–5746, both in the on-peak and *Bridge* regions, also agree at 95% CL. The point-like source, however, is not

detected if selecting only off-peak events. In this region, only upper limits for the flux of PSR J1023–5746, represented as red arrows in the left panel of Figure 5.8, could be derived. Its non-detection points to reduced contamination of the defined off-peak interval compared to the *Bridge*. Admittedly, however, the comparable flux level between both regions complicates this distinction.

5.3.3.3 FGES J1023.3–5747: Position, detection significance, spectrum, and morphology

We next focused on analyzing the emission associated with the extended source FGES J1023.3–5747 in the off-peak interval, i.e., from 0.58 to 1 in phase, minimizing the contamination from PSR J1023–5746 (see Figure 5.7). In this region, a significant detection of FGES J1023.3–5747, with $\sqrt{(TS)} \approx 14$ and the source located at RA $= 155.93^\circ \pm 0.03^\circ$ and DEC $= -57.79^\circ \pm 0.03^\circ$ (see Table 5.1), was achieved. Table 5.2 summarizes the parameters of the best-fit power-law spectrum (showed in the right panel of Figure 5.8) for FGES J1023.3–5747. A (symmetric) 2D Gaussian model best described the source's spatial component, and the extension fitting method indicated a 68% containment radius of $r_{68} = 0.24^\circ \pm 0.03^\circ$, i.e., an intrinsic size of $\sigma = 0.16 \pm 0.02$ (where $r_{68,\mathrm{Gaussian}} = 1.51\sigma$, see Lande et al., 2012). Also, a 0.29° upper limit for the 95% containment radius was derived. In addition, we tested a (symmetric) 2D disk model. However, it does not improve the log-likelihood compared to the best-fit Gaussian model. In this case, we obtained a 68% containment radius of $0.25^\circ \pm 0.02^\circ$, compatible with the extension above. Furthermore, the log-likelihood of the best-fit Gaussian model with an extension fixed to the value measured by H.E.S.S. (for HESS J1023-575), i.e., $\sigma = 0.18^\circ$ (H.E.S.S. Collaboration et al., 2011) is, although slightly smaller, not significantly different than that corresponding to the best-fit extension described above (ΔTS ≈ 1.6). It was expected given the similar extension of the GeV and TeV excesses. We also computed the extension and position of FGES J1023.3–5747 for the on-peak and *Bridge* components, with an extended source model fitted simultaneously to the PSR J1023–5746 emission. No significant difference compared to the off-peak region analysis was observed.

The 'OFF' region of PSR J1023–5746 has already been analyzed with LAT data in previous works. Hence, we will make a brief interlude to compare our results with those available in the literature. For instance, the paper describing the second catalogue of LAT gamma-ray pulsars (2PC, see Abdo et al., 2013) analyzed the PSR J1023–5746 off-pulse region. The cited work reported an unidentified source in the off-peak of the pulsar, defined from 0.76 to 0.02 in phase. This definition does not seem to justify significantly different results in the 'OFF' region than those we obtained (see Figure 5.6). Furthermore, the analysis of this source showed some indication of spatial extension ($\sqrt{TS_{\mathrm{ext}}} = 5.5$). Interestingly, the integrated flux for such source, computed from 100 MeV to 316 GeV

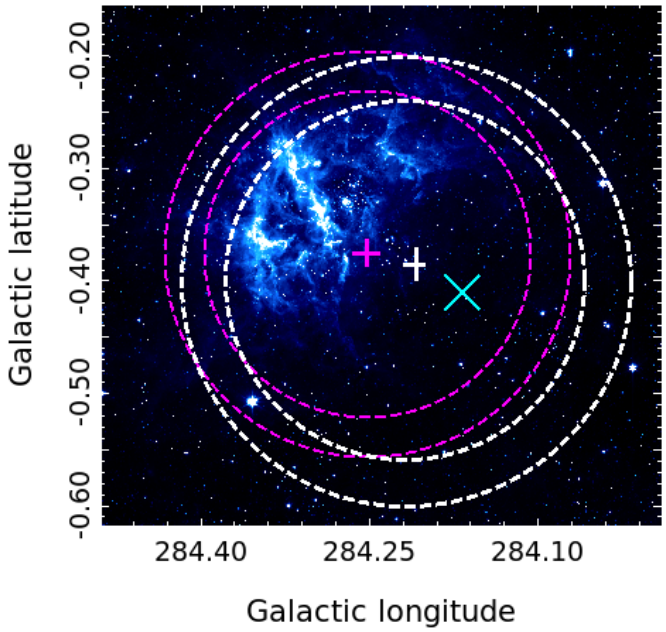

Figure 5.9: *Spitzer*/IRAC GLIMPSE Mosaic obtained from the GLIMPSE survey archival data. The magenta dashed lines correspond to the (1σ) error interval for the best-fit extension of FGES J1023.3–5747, with the central cross marking the best-fit position (with the 1σ error). Similarly, the white dashed lines (and the cross) correspond to the morphological characteristics of the H.E.S.S. source HESS J1023-575, as described in H.E.S.S Collaboration et al. (2011). The cyan cross corresponds to the position of PSR J1023–5746.

of energy, i.e., 1.79×10^{-8} cm^{-2}s^{-1} (with large uncertainty), is compatible with the one derived (in this work) for FGES J1023.3–574 in the same energy regime, i.e., $(1.97 \pm 0,49) \times 10^{-8}$ cm^{-2}s^{-1} (with only statistical errors). Similarly, Ackermann et al. 2011b analyzed the off-peak region with 16 months of LAT data. In this case, the off-peak emission was reported only at energies above 10 GeV. The off-pulse region (from 0.85 to 1.13 in phase, in the cited paper) differs significantly from the definition in this work (partially overlapping with our definition of P1), and the amount of data used is small compared to the reanalysis we present. However, we conclude the integral flux of the source reported (from 10 GeV to 100 GeV of energy), i.e., $(4.6 \pm 2.2) \times 10^{-10}$ cm^{-2}s^{-1}, agrees well with the one derived for FGES J1023.3–574 (in the same interval), i.e., $(2.62 \pm 0.37) \times 10^{-10}$ cm^{-2}s^{-1}. To conclude, a more recent reanalysis of the detected off-pulse emission with 45 months of LAT data (see Acero et al. 2013) reported a similar integrated flux above 10 GeV of energy, i.e., $(4.6 \pm 0.9_{stat} \pm 1.2_{sys}) \times 10^{-10}$ cm^{-2}s^{-1}. Furthermore, in this case, a 2 (i.e., $1.99 \pm 0.24_{stat} \pm 0.32_{sys}$) power-law spectrum was derived.

Resuming our analysis, the position of the sources, fitted for the different components of the phase curve, implies a separation between PSR J1023–5746 and the FGES J1023.3–5747 centroid of 5.3 ± 1.1 arcminutes. Given the size derived for FGES J1023.3–5747, PSR J1023–5746 is (clearly) located within the extended source's emission (see Figure 5.9). Besides, the best-fitted position of FGES J1023.3–5747 (in the off-peak region) is in good agreement with the one estimated by H.E.S.S (for HESS J1023-575, i.e., RA = 155.85° and DEC = −57.79°, H.E.S.S. Collaboration et al., 2011), being the separation between the sources of 3.3 ± 1.4 arcminutes (accounting for statistical errors only, see Figure 5.9).

To further investigate the spectrum and morphology of the high energy part of FGES J1023.3–5747, we analyzed the data set above 10 GeV (see Table 5.2 and the right panel of Figure 5.8). Additional cuts in phase are not necessary at these energies due to the exponential decrease of the pulsed emission above $\sim$ 3 GeV. We included the emission of PSR J1023–5746 (modeled as a point-like source with the spectrum shown in Table 5.2) on this analysis, being the same only detected at low significance at energies above 10 GeV ($\sqrt{TS} \approx 3$). The extension fitted in this case for FGES J1023.3–5747 was $r_{68} = 0.23^\circ\ +0.03^\circ\ -0.02^\circ$ (or $\sigma = 0.15^\circ\ +0.02^\circ\ -0.01^\circ$, for a 2D Gaussian model, see Table 5.2). Note that both the position of the extended source and the best-fitted (power-law) spectral model are in good agreement with those obtained in the off-peak region (at 95% CL, see the right panel of Figure 5.8 and Table 5.1). The spectral index, computed both in the off-peak region and at energies above 10 GeV, is also compatible with $\Gamma = 2$, within the uncertainties (at 95% CL, see Table 5.2).

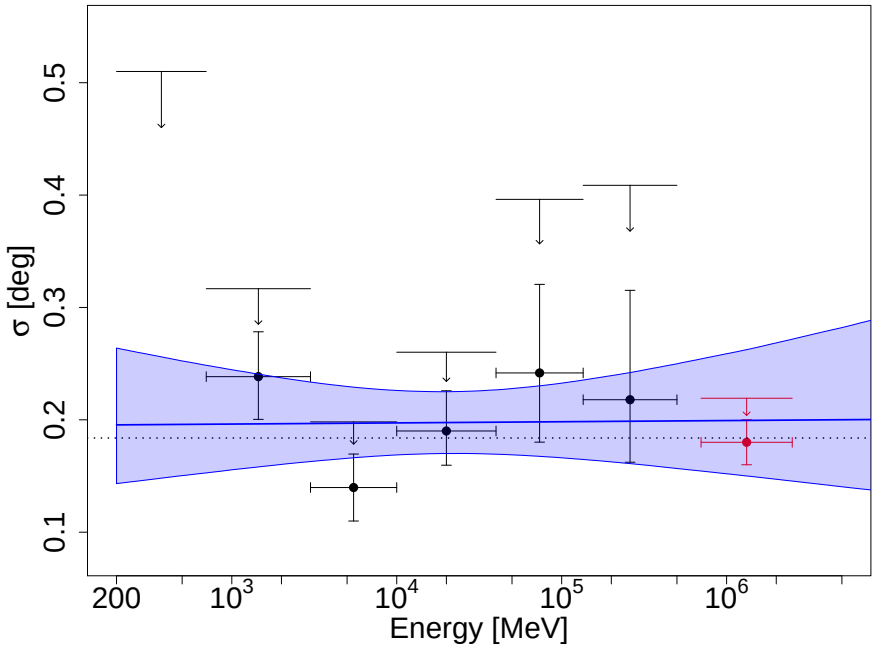

Figure 5.10: Intrinsic (Gaussian) width of FGES J1023.3–574 measured for different energy bins (in black points for LAT data, with only statistical errors). The red point corresponds to the intrinsic width of HESS J1023-575. The best-fitted power-law model (for the joint LAT/H.E.S.S. data) is plotted in a blue line (with the 1σ error region noted in shaded area), together with the mean size (black dashed line). The arrows correspond to the extension upper limit at 95% CL, except that in the first energy bin, which depicts the 95% containment radius instead (r_{95} UL).

5.3.3.4 FGES J1023.3–5747: Search for energy-dependent morphology and radial profile

To conclude the morphological study of FGES J1023.3–5747, we fitted the extension of the source (measured for a Gaussian profile, i.e., 68% containment radius) as a function of the energy (see Figure 5.10). For this purpose, we computed the (Gaussian) extension in the off-peak component for six energy bins (with breakpoints in 200 MeV, 700 MeV, 3 GeV, 10 GeV, 40 GeV, 70 GeV, and 500 GeV). Then, we tested an energy-dependent shrinking model of the form $\sigma \propto E^{-\alpha}$. However, there is no significant variation of the (FGES J1023.3–5747) extension observed (even accounting for the extension reported for HESS J1023-575 at TeV energies, see Figure 5.10).

The flux fitted for FGES J1023.3–5747 in each energy bin was compatible with the one expected from the spectrum derived in the entire energy range (i.e., from 200 MeV to 500 GeV, see the left panel in Figure 5.11), and the spectral index of the best-fit model is compatible with $\Gamma = 2$ (at 3σ), for each energy bin (see the right panel of the cited figure).

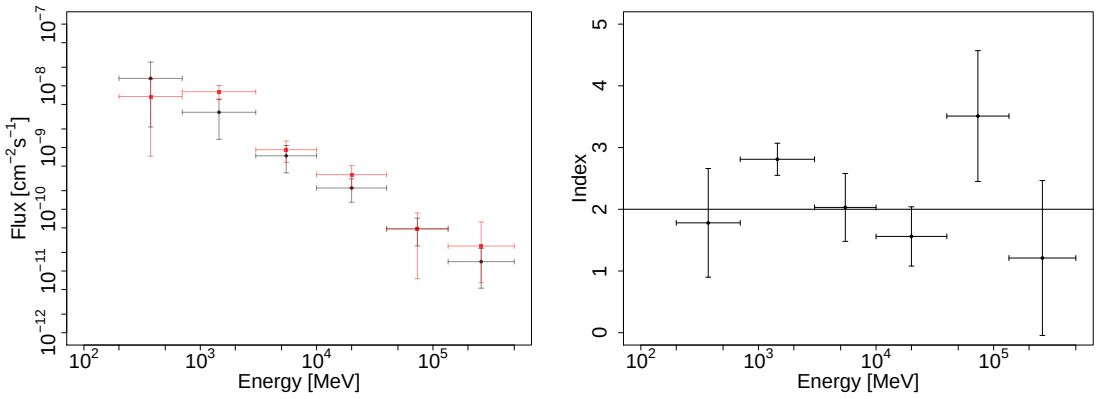

Figure 5.11: The left panel shows the integral flux from the best-fit FGES J1023.3–5747 spectrum computed in differential energy bins (in red squares) compared to that predicted given the best-fit spectrum in the entire energy range, i.e., from 200 MeV to 500 GeV (in black dots, see the last column in the upper part of Table 5.2). The right panel shows the best-fit (power-law) index obtained in differential energy bins.

However, the angular resolution of *Fermi*-LAT, i.e., $\sim$ 0.8° at 1 GeV (see Abdollahi et al., 2020), limits the fit of the FGES J1023.3–5747 extension for energies below a few GeV. Note that, since the *Fermi*-LAT PSF is $\sim$ 0.2° at 3 GeV (68% containment radius), the imperfect diffuse modeling can bias the extension measured at lower energies. The large-scale diffuse emission, dominant at low energies ($\sim$ 500 MeV), limits the extension measurements performed in this regime, as seen in Figure 5.10 (note the upper limit in the lowest energy bin). The contamination from the same, however, is decreasingly relevant at higher energies.

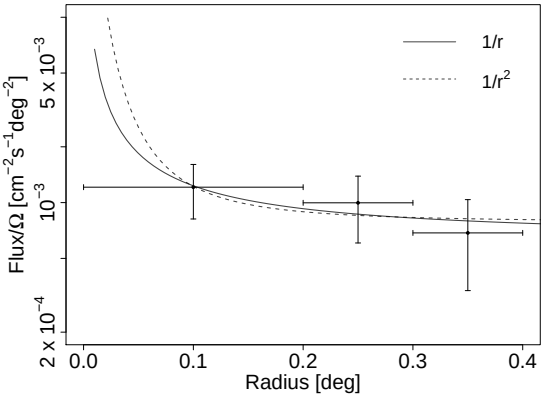

Figure 5.12: The figure (above) shows the radial profile obtained for FGES J1023.3–5747 with the best-fit $1/r$ and $1/r^2$ models depicted. We merged the first two rings with 0.1° of radius each.

Finally, we obtained the extended source's radial profile by fitting the emission simultaneously to concentric circular ring templates of 0.1° of width (see Figure 5.12). Then, we fitted two models to the data, corresponding with a decay $\propto 1/r$ and $\propto 1/r^2$, expected for continuous injection of cosmic rays from Westerlund 2 and if cosmic rays are advected in the winds, respectively. However, we ultimately merged the first two rings, which resulted in better statistics. In any case,

Parameter	PSR J1023–5746 (On-peak)	PSR J1023–5746 (*Bridge*)	FGES J1023.3–574 (Off-peak)
RA	155.772 ± 0.005	155.79 ± 0.01	155.93 ± 0.03
DEC	-57.764 ± 0.005	-57.77 ± 0.01	-57.79 ± 0.03
l	284.168 ± 0.005	284.18 ± 0.01	284.25 ± 0.02
b	-0.401 ± 0.005	-0.40 ± 0.01	-0.38 ± 0.03

Parameter	FGES J1023.3–574 ($E > 10$ GeV)	FGES J1023.3–574 (On-peak)	FGES J1023.3–574 (*Bridge*)
RA	155.93 ± 0.02	155.98 ± 0.04	155.83 ± 0.03
DEC	-57.76 ± 0.02	-57.77 ± 0.03	-57.81 ± 0.03
l	284.24 ± 0.02	284.27 ± 0.05	284.22 ± 0.03
b	-0.35 ± 0.02	-0.35 ± 0.03	-0.43 ± 0.03

Table 5.1: Best-fitted positions (in equatorial and Galactic coordinates) for PSR J1023–5746 and FGES J1023.3–574 (in degrees, accounting only for statistical errors).

Parameter	PSR J1023–5746 (On-peak)	PSR J1023–5746 (*Bridge*)	FGES J1023.3–5747 (Off-peak)
N_0	$(2.51 \pm 0.18_{stat} \pm 0.24_{sys}) \times 10^{-11}$	$(6.57 \pm 1.22_{stat} \pm 2.44_{sys}) \times 10^{-12}$	$(1.02 \pm 0.14_{stat} \pm 0.16_{sys}) \times 10^{-14}$
Γ	$1.74 \pm 0.05_{stat} \pm 0.16_{sys}$	$1.61 \pm 0.17_{stat} \pm 0.56_{sys}$	$2.05 \pm 0.06_{stat} \pm 0.33_{sys}$
E_0 [GeV]	1.95	1.95	17
$E_{\rm cutoff}$ [GeV]	$2.74 \pm 0.24_{stat} \pm 0.39_{sys}$	$2.7 \pm 0.57_{stat} \pm 1.2_{sys}$	-
σ [deg]	-	-	0.16 ± 0.02

Parameter	FGES J1023.3–5747 ($E > 10$ GeV)	FGES J1023.3–5747 (On-peak)	FGES J1023.3–5747 (*Bridge*)
N_0	$(1.09 \pm 0.16_{stat} \pm 0.04_{sys}) \times 10^{-14}$	$(1.03 \pm 0.21_{stat} \pm 0.10_{sys}) \times 10^{-14}$	$(9.83 \pm 2.0_{stat} \pm 0.5_{sys}) \times 10^{-15}$
Γ	$2.07 \pm 0.15_{stat} \pm 0.02_{sys}$	$(2.01 \pm 0.16_{stat} \pm 0.26_{sys})$	$(2.11 \pm 0.14_{stat} \pm 0.22_{sys})$
E_0 [GeV]	17	19.6	19.6
$E_{\rm cutoff}$ [GeV]	-	-	-
σ [deg]	0.15 ± 0.02	0.16 ± 0.04	0.16 ± 0.03

Table 5.2: Best-fitted models for PSR J1023–5746 and FGES J1023.3–5747. The units of N_0 are $\rm cm^{-2}s^{-1}MeV^{-1}$ for PSR J1023–5746 and $\rm cm^{-2}s^{-1}MeV^{-1}sr^{-1}$ in the case of FGES J1023.3–5747.

the poor angular resolution prevented us from rejecting any of the hypotheses mentioned, with an integral flux between 3 GeV and 500 GeV of $\sim 1.5 \times 10^{-4}$ cm^{-2} s^{-1} sr^{-1}, in each ring.

5.3.4 Modeling the high-energy spectrum of Westerlund 2

We showed previously how the analysis of the gamma-ray emission from FGES J1023.3–5747, after gating off the ON- and *Bridge* regions of PSR J1023–5746, combined with the large dataset, allowed us to investigate in detail the (underlying) extended source's spectral shape and morphology. In summary, the measured size of the GeV source resulted in good agreement with the one reported by H.E.S.S. (at TeV energies) for HESS J1023-575 (see Figure 5.9), while the spectrum obtained from the $\sim$0.2° region is hard (i.e., $\Gamma = 2$, at GeV energies) and connected the LAT emission smoothly with that observed in the TeV regime (see Figure 5.14). Consequently, we can (clearly) identify FGES J1023.3–5747 as the GeV counterpart of HESS J1023-575.

The spectral results of FGES J1023.3–5747 agree with those reported in Ackermann et al. (2017). However, our results are in tension with those presented in Yang et al. (2018). For the latter, the ephemeris used was valid only for a reduced period compared to the temporal span of the data analyzed. It means that at some point in the event phases computation, the coherence of the pulsar timing analysis was lost. Thus, the contamination from the pulsar most likely affected the spectral analysis of the extended source. For this work, in turn, we have used the most updated ephemeris for the pulsar, valid for the entire data set analyzed. Thanks to the larger data set and better source discrimination, the new characterization of the emission performed provided us new clues to establish the origin of the gamma-ray emission. In the following, we discuss several scenarios for the observed radiation in the context of the new morphology and spectral features found.

5.3.4.1 Pulsar wind nebula hypothesis

Given the proven efficiency of PWNe to produce TeV gamma-rays, the discovery of the energetic pulsar PSR J1023–5746 immediately triggered the interpretation of HESS J1023-575 as an unassociated PWN powered by PSR J1023–5746 (Ackermann et al., 2011b). Furthermore, the diffuse X-ray emission found in *Chandra* data around PSR J1023–5746 (in a radius $> 1'$) was related to a PWN (associated with PSR J1023–5746, see Townsley et al., 2019). Also, the radio shell described by Whiteoak & Uchida (1997, at the southwest of RCW 49) appeared to be filled with hard diffuse X-ray radiation (as seen by *Chandra*, see Figure 38 of the cited paper). For this reason, it was suggested to trace a cavity SNR. We will examine the PWN hypothesis first.

Several detailed time-dependent modelings of a pulsar with its pulsar wind nebula scenario proposed to connect HESS J1023-575 with PSR J1023-5746 (Ackermann et al., 2011b; H.E.S.S. Collaboration et al., 2018). Ackermann et al. (2011b) noted, however, some problems arising from this assumption. The separation of the pulsar and the cluster (i.e., $8'$), together with the distance to the stellar cluster (of ~ 6 kpc from the CO emission and 21 cm absorption along the line of sight, Dame et al., 2007) and the pulsar's characteristic age (of 4.6 kyr), implies an extremely high transverse velocity of ~ 3000 km s^{-1}. Thus, the association of the stellar cluster as the pulsar birth site is not straightforward. Furthermore, the 0.18° extension of the TeV source, which translates to ~ 19 pc of distance (at 6 kpc), would signify a very fast (mean) expansion velocity of about 4000 km s^{-1} over 4.6 kyr. The distance to the pulsar is somewhat uncertain. The pseudo-luminosity distance of PSR J1023-5745 locates the pulsar at ~ 2.4 kpc, although the uncertainties in this estimate can be of the order of factor 2-3 (Saz Parkinson et al., 2010).

In the reanalysis presented in this Chapter, we found a noticeable morphological (see Figure 5.9) and spectral (see Figure 5.14) overlap between the extended GeV source FGES J1023.3–5747 and the TeV source HESS J1023-575, which provides strong constraints on the PWN interpretation. In this scenario, we expect the gamma-ray spectrum to show a peak in the TeV regime, i.e., at energies just below the cutoff energy of the electron spectrum. Given that inverse Compton and synchrotron loss times are much longer in a typical pulsar wind nebula environment, the gamma-ray spectrum, due to electrons interacting with magnetic and radiation fields, is effectively uncooled up to the cutoff energy. The inverse Compton cooling time for the different photon fields present in the region where the pulsar is located, i.e., dust IR photons, stellar photons, and CMB (see Table 5.3, where the density ratio of the dust and stellar photon fields at temperature $T_{FIR/*}$, i.e., $\omega_{FIR/*}$, is given), is $> 10^4$ yr. Besides, we should consider a magnetic field $B > 400$ μG to efficiently cool (a few GeV) electrons ($\tau_{syn,yr} \simeq 1.3 \times 10^7 B_{\mu G}^{-2} E_{e,TeV}^{-1}$). In this case, the uncooled $\Gamma_\gamma \sim 2$ spectrum observed extends from ~ 200 MeV to a few hundreds of GeV, where meets smoothly the one measured by H.E.S.S. (see Figure 5.14). This photon spectrum would correspond to an electron spectrum of index $\alpha = 2\Gamma_\gamma - 1 = 3$. Such a spectral index is difficult to reconcile with acceleration theories and typical injection spectra in pulsar wind nebulae (Bell, 1978; Torres et al., 2014).

To further probe this hypothesis, we modeled the data using a PWN radiative scenario, in which the particle evolution and radiation are evolving in time according to the approach taken in Torres et al. (2014). We obtained the time-dependent gamma-ray spectrum using the GAMERA software (Hahn, 2015) with a broken power-law injection spectrum with a similar shape to those found for young PWNe (see Table 2 in Torres et al., 2014). Table 5.3 shows in more detail the parameters used to obtain the time-dependent gamma-ray

emission. Note that this time-dependent modeling does not account for morphological changes, i.e., we assumed energy-independent morphology.

The best model representing the data is shown in Figure 5.14, integrating in time up to the estimated pulsar age (τ_c ∼4.6 kyr). The upper limit on the X-ray emission was taken from Fujita et al. (2009) using *Suzaku* observations (in a 17′.8 ×17′.8 field). The disagreement between the LAT data and the model is evident, especially at the lowest energies. Therefore, one should consider more complex modeling, e.g., with more than one electron population, to obtain a good representation of the data. Another possibility to flatten the spectrum is to invoke the contribution of different stellar photon fields, which would be indeed expected from a region like Westerlund 2 (Vargas Álvarez et al., 2013b; Guarnieri et al., 1995). However, in the last case, such a source's morphology, peaking at the regions of high stellar radiation density, would differ from the one observed, rendering this possibility unlikely. Additionally, the similar extension found between the LAT and the H.E.S.S. sources disfavors further the PWN scenario, where usually a larger GeV nebula, due to cooling or/and energy-dependent diffusive transport, is observed (H.E.S.S. Collaboration et al., 2019, 2012).

5.3.4.2 Association with Westerlund 2 stellar cluster

The electrons in open clusters can also be efficiently accelerated via shocks, e.g., in massive stars (Bednarek et al., 2014), generating gamma-rays via inverse Compton or bremsstrahlung radiation. However, in this case, a strong correlation of the resulting gamma-rays with the region of high photon density is expected. We derived (from our analysis) that the gamma-ray emission extends up to $\sim 25_{d_{5kpc}}$ pc, contrasting with the $\sim 4_{d_{5kpc}}$ pc core radius of the cluster. Thus, our results disfavor a pure leptonic origin of the GeV and TeV emission. Moreover, the source's extension remains constant (within the uncertainties) for different energy bands, which indicates a stable dependency of the cooling time with energy, contrary to what we expect in a leptonic scenario.

We found that a hadronic interpretation of the emission naturally fits the hard spectrum derived for the source from ∼ 200 MeV up to a few tens of GeV, where meets the H.E.S.S. spectrum, continuing up to a few TeVs before showing a drop of the flux. We will next describe the results for this hypothesis.

5.3.4.3 Hadronic scenario

We first constrained the proton population powering the gamma-ray source to probe the hadronic origin of the FGES J1023.3–5747 and HESS J1023-575 gamma-ray emissions. For this purpose, we modeled the 200 MeV to 20 TeV emission using the NAIMA package (version 0.8.4, Zabalza, 2015). To compute the spectral energy distribution, we used a

Pulsar & Ejecta	
f (Hz)	8.97
$\dot{f}(-10^{-12}$ Hz s$^{-1})$	30.88
τ_c (kyr)	4.6
$L(t_{age})$ (erg/s)	1.1 $\times 10^{37}$
n	2.509
D (kpc)	5
M_{ej} ($M_\odot$)	10
Environment	
T_{FIR} (K)	30
w_{FIR} (eV/cm^3)	1
T_* (K)	2500
w_* (eV/cm^3)	2
n_H	1.0
Particles and field	
γ_b	5×10^5
α_1	1.5
α_2	3.0
$B(t_{age})$ (μG)	7

Table 5.3: Physical parameters of PSR J1023–5746 and its putative PWN. The pulsar rotation parameters f and $\dot{f}$ are obtained from the ATNF catalogue. The braking index n and ejecta mass M_{ej} are fixed, following the results from Torres et al. (2014). The broken power-law spectral shape of electrons (defined with the indices $\alpha_{1,2}$ and breaking energy γ_b), and magnetic field in the region (B), best representing the data, are listed in the third section of the table.

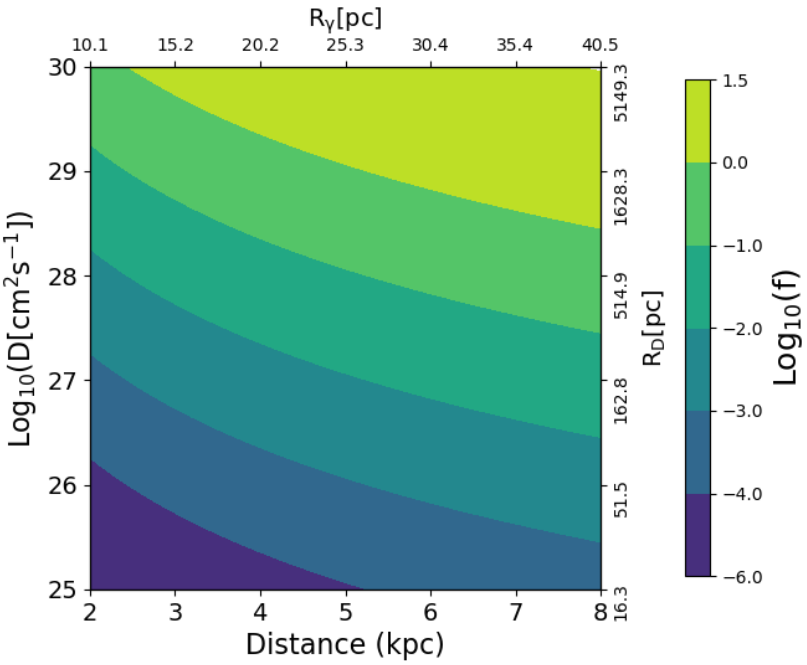

Figure 5.13: Acceleration efficiency (f) obtained in function to the distance and diffusion coefficient (D) assumed (for a fiducial target mass in molecular clouds of 4.5×10^5 $M_\odot$). The upper and right axes correspond to the estimated gamma-ray source and CRs diffusion radius, respectively.

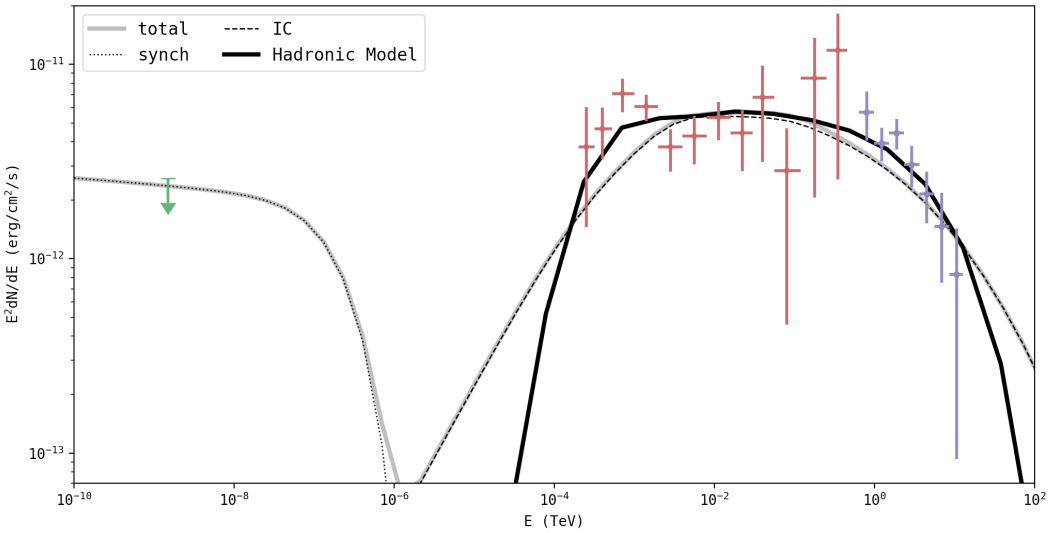

Figure 5.14: The lines depicted represent the best-fitted models for the FGES J1023.3–5747 spectrum according to the pion decay (solid line) and PWN (dashed line) hypotheses. The red points correspond to the *Fermi*-LAT data analysis (with only statistical errors), and the purple ones to H.E.S.S. (H.E.S.S. Collaboration et al., 2011). We obtained the upper limit in the X-ray domain from Fujita et al. (2009).

reference distance of 5 kpc. However, a distance ranging from 2 kpc to 8 kpc will be considered when discussing the results.

Several authors have deeply investigated the region's molecular content (see Dame, 2007; Furukawa et al., 2014) using millimeter-wave CO spectroscopy. These studies concluded the presence of several massive molecular clouds within the surroundings of Westerlund 2, with an estimated total mass of $(1.7 - 7.5) \times 10^5 M_\odot$. To our model, we assumed a proton distribution described by a particle index s, amplitude N_p, and cutoff energy $\mathrm{E_{cutoff}}$. We calculated the emitted gamma-ray emission due to pion decay (see Section 2.3.5) using the parametrization described in Kafexhiu et al. (2014) and compared it to the experimental data.

We implemented this method using the NAIMA PYTHON package. For this purpose, we assume a fixed proton index (s) ranging from 1 to 3 in steps of 0.1 and a (free) cutoff energy located between 1 TeV and 1 PeV of energy. We first fitted a (simple) power-law proton population to the data for later comparisons, computing the best-fit parameters (amplitude and index) employing a log-likelihood maximization process. For this fitting method, we used the optimization algorithms from the SCYPY PYTHON package[2]. Next, we sample, for each fixed value of s mentioned, the best-fit cutoff energy for a power-law

[2]See `https://docs.scipy.org/doc/scipy/reference/optimize.html#module-scipy.optimize`

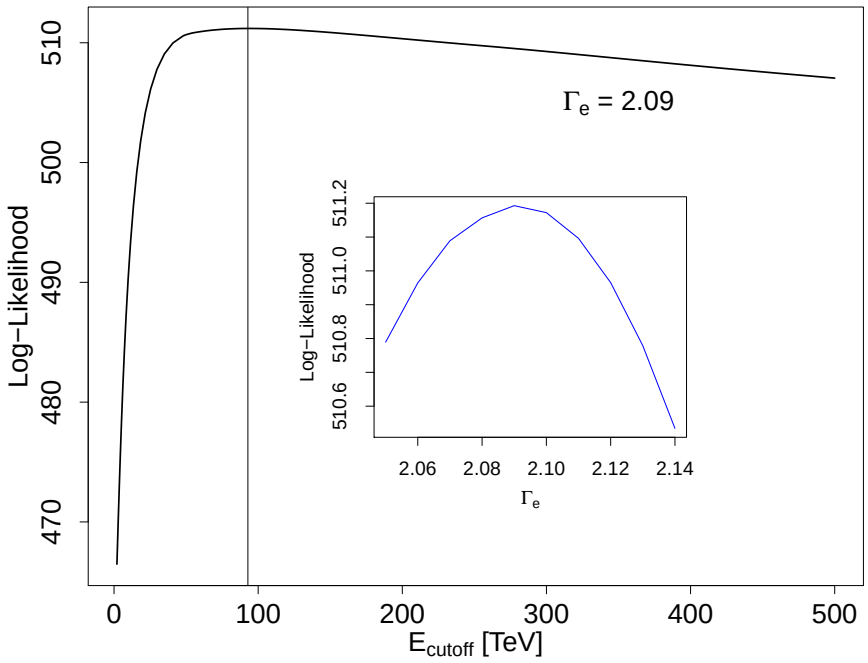

Figure 5.15: The black line represents the log-likelihood for the best-fit (power-law with an exponential cutoff) proton spectrum (to the joint LAT and H.E.S.S. data of FGES J1023.3-5747) as a function of the cutoff energy and particle index (in the inset plot).

with an exponential cutoff particle population. The initial value of cutoff energy provided to the fitting method significantly influences the best-fit value. Hence, we chose it from a preliminary blind search, which interactively locates a sensible initial value for the cutoff energy parameter. We obtain the final best-fit amplitude and cutoff energy with the cited log-likelihood maximization process. Therefore, this method (basically) computes a log-likelihood 2D surface, being the index and cutoff energy of the particle population the surface's dimensions. Each point of the surface represents the log-likelihood of the best-fitted model for a given s and $E_{\rm cutoff}$, with a surface's grid spacing constant in s (in steps of 0.1) and varying along with the $E_{\rm cutoff}$ axis (with smaller steps around the final best-fitted cutoff energy).

Figure 5.15 shows the results of the particle population fitting process for the joint LAT and H.E.S.S. data. The best-fit model corresponds to an exponential cutoff power-law proton spectrum with $\mathrm{E_{cutoff}} = 93 \pm 8$ TeV, particle index of $s = 2.09 \pm 0.01$, and $N_p = 3.52 \times 10^{37}$ eV^{-1} of amplitude referenced to 1 TeV (for a fiducial target density of $n = 1$ cm^{-3}). The solid black line in Figure 5.14 represents the corresponding gamma-ray spectrum. We can estimate the total energy in protons from the integration of the particle spectrum above. For a distance of 5 kpc, we obtained the total energy above 1.22 GeV (the threshold energy for pion production in pp interactions, Mannheim & Schlickeiser 1994)

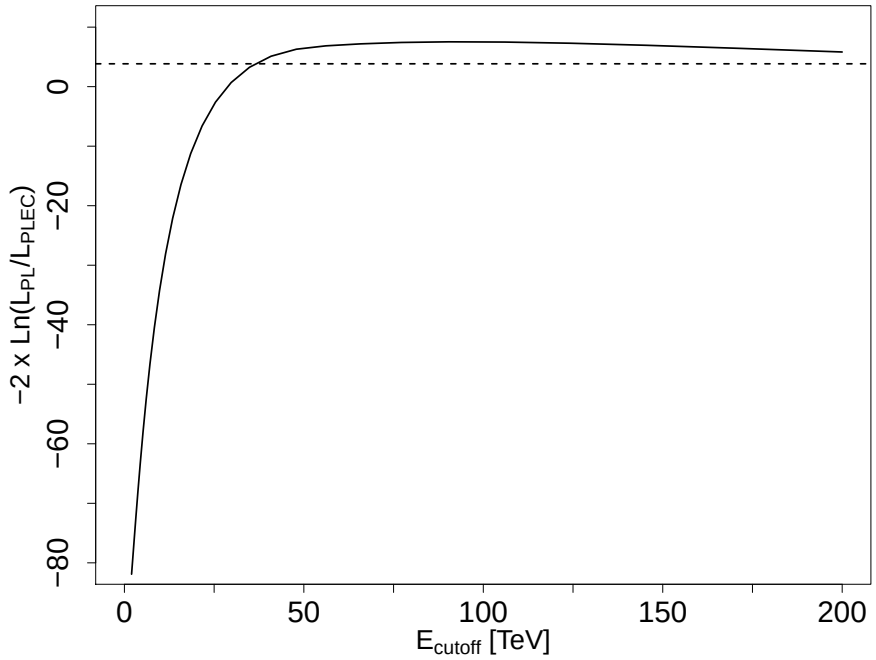

Figure 5.16: In a solid black line, we represent the likelihood ratio test statistic as a function of the cutoff energy. The null hypothesis of the likelihood ratio test (H_0) corresponds to a proton power-law spectrum and the alternative one (H_1) to the exponential cutoff power-law model. The black dashed line indicates the critical value of the χ^2 distribution at 95% CL (with one degree of freedom, i.e., 3.841).

of $W_{\rm p} = (1.3 - 5.9) \times 10^{48}$ erg, for densities of n = (7.5 - 1.7)$\times 10^5$ $M_\odot/V_{24pc}$, as derived by Furukawa et al. (2014) and Dame (2007), respectively. Comparing the maximum likelihoods of the data obtained for the exponential cutoff power-law and power-law models with the likelihood-ratio test, we could also estimate a lower limit for the cutoff energy on the proton spectrum of ≈ 37 TeV (at 95% CL, see Figure 5.16). The likelihood ratio test mentioned compares the best-fit proton power-law spectrum (i.e., null hypothesis, or H_0) with the exponential cutoff power-law model for the particle distribution (i.e., alternative hypothesis, or H_1). We computed the log-likelihood for particle cutoff energies ranging from 2 TeV to 200 TeV for the latter assumption. Figure 5.16 shows the results for the likelihood ratio test, representing the black dashed line, the critical value for the test statistic (at 95% CL). The power-law model is rejected at 95% CL (i.e., the test statistic is larger than the critical value) in favor of the exponential cutoff power-law one if the cutoff energy is $\rm E_{cutoff} \gtrsim 37$ TeV.

The total energy in protons (above 1.22 GeV) obtained can be compared with the total mechanical power of the stellar winds in the Westerlund 2 cluster: $\rm W_{tot} = f L_0 T_0$, which results in a modest acceleration efficiency of $f = 10^{-4}$ (10^{-6} / 5×10^{-3}), for the well-known age of the cluster ($T_0 = 2 \times 10^6$ yr), a distance of 5 kpc (2 kpc / 8 kpc), and the available energy budget in the form of the kinetic energy of stellar winds ($L_0 = 2 \times 10^{38}$ erg $\rm s^{-1}$).

If we consider the total volume defined by the size of the GeV source, i.e., $\sim$ 24 pc (with $V_{24\rm pc}$ of volume for a spherical source) at 5 kpc (or 10-40 pc for a distance from 2 kpc to 8 kpc), the energy density of protons in the region derived is $\omega_{\rm p}$ = (1.3-5.9)$\times 10^{48}$ erg/$\rm V_{24pc} \simeq (0.5 - 2.2)$ eV/$\rm cm^3$ (or 0.1-5.6 eV/$\rm cm^3$ if considering the uncertainty due to the distance to the source), which is comparable to the density of protons found in others massive clusters (Aharonian et al., 2019). The best-fit model described above constrains the proton population's maximum energy to $\sim$90 TeV, with a lower limit of 37 TeV on the cutoff energy. However, it would be possible that a significant part of these CRs has already escaped from the gamma-ray emission region, where the molecular content is enhanced, and therefore also the gamma-ray radiation. Following the formalism in Aharonian & Atoyan (1996), the relation between the observed energy emitted by protons (W_{em}) and the total energy (in protons) available (W_{tot}), assuming isotropic diffusion, is:

$$W_{em}/W_{tot} = (R_\gamma/R_D)^2 \tag{5.2}$$

where R_γ is the radius of the gamma-ray source and R_D is the diffusion radius. Employing the diffusion coefficient usually assumed for the interstellar medium, i.e., $\rm D \sim 10^{28} cm^2 s^{-1}$ and $R_{\rm D} = 2\sqrt{T_0 D} = 515$ pc, we obtain that the total energy released in the form of CRs could reach $W_{\rm tot} \sim 5 \times 10^{50}$ erg (for a distance of 5 kpc), which is still a few percent of the total available energy in the kinetic winds ($L_0 T_0 \sim 10^{52}$ erg). Note that this result is

affected by the uncertainties in the distance. For instance, the efficiency obtained is larger than 10% for a distance of 8 kpc with the quoted diffusion coefficient of the ISM. Likewise, formally, the value of the diffusion coefficient could be larger, and correspondingly, the CR halo could reach up to 5 kpc (for $D \sim 10^{30}\mathrm{cm}^2\mathrm{s}^{-1}$). These uncertainties affect the total efficiency, reaching in some extreme cases an unrealistically large fraction of the total energy to be transferred to CRs.

If the region is, instead, affected by large turbulence, expected in the surrounding of an accelerator, the CRs diffusion could be much slower (see, e.g., Schroer et al., 2020). If the size observed at GeV and TeV energies ($R_\gamma \sim 24\,(d/5\mathrm{kpc})$ pc) reflects the propagation depth of CRs, the diffusion coefficient would be much lower than in the ISM $D \sim 3 \times 10^{25}\mathrm{cm}^2\mathrm{s}^{-1}$ (or (0.4 - 6)$\times 10^{25}\mathrm{cm}^2\mathrm{s}^{-1}$ for 2 and 8 kpc, respectively), which is in tension with the value of the diffusion coefficient at these energies in the Bohm regime (Aharonian et al., 2019). That points to a certain CR halo around Westerlund 2, beyond the size traced by LAT and H.E.S.S., that could, in principle, extend up to a few tens of parsecs. Figure 5.13 summarizes the discussion above. We also show in the cited figure the acceleration efficiency resulting from different assumptions on the distance to the cluster and the diffusion coefficient, and the corresponding diffusion and gamma-ray source radius. More precise estimations of the distance to the cluster, foreseen with Gaia DR3 (Zeidler et al., 2018, and therefore of the actual gamma-ray size), would provide constraining limits on the diffusion of CRs around the source for a range of acceleration efficiency f.

Another possibility to explain the gamma-ray emission involves energetic SNR explosions within the cluster, injecting CRs in the surrounding. The lack of shell-like structure and the high efficiency required in the diffusive CRs scenario (50% E_{SN}, for a standard $E_{\mathrm{SN}} = 10^{51}$ erg) renders this hypothesis less attractive (at least for a single SNR event) than that attributing the origin of CRs to the stellar winds.

Chapter 6

Conclusions

6.1 General remarks

As we have seen along with this work, the presence of highly relativistic particles is indubitably proved in several types of astrophysical sources (see, e.g., Sections 2.1 and 2.4), and both direct and indirect evidence of this statement has been collected for decades through astronomical observations along the electromagnetic spectrum. The varied population of sources that are believed to accelerate these cosmic particles are ubiquitous in the universe and include, e.g., pulsars, PWNe, SNRs, or stellar clusters. The mechanism behind the acceleration of particles, although theorized for long, however, is not still exempt from the debate for the sources observed when individually examined. Some of the mechanisms studied, as discussed in Section 2.2, for example, invoke relativistic shocks, interstellar gas clouds, or regions of magnetic reconnection as sites of particle acceleration. The processes involved in the radiation emitted by accelerated particles were also extensively studied, and different emission mechanisms were described in detail (see Section 2.3). However, applying these prescriptions to particular sources, discriminating among the various possible origins of the observed radiation, has usually been complicated. A detailed characterization of the source non-thermal spectral energy distribution at both very high energies and other wavelengths can shed light on the origin of the emission and the different mechanisms at play.

The physical processes leading to the emission of VHE radiation studied share a common ground (Section 2.2), i.e., being ruled by the interaction between plasma and magnetic fields. In this context, we can identify different regimes, such as weak magnetic fields in low-density (e.g., pulsars winds and young SNRs, see Sections 2.4.2 and 2.4.3) or high-density plasma (e.g., old SNRs evolving in dense clouds, see Section 5.2), or more moderate magnetic fields in low-density plasma (e.g., in cold pulsar winds, see Section 4.2) or in plasma of higher density (e.g., massive stellar clusters, see Section 5.3). Figure 6.1 illustrates the different regimes mentioned.

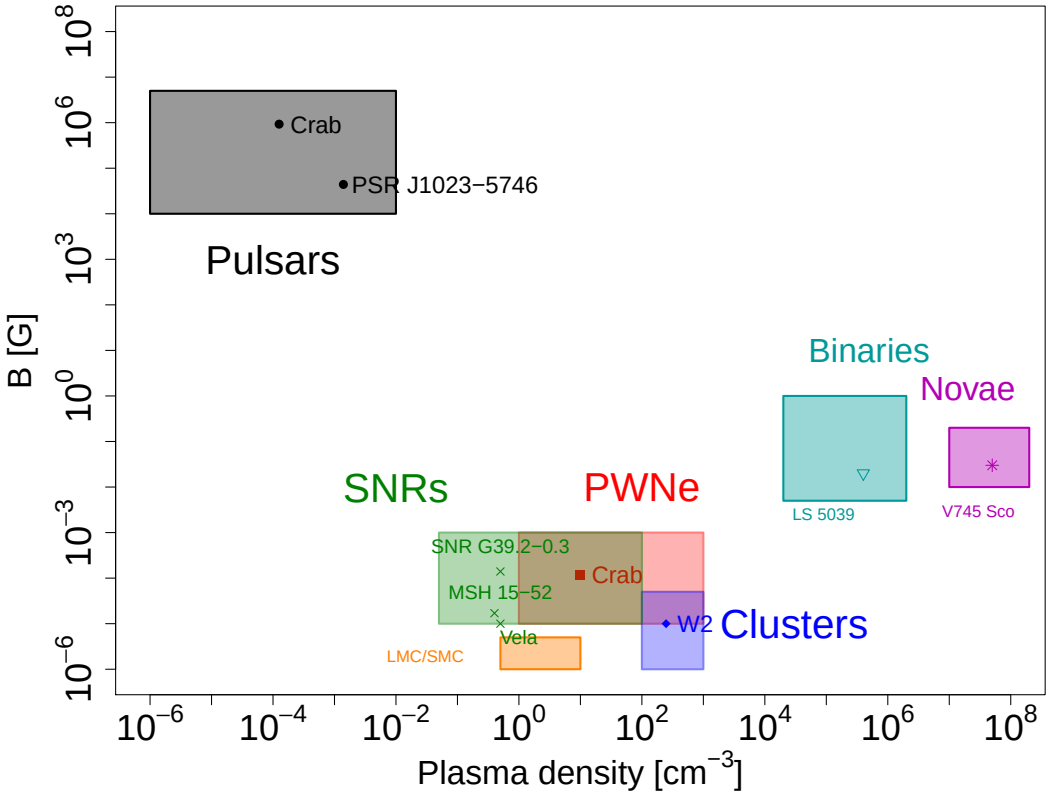

Figure 6.1: Characteristic magnetic field compared to plasma density for different (Galactic) astrophysical environments. The fiducial values depicted were taken from; Goldreich & Julian, 1969; Saz Parkinson et al., 2010; Bucciantini et al., 2010; and Sironi & Spitkovsky A., 2011, for the Crab pulsar and PSR J1023-5746 (cold wind, in black); Martín et al., 2012; and Torres et al., 2014, for the Cran Nebula (PWNe region, in red); Dubner et al., 2002; Aharonian et al., 2005a; Sushch & Hnatyk, 2014, Slane et al., 2018; and de Oña Wilhelmi et al., 2020, for SNR G39.2-0.3, MSH 15-52 and Vela (SNRs region, in green); Bednarek, 2007; and this thesis results for Westerlund 2 (clusters, in blue); Gaensler, 2005; and Mao et al., 2012, for the LMC/SMC (in orange); Delgado & Hernanz, 2019, for V745 Sco (novae, in purple); and Dubus, 2008; and Marcote et al., 2016, for LS 5039 (gamma-ray binaries, in cyan).

6.2 Plasma-magnetic field interaction: the Physics behind the sources under study

6.2.1 The Crab Nebula and pulsar

As commented, the Crab Nebula is the most prominent source consisting of a pulsar and its PWN and the best-studied source in the high-energy regime. Furthermore, it was used on many occasions both as a standard candle in the field and as a classical target for Cherenkov telescopes testing during their science verification period. Given the Crab pulsar and nebula have been broadly studied for decades (with many different instruments), in this thesis (see Chapter 4), we focused on analyzing the prospects regarding the progress in the physical knowledge underlying the Crab, as expected from the (future) CTA observatory. On a general basis, plasma and magnetic field interactions play a determining role in pulsars and their nebulae. Indeed, the most significant part of the rotational energy lost from the pulsar is (supposedly) released in a relativistic flow of magnetized plasma (predominantly composed of electron-positron pairs). This pulsar wind is (apparently) radiationless until the interaction with the ambient medium occurs.

The interaction between plasma and magnetic fields is in the core of the physical processes at play (in pulsars/PWNe environments), from the spatial scales of the neutron stars ($\sim$ 10 km) and the sub astronomical scales of their magnetospheres ($\sim 10^8$ cm) to the $\sim$ 0.2 pc scales of the cold wind and the parsecs sizes of the SNR shells in young sources like the Crab (i.e., of $\sim$ 1000 years age). The pulsed emission observed from Crab, e.g., is usually attributed to synchrotron-curvature radiation up to $\sim$ 100 GeV (at least, see Section 4.2). Given the nebula's high average magnetic field ($\sim$ 100 μG), the most energetic parent particles dissipate their energies via synchrotron radiation. At higher energies, i.e., above $\sim$ 1 GeV, the inverse Compton component from these particles against the CMB, FIR, NIR backgrounds, and the synchrotron photons of the nebula itself rises (see in Section 4.3). Besides this picture of the nebula in its normal state, the VHE emission detected during Crab's flaring events (discussed in Section 4.4) seems to rule out the usual synchrotron (i.e., in ideal MHD conditions) and inverse Compton mechanisms. Consequently, other scenarios, e.g., a reconnection region of the magnetic field, have been explored (Section 4.4.4).

6.2.2 SNR G39.2-0.3

Section 5.2 summarizes the reanalysis described in de Oña Wilhelmi et al. (2020) of the LAT data from SNR G39.2-0.3. This source, as explained, was identified as a hadronic accelerator through its multi-wavelength properties. The combination of the LAT data at GeV energies and observations in radio wavelengths, together with the non-detection

of non-thermal X-rays from the remnant, clearly points to a hadronic scenario, where accelerated cosmic rays interact with the rich interstellar medium surrounding the remnant. Neither inverse Compton emission nor bremsstrahlung radiation was found to be responsible for the observed emission. According to the cited work, on the one hand, a very large far-infrared photon density field must be invoked to raise the inverse Compton emission to the gamma-ray flux level detected from the remnant. On the other hand, bremsstrahlung radiation can not reproduce the source's spectral shape at high energies.

On the contrary, the hadronic origin assumption reproduces relatively successfully the spectral energy distribution of SNR G39.2-0.3 above tens of MeV. The best-fit model corresponds to a proton population with a soft particle index of ~ 2.75 with a turnover at low energies (i.e., $\sim$ 2.3 GeV). Such a soft spectrum above the cited break energy (reflecting the maximum current energy of accelerated protons) is in good agreement with a dynamically old SNR scenario, given the considerable escape rate of cosmic rays and the decrease of the acceleration efficiency implied by the proton spectral shape. The total energy estimated (in cosmic rays) reaches $\sim 10^{49}$ erg, which translates to a few percent of efficiency in converting kinetic energy into cosmic rays. The scenario is similar to those observed in other SNR interacting with dense gas in large molecular clouds (Acero et al., 2016). Despite SNR G39.2-0.3 seems in general fainter than the standard interacting supernova remnants listed in the last *Fermi*-LAT SNR catalogue, it is still within the main distribution (if compared with the radio emission, see Figure 12 in Acero et al., 2016).

The dense medium, explored with CO observations from the MWISP survey, in which this remnant is evolving, means that a large emission of bremsstrahlung is produced. From the same, in combination with observed GeV emission, a lower limit on the magnetic field of around $\sim$ 100 μG was reported. However, the strong magnetic field derived is not (typically) expected for evolved remnants. Instead, it is expected from supernova remnants interacting with molecular clouds since the thick medium compresses the shock region, amplifying the magnetic field. In principle, such amplified magnetic fields favor the acceleration of protons to high energies. However, the dense matter also slows down the shock, preventing the acceleration of protons to energies larger than a few tens of GeV. This consideration, nonetheless, still does not explain the very low break energy obtained in de Oña Wilhelmi et al. (2020) for SNR G39.2-0.3 if considering the evolution models of SNRs and its synchrotron spectrum (observed in radio).

Several hypotheses were proposed in the cited paper further to explain the detailed spectral shape of the remnant. The low-energy peak in the gamma-ray spectrum points to a very low proton maximum energy and/or a softer ($\gtrsim$ 2.3 index) proton spectrum than expected from the classical diffusive shock acceleration mechanism. These requirements are not trivial to fulfill, even considering the remnant's old dynamical age and its interaction with dense molecular clouds. However, the remnant's core-collapse

nature, indicating a progenitor star that underwent a red supergiant phase, implies a rich and heavy composition of the surrounding medium. Thus, the resulting cosmic-ray and gamma-ray spectra should reflect it. The interactions involving heavy nuclei should originate a peak of the gamma-ray emission at significantly lower energies than proton-proton interactions. Under this hypothesis (i.e., a heavy composition of the circumstellar medium), the observed gamma-ray spectrum may be better explained (without the need for an unusually soft spectrum or low break energy), although requiring a Wolf-Rayet progenitor star. More precise measurements of the gamma-ray emission from core-collapse supernova remnants are needed to probe the composition of the circumstellar medium and the progenitor star's nature.

6.2.3 Westerlund 2

We have presented a reanalysis of the ($\sim$ 11 years) LAT data towards the Westerlund 2 massive stellar cluster (in Section 5.3). This region presents several interesting GeV and TeV gamma-ray sources revealed by H.E.S.S. and *Fermi*-LAT, including pulsars, a gamma-ray binary, and likely, PWNe. We focused on the gamma-ray emission towards the pulsar PSR J1023–5746 and the underlying extended source FGES J1023.3-5747, coincident with the HESS J1023-575 TeV emission. We took advantage of the large data set available and the latest and extended ephemeris for PSR J1023–5746 to probe the observed radiation's origin.

As discussed in Chapter 5, our analysis resulted in the clear identification of the extended LAT source FGES J1023.3-5747 as the GeV counterpart of the TeV source HESS J1023-575. We found a noticeable matching spectral and morphological agreement between the sources and searched for hints of energy-dependent morphology. The source's positional and spatial agreement, with no signs of cooling features in the extension of the same, and the spectra of the sources, connecting the GeV and TeV regimes smoothly, point to a common origin of the emission. Furthermore, the extension of FGES J1023.3-5747 together with the one of HESS J1023-575, beyond the size of the cluster, and the hard spectrum of the GeV source above 200 MeV up to TeV energies, without showing a drop of the flux, provides evidence of the hadronic origin of the gamma-ray emission detected in the *Fermi*-LAT and H.E.S.S. observations.

We then evaluated different scenarios proposed to explain the gamma-ray emission from FGES J1023.3–5747 (and HESS J1023-575). First, we considered if the GeV and TeV sources radiation could be related to the (unassociated) PWN of PSR J1023–5746, despite the association of the stellar cluster with the birth site of the pulsar, implying an unrealistic transverse velocity, is (from the beginning) problematic. Even though the photon spectrum found would be difficult to reconcile with acceleration theories and typical injection spectra in PWNe, we used a PWN radiative scenario to derive the time-dependent

gamma-ray spectrum and compared it to the observations. However, this calculation resulted in a noticeable disagreement between the LAT data and the model at the lowest energies studied. In contrast, a hadronic scenario explains the hard spectrum obtained from 200 MeV to GeV energies, connecting flatly with the TeV emission and accounting for the radiation observed up to TeV energies. This scenario proposed was then modeled with NAIMA (see Appendix C), deriving the possible proton population originating the emission observed. In light of the new clues provided by LAT, particularly from the analysis of its gamma-ray spectrum, we concluded that the gamma-ray source is compatible with being of hadronic nature. Therefore, we suggest the gamma-ray emission analyzed is related to the Westerlund 2 stellar cluster rather than to leptonic emission from either a PWN associated with PSR J1023–5746 or the cluster itself. However, given that the hypotheses examined are not entirely exempt from reasonable uncertainties, the former, i.e., the PWN hypothesis, was not (definitely) ruled out.

The results obtained in the Westerlund 2 region analysis reinforce the hypothesis of stellar clusters as significant contributors to the Galactic cosmic-ray sea (or, at least, are better understood within that framework). These cosmic rays steaming from Westerlund 2, particularly, seem to extend in a very large halo (i.e., ~ 200 pc radius) around the cluster, as was already proposed in Yang et al. (2018). The total energy in protons derived in our work (i.e., $\sim 5 \times 10^{50}$ erg) could easily account for the total luminosity observed in gamma-rays. Furthermore, the acceleration efficiency required in the cluster for such flux, i.e., smaller than $f = 0.1$ for the typical diffusion coefficient of the interstellar medium (or lower values) even considering the uncertain distance to the source, is still moderate for acceleration theories in wind shocks. The spectrum at TeV energies seems to change the hard 2 (power-law) index trend found in the LAT data, softening towards higher energies. We showed that the spectral energy distribution's shape indicates a relatively low cutoff energy (~ 100 TeV) for a PeVatron accelerator, disfavoring thus Westerlund 2 as a good candidate for such type of sources (at present). More exhaustive observations with H.E.S.S. or with sensitive TeV instruments in the southern hemisphere such as CTA (Cherenkov Telescope Array Consortium et al., 2019) may soon provide a definitive answer to the PeVatron nature of HESS J1023-575.

6.3 Prospects for future studies

Up to date, different techniques have been employed to detect and characterize the emission from the different types of sources appearing in the sky at VHEs (see Section 3.1). In particular, pair detectors (e.g., Fermi-LAT), IACTs (as CTA or H.E.S.S.), and air-shower experiments have been treated in this work. However, a new generation of Cherenkov telescopes, indeed, is in preparation. CTA represents this new generation

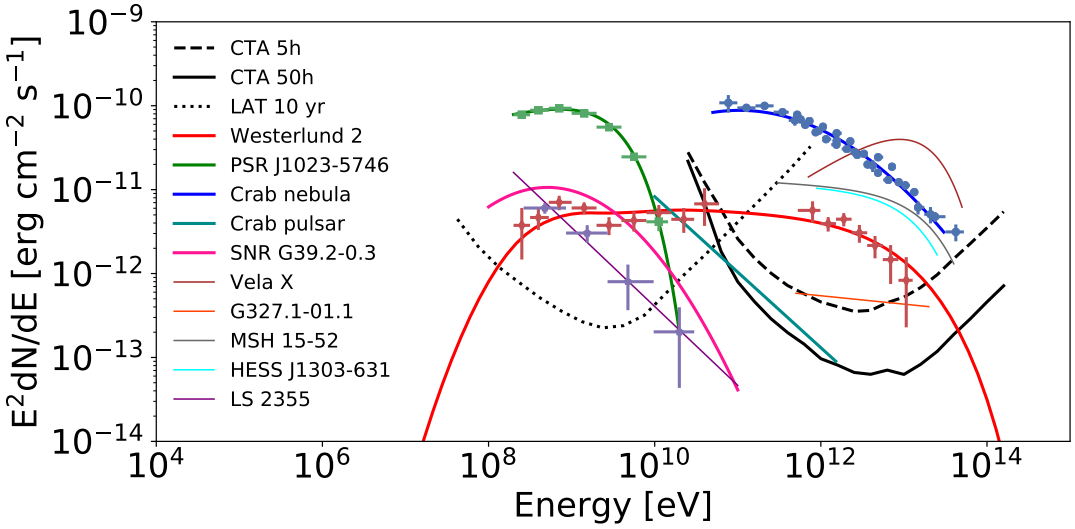

Figure 6.2: In color lines, we show the spectral energy distribution of the different sources treated in this thesis. The black lines depict the CTA/LAT sensitivity (for comparison).

of instruments for the VHE regime. With its unprecedented sensitivity, it is expected to provide valuable data that may clarify, shortly, the picture of the origin and role of relativistic cosmic particles and non-thermal phenomena in the universe.

6.3.1 Simulating CTA data

We probed, through simulations, the sensitivity of the CTA Observatory (currently under construction) regarding different gamma-ray sources (see, for example, the case of stellar bowshocks in Section 3.3.3 and Figure 6.2). For this purpose, we applied the various tools in development for the future analysis of CTA data, i.e., GAMMAPY and CTOOLS and the IRFs provided by the CTA collaboration (from Monte Carlo simulations of the instrument performance, see Section 3.2). In particular, we implemented a simulation scheme of 3D GAMMAPY cubes, made public and available together with other tools developed for the simulated cubes analysis (as described in Section 3.3.1 and detailed in Appendix A). This tool allowed us to simulate the observation of two sources (plus background), with different spectra and morphology, on top of each other with CTA (in various configurations). The spectral energy distribution of the sources could be simulated and derived by projecting the cubes along the energy axis, while projecting the cubes onto the spatial dimensions facilitated the simulation and study of their morphological properties. Consequently, the tools developed (both for the cubes simulation and analysis) constitute a valuable framework for analyzing, e.g., the prospects regarding the Crab's (formed by a pulsar and its PWN) characterization.

6.3.1.1 The source confusion problem

A major problem expected to arise in the future CTA Galactic survey is the source confusion problem in crowded regions (also examined in Chapter 3), given the large extension of some sources at VHEs (as PWNe, which at these energies, depending on the age and distance, can extend even more than 1°) and the low spatial resolution that the Cherenkov technique suffers. However, we could also probe this complication with the tools presented (see Section 3.3.2). With a relatively simple approach, we illustrated how an empirical or theoretical template for the morphology of a PWN (e.g., from other Cherenkov telescopes surveys or magneto-hydrodynamic simulations) could be directly compared with CTA data. Furthermore, we proved that a combination of different templates on top of each other could also be compared with CTA observations, both superposing the templates or the observation simulations of each (individual) source.

The tests performed open the possibility of discrimination between a single source and different (confused) sources if a library of such morphological templates is finally accomplished. Under some circumstances, depending on the separation between the sources, the flux, extension, spectrum, and morphology of each of the confused sources might be retrieved with precision (after discriminating them from the single source assumption) applying the method described in the cited section. The advantage of associating CTA observations to empirical or simulated templates is to relate the CTA data with the physical parameters (and/or properties) behind the template's choice (and/or generation). For example, this approach provides further information of a source morphology than fitting the corresponding CTA data with a simple Gaussian model, which only provides a centroid position plus a spatial scale.

6.3.2 Future studies with CTA

The capabilities of CTA regarding the observation of the Crab have significant importance for the collaboration of the future observatory, given the mentioned importance of the source in the high-energy and very-high-energy regimes. For this reason, we have presented, by testing in depth the main existing tools for CTA simulations and data analysis, detailed prospects derived for the observation of Crab (with CTA). The study performed, of course, is limited in some respects. In the first place, the IRFs used for this work are not optimized for the specific simulations described in Chapter 4. For instance, the IRFs of the southern CTA telescope array (expected to optimize the spectral results at high energies) are used, in this case, for large zenith angles, which may introduce more considerable uncertainties in the simulations. Furthermore, the analysis was not optimized for angular resolution, in contrast, e.g., to the more advanced analysis performed by H.E.S.S. (so far). Despite the mentioned difficulties, we derived interesting results in our

first approach (as detailed in Chapter 4). The application of the two leading analysis chains cited (i.e., GAMMAPY and CTOOLS), developed by the CTA Consortium, actually proves that both tools produce statistically compatible simulations and results concerning (at least) the spectral analysis of the Crab pulsar and nebula.

6.3.2.1 Characterizing the Crab pulsar and nebula

With the statistical approach explained, we aimed to estimate the CTA potential to answer the open questions concerning the gamma-ray emission attributed to the Crab. Both the pulsar and the nebula were detected in a short or moderate observation time (from both the northern and southern sites), along most of the broad CTA energy band, i.e., from hundreds of GeV to tens of TeV energies (in the case of the nebula). As we saw, a hard cutoff of the nebula's spectrum, if located below an energy of 20 TeV, could prevent, in principle, its detection at energies above 50 TeV. However, recent measurements (in the TeV regime) with air-shower experiments seem to rule out this scenario, pointing to the nebula's detection with CTA up to energies close (or larger) than 100 TeV (Abeysekara et al., 2019). CTA will also characterize the pulsed emission with unprecedented precision, and its spectrum could be extended (according to our simulations) up to several TeVs of energy. This result, together with the capabilities of CTA to detect features in the pulsar spectrum at energies of hundreds of GeV (as probed in Section 4.2), could shed light on the component emerging at tens of GeV that revolutionized in the last decade our picture of the Crab pulsar. Concretely, we established the minimum detectable (spectral) index variation (~ 0.6) for an energy break occurring between 80 GeV and 150 GeV. In this approach, we included (when possible) the usually overlooked systematic errors (see Section 3.2.3). Even considering the latest, which are the largest source of uncertainties in the current measurements, we showed that CTA would discriminate between different characterizations and hypotheses on the nebula spectrum (in a moderate observation time).

The huge energy range covered by CTA, given the source's luminosity, is the key to disentangle between the different mathematical descriptions proposed to characterize the nebula spectrum, i.e., log-parabola, exponential cutoff power-law, and simple power-law, within less than 50 hours (with high confidence). Similarly, thanks to the instrument's extensive coverage (in energy), we could also derive the minimum cutoff energy (probed up to more than 100 TeV in 50 hours) and the ability to parametrize the shape of this cutoff (if detected, within a precision of $\Delta\beta = 0.2$). These results provide moderate possibilities to determine the domain in which particles are accelerated and cooled (see Lefa et al., 2012).

Chapter 4 also shows several approaches concerning the Crab Nebula morphological characterization (with CTA). First, we derived a general shape for the minimum size

detectable that can be easily scaled to the latest and more realistic IRFs, obtaining better than $30''$ resolution at TeV energies (with a relatively conservative approach). Secondly, we already proved that CTA data would provide invaluable input if compared with theoretical predictions, such as hydrodynamical or magneto-hydrodynamical simulations. According to the simulations performed, CTA will disentangle sub-parsecs structures ($\sim 0.02^\circ$ for a distance of ~ 2.2 kpc), which might be crucial to understand the origin of the emission observed. Furthermore, our simulations indicate that CTA will image the nebula (at TeV energies) for the first time and possibly determine its asymmetry, allowing, for instance, its comparison with the high-energy resolution images in the X-ray regime. The cited result opens the possibility of retrieving valuable information on the effect of cooling processes of the electrons powering the nebula, given that CTA could provide a continuous resolved image from a few tens of GeV to tens TeV. Thus, the gap between the size measured by *Fermi*-LAT and the one by H.E.S.S. (H.E.S.S. Collaboration, 2020) could be closed in the upcoming years, tracing the behavior of multiple-energy electron populations.

CTA will probe the maximum energy to which the particles are accelerated in the Crab pulsar since the pulsed spectrum will be measured at the highest energies ever achieved. According to our simulations, CTA will detect pulsed photons up to 7 TeV in a time of 300 hours. Even if this observation time (which is nevertheless conservatively estimated) looks high, it is necessary to mention that Crab is considered the standard candle in the gamma-ray domain. Therefore, it will be (deeply) observed from the beginning of the observatory working time. If the spectrum extends indeed well beyond 1 TeV, some of the models proposed to explain the extension of the pulsed emission, such as the ones based on synchrotron emission, will be heavily challenged. Likewise, the maximum energy detected will provide direct evidence of the region in which the radiation is located and, therefore, on the pulsar wind nebula's inner structure.

We also studied the Crab pulsar phase curve's determination (with CTA) in detail, determining (in a conservative approach) the precision achievable in the characterization of the pulses. Moreover, we provided a general description of the power of CTA to detect different light curves shapes, from sharp peaks as in the Crab (i.e., 0.01 gaussian sigma width in phase) up to four times broader peaks. Measuring with high-quality data the shape of the VHE pulse profile and comparing it with those obtained at lower energies can constrain the location of the emission regions in different bands. The periodicity of sources with a flux of ~ 0.1 (in Crab units) was detected (at 5σ) within 300 hours (for different peak widths).

Our knowledge of the instrument's response will undoubtedly increase during the observatory construction and scientific verification phase (in the upcoming months). The results we summarized are a conservative estimation of the potential of CTA to unveil the many unknowns behind the physics of the gamma-ray radiation from the Crab. For

instance, we probed the capabilities of CTA with other potential gamma-ray sources that will challenge (due to the small flux expected) the CTA sensitivity, as bowshocks from massive runaway stars (Section 3.3.3). More realistic studies (and simulations) of Crab and other sources will emerge from the science verification phase describing the real power of CTA.

6.3.2.2 Detecting the Crab flares with CTA

The bright and rapid flares in the Crab Nebula, detected at hundreds of MeV, are among the most puzzling phenomena in Crab still to explain. Detecting these flares, hence, is one of the most challenging goals concerning future observations of the Crab with the CTA observatory. For this reason, we explored different scenarios in various energy regimes within the CTA band, which may be promising for achieving the detection of the flares in the nebula with both the northern and southern telescope arrays. To investigate these scenarios, we combined the simulations of the steady nebula (previously presented), the physical conditions that we expect in the same, the *Fermi* data of two flares detected (in April 2011 and March 2013, together with the H.E.S.S. and VERITAS upper limits for the one in 2013), and different hypotheses for the particle population and origin of the flares observed. Putting together all these factors led us to varied characterizations of (simulated) flares, with similar fluxes (in the *Fermi* band) than those detected during the cited flares. Our ultimate goal is to develop tools to constrain the physical parameters ruling the flare emission by comparing CTA data and the *Fermi*-LAT observations at lower energies.

The simulations performed for the Crab Nebula in the flaring state (see Appendix B) suggest exciting prospects for CTA, particularly for the Large Size Telescopes that sample the GeV energy regime with the best sensitivity. On the one hand, we showed that CTA could achieve the flares detection in the Crab Nebula at tens of GeV in the case of classical synchrotron radiation, concretely, if we assume a parent particle population with hard index ($\Gamma_e = 1.5 - 2.0$) and magnetic fields similar to, or stronger than, the estimated average magnetic field in the nebula (i.e., B $\sim$ 150 μG). On the other hand, we compared the TeV electrons energy involved in the models with the total energy available (when considering the gamma-ray luminosity of the nebula and the synchrotron cooling time). Even without accounting for the reacceleration of particle processes that may occur, we found a space of parameters (within plausible particle indices and magnetic fields) in which the flare models detected imply electron energies below the upper limit established (i.e., 5×10^{43} erg).

However, the formulation of the synchrotron radiation used in NAIMA is somehow conservative. Several works (Derishev & Aharonian, 2019; Khangulyan et al., 2020a) demonstrated that the spectrum of synchrotron radiation could significantly deviate from

the one obtained in random magnetic fields (Aharonian et al., 2010). Interestingly, under some conditions, the spectrum's tail can extend into the VHE regime following a power-law decay (instead of an exponential one). Observations of the Crab flares with Cherenkov telescopes, ensuring an optimal energy threshold, provide a unique opportunity to investigate the magnetic structure in astrophysical environments with great detail. Chapter 4 compared the synchrotron tail emission, derived for hundreds of flare models, with the sensitivity curves corresponding to four CTA Large Size Telescopes and the MAGIC experiment (which can observe the Crab Nebula with a low-energy threshold). We showed that observations of bright flares (similar to the one in 2011) could already provide strong constraints, even in the most pessimistic synchrotron approach considered.

Next, we simulated flares of different flux levels, re-scaling the *Fermi*-LAT 2011 April flare data by two factors (i.e., 0.5 and 0.1). For moderate magnetic fields, i.e., $B < 500$ μG, we were able to achieve (in less than ten hours of effective observation time) the detection at TeV energies of flares with half the integrated flux (in the LAT energy band) of the April 2011 one. Furthermore, some of these models did not imply TeV electrons energies larger than the upper limit considered (without particle re-acceleration processes). In contrast, the flare models ten times dimmer than the 2011 April flare (at LAT energies), challenging this maximum energy in electrons established, could be detected at tens of GeV even in less than an hour of observations.

The inverse Compton component arising from the flares faces, in general, more complications. On the one hand, one needs to observe the variability over the overwhelming nebular background. On the other hand, low magnetic fields should be involved to boost the IC emission. The latter, even if theoretically possible, seems unlikely when considering the fast variations observed during the flares in the Crab Nebula's light curve. Additionally, we found an important drawback, i.e., to achieve detectable TeV fluxes, in most cases, the total energy required exceeded the one in TeV emitting electrons in the nebula. Despite such difficulties, several models with soft particle spectra ($\Gamma_e > 2.5$) and mG magnetic fields show that the flares detection at TeV energies can be, in principle, achieved. Furthermore, the prospects obtained for the inverse Compton component's detection can significantly improve if some re-acceleration of particle process boosts the energy in electrons available above the upper limit established. Nonetheless, the non-detection of flares in the TeV regime with the CTA MSTs and SSTs (with the best sensitivity at TeV energies) would constrain the parameters space of the particle population behind the flares.

To summarize, observations with CTA will constrain many physical parameters in the acceleration and emission regions. We showed how different hypotheses could be tested, besides strongly constraining the particle spectrum and magnetic field. The Jitter mechanism, improving the prospects very significantly for the flares detection with the

CTA LSTs at GeV energies, could be easily proven if at work. Similarly, the dynamic of relativistic blobs can be derived if an MHD outflow is considered, in this case, limiting through CTA observations both the Doppler boosting factor and the blob's size. For completeness, we discussed a third scenario, based on a non-MHD approach, that should be further (theoretically) investigated to infer more accurate predictions (to be later compared with observations). We conclude that even if the detection of the flares in the Crab seems difficult to achieve in the TeV regime, the prospects for detecting them in the sub-100 GeV regime are bright and feasible in the early stages of the CTA operations.

6.3.2.3 Final remarks

The prospects that we present, through simulations, for future studies (with CTA) of gamma-ray sources, as, e.g., the Crab Nebula and its pulsar, are based, of course, on the current prospects regarding the CTA northern and southern arrays sensitivities. We indeed reached the conclusions presented in this thesis from somewhat optimistic assumptions, as commented in different parts of the dissertation. For example, we did not always account for the systematical errors. Likewise, the spectral energy distribution of the simulated sources, for some simulations performed, was (admittedly) an optimistic choice. For instance, it is the case of the flaring nebula simulations, which primarily relied on data from the most luminous flares detected (up to date). Hence, our prospects may significantly deviate from future results if, in the end, the CTA observatory does not match the planned requirements considered in this thesis.

The number of Cherenkov telescopes, particularly, may suffer a reduction in comparison to current projections. Note that the results related to the Crab Nebula and pulsar at the highest energies, as, e.g., the maximum energies at which we can still detect the sources, the precision of the nebula's spectral shape measurements in the cutoff region (i.e., above 8 TeV), or the discrimination of different spectral models at tens of TeV, are sensitive to changes in the number (or performance) of MSTs and SSTs (with the best performance at $E > 1$ TeV). In contrast to the case of the steady nebula, the prospects obtained for the detection of flares in Crab, which according to the simulations performed are best at energies below ~ 200 GeV, critically depend on the final number and performance (at tens of GeV) of the LSTs. Nonetheless, the construction and future availability of the four LSTs planned for the northern array is likely guaranteed. Hence, we think that our prospects for detecting flares at tens/hundreds of GeV will not be limited in this aspect.

Furthermore, it is hardly expected more than a factor of two of difference between the instrument's current predicted sensitivity (or PSF) and the final one, either in the sense of better or worst performance than planned. We could detect most of the simulated sources at TeV energies at large significance in modest observation times, suggesting that

our conclusions are robust. It may not be the case for the faintest source individually examined, i.e., G327.1-01.1, with a differential flux of $\sim 2 \times 10^{-13}$ cm^{-2} s^{-1} TeV^{-1} at 1 TeV and a detection significance $\sqrt{\mathrm{TS}} \lesssim 10$ (in 50 hours). In any case, our simulations showed at least one case of clear discrimination between two (confused) sources and the singular source assumption (see Table 3.6), indicating that the conclusions reached will hold (in general). According to our simulations, CTA will also detect the Crab Nebula at tens of TeV with considerable significance. Recent results with air-shower experiments (cited in the discussion) reject a low energy cutoff at $E \lesssim 20$ TeV. In light of the results presented in Chapter 4, it points to a precise characterization of the nebula's spectrum even beyond energies of 50 TeV. Also, the reconstructed size of the nebula at ~ 1 TeV is clearly differentiated from the point-like assumption, even considering systematics comparable to those reported by H.E.S.S. and significantly worst statistical errors than predicted. Considering a PSF larger than expected, however, could complicate the determination of the nebula's asymmetry. As commented in Section 4.3.2, CTA will most likely not resolve the jet-torus structure seen at X-rays. A natural solution to the cited limitations is to update the prospects obtained with future and more realistic assessments of the CTA systematics and IRFs, when possible.

Bibliography

[1] Abdo, A. A. and others, 2007a, The Astrophysical Journal, Volume 664, Issue 2, pp. L91-L94.

[2] Abdo, A. A. and others, 2007b, The Astrophysical Journal, Volume 658, Issue 1, pp. L33-L36.

[3] Abdo, A. A. and others, 2008, Science, 322, 1218-1221.

[4] Abdo, A. A. and others, 2009, Science, Volume 325, Issue 5942, pp. 840.

[5] Abdo et al., Fermi collaboration, 2010a, The Astrophysical Journal, 710, L92–L97.

[6] Abdo A.A., Ackermann M., Ajello M. et al., 2010b, The Astrophysical Journal Supplement Series, Volume 187, Number 2.

[7] Abdo A.A., Ackermann M., Ajello M. et al., 2010c, Astronomy and Astrophysics, 523, L2.

[8] Abdo A.A., Ackermann M., Ajello M. et al., 2010d, The Astrophysical Journal, 709, L152.

[9] Abdo A. A., et al., 2010e, The Astrophysical Journal, 708, 1254.

[10] Abdo A. A., et al., 2011a, Science, 331, 739.

[11] Abdo A. A., et al., 2011b, The Astrophysical Journal, 734, Issue 1, 28, 9.

[12] Abdo, A. A. and others, 2013, The Astrophysical Journal Supplement, vol. 208, no. 2.

[13] Abdollahi, S. and others, 2020, The Astrophysical Journal Supplement Series, 247, 1, 33.

[14] Abeysekara, A. U. and others, 2013, Astroparticle Physics, Volume 50, pp. 26-32.

[15] Abeysekara, A. U. and others, 2016, The Astrophysical Journal, Volume 817, Issue 1, article id. 3, 10 pp.

[16] Abeysekara, A. U., Albert, A., Alfaro, R., et al., 2017, Science, 358, 911.

[17] Abeysekara, A. U., 2018, The Astrophysical Journal, vol. 861, no. 2.

[18] Abeysekara, A. U., and others, 2019, The Astrophysical Journal, 881, 2, 134.

[19] Abramowski A., Acero F., Aharonian F., et al., 2012a, Astronomy and Astrophysics, 537, A114.

[20] Abramowski, A., and others, 2012b, Astronomy and Astrophysics, vol. 548, id.A38, 11 pp.

[21] Acciari, V. A., et al. (VERITAS), 2009, Nature, 462, 770-772.

[22] Acciari et al., V. A., (VERTAS), 2010, The Astrophysical Journal, 714, 163–169.

[23] Acciari, V. A., et al., 2011, The Astrophysical Journal, vol. 730, no. 2.

[24] Acero, F., et al. (H.E.S.S.), 2009, Science, 326, 1080-1082.

[25] Acero, F., Djannati Ataï, A., Forster, A., Gallant, Y., Renaud, M., 2011, International Cosmic Ray Conference, vol. 7, pp. 185. doi:10.7529/ICRC2011/V07/0928.

[26] Acero F., et al., 2013, The Astrophysical Journal, 773, 77.

[27] Acero F., et al., 2016, The Astrophysical Journal Supplement Series, 224, 8.

[28] Acharya B. S., et al., 2013, Astroparticle Physics, 43, 3.

[29] Ackermann M., et al., 2011a, Science, 334, 1103.

[30] Ackermann M., et al., 2011b, The Astrophysical Journal, 726, 35.

[31] Ackermann M., et al., 2012, Astronomy and Astrophysics, Volume 538, id. A71, 15 pp.

[32] Ackermann M., et al., 2013, Science, Volume 339, Issue 6121, pp. 807-811.

[33] Ackermann M., et al., 2017, The Astrophysical Journal, 843, 139.

[34] Adriani O., Akaike Y., Asano K., Asaoka Y., Bagliesi M. G., Bigongiari G., Binns W. R., et al., 2017, Physical Review Letters, Volume 119, Issue 18, id.181101.

[35] Aharonian, F. A.; Hofmann, W.; Konopelko, A. K.; Völk, H. J., 1997a, Astroparicle Physics, Volume 6, Issue 3-4, pp. 343-368.

[36] Aharonian F. A., Atoyan A. M., Kifune T., 1997b, Monthly Notices of the Royal Astronomical Society, 291, 162.

[37] Aharonian et al., HEGRA collaboration, 2001a, Astronomy and Astrophysics, 370, 112–120.

[38] Aharonian, F. A., Konopelko, A. K., Völk, H. J., Quintana, H., 2001b, Astroparticle Physics, Volume 15, Issue 4, pp. 335-356.

[39] Aharonian, F. A., Akhperjanian, A. G., Beilicke, M., et al. 2002, Astronomy and Astrophysics, 395, 803.

[40] Aharonian, Felix A., 2004, Very High Energy Cosmic Gamma Radiation: a Crucial Window on the Extreme Universe. World Scientific.

[41] Aharonian, F., Akhperjanian, A.G., Aye, K.-M., et al., 2005a, Astronomy and Astrophysics, Volume 435, Issue 1, May III, pp. L17-L20.

[42] Aharonian, F., 2005b, Astronomy and Astrophysics, vol. 439, no. 3, pp. 1013–1021.

[43] Aharonian F., et al., 2006a, Astronomy and Astrophysics, 457, Issue 3, October III, pp. 899-915.

[44] Aharonian, F., et al., 2006b, Astronomy and Astrophysics, vol. 448, no. 2, pp. L43–L47.

[45] Aharonian F., et al., 2007, Astronomy and Astrophysics, 467, 1075.

[46] Aharonian F. A., Kelner S. R., Prosekin A. Y., 2010, Physical Review D, 82, 043002.

[47] Aharonian F. A., Bogovalov S. V., Khangulyan D., 2012, Nature, 482, 507.

[48] Aharonian, F. A., 2013, Astroparticle Physics, vol. 43, pp. 71–80.

[49] Aharonian F., Yang R., de Oña Wilhelmi E., 2019, Nature Astronomy, 3, 561.

[50] Aharonian, F., and others, 2021, Chinese Physics C, vol. 45, no. 2. arXiv:2010.06205.

[51] Ahnen, M. L., et al, 2017a, Astroparticle Physics, Volume 94, Pages 29-41.

[52] Ahnen M. L., et al., 2017b, Monthly Notices of the Royal Astronomical Society, 472, 2956.

[53] Albert, J., et al., MAGIC collaboration, 2007, Astronomy and Astrophysics, 474, 937–940.

[54] Aleksić, et al., 2011, The Astrophysical Journal, 742, 43.

[55] Aleksić, J., et al., 2012, Astronomy and Astrophysics, 540, A69.

[56] Aleksić, J., et al., 2014, The Astrophysical Journal, 565, L12.

[57] Aleksić, J., et al., 2015, Journal of High Energy Astrophysics, vol. 5, pp. 30–38.

[58] Aleksić, J., et al., 2016, Astroparticle Physics, Volume 72, pp. 76-94.

[59] Aliu E., et al., 2008, Science, 322, 1221.

[60] Aliu E., et al., 2011, Science, 334, 69.

[61] Aliu E., et al., 2014, The Astrophysical Journal, 781, L11.

[62] Ambrogi L., Zanin R., Casanova S., De Oña Wilhelmi E., Peron G., Aharonian F., 2019, Astronomy and Astrophysics, 623, A86.

[63] Amenomori, M., et al., 2001, Proceedings of the 27th International Cosmic Ray Conference. Hamburg, Germany. Under the auspices of the International Union of Pure and Applied Physics (IUPAP)., pp. 573.

[64] Amenomori, M., and others, 2019, Physical Review Letters, 123, 051101.

[65] Ansoldi, S., et al., 2016, Astronomy and Astrophysics, vol. 585.

[66] Arakawa M., Hayashida M., Khangulyan D., Uchiyama Y., 2020, The Astrophysical Journal, Volume 897, Issue 1, id.33, 12 pp.

[67] Ascenso J., Alves J., Beletsky Y., Lago M. T. V. T., 2007, Astronomy and Astrophysics, 466, 137.

[68] Aschenbach, B., 1985, Reports on Progress in Physics, 48, 579.

[69] Astropy Collaboration, 2013, Astronomy and Astrophysics, Volume 558, id. A33, 9 pp.

[70] Astropy Collaboration, 2018, The Astronomical Journal, Volume 156, Issue 3, article id. 123, 19 pp.

[71] Atkins, R., and others, 2001, Nuclear Instruments and Methods in Physics Research Section A, Volume 449, Issue 3, pp. 478-499.

[72] Atoyan A. M., Aharonian F. A., 1996, Monthly Notices of the Royal Astronomical Society, 278, 525.

[73] Atwood W. B., et al., 2009, The Astrophysical Journal, 697, 2, 1071-1102.

[74] Atwood W., et al., 2013, arXiv:1303.3514.

[75] Bai, X., et al., 2019, eprint arXiv:1905.02773.

[76] Balbo M., Walter R., Ferrigno C., Bordas P., 2011, Astronomy and Astrophysics, 527, L4.

[77] Bamba, A., Ueno, M., Nakajima, H., Koyama, K., 2004, The Astrophysical Journal, Volume 602, Issue 1, pp. 257-263.

[78] Bartoli B., et al., 2015, The Astrophysical Journal, 798, 119.

[79] Bartos I., Veres P., Nieto D. et al., 2014, Monthly Notices of the Royal Astronomical Society, 443, 738.

[80] Bednarek, W., 2007, Monthly Notices of the Royal Astronomical Society, Volume 382, Issue 1, Pages 367–376.

[81] Bednarek W., Idec W., 2011, Monthly Notices of the Royal Astronomical Society, 414, 2229.

[82] Bednarek W., 2013, Astroparticle Physics, 43, 81.

[83] Bednarek W., Pabich J., Sobczak T., 2014, Physical Review D, 90, 103008.

[84] Bell A. R., 1978, Monthly Notices of the Royal Astronomical Society, 182, 147.

[85] Bernlöhr, K., et al., 2003, Astroparticle Physics, Volume 20, Issue 2, pp. 111-128.

[86] Bernlöhr, K., 2008, Astroparticle Physics, 30, 3, 149–158.

[87] Bernlöhr, K., et al., 2013, Astroparticle Physics, 43, 171–188.

[88] Binns, W. R., Wiedenbeck, M. E., Arnould, M., et al., 2005, Astrophysical Journal, 634(1), 351–364.

[89] Bhatt M., Sushch I., Pohl M., Fedynitch A., Das S., Brose R., Plotko P., Meyer D. M. A., 2020, Astroparticle Physics, 123, 102490.

[90] Blackman, E. G., & Field, G. B., 1994, Physical Review Letters, 72, 494.

[91] Blasi, P., Amato, E., 2012, Journal of Cosmology and Astroparticle Physics, Issue 01, id. 011.

[92] Blasi, P., 2013, Nuclear Physics B - Proceedings Supplements, Volumes 239–240, Pages 140-147.

[93] Bonanos A. Z., et al., 2004, The Astrophysical Journal, 611, L33.

[94] Brazier, K.T.S., Becker, W., 1997, Monthly Notices of the Royal Astronomical Society, 284, 335.

[95] Bruel P., Burnett T. H., Digel S. W., Johannesson G., Omodei N., Wood M., 2018, Fermi-LAT improved Pass 8 event selection, arXiv:1810.11394.

[96] Bucciantini N., Arons J., Amato E., 2010, Monthly Notices of the Royal Astronomical Society, 410, 381.

[97] Buehler R., D'Ammando F., Cannon A., 2011, The Astronomer's Telegram, 3276, 1.

[98] Buehler R., et al., 2012, The Astrophysical Journal, 749, Issue 1, article id. 26, 8 pp.

[99] Bühler, R. and Blandford, R., Reports on Progress in Physics, 2014, vol. 77, no. 6.

[100] Bulgarelli, A., and others, 2019, Astronomy and Astrophysics, Volume 627, id. A13, 36 pp.

[101] Burnham K. P., R Anderson D., 2004, Sociological Methods Re-search, 33, 261.

[102] Burtovoi, A., Zampieri, L., 2016, Monthly Notices of the Royal Astronomical Society, Volume 459, Issue 4, 11 July, Pages 3783–3791.

[103] Burtovoi,A., Saito, T. Y., Zampieri, L., Hassan, T., 2017, Monthly Notices of the Royal Astronomical Society, Volume 471, Issue 1, October, Pages 431–446.

[104] Bykov, A. M., Toptygin, I. N., 2001, Astronomy Letters, 27(10), 625–633.

[105] Bykov A. M., Pavlov G. G., Artemyev A. V., Uvarov Y. A., 2012, Monthly Notices of the Royal Astronomical Society, 421, L67.

[106] Bykov, A. M., 2014, Astronomy and Astrophysics Review, volume 22, article id.77, 54 pp.

[107] Bykov A. M., Marcowith A., Amato E., Kalyashova M. E., Kruijssen J. M. D., Waxman E., 2020, Space Sci. Rev., 216, 42.

[108] Camilo, F. et al. 2001, The Astrophysical Journal, 557, 51.

[109] Carraro G., Munari U., 2004, Monthly Notices of the Royal Astronomical Society, 347, 625.

[110] Cash W., 1979, The Astrophysical Journal, 228, 939.

[111] Casse M., Paul J. A., 1980, The Astrophysical Journal, 237, 236.

[112] Caswell, J. L., Milne, D.K., Wellington, K.J., 1981, Monthly Notices of the Royal Astronomical Society, 195, 89.

[113] Cerutti B., Werner G. R., Uzdensky D. A., Begelman M. C., 2012, The Astrophysical Journal, 754, L33.

[114] Cerutti B., Philippov A. A., Spitkovsky A., 2016, Monthly Notices of the Royal Astronomical Society, 457, 2401.

[115] Cesarsky C. J., Montmerle T., 1983, Space Sci. Rev., 36, 173.

[116] Cheng K. S., Ho C., Ruderman M., 1986, The Astrophysical Journal, 300, 500.

[117] Cherenkov Telescope Array Consortium et al., 2019, Science with the Cherenkov Telescope Array, doi:10.1142/10986.

[118] Contopoulos I., Kazanas D., Fendt C., 1999, The Astrophysical Journal, 511, 351.

[119] Cowsik, R., Pal, Y., Tandon, S. N., Verma, R. P., 1967, Phys. Rev. 158 1238.

[120] Cruciani A., et al., 2016, Monthly Notices of the Royal Astronomical Society, 459, 4224.

[121] Crutcher R. M., Wandelt B., Heiles C., Falgarone E., Troland T. H., 2010, The Astrophysical Journal, 725, 466.

[122] Dame T. M., 2007, The Astrophysical Journal, 665, L163.

[123] De Jager O. C., Raubenheimer B. C., Swanepoel J. W. H., 1989, Astronomy and Astrophysics, 221, 180.

[124] De Jager O. C., Büsching I., 2010, Astronomy and Astrophysics, 517, L9.

[125] de Oña Wilhelmi, E., Rudak B., Barrio J.A. et al., 2013, Astroparticle Physics, 43, 287.

[126] de Oña Wilhelmi, E., and Sushch, I., and Brose, R., and Mestre, E., and Su, Y., and Zanin, R., 2020, Monthly Notices of the Royal Astronomical Society, Vol 497, 3, p 3581-3590, https://doi.org/10.1093/mnras/staa2045.

[127] Deil C., et al., 2017, 35th International Cosmic Ray Conference. 10-20 July, 2017. Bexco, Busan, Korea, Proceedings of Science, Vol. 301, id.766.

[128] Delgado, L., Hernanz, M., 2019, Monthly Notices of the Royal Astronomical Society, Volume 490, Issue 3, pp. 3691-3704.

[129] Derishev E., Aharonian F., 2019, The Astrophysical Journal, 887, 181.

[130] del Valle, M. V., & Romero, G. E. 2012, Astronomy and Astrophysics, 543, A56, doi: 10.1051/0004-6361/201218937.

[131] del Valle, M. V., & Romero, G. E., 2014, Astronomy and Astrophysics, 563, A96, doi: 10.1051/0004-6361/201322308.

[132] Drew J. E., Herrero A., Mohr-Smith M., Monguió M., Wright N. J., Kupfer T., Napiwotzki R., 2018, Monthly Notices of the Royal Astronomical Society, 480, 2109.

[133] Dubner, G. M., Gaensler, B. M., Giacani, E. B, Goss, W. M., and Green, A. J., 2002, The Astronomical Journal, Volume 123, Number 1.

[134] Dubner G., Castelletti G., Kargaltsev O., Pavlov G. G., Bieten-holz M., Talavera A., 2017, The Astrophysical Journal, 840, 82.

[135] Dubus, G., Cerutti, B., Henri, G., 2008, Astronomy and Astrophysics, 477, 691-700.

[136] Dubus G., Contreras J.L., Funk S. et al., 2013, Astroparticle Physics, 43, 317.

[137] Dubus G, 2015, Comptes Rendus Physique, 16, 661.

[138] Hobbs, G. B., Edwards, R. T., Manchester, R. N., 2006a, Monthly Notices of the Royal Astronomical Society, Volume 369, Issue 2, pp. 655-672.

[139] Hobbs, G. B., Edwards, R. T., Manchester, R. N., 2006b, Monthly Notices of the Royal Astronomical Society, Volume 372, Issue 4, pp. 1549-1574.

[140] Efron B., 1979, Annals of Statistics, 7, 1.

[141] Eichler, D., Usov, V., 1993, Astrophysical Journal vol. 402, pp. 271.

[142] Ellison, D. C, Slane, P., Patnaude, D. J., and Bykov, A. M, 2012, The Astrophysical Journal, 744, 39.

[143] Engel, R., and Heck, D., and Pierog, T., 2011, Annual Review of Nuclear and Particle Science, 61, 1, 467-489.

[144] Fabjan, C. W., and Ludlam, T., 1982, Annual Review of Nuclear and Particle Science, 32, 335-89.

[145] Feinberg, E., and Primakoff, H., 1948, Phys. Rev. 73,449.

[146] Fiandrini, E. and Tomassetti, N. and Bertucci, B. and Donnini, F. and Graziani, M. and Khiali, B., 2020, arXiv.

[147] Fleishman G. D., 2006, The Astrophysical Journal, 638, 348.

[148] Foreman-Mackey, D., Hogg, D. W., Lang, D., Goodman, J., 2013, Publications of the Astronomical Society of the Pacific, Volume 125, Issue 925, pp. 306.

[149] Frank, I. M. & Tamm, I. E., 1937, Compt. Rend. Acad. Sci. URSS, vol. 14, no. 3, pp. 109-114.

[150] Freeman P., Doe S., Siemiginowska A., 2001, in Starck J.- L., Murtagh F. D., eds, Proc. SPIE Vol. 4477, Astronomical Data Analysis. pp 76–87.

[151] Friedlander, M. A century of cosmic rays, 2012, Nature 483, 400–401.

[152] Fujita Y., Hayashida K., Takahashi H., Takahara F., 2009, Publications of the Astronomical Society of Japan, Volume 61, Issue 6, 25 December, Pages 1229–1235.

[153] Furukawa N., Dawson J. R., Ohama A., Kawamura A., Mizuno N., Onishi T., Fukui Y., 2009, The Astrophysical Journal, 696, L115.

[154] Furukawa N., et al., 2014, The Astrophysical Journal, 781, 70.

[155] Gabici S., Gaggero D., Zandanel F., 2016, arXiv e-prints, p.arXiv:1610.07638.

[156] Gaensler, B. M., Haverkorn, M., Staveley-Smith, L., Dickey, J. M., McClure-Griffiths, N. M., Dickel, J. R., Wolleben, M., 2005, Science, Vol. 307, Issue 5715, pp. 1610-1612.

[157] Gaensler, B. M., and Slane, P.O., 2006, Annual Reviews, 44, 17–47.

[158] Gaisser, T.K., Stanev, T., and Tilav, S., 2013, Frontiers of Physics, 8, 748–758.

[159] Gao, H., Lei, W. H., Wu, X. F., and Zhang, B., 2013, Monthly Notices of the Royal Astronomical Society, vol. 435, no. 3, pp. 2520–2531.

[160] Gerard L., 2015, Divergent pointing with the Cherenkov Telescope Array for surveys and beyond. arXiv:1508.06197.

[161] Giordano, F., 2012, The Astrophysical Journal, vol. 744, no. 1.

[162] Ginzburg, V. L., 1965, Soviet Astronomy, Vol. 9, pp. 877.

[163] Giuliani, G., (AGILE Team), 2011, Memorie della Societa Astronomica Italiana, v.82, pp. 747.

[164] Goldreich, P., Julian, W. H., 1969, The Astrophysical Journal, vol. 157, pp. 869.

[165] Greisen, K., 1966, Physical Review Letters 16, 748–750.

[166] Guarnieri M. D., Lattanzi M. G., Massone G., Munari U., Moneti A., 1995, in The Formation of the Milky Way. pp 183–184.

[167] Guilbert P. W., Fabian A. C., Rees M. J., 1983, Monthly Notices of the Royal Astronomical Society, 205, 593.

[168] Guo, F., Li, H., Daughton, W., & Liu, Y.H. 2014, Physical Review Letters, 113, 155005.

[169] Guo, F., Liu, Y. H., Daughton, W., & Li, H. 2015, The Astrophysical Journal, 806, 167.

[170] Guo, F., Liu, Y. H., Li, X., Li, H., Daughton, W., and Kilian, P., 2020, Physics of Plasmas, vol. 27, no. 8.

[171] Hahn J., 2015, in 34th International Cosmic Ray Conference (ICRC2015). pp. 917.

[172] Harris, C.R., Millman, K.J., van der Walt, S.J. et al., 2020, Nature, 585, 357–362.

[173] Harrison, C. M., Thomson, A. P., Alexander, D. M., Bauer, F. E., Edge, A. C., Hogan, M. T., Mullaney, J. R., and Swinbank, A. M., 2015, The Astrophysical Journal, Vol. 800, No. 1.

[174] Harrus, I. M. and Slane, P. O., 1999, The Astrophysical Journal, Volume 516, Number 2.

[175] Hassan, T., et al., 2015, Proceedings of Science, 34th ICRC, The Hague.

[176] Hassan, Tahira and Arrabito, Luisa and Bernlör, Konrad and Bregeon, Johan and Hinton, James and Jogler, Tobias and Maier, Gernot and Moralejo, Abelardo and Di Pierro, Federico and Wood, Matthew, 2016, Proceedings of Science, 8, 971.

[177] Hassan, T. and Arrabito, L. and Bernlöhr, K. and Bregeon, J. and Cortina, J. and Cumani, P. and Di Pierro, F. and Falceta-Goncalves, D. and Lang, R. G. and Hinton, J. and Jogler, T. and Maier, G. and Moralejo, A. and Morselli, A. and Todero Peixoto, C. J. and Wood, M., 2017, Astroparticle Physics, 93, 76-85.

[178] HAWC Collaboration et al., 2019, The Astrophysical Journal, Volume 881, Issue 2, article id. 134, 13 pp.

[179] Hayakawa, S., 1952, Progress of Theoretical Physics, 8, 571.

[180] Helfand, D. J., Gotthelf, E. V., & Halpern, J. P. 2001, The astrophysical Journal, 556, 380.

[181] H.E.S.S. Collaboration et al., 2011, Astronomy and Astrophysics, 525, A46.

[182] H.E.S.S. Collaboration., et al., 2012a, Astronomy and Astrophysics, 548, A46.

[183] H.E.S.S. Collaboration., et al., 2012b, Astronomy and Astrophysics, Volume 541, id. A5, 9 pp.

[184] H.E.S.S. Collaboration et al., 2014, Astronomy and Astrophysics, 562, id. L4, 5 pp.

[185] H.E.S.S. Collaboration et al., 2015a, Science, 347, 406.

[186] H.E.S.S. Collaboration, 2015b, Astronomy and Astrophysics, vol. 577.

[187] H.E.S.S. Collaboration, 2018, Astronomy and Astrophysics, vol. 612, id. A1, 61 pp.

[188] H.E.S.S. Collaboration, 2020, Nature Astronomy, Volume 4, pp. 167-173.

[189] Hess, V. F., Physik. Zeitschr. 13 (1912) 1084; Physik. Zeitschr. 14 (1913) 610.

[190] Hester, J., and others, 1995, Astrophysical Journal v.448, pp. 240.

[191] Hester J. J., 2008, Annual Review of Astronomy and Astrophysics, 46, 127.

[192] Hillas, A., 1996. Differences between gamma-ray and hadronic showers. Space Science Review 75, 17–30.

[193] Hillas A. M., et al., 1998, The Astrophysical Journal, 503, 744.

[194] Hillas, A., 2006, Conference on Cosmology, Galaxy Formation and Astro-Particle Physics on the Pathway to the SKA, arXiv, astro-ph/0607109.

[195] Holder, J., et al., 2006, Astroparticle Physics, Volume 25, Issue 6, p. 391-401.

[196] Holler M., et al., 2015, preprint (arXiv:1509.02902).

[197] Holler M., Berge D., Hahn J., Khangulyan D., Parsons R. D., for the H.E.S.S. collaboration 2017, 35th International Cosmic Ray Conference. 10-20 July, 2017. Bexco, Busan, Korea, Proceedings of Science, Vol. 301.

[198] Hörandel, Jörg R., 2006, Journal of Physics Conference Series, 47, 41-50.

[199] Horns D., Aharonian F. A., 2004, in Schoenfelder V., Lichti G., Winkler C., eds, ESA Special Publication Vol. 552, 5th INTEGRAL Workshop on the INTEGRAL Universe. pp. 439 (arXiv:astro-ph/0407119).

[200] Hutchinson, W., 1952, Phil. Mag. 43, 847.

[201] Inoue, Y., 2011, The Astrophysical Journal, 733, 1, 66, 66.

[202] Inoue S., Granot J., O'Brien P.T. et al., 2013, Astroparticle Physics, 43, 252.

[203] Ipavich, F. M., 1975, The Astrophysical Journal, 196, 107.

[204] Jansen, F., Lumb, D., Altieri, B., Clavel, J., Ehle, M., Erd, C., Gabriel, C., Guainazzi, M., Gondoin, P., Much, R., Munoz, R., Santos, M., Schartel, N., Texier, D., Vacanti, G., 2001, Astronomy and Astrophysics, v.365, pp. L1-L6.

[205] Jogler, T., and Funk, S., 2016, The Astrophysical Journal, Volume 816, Issue 2, article id. 100, 6 pp.

[206] Jones, C. F., Crawford, J. H., Engelage, J., Guzik, G. T., Mitchell, W. J., Waddington, J. C., 1990, Proceedings of the 21st International Cosmic Ray Conference. Volume 3 (OG Sessions), pp. 333.

[207] Kafexhiu E., Aharonian F., Taylor A. M., Vila G. S., 2014, Physical Review D, 90, 123014.

[208] Kanbach, G., Arzoumanian, Z., Bertsch, D. L., et al. 1994, Astronomy and Astrophysics, 289, 855.

[209] Kargaltsev, O., Rangelov, B., and Pavlov, G. G., 2013, arXiv e-prints.

[210] Kashti, T., Waxman, E., 2005, Physical Review Letters, vol. 95, Issue 18, id. 181101.

[211] Kaufmann, S.; Tibolla, O., 2018, Nuclear and Particle Physics Proceedings, Volume 297-299, pp. 91-95.

[212] Kelner S. R., Aharonian F. A., Khangulyan D., 2013, The Astrophysical Journal, 774, 61.

[213] Kennel C. F., Coroniti F. V., 1984, The Astrophysical Journal, 283, 710.

[214] Kerr M., Ray P. S., Johnston S., Shannon R. M., Camilo F., 2015, The Astrophysical Journal, 814, 128.

[215] Khangulyan D., Aharonian F. A., Kelner S. R., 2014, The Astrophysical Journal, 783, 100.

[216] Khangulyan D., Aharonian F., Romoli C., Taylor A., 2020a, arXiv e-prints, pp. arXiv:2003.00927.

[217] Khangulyan D., Arakawa M., Aharonian F., 2020b, Monthly Notices of the Royal Astronomical Society, 491, 3217.

[218] Kirk J. G., Giacinti G., 2017, Physical Review Letters, 119, 211101.

[219] Knoedlseder, J., and Mayer, M., and Deil, C., and Cayrou, J.-B., and Owen, E., and Kelley-Hoskins, N., and Lu, C.-C., and Buehler, R., and Forest, F., and Louge, T., and Siejkowski, H., and Kosack, K., and Gerard, L., and Schulz, A., and Martin, P., and Sanchez, D., and Ohm, S. and Hassan, T., and Brau-Nogue, S., 2016, Astronomy and Astrophysics, 593, A1.

[220] Krause, O., Birkmann, S. M., Usuda, T., Hattori, T., Goto, M., Rieke, G. H., Misselt, K. A., 2008a, Science, Volume 320, Issue 5880, pp. 1195.

[221] Krause, O., Tanaka, M., Usuda, T., Hattori, T., Goto, M., Birkmann, S., Nomoto, K., 2008b, Nature, 456, 617–619.

[222] Ku W., Kestenbaum H. L., Novick R., Wolff R. S., 1976, The Astrophysical Journal, 204, L77.

[223] Kuiper L., Hermsen W., Cusumano G., Diehl R., Schönfelder V.,Strong A., Bennett K., McConnell M. L., 2001, Astronomy and Astrophysics, 378, 918.

[224] Lagarias J., A. Reeds J., H. Wright M., Wright P., 1998, SIAM Journal on Optimization, 9, 112.

[225] Lande J., et al., 2012, The Astrophysical Journal, 756, 5.

[226] Lee H.-G., Moon D.-S., Koo B.-C., Lee J.-J., Matthews K., 2009, The Astrophysical Journal, 691, 1042.

[227] Lefa E., Kelner S. R., Aharonian F. A., 2012, The Astrophysical Journal, 753, 176.

[228] Lemoine-Goumard, M., Ferrara, E., Grondin, M. H., Martin, P., Renaud, M., 2011, Memorie della Societa Astronomica Italiana, v. 82, pp. 739.

[229] Li T.-P., Ma Y.-Q., 1983, The Astrophysical Journal, 272, 317.

[230] Li, W., Jesse Leaman, R.C., Filippenko, A. V., Poznanski, D., Wang, X., Ganeshalingam, M., Mannucci, F., 2011, Monthly Notices of the Royal Astronomical Society, vol. 412, no. 3, pp. 1473–1507.

[231] Linden, T., Auchettl, K., Bramante, J., Cholis, I., Fang, K., Hooper, D., Karwal, T., Li, S. W., 2017, Physical Review D, Volume 96, Issue 10, id. 103016.

[232] Lingenfelter, 2019, The Astrophysical Journal Supplement Series, vol. 245, no. 2.

[233] Liu, Y. H., Guo, F., Daughton, W., Li, H., & Hesse, M. 2015, Phisixal Review Letters, 114, 095002.

[234] Lobanov A. P., Horns D., Muxlow T. W. B., 2011, Astronomy and Astrophysics, 533, A10.

[235] Longair M. S., 1981, High energy astrophysics: an informal introduction for students of physics and astrophysics. Cambridge Univ. Press, Cambridge.

[236] Lorimer D., Kramer M., 2005, Handbook of Pulsar Astronomy. Vol. 4. Cambridge, UK, Cambridge University Press.

[237] Lyubarsky, Y. E., 2003, Monthly Notices of the Royal Astronomical Society, vol. 345, no. 1, pp. 153–160.

[238] Lyubarsky, Y. E. 2005, Monthly Notices of the Royal Astronomical Society, 358, 113.

[239] Lyubarsky Y. E., 2012, Monthly Notices of the Royal Astronomical Society, 427, 1497.

[240] Lyutikov, M., 2003, Monthly Notices of the Royal Astronomical Society, 346, 540.

[241] Lyutikov M., Otte N., McCann A., 2012, The Astrophysical Journal, 754, 33.

[242] Lyutikov M., Komissarov S., Sironi L., Porth O., 2018, Journal of Plasma Physics, 84, 635840201.

[243] MacKay, D. J. C., Cambridge University Press, 40 W. 20 St. New York, NY, United States, ISBN:978-0-521-64298-9.

[244] Mangano S., Delgado C., Bernardos M., Lallena M., Rodríguez Vázquez J. J., 2018, arXiv e-prints, p. arXiv:1810.00592.

[245] Mannheim K., Schlickeiser R., 1994, Astronomy and Astrophysics, 286, 983.

[246] Mao, S. A, McClure-Griffiths, N. M., Gaensler, B. M., Haverkorn, M.. Beck, R., McConnell, D.;, Wolleben, M., Stanimirović, S., Dickey, J. M., Staveley-Smith, L., 2012, The Astrophysical Journal, Volume 759, Issue 1, article id. 25, 25 pp.

[247] Marcote, B., Ribó, M., Paredes, J. M., Ishwara-Chandra, C. H. 2015, Monthly Notices of the Royal Astronomical Society, 451, 4578.

[248] Markwardt, C. B., & Ögelman, H. 1995, Nature, 375, 40.

[249] Marsden, P. L., Gillett, F. C., Jennings, R. E., Emerson, J. P., de Jong, T., and Olnon, F. M., 1984, Astrophysical Journal, vol. 278, March 1, 1984, pp. L29-L32.

[250] Martín J., Torres D. F., Rea N., 2012, Monthly Notices of the Royal Astronomical Society, 427, 415.

[251] Matthews, J. H., Bell, A. R., and Blundell, K. M., 2020, New Astronomy Reviews, vol. 89.

[252] Mattox J. R., et al., 1996, The Astrophysical Journal, 461, 396.

[253] Mayer M., Buehler R., Hays E., Cheung C. C., Dutka M. S., Grove J. E., Kerr M., Ojha R., 2013, The Astrophysical Journal Letters, Volume 775, Issue 2, article id. L37, 6 pp.

[254] Mazin D., Raue M., Behera B. et al., 2013, Astroparticle Physics, 43, 241.

[255] Mazin, D., 2019, 36th International Cosmic Ray Conference (ICRC2019), held July 24th-August 1st, 2019 in Madison, WI, U.S.A. Online at https://pos.sissa.it/cgi-bin/reader/conf.cgi?confid=358, id. 741.

[256] Meagher K., VERITAS Collaboration 2015, in 34th International Cosmic Ray Conference (ICRC2015). pp. 792 (arXiv:1508.06442).

[257] Mestre E., de Oña Wilhelmi E., Zanin R., Torres D. F., Tibaldo L., 2020, Monthly Notices of the Royal Astronomical Society, 492, 708.

[258] Mestre E., de Oña Wilhelmi E., Khangulyan, D., Zanin, R., Acero, F., Torres, D. F., 2021, Monthly Notices of the Royal Astronomical Society, V501, I1, February, 337–346.

[259] Meyer M., Horns D., Zechlin H. S., 2010, Astronomy and Astrophysics, 523, A2.

[260] Mochol I., Pétri J., 2015, Monthly Notices of the Royal Astronomical Society, 449, L51.

[261] Moffat A. F. J., Shara M. M., Potter M., 1991, The Astrophysical Journal, 102, 642.

[262] Morrison, P., 1958, Il Nuovo Ciment 7, 858.

[263] Naurois, M. & Mazin, D., 2015, Comptes rendus - Physique, Volume 16, Issue 6-7, pp. 610-627.

[264] Nazé, Y., Rauw, G. and Manfroid, J. 2008, Astronomy and Astrophysics, 483, 171.

[265] Nečesal, P., (Pierre Auger Collaboration), 2011, Journal of Physics: Conference Series, Volume 293, Issue 1, id. 012036.

[266] Nigro, C. and Deil, C. and Zanin, R. and Hassan, T. and King, J. and Ruiz, J. E. and Saha, L. and Terrier, R. and Brügge, K. and Nöthe, M. and et al., 2019, Astronomy and Astrophysics, 625, 1432-0746.

[267] Ögelman, H., Finley, J. P., & Zimmerman, H. U. 1993, Nature, 361, 136.

[268] Ojha R., Hays R., Buehler E., Dutka M., 2013, The Astronomer's Telegram, 4855.

[269] Olbert C. M., Keohane J. W., Arnaud K. A., Dyer K. K., Reynolds S. P., Safi-Harb S., 2003, The Astrophysical Journal, 592, L45.

[270] Pacini F., Salvati M., 1973, The Astrophysical Journal, 186, 249.

[271] Paredes J.M., Bednarek W., Bordas P. et al, 2013, Astroparticle Physics, 43, 301.

[272] Parker, E. N. 1957, Journal of Geophysical Research, 62, 509.

[273] Parker, E. N., 1969, Space Science Reviews, Volume 9, Issue 5, pp. 651-712.

[274] Peterson, J. D., and Webber, W. R., 2002, Astrophysical Journal, 575, 217–224.

[275] Petschek, H. E. 1964, in Magnetic Field Annihilation in AAS/NASA Symposium on the Physics of Solar Flares, ed. W. N. Ness (Washington, DC: NASA), 425.

[276] Piatti A. E., Bica E., Claria J. J., 1997, VizieR Online Data Catalog, pp J/A+AS/127/423.

[277] Piron F., et al., 2001, Astronomy and Astrophysics, 374, 895.

[278] Popkow A., (VERITAS Collaboration), 2015, Proceedings of the 34th International Cosmic Ray Conference (ICRC2015). 30 July - 6 August, 2015. The Hague, The Netherlands.

[279] Porth O., Komissarov S. S., Keppens R., 2014, in International Journal of Modern Physics Conference Series. pp. 1460168.

[280] Preibisch T., Ratzka T., Kuderna B., et al., 2011, Astronomy and Astrophysics, 530, A34.

[281] Price-Whelan, A. M. and Sipőcz, B. M. and Günther, H. M. and Lim, P. L. and Crawford, S. M. and Conseil, S. and Shupe, D. L. and Craig, M. W. and Dencheva, N. and et al., 2018, The Astronomical Journal, 156, 1538-3881, 123.

[282] Ptuskin, V. S, and Rogovaya, S. I., and Zirakashvili, V. N., and Chuvilgin, L. G., and Khristiansen, G. B., and Klepach, E. G., and Kulikov, G. V., 1993. Astronomy and Astrophysics, 268, 2, 726-735.

[283] Ptuskin, V., 2006, Journal of Physics: Conference Series, Volume 47, 113-119.

[284] Rauw G., et al., 2004, Astronomy and Astrophysics, 420, L9.

[285] Rauw G., et al., 2005, Astronomy and Astrophysics, 432, 985.

[286] Rauw G., Manfroid J., Gosset E., Nazé Y., Sana H., De Becker M., Foellmi C., Moffat A. F. J. 2007, Astronomy and Astrophysics, 463, 981.

[287] Reach W. T., et al., 2006, The Astrophysical Journal, 131, 1479.

[288] Refsdal B. L., et al., 2009, in Varoquaux G., van der Walt S., Millman J., eds, Proceedings of the 8th Python in Science Conference. Pasadena, CA USA, pp 51 – 57.

[289] Richardson, J. D., 2008, Geophysical Research Letters, Vol. 35, L23104.

[290] Rishbeth, H. 1958, Australian Journal of Physics, 11, 550.

[291] Rodgers A.W., Campbell C.T., Whiteoak J.B., 1960, Monthly Notices of the Royal Astronomical Society, 121, 103.

[292] Romoli C., Taylor A. M., Aharonian F., 2017, Astroparticle Physics, 88, 38.

[293] Rudak B., Dyks J., 1998, Monthly Notices of the Royal Astronomical Society, 295, 337.

[294] Saha L., Domínguez A., Tibaldo L., Marchesi S., Ajello M., LemoineGoumard M., López M., 2020, The Astrophysical Journal, 897, 131.

[295] Sajjad, S. and Falvard, A., arXiv e-prints, (arXiv:2010.13822) 2020.

[296] Salpeter E. E., 1955, The Astrophysical Journal, 121, 161.

[297] Sánchez-Ayaso, E., del Valle, M. V., Martí, J., Romero, G. E., and Luque-Escamilla, P. L., 2018, The Astrophysical Journal, Vol 861, Number 1.

[298] Saz Parkinson P. M., et al., 2010, The Astrophysical Journal, 725, 571.

[299] Schroer B., Pezzi O., Caprioli D., Haggerty C., Blasi P., 2020, arXiv e-prints,p. arXiv:2011.02238.

[300] Serlemitsos, P. J., 2007, Publications of the Astronomical Society of Japan, Volume 59, Issue sp1.

[301] Seward, F.D., Harnden, F.R., Jr., 1982, The Astrophysical Journal, 256, L45.

[302] Sezer A., Ergin T., Cesur N., Tanaka S. J., Kisaka S., Ohira Y.,Yamazaki R., 2020, Monthly Notices of the Royal Astronomical Society, 492, 1484.

[303] Shilon I., et al., 2019, Astroparticle Physics, 105, 44.

[304] Shu, F. H., Adams, F. C., & Lizano, S., 1987, Annual Review of Astronomy and Astrophysics, 25, 23–81.

[305] Sironi, L. and Spitkovsky, A., 2011, The Astrophysical Journal, vol. 726, no. 2, doi:10.1088/0004-637X/726/2/75.

[306] Sironi, L. and Spitkovsky, A., 2014, The Astrophysical Journal Letters, Vol. 783, no. 1.

[307] Slane, P., Lovchinsky, I., Kolb, C., Snowden, S. L., Temim, T., Blondin, J., Bocchino, F., Miceli, M., Chevalier, R. A., Hughes, J. P., Patnaude, D. J., Gaetz, T., 2018, The Astrophysical Journal, Volume 865, Issue 2, article id. 86, 12 pp.

[308] Smith, D. A., Wang, Q. D., 2004, The Astrophysical Journal, Volume 611, Issue 2, pp. 881-891.

[309] Striani E., et al., 2011, The Astrophysical Journal, 741, L5.

[310] Striani E., et al., 2013, The Astrophysical Journal, 765, 52.

[311] Su, Meng and Slatyer, Tracy R. and Finkbeiner, Douglas P., 2010, The Astrophysical Journal, 724, 2, 1044–1082.

[312] Su Y., Chen Y., Yang J., Koo B.-C., Zhou X., Lu D.-R., JeongI.-G., DeLaney T., 2011, The Astrophysical Journal, 727, 43.

[313] Sun, X. -N., Yang, R. -Z., Liang, Y. -F., Peng, F. -K., Zhang, H. -M., Wang, X. -Y., Aharonian, F., 2020a, Astronomy and Astrophysics, Volume 639, id.A80, 7 pp.

[314] Sun, X. -N., Yang, R. -Z., Wang X. -Y., 2020b, Monthly Notices of the Royal Astronomical Society, Volume 494, Issue 3, Pages 3405–3412.

[315] Sushch, I.; Hnatyk, B., 2014, Astronomy and Astrophysics, Volume 561, id.A139, 8 pp.

[316] Sushch, I., Oya, I., Schwanke, U., Johnston, S., and Dalton, M. L., 2017, Astronomy and Astrophysics, vol. 605.

[317] Sweet, P. A. 1958, in IAU Symp. 6, Electromagnetic Phenomena in Cosmical Physics, ed. B. Lehnert (New York: Cambridge Univ. Press), 123.

[318] Szanecki M., Sobczynska D., Niedzwiecki A., et al., 2015, Astroparticle Physics, 67, 33.

[319] Takamoto, M., 2013, Astrophysical Journal, 775, 50.

[320] Tamura, K., Kawai, N., Yoshida, A., 1996, Publications of the Astronomical Society of Japan, 48, L33.

[321] Tanaka S. J., Takahara F., 2010, arXiv e-prints, p. arXiv:1001.2360.

[322] Tavani, M., et al., 2009, Astronomy and Astrophysics, Volume 502, Issue 3, pp. 995-1013.

[323] Tavani M., et al., 2011, Science, 331, 736.

[324] Temim, T., Slane, P., Gaensler, B. M., Hughes, J. P., and Van Der Swaluw, E., 2009, The Astrophysical Journal, vol. 691, no. 2, pp. 895–906.

[325] Teraki Y., Takahara F., 2013, The Astrophysical Journal, 763, 131.

[326] The Fermi-LAT Collaboration., 2012, Science, Volume 335, Issue 6065, pp. 189.

[327] The Fermi-LAT Collaboration., 2017, The Astrophysical Journal Supplement Series, Volume 232, Issue 2, article id. 18, 23 pp.

[328] The Fermi-LAT Collaboration and Biteau J., 2018, The Astrophysical Journal, 237, 32.

[329] The Fermi-LAT collaboration, 2019, The Astrophysical Journal Supplement Series, Volume 247, Issue 1, id.33, 37 pp.

[330] The Pierre Auger Collaboration, Contributions to the 33rd International Cosmic Ray Conference (ICRC 2013), arXiv e-prints, 2013.

[331] Thompson, D. J., Fichtel, C. E., Kniffen, D. A., & Ögelman, H. B. 1975, ¨ The Astrophysical Journal, 200, L79.

[332] Tibaldo, L., Grenier, I. A., (The Fermi-LAT collaboration), Nuclear Physics B (Proceedings Supplements), Volume 239, pp. 70-75.

[333] Torres D. F., Martín J., de Oña Wilhelmi E., Cillis A., 2013, Monthly Notices of the Royal Astronomical Society, 436, 3112.

[334] Torres D. F., Cillis A., Martín J., de Oña Wilhelmi E., 2014, Journal of High Energy Astrophysics, 1-2, 31.

[335] Townsley, L. K., Broos, Patrick S., Garmire, G. P., Povich, M. S., 2019, The Astrophysical Journal Supplement Series, Volume 244, Issue 2, article id. 28, 44 pp.

[336] Trussoni, E., Massaglia, S., Caucino, S., Brinkmann, W., Aschenbach, B., 1996, Astronomy and Astrophysics, 306, 581.

[337] Tsirou, M., Gallant, Y., Zanin, R., Terrier, R., and H.E.S.S. Collaboration, 35th International Cosmic Ray Conference (ICRC2017), 2017, vol. 301.

[338] Tsujimoto M., et al., 2007, The Astrophysical Journal, 665, 719.

[339] Uzpen B., et al., 2005, The Astrophysical Journal, 629, 512.

[340] Vargas Álvarez C. A., Kobulnicky H. A., Bradley D. R., Kannappan S. J., Norris M. A., Cool R. J., Miller B. P., 2013a, The Astrophysical Journal, 145, 125.

[341] Vargas Álvarez C. A., Kobulnicky H. A., Bradley D. R., Kannappan S. J., Norris M. A., Cool R. J., Miller B. P., 2013b, The Astronomical Journal, 145, 125.

[342] Viganó and D., Torres D. F., 2015, Monthly Notices of the Royal Astronomical Society, 449, 3755.

[343] Virtanen, Pauli and Gommers, Ralf and Oliphant, Travis E. and Haberland, Matt and Reddy, Tyler and Cournapeau, David and Burovski, Evgeni and Peterson, Pearu and Weckesser, Warren and Bright, Jonathan and van der Walt, Stéfan J. andBrett, Matthew and Wilson, Joshua and Millman, K. Jarrod andMayorov, Nikolay and Nelson, Andrew R. J. and Jones, Eric andKern, Robert and Larson, Eric and Carey, C J and Polat, İlhan and Feng, Yu and Moore, Eric W. and VanderPlas, Jake and Laxalde, Denis and Perktold, Josef and Cimrman, Robert and Henriksen, Ian and Quintero, E. A. and Harris, Charles R. and Archibald, Anne M. and Ribeiro, Antônio H. and Pedregosa, Fabian and van Mulbregt, Paul and SciPy 1.0 Contributors, 2020, Nature Methods, 17, 261-272.

[344] Voelk H. J., Forman M., 1982, The Astrophysical Journal, 253, 188.

[345] Völk, H. J., and Zirakashvili, V. N., Astronomy and Astrophysics, 2004, 417, 807-817.

[346] Volpi D., Del Zanna L., Amato E., Bucciantini N., 2008, Astronomy and Astrophysics, 485, 337.

[347] Wallace, P. T., Peterson, B. A., Murdin, P. G., et al. 1977, Nature, 266, 692.

[348] Weekes, T. C., et al., 1989, The Astrophysical Journal, 342, 379.

[349] Weisskopf M. C., et al., 2013, The Astrophysical Journal, 765, 56.

[350] Wentzel, D. G., 1974, Annual Review of Astronomy and Astrophysics, Vol. 12, 71-96.

[351] White R. L., 1985, The Astrophysical Journal, 289, 698.

[352] White, R. L., & Chen, W., 1992, Astrophysical Journal Letters vol. 387, pp. L81.

[353] White, R. L., & Chen, W., 1995, in Proc. IAU Symp. 163, ed. K. A. van der Hucht, & P. M. Williams (Dordrecht: Kluwer Academic Publishers), 438.

[354] Whiteoak, J. B. Z. and Green, A. J., 1996, Astronomy and Astrophysics Supplement Series, vol. 118, pp. 329–380.

[355] Whiteoak J. B. Z., Uchida K. I., 1997, Astronomy and Astrophysics, 317, 563.

[356] Whitney B. A., et al., 2004, The Astrophysical Journal Supplement Series, 154, 315.

[357] Winkler, C., et al., 2003, Astronomy and Astrophysics, v.411, pp. L1-L6.

[358] Wright M., 1996, Direct search methods: Once scorned, now respectable. Addison-Wesley, pp 191–208.

[359] Wood, M. and Caputo, R. and Charles, E. and Di Mauro, M. and Magill, J. and Perkins, J. S. and Fermi-LAT Collaboration, 2017, ICRC2017, International Cosmic Ray Conference, 301, 824.

[360] Yang R.-z., de Oña Wilhelmi E., Aharonian F., 2018, Astronomy and Astrophysics, 611, A77.

[361] Yang, R. -Z. and Wang, Y., 2020, Astronomy and Astrophysics, Volume 640, id. A60, 7 pp.

[362] Yamaguchi, H., Bamba, A., Koyama, k., 2009, Publications of the Astronomical Society of Japan, Volume 61, Issue sp1, Pages S175–S181.

[363] Yeung P. K. H., Horns D., 2019, The Astrophysical Journal, 875, 123.

[364] Zabalza V., 2015, Proc. of International Cosmic Ray Conference 2015, pp. 922.

[365] Zatsepin, G. T., and Kuzmin, V. A., 1966, JETP Lett., 4 78–80.

[366] Zeidler P., et al., 2018, The Astrophysical Journal, 156, 211.

[367] Zenitani S., Hesse M., Klimas A., 2009, The Astrophysical Journal, 696, 1385.

List of Figures

2.1 Half-absorption altitude with respect to photon energy. The data were taken from the *National Radio Astronomy Observatory* (NRAO). 11

2.2 Spectral energy distribution of cosmic rays (taken from Hillas, 2006). . . . 12

2.3 Schematic illustration of the Fermi second-order acceleration mechanism in an interstellar gas cloud. 15

2.4 An example of shock. The temperature observed by the Voyager 2 spacecraft in the solar wind and heliosheath at crossing the termination shock in 2007 (taken from Richardson, 2008). 16

2.5 Schematic illustration of the diffusive shock acceleration mechanism in a shock front. 17

2.6 Sketch of a reconnection region. Two magnetized flows with oppositely directed magnetic field (B) converge with velocity v_{in} in the reconnection region, where the electric field (E) is co-directed in the converging flow (thick red arrow). The particles emit synchrotron and IC (in-figure boxes) along their trajectories (red lines). Credits: D. Khangulyan (taken from Mestre et al., 2020). 19

2.7 Sketch representing the geometries of different radiation mechanisms. See chapters 6, 8, and 9 of Longair's book for an in-depth discussion. 21

2.8 Sketch representing the geometry of curvature radiation. 22

2.9 Spectral energy distribution of a particle population with index 2, cutoff energies ranging from 100 GeV to 10 TeV, and arbitrary amplitude, for different radiation mechanisms. The plot was produced with the NAIMA PYTHON package. 26

2.10 Full gamma-ray sky from the *Fermi Large Area Telescope Fourth Source Catalog* (4FGL, taken from Abdollahi and others, 2020). 27

3.1 Sketch of the geometry of Cherenkov radiation. 36

3.2 The panels (above) illustrate an electromagnetic (in the left) and proton-induced (in the right) atmospheric shower. We based the illustrations on Sajjad and Falvard (2020) and Engel et al.'s (2011) papers for the electromagnetic- and hadronic- cases. 37

3.3 First (at the left) and second (at the right) iterations of the FERMIPY localization method applied to Westerlund 2. 42

3.4 The solid lines depict the CTA-N angular resolution (in black), and the same improved by a factor 2 (in blue) and 5 (in green). The black dashed line depicts the CTA-N system requirements. 42

3.5 The different lines depict the sensitivity and angular resolution of the CTA observatory compared to other instruments. The plots were taken from `https://www.cta-observatory.org/science/cta-performance`. 43

3.6 Comparison between GAMMAPY and CTOOLS simulations. 45

3.7 We show an example of simulated 3D sky cubes. In particular, we display four energy bins taken from an 'ON' (in the upper panel) and 'OFF' (below) cube. We smoothed the plots (in counts units) by applying a small Gaussian kernel convolution. 48

3.8 (a) Vela X template employed in the simulations. (b) Observation simulation of Vela X with the CTA northern array and 25 hours of observation time. (c) Same as (b) but with the CTA southern array instead. The sky region plotted is a square of 3.4° of side. 52

3.9 (a) G327.1-01.1 template used for the simulations. (b) Observation simulation of G327.1-01.1 for 50 hours with the CTA northern array. (c) Same as (b) but with the CTA southern array instead. The sky region plotted is a square of 0.85° of side. 55

3.10 (a) MSH 15-52 template used for the simulations. (b) Observation simulation of MSH 15-52 for 25 hours with the CTA northern array. (c) The same as (b) but with the CTA southern array instead. The sky region plotted is a square of 1.6° of side. 59

3.11 (a) HESS J1303-631 template used for the simulations. (b) Observation simulation of HESS J1303-631 for 25 hours with the CTA northern array. (c) The same as (b) but with the CTA southern array instead. The sky region plotted is a square of 1.7° of side. 61

3.12 Simulation observation of HESS J1303-631 and MSH 15-52 sources with a separation of 0.2° (without background). The simulations correspond to 25 hours with the CTA southern array. 67

3.13 (a) Simulation observation of HESS J1303-631 for 25 hours of observation time with the CTA southern array (b) Same as (a) but rescaling the HESS J1303-631 template at twice its distance (c) The same rescaled at fourth times the distance of (a). 69

3.14 Expected gamma-ray emission from two stellar bowshocks compared with the predicted CTA sensitivity. Credits: Estrella Sánchez-Ayaso 70

3.15 The SED of the LS 2355 bowshock at an assumed distance of 2.1 kpc. The plot was taken from Sánchez-Ayaso et al. (2018). 71

4.1 We obtained the phase curve depicted from a simulation (carried out with CTOOLS) of the Crab pulsar above 400 GeV of energy with the CTA northern array (for 100 h of observation time). 74

4.2 The Crab Nebula and pulsar spectra are depicted with data taken from Ansoldi et al. (2016) and Buehler et al. (2012). 75

4.3 Panel (a) depicts the statistical error retrieved from the Crab pulsar simulations for the positions and Gaussian σ of P1 and P2 peaks above 40 GeV, with different observation times. The panel (b) corresponds to the same but above 400 GeV. 76

4.4 Minimum index variation detected (at 95% CL) resulting from fitting the pulsar spectrum to a smoothed broken power-law at different observation times. The legend shows the different (fixed) energy breaks employed. The plot was taken from Mestre et al. (2020). 77

4.5 Minimum source flux (in Crab units) necessary to detect a periodicity at a 5σ-level as a function of the observation time (for the Gaussian peak templates described). The shadowed regions depict the 3σ error. The plot was taken from Mestre et al. (2020). 78

4.6 The different panels depict the evolution in time of the periodicity detection's significance (3σ region). The source's flux is (a) 0.2, (b) 0.5, (c) 1, (d) and 2, in Crab units. We smoothed the curves through the interpolation method, and the 3σ region was computed by bootstrapping (Efron, 1979) of the H-statistic and simulations. The plots were taken from Mestre et al. (2020). 80

4.7 In panel (a), the statistical error in the peak's best-fit position (for different Gaussian peak widths, with the 1σ error region noted). In panel (b), the same for the Gaussian sigma. We smoothed the curves through the interpolation method and computed the 1σ error region by bootstrapping (Efron, 1979) the (simulated) events phases. 81

4.8 The different lines depict the detection significance of the Crab Nebula with the CTA northern (in the left panel) and southern (in right panel) arrays as a function of the observation time for the different assumptions on the spectral shape listed in Table 4.1 (at energies above 50 TeV). The plots correspond to observation times larger than one hour. 85

4.9 The different histograms above depict the average number of (excess) events obtained in discrete energy bins for the Crab Nebula simulations (according to the different assumptions for the spectral shape in Table 4.1) with the CTA northern array and 50 hours of observation time. 88

4.10 Result of fitting all the spectral shapes considered to the nebula simulations with the LP-MAGIC model (see Table 4.1), with the 3σ error region noted. On the left, the results under the assumption of the systematic error requirements in Section 3.2.3. On the right, we improved the systematic uncertainty by a factor 2. The plots were taken from Mestre et al. (2020). 90

4.11 The black line depicts the energy cutoff lower limit at 95% CL for different observation times. The plot was taken from Mestre et al. (2020). 91

4.12 The panels represent the CTA capabilities to disentangle between different shapes of an exponential spectral cutoff, i.e., different values of k, as defined in Equation 4.4. In particular, we show the cases $k = 1$ and $k = 3/2$. The shaded area represents the systematical and statistical errors, quadratically added. On the left, we calculated the errors using the systematic error requirements, whereas, on the right, we used the systematic errors reduced by a factor 2. The plots were taken from Mestre et al. (2020). 91

4.13 On the left, we represent the minimum size resolvable (in the simulations) versus the lower energy bound of the energy interval simulated (we permanently fixed the upper bound to 300 TeV), using the CTA IRFs, with the 1σ error region noted. We added the Crab Nebula's measured size with H.E.S.S. for energies above 0.7 TeV (black dot) and the one measured from 5 GeV to 500 GeV with *Fermi* (black star) with the 1σ error bars for comparison. On the right, the measured extension versus the input size for the simulations. The plot on the left was taken from Mestre et al. (2020). 94

4.14 (a) Morphological template used for the jet-torus scenario. The white circles represent the PSF one sigma for the full system requirements (of approximately 0.04° for the energy bin spanning from 0.8 TeV to 1.25 TeV), and the same improved by a factor of five (i.e., 0.008° referred to the same energy bin). It is a surface-brightness map in units of erg $cm^{-2}sr^{-1}s^{-1}Hz^{-1}$. (b) Observation simulation of 100 hours with the CTA full system requirements for the angular resolution plotted with the corresponding PSF (white circle) in counts (after background subtraction). (c) Observation simulation as in (b), but with the angular resolution improved by a factor of five (exceeding by far the current CTA system requirements), again with the corresponding PSF depicted. The plots were taken from Mestre et al. (2020). 95

4.15 Schematic summary of the flare simulations workflow. 100

4.16 In the left panel (taken from Mestre et al., 2021), we represented the fitted amplitude of the electron energy distribution (N_e) as a function of Γ_e, E_p, and B for the April 2011 flare. For each value of Γ_e, the points correspond from left to right to 11 values of magnetic field logarithmically spaced from 5 mG to 50 μG. The right panel depicts the integrated energy in electrons above 1 TeV (W_e) in the same manner of the left panel. 101

4.17 The different lines depict the synchrotron and IC emission of a simulated flare (fitted to the 2011 April flare spectrum) with B = 100 μG and $\Gamma_e = 1.5$. The green squares correspond to the nebula spectrum during the 2011 April flare (as seen by *Fermi*-LAT). The rest of the data correspond to the steady nebula emission (the compilation was taken from Meyer et al., 2010, and Buehler et al., 2012). The plot was taken from Mestre et al. (2021). . . . 101

4.18 The different black lines depict the synchrotron emission for flares (fitted to the LAT 2011 April flare data) of various indices ($\Gamma_e = 1, 2, 2.5$) and magnetic fields ($B = 100$ μG in the left panel, and 500 μG in the right one) together with the simulations of the Crab Nebula steady spectrum (in black line with dots), with the (3σ) error region noted (see the black shaded area, accounting only for statistical errors). The data recorded by LAT of the 2011 flare is shown in red squares. The magenta solid (and dashed) lines correspond to the CTA northern array's sensitivity (when considering only its four Large Size Telescopes) for five hours of observation time. The magenta dot-dashed line corresponds to the MAGIC's sensitivity at a low zenith angle, i.e., $z < 30°$ (see Tables A.5 and A.6 in Alecsić et al., 2016). The plot was taken from Mestre et al. (2021). 108

4.19 The different lines depict the IC emission for different flares models (fitted to the LAT 2011 April flare data, in black if the flare is detected in the TeV regime and in red otherwise). In these cases, $\Gamma_e = 1.5$ (left) and $\Gamma_e = 2$ (right). On top is the (simulated) Crab steady nebula spectrum (in black line with dots) with the (3σ) error region noted (in a black shaded area, accounting only for statistical errors). We accounted for the SSC emission in a region of 2.8×10^{-4} pc in size. The sensitivity curves (in magenta) were defined in Figure 4.18. The plot was taken from Mestre et al. (2021). 109

4.20 The different lines show the enhancement of integral flux above 1 TeV (in Equation 4.6) for various flare models (fitted to the LAT 2011 April flare data and accounting for the SSC). The plot was taken from Mestre et al. (2021). 110

4.21 The plot summarizes the flaring nebula observation simulations for the different models fitted to the LAT data of the April 2011 flare. The models below the solid line are detectable in the TeV and GeV regimes (i.e., from 1.25 TeV to 50 TeV of energy, and below 200 MeV) if observed with CTA. In contrast, we only detected the models above the solid line in the GeV regime. However, the models below the dash-dotted line (red shaded area) require an energy in electrons $W_e > 5 \times 10^{43}$ erg. The plot was taken from Mestre et al. (2021). 111

4.22 The plot summarizes the flaring nebula observation simulations for the different models fitted to the LAT data of the March 2013 flare, compared to the upper limits established by H.E.S.S. and VERITAS observations. The models located below the dashed line imply an enhancement of integral flux above 1 TeV larger than 60% (i.e., $Z > 1.6$ in Equation 4.6). Therefore, these models violate the upper limits established by the H.E.S.S. and VERITAS observations of the 2013 flare. The exclusion region (for the integral flux upper limit above 1 TeV) extends up to the solid line ($Z > 1.01$, with only statistical errors), supposing the flare is not detectable in 50 hours with the CTA northern array. The models below the dashed-dotted line (red shaded area) violate the upper limit estimated for the (TeV electrons) total energy. The plot was taken from Mestre et al. (2021). 112

4.23 We depict the synchrotron (green lines), IC (purple lines), and total (black lines) emissions for different flare models. We fitted the flare depicted in solid line to the LAT 2011 flare data (above 80 MeV) for a 2.5 index. The dashed (dotted) lines correspond to the same model re-scaled by a factor of 0.5 (0.1). All models assume $B = 500$ μG. The red solid (dashed) line indicates the sensitivity of CTA-N (accounting only for five hours with its four LSTs). We noted the simulated steady spectrum (for 50 h of CTA-N) in a gray shaded area (3σ region). 114

4.24 In the left panel (taken from Mestre et al., 2021), we represent the Doppler boosting factor lower and upper limits from Equations 4.11 and 4.12. The simulations plotted in red are not consistent with the relativistic moving outflow scenario for any Doppler factor since the particle spectrum's cutoff energy (E'_{PeV}) fitted in these cases is too small compared to the Doppler boosting factor upper limit derived with Equation 4.12. In the right panel, we plotted the different lower limits for the blob size obtained with Equations 4.7 (in black) and 4.13 (in red), as a function of the particle index and magnetic field assumed. We derived the Doppler boosting factor depicted in the right axis from the simulations. 118

4.25 We represent the LAT data of the 2011 and 2013 flares fitted to a power-law model above 400 GeV (with the 1σ error region noted) and compared to the nebula steady emission and the CTA/MAGIC sensitivity. 119

5.1 On the top left, (a) depicts the ^{13}CO large-scale intensity map integrated between 67 km s^{-1} and 74 km s^{-1} obtained from the MWISP survey. On the top right, (b) shows the intensity map integrated between 80 and 88 km s^{-1}. The red dashed-line circle marks the 99% localization error of the *Fermi* reanalysis. The green contours correspond to the radio shell, derived from the image compiled by Ferrand & Safi-Harb (2012). The bottom panels show the ^{12}CO channel (MWISP survey), centered on the position of SNR G39.2-0.3. The left one (c) for the 69 km s^{-1} map and the right one (d) for the 88 km s^{-1} one. White contours are obtained from the LAT significance map above 3 GeV, starting on TS=25 (or $\sim 5\sigma$ significance in steps of 10). The plot was taken from de Oña Wilhelmi et al. (2020). . . . 126

5.2 Spectral energy distribution of 4FGL J1903.8+0531, associated with SNR G39.2–0. The black lines represent the best-fitting shape, and the 1σ error derived for the energy range between 100 MeV and 100 GeV. The plot was taken from de Oña Wilhelmi et al. (2020). 127

5.3 Multiwavelength spectral energy distribution of the SNR G39.2–0.3. The lines indicate the best-fitting models for both leptonic and hadronic interpretations of the high-energy emission. The plot was taken from de Oña Wilhelmi et al., (2020). 128

5.4 The panels above correspond to images of the core of RCW 49 at 0.843 GHz (taken from Whiteoak & Uchida, 1997). In (a) with a resolution of 43″, in (b) with a greyscale that enhances fainter structure, in (c) at a resolution of 25″, and in (d) a sketch of the wind-blown shells (A and B) with the blister outlined by a dotted curve. WR 20a and b are indicated by the cross-mark and plus sign, respectively. The box encloses the Westerlund 2 cluster location. 132

5.5 The left panel, taken from Yang et al. (2018), shows the gamma-ray emission (in counts) above 10 GeV for a ($8° \times 8°$) region around Westerlund 2. The black crosses and blue circles represent identified and unassociated sources from the 3FGL catalogue. The white dashed line shows the extended emission of FGES J1036.4–5834. At the right, the Westerlund 2 field in H.E.S.S. data showing the significance of the VHE gamma-ray emission. The black (dashed) and green (solid) contours correspond to $0.7 < E < 2.5$ TeV and $E > 2.5$ TeV, respectively. The right panel is taken from HESS Collaboration (2011). 133

5.6 Phase curve of PSR J1023.1-5745 obtained at different energies in a region of 0.6° around the pulsar's position (normalized by the height of P2) with the various components of the phase curve noted. The horizontal blue line corresponds to the expected contribution in the phase curve of background sources (i.e., all the sources in the field of view except FGES J1023.3–5747 and PSR J1023.1-5745). 137

5.7 Test statistic map centered on the position of FGES J1023.3–5747 at energies above: 200 MeV (upper left), 700 MeV (upper right), and 3 GeV (below left), cut in phase from 0.58 to 1, and above 10 GeV without cutting in phase. It was computed for a point-like test source with an index 2 power-law spectrum. 138

5.8 On the left, a) Spectral energy distribution (with only statistical errors) of PSR J1023–5746 derived from the on-peak (in black, with dot markers), the *Bridge* (in blue, with star markers), and off-peak-region (red upper limits). On the right, b) The SED (only statistical errors) derived from FGES J1023.3–5747 after gating the pulsed emission (in black) and analyzing only the gamma-ray emission above 10 GeV (without cutting in phase, in blue). The shaded area marks the 1σ error on the fitted spectral model. 138

5.9 *Spitzer*/IRAC GLIMPSE Mosaic obtained from the GLIMPSE survey archival data. The magenta dashed lines correspond to the (1σ) error interval for the best-fit extension of FGES J1023.3–5747, with the central cross marking the best-fit position (with the 1σ error). Similarly, the white dashed lines (and the cross) correspond to the morphological characteristics of the H.E.S.S. source HESS J1023-575, as described in H.E.S.S Collaboration et al. (2011). The cyan cross corresponds to the position of PSR J1023–5746. 141

5.10 Intrinsic (Gaussian) width of FGES J1023.3–574 measured for different energy bins (in black points for LAT data, with only statistical errors). The red point corresponds to the intrinsic width of HESS J1023-575. The best-fitted power-law model (for the joint LAT/H.E.S.S. data) is plotted in a blue line (with the 1σ error region noted in shaded area), together with the mean size (black dashed line). The arrows correspond to the extension upper limit at 95% CL, except that in the first energy bin, which depicts the 95% containment radius instead (r_{95} UL). 143

5.11 The left panel shows the integral flux from the best-fit FGES J1023.3–5747 spectrum computed in differential energy bins (in red squares) compared to that predicted given the best-fit spectrum in the entire energy range, i.e., from 200 MeV to 500 GeV (in black dots, see the last column in the upper part of Table 5.2). The right panel shows the best-fit (power-law) index obtained in differential energy bins. 144

5.12 The figure (above) shows the radial profile obtained for FGES J1023.3–5747 with the best-fit $1/r$ and $1/r^2$ models depicted. We merged the first two rings with 0.1° of radius each. 144

5.13 Acceleration efficiency (f) obtained in function to the distance and diffusion coefficient (D) assumed (for a fiducial target mass in molecular clouds of 4.5×10^5 $M_\odot$). The upper and right axes correspond to the estimated gamma-ray source and CRs diffusion radius, respectively. 150

5.14 The lines depicted represent the best-fitted models for the FGES J1023.3–5747 spectrum according to the pion decay (solid line) and PWN (dashed line) hypotheses. The red points correspond to the *Fermi*-LAT data analysis (with only statistical errors), and the purple ones to H.E.S.S. (H.E.S.S. Collaboration et al., 2011). We obtained the upper limit in the X-ray domain from Fujita et al. (2009). 151

5.15 The black line represents the log-likelihood for the best-fit (power-law with an exponential cutoff) proton spectrum (to the joint LAT and H.E.S.S. data of FGES J1023.3-5747) as a function of the cutoff energy and particle index (in the inset plot). 152
5.16 In a solid black line, we represent the likelihood ratio test statistic as a function of the cutoff energy. The null hypothesis of the likelihood ratio test (H_0) corresponds to a proton power-law spectrum and the alternative one (H_1) to the exponential cutoff power-law model. The black dashed line indicates the critical value of the χ^2 distribution at 95% CL (with one degree of freedom, i.e., 3.841). 153

6.1 Characteristic magnetic field compared to plasma density for different (Galactic) astrophysical environments. The fiducial values depicted were taken from; Goldreich & Julian, 1969; Saz Parkinson et al., 2010; Bucciantini et al., 2010; and Sironi & Spitkovsky A., 2011, for the Crab pulsar and PSR J1023-5746 (cold wind, in black); Martín et al., 2012; and Torres et al., 2014, for the Cran Nebula (PWNe region, in red); Dubner et al., 2002; Aharonian et al., 2005a; Sushch & Hnatyk, 2014, Slane et al., 2018; and de Oña Wilhelmi et al., 2020, for SNR G39.2-0.3, MSH 15-52 and Vela (SNRs region, in green); Bednarek, 2007; and this thesis results for Westerlund 2 (clusters, in blue); Gaensler, 2005; and Mao et al., 2012, for the LMC/SMC (in orange); Delgado & Hernanz, 2019, for V745 Sco (novae, in purple); and Dubus, 2008; and Marcote et al., 2016, for LS 5039 (gamma-ray binaries, in cyan). 157
6.2 In color lines, we show the spectral energy distribution of the different sources treated in this thesis. The black lines depict the CTA/LAT sensitivity (for comparison). 162

List of Tables

3.1 Vela X input model and best-fit parameters to the CTA observations simulations depicted in (b) and (c) panels of Figure 3.8. We fitted the simulations using the Vela X template morphology, i.e., the panel (a) in the cited figure and a Gaussian model. 54

3.2 G327.1-01.1 input model and best-fit parameters to the CTA observations simulations in (b) and (c) panels of Figure 3.9. We fitted the simulations both to a source with the template morphology shown in panel (a) (of the cited figure) and a Gaussian model. 56

3.3 MSH 15-52 input model and best-fit parameters to the CTA observations simulations in (b) and (c) panels of Figure 3.10. We fitted the simulations both to a source with the MSH 15-52 template morphology, i.e., in panel (a) of the cited figure and a Gaussian model. 58

3.4 HESS J1303-631 input model and best-fit parameters to the CTA observations simulations in the (b) and (c) panels of Figure 3.11. We fitted the simulations both to a source with the HESS J1303-631 template morphology, i.e., in (a) panel of the cited figure and Gaussian model. . . . 62

3.5 The TS obtained from fitting the CTA observations simulations of MSH 15-52 and HESS J1303-631 (artificially confused) to; (1) The MSH 15-52 template morphology. (2) The HESS J1303-631 template morphology. (3) A Gaussian model. (4) A source with the morphology of the MSH 15-52 plus HESS J1303-631 templates. 64

3.6 The TS obtained from fitting the CTA observations simulations of MSH 15-52 and Vela X (artificially confused) to; (1) The MSH 15-52 template morphology. (2) The Vela X template morphology. (3) A Gaussian model. (4) A source with the morphology of the MSH 15-52 plus Vela X templates. 65

3.7 The TS obtained from fitting the CTA observations simulations of G327.1-01.1 and HESS J1303-631 (artificially confused) to; (1) The G327.1-01.1 template morphology. (2) The HESS J1303-631 template morphology. (3) A Gaussian model. (4) A source with the morphology of the G327.1-01.1 plus HESS J1303-631 templates. 65

3.8 We summarize (above) the computation time ($t_{\rm simul}$) required for the simulation of two (confused) sources (from a morphological spatial template, with CTOOLS) for different input parameters. The input parameters varied are the radius of the field-of-view, observation time ($t_{\rm obs}$), energy threshold ($E_{\rm th}$), and total flux of the (confused) sources above 1 TeV of energy ($\rm F_{1TeV}$). The first two parts of the table are referenced to a simulation with a (FoV) radius of 0.1°, $t_{\rm obs} = 1$ hour, $E_{\rm th} = 1$ TeV, and $\rm F_{1TeV} = 10^{-12}$ $\rm cm^{-2}s^{-1}$ (lasting $t_{\rm simul} = 2.236 \pm 0.011$ s). We indicate in each column of the table the parameter that changed compared to the cited ones. The third and bottom part of the table is referenced to a simulation with (FoV) radius of 10°, $t_{\rm obs} = 25$ hours, and $\rm F_{1TeV} = 2 \times 10^{-12}$ $\rm cm^{-2}s^{-1}$, indicating that the combination of increasing observation times and lower energy thresholds boosts the computation time needed per simulation. 66

4.1 The table below summarizes the spectral models (taken from the literature) used for the Crab Nebula's IC component. The corresponding references, in order of appearance, are Aharonian et al. (2004); Aleksić et al. (2015); Holler et al. (2015); Aharonian et al. (2006a); HAWC Collaboration et al. (2019). 84

4.2 In the tables below, we summarize the minimum observation time (in hours) needed to detect the Crab Nebula (at 5σ) in various energy ranges and under different assumptions for the spectral model. We considered the spectral models listed in Table 4.1. The upper part of the table corresponds to the CTA northern array, whereas the bottom part is for the southern one. . . 86

4.3 On the left, a summary of the systematic errors applied. On the right, resulting AIC values for the different characterizations fitted to the LP-MAGIC model simulations. 89

4.4 We summarize below the properties of the 2011 and 2013 flares, obtained from Buehler et al. (2012), Mayer et al. (2013), and H.E.S.S. Collaboration et al. (2014). 97

4.5 We provide (above) the observation time (in hours) necessary to detect different models of flares (fitted to the LAT 2011 April flare data) at energies from 20 GeV to 120 GeV with the chi-square test applied to the excess distributions (at 99% CL). Note that we assume that Crab is flaring during the entire time of observation. 104
4.6 We summarize (above) the observation time (in hours) necessary to detect different models of flares (fitted to the LAT 2011 April flare data) at energies from 1.25 TeV to 50 TeV, obtained as Table 4.5. The table's left part corresponds to the CTA northern array, whereas the right part corresponds to the southern one. We assume that Crab is flaring during the entire time of observation. The models indicated with asterisks imply $W_{\rm e} > 5 \times 10^{43}$ erg if the flare duration is the one noted. 106
4.7 We summarize (above) the observation time (in hours) necessary to detect different models of flares from 1.25 TeV to 50 TeV with the CTA northern (left) and southern (right) arrays. The first column (F_{2011}) corresponds to flare models fitted to the LAT data of the April 2011 flare. The models with an asterisk imply that the energy in electrons (above 1 TeV) is larger than 5×10^{43} erg. We assume the Crab is flaring during the entire observation time. 113

5.1 Best-fitted positions (in equatorial and Galactic coordinates) for PSR J1023–5746 and FGES J1023.3–574 (in degrees, accounting only for statistical errors). 145
5.2 Best-fitted models for PSR J1023–5746 and FGES J1023.3–5747. The units of N_0 are $\mathrm{cm^{-2}s^{-1}MeV^{-1}}$ for PSR J1023–5746 and $\mathrm{cm^{-2}s^{-1}MeV^{-1}sr^{-1}}$ in the case of FGES J1023.3–5747. 145
5.3 Physical parameters of PSR J1023–5746 and its putative PWN. The pulsar rotation parameters f and $\dot{f}$ are obtained from the ATNF catalogue. The braking index n and ejecta mass M_{ej} are fixed, following the results from Torres et al. (2014). The broken power-law spectral shape of electrons (defined with the indices $\alpha_{1,2}$ and breaking energy γ_b), and magnetic field in the region (B), best representing the data, are listed in the third section of the table. 149

Acronyms

AGILE Astro-rivelatore Gamma a Immagini LEggero

AGN Active Galactic Nucleus

AIC Akaike Information Criterion

AMS Alpha Magnetic Spectrometer

ASCA Advanced Satellite for Cosmology and Astrophysics

ATCA Australia Telescope Compact Array

CGRO Compton Gamma Ray Observatory

CL Confidence Level

CMB Cosmic Microwave Background

CR Cosmic rays

CTA Cherenkov Telescope Array

FGES Fermi Galactic Extended Source

FGL Fermi Gamma-ray LAT

FIR Far-infrared

FoV Field-of-View

FWHM Full Width at Half Maximum

H.E.S.S. High Energy Stereoscopic System

HAWC High-Altitude Water Cherenkov

HE High-energy

HEGRA High Energy Gamma Ray Astronomy

HGPS H.E.S.S. Galactic Plane Survey

IACT Imaging Atmospheric (or Air) Cherenkov Telescope

IC inverse Compton

INTEGRAL INTErnational Gamma-Ray Astrophysics Laboratory

IR Infrared

IRF Instrument Response Function

ISM Interstellar Medium

K-N Klein-Nishina

KSP Key Science Project

LAT Large Area Telescope

LHAASO Large High Altitude Air Shower Observatory

LMC Large Magellanic Cloud

LP Log-Parabola

LST Large-Sized Telescope

MAGIC Major Atmospheric Gamma Imaging Cherenkov

MCMC Markov Chain Monte Carlo

MHD Magneto-hydrodynamic

MJD Modified Julian Date

MST Medium-Sized Telescope

MWISP Milky Way Imaging Scroll Painting

NIR Near-infrared

NRAO National Radio Astronomy Observatory

OSO Orbiting Solar Observatory

PAMELA Payload for Antimatter Matter Exploration and Light-nuclei Astrophysics

PIC Particle-In-Cell

PL Power-law

PLEC Power-law with Exponential Cutoff

PSF Point Spread Function

PWN Pulsar Wind Nebula

ROI Region of Interest

ROSAT RöntgenSATellit

RSG Red supergiant

SAS Small Astronomy Satellite

SB SuperBubble

SED Spectral Energy Distribution

SFR Star-forming region

SMC Small Magellanic Cloud

SNR Supernova Remnant

SSC Synchrotron-Self-Compton

SST Small-Sized Telescope

TS Test Statistic

UL Upper limit

UV Ultraviolet

VERITAS Very Energetic Radiation Imaging Telescope Array System

VHE Very-high-energy

WR Wolf-Rayet

XMM-Newton X-ray Multi-mirror Mission - Newton

Appendices

Appendix A

Generation and analysis of 3D sky cubes

Introduction

In the following appendices, we first present a list of codes (sorted following the dissertation order) that were of relevant importance for obtaining the results described in this thesis. Most of these scripts are also available on *Github*; see `https://github.com/emestregui?tab=repositories`. Next, we included the papers made public to explain the results of our research work.

Please note that the compilation of scripts we present has to be taken only as a guide for reproducing the results explained. The complete list of materials used for this work is too long. Hence, it is impractical to append them all here. However, the corresponding authors of the papers shown below can provide further information on the scripts and tools employed (under request). Note also that the scrips appended are based on deprecated versions of GAMMAPY and CTOOLS and may worth using the most recent versions instead.

Appendix A is dedicated to the simulation and analysis of 3D GAMMAPY cubes, as described in Section 3.3.1 of this work. We used this tool for several results summarized in Chapter 4 (as explained). Appendix B presents the primary tool employed to simulate flares in the Crab Nebula, as described in Section 4.0.4 of the dissertation. Finally, Appendix C shows the script used to fit the particle spectrum of a source, giving its high-energy spectrum, if assuming a hadronic origin of the radiation. In particular, it was used for the Westerlund 2 emission modeling (explained in Section 5.0.3). Appendix D consists of the works we published.

A.1 Generator of 3D sky cubes

You can see below an example of the initial XML definition files. For the nebula, e.g.:

```
binning: {binsz: 0.005, coordsys: CEL, enumbins: 20, nxpix: 500, nypix: 500,
          proj: TAN}
logging: {working_dir: .}
model: {alphapar: 2.47, beta: 0.10423, dec: 22.0144, pivot_energy: 1,
        prefactor: 3.23e-11, ra: 83.6333, rad: 0.1, source:"Nebula",
        spectrum: LogParabola, template: Sphere2D, use_psf: false}
pointing: {dec: 22.0144, livetime: 50.0 hour, ra: 83.6333}
selection: {ROI: 5 deg, emax: 300.0, emin: 0.02, offset_fov: 2}
```

For the pulsar:

```
binning: {binsz: 0.005, coordsys: CEL, enumbins: 20, nxpix: 500, nypix: 500,
          proj: TAN}
logging: {working_dir: .}
model: {dec: 22.0144, index: 2.9, pivot_energy: 0.15, prefactor: 2.0e-11,
        ra: 83.6333, rad: 0.005, source: "pulsar", spectrum: pl,
        template: Sphere2D, use_psf: false}
pointing: {dec: 22.0144, livetime: 50.0 hour, ra: 83.6333}
selection: {ROI: 5 deg, emax: 300.0, emin: 0.02, offset_fov: 2}
```

Finally, for the generation of the cubes:

```
"""
An example how to simulate a 3D n_pred, n_obs cube, n_off cube.
Using CTA IRFs.
"""
#from __future__ import absolute_import,division,print_function,
#unicode_literals
import astropy.units as u
import numpy as np
import yaml
from astropy.coordinates import SkyCoord, Angle
from gammapy.cube import make_exposure_cube
from gammapy.cube.utils import SkyCube
from gammapy.irf import EffectiveAreaTable2D, EnergyDispersion2D
from gammapy.irf import EnergyDependentMultiGaussPSF
from configuration import get_model_gammapy, make_ref_cube
from astropy.io import fits
from gammapy.utils.energy import EnergyBounds
from gammapy.cube import make_background_cube
from gammapy.irf import Background3D
```

```
from time import time
import pyfits
from astropy.units import Quantity

def _validate_inputs(flux_cube, exposure_cube):
    if flux_cube.data.shape[1:] != exposure_cube.data.shape[1:]:
        raise ValueError('flux_cube and exposure cube must have the same
                         shape! \n''flux_cube: {0}\nexposure_cube: {1}'
                          ''.format(flux_cube.data.shape[1:],
                          exposure_cube.data.shape[1:])
                          )

def read_config(filename):
    '''Read configuration from yaml file.

    Parameters
    ----------
    filename : yaml file
        Configuration file.

    Returns
    -------
    config : `dict`
        Configuration dictionary.
    '''
    with open(filename) as fh:
        config = yaml.load(fh)
    config['model']['prefactor'] = float(config['model']['prefactor'])
    return config

def get_irfs(config, filename):
    '''Get IRFs from file.

    Parameters
    ----------
    config : `dict`
        Configuration dictionary.
    filename : fits file
        IRFs file

    Returns
    -------
    irfs : `dict`
```

```
        IRFs dictionary.
    '''
    offset = Angle(config['selection']['offset_fov']*u.deg)
    psf_fov = EnergyDependentMultiGaussPSF.read(filename,hdu=
        'POINT SPREAD FUNCTION')
    psf=psf_fov.to_energy_dependent_table_psf(theta=offset)
    print(' psf', psf)
    aeff = EffectiveAreaTable2D.read(filename, hdu='EFFECTIVE AREA')
    edisp_fov = EnergyDispersion2D.read(filename, hdu='ENERGY DISPERSION')
    table = fits.open('irf_file.fits')['BACKGROUND']
    table.columns.change_name(str('BGD'), str('Bgd'))
    table.header['TUNIT7'] = '1/(MeV s sr)'
    bkg = Background3D.read(filename, hdu='BACKGROUND')
    irfs = dict(psf=psf, aeff=aeff, edisp=edisp_fov, bkg=bkg, offset=offset)
    return irfs

def compute_spatial_model_integral(model, image):
    '''Compute integral of spatial model.

    Parameters
    ----------
    model : `CombinedModel3D`
        Source model
    image : `SkyImage`
        Spatial model sky image

    Returns
    -------
    Spatial model integral.
    '''
    coords = image.coordinates()
    surface_brightness=model(coords.data.lon.deg,coords.data.lat.deg)
        *u.Unit('deg-2')
    solid_angle = image.solid_angle()
    return (surface_brightness*solid_angle).sum().to('')

def compute_sum_cube(flux_cube, flux_cube2, config):
    """Compute sum of two flux cubes.

    Parameters
    ----------
    flux_cube : `SkyCube`
        Flux cube, differential surface brightness in 'cm-2 s-1 TeV-1 sr-1'.
```

```
    flux_cube2 : `SkyCube`
        Flux cube 2.
    config : `dict`
        Configuration dictionary.

    Returns
    -------
    nflux_cube_sum: `SkyCube`
        Sum of flux_cube and flux_cube2.

    See also
    -------
    read_config
    """
    ebin = flux_cube.energies(mode="edges")
    ebounds = EnergyBounds(ebin)
    nflux_cube_sum = make_ref_cube(config)
    for idx in range(len(ebounds)-1):
        npred1 = flux_cube.sky_image_idx(idx)
        npred2 =flux_cube2.sky_image_idx(idx)

        #DEBUG
        #print npred1.data
        #print npred2.data

        nflux_sum=u.Quantity(npred1.data.value+npred2.data.value,
            '1/(cm2 s sr TeV)')
        nflux_cube_sum.data[idx] = nflux_sum.value
    return nflux_cube_sum

def compute_npred_cube(flux_cube, exposure_cube, ebounds, config, irfs,
                       integral_resolution=10):
    """Compute predicted counts cube.

    Parameters
    ----------
    flux_cube : `SkyCube`
        Flux cube, differential surface brightness in cm-2 s-1 TeV-1 sr-1.
    exposure_cube : `SkyCube`
        Exposure cube.
    ebounds : `~astropy.units.Quantity`
        Energy bounds for the output cube.
    config : `dict`
```

```
    Configuration dictionary.
irfs : `dict`
    IRFs dictionary.
integral_resolution : int (optional)
    Number of integration steps in energy bin when computing
    integral flux.

Returns
-------
npred_cube : `SkyCube`
    Predicted counts cube with energy bounds as given by the
    input "ebounds".

See also
--------
compute_npred_cube_simple
read_config
See get_irfs
"""
_validate_inputs(flux_cube, exposure_cube)

#Make an empty cube with the requested energy binning
sky_geom = exposure_cube.sky_image_ref
energies = EnergyBounds(ebounds)
npred_cube = SkyCube.empty_like(sky_geom,energies=energies,unit='',
    fill=np.nan)

#Process and fill one energy bin at a time
for idx in range(len(ebounds)-1):
    emin, emax = ebounds[idx:idx+2]
    ecenter = np.sqrt(emin*emax)
    flux = flux_cube.sky_image_integral(emin,emax,interpolation='linear',
        nbins=integral_resolution)

    exposure = exposure_cube.sky_image(ecenter, interpolation='linear')
    solid_angle = exposure.solid_angle()
    flux.data.value[np.isnan(flux.data.value)] = 0
    exposure.data.value[np.isnan(exposure.data.value)] = 0
    npred=flux.data.value*u.Unit('1/(cm2 s sr)')*exposure.data*solid_angle

    #Debug
    #print npred.to('')
    npred_cube.data[idx] = npred.to('')
```

```
    #Apply EnergyDispersion
    edisp = irfs['edisp']
    offset = irfs['offset']
    edisp_idx = edisp.to_energy_dispersion(offset=offset,e_reco=ebounds,
        e_true=ebounds)

    for pos_x in range(npred_cube.data.shape[1]):
        for pos_y in range(npred_cube.data.shape[2]):
            npred_pos = npred_cube.data[0:len(ebounds)-1,pos_x,pos_y]
            if npred_pos.sum() != 0:
                for idx in range(len(ebounds)-1):
                    npred_cube.data[idx][pos_x][pos_y]=np.dot(npred_pos,
                        edisp_idx.data.data[idx])

    return npred_cube

def compute_npred_cube_simple(flux_cube, exposure_cube):
    """Compute predicted counts cube (using a simple method).

    *Multiplies flux, exposure, pixel solid angle and energy bin width.
    *No spatial reprojection, interpolation or integration in energy.
    *This is fast, but can be inaccurate, e.g., for too large energy bins.
    *If you want a more fancy method, call compute_npred_cube instead.

    Output cube energy bounds will be the same as for the exposure cube.

    Parameters
    ----------
    flux_cube : `SkyCube`
        Differential flux cube.
    exposure_cube : `SkyCube`
        Exposure cube.

    Returns
    -------
    npred_cube : `SkyCube`
        Predicted counts cube.

    See also
    --------
    compute_npred_cube
    """
```

```
    _validate_inputs(flux_cube, exposure_cube)
    solid_angle = exposure_cube.sky_image_ref.solid_angle()
    de = exposure_cube.energy_width
    flux = flux_cube.data*u.Unit('1/(cm2 s sr TeV)')
    exposure = exposure_cube.data
    npred = flux*exposure*solid_angle*de[:, np.newaxis,np.newaxis]
    npred_cube = SkyCube.empty_like(exposure_cube)
    npred_cube.data = npred.to('')
    return npred_cube

def compute_nexcess_cube(npred_cube,livetime,pointing,offset_max,
    bkg_rate,config):
    '''Compute excess cube.

    Parameters
    ----------
    npred_cube : `SkyCube`
        Predicted counts cube.
    livetime : `Quantity`
        Observation time.
    pointing : `SkyCoord`
        Pointing coordinates.
    offset_max : `Angle`
        Offset.
    bkg_rate : `Background3D`
        Background rate.
    config : `dict`
        Configuration dictionary.
    Returns
    -------
    nexcess_cube : `SkyCube`
        Predicted counts cube.

    non_cube : `SkyCube`
        On observation.
    noff_cube : `SkyCube`
        Off observation.

    See also
    --------
    read_config
    See get_irfs
    '''
```

```
    ebin = npred_cube.energies(mode="edges")
    ebounds = EnergyBounds(ebin)
    nexcess_cube = make_ref_cube(config)
    non_cube = make_ref_cube(config)
    noff_cube = make_ref_cube(config)

    #Compute two background cubes
    nbkg1_cube =  make_background_cube(pointing=pointing,obstime=livetime
        ,bkg=bkg_rate,ref_cube=npred_cube, offset_max=offset_max)
        #compute_bkg_cube(npred_cube,bkg_rate,livetime)
    nbkg2_cube =  make_background_cube(pointing=pointing,obstime=livetime
        ,bkg=bkg_rate,ref_cube=npred_cube,offset_max=offset_max)
        #compute_bkg_cube(npred_cube,bkg_rate,livetime)

    #For each energy bin, I need to obtain the correct background rate
    #i.e., two, one for the on and one for the off.
    for idx in range(len(ebounds)-1):
        emin, emax = ebounds[idx:idx+2]
        ecenter = np.sqrt(emin*emax)
        print('Energy bins:')
        print emin, emax
        npred = npred_cube.sky_image_idx(idx)
        npred.unit = u.Unit('TeV')
        solid_angle = npred.solid_angle()
        npred.data.value[np.isnan(npred.data.value)]=0.

        nbkg1_ebin = nbkg1_cube.data[idx]
        nbkg2_ebin = nbkg2_cube.data[idx]

        #DEBUG
        #print npred

        n_on=np.random.poisson(npred.data)+np.random.poisson(abs(nbkg1_ebin))
        n_off = np.random.poisson(abs(nbkg2_ebin))
        nexcess = n_on-n_off
        nexcess_cube.data[idx] = nexcess
        non_cube.data[idx] = n_on
        noff_cube.data[idx] = n_off
    return nexcess_cube, non_cube, noff_cube

def psf_fromfits(filename):
    '''Get PSF from fits file.
```

```
    Parameters
    ----------
    filename : Fits file
        IRFS fits file.

    Returns
    -------
    energy_lo : `Quantity`
        Low energy bounds.
    energy_hi : `Quantity`
        High energy bounds.
    theta : `Angle`
        Offset angle.
    sigmas : `list`
        PSF sigmas.
    norms : `list`
        PSF norms.
    '''
    hdulist = pyfits.open(filename)
    hdu = hdulist[2]
    energy_lo = Quantity(hdu.data['ENERG_LO'][0], 'TeV')
    energy_hi = Quantity(hdu.data['ENERG_HI'][0], 'TeV')
    theta = Angle(hdu.data['THETA_LO'][0], 'deg')

    #Get sigmas
    shape = (len(theta), len(energy_hi))
    sigmas = []
    for key in ['SIGMA_1','SIGMA_2','SIGMA_3']:
        sigma = hdu.data[key].reshape(shape).copy()
        sigmas.append(sigma)

    #Get amplitudes
    norms = []
    for key in ['SCALE','AMPL_2','AMPL_3']:
        norm = hdu.data[key].reshape(shape).copy()
        norms.append(norm)
    return [energy_lo, energy_hi, theta, sigmas, norms]

def main():
    t0 = time()

    #Read configuration
    config = read_config('config.yaml')
```

```
config2 = read_config('config2.yaml')

#Getting the IRFs, effective area and PSF
filename = 'irf_file.fits'
irfs = get_irfs(config, filename)

#Create empty references cubes
ref_cube = make_ref_cube(config)

if config['binning']['coordsys'] == 'CEL':
    pointing=SkyCoord(config['pointing']['ra'],config['pointing']['dec']
        ,frame='icrs',unit='deg')
if config['binning']['coordsys'] == 'GAL':
    pointing=SkyCoord(config['pointing']['glat'],config['pointing']
        ['glon'],frame='galactic',unit='deg')

ref_cube2 = make_ref_cube(config2)
livetime = u.Quantity(config['pointing']['livetime']).to('second')
offset_max = Angle(config['selection']['ROI'])

#Make exposure cube
exposure_cube = make_exposure_cube(
    pointing=pointing,
    livetime=livetime,
    aeff=irfs['aeff'],
    ref_cube=ref_cube,
    offset_max=offset_max,
)
print('exposure sum: {}'.format(np.nansum(exposure_cube.data)))
exposure_cube.data = exposure_cube.data.to('m2 s')
print(exposure_cube)

#Define model and do some quick checks
model = get_model_gammapy(config)
model2 = get_model_gammapy(config2)

#Normalize spatial model
norm_factor = compute_spatial_model_integral(model.spatial_model
    ,exposure_cube.sky_image_ref)
norm_factor2 = compute_spatial_model_integral(model2.spatial_model
    ,exposure_cube.sky_image_ref)

model.spatial_model.amplitude.value = 1./norm_factor
```

```
        model2.spatial_model.amplitude.value = 1./norm_factor2

        spatial_integral = compute_spatial_model_integral(model.spatial_model
            ,exposure_cube.sky_image_ref)
        spatial_integral2 = compute_spatial_model_integral(model2.spatial_model
            ,exposure_cube.sky_image_ref)
        print('Spatial integral (should be 1): ',round(spatial_integral,3))
        print('Spatial integral (should be 1): ',round(spatial_integral2,3))
        #flux_integral=model.spectral_model.integral(emin='1 TeV',emax='10 TeV')
        #print('Integral flux in range 1 to 10 TeV:',flux_integral.to('cm-2 s-1'))
        flux_integral2=model2.spectral_model.integral(emin='1 TeV',emax='10 TeV')
        print('Integral flux in range 1 to 10 TeV:',flux_integral2.to('cm-2 s-1'))

    #import IPython; IPython.embed()
        #Make and sum flux cubes
        flux_cube = model.evaluate_cube(ref_cube)
        flux_cube2 = model2.evaluate_cube(ref_cube2)
        flux_sum = compute_sum_cube(flux_cube,flux_cube2,config)

        #Make npred cube
        npred_cube = compute_npred_cube(
            flux_sum, exposure_cube,
            ebounds=flux_sum.energies('edges'),
            config = config, irfs = irfs, integral_resolution=2
        )
        bkg = irfs['bkg']

        t1 = time()
        npred_cube_simple = compute_npred_cube_simple(flux_sum, exposure_cube)
        t2 = time()
        print('npred_cube: ', t1-t0)
        print('npred_cube_simple: ', t2-t1)
        print('npred_cube sum: {}'.format(np.nansum(npred_cube.data)))
        print('npred_cube_simple sum: {}'.format(np.nansum(npred_cube_simple.data)))

        #Make ON, OFF and excess cubes
        on_excess = compute_nexcess_cube(npred_cube,livetime,pointing,
            offset_max,bkg_rate=bkg,config=config)
        nexcess_cube = on_excess[0]
        non_cube = on_excess[1]
        noff_cube = on_excess[2]

        #Apply PSF convolution here
```

```
#kernels = irfs['psf'].kernels(npred_cube_simple)
#npred_cube_convolved = npred_cube_simple.convolve(kernels)

#Make PSF Kernels
kernels = []
psf_table = psf_fromfits('irf_file.fits')
energ_lo = psf_table[0].value
sigmas = psf_table[3]
energ_array = nexcess_cube.energies('edges')
s = np.argmin(np.abs(irfs['offset'].value-psf_table[2].value))

for i in range(nexcess_cube.data.shape[0]):
    v = np.argmin(np.abs(energ_array[i].value-energ_lo))
    kernels.append(irfs['psf'].kernels(nexcess_cube,
        Angle(sigmas[0][s][v]*u.deg))[i])
    #Debug
    #print(sigmas[0][s][v]*u.deg)

#Apply kernels convolution
nexcess_cube_convolved = nexcess_cube.convolve(kernels)
npred_cube_convolved = npred_cube_simple.convolve(kernels)
print('npred_cube sum: {}'.format(np.nansum(npred_cube.data)))
#print('npred_cube_convolved sum: {}'
#.format(np.nansum(npred_cube_convolved.data)))
noff_cube_convolved = noff_cube.convolve(kernels)
non_cube_convolved = non_cube.convolve(kernels)

#Write cubes
exposure_cube.write('exposure_cube.fits',overwrite=True,
    format='fermi-exposure')
flux_sum.write('flux_cube.fits',overwrite=True)
npred_cube.write('npred_cube.fits',overwrite=True)
npred_cube_convolved.write('npred_cube_convolved.fits',overwrite=True)
noff_cube.write('noff_cube.fits',overwrite=True)
noff_cube_convolved.write('noff_cube_convolved.fits',overwrite=True)
nexcess_cube.write('nexcess_cube.fits',overwrite=True)
nexcess_cube_convolved.write('nexcess_cube_convolved.fits',overwrite=True)
non_cube.write('non_cube.fits',overwrite=True)
non_cube_convolved.write('non_cube_convolved.fits',overwrite=True)

#If the amplitude of one of the sources in null then also try:
#non_cube.write('noff_withneb_cube.fits', overwrite=True)
#non_cube_convolved.write('noff_withneb_cube_convolved.fits',
```

```
    #overwrite=True)
    #non_cube.write('noff_withpuls_cube.fits', overwrite=True)
    #non_cube_convolved.write('noff_withpuls_cube_convolved.fits',
    #overwrite=True)

    t3 = time()
    print('Done in: ', t3-t0)


if __name__ == '__main__':
    main()
```

A.2 Analysis of 3D sky cubes

We list below some simple scripts for the analysis of generated 3D cubes. To compute the source's detection significance:

A.2.1 Detection significance

```
"""
How to compute the significances for a 3D n_pred, n_obs cube, n_off cube
Using CTA IRFs.
"""
from __future__ import absolute_import,division,print_function,
    unicode_literals
import numpy as np
from gammapy.cube import SkyCube
from astropy.coordinates import SkyCoord, Angle
from regions import CircleSkyRegion
from astropy.table import Table
import astropy.units as u
import yaml
import pyfits
from astropy.units import Quantity

def psf_fromfits(filename):
    '''Get PSF from fits file.

    Parameters
    ----------
    filename : Fits file
```

```
    IRFS fits file.

    Returns
    -------
    energy_lo : `Quantity`
    Low energy bounds.
    energy_hi : `Quantity`
    High energy bounds.
    theta : `Angle`
    Offset angle.
    sigmas : `list`
    PSF sigmas.
    norms : `list`
    PSF norms.
    '''
    hdulist = pyfits.open(filename)
    hdu = hdulist[2]
    energy_lo = Quantity(hdu.data['ENERG_LO'][0],'TeV')
    energy_hi = Quantity(hdu.data['ENERG_HI'][0],'TeV')
    theta = Angle(hdu.data['THETA_LO'][0], 'deg')

    #Get sigmas
    shape = (len(theta), len(energy_hi))
    sigmas = []
    for key in ['SIGMA_1','SIGMA_2','SIGMA_3']:
        sigma = hdu.data[key].reshape(shape).copy()
        sigmas.append(sigma)

    #Get amplitudes
    norms = []
    for key in ['SCALE','AMPL_2','AMPL_3']:
        norm = hdu.data[key].reshape(shape).copy()
        norms.append(norm)
    return [energy_lo, energy_hi, theta, sigmas, norms]

def main():
    #Read cubes
    cube_on = SkyCube.read('non_cube.fits')
    cube_off = SkyCube.read('noff_cube.fits')

    #Read config
    config = yaml.load(open('config.yaml'))
    binsz = config['binning']['binsz']
```

```
offset_fov = config['selection']['offset_fov']

diff_vals = np.ones(int(config['binning']['enumbins']))
sigmaslimas = np.ones(int(config['binning']['enumbins']))

#Define PSF region
irffile = 'irf_file.fits'
psf_table = psf_fromfits(irffile)
psfs = psf_table[3]
on_sizes = np.ones(int(config['binning']['enumbins']))*u.deg
energarr = cube_on.energies('edges')
for idx in range(len(cube_on.energies('center'))):
    i = np.argmin(np.abs(energarr[idx].value-psf_table[0].value))
    j = np.argmin(np.abs(offset_fov-psf_table[2].value))
    on_sizes.value[idx] = psfs[0][j][i]*2.12
alpha_obs = 0.2
on_pos = SkyCoord(83.6333*u.deg,22.0144*u.deg,frame='icrs')

#Debug
#print(on_sizes/binsz)

off_pos = SkyCoord(83.6333*u.deg,22.0144*u.deg,frame='icrs')
off_sizes = on_sizes/np.sqrt(alpha_obs)
on_data = Table()
off_data = Table()
on_data['value'] = np.zeros(len(on_sizes))
off_data['value'] = np.zeros(len(on_sizes))

for i in range(cube_on.data.shape[0]):
    #Make PSF region
    on_region = CircleSkyRegion(on_pos, on_sizes[i])
    off_region = CircleSkyRegion(off_pos, off_sizes[i])

    #Take spectrum
    on_data['value'][i] = cube_on.spectrum(on_region)['value'][i]
    off_data['value'][i] = cube_off.spectrum(off_region)['value'][i]
    non_val = on_data['value'][i]
    noff_val = off_data['value'][i]
    diff_vals[i] = non_val-noff_val

    if non_val != 0 and noff_val != 0:
        siglima = 2**0.5*np.sqrt(non_val*np.log((1.0+(1.0/alpha_obs))
            *non_val/(non_val+noff_val))+noff_val*np.log((alpha_obs+1.0)
```

```
            *noff_val/(non_val+noff_val)))
    elif non_val != 0 and noff_val == 0:
        siglima = 2**0.5*np.sqrt(non_val*np.log((1.0+(1.0/alpha_obs))))
    else:
        siglima = 0
    sigmaslimas[i] = siglima

#Debug
#non_val = cube_on.data.sum().value
#noff_val = cube_off.data.sum().value

lo_lim_idx = np.where(abs(cube_on.energies('edges').value-0.4)
    ==np.min(abs(cube_on.energies('edges').value-0.4)))[0][0]
max_energ_idx = np.where(abs(cube_on.energies('edges').value-3.0)
    ==np.min(abs(cube_on.energies('edges').value-3.0)))[0][0]
non_val = on_data['value'][lo_lim_idx:max_energ_idx].sum()
noff_val = off_data['value'][lo_lim_idx:max_energ_idx].sum()
siglima = 2**0.5*np.sqrt(non_val*np.log((1.0+(1.0/alpha_obs))
    *non_val/(non_val+noff_val))+noff_val*np.log((alpha_obs+1.0)
    *noff_val/(non_val+noff_val)))

#print('On events: ', on_data)
#print('Off events: ', off_data)
diff_vals[np.isnan(diff_vals)] = 0
sigmaslimas[np.isnan(sigmaslimas)] = 0
print('Excess: ', diff_vals)
print('Total positive Excess: ', diff_vals[diff_vals > 0].sum())
print('LiMa by energy bins: ', sigmaslimas)
print('Total LiMa: ', siglima, 'Energy range: ',
    cube_on.energies('edges')[lo_lim_idx],' - ',
    cube_on.energies('edges')[max_energ_idx])

lo_lim_idx = np.where(abs(cube_on.energies('edges').value-1.0)
    ==np.min(abs(cube_on.energies('edges').value-1.0)))[0][0]
non_val = on_data['value'][lo_lim_idx:max_energ_idx].sum()
noff_val = off_data['value'][lo_lim_idx:max_energ_idx].sum()
siglima_tves=2**0.5*(non_val*np.log(2*non_val/(non_val+noff_val))
    +noff_val*np.log(2*noff_val/(non_val+noff_val)))**0.5

print('Total LiMa: ', siglima_tves, 'Energy range: ',
    cube_on.energies('edges')[lo_lim_idx],' - ',
    cube_on.energies('edges')[max_energ_idx])
return [siglima,siglima_tves,on_data,off_data,diff_vals,sigmaslimas]
```

```
if __name__ == '__main__':
    main()
```

To perform a spectral analysis of the cubes:

A.2.2 Spectral analysis

```
"""
An example of how to do spectral analysis of a 3D n_pred/n_obs cube.
Using CTA IRFs.
"""
#from __future__ import absolute_import,division,print_function,
#unicode_literals
import astropy.units as u
import numpy as np
import yaml
import matplotlib.pyplot as plt
from astropy.coordinates import SkyCoord, Angle
from astropy.io import fits
from sherpa.astro.ui import *
from gammapy.cube import SkyCube
from regions import CircleSkyRegion
from astropy.table import Table
from gammapy.spectrum.models import LogParabola
from gammapy.spectrum.models import PowerLaw
from gammapy.spectrum.models import ExponentialCutoffPowerLaw
from gammapy.spectrum import SpectrumFit
from gammapy.spectrum import SpectrumObservation
from gammapy.spectrum import PHACountsSpectrum
from gammapy.irf import EffectiveAreaTable2D, EnergyDispersion2D
from gammapy.irf import EnergyDependentMultiGaussPSF
from regions.shapes import CircleAnnulusSkyRegion
from gammapy.irf import Background3D
from gammapy.background import FOVCube
#from gammapy.image import SkyImage
#from configuration import make_ref_cube

def read_config(filename):
    '''Read configuration from yaml file.

    Parameters
    ----------
```

```
    filename : yaml file
        Configuration file.

    Returns
    -------

    config : `dict`
        Configuration dictionary.
    '''
    with open(filename) as fh:
        config = yaml.load(fh)
    config['model']['prefactor'] = float(config['model']['prefactor'])
    return config

def get_irfs(config):
    '''Get IRFs from file.

    Parameters
    ----------
    config : `dict`
        Configuration dictionary.
    filename : fits file
        IRFs file

    Returns
    -------
    irfs : `dict`
        IRFs dictionary.
    '''
    filename = 'irf_file.fits'
    offset = Angle(config['selection']['offset_fov']*u.deg)
    psf_fov = EnergyDependentMultiGaussPSF.read(filename,
        hdu='POINT SPREAD FUNCTION')
    psf = psf_fov.to_energy_dependent_table_psf(theta=offset)
    print(' psf', psf)
    aeff_tab=EffectiveAreaTable2D.read(filename, hdu='EFFECTIVE AREA')
    edisp_fov=EnergyDispersion2D.read(filename, hdu='ENERGY DISPERSION')
    table = fits.open('irf_file.fits')['BACKGROUND']
    table.columns.change_name(str('BGD'), str('Bgd'))
    table.header['TUNIT7'] = '1/(MeV s sr)'
    bkg = Background3D.read(filename, hdu='BACKGROUND')
    return dict(psf=psf, aeff=aeff_tab, edisp=edisp_fov, bkg=bkg)
```

```
def make_annular_spectrum(on_pos, off_pos, on_rad_sizes, off_rad_sizes,
    out_rad_sizes, cube_on, cube_off, alpha_obs):
    '''Take ON and OFF counts from an annular region.

    Parameters
    ----------
    on_pos : `SkyCoord`
        Center of ON annular region coordinates.
    off_pos : `SkyCoord`
        Center of OFF annular region coordinates.
    on_rad_sizes : numpy array
        Inner radius of ON size for each energy bin for an annular region.
    off_rad_sizes : numpy array
        Inner radius of OFF size for each energy bin for an annular region.
    out_rad_sizes : numpy array
        Outer radius of ON size for each energy bin and a annular radius.
    cube_on : `SkyCube`
        3D ON sky cube.
    cube_off : `SkyCube`
        3D OFF sky cube.
    alpha_obs : float
        On region area/Off region area
    Returns
    -------

    ann_on_data : `Table`
        ON annular region information table.
    ann_off_data : `Table`
        OFF annular region information table.
    ann_stats : numpy array
        Array of ones and zeros.
        Depending on if each energy satisfy a certain condition (1) or not (0).
    '''
    ann_on_data = Table()
    ann_off_data = Table()
    ann_on_data['value'] = np.zeros(len(on_rad_sizes))
    ann_off_data['value'] = np.zeros(len(on_rad_sizes))
    ann_stats = np.zeros(len(on_rad_sizes))

    for i in range(len(on_rad_sizes)):
        on_region = CircleSkyRegion(on_pos, on_rad_sizes[i])
        off_region = CircleSkyRegion(off_pos, off_rad_sizes[i])
```

```
        on_data = cube_on.spectrum(on_region)
        off_data = cube_off.spectrum(off_region)

        out_region = CircleSkyRegion(on_pos, out_rad_sizes[i])
        out_on_data = cube_on.spectrum(out_region)
        out_off_data = cube_off.spectrum(out_region)

        ann_on_data['value'][i]=out_on_data['value'][i]-on_data['value'][i]
        ann_off_data['value'][i]=out_off_data['value'][i]-off_data['value'][i]

        limasig = 2**0.5*(ann_on_data['value'][i]
            *np.log(((1+alpha_obs)/alpha_obs)*ann_on_data['value'][i]
            /(ann_on_data['value'][i]+ann_off_data['value'][i]))
            +ann_off_data['value'][i]*np.log((1+alpha_obs)
            *ann_off_data['value'][i]/(ann_on_data['value'][i]
            +ann_off_data['value'][i])))**0.5

        exss_dat = ann_on_data['value'][i]-ann_off_data['value'][i]
        aodt = 0.03*ann_off_data['value'][i]
        if limasig>=3 and exss_dat>=7 and exss_dat>=aodt:
            ann_stats[i] = 1.

    ann_on_data['e_min'] = on_data['e_min']
    ann_on_data['e_max'] = on_data['e_max']
    ann_on_data['e_ref'] = on_data['e_ref']

    ann_off_data['e_min'] = off_data['e_min']
    ann_off_data['e_max'] = off_data['e_max']
    ann_off_data['e_ref'] = off_data['e_ref']

    return ann_on_data, ann_off_data, ann_stats

def make_circular_spectrum(on_pos, off_pos, on_sizes, off_sizes, cube_on,
    cube_off, alpha_obs):
    '''Take ON and OFF counts from an circular region.

    Parameters
    ----------
    on_pos : `SkyCoord`
        Center of ON circular region coordinates.
    off_pos : `SkyCoord`
        Center of OFF circular region coordinates.
    on_sizes :
```

```
    Radius of ON size for each energy bin for an circular region.
off_sizes :
    Radius of OFF size for each energy bin for an circular region.

cube_on : `SkyCube`
    3D ON sky cube.
cube_off : `SkyCube`
    3D OFF sky cube.
alpha_obs : float
    On region area/Off region area

Returns
-------

ann_on_data : `Table`
    ON circular region information table.
ann_off_data : `Table`
    OFF circular region information table.
ann_stats : numpy array
    Array of ones and zeros
    Depending on if each energy satisfy a certain condition (1) or not (0).
'''

on_data = Table()
off_data = Table()
on_data['value'] = np.zeros(len(on_sizes))
off_data['value'] = np.zeros(len(on_sizes))
circ_stats = np.zeros(len(on_sizes))

for i in range(len(on_sizes)):

    on_region = CircleSkyRegion(on_pos, on_sizes[i])
    off_region = CircleSkyRegion(off_pos, off_sizes[i])

    on_data['value'][i] = cube_on.spectrum(on_region)['value'][i]
    off_data['value'][i] = cube_off.spectrum(off_region)['value'][i]

    limasig=2**0.5*np.sqrt(on_data['value'][i]
        *np.log(((1+alpha_obs)/alpha_obs)*on_data['value'][i]
        /(on_data['value'][i]+off_data['value'][i]))+off_data['value'][i]
        *np.log((1+alpha_obs)*off_data['value'][i]
        /(on_data['value'][i]+off_data['value'][i])))
```

```
            #Debug
            #print(limasig,'Energy range: ',cube_on.energies('edges')[i],' - ',
            #cube_on.energies('edges')[i+1])
            #print('On: ',on_data['value'][i],'Off: ',off_data['value'][i])
            exss_dat = on_data['value'][i]-off_data['value'][i]
            if exss_dat >= 7 and limasig > 3:
                circ_stats[i] = 1.
    return on_data, off_data, circ_stats

def main():
    #Low energy of spectral fitting range.
    lo_fit_energ = 0.1*u.Unit('TeV')
    hi_fit_energ = 10*u.Unit('TeV')

    #If you want an internal estimation of a high energy limit for the
    #fitting range: est_hi_lim = 'yes'.
    #If 'no' the hi_fit_energ will be used.
    est_hi_lim = 'yes'

    #Read ON and OFF cubes
    filename_on = 'non_cube.fits'
    cube_on = SkyCube.read(filename_on)

    ann_filename_off = 'noff_withpuls_cube.fits'
    ann_cube_off = SkyCube.read(ann_filename_off)
    circ_filename_off = 'noff_withneb_cube.fits'
    circ_cube_off = SkyCube.read(circ_filename_off)

    #Read config and IRFs
    config = read_config('config.yaml')
    irfs = get_irfs(config)
    offset = Angle(config['selection']['offset_fov']*u.deg)
    livetime = u.Quantity(config['pointing']['livetime']).to('second')
    alpha_obs = 1.
    binsz = config['binning']['binsz']
    aeff = irfs['aeff'].to_effective_area_table(offset = offset,
        energy = cube_on.energies('edges'))
    edisp = irfs['edisp'].to_energy_dispersion(offset = offset,
        e_true = aeff.energy.bins,e_reco=cube_on.energies('edges'))

    #Define circular on/off Regions parameters
    on_pos = SkyCoord(83.6333*u.deg,22.0144*u.deg,frame='icrs')
    on_sizes = np.ones(20)*binsz*u.deg
```

```
off_pos = SkyCoord(83.6333*u.deg,22.0144*u.deg,frame='icrs')
off_sizes = on_sizes*np.sqrt(1./alpha_obs)

#Make Annular region
on_rad_sizes = np.ones(len(on_sizes))*0.1*binsz*u.deg
off_rad_sizes = on_rad_sizes*np.sqrt(1./alpha_obs)
widths = np.ones(len(on_sizes))*22*binsz*u.deg
out_rad_sizes = on_rad_sizes+widths
ann_on_data,ann_off_data,ann_stats=make_annular_spectrum(on_pos,off_pos,
    on_rad_sizes, off_rad_sizes, out_rad_sizes,
    cube_on, ann_cube_off, alpha_obs)

#Make circular region
circ_on_data,circ_off_data,circ_stats = make_circular_spectrum(on_pos,
    off_pos,on_sizes,off_sizes,cube_on,circ_cube_off,alpha_obs)

#Undo "holes" in circ/ann_stats
if np.max(np.where(circ_stats==1))+1 != circ_stats.sum():
    circ_stats[0:np.max(np.where(circ_stats == 1))+1]
        [circ_stats[0:np.max(np.where(circ_stats==1))+1]==0]=1.
if np.max(np.where(ann_stats == 1))+1 != ann_stats.sum():
    ann_stats[0:np.max(np.where(ann_stats == 1))+1]
        [ann_stats[0:np.max(np.where(ann_stats == 1))+1]==0]=1.

#Make on/off vector
ann_on_vector=PHACountsSpectrum(energy_lo=cube_on.energies('edges')[:-1]
    ,energy_hi=cube_on.energies('edges')[1:],data=ann_on_data['value'].data
    *ann_stats*u.ct,backscal=on_sizes[0].value,
    meta={'EXPOSURE' : livetime.value})
circ_on_vector=PHACountsSpectrum(energy_lo=cube_on.energies('edges')[:-1]
    ,energy_hi=cube_on.energies('edges')[1:],data=circ_on_data['value'].data
    *circ_stats*u.ct,backscal=on_sizes[0].value,
    meta={'EXPOSURE' : livetime.value})

ann_off_vector=PHACountsSpectrum(energy_lo=ann_cube_off.energies('edges')
    [:-1],energy_hi=ann_cube_off.energies('edges')[1:],
    data=ann_off_data['value'].data*ann_stats*u.ct,
    backscal=off_sizes[0].value,
    meta={'EXPOSURE':livetime.value, 'OFFSET':0.3*u.deg})
circ_off_vector=PHACountsSpectrum(energy_lo=circ_cube_off.energies('edges')
    [:-1],energy_hi=circ_cube_off.energies('edges')
        [1:],data=circ_off_data['value'].data*circ_stats*u.ct,
```

```
        backscal=off_sizes[0].value,
    meta={'EXPOSURE' : livetime.value, 'OFFSET' : 0.3*u.deg})

#Make SpectrumObservation
ann_sed_table = SpectrumObservation(on_vector = ann_on_vector,
    off_vector = ann_off_vector, aeff = aeff, edisp = edisp)
circ_sed_table=SpectrumObservation(on_vector = circ_on_vector,
    off_vector = circ_off_vector, aeff = aeff, edisp = edisp)

#Debug
#print(ann_stats)
#print(circ_stats)

#Define Spectral Model
model2fit1 = LogParabola(amplitude=1e-11*u.Unit('cm-2 s-1 TeV-1'),
    reference=1*u.TeV,alpha=2.5*u.Unit(''),beta=0.1*u.Unit(''))
model2fit2 = ExponentialCutoffPowerLaw(index=1.*u.Unit(''),
    amplitude=1e-11*u.Unit('cm-2 s-1 TeV-1'),
    reference=1*u.TeV,lambda_=0.*u.Unit('TeV-1'))
model2fit3 = PowerLaw(index=2.5*u.Unit(''),
    amplitude=5e-11*u.Unit('cm-2 s-1 TeV-1'),reference=0.15*u.TeV)

model2fit3.parameters['amplitude'].parmin = 1e-12
model2fit3.parameters['amplitude'].parmax = 1e-10

model2fit3.parameters['index'].parmin = 2.0
model2fit3.parameters['index'].parmax = 4.0

#Models to fit the circular and annular observations
models_ann_fit = [model2fit1, model2fit2, model2fit3]
models_circ_fit = [model2fit1, model2fit2, model2fit3]

#Fit
if est_hi_lim = 'yes':
    hi_fit_energ = cube_on.energies('edges')[int(np.sum(ann_stats))]

for k in range(len(models_ann_fit)):
    fit_source=SpectrumFit(obs_list=ann_sed_table,model=models_ann_fit
        [k],forward_folded=True,fit_range=(lo_fit_energ,hi_fit_energ))
    fit_source.fit()
    fit_source.est_errors()
    results = fit_source.result
    ax0, ax1 = results[0].plot(figsize=(8,8))
```

```
        print(results[0])

    if est_hi_lim = 'yes':
        hi_fit_energ = cube_on.energies('edges')[int(np.sum(circ_stats))]

    for k in range(len(models_circ_fit)):
        fit_source=SpectrumFit(obs_list=circ_sed_table,model=models_circ_fit
            [k],forward_folded=True,fit_range=(lo_fit_energ,hi_fit_energ))
        fit_source.fit()
        fit_source.est_errors()
        results = fit_source.result
        print(results[0])


if __name__ == '__main__':
    main()
```

To fit the source morphology:

A.2.3 Morphological analysis

```
"""
An example of how to fit the size of a source from a 3D n_pred/n_obs cube.
Using CTA IRFs.
"""
#from __future__ import absolute_import, division, print_function,
#unicode_literals
import astropy.units as u
import numpy as np
import yaml
import pyfits
from astropy.coordinates import SkyCoord, Angle
from configuration import make_ref_cube
from astropy.io import fits
from sherpa.astro.ui import *
from gammapy.cube import SkyCube
from astropy.units import Quantity
from time import time
from regions import CircleSkyRegion
from astropy.table import Table

def read_config(filename):
    '''Read configuration from yaml file.
```

```
    Parameters
    ----------
    filename : yaml file
        Configuration file.

    Returns
    -------

    config : `dict`
        Configuration dictionary.
    '''
    with open(filename) as fh:
        config = yaml.load(fh)

    config['model']['prefactor'] = float(config['model']['prefactor'])
    return config

def do_fit():
    fit()
    image_resid()
    for mod in list_models:
        mtype = get_model_component(mod)
        if mtype:
            coord = get_pos(mtype.xpos.val,mtype.ypos.val)[0]
            print "Fitted position of ", mod ," : ", coord

def get_pos(xpix,ypix):
    pixcrd = np.array([[xpix,ypix]], np.float_)
    return im_proj.wcs_pix2world(pixcrd,1)

def do_conf():
    conf()
    res_conf = get_conf_results()
    for im in range(len(res_conf.parnames)):
        cparam = res_conf.parnames[im]
        [model,param] = cparam.split('.')
        if param == "xpos":
            smin = res_conf.parmins[im]*abs(im_proj.wcs.cdelt[0])
            smax = res_conf.parmaxes[im]*abs(im_proj.wcs.cdelt[0])
            print "Fitted X position error of ",model," : -",smin," +",smax
        elif param == "ypos":
            smin = res_conf.parmins[im]*abs(im_proj.wcs.cdelt[1])
            smax = res_conf.parmaxes[im]*abs(im_proj.wcs.cdelt[1])
```

```
            print "Fitted Y position error of ",model," : -",smin," +",smax
        elif param == "size" or param == 'r1' or param == 'thick':
            smean = res_conf.parvals[im]*abs(im_proj.wcs.cdelt[0])
            smin = res_conf.parmins[im]*abs(im_proj.wcs.cdelt[0])
            smax = res_conf.parmaxes[im]*abs(im_proj.wcs.cdelt[0])
            print "Fitted ",param," of ",model," :",smean,"+-",smin," +",smax

def GaussianSource(pars,x,y):
    (sigma1, sigma2, sigma3, alpha, beta, ampl, size, xpos, ypos) = pars
    r2 = (x-xpos)**2+(y-ypos)**2
    s1sq = sigma1*sigma1
    s2sq = sigma2*sigma2
    s3sq = sigma3*sigma3
    v1 = sigma1*sigma1+size*size
    v2 = sigma2*sigma2+size*size
    v3 = sigma3*sigma3+size*size
    s1 = s1sq*np.exp(-0.5*r2/v1)/(2*pi*v1)
    s2 = alpha*s2sq*np.exp(-0.5*r2/v2)/(2*pi*v2)
    s3 = beta*s3sq*np.exp(-0.5*r2/v3)/(2*pi*v3)
    return ampl*(s1+s2+s3)/(s1sq+alpha*s2sq+beta*s3sq)

def psf_fromfits(filename):
    '''Get PSF from fits file.

    Parameters
    ----------
    filename : Fits file
        IRFS fits file.

    Returns
    -------
    energy_lo : `Quantity`
        Low energy bounds.
    energy_hi : `Quantity`
        High energy bounds.
    theta : `Angle`
        Offset angle.
    sigmas : `list`
        PSF sigmas.
    norms : `list`
        PSF norms.
    '''
```

```
    hdulist = pyfits.open(filename)
    hdu = hdulist[2]
    energy_lo = Quantity(hdu.data['ENERG_LO'][0], 'TeV')
    energy_hi = Quantity(hdu.data['ENERG_HI'][0], 'TeV')
    theta = Angle(hdu.data['THETA_LO'][0], 'deg')

    #Get sigmas
    shape = (len(theta), len(energy_hi))
    sigmas = []
    for key in ['SIGMA_1','SIGMA_2','SIGMA_3']:
        sigma = hdu.data[key].reshape(shape).copy()
        sigmas.append(sigma)

    #Get amplitudes
    norms = []
    for key in ['SCALE','AMPL_2','AMPL_3']:
        norm = hdu.data[key].reshape(shape).copy()
        norms.append(norm)
    return [energy_lo, energy_hi, theta, sigmas, norms]

pi = 3.141592653589793

def PSFGauss(pars,x,y):
    (sigma1, ampl, xpos, ypos) = pars
    r2 = (x-xpos)**2+(y-ypos)**2
    v1 = sigma1*sigma1
    return ampl*np.exp(-0.5*r2/v1)/(2*pi*v1)

def PSFtripleGauss(pars,x,y):
    (sigma1, sigma2, sigma3, alpha, beta, ampl, xpos, ypos) = pars
    r2 = (x-xpos)**2+(y-ypos)**2
    s1sq = sigma1*sigma1
    s2sq = sigma2*sigma2
    s3sq = sigma3*sigma3
    v1 = sigma1*sigma1
    v2 = sigma2*sigma2
    v3 = sigma3*sigma3
    s1 = s1sq*np.exp(-0.5*r2/v1)/(2*pi*v1)
    s2 = alpha*s2sq*np.exp(-0.5*r2/v2)/(2*pi*v2)
    s3 = beta*s3sq*np.exp(-0.5*r2/v3)/(2*pi*v3)
    return ampl*(s1+s2+s3)/(s1sq+alpha*s2sq+beta*s3sq)

def main():
```

```
#Read file to fit
#filename = 'nexcess_cube.fits'
filename = 'non_cube_convolved.fits'
cube = SkyCube.read(filename)

#Read configuration
config = read_config('config.yaml')
binsz = config['binning']['binsz']
offset_fov = config['selection']['offset_fov']

#Take PSF data
irffile = 'irf_file.fits'
psf_table = psf_fromfits(irffile)
energarr = cube.energies('edges')
sigmas = psf_table[3]
norms = psf_table[4]

hdu = pyfits.open(filename)

im_sizex = hdu[0].header['NAXIS1']
im_sizey = hdu[0].header['NAXIS2']
cx = 0.5*im_sizex
cy = 0.5*im_sizey

#Check the significance
filename_on = 'non_cube.fits'
cube_on = SkyCube.read(filename_on)

filename_off = 'noff_cube.fits'
cube_off = SkyCube.read(filename_off)
alpha_obs = 1.

on_pos = SkyCoord(83.6333*u.deg,22.0144*u.deg,frame='icrs')
on_sizes = np.ones(len(cube.energies('center')))*120*binsz*u.deg

off_pos = SkyCoord(83.6333*u.deg,22.0144*u.deg,frame='icrs')
off_sizes = on_sizes*alpha_obs

on_data = Table()
off_data = Table()
on_data['value'] = np.zeros(len(on_sizes))
off_data['value'] = np.zeros(len(on_sizes))
for idx in range(len(cube.energies('center'))):
```

```
on_region = CircleSkyRegion(on_pos, on_sizes[idx])
off_region = CircleSkyRegion(off_pos, off_sizes[idx])

on_data['value'][idx] = cube_on.spectrum(on_region)['value'][idx]
off_data['value'][idx] = cube_off.spectrum(off_region)['value'][idx]

limasig = 2**0.5*(on_data['value'][idx]
    *np.log(((1+alpha_obs)/alpha_obs)*on_data['value'][idx]
    /(on_data['value'][idx]+off_data['value'][idx]))
    +off_data['value'][idx]
    *np.log((1+alpha_obs)*off_data['value'][idx]
    /(on_data['value'][idx]+off_data['value'][idx])))**0.5
print(limasig,'Energy range: ',cube_on.energies('edges')[idx],
    ' - ',cube_on.energies('edges')[idx+1])

#Fit only if data is enough
#on_data['value'][i]-off_data['value'][i]>=0.01*off_data['value'][i]
if limasig>=3 and on_data['value'][idx]-off_data['value'][idx]>=7:
    #Make image cube from slice excess convolved cube
    cube_sum=np.zeros((cube.data.shape[1],cube.data.shape[2]))*u.ct
    cube_sum = np.add(cube_sum, cube.data[idx])

    cube_sum.value[np.isnan(cube_sum.value)]=0
    cube_sum.value[cube_sum.value<0]=abs(cube_sum.value
        [cube_sum.value<0])

    image_sum = SkyCube.empty_like(cube)
    image_sum.data = cube_sum

    image_sum.write('sum_image.fits', overwrite=True)

    #Find nearest energy and theta value
    i = np.argmin(np.abs(energarr[idx].value-psf_table[0].value))
    j = np.argmin(np.abs(offset_fov-psf_table[2].value))

    #Make PSF
    #psfname="mypsf"
    #load_user_model(PSFGauss,psfname)
    s1 = sigmas[0][j][i]/binsz
    s2 = sigmas[1][j][i]/binsz
    s3 = sigmas[2][j][i]/binsz
    print(sigmas[0][j][i],sigmas[1][j][i],sigmas[2][j][i])
    ampl = norms[0][j][i]
```

```
ampl2 = norms[1][j][i]
ampl3 = norms[2][j][i]

t0 = time()

#Morphological fitting
load_image("sum_image.fits")
#image_data()
#set_coord("physical")

set_method("simplex")
set_stat("cash")

#Position and radius
x0 = 125
y0 = 125
rad0 = 80.0

image_getregion(coord="physical")
'circle(x0,y0,rad0);'

notice2d("circle("+str(x0)+","+str(y0)+","+str(rad0)+")")

load_user_model(GaussianSource, "sph2d")
add_user_pars("sph2d",["sigma1","sigma2","sigma3","alpha","beta",
    "ampl","size","xpos","ypos"])
set_model(sph2d+const2d.bgnd)

#Constant PSF
#gpsf.fwhm = 4.2
#gpsf.xpos = x0
#gpsf.ypos = y0
#gpsf.ellip = 0.2
#gpsf.theta = 30*np.pi/180

#Set PSF
set_par(sph2d.sigma1,val=s1,frozen=True)
set_par(sph2d.sigma2,val=0,frozen=True)
set_par(sph2d.sigma3,val=0,frozen=True)
set_par(sph2d.alpha,val=0,frozen=True)
set_par(sph2d.beta,val=0,frozen=True)

#HESS PSF
```

```
            #set_par(sph2d.sigma1,val=0.025369,frozen=True)
            #set_par(sph2d.alpha,val=0.691225,frozen=True)
            #set_par(sph2d.sigma2,val=0.0535014,frozen=True)
            #set_par(sph2d.beta,val=0.13577,frozen=True)
            #set_par(sph2d.sigma3,val=0.11505,frozen=True)

            set_par(sph2d.xpos,val=x0,frozen=True)
            set_par(sph2d.ypos,val=y0,frozen=True)

            set_par(sph2d.ampl,val=10000,min=1e-11,max=100000000)
            set_par(sph2d.size,val=10,min=1e-11,max=100)

            set_par(bgnd.c0,val=1,min=0,max=100)

            show_model()
            fit()
            #do_fit()
            conf()
            #do_conf()
            #image_fit()
            #save_model("model_"+str(idx)+".fits")
            #save_resid("resid_"+str(idx)+".fits")

            t1 = time()
            print('Simul time', t1-t0)

if __name__ == '__main__':
    main()
```

Appendix B

Simulations of Crab flares

```
#!/usr/bin/env python
# coding: utf-8

#get_ipython().magic(u'matplotlib inline')
import naima
from astropy import table
import numpy as np
import math
from astropy.io import ascii
from astropy.constants import c,m_e
import astropy.units as u
from naima.models import (ExponentialCutoffPowerLaw, Synchrotron,
                          InverseCompton)
from matplotlib import pyplot as plt
from matplotlib.ticker import FormatStrFormatter
from ipywidgets.widgets.interaction import interact, fixed
from matplotlib.backends.backend_pdf import PdfPages
from scipy.optimize import minimize
from astropy.table import Table, Column
import csv

flarename = '2011'
mcc = (m_e*c**2).cgs
crab_distance=  2.2*u.kpc
amp0=2.e42
make_plot = True
make_tables = False
syn_max_0 = 200*u.MeV
tvar = 6*u.h
```

```
nloops = 4
sizeloops = 20

comovf = False

def lorentzfactor(B=140*u.mG):
    return (10*(syn_max_0.to('MeV')/(600*u.MeV))**-1*(tvar.to('s')/(4e4*u.s))
        **-2*B.to('mG').value**-3)

def eprimpev(syn_max_0,tvar,delta=1.0):
    return ((syn_max_0.to('MeV')/(600*u.MeV))**(2./3.)
    *(tvar.to('s')/(4e4*u.s))**(1./3.)*(delta/10.0)**(-1./3.))*u.PeV

#Analytic estimate for the cutoff energy
def ecutoff(index,B,syn_max):
    Bint=((B).to(u.Gauss)).value
    ecut_a=((syn_max/mcc)/((-index+3.5)**3*4/27.*3.4e-14*Bint*4/3.))**0.5*mcc
    return (ecut_a).cgs

def cutoffinitval(index,B,init_ecut=1*u.PeV,index_ref=1.5,b_ref=1.99*u.mG):
    correcut_factor = (init_ecut.to('PeV').value/((3.5-index_ref)**(-3/2.)
        *(b_ref.to('mG').value)**(-0.5)))
    ecut_scl = correcut_factor*(3.5-index)**(-1.5)*(B.to('mG').value)**(-0.5)
    return ecut_scl*u.PeV

#Definitions for E_cutoff, amplitude fittings
def log_likelihood(e_cutoff, data, amplitude, alpha, B, Eemin, Eemax):
    crab_distance=  2.2*u.kpc
    ECPL = ExponentialCutoffPowerLaw(amplitude=amplitude/u.eV,
                                     e_0=1*u.TeV,
                                     alpha=alpha,
                                     e_cutoff=abs(e_cutoff)*u.erg)
    SYN = Synchrotron(ECPL,B=B,Eemin=Eemin,Eemax=Eemax)
    model=SYN.sed(data['energy'].quantity,distance=crab_distance)
    sigma=(data['flux_error_lo'].quantity+data['flux_error_hi'].quantity)/2
    sigma2=np.where(sigma != 0, sigma, np.ones_like(sigma))
    loglik = np.sum(np.log((model.value-data['flux'].data)**2))
    return loglik-2*np.sum(np.log(sigma2))

def trylik(e_cutoff, data, amplitude, alpha, B, Eemin, Eemax):
    nll = lambda *args: -log_likelihood(*args)
    initial = e_cutoff
```

```
    soln=minimize(nll,initial.value,args=(data,amplitude,alpha,B,Eemin,Eemax))
    m_ecut = soln.x
    llkh = log_likelihood(m_ecut,data,amplitude,alpha,B,Eemin,Eemax)
    return llkh

def tryecut(ecut_arr, data, amplitude, alpha, B, Eemin, Eemax):
    liktrial = np.zeros(len(ecut_arr))
    for i in range(len(ecut_arr)):
        ECPL = ExponentialCutoffPowerLaw(amplitude=amplitude/u.eV,
                                         e_0=1*u.TeV,
                                         alpha=alpha,
                                         e_cutoff=ecut_arr[i])
        SYN = Synchrotron(ECPL,B=B,Eemin=Eemin,Eemax=Eemax)
        amp_cor=fitfactor(data,SYN)
        liktrial[i]=trylik(ecut_arr[i],data,amplitude*amp_cor,alpha,B,
            Eemin,Eemax)
    result = ecut_arr[np.where(liktrial==np.min(liktrial))]
    dof = len(np.asarray(data['flux'].data))
    if np.min(liktrial) > dof:
        print('Warning: Minimum Log-likelihood > degrees of freedom')
    return result

#Analytic fitting for the spectrum normalization
def fitfactor(data,spectrum):
    #One should be careful here: in data_flare.flux corresponds to nuFnu
    model=spectrum.sed(data['energy'].quantity,distance=crab_distance)
    flux_error=(data['flux_error_lo'].quantity+data['flux_error_hi'].quantity)/2
    flux_error2=np.where(flux_error!= 0,flux_error,np.ones_like(flux_error))
    s1=np.where(flux_error!=0,model**2/flux_error2**2,
        np.zeros_like(flux_error))
    sum1=sum(s1)
    s2=np.where(flux_error!=0,model*data['flux']/flux_error2**2,
        np.zeros_like(flux_error))
    sum2=sum(s2)
    return (sum2/sum1)

#Final fitting for the Cutoff energy
def fitcutoff(e_cutoff, data, amplitude, alpha, B, Eemin, Eemax):
    nll = lambda *args: -log_likelihood(*args)
    initial = e_cutoff
    soln=minimize(nll,initial.value,args=(data,amplitude,alpha,B,Eemin,Eemax))
    m_ecut = soln.x
    print("Initial value: ", initial.to(u.PeV))
```

```
    llkh = log_likelihood(m_ecut, data, amplitude, alpha, B, Eemin, Eemax)
    dof = len(np.asarray(data['flux'].data))
    print("Maximum likelihood estimates: ",soln.nfev," iterations",llkh,
        "Log-likelihood",dof,'dof')
    if llkh > dof:
        print('Warning: Final Log-likelihood > degrees of freedom')
    return(m_ecut*u.erg)

def flare_rad(index,LE_cutoff,Ee_syn_max,B_flare,Ecut_0):
    ECPL = ExponentialCutoffPowerLaw(amplitude=amp0/u.eV,
                                     e_0=1*u.TeV,
                                     alpha=index,
                                     e_cutoff=Ecut_0)
    SYN = Synchrotron(ECPL,B=B_flare,Eemin=LE_cutoff,Eemax=Ee_syn_max)
    amp_cor=fitfactor(data_flare,SYN) # Fit particle distribution prefactor
    #Fit particle cutoff, with analytic initial value
    Ecut_flare=fitcutoff(Ecut_0,data_flare,amp0*amp_cor,index,B_flare,
        LE_cutoff,Ee_syn_max)
    print('Correct ecut: ', Ecut_flare.to(u.PeV))
    #Final particle spectrum and synchrotron
    ECPL = ExponentialCutoffPowerLaw(amplitude=amp0*amp_cor/u.eV,
                                     e_0=1*u.TeV,
                                     alpha=index,
                                     e_cutoff=Ecut_flare)
    SYN = Synchrotron(ECPL,B=B_flare,Eemin=LE_cutoff,Eemax=Ee_syn_max)
    if flarename == '2011':
        Rflare = 2.8e-4*u.pc
    elif flarename == '2013':
        Rflare = 1.7e-4*u.pc
    else:
        Rflare == 3.2*u.pc
    Esy = np.logspace(0.0,12,100)*u.eV #np.exp(14)
    Lsy = SYN.flux(Esy,distance=0*u.cm)
    #Use distance 0 to get luminosity
    phn_sy = Lsy/(4*np.pi*Rflare**2*c)*2.24
    fields=['CMB',['FIR',70*u.K,0.5*u.eV/u.cm**3],
        ['NIR',5000*u.K,1*u.eV/u.cm**3],
        ['SSC',Esy, phn_sy]]
    IC=InverseCompton(ECPL,seed_photon_fields=fields,Eemin=LE_cutoff,
        Eemax=Ee_syn_max)
    We = IC.compute_We(Eemin=1*u.TeV)
    return SYN,IC,amp_cor,We,Ecut_flare
```

```
#Start
#Paper models
index_models = np.linspace(1.0, 3.0, 21)
B_flare_models = np.concatenate((10**(np.linspace(math.log10(50.0),
    math.log10(5000.0),11)),np.asarray([1000,100,10,3])))
B_flare_models = np.sort(B_flare_models)*u.uG

with open('total_energy_'+flarename+'_'+str(len(index_models)*
        len(B_flare_models))+'models.csv','w') as totenergtab:
    writer_totenerg = csv.writer(totenergtab)
    if comovf == False:
        writer_totenerg.writerows([str('B_microG'),str('Index'),
            str('We_ergs'),str('Ep.erg.'),str('Amplitude.1.eV')])
    else:
        writer_totenerg.writerows([str('B_microG'),str('Index'),str('We_ergs'),
            str('Ep.erg.'),str('sigma10'),str('Rpc')])
    for m in range(len(np.asarray(B_flare_models.value))):
        for n in range(len(index_models)):
            if comovf == False:
                data_flare=ascii.read('CrabNebula_spectrum_flare'+flarename
                    +'_fermi.ecsv.txt')
            else:
                data_flare=ascii.read('CrabNebula_spectrum_flare'+flarename
                    +'_fermi.ecsv.txt')
                delta = lorentzfactor(B=B_flare_models[m])
                print('Lorentz factor required: ', delta)
                data_flare['energy'] = data_flare['energy']/delta

            #Analytic estimate:cutoffinitval(index_models[n],B_flare_models[m])
            #ecutoff(index_models[n],B_flare_models[m],syn_max_0)
            minindex = np.min(index_models)
            maxindex = np.max(index_models)
            minbfield = np.min(B_flare_models)
            maxbfield = np.max(B_flare_models)
            minfact = 0.2
            maxfact = 1.2
            ecut_0_arr=np.logspace(np.log10(minfact*cutoffinitval(index=
                minindex,B=maxbfield).value),maxfact*np.log10(cutoffinitval(
                index=maxindex,B=minbfield).value),sizeloops)*u.PeV

            if comovf == False:
                ecut_0_arr = ecut_0_arr.to('erg')
```

```
else:
    ecut_0_arr = ecut_0_arr.to('erg')*0.1*
        (B_flare_models[m].to('mG').value*
        ((syn_max_0.to('MeV').value/600)*(tvar.to('s').value/4e4)))
for k in range(nloops):
    if k == 0:
        ecut_i_arr = ecut_0_arr
        res = ecut_0_arr
        nbin = sizeloops
        print('Executing realization: ',k+1,'searching from',
            min(ecut_i_arr.to('PeV')),'to',
            max(ecut_i_arr.to('PeV')))
    if k > 0:
        if int(np.where(res==initial_ecut)[0]) == 0:
            lolim = res[0]-abs(res[1]-res[0])*2.0
            hilim = res[int(np.where(res==initial_ecut)[0])+1]
        elif int(np.where(res==initial_ecut)[0])==int(len(res)-1):
            lolim = res[int(np.where(res==initial_ecut)[0])-1]
            hilim = res[int(len(res)-1)]+abs(res[int(len(res)-1)]
                -res[int(len(res)-2)])*2.0
        else:
            lolim = res[int(np.where(res==initial_ecut)[0])-1]
            hilim = res[int(np.where(res==initial_ecut)[0])+1]
        nbin = int(1+(sizeloops//(k+1)))
        ecut_i_arr=np.linspace(lolim.value,hilim.value,nbin)*u.erg
        res = ecut_i_arr
        print('Executing realization: ',k+1,'searching from',
            min(ecut_i_arr.to('PeV')),'to',
            max(ecut_i_arr.to('PeV')))


    initial_ecut=tryecut(ecut_i_arr,data_flare,amp0,
        index_models[n],B_flare_models[m],Eemin=50*u.GeV
        ,Eemax=15000*np.log10(cutoffinitval(index=maxindex
        ,B=minbfield).value)
        *u.PeV)

print([B_flare_models[m],index_models[n],initial_ecut])

SYN_f,IC_f,amp_cor,We,Ecut_flare=flare_rad(index=index_models[n],
    LE_cutoff=50.0*u.GeV,Ee_syn_max=15000*initial_ecut.to('PeV'),
    B_flare=B_flare_models[m],Ecut_0=initial_ecut)
if comovf == True:
```

```
        eprimpev_ =  eprimpev(syn_max_0,tvar,delta)
        print('Predicted E^prime_PeV',eprimpev_)
    print('Amplitude correction: ', amp_cor, amp0*amp_cor/u.eV)
    try:
        err_ep=res[int(np.where(abs(Ecut_flare-res)==
            min(abs(Ecut_flare-res)))[0])+1]
            -res[int(np.where(abs(Ecut_flare-res)==
            min(abs(Ecut_flare-res)))[0])]
    except:
        err_ep = abs(res[int(np.where(abs(Ecut_flare-res)==
            min(abs(Ecut_flare-res)))[0])-1]-
            res[int(np.where(abs(Ecut_flare-res)==
            min(abs(Ecut_flare-res)))[0])])

    print('Energy cutoff: ',Ecut_flare, '+-', str(err_ep/2.))
    print('Energy in electrons (> 1 TeV): ',We.value,' erg')

    energy = np.logspace(-7, 15, 100)*u.eV

    if make_plot == True:
        figure, ax = plt.subplots(1, 1, figsize=(10,5))
        data_steady = ascii.read('CrabNebula_spectrum.ecsv.txt')
        naima.plot_data(data_steady, e_unit=u.eV,figure=figure)
        naima.plot_data(data_flare, e_unit=u.eV,figure=figure)

        ax.loglog(energy,SYN_f.sed(energy,crab_distance),lw=3,c='r'
            ,label='SYN')

        ax.loglog(energy,IC_f.sed(energy,crab_distance,seed='CMB')
            +IC_f.sed(energy,crab_distance,seed='FIR')
            +IC_f.sed(energy,crab_distance,seed='NIR')
            +IC_f.sed(energy,crab_distance,seed='SSC'),
            lw=3,c='r',ls='--',label='IC')

        for i, seed, ls in zip(range(4),['CMB','FIR','NIR','SSC'],
            [':','-.',':','--']):
            ax.loglog(energy,IC_f.sed(energy,crab_distance,seed=seed)
                      ,lw=3,c=naima.plot.color_cycle[i+1],label=seed
                      ,ls=ls)

        #Sensitivity curves
        CTAsN=ascii.read('CTA_prod3b_v2_North_20deg_05h_DiffSens.txt')
        ax.loglog(1e12*CTAsN['energy'],CTAsN['flux'],lw=3
```

```
            ,c='darkmagenta',label='CTA-N 5h')

        ax.set_ylim(1e-19, 9e-8)
        ax.set_xlim(1e0, 1e15)
        ax.legend(loc='lower left', frameon=False, fontsize=20)
        ax.tick_params(axis='x', labelsize=22)
        ax.tick_params(axis='y', labelsize=22)
        ax.xaxis.label.set_size(22)
        ax.yaxis.label.set_size(22)
        figure.tight_layout()

        pdf_name = flarename+'_flare_'+str(B_flare_models[m])
            +'_'+str(index_models[n])+'.pdf'
        with PdfPages(pdf_name) as pdf:
            pdf.savefig(figure)
        plt.show()


    if make_tables == True:
        table = Table()

        table['Energy']=Column(energy.to('TeV').value,unit='TeV')
        table['IC_flux_CMB']=Column(IC_f.sed(energy,crab_distance,
            seed='CMB').to('cm-2 s-1 TeV').value,unit='cm-2 s-1 TeV')
        table['IC_flux_FIR']=Column(IC_f.sed(energy,crab_distance,
            seed='FIR').to('cm-2 s-1 TeV').value,unit='cm-2 s-1 TeV')
        table['IC_flux_NIR']=Column(IC_f.sed(energy,crab_distance,
            seed='NIR').to('cm-2 s-1 TeV').value,unit='cm-2 s-1 TeV')
        table['IC_flux_SSC']=Column(IC_f.sed(energy,crab_distance,
            seed='SSC').to('cm-2 s-1 TeV').value,unit='cm-2 s-1 TeV')


        #Write it
        with open('./table_models/'+flarename+'/IC_sedTable'+'_'
                +str(round(B_flare_models.value[m],1))+'uG_'
                +str(round(index_models[n],1))+'.csv','w') as csvfile:
            writer = csv.writer(csvfile)
            [writer.writerow(r) for r in table]


        table2 = Table()
        table2['Energy'] = Column(energy.to('TeV').value,unit='TeV')
        table2['SYN_flux'] = Column(SYN_f.sed(energy,
```

```
                    crab_distance).to('cm-2 s-1 TeV').value,
                    unit='cm-2 s-1 TeV')

                with open('./table_models/'+flarename+'/SYN_sedTable'+'_'
                        +str(round(B_flare_models.value[m],1))+'uG_'+
                        str(round(index_models[n],1))+'.csv','w') as csvfile:
                    writer = csv.writer(csvfile)
                    [writer.writerow(r) for r in table2]
            if comovf == True:
                rcm = 3e15*(eprimpev_.value*
                    B_flare_models[m].to('mG').value**-1)*u.cm
                rpc = float(rcm.to('pc').value)
                print('Gyro radius [pc]: ', rpc)
            if comovf == True:
                writer_totenerg.writerow([B_flare_models.value[m],
                    index_models[n],float(We.value),
                    float(Ecut_flare.value),delta/10.0,rpc])
            else:
                writer_totenerg.writerow([B_flare_models.value[m],
                    index_models[n],float(We.value),
                    float(Ecut_flare.value),amp0*amp_cor])
totenergtab.close()
```

Appendix C

Particle spectrum fit with NAIMA

```
import naima
from astropy import table
import numpy as np
import math
from astropy.io import ascii
from astropy.constants import c,m_e
import astropy.units as u
from naima.models import (PowerLaw, ExponentialCutoffPowerLaw, Synchrotron,
                          InverseCompton,PionDecay)
import matplotlib
from matplotlib import pyplot as plt
from matplotlib.ticker import FormatStrFormatter
from ipywidgets.widgets.interaction import interact, fixed
from matplotlib.backends.backend_pdf import PdfPages
from scipy.optimize import minimize
from astropy.table import Table, Column
import csv
import sys

mcc = (m_e*c**2).cgs
amp0=9.e37
make_plot = True
make_tables = True
distance_src = 1*u.kpc

srcname = 'j1023'
nloops = 1
sizeloops = 10
```

```
#Definitions for E_cutoff, amplitude fittings
def log_likelihood(e_cutoff,data,amplitude,alpha):

    ECPL = ExponentialCutoffPowerLaw(amplitude=amplitude/u.eV,
                                     e_0=1*u.TeV,
                                     alpha=alpha,
                                     e_cutoff=abs(e_cutoff)*u.erg)
    PP = PionDecay(ECPL,nh=1.*u.cm**-3)
    model=PP.sed(data['energy'].quantity,distance=distance_src)
    sigma=(data['flux_error_lo'].quantity+data['flux_error_hi'].quantity)/2
    sigma2=np.where(sigma != 0, sigma, np.ones_like(sigma))
    loglik = 0.5*np.sum((model.value-data['flux'].data)**2/(sigma2**2))
    return -loglik-np.sum(np.log(sigma2))

def log_likelihood_PL(alpha,data, amplitude):
    PL = PowerLaw(amplitude=amplitude/u.eV,
                  e_0=1*u.TeV,
                  alpha=alpha,
                  )
    PP = PionDecay(PL,nh=1.*u.cm**-3)
    model=PP.sed(data['energy'].quantity,distance=distance_src)
    sigma=(data['flux_error_lo'].quantity+data['flux_error_hi'].quantity)/2
    sigma2=np.where(sigma!=0,sigma,np.ones_like(sigma))
    loglik = 0.5*np.sum((model.value-data['flux'].data)**2/(sigma2**2))
    return -loglik-np.sum(np.log(sigma2))

def aplpy_constraint(amplitude,alpha):
    PL = PowerLaw(amplitude=amplitude/u.eV,
                  e_0=1*u.TeV,
                  alpha=alpha,
    )
    PP = PionDecay(PL, nh=1.*u.cm**-3)
    return (fluxUL-PP.sed(eneUL,distance=distance_src)).value

def aplpy_constraint_exp(amplitude,alpha,e_cutoff):
    ECPL = ExponentialCutoffPowerLaw(amplitude=amplitude/u.eV,
                                     e_0=1*u.TeV,
                                     alpha=alpha,
                                     e_cutoff=e_cutoff)
    PP = PionDecay(ECPL,nh=1.*u.cm**-3)
    return (fluxUL-PP.sed(eneUL,distance=distance_src)).value

def trylik(e_cutoff, data, amplitude, alpha):
```

```
    nll = lambda *args: -log_likelihood(*args)
    initial = e_cutoff
    cons={'type':'ineq','fun':aplpy_constraint_exp,
        'args':[amplitude,alpha,e_cutoff]}
    soln = minimize(nll,initial.value,args=(data,amplitude,alpha),
        bounds=[(e_cutoff.value*0.5, e_cutoff.value*1.5)])
    m_ecut = soln.x
    llkh = log_likelihood(m_ecut, data, amplitude, alpha)
    if np.any(aplpy_constraint_exp(amplitude,alpha,e_cutoff)<0):
        llkh=-1
    return llkh

def tryecut(ecut_arr, data, amplitude,alpha, max_PL):
    liktrial = np.zeros(len(ecut_arr))
    liktrial_PL = np.zeros(len(ecut_arr))
    for i in range(len(ecut_arr)):
        ECPL = ExponentialCutoffPowerLaw(amplitude=amplitude/u.eV,
                                         e_0=1*u.TeV,
                                         alpha=alpha,
                                         e_cutoff=ecut_arr[i])
        PP = PionDecay(ECPL,nh=1.*u.cm**-3)
        amp_cor=fitfactor(data,PP)
        liktrial[i] = trylik(ecut_arr[i],data,amplitude*amp_cor,alpha)
        liktrial_PL[i] = max_PL

    result = ecut_arr[np.where(liktrial==np.max(liktrial))]
    dof = len(np.asarray(data['flux'].data))
    LR = -2*(np.asarray(np.array(liktrial_PL)-np.asarray(liktrial)))
    return result,LR,liktrial

def trylik_pwl(data, amplitude, alpha):
    nll = lambda *args: -log_likelihood_PL(*args)
    initial = alpha
    cons = {'type':'ineq','fun': aplpy_constraint,
        'args':[amplitude,alpha]}
    soln = minimize(nll,initial,args=(data,amplitude),
        bounds=[(alpha-1.5,alpha+ 1.5)])
    m_alpha = soln.x
    llkh_pwl = log_likelihood_PL(m_alpha,data, amplitude)
    if np.any(aplpy_constraint(amplitude,alpha)<0):
        llkh=-1
    return llkh_pwl,m_alpha
```

```
def trypl(data,amplitude,alpha):
    PL = PowerLaw(amplitude=amplitude/u.eV,
                  e_0=1*u.TeV,
                  alpha=alpha,
    )
    PP = PionDecay(PL,nh=1.*u.cm**-3)
    amp_cor=fitfactor(data,PP)
    liktrial_PL,m_alpha = trylik_pwl(data,amplitude*amp_cor, alpha)
    alpha_result=m_alpha
    return liktrial_PL,m_alpha

# Analytic fitting for the spectrum normalization
def fitfactor(data,spectrum):
    #One should be careful here: in data_src.flux corresponds to nuFnu
    model=spectrum.sed(data['energy'].quantity,distance=distance_src)
    flux_error=(data['flux_error_lo'].quantity+data['flux_error_hi'].quantity)/2
    flux_error2=np.where(flux_error!=0,flux_error,np.ones_like(flux_error))
    s1=np.where(flux_error!=0,model**2/flux_error2**2,np.zeros_like(flux_error))
    sum1=sum(s1)
    s2=np.where(flux_error!=0,model*data['flux']/flux_error2**2,
        np.zeros_like(flux_error))
    sum2=sum(s2)
    return (sum2/sum1)

#Final fitting for the Cutoff energy
def fitcutoff(e_cutoff, data, amplitude, alpha):
    nll = lambda *args: -log_likelihood(*args)
    initial = e_cutoff
    soln = minimize(nll,initial.value,args=(data,amplitude,alpha))
    m_ecut = soln.x
    llkh = log_likelihood(m_ecut, data, amplitude, alpha)
    dof = len(np.asarray(data['flux'].data))
    print("Maximum likelihood estimates: ",soln.nfev," iterations",llkh,
        "Log-likelihood",dof,'dof')
    sigma=(data['flux_error_lo'].quantity+data['flux_error_hi'].quantity)/2
    sigma2=np.where(sigma != 0, sigma, np.ones_like(sigma))
    if -llkh > dof+np.sum(np.log(sigma2)):
        print('Warning: Final Log-likelihood > degrees of freedom')
    return (m_ecut*u.erg).to('TeV'), llkh

def src_rad(index,Ecut_0):
    ECPL = ExponentialCutoffPowerLaw(amplitude=amp0/u.eV,
                                     e_0=1*u.TeV,
```

```
                                        alpha=index,
                                        e_cutoff=Ecut_0)
    PP = PionDecay(ECPL,nh=1.*u.cm**-3)
    amp_cor=fitfactor(data_src,PP)
    #Fit particle distribution prefactor
    #Fit particle cutoff, with analytic initial value
    Ecut_src, llkh = fitcutoff(Ecut_0, data_src, amp0*amp_cor, index)
    #Final particle spectrum and synchrotron
    ECPL = ExponentialCutoffPowerLaw(amplitude=amp0*amp_cor/u.eV,
                                        e_0=1*u.TeV,
                                        alpha=index,
                                        e_cutoff=Ecut_src)
    PP = PionDecay(ECPL,nh=1.*u.cm**-3)

    return PP,amp_cor,Ecut_src, llkh

#Start
index_models = np.linspace(1.5,3.0,16)
if nloops > 1:
    LRS_array=np.ndarray(shape=(len(index_models),int(1+(sizeloops//nloops)))
        ,dtype=float)
    ecut_LR_array=np.ndarray(shape=(len(index_models),
        int(1+(sizeloops//nloops))),dtype=float)
    liktrial_array=np.ndarray(shape=(len(index_models),
        int(1+(sizeloops//nloops))),
        dtype=float)
else:
    LRS_array=np.ndarray(shape=(len(index_models),sizeloops),dtype=float)
    ecut_LR_array=np.ndarray(shape=(len(index_models),sizeloops),dtype=float)
    liktrial_array=np.ndarray(shape=(len(index_models),sizeloops),dtype=float)
llkh_array = np.ndarray(shape=(len(index_models),),dtype=float)
ecut_array = np.ndarray(shape=(len(index_models),2),dtype=float)
ampl_array = np.ndarray(shape=(len(index_models),),dtype=float)
alpha_array = []

ene_ul=[]
ul=[]
data_ul=ascii.read(str(srcname)+'.csv')
for i in range(0, len(data_ul['ul'])):
    if data_ul['ul'][i]==True:
        ene_ul.append(data_ul['energy'][i])
        ul.append(data_ul['flux'][i])
```

```
eneUL=ene_ul*u.MeV
fluxUL=ul*u.erg/u.cm**2/u.s
for n in range(len(index_models)):
    data_src = ascii.read(str(srcname)+'.csv')
    liktrial_PL = trypl(data_src, amp0, index_models[n])
    alpha_array.append(liktrial_PL)

maxLL_PL=np.amax(alpha_array,axis=0)[0].mean()
index=np.where(alpha_array==np.amax(alpha_array,axis=0)[0])[0].mean()
alpha_PL=alpha_array[int(index)][1].mean()

with open('./results_'+str(srcname)+'_'+str(len(index_models))+
        'models_1loop.csv','w') as totenergtab:
    writer_totenerg = csv.writer(totenergtab)
    writer_totenerg.writerows([str('Index'),str('Eperg'),str('Amplitude')])


    for n in range(len(index_models)):
        data_src = ascii.read(str(srcname)+'.csv')
        ecut_0_arr=np.exp(np.linspace(np.log(1.),np.log(5000.),sizeloops))*u.TeV
        ecut_0_arr = ecut_0_arr.to('erg')
        print(ecut_0_arr)
        for k in range(nloops):
            if k == 0:
                ecut_i_arr = ecut_0_arr
                res = ecut_0_arr
                nbin = sizeloops
                print('Executing realization: ',k+1,'searching from',
                    min(ecut_i_arr.to('PeV')),'to',
                    max(ecut_i_arr.to('PeV')))
            if k > 0:
                if int(np.where(res==initial_ecut)[0]) == 0:
                    lolim = res[0]-abs(res[1]-res[0])*2.0
                    hilim = res[int(np.where(res==initial_ecut)[0])+1]
                elif int(np.where(res==initial_ecut)[0]) == int(len(res)-1):
                    lolim = res[int(np.where(res==initial_ecut)[0])-1]
                    hilim = res[int(len(res)-1)]+abs(res[int(len(res)-1)]
                    -res[int(len(res)-2)])*2.0
                else:
                    lolim = res[int(np.where(res==initial_ecut)[0])-1]
                    hilim = res[int(np.where(res==initial_ecut)[0])+1]
                nbin = int(1+(sizeloops//(k+1)))
                ecut_i_arr = np.linspace(lolim.value,hilim.value,nbin)*u.erg
```

```
        res = ecut_i_arr
        print('Executing realization: ',k+1,'searching from',
            min(ecut_i_arr.to('PeV')),'to',max(ecut_i_arr.to('PeV')))


    initial_ecut,LR_i,liktrial_i=tryecut(ecut_i_arr,data_src,amp0,
        index_models[n],maxLL_PL)

    PP_f,amp_cor,Ecut_src, llkh_i=src_rad(index=index_models[n],
        Ecut_0=initial_ecut)
    try:
        err_ep=res[int(np.where(abs(Ecut_src-res)
            ==min(abs(Ecut_src-res)))[0])+1]-
            res[int(np.where(abs(Ecut_src-res)
            ==min(abs(Ecut_src-res)))[0])]
    except:
        err_ep=abs(res[int(np.where(abs(Ecut_src-res)
            == min(abs(Ecut_src-res)))[0])-1]-
            res[int(np.where(abs(Ecut_src-res)
            ==min(abs(Ecut_src-res)))[0])])

    energy = np.logspace(-7,15,100)*u.eV

    PP_PL = PionDecay(PowerLaw(amplitude=amp0*amp_cor/u.eV,e_0=1*u.TeV
        ,alpha=index_models[n]),nh=1.*u.cm**-3)

    if make_plot == True:
        figure, ax = plt.subplots(1, 1, figsize=(10,5))
        data_steady = ascii.read(str(srcname)+'.csv')
        naima.plot_data(data_steady, e_unit=u.eV,figure=figure)
        ax.loglog(energy,PP_f.sed(energy,distance_src),lw=3,c='r'
            ,label='PP(ECPL)')
        ax.loglog(energy,PP_PL.sed(energy, distance_src),lw=2,c='b'
            ,label='PP(PL)')
        ax.set_ylim(1e-14, 5e-11)
        ax.set_xlim(1e10, 1e15)
        ax.legend(loc='lower left', frameon=False, fontsize=22)
        ax.tick_params(axis='x', labelsize=22)
        ax.tick_params(axis='y', labelsize=22)
        ax.xaxis.label.set_size(22)
        ax.yaxis.label.set_size(22)
        figure.tight_layout()
```

```
                pdf_name = srcname+'_'+str(index_models[n])+'.pdf'
                with PdfPages(pdf_name) as pdf:
                    pdf.savefig(figure)

                plt.clf()
            if make_tables == True:
                table2 = Table()
                table2['Energy'] = Column(energy.to('TeV').value,unit='TeV')
                table2['PP_flux']=Column(PP_f.sed(energy,
                    distance_src).to('cm-2 s-1 TeV').value,
                    unit='cm-2 s-1 TeV')

                with open('./'+srcname+'_'+'PP_sedTable'+'_'+
                    str(round(index_models[n],1))+'.csv','w') as csvfile:
                    writer = csv.writer(csvfile)
                    writer.writerow([str('Energy[TeV]'),
                        str('Flux[cm-2 s-1 TeV]')])
                    [writer.writerow(r) for r in table2]
                writer_totenerg.writerow([index_models[n],float(Ecut_src.value)
                    ,amp0*amp_cor])
        LRS_array[n] = LR_i
        llkh_array[n] = llkh_i
        ecut_array[n][0], ecut_array[n][1]=Ecut_src.to('TeV').value,
            err_ep.to('TeV').value/2.
        ampl_array[n] = amp0*amp_cor
        ecut_LR_array[n] = ecut_i_arr.to('TeV').value
        liktrial_array[n] = liktrial_i
    result_dict = dict([('Index',index_models),('Log-likelihood',llkh_array),
        ('Ecutoff[TeV]',ecut_array), ('Amplitude[1/eV]',ampl_array),
        ('Ecut_array(LR)[TeV]',ecut_LR_array),('LR',LRS_array),
        ('ECPL Log-Likelihood',liktrial_array)])
    print(result_dict)
    np.save(srcname+'_Results_1loop.npy',result_dict)
totenergtab.close()
```

Appendix D

Publications

List of papers:

- E. Mestre, E. de Oña Wilhelmi, R. Zanin, D. F. Torres and L. Tibaldo. "The Crab nebula variability at short timescales with the Cherenkov Telescope Array. Monthly Notices of the Royal Astronomical Society", doi:10.1093/mnras/staa3599.
- E. Mestre, E. de Oñna Wilhelmi, D. Khangulyan, R. Zanin, F. Acero, D. F. Torres. "Prospects for the characterization of the VHE emission from the Crab Nebula and Pulsar with the Cherenkov Telescope Array". Monthly Notices of the Royal Astronomical Society, Volume 492, Issue 1, February 2020, Pages 708-718, https://doi.org/10.1093/mnras/stz3421
- E. de Oñna Wilhelmi, I. Sushch, R. Brose, E. Mestre, Y. Su and R. Zanin. "SNR G39.2-0.3, an hadronic cosmic rays accelerator". Notices of the Royal Astronomical Society, 497, Issue 3, September 2020, Pages 3581-3590, https://doi.org/10.1093/mnras/staa2045
- E. Mestre, E. de Oñna Wilhelmi, D. F. Torres, T. L. Holch, U. Schwanke, F. Aharonian, P. Saz Parkinson, R. Yang, R. Zanin. "Probing the hadronic nature of the gamma-ray emission associated with Westerlund 2" (sent to Monthly Notices of the Royal Astronomical Society).

MNRAS **000**, 000–000 (2018) Preprint 5 December 2019 Compiled using MNRAS LATEX style file v3.0

Prospects for the characterization of the VHE emission from the Crab Nebula and Pulsar with the Cherenkov Telescope Array

E. Mestre[1,2], E. de Oña Wilhelmi[1,2,3], R. Zanin[4], D. F. Torres[1,2,5] and L. Tibaldo[6]
[1] *Institute of Space Sciences (ICE/CSIC), Campus UAB, Carrer de Can Magrans s/n, 08193 Barcelona, Spain*
[2] *Institut d' Estudis Espacials de Catalunya (IEEC), 08034 Barcelona, Spain*
[3] *Deutsches Elektronen Synchrotron DESY, 15738 Zeuthen, Germany*
[4] *Max-Planck-Institut für Kernphysik, P.O. Box 103980, D 69029 Heidelberg, Germany*
[5] *Institució Catalana de Recerca i Estudis Avançats (ICREA), E-08010 Barcelona, Spain*
[6] *Institut de Recherche en Astrophysique et Planétologie, CNRS-INSU, Université Paul*

5 December 2019

ABSTRACT

The Cherenkov Telescope Array (CTA) will be the next generation instrument for the very high energy gamma-ray astrophysics domain. With its enhanced sensitivity in comparison with the current facilities, CTA is expected to shed light on a varied population of sources. In particular, we will achieve a deeper knowledge of the Crab nebula and pulsar, which are the best characterized pulsar wind nebula and rotation powered pulsar, respectively. We aim at studying the capabilities of CTA regarding these objects through simulations, using the main tools currently in development for the CTA future data analysis: *Gammapy* and *ctools*. We conclude that, even using conservative Instrument Response Functions, CTA will be able to resolve many uncertainties regarding the spectrum and morphology of the pulsar and its nebula. The large energy range covered by CTA will allow us to disentangle the nebula spectral shape among different hypotheses, corresponding to different underlying emitting mechanisms. In addition, resolving internal structures (smaller than $\sim 0.02^\circ$ in size) in the nebula and unveiling their location, would provide crucial information about the propagation of particles in the magnetized medium. We used a theoretical asymmetric model to characterise the morphology of the nebula and we showed that if predictions of such morphology exist, for instance as a result of hydrodynamical or magneto-hydrodynamical simulations, it can be directly compared with CTA results. We also tested the capability of CTA to detect periodic radiation from the Crab pulsar obtaining a precise measurement of different light curves shapes.

Key words: instrumentation: detectors – (stars:) pulsars: individual: Crab – (stars:) supernovae: individual: Crab Nebula

1 INTRODUCTION

Due to the high luminosity and seemingly long-term flux stability, the Crab pulsar and its pulsar wind nebula (PWN) is one of the most studied sources in the very high energy (VHE, E > 100 GeV) regime. For many years, Crab has been used as a standard candle in X- and gamma-ray astronomy (Hester 2008). The Crab nebula was the first TeV gamma-ray source discovered (in 1989 by the Whipple 10 meters telescope, Weekes et al. 1989), and soon after detected by numerous facilities above 100 GeV (Smith et al. 2000; Aharonian et al. 2006; Abdo et al. 2012; Aleksić et al. 2015; Meagher & VERITAS Collaboration 2015; Abeysekara et al. 2017). It has a (energy-dependent) angular size of $\sim 0.1^\circ$ and its distance has been estimated to be ≈ 2.2 kpc, corresponding to a physical size of ≈ 3.8 pc (Trimble 1973; Davidson & Fesen 1985; Kaplan et al. 2008). The nebula non-thermal spectrum can be described by two components, a synchrotron component extending from radio to high energy gamma-rays and a second component emerging above 1 GeV (Atoyan & Aharonian 1996). The latter is interpreted as inverse Compton scattering (IC) of the same particles against soft background photons: cosmic microwave background (CMB), far-infrared (FIR) and near-infrared (NIR) background, and the synchrotron photons of the nebula itself or Synchrotron Self Compton (SSC). The pulsar has a spin period of P = 33 ms, a spin down rate of $\dot{\mathrm{P}} = 4.21 \times 10^{-13}$ and a spin down luminosity of $\mathrm{L_{spin}} = 3.8 \times 10^{38}$ erg s^{-1}.

The pulsed emission between 0.1 GeV and 100 GeV is believed to be due to synchrotron-curvature radiation (Abdo et al. 2010; Ansoldi et al. 2016) and its spectrum is well parametrized by a power law with a sub-exponential cutoff function of spectral index $\gamma_{\rm P} = 1.59$, the break located at an energy of about 500 MeV and curvature index of $\kappa = 0.43$. In addition, a power law component emerges above the cutoff extending above 100 GeV (Aliu et al. 2011; Aleksić et al. 2012; Ansoldi et al. 2016).

Despite the high-precision spectral measurements performed by the last generation of IACTs, with points with a 5% statistical uncertainty at energies below 100 GeV (Aleksić et al. 2015), the spectral shape of the IC component of the Crab nebula is still not firmly established. The main ambiguities appear at the highest energies, above tens of TeV. They are the result of the decrease of the photon statistics, and, on the other hand, of the large systematic uncertainties that the imaging Cherenkov technique suffers.
At the lowest energies (from few up to hundreds of GeV), instead, *Fermi*-LAT and MAGIC closed the previously existing gap between space- and ground-based measurements, hence providing for the first time a complete coverage of the IC peak. A joint analysis of *Fermi*-LAT and MAGIC shows a rather flat peak. Given the small uncertainties, this peak is not trivial to reproduce (see Aleksić et al. 2015 for an in-depth discussion). Different theoretical models were used to reproduce the rich Crab data sample, following different prescriptions of the time evolution of the system and particle populations (see, i.e. Pacini & Salvati 1973; Hillas et al. 1998; Aharonian et al. 2004; Meyer et al. 2010; Tanaka & Takahara 2010; Bucciantini et al. 2010; Torres et al. 2014 and references therein). However, none of them fully describe the spectral shape and the morphology observed with high precision: detailed studies of the spectral shape of the VHE emission should allow us to finally disentangle the strength and structure of the magnetic field, together with the particle distribution function in the nebula. The characterization of the spectral energy distribution (SED) peak is of special importance, since the SSC scattering becomes relevant only for the highly energetic (∼70 percent of the Crab rotational power), particle dominated nebulae at low ages (of less than a few kyr), which are located in a FIR background with relatively low energy density (Torres et al. 2013). It is particularly interesting the still poorly explored energy interval above few tens of TeV. The so-called cutoff region is related to the maximum energy of the parent particles as well as to the energy losses, encompassesing significant information on particle acceleration and evolution. However, in the specific case of the Crab nebula, the spectral steepening at VHEs is a radiative or a propagation feature. Given the high magnetic field of $\sim 100\ \mu$G (Kennel & Coroniti 1984; Meyer et al. 2010; Martín et al. 2012), in fact, the most energetic parent particles dissipate their energies via synchrotron radiation. On one hand, the spectrum steepens due to the transition of the IC mechanism from the Thomson to the Klein-Nishina (KN) regime that occurs at different energies for the three dominant target photon fields: the synchrotron-self-Compton, the far infrared and the CMB (Atoyan & Aharonian 1996). The overall spectral shape is, therefore, given by the overlap of the three contributions. On the other hand, also the energy-dependence of the particle diffusion mechanism can generate possible spectral breaks (Lefa et al. 2012).

Empirically, several analytical models were proposed to describe the VHE emission. It is already clear that there is no simple mathematical function that can properly describe the entire IC component, from ∼1 GeV to tens of TeV, but there are good approximations in reduced energy intervals. At energies larger than a few hundreds of GeV, above the IC peak, the emission was fitted by a power law up to 80 TeV (PL: Aharonian et al. 2004), a power law with an exponential cutoff at 14.3 TeV (PLEC-HESS, Aharonian et al. 2006), and a log-parabola (LP-MAGIC: Aleksić et al. 2015; LP-HESS: Holler et al. 2015, see also Meagher & VERITAS Collaboration 2015) reaching up to 100 TeV (HAWC Collaboration et al. 2019). Although it is, currently, commonly accepted that the Crab nebula spectrum exhibits a curvature above 10 TeV, the exact position and shape of this spectral break is still under debate. In this work we test CTA capabilities to answer this question.

The size of the Crab nebula results from the interplay between radiation losses and particle transport mechanisms and depends on the energy of the underlying particle population. The morphology of the synchrotron component has been studied in detail from radio to gamma rays (see for a review Hester 2008), showing a clear dependence on the energy range. At X-ray energies the Crab exhibits a complex structure consisting of a torus and two narrow jets emerging from the direction perpendicular to the torus plane. The size of the Crab nebula is energy dependent as a consequence of the energy losses due to synchrotron burn-off, which limits the particle energy as a function of the distance from the shock, and therefore the size of the nebula.

The morphology of the IC nebula is, instead, poorly known due to the limited angular resolution of the gamma-ray telescopes which is of the order of 0.5° for the *Fermi*-LAT detector at few GeV and of few arcminutes for the current generation of IACTs. We expect its extension to be related with that of the synchrotron nebula, since it depends on the same population of the synchrotron electrons convolved with the spatial distribution of the photon field. At energies above 1 GeV an extension of 0.03° (Fermi-LAT Collaboration & Biteau 2018; Yeung & Horns 2019) was derived using data from *Fermi*-LAT. At higher energies the nebular shrinking due to synchrotron burn-off (Atoyan & Aharonian 1996) was finally established by the H.E.S.S. collaboration thanks to the use of advanced analysis techniques that improved the angular resolution down to 0.05° above 700 GeV. The sigma of the measured Gaussian morphology is $52.2'' \pm 2.9''_{stat} \pm 7.8''_{sys}$ (Holler et al. 2017). Such extension is in good agreement with the theoretical expectations probing for the first time electron energies in the 1-10 TeV range. This electron population is, in fact, responsible for the 0.1 keV synchrotron emission that is inaccessible because of its absorption with the interstellar medium.

The Crab pulsar is one of the few pulsars detected across the entire electromagnetic spectrum, from radio frequencies to γ rays. At high energies, above 100 MeV, the significant improvement in sensitivity and the unprecedented statistics afforded by *Fermi*-LAT, with respect to the previous generation of instruments, established precise measurements of the Crab pulsar spectrum. The phase-averaged spectrum is well represented by a 1.97 power law function with an energy cutoff at $(5.8 \pm 0.5 \pm 1.2)$ GeV (Abdo et al. 2010), in agreement with the theoretical prediction of a synchro-curvature emis-

sion component (Viganó & Torres 2015) with a maximum energy limited by either magnetic and gamma pair absorption or radiation losses. In particular, the *Fermi*-LAT result, together with the MAGIC detection of the Crab pulsar at ∼25 GeV (Aliu et al. 2008), suggested an emission originating at high-altitudes inside the magnetosphere, i.e. the outer gap models (Cheng et al. 1986). Few years later, in 2011, the unexpected discovery of a new spectral component emerging above the cutoff at ∼6 GeV, and extending up to hundreds of GeV opened a new window in the pulsar physics. Discovered by VERITAS (Aliu et al. 2011), and later confirmed by MAGIC (Aleksić et al. 2011, 2012), this results implies the existence of relativistic particles close to or beyond the light cylinder where absorption is negligible. It has been proposed that a new emission mechanism must be invoked to account for this new component, namely IC of lower energy synchrotron pulsed photons. The location of the emission, if magnetospheric (Aleksić et al. 2011; Lyutikov et al. 2012), in the pulsar wind region (Aharonian et al. 2012), or in the current sheets (Contopoulos et al. 1999; Cerutti et al. 2016) extending beyond the light cylinder (Mochol & Pétri 2015) still remains an open question. Normal synchro-curvature emission (as it is the case for other pulsars, see Torres 2018) could also play a role. The full (infrared to gamma-rays, with a continuous coverage) pulsed spectrum of Crab could be described with synchro-curvature radiation in a model using seven parameters (even less than needed to generate the Crab spectrum via a cyclotron self-Compton model Lyutikov 2013). And it is not even discarded that to represent the TeV component with a small population of particles emitting towards us, but requiring a larger accelerating field (see figure 14 of Torres et al. 2019 and the associated discussion). The presence of two different mechanisms for the production of the high-energy and the VHE components leads to the production of spectral features whose detection could shed light on the understanding of the mechanisms at work.

The Cherenkov Telescope Array (CTA, Acharya et al. 2013), currently in the pre-construction phase, is the next generation ground-based observatory for very-high-energy gamma-ray astronomy (up to more than 300 TeV). CTA will be located on two sites, a northern location in La Palma (Spain), and a southern one in Paranal (Chile). It will observe with an array of Small, Medium and Large Size Telescopes (SSTs, MSTs and LSTs), improving the sensitivity of the existing VHE instruments by a factor of five to ten depending on the energy range. The angular resolution of both arrays will be equal to or better than 0.1° at 0.1 TeV and 0.05° at energies above 1 TeV, and the energy resolution will be equal to or better than 30% at 50 GeV and 10% at all energies above 1 TeV (Hassan et al. 2015).

In this paper we aim at understanding the potential of CTA to study different characteristics of the Crab pulsar and nebula (De Oña-Wilhelmi et al. 2013; Burtovoi & Zampieri 2016), which have direct implications on the physics mechanisms behind the multi-wavelength radiation. In particular, (1) What is the maximum energy that CTA can achieve with deep observations of the nebula? or in other words, what is the largest-energy particles CTA can probe (2) How well can CTA constrain the nebula spectral shape, which depends on the particles acceleration and emission mechanisms at play? (3) Can CTA resolve the morphology of the Crab nebula? that is, how well can we study the transport and evolution of particles in a magnetised medium (4) What can we expect from deep observations of the pulsar with CTA? can we disentangle between different spectral components in the GeV/TeV regimes by means of CTA observations? In this work we only consider the Crab nebula in a steady state (out of a state similar to the several gamma-ray flares that have been observed Abdo et al. 2011).

It is important to note that the simulations showed in this paper are based in a conservative estimation of the CTA response functions, which are aimed to describe the general behavior of the instrument and based on standard Hillas reconstruction Hillas et al. (1998). To account for this, we also tested a more realistic and improved response modifying artificially some of the simulated telescope parameters. Thus, §2 describes the Instrument Response Functions (IRF) of CTA, the modifications of those reflecting the foreseen improvement by using more sophisticated techniques, and the tools (§2.1) we used in this study. §3 describes the hypotheses we assumed for this work and the results of the simulations regarding the Crab nebula spectral shape and morphology. §4 presents the results of the simulations concerning the pulsar and §5 provides a few concluding remarks.

2 SIMULATIONS AND ANALYSIS

We simulated the energy spectrum and the morphology of both the Crab nebula and pulsar. The simulations of both the spectral and the morphological behaviour require an a priori assumption on the model, which must be convoluted with the IRFs.

The IRF comprises the mathematical description that relates the observable of the events measured by the instrument (measured energy E', measured incident direction p' and arrival time t'), with the physical quantities of the incident photon (true energy E, true incident direction p and true arrival time t). It is factorized into the effective area $\mathrm{A_{eff}(p, E, t)}$, the point spread function $\mathrm{PSF(p'|p, E, t)}$, and the energy dispersion $\mathrm{E_{disp}(E'\ |p, E, t)}$. The factorization of the instrument response is given by the following expression:

$$\begin{aligned}\mathrm{R(p', E', t'\ |p, E, t)} &= \mathrm{A_{eff}(p, E, t)} \\ &\times \mathrm{PSF(p'\ |p, E, t)} \times \mathrm{E_{disp}(E'\ |p, E, t)}\end{aligned} \quad (1)$$

In this work we used version prod3b of the publicly available IRFs [1]. A detailed description on how these IRFs are obtained can be found in Hassan et al. (2015). These IRFs have been optimized for the detection of isolated point-like sources against residual cosmic-ray background for exposure times of 0.5, 5 and 50 hr and at two different zenith angles of 20° and 40°. We considered the IRFs for the Northern site at 20° zenith angle where the Crab culminates almost at zenith, thus being observable at small zenith angles which guarantee the lowest energy threshold possible. It should also be emphasized that the available IRFs do not account yet for the foreseen improvement that will be achieved by the use of advance analysis techniques (see for instance Mangano et al. 2018 or Shilon et al. 2019). We expect that more advanced IRFs will improve significantly key parameters such the angular and energy resolution. To take this into account, we

[1] https://www.cta-observatory.org/science/cta-performance/

also evaluated the expected results assuming some degree of improvement beyond the current IRFs, as described in §3.2.

2.1 Analysis science tools

In this work we used both prototypes for the CTA Science Tools (STs): *gammapy* (Deil et al. 2017) version 0.7 and *ctools* (Knödlseder et al. 2016) version 1.5.0.

We implemented a simulation scheme within *Gammapy* that works as a generator of simulated 3D sky cubes, which we have also made public[2], with two spatial dimensions (sky direction) plus an energy axis discretised in bins. These cubes contain the predicted counts for the simulated Crab nebula and pulsar, supposing that both sources are in the same position but with different morphology and spectra. The set of simulated cubes comprise the predicted counts from the two sources (without background), an observation simulation with an ON and OFF cube, a cube of excess (ON minus OFF), and secondary products (also in the form of 3D sky cubes) such as an exposure cube (effective area times observation time) or a cube with the total flux from the sources. The ON cube comprises the predicted counts of both sources and background counts (being the three components smeared by Poisson noise). The OFF cube contains only predicted background counts smeared by Poisson noise. This is computed including the cosmic-ray background provided by the CTA IRFs for each particular offset (distance to the center of the field of view) and energy bin. The simulations take into account the CTA IRFs (effective area, energy resolution and the energy dependent point spread function) and the offset.

The sky cubes allow us to perform 1D spectral analysis projecting the cubes along the energy axis, and 2D morphological analysis using the *Sherpa* software (Freeman et al. 2001; Refsdal et al. 2009) for each energy bin of the cube. *Gammapy* provides a 1D *Sherpa* spectral fitting with maximum likelihood functions (Cash or Wstat, see Cash 1979) statistics and Nelder-Mead Simplex optimization method (Wright 1996; Lagarias et al. 1998) based on a forward-folding technique (Piron et al. 2001). The input of the sky cube generator is an analytical spectral model (Table 1) and a morphological model for each source together with the desired configuration of the cubes (spatial and energy axis binning, energy limits, pointing coordinates and cube size, coordinate system and projection, observation time and offset). We produced the cubes in the whole energy range of CTA covered by the IRFs, and observation times from seconds up to 300 hours. The best-fit spectral parameters are derived following the procedure explained in `http://docs.gammapy.org/dev/spectrum/fitting.html#spectral-fitting`.

The *ctools*[3] software package (Knödlseder et al. 2016) has been developed to perform analysis of gamma-ray instruments. *ctools* is based on *GammaLib*. The spectral studies of the Crab nebula we present (§3.1) have been checked using the two frameworks, *ctools* and *Gammapy*, independently. To make this comparison we performed observation simulations of the Crab nebula and pulsar with *ctools* in addition to the simulated 3D sky cubes. *ctools* performs maximum likelihood fitting of a model to unbinned or binned data, or joint maximum likelihood analysis in the case of data coming from different observations or instruments. We used maximum likelihood fitting in unbinned mode. The results obtained with the two analysis chains were compatible within 1σ error.

We performed simulations of the Crab pulsar (point-like source with the spectrum model detailed in §4) for different observation times and fluxes in the energy range between 20 GeV and 180 TeV (with the mentioned CTA IRFs). We used templates for different phase curve models, which are also explained in §4. We assigned the events phases in the region of interest (defined as a circle of 0.1° of radius) according to the timing model from Zampieri et al. 2014 at epoch 55178 MJD. The *ctools* tool *ctprob* computes the probability for each event to either belong to the source or to the background component. This tool was used to reject the events with probability of belonging to the source smaller than 95% from the simulations. Once the time properties were applied to the events, the signal was evaluated fitting the individual peaks to normal distributions (applying maximum likelihood estimation) and the periodicity was analyzed with the H-test statistic (De Jager et al. 1989).

2.2 Systematic errors

The systematic errors are the dominant source of uncertainty when studying in detail a bright source such as the Crab. For this reason, we need to take them into account in our simulations to guarantee a correct assessment of the CTA capabilities.

The reconstruction of events, the Monte Carlo determination of the effective area, and the uncertainty in atmospheric conditions and background are some of the many sources of systematic errors in air Cherenkov telescope measurements. The systematic error in the energy scale (E_0), for example, is requested to not exceed 4% (CTA 2018), which constitutes an improvement of at least a factor of 2 over the current measurements (Aharonian et al. 2004, 2006; Aleksić et al. 2015; Holler et al. 2015). We have taken into account that the systematic error of the flux (at a given apparent energy) must be less than a 10% between 50 GeV and 300 TeV (CTA 2018). To include these errors on the spectral models considered in the Crab nebula studies (see §3.1.), we first simulate the spectrum taking into account only statistical errors by performing 1D analysis fitting over the simulated data, obtained from the convolution of the analytical models (Table 1) with the CTA IRFs. The expected flux for each of the energy bins was then computed and smeared by adding quadratically the systematic errors to the statistical ones. The systematic error on the energy scale is already taken into account prior to the smearing of the expected flux in each energy bin. To include it, we allowed the energy scale to fluctuate according to a 4% of systematic error, as discussed above. We refit the new spectral points, in which both the statistical error and the systematic ones are added, and we use these results as input for the discrimination tests (see §3.1). Finally, we have considered a factor 2 improvement over the fiducial requirements for the systematic errors.

[2] https://github.com/emestregui/The-CTA-Crab-Nebula-and-Pulsar/tree/master/3D_cubes_simulator_archive
[3] http://cta.irap.omp.eu/ctools/

3 THE CRAB PULSAR WIND NEBULA

3.1 Spectral shape

First of all, we estimated the minimum observation time that is needed to detect the Crab nebula at 5σ level at different energy ranges. In particular, the highest energy bin (E > 50 TeV) considered is the energy interval that will allow the definitive discrimination between the different above-mentioned spectral models. We simulated the Crab nebula spectrum from 20 GeV up to 300 TeV under the different spectral assumptions that are listed in Table 1. The simulations are performed with *Gammapy* over equally spaced moving intervals of observation time spanning between 0.001 hr and 300 hr, with steps of increasing width within the $10^{-4} - 0.1$ hr. We computed the significance of each observation simulation using equation 17 of Li & Ma (1983). We performed 5000 realizations for each spectral model and observation time considered. Table 2 shows the minimum observation time needed to achieve a mean significance of 5σ. In addition, it also shows that the Crab can be detected at 5σ in less than 25 seconds for either model from Table 1 in the most sensitive among the computed bins [0.1-1] TeV. The highest energy bin containing a 5σ signal in 300 hr extends up to $E \approx 60$ TeV for the PLEC-HESS, and $E \approx 100$ TeV for the LP-MAGIC and the LP-HAWC assumptions. We estimated the CTA capabilities to disentangle between the different mathematical approximations listed in Table 1. We computed thus the expected distribution of the excess events in bins of energy for each of the considered spectral models and for 50 hr of observations. To evaluate the statistical uncertainties on the excess, each of the spectral models was simulated 5×10^3 times, and from these distributions the mean and deviance were obtained. We compared the distributions in pairs using a chi-square test. The probability of two distributions resulting from two different hypotheses to be compatible is rejected in all cases (with a probability of 95% CL) when comparing the whole energy range of the simulations. This is mainly due to the differences of the hypotheses in the lower energy range. Even when considering only the cutoff region, above 8 TeV it is possible to discriminate between LP-MAGIC and PLEC-HESS at 95% CL. Also, the LP-MAGIC, LP-HAWC and LP-HESS models were distinguishable among each other above 8 TeV of energy. In addition, at energies above 50 TeV the HESS-PLEC model was distinguished from MAGIC/HAWC log-parabolas and vice versa.

We also fitted the data obtained simulating the LP-MAGIC spectrum for 50h of observation time to each of the spectral shapes listed in Table 1 (log-parabola, power law and power law with an exponential cutoff). All the parameters of the models fitted to the data were free except for the energy of reference (fixed to 1 TeV). The most energetic bin at which the source was detected was 50 TeV - 80 TeV with a significance of 5σ (80 TeV - 125 TeV with a significance of 3σ). We used the Akaike's Information Criterion (AIC) (P Burnham & R Anderson 2004) to evaluate the goodness of the fitted model. The AIC took a value of 33.7 for the log-parabola model (33.0 if the systematic errors added to the simulated spectrum are improved by a factor 2). For the power law and power law with an exponential cutoff fitted models, the value of the AICs were 84.4 and 126.2 respectively (or 190.2 and 461.2 respectively with the mentioned systematic improvement). Figure 1 shows the comparison between the models using the current systematic errors on the CTA requirements (left) and those ones improved by a factor 2 (right).

Our second goal is to compute the lower limit on the energy cutoff as a function of the observation time. We simulated a power law spectral model with the same α and N_0 value of the LP-MAGIC function for different observation times, spanning from 8 hr to 300 hr and 10^5 realizations for each observation time, then we fitted the obtained results with a power law with an exponential cutoff and computed the lower limit of the energy cutoff at 95% confidence level (CL). The results are illustrated in Figure 2.

Finally, we test the CTA capabilities to disentangle between different cutoff shapes, thus we considered the following modified power law with exponential cutoff function:

$$\frac{dN}{dE} = N_0 \left(\frac{E}{E_0}\right)^{-\alpha} \exp\left[-\left(\frac{E}{E_{\rm cutoff}}\right)^{k}\right] \qquad (2)$$

Different values of k can reflect either the energy-dependence of the particle propagation mechanisms with k=1/3, 3/11, 1/4, and 1/5 being the Bohm, Kraichnan, Kolmogorov, and hard-sphere turbulence spectral models (in Thomson regime), respectively (Romoli et al. 2017) or the transition from the Thomson to the KN region of the IC mechanism. In the specific case of IC scattering of synchrotron photons in the KN regime, which is the dominant regime in the Crab nebula, Lefa et al. 2012 computed the following possibilities: k= 3/2, 5/3, 2, 3 (corresponding, in this regime, to the same electron cutoff shape; $k = \beta_e$, see Table 1 of the cited paper). We assumed as primary hypothesis the PLEC-HESS spectral model which is the $k = 1$ specific case of Eq. 2. This can be considered as a rather optimistic case, since the latest results by MAGIC (Aleksić et al. 2015), H.E.S.S. (Holler et al. 2015) and HAWC (HAWC Collaboration et al. 2019) indicate that the spectral break should occur at higher energies, where the statistics becomes more and more an issue. We simulated a power law with an exponential cutoff spectrum following the PLEC-HESS assumption for 50 h of observation time and then we fitted the results with Eq. 2 and k=1, 3/2, 5/3, 2, 3. The AIC computed for each of these fitting functions with respect to case of k=1 (taking the values of 34.6, 52.7, 79.6, 196.31 for k=1, 3/2, 5/3 and 2, and a value >> 200 for k=3) is always positive and indicates that it is possible to disentangle between an exponential and a super-exponential cutoff shape with a minimum k value of 3/2 (see Figure 3). We also simulated the various Eq. 2 using the above k values to be compared against each other. The results show that it will be possible to discriminate within each other, even when including systematic uncertainties. The smallest difference in the β parameter that was distinguished at 95% CL from the $\beta = 1$ model (for the observation time and systematic error improvement considered) was $\Delta\beta \approx 0.2$.

The comparison of the fitting results obtained with the two science tools is shown in the appendix. The results obtained with the two different science tools are consistent within the statistical uncertainties.

	N_0 [$cm^{-2}s^{-1}TeV^{-1}$]	E_{ref} [TeV]	α	β	E_{cutoff} [TeV]
PL	2.83×10^{-11}	1	2.62	-	-
LP-MAGIC	3.23×10^{-11}	1	2.47	0.104[1]	-
LP-HESS	17.9×10^{-11}	0.521	2.1	0.24	-
PLEC-HESS	3.76×10^{-11}	1.0	2.39	-	14.3
LP-HAWC	2.35×10^{-13}	7.0	2.79	0.1	-

Table 1. Spectral models for the IC component of the Crab nebula used in literature. The corresponding references, in order of appearance, are Aharonian et al. (2004); Aleksić et al. (2015); Holler et al. (2015); Aharonian et al. (2006); HAWC Collaboration et al. (2019).

[1] In Aleksić et al. (2015) the log-parabola formula is written with decimal logarithm, in this work we used the natural logarithm instead.

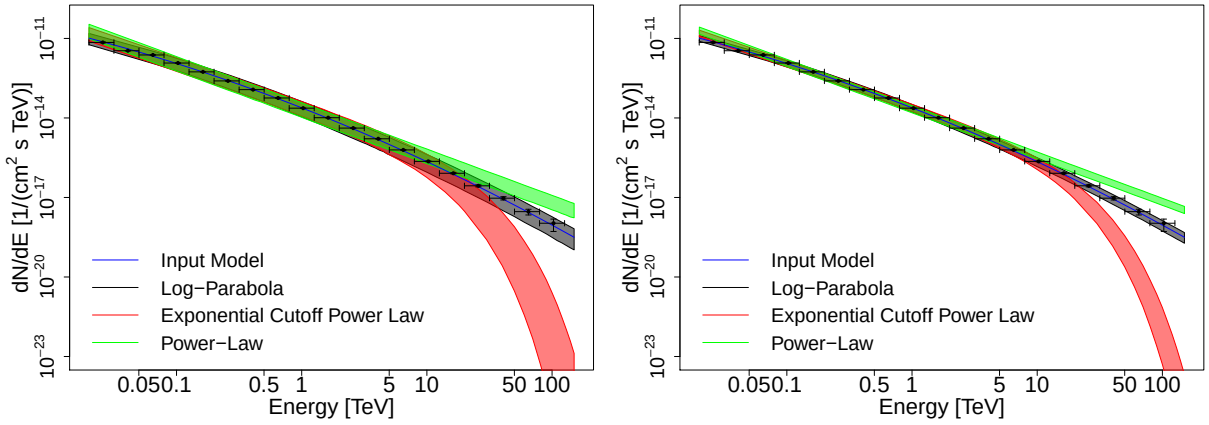

Figure 1. Result of fitting all the spectral shapes considered to the simulations for the nebula of LP-MAGIC model (Table 1), with 3σ error region noted. Results under the assumption of the systematic error requirements in §2.2 (left), and with the systematic uncertainty improved by a factor of 2 (right) are shown.

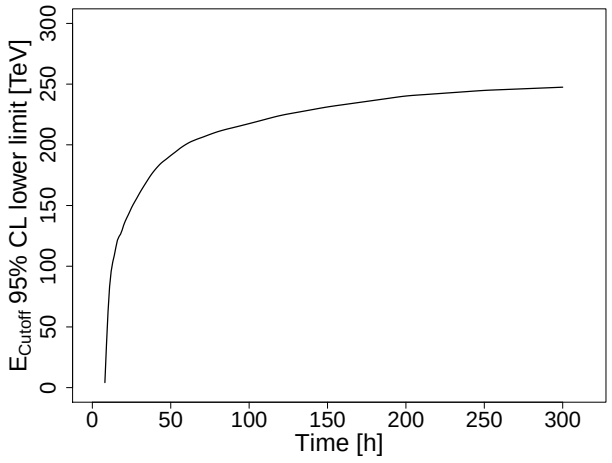

Figure 2. Energy cutoff lower limit at 95% CL for different observation times.

Table 2. Minimum observation time (in hours) needed to obtain a 5σ detection of the Crab nebula in various energy ranges and under different assumptions for the spectral model. We considered the spectral models listed in Table 1

Energy [TeV]	PL	LP-HAWC	LP-MAGIC	LP-HESS	PLEC-HESS
$E < 0.1$	0.027	0.40	0.37	3.8	0.059
$0.1 < E < 1$	0.0053	0.0037	0.0056	0.007	0.0046
$E > 5$	0.16	0.13	0.17	0.22	0.15
$E > 50$	10.1	18.4	30.3	233	298

3.2 Morphology

In the following, we study the capabilities of CTA to measure the nebular shrinking with increasing energies, hence to determine what is the maximum energy at which the Crab can be significantly resolved by CTA. In addition, we will assess the potentialities of CTA in detecting asymmetries in the Crab morphology. The Crab at ten TeV is expected to

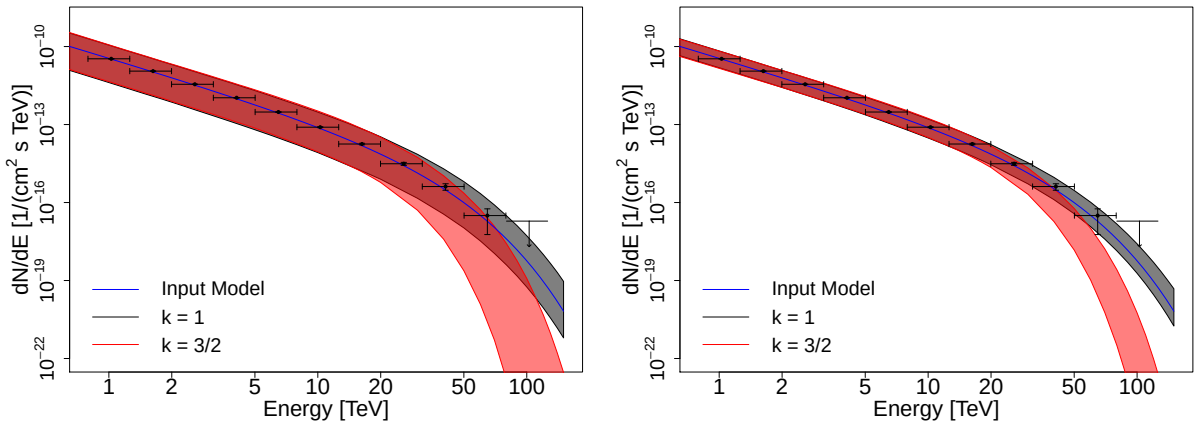

Figure 3. CTA capabilities to disentangle between different shapes of an exponential spectral cutoff, i.e. different values of k, as in Eq. 2. In particular, we show the two cases of k=1 and k=3/2. The shaded area represent the systematic and statistic errors, quadratically added. On the left, the errors are calculated using the systematic error requirements, whereas on the right, the systematic errors have been reduced by a factor 2.

exhibit the jet-torus structure revealed by *Chandra* (Volpi et al. 2008) and although the arcsecond resolution of the X-ray detectors is certainly beyond the CTA performance, such a complex structure translates on a clear asymmetry in the two spatial dimensions.

For all simulations performed in this section we accounted for 50 hr of observations and we assumed a spectral shape following the prescription of the LP-MAGIC model.

To evaluate the capabilities of CTA to resolve the extension of the Crab nebula, we simulated in *Gammapy* 3D sky cubes a 2D projected spherical source with a LP-MAGIC spectral model. We varied the sphere radius from 0.004° (the smallest value of size per bin considered in the simulated sky cubes was of 0.002°/bin) to 0.03° in steps of 0.002° for 14 different integral energy bins of lower energy bounds equally spaced in a log-scale spanning from 50 GeV to 50 TeV and a fixed upper bound of 300 TeV. We assume a Gaussian-shaped PSF and obtained the 68% containment radius from the CTA IRFs. After convolving the energy-binned sky maps with the corresponding PSF, we fit the resulting image with a projected 2D sphere convolved with the PSF using the sherpa tool. We called the minimum resolvable radius at a given energy bin to the smallest radius of the source for which the fitted size is significantly greater than zero (at 3σ) and also compatible with the input radius at 95% CL. The minimum resolvable radius is shown in Fig. 4, which reflects the effect of the PSF and the spectral shape. The cross and dot mark respectively the extension of the Crab nebula as measured with *Fermi*-LAT and H.E.S.S. The results show that CTA will be able to resolve the Crab nebula at a large energy range, from tens of GeV to TeV energies.

To prove the capabilities to detect asymmetries in the morphology of the Crab at different energies, we used as spatial template for our simulations the synthetic surface brightness map at 1 TeV resulting from the 2-dimensional MHD simulations of the Crab performed in Volpi et al. (2008) (see Fig. 5a). To perform this simulation, we used *ctools* to import the 2D fits image provided by Volpi et al. 2008 and the CTA North full system requirements for the angular resolution (which are in good agreement with the

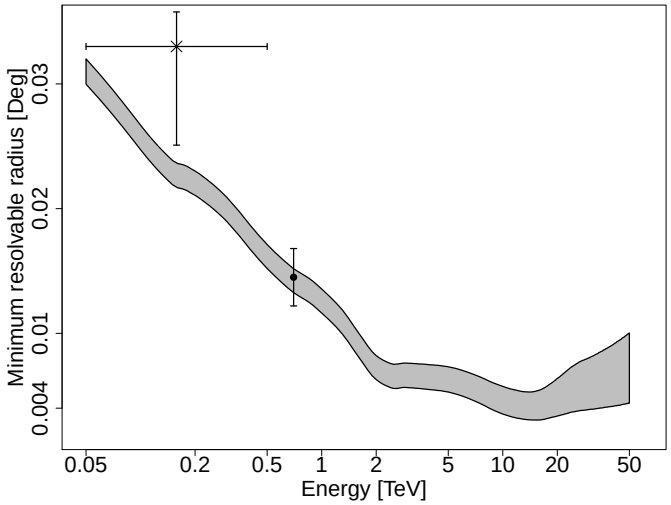

Figure 4. Minimum size resolvable in the simulations versus the lower energy bound of the energy interval simulated (the upper bound is always fixed to 300 TeV), using the CTA IRFs with the 1σ region noted. The measured size for the Crab nebula with H.E.S.S. for energies above 0.7 TeV (black dot), and the one measured from 5 GeV to 500 GeV with *Fermi*-LAT (black star) are plotted with the 1σ error bars for comparison.

angular resolution provided by the version of the IRFs used for previous analysis). The resulting sky map is shown in Fig. 5b for 100 h of observation time and an energy range spanning from 0.7 TeV to 100 TeV. To test the asymmetry of the resulting simulated events maps we performed 2D *Sherpa* morphological fittings. We compared the fitting results obtained by using a symmetric 2D Gaussian function and an asymmetric one. In the first case, a reconstructed size of $(0.017(8) \pm 0.0002)^\circ$ is obtained, whereas the asymmetric function is favored (with a $\sqrt{\mathrm{TS}} \simeq 21$) resulting in a σ_x of $(0.021(1) \pm 0.0002)^\circ$ and a σ_y of $(0.013(8) \pm 0.0003)^\circ$ along the major and minor axis respectively. For illustrative

purposes, we improve artificially the angular resolution by a factor 5, to show that in this case a jet-torus structure would be easily established (see Figure 5c, in fact a hint of the torus shape is already visible with a factor 4 of improvement). Also, in this case, the error in the reconstructed major and minor axis (σ_x and σ_y) for an assymetric Gaussian fit is improved by a factor ~ 10, retrieving an asymmetry of $\sigma_x/\sigma_y \sim 1.31 \pm 0.03$.

4 THE CRAB PULSAR

The state-of-the-art measurements of the Crab pulsar at VHEs show a three-feature light curve with two peaks, the main pulse P1 and the interpulse P2, and an extra emission component between P1 and P2 dubbed bridge emission. P1, which is the main pulse at GHz frequencies, defines the phase 0, whereas P2 is shifted by ~ 0.4 with respect to P1. Both width and intensity of the pulses, as well as of the bridge emission, are energy-dependent (Kuiper et al. 2001). In particular, in gamma rays, P2 becomes the dominant emission component at around 50 GeV (Aleksić et al. 2014), and both pulses are much narrower than in the *Fermi*-LAT energy band. In this work we assume as definition of the phase intervals the one in Aleksić et al. (2012) that is based on the VHE light curve fit results: $[-0.017 - 0.026]$, and $[0.377 - 0.422]$ for P1 and P2, respectively and the range in between for the bridge emission. The energy spectrum of the three components is well described by power law functions from 10 GeV on with P1 ($\Gamma = 3.5 \pm 0.1$) being 0.5 ± 0.1 steeper than P2 (Ansoldi et al. 2016). MAGIC reconstructed spectral points of the harder and brighter interpulse up to $\sim$1 TeV, with a lower limit on the energy of a possible cut-off at $\sim$700 GeV (Ansoldi et al. 2016). The bridge emission, that is very prominent at the energies accessible by *Fermi*-LAT, is well represented by a 3.35 power law function above 50 GeV and fades away at 150 GeV (Aleksić et al. 2014).

We simulated in *Gammapy* 3D sky cubes a point-like source at the position of the radio Crab pulsar (RA = 05:34:31.992 and DEC = +22:00:51.84, Lobanov et al. 2011) from 20 GeV to 180 TeV of energy and with a spectral index of 2.9 for a power law spectral model of 2×10^{-11} cm^{-2}s^{-1}TeV^{-1} of flux at 150 GeV (Ansoldi et al. 2016). We included in our background model the continuous emission from the Crab nebula, that was simulated as an extended source with the LP-MAGIC spectral shape. The maximum energies at which the source was detected for 300 hr of observation time were achieved in the energy bin spanning from 3 TeV to 7 TeV, at 3σ. Note that in the spectral studies performed for the Crab pulsar, the phase-average emission was simulated considering the spectrum of P2 (Ansoldi et al. 2016), which is harder than P1. Therefore, our approach to the observation simulations of the Crab pulsar can be considered as a somewhat optimistic case.

To explore the presence of spectral features, for example, a 'kink' at ~ 100 GeV resulting from two different spectral components we fitted the simulations of the pulsar to a smoothed broken power law fixing different values for the energy break, ranging from 80 to 150 GeV. From the fitted models, we retrieve the precision on the measurement of the spectral indices below and above the break energy assumed. The minimum difference between the two indices for which the total spectrum is no longer compatible with the single power-law input function at 95% CL, is defined as minimum index variation detectable. We obtained that the minimum index variation that could be detected was of ~ 0.6 at 95% CL in 300 hours with the energy break located at 150 GeV (see Fig. 6). The minimum index variation detectable improved as the break was located at a higher energy, in part because of the improvement of the CTA sensitivity and the reduction of noise, but mostly because the spectrum fit below the break (down to 20 GeV of energy) improves rapidly with the enlargement of the fitted energy range (and therefore with the increasing amount of energy bins to fit). The spectral fit above the break, however, is less sensitive to the energy break location, since the fitted energy range can be extended up to TeV energies. Note that the spectral index below the break energies considered can be better constrained combining CTA with measurements at energies below 20 GeV performed with other instruments (as e.g. MAGIC and/or VERITAS). The minimum index variation detectable above the break energies with respect to the input model index (of 2.9) corresponds approximately to the one in Figure 6 improved by a factor $0.5 - 0.7$, depending on the break location and observation time.

Finally, we extended the simulations to study the capability of CTA to detect pulsed emission, considering different light curve shapes. For that, we used in *ctools* different templates with a single Gaussian peak (discretised in bins of 0.01 of width in phase) in the position of P2 and gaussian σ of 0.01, 0.02 and 0.04 in phase, at different levels of flux. The periodicity was proved with the H-test statistic for the events with folded phases (De Jager et al. 1989), and the probability associated with an H-test statistic for the best number of harmonics was taken from De Jager & Büsching (2010) result and converted into a Gaussian sigma (with the area under the Gaussian probability density function integrated from σ to infinity). The results are shown in Figure 7. We also tested the minimum flux necessary to detect the periodicity at 5σ, fixing the observation time (Fig. 8). Figures 7 and 8 then represent the sensitivity of CTA to detect pulsars displaying different light curves and flux levels above 80 GeV, and can be used for future pulsar population studies.

5 DISCUSSION AND CONCLUSIONS

We have studied the expected capabilities of the future CTA observatory regarding the observation of the Crab nebula and pulsar, testing the main existing tools for CTA simulations and data analysis, *Gammapy* and *ctools*. Note that this study is limited in some respects; the CTA IRFs used for this work are not optimized for the specific simulations described in this paper, and do not take into account the IRFs of the southern CTA telescope array, which is expected to optimize the spectral results at high energy. In addition, the analysis has not been optimized for angular resolution. However, from this first approach and considering the limitations of the available simulations, we can derive the following statements:

- (1) Our approach to the problem, the 3D *Gammapy* sky cube generation allow us to place simulations of two objects in the same position with different morphology and spectral

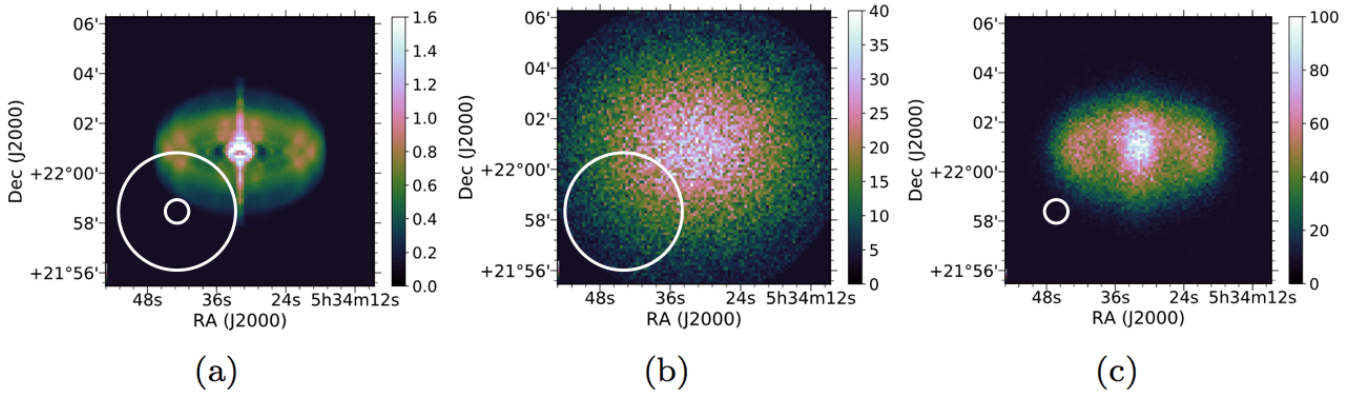

Figure 5. a) Morphological template used for the jet-torus scenario. The white circles represent the PSF one sigma for the full system requirements (of approximately 0.04° for the energy bin spanning from 0.8 TeV to 1.25 TeV), and the same improved by a factor of 5 (i.e. 0.008° referred to the same energy bin). It is a surface-brightness map in units of erg $cm^{-2}sr^{-1}s^{-1}Hz^{-1}$. b) Observation simulation of 100 hours with the CTA full system requirements for the angular resolution plotted with the corresponding PSF (white circle), in counts (after background subtraction). c) Observation simulation as in b), but with the angular resolution improved by a factor of 5 (exceeding by far the current CTA system requirements), again with the corresponding PSF.

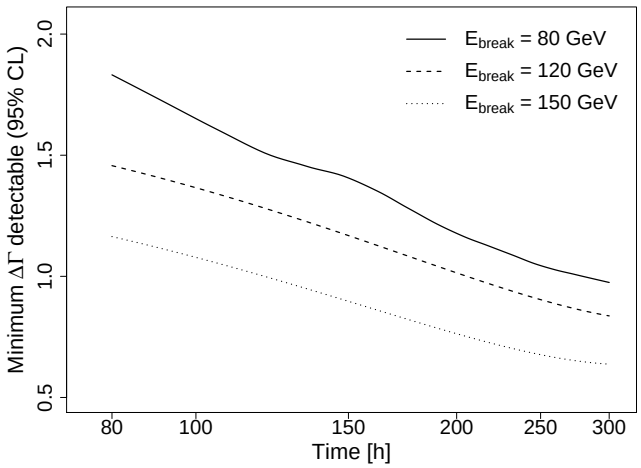

Figure 6. Minimum index variation detected (at 95% CL) resulting from fitting the pulsar spectrum to a smoothed broken power law, fixing different energy breaks (in the legend) at different observation times.

characteristics, plus the background. Therefore, this tool can be used for other complex systems or to study other important problems like source confusion in crowded regions of the sky. We also tested the two main analysis chains developed by the CTA Consortium, *ctools* and *gammapy*, and demonstrated they produce statistically compatible simulations and results of the spectral analysis.

• (2) We applied a statistically approach to estimate the CTA potential to answer all the open questions with respect the gamma-ray emission attributed to the Crab Nebula. We also included the, usually overlooked, systematic errors. Even considering the latest, which are the largest source of uncertainties in the current measurements, we showed that CTA will be able to discriminate between different hypotheses in a moderate observation time. Given the large energy range covered by the detector, CTA will disentangle between the different mathematical descriptions proposed (log-parabola, exponential cutoff power-law and simple power-law) within less than 50 h with high confidence. We estimated not only the minimum cutoff that can be proved, but also the ability to parametrize the shape of this cutoff within a precision of $\Delta\beta = 0.2$, CTA will determine the domain in which particles are accelerated and cooled (see Lefa et al. 2012).

• (3) Concerning the morphology, we derived a general shape for the minimum size detectable that can be easily scaled when more realistic IRFs are used. Within this conservative approach, we already proved that CTA will provide invaluable input when comparing with theoretical predictions, for instance as a result of hydrodynamical or magneto-hydrodynamical simulations. We proved that CTA will be able to disentangle sub-parsecs structures ($\sim 0.02°$ for a distance of ~ 2.2 kpc), which is crucial to understand the origin of the emission observed. In fact, our simulation shows that CTA will be able to image the nebula for the first time, allowing for instance the comparison with high energy resolution images in the X-ray regime. The simulations also show that CTA will access the effect of cooling processes of the electrons powering the nebula (see Fig. 4), and provide a continuous resolved image from a few tens of GeV to tens TeV. This will close the gap between the size measured by *Fermi*-LAT and the one by H.E.S.S. (Holler et al. 2017), tracing the behavior of multiple-energy electron populations.

• (4) With respect to the Crab pulsar, we studied the energy range in which the pulsed spectrum can be measured, and therefore the maximum energy to which the particles are accelerated. CTA will be able to detect pulsed photons up to 7 TeV in a time of 300 h. Even if this observation time (which is nevertheless conservatively estimated) looks high, it is important to mention that Crab is considered the standard candle in the gamma-ray domain, and therefore will be deeply observed from the beginning of the observatory working time. If the spectrum extends indeed well beyond 1 TeV, some of the models proposed to explain the extension

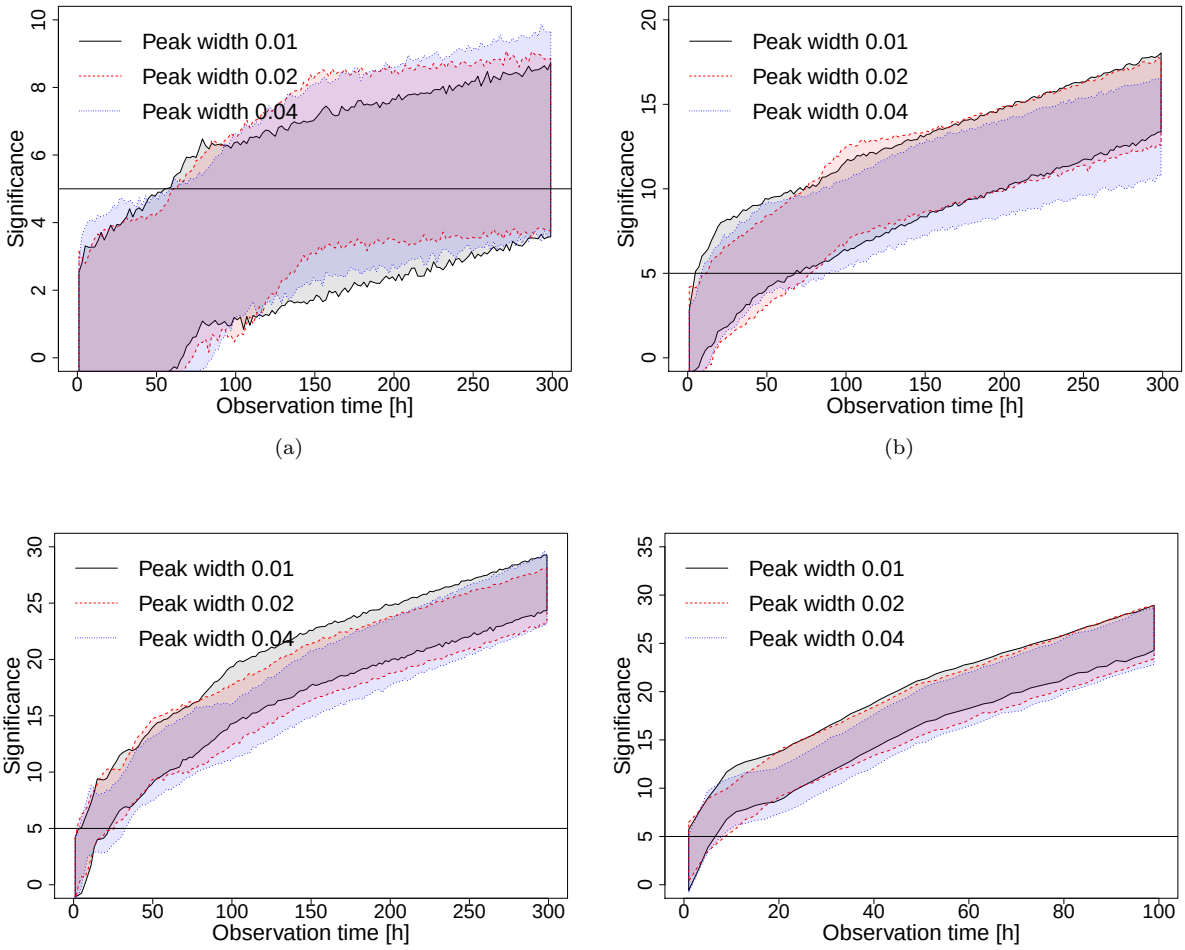

Figure 7. Evolution of the significance of the periodicity detection (3σ region) with time for a source of flux (a) 0.2, (b) 0.5, (c) 1, (d) 2, times the integral flux of the Crab pulsar from 20 GeV to 180 TeV of energy and the spectrum considered

. The curves are smoothed by interpolation method and the 3σ region was computed by bootstrapping (Efron 1979) of the H-statistic and simulations.

of the pulsed emission, such as the ones based on synchrotron emission, will be heavily challenged. Likewise, the maximum energy detected will provide direct evidence of the region in which the radiation is located and therefore on the inner structure of the pulsar wind nebula. Also, the minimum spectral index variation that could be detected if an energy break occurs between 80 GeV and 150 GeV was established. Finally, we derived a general description of the power of CTA to detect different light curves shapes (from sharp peaks as in Crab, 0.01 gaussian sigma width in phase, up to 4 times wider peaks). Measuring with high-quality data the shape of the VHE pulse profile and comparing it with those obtained at lower energies can be used for constraining the location of the emission regions in different bands.

Certainly, our knowledge of the instrument response will increase in the upcoming months, during the construction and scientific verification phase of the observatory. The results summarised in this work are a conservative estimation of the potential of CTA to unveil the many unknowns behind the physics of the Crab Nebula and pulsar gamma-ray radiation. More realistic studies will emerge from the science verification phase describing the real power of CTA.

6 ACKNOWLEDGEMENTS

This research was supported by the grants AYA2017-92402-EXP, SGR2017-1383, PGC2018-095512-B-I00, SGR2017-1383 and iLink 2017-1238. This research made use R Project for Statistical Computing (R Core Team 2013). This research made use of the CTA instrument response functions provided by the CTA Consortium and Observatory, see http://www.cta-observatory.org/science/cta-performance/ (version prod3b-v1) for more details. This research made use of *ctools*, a community-developed analysis package for Imaging Air Cherenkov Telescope data. *ctools* is based on *GammaLib*, a community-developed toolbox for the high-level analysis of astronomical gamma-ray data. This research also made use of *Astropy*, a community-developed

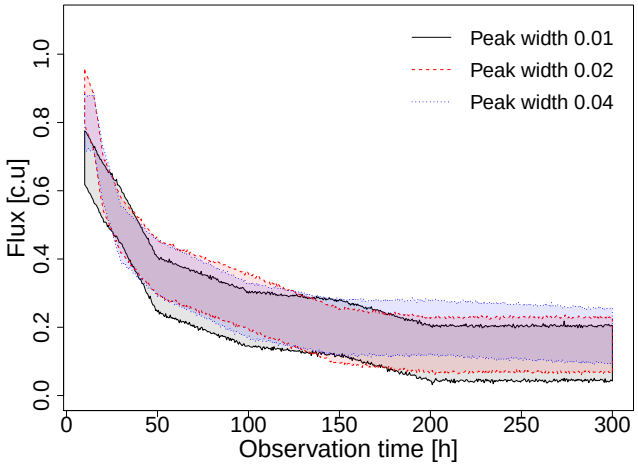

Figure 8. Minimum source flux (in the same units of Figure 7) necessary to detect a periodicity at a 5σ-level as a function of the observation time for Gaussian peak templates. The shadowed regions depict the 3σ error.

core Python package for Astronomy (*Astropy* Collaboration, 2018).

We are very thankful to D. Volpi, L. Del Zanna, E. Amato and N. Bucciantini for providing us with the synthetic surface brightness map of Crab at 1TeV published in Volpi et al. (2008). E. de O. W. acknowledges the Alexander von Humboldt Foundation for financial support.

7 APPENDIX

7.1 Comparison of Gammapy and ctools results

Figure 9 proves that the spectral fitting results of *Gammapy* and *ctools* are compatible between each other. Also, *ctools* and *Gammapy* fitting results present similar statistical errors.

REFERENCES

Abdo A. A., et al., 2010, The Astrophysical Journal, 708, 1254
Abdo A. A., et al., 2011, Science, 331, 739
Abdo A. A., et al., 2012, ApJ, 750, 63
Abeysekara A. U., et al., 2017, ApJ, 843, 39
Acharya B. S., et al., 2013, Astroparticle Physics, 43, 3
Aharonian F., et al., 2004, The Astrophysical Journal, 614, 897
Aharonian F., et al., 2006, Astronomy and Astrophysics, 457, 899
Aharonian F. A., Bogovalov S. V., Khangulyan D., 2012, Nature, 482, 507
Aleksić J., et al., 2011, The Astrophysical Journal, 742, 43
Aleksić J., et al., 2012, Astronomy and Astrophysics, 540, A69
Aleksić J., et al., 2014, ApJ, 565, L12
Aleksić J., et al., 2015, Journal of High Energy Astrophysics, 5, 30
Aliu E., et al., 2008, Science, 322, 1221
Aliu E., et al., 2011, Science, 334, 69
Ansoldi S., et al., 2016, A&A, 585, A133
Atoyan A. M., Aharonian F. A., 1996, Monthly Notices of the Royal Astronomical Society, 278, 525
Bucciantini N., Arons J., Amato E., 2010, Monthly Notices of the Royal Astronomical Society, 410, 381
Burtovoi A., Zampieri L., 2016, Monthly Notices of the Royal Astronomical Society, 459, 3783
CTA c., 2018, CTA System-Level Science Performance Requirements.,
Cash W., 1979, Astrophysical Journal, 228, 939
Cerutti B., Philippov A. A., Spitkovsky A., 2016, MNRAS, 457, 2401
Cheng K. S., Ho C., Ruderman M., 1986, ApJ, 300, 500
Contopoulos I., Kazanas D., Fendt C., 1999, Astrophys. J., 511, 351
Davidson K., Fesen R. A., 1985, Annual review of astronomy and astrophysics, 23, 119
De Jager O. C., Büsching I., 2010, Astronomy and Astrophysics, 517, L9
De Jager O. C., Raubenheimer B. C., Swanepoel J. W. H., 1989, Astronomy and Astrophysics, 221, 180
De Oña-Wilhelmi E., et al., 2013, Astroparticle Physics, 43, 287
Deil C., et al., 2017, International Cosmic Ray Conference, 35, 766
Efron B., 1979, Annals of Statistics, 7, 1
Fermi-LAT Collaboration Biteau J., 2018, Astrophysical Journal, 237, 32
Freeman P., Doe S., Siemiginowska A., 2001, in Starck J.-L., Murtagh F. D., eds, Proc. SPIE Vol. 4477, Astronomical Data Analysis. pp 76–87 (arXiv:astro-ph/0108426), doi:10.1117/12.447161
HAWC Collaboration et al., 2019, arXiv e-prints
Hassan T., et al., 2015, preprint (arXiv:1508.06075)
Hester J. J., 2008, Annual Review of Astronomy & Astrophysics, 46, 127
Hillas A. M., et al., 1998, The Astrophysical Journal, 503, 744
Holler M., et al., 2015, preprint (arXiv:1509.02902)
Holler M., Berge D., Hahn J., Khangulyan D., Parsons R. D., for the H. E. S. S. collaboration 2017, preprint, (arXiv:1707.04196)
Kaplan D. L., Chatterjee S., Gaensler B. M., Anderson J., 2008, The Astrophysical Journal, 677, 1201
Kennel C. F., Coroniti F. V., 1984, ApJ, 283, 710
Knödlseder J., et al., 2016, Astronomy & Astrophysics, 593, A1
Kuiper L., Hermsen W., Cusumano G., Diehl R., Schönfelder V., Strong A., Bennett K., McConnell M. L., 2001, A&A, 378, 918
Lagarias J., A. Reeds J., H. Wright M., Wright P., 1998, SIAM Journal on Optimization, 9, 112
Lefa E., Kelner S. R., Aharonian F. A., 2012, ApJ, 753, 176
Li T.-P., Ma Y.-Q., 1983, Astrophysical Journal, 272, 317
Lobanov A. P., Horns D., Muxlow T. W. B., 2011, Astronomy and Astrophysics, 533, A10
Lyutikov M., 2013, Monthly Notices of the Royal Astronomical Society, 431, 2580
Lyutikov M., Otte N., McCann A., 2012, ApJ, 754, 33
Mangano S., Delgado C., Bernardos M., Lallena M., Rodríguez Vázquez J. J., 2018, arXiv e-prints, p. arXiv:1810.00592
Martín J., Torres D. F., Rea N., 2012, MNRAS, 427, 415
Meagher K., VERITAS Collaboration 2015, in 34th International Cosmic Ray Conference (ICRC2015). p. 792 (arXiv:1508.06442)
Meyer M., Horns D., Zechlin H. S., 2010, A&A, 523, A2
Mochol I., Pétri J., 2015, Monthly Notices of the Royal Astronomical Society, 449, L51
P Burnham K., R Anderson D., 2004, Sociological Methods Research, 33, 261
Pacini F., Salvati M., 1973, ApJ, 186, 249
Piron F., et al., 2001, Astronomy and Astrophysics, 374, 895
R Core Team 2013, R: A Language and Environment for Sta-

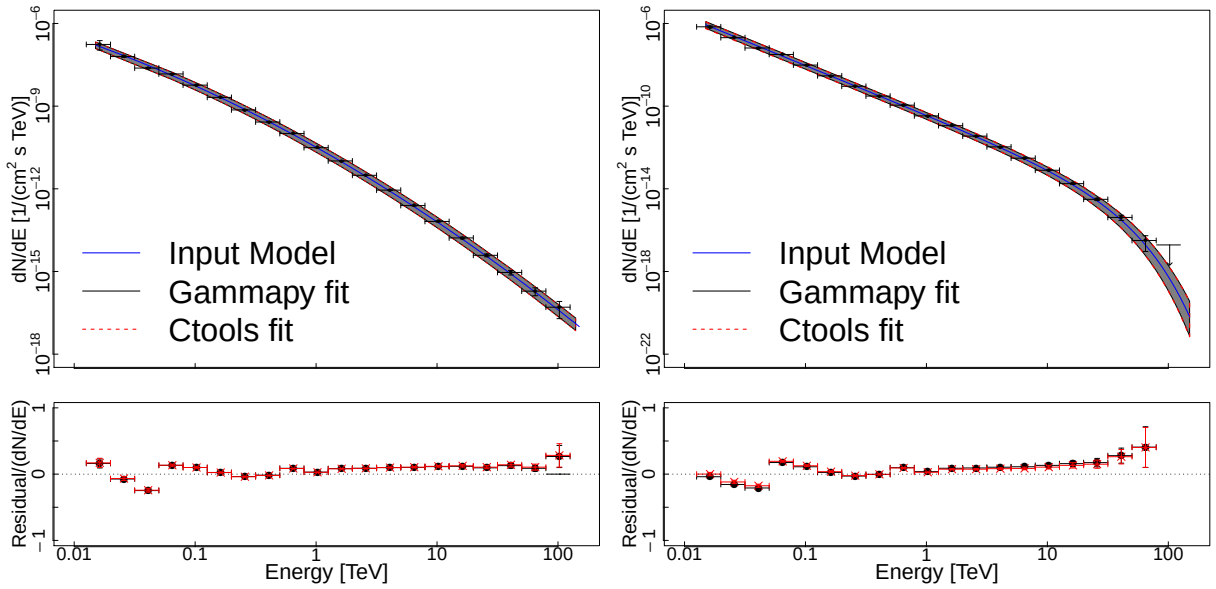

Figure 9. Results of the simulations with LP-MAGIC (left) and a PLEC-HESS (right) models fitted with *Gammapy* and *ctools*.

tistical Computing. R Foundation for Statistical Computing, Vienna, Austria, http://www.R-project.org/
Refsdal B. L., et al., 2009, in Varoquaux G., van der Walt S., Millman J., eds, Proceedings of the 8th Python in Science Conference. Pasadena, CA USA, pp 51 – 57
Romoli C., Taylor A. M., Aharonian F., 2017, Astroparticle Physics, 88, 38
Shilon I., et al., 2019, Astroparticle Physics, 105, 44
Smith D. A., et al., 2000, Nuclear Physics B Proceedings Supplements, 80, 163
Tanaka S. J., Takahara F., 2010, arXiv e-prints, p. arXiv:1001.2360
Torres D. F., 2018, Nature Astronomy, 2, 247
Torres D. F., Martín J., de Oña Wilhelmi E., Cillis A., 2013, Monthly Notices of the Royal Astronomical Society, 436, 3112
Torres D. F., Cillis A., Martín J., de Oña Wilhelmi E., 2014, JHEAp, 1-2, 31
Torres D. F., Viganò D., Coti Zelati F., Li J., 2019, Monthly Notices of the Royal Astronomical Society, 489, 5494
Trimble V., 1973, Publications of the Astronomical Society of the Pacific, 85, 579
Viganó D., Torres D. F., 2015, Monthly Notices of the Royal Astronomical Society, 449, 3755
Volpi D., Del Zanna L., Amato E., Bucciantini N., 2008, Astronomy and Astrophysics, 485, 337
Weekes T. C., et al., 1989, Astrophysical Journal, 342, 379
Wright M., 1996, Direct search methods: Once scorned, now respectable. Addison-Wesley, pp 191–208
Yeung P. K. H., Horns D., 2019, ApJ, 875, 123
Zampieri L., et al., 2014, Monthly Notices of the Royal Astronomical Society, 439, 2813

MNRAS **000**, 000–000 (2018) Preprint November 18, 2020 Compiled using MNRAS LATEX style file v3.0

The Crab nebula variability at short timescales with the Cherenkov Telescope Array

E. Mestre[1,2], E. de Oña Wilhelmi[1,2,3], D. Khangulyan[4], R. Zanin[5], F. Acero[6], D. F. Torres[1,2,7]

[1] *Institute of Space Sciences (ICE/CSIC), Campus UAB, Carrer de Can Magrans s/n, 08193 Barcelona, Spain*
[2] *Institut d' Estudis Espacials de Catalunya (IEEC), 08034 Barcelona, Spain*
[3] *Deutsches Elektronen Synchrotron DESY, 15738 Zeuthen, Germany*
[4] *Department of Physics, Rikkyo University, Nishi-Ikebukuro 3-34-1, Toshima-ku, Tokyo 171-8501, Japan*
[5] *CTA Observatory GmbH, Via Piero Gobetti 93, I-40129 Bologna, Italy*
[6] *AIM, CEA, CNRS, Université Paris-Saclay, F-91191 Gif-sur-Yvette Cedex, France*
[7] *Institució Catalana de Recerca i Estudis Avançats (ICREA), E-08010 Barcelona, Spain*

November 18, 2020

ABSTRACT

Since 2009, several rapid and bright flares have been observed at high energies (>100 MeV) from the direction of the Crab Nebula. Several hypotheses have been put forward to explain this phenomenon, but the origin is still unclear. The detection of counterparts at higher energies with the next generation of Cherenkov telescopes will be determinant to constrain the underlying emission mechanisms. We aim at studying the capability of the Cherenkov Telescope Array (CTA) to explore the physics behind the flares, by performing simulations of the Crab Nebula spectral energy distribution, both in flaring and steady state, for different parameters related to the physical conditions in the nebula. In particular, we explore the data recorded by *Fermi* during two particular flares that occurred in 2011 and 2013. The expected GeV and TeV gamma-ray emission is derived using different radiation models. The resulting emission is convoluted with the CTA response and tested for detection, obtaining an exclusion region for the space of parameters that rule the different flare emission models. Our simulations show different scenarios that may be favourable for achieving the detection of the flares in Crab with CTA, in different regimes of energy. In particular, we find that observations with low sub-100 GeV energy threshold telescopes could provide the most model-constraining results.

Key words: instrumentation: detectors — stars: supernovae: individual: Crab Nebula – stars: flare

1 INTRODUCTION

The Crab nebula has been used as standard candle in gamma-ray astronomy since the first Imaging Air Cherenkov Telescopes (IACTs) began to operate. The science verification period of the current and future IACTs rely on observations of the, in principle, stable gamma-ray flux detected in the bright nebula, and it has been used to characterise the performance of different instruments (Aharonian et al. 2000; Aleksić et al. 2015; Holler et al. 2015; Meagher & VERITAS Collaboration 2015; Aleksić et al. 2016; Abeysekara et al. 2019; Amenomori et al. 2019). However, several flares of different magnitude have been detected in the last years with spaceborne gamma-ray instruments (Abdo et al. 2011; Tavani et al. 2011; Buehler et al. 2012; Ojha et al. 2013; Mayer et al. 2013; Striani et al. 2013; Arakawa et al. 2020a) in the high-energy regime (HE, ≥ 100 MeV) with variability time scales of hours (Abdo et al. 2011, Tavani et al. 2011, Balbo et al. 2011). During these flaring periods, the flux of the nebula shows rapid variations, releasing a huge amount of energy: for example, during the April 2011 flare, first detected by *Fermi*-LAT (Buehler et al. 2011; Buehler et al. 2012) and later confirmed by AGILE (Striani et al. 2011), the nebula doubled its HE flux level with respect to the steady state in less than 8 hours. A review of the different flares detected up to September 2013 can be found in Bühler & Blandford (2014). The rapid variability and the energy range in which the flares are detected point to a phenomenon associated to fast variation of magnetic fields and/or compact regions. These two ingredients do not favour a rapid variation (at a detectable level with the current generation of Cherenkov telescopes) in the inverse Compton (IC) component that emerges in the TeV regime (Horns & Aharonian 2004). A large effort was done to follow those flares in several multi-wavelength campaigns (Weisskopf et al. 2013; H. E. S. S. Collaboration et al. 2014) to search for a new ingredient that could shed light on the mechanisms underlying the flares observed. These observations did not result in any positive correlation between spectral and/or morphological variations of the nebula and the (hundreds of) MeV flares.

Several theoretical works have been put forward to explain the characteristics of the observed emission, which results in different predictions of the flux level at different wavelengths. In particular, the GeV regime can be accessed by current

and future IACTs with great sensitivity (CTA, Acharya et al. 2013; MAGIC Collaboration et al. 2019; Abdalla et al. 2019).

The detection of transients is one of the Key Science Programs (KSPs) of the Cherenkov Telescope Array (CTA, Acharya et al. 2013). It comprises the ability to rapidly respond to a broad range of multi-wavelength alerts from other observatories, being the design of the telescopes optimized for rapid movement. In this paper, we explore the capability of CTA to constrain the flare contribution in the GeV and TeV regime. For that purpose, we performed a number of simulations to reproduce the ∼400 MeV emission detected by gamma-ray satellites, and derived the expected emission in the high energy regime, under different conditions of magnetic and photon fields, and particle spectral energy distribution. The comparison with the CTA simulated data (see Mestre et al. 2020), and previous IACTs observations (H. E. S. S. Collaboration et al. 2014) result in constraints on the physical parameters ruling the flare emission.

The paper is structured as follows: in Section 2 we describe the analysis technique, including the parameters and variables chosen for the simulations. We show the results of the simulations in Section 3. In Section 4, we discuss the potential of CTA to constrain different theoretical scenarios proposed to explain the flare emission. Finally, in Section 5 we emphasise some of the conclusions we reached in this work.

2 SIMULATIONS AND METHODS

To evaluate the capability of CTA to explore the properties of the population of electrons behind the flares in the Crab nebula, we first explore its basic physical parameters (in Section 2.1) and the properties of its flares (Section 2.2). Second, we fit the flare spectrum assuming a classical synchrotron emission as coded in the NAIMA PYTHON package (Zabalza 2015) and calculate the corresponding IC component for different realizations of magnetic field strengths (Section 2.3). Finally we convolve the synchrotron tail and IC components with the CTA response, including the expected emission from the nebula and derive the CTA sensitivity for different population of electrons compatible with the flare emission observed (Section 2.4).

2.1 General physical properties of the Crab nebula

The broad-band spectrum of the nebula consists of a wide synchrotron component and a narrow IC peak. Synchrotron radiation is expected to be the dominant channel in which particles cool down. Therefore, the radiation observed critically depends on the strength of the magnetic field. The average magnetic field strength in the nebula is well-constrained through the multi-wavelength properties of the Crab Nebula to be $\bar{B} \sim 120\mu$G (see,e.g., Atoyan & Aharonian 1996; Hillas et al. 1998; Martín et al. 2012; Khangulyan et al. 2020b). The flares can occur however in particular locations of the nebula, where the magnetic field can be very different from the average one (see, e.g., Kennel & Coroniti 1984; Lyubarsky 2012; Porth et al. 2014). The flare spectral index also shows a large variability from flare to flare (Bühler & Blandford 2014; Arakawa et al. 2020b), which results on a large range of particle indices to consider, when calculating the parent particle population.

The IC component emerges from high energy electrons upscattering several photon targets: the cosmic microwave background (CMB), far-infrared (FIR), near-infrared (NIR) photon background fields, and the synchrotron emission, which is believed to dominate the total gamma-ray emission of the nebula. The FIR background is typically attributed to an isotropic photon field emitted by dust, at a temperature of 70 K with an energy density of 0.5 eV/cm^3, while the NIR background photon field is usually described for starlight with temperature of 5000 K and energy density of 1 eV/cm^3 (Atoyan & Aharonian 1996). These background fields can be approximated as diluted Planckian distributions and the corresponding emission spectra can be obtained based on an approximate treatment (Khangulyan et al. 2014). The Synchrotron Self-Compton (SSC) component however depends on the size of the emission region. For the total nebula, with a radius of $R_{\rm SYN} \sim 1.5$ pc, the total energy density provided by the synchrotron photons amounts:

$$\omega_{\rm SSC} = \frac{2.24 L_{\rm SYN}}{4\pi c R_{syn}^2} \simeq 2 \text{ eV cm}^{-3}$$

(where the factor 2.24 is obtained for a homogeneous spherical source, Atoyan & Aharonian 1996), for a total luminosity in the synchrotron regime of the nebula of $L_{\rm SYN} \sim 10^{37}$erg s^{-1} (see Table 1 in Aharonian et al. 1997). The fast variability observed on the flares nonetheless, limits the size of the emission regions (due to causality arguments). For a duration of t_{var}, the size of the emission region should be limited to $c \times t_{var}$.

Considering the uncertainties described above, we simulate our particle population using a range of particle indices between $\Gamma_{\rm e}$=[1–3] (associated to non-thermal acceleration processes, Longair 1981). To calculate the corresponding synchrotron emission we use a relatively broad range of magnetic field intensities, for particular regions in which the flares might occur, spanning from a few μG and mG. Likewise, the IC part is calculated using the CMB and IR photon targets, whereas the SSC contribution is obtained for each particular flare duration considered. Finally, the space of parameters is also a priori limited by the total energy budget stored in the nebula. The latest can be estimated as the product of the nebula luminosity in γ-rays ($L_\gamma \sim 2 \times 10^{35}$ erg s^{-1}, see Rudak & Dyks 1998) and synchrotron cooling time ($\tau_{\rm SYN}$) for the electrons (with energy E_e) of the nebula:

$$\tau_{\rm SYN} L_\gamma = \frac{3 m_e^4 c^7}{2e^4} E_{\rm e}^{-1} B^{-2} \sim 5 \times 10^{43} (B/100\,\mu\text{G})^{-2} \text{ erg} \quad (1)$$

Note however, that this energy limit does not account for reacceleration of particles, that can result on additional boosts of energy.

2.2 Gamma-ray properties of the Crab Nebula flares

We performed the simulations for two flares with different characteristics: a very bright one with parameters similar to the one observed by *Fermi*-LAT in April 2011 (Striani et al. 2011; Buehler et al. 2012), and a moderated-flux flare as the one observed in March 2013 (Ojha et al. 2013; Mayer et al. 2013). For the latest, simultaneous observations with the H.E.S.S. and VERITAS experiments were performed (H. E. S. S. Collaboration et al. 2014; Aliu et al. 2014), which allow us to test the limits on the parameters space with the

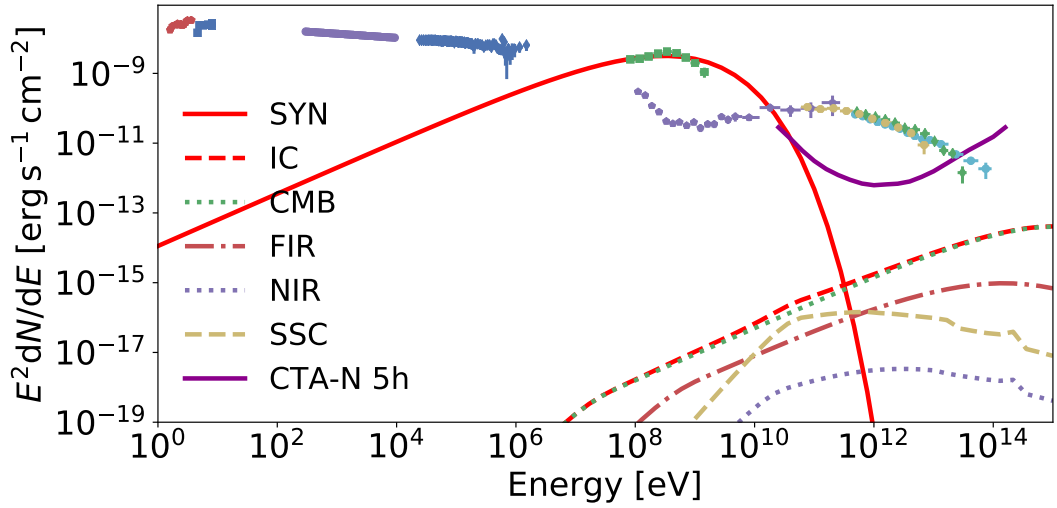

Figure 1. Synchrotron and IC of a simulated flare (fitted to the 2011 April flare spectrum) with B = 100 μG and $\Gamma_e = 1.5$. The synchrotron and total IC emissions are plotted in red solid and dashed line, respectively. The rest of the lines represent the IC with CMB, FIR and NIR background photon fields and the SSC. The magenta solid line represents the sensitivity of the CTA northern array (for 5 h of observation time, see the instrument response functions[1]). The green squares correspond to the nebula spectrum during the 2011 April flare (as seen by *Fermi*). The rest of the data correspond to the steady nebula emission (the compilation was taken from Meyer et al. 2010 and Buehler et al. 2012).

current IACT sensitivity. In the following we briefly describe the main characteristics of both flares. The data points are extracted from Bühler & Blandford 2014.

The gamma-ray flare detected in April 2011 (Striani et al. 2011; Buehler et al. 2012) lasted nine days, reaching a peak photon flux of $(186 \pm 6) \times 10^{-7}$ cm^{-2}s^{-1} above 100 MeV, implying a flux enhancement by approximately a factor 30 compared to the average flux from the Crab nebula (Buehler et al. 2012). The γ-ray flares from the Crab show complex substructures with sub-flares of duration of a few hours. For instance, the April 2011 flare had two sub-peaks centered around the dates 55665 and 55667 (in MJD), both with a doubling timescale (t_{var}) smaller than 8 h, implying (because of causality arguments) a compact emission region smaller than $c \times t_{var} \sim 2.8 \times 10^{-4}$ pc in size. The flare spectral energy distribution (SED) had a distinctive narrow shape, peaking at $E_{peak} \simeq 400$ MeV.

The Crab flare of March 4, 2013 was reported by *Fermi*-LAT (Ojha et al. 2013; Mayer et al. 2013) and AGILE (Striani et al. 2013) when the peak photon flux of the synchrotron emission for energies above 100 MeV was $(103.4 \pm 0.8) \times 10^{-7}$ cm^{-2}s^{-1}, about 17 times above the level of the steady component. The flare lasted for approximately two weeks and the variability was measured on timescales of $\sim$ 5 hours, which results on a region size of $\lesssim 1.7 \times 10^{-4}$ pc (Mayer et al. 2013). Interestingly, the SED peaked at an energy of $\sim$ 400 MeV at the time of the highest flux, as in the case of the April 2011 flare. Observations of the flare were carried out with different instruments, providing the opportunity to study the emission during the flaring state at multiple wavelengths, from infrared to X-rays (Mayer et al. 2013) and also in the very high energy (VHE) regime (Aliu et al. 2014; H. E. S. S. Collaboration et al. 2014). A blind search of flares in Crab by ARGO-YBJ air shower detector reported no significant excess of events during the 2011 and 2013 flares (Bartoli et al. 2015). The observations conducted with VERITAS and H.E.S.S. the following days after the 2013 flare reported also no significant changes in the flux of the nebula (above 1 TeV). Considering systematical and statistical errors, both observations result in similar upper limits to the variability of the integral flux of $\sim 55 - 65\%$ (for a 95% CL). We used a fiducial value of 60% to compare with our simulations.

2.3 Simulation of the electron particle distribution

The electron particle distribution simulated to reproduce the observed flares is characterized by a power-law distribution with an exponential cutoff:

$$\frac{dN_e}{dE} = N_0 \left(\frac{E}{1\mathrm{TeV}}\right)^{-\Gamma_e} \exp\left(-\frac{E}{E_p}\right) \quad (2)$$

The magnetic field (B) and the particle index (Γ_e) are the only parameters left free in order to derive the resulting SED of synchrotron radiation from the electron population. The maximum energy reached, the amplitude of the gamma-ray spectrum (which is determined by the amplitude of the electron particle distribution, N_0), and the particle spectrum cutoff energy are obtained from fitting the spectrum at hundreds of MeV to the different data sets employed (the LAT measurements of the April 2011 and March 2013 flares). The fitting is performed by means of a log-likelihood optimization method, implemented using the open-source software NAIMA (Zabalza 2015).

We compute, first, the amplitude (N_0) and the cutoff energy of the particle spectrum (E_p), for the chosen particle index and magnetic field, by fitting the resulting synchrotron emission to the Fermi-LAT flare data.

We considered Γ_e ranging from 1 to 3 as argumented above (in linearly spaced bins of 0.1) and the magnetic field (B) ranging from 10 μG to 5 mG in 14 bins (10 μG, 100 μG and

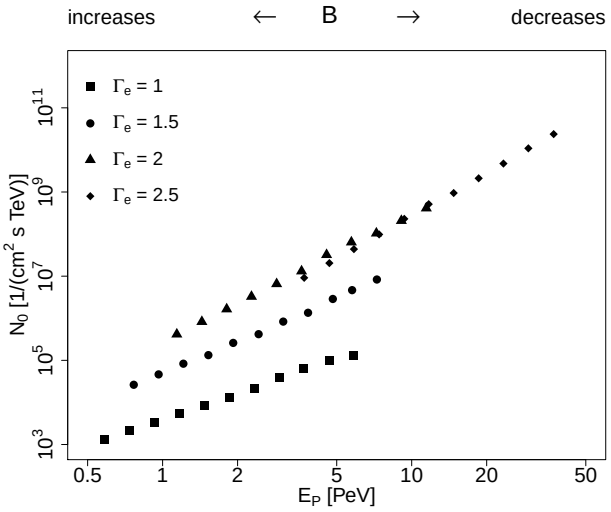

Figure 2. The fitted amplitude of the electron energy distribution (N_e), with respect to Γ_e, E_p, and B for the April 2011 flare. For each value of Γ_e, the points correspond from left to right to 11 values of magnetic field logarithmically spaced from 5 mG to 50 µG.

1 mG, plus 11 values logarithmically spaced from 50 µG to 5 mG). Note that both very low (10µG) and very large (few mG) magnetic fields are difficult to justify in standard pulsar wind nebula (PWN) theory. However, we include them to cover all possible hypotheses, and to probe the performance of the simulations over a very large parameters space. In the discussion section, we will only focus then on results for $B >$ 50 µG.

The synchrotron emission is computed using the NAIMA PYTHON package (Zabalza 2015), according to the approximation of the synchrotron emissivity in a random magnetic field in Aharonian et al. 2010. We selected a minimum electron energy of 50 GeV. The amplitude and cutoff energy of the resulting emission spectrum for each fixed value of Γ_e and B is fitted to the 2011 (or 2013) flare observations. Using the resulting amplitude, we obtain the total density of electrons N_0 and compute the corresponding IC on all relevant photon targets. The total SED of the flare (see Figure 1 as an example) is obtained as the sum of these different contributions. Both the synchrotron and IC are computed for 100 bins of energy logarithmically spaced from 10^{-7} eV to 1 PeV. Finally, from the IC component integration, we obtained the total energy in electrons above 1 TeV (W_e) for the different flare models, which can be directly compared with the upper limit estimated in Section 2.1.

To illustrate the effect of the different parameters on the simulation, we plot in Fig. 2 the obtained amplitude (N_0) with respect to the fitted cutoff energy (E_p), for different values of Γ_e.

Additionally, we considered an alternative approximation for which we used a power-law decay for the synchrotron radiation model, instead of an exponential one (as expected for jitter radiaton, Kelner et al. 2013). In particular, we fitted the *Fermi* data above 400 MeV with simple power-law models of fixed index (Γ_{Jit}), ranging from 2.5 to 3.5 in bins of 0.1, and fitted the amplitude of the emission normalized to 0.85 GeV of energy.

2.4 Simulation of the CTA observations

The simulations of the observations were performed folding the result from the radiation model with the CTA Instrument Response Functions (IRFs, Hassan et al. 2015, version prod3b[1]). The later was done using the CTA GAMMAPY PYTHON tool (version 0.7, Deil et al. 2017). We used the IRFs corresponding to observations at low zenith angle (20°) from the northern array (aiming to guarantee the lowest energy threshold possible), and optimized for an exposure time of 5 h. The results of the simulations are presented here for a fiducial observation time of 10 h.

The resulting spectrum is then reconstructed by means of a fitting process, using maximum likelihood (implemented in SHERPA, see Cash 1979) and Nelder-Mead Simplex optimization method (Wright 1996; Lagarias et al. 1998) based on a forward-folding technique (Piron et al. 2001). To avoid possible problems arising from the discretization of the radiation model, we parametrized the result of our model using an exponential power-law function (from 20 GeV to 200 GeV) and a power-law one (from 1.25 TeV to 50 TeV) to account for the MeV/GeV synchrotron contribution and the IC one at TeV's, respectively. The detection of flares at energies from 200 GeV to 1 TeV is considerably more difficult to achieve, since both the synchrotron and IC emissions from the flare are expected to be several orders of magnitude dimmer than at tens of GeVs and TeVs, respectively (see Fig. 1).

In our simulations, the background is dominated by the emission from the nebula, specially in the TeV regime. To account for that, we used the results from the simulations presented in our previous work (Mestre et al. 2020). In particular, we used the spectral shape described as a log-parabola as in Aleksić et al. 2015. The cosmic-ray background is provided by the CTA IRFs and computed in the simulations of the nebula, both in flaring and steady state. To evaluate the capability of CTA to disentangle variations on the large Crab nebula steady emission, we proceed as following:

- We fit the simulated spectrum (flare plus steady emission) in the GeV (i.e from 20 GeV to 200 GeV) and TeV regimes (from 1.25 TeV to 50 TeV) to simple power-laws.
- We compute the integral flux in both GeV and TeV regimes, using the best-fitted models.
- We compute the mean total expected excess (i.e., expected counts from the source, with background subtraction) and its standard deviation, by iterating over 10^4 realisations for each model of flare (and 10 h of observation time).
- The integral flux and mean expected excess in both GeV and TeV regimes are also computed for the flare and steady components individually, to use them as reference.
- To compare the non-flaring and flaring SED, we use a Pearson's chi-squared test, being the excess distribution the observed data (H_1), to be compared to the steady state as expected data (null hypothesis H_0). This test is then done for each of the 10^4 realisations. We consider that a flare is detected when the null hypothesis can be rejected at 99% CL.
- Finally, we compute the enhancement of integral flux

[1] The version prod3b of the IRFs and the CTA science performance requirements are public and available in https://www.cta-observatory.org/science/cta-performance/

above 1 TeV (with respect to the simulations of the nebula in steady state) expected for the different models of flares, defined as:

$$Z = \frac{\int_{1\mathrm{TeV}}^{300\mathrm{TeV}} \mathrm{F}_{\mathtt{flare,E}}\,\mathrm{d}E + \int_{1\mathrm{TeV}}^{300\mathrm{TeV}} \mathrm{F}_{\mathtt{Steady,E}}\,\mathrm{d}E}{\int_{1\mathrm{TeV}}^{300\mathrm{TeV}} \mathrm{F}_{\mathtt{Steady,E}}\,\mathrm{d}E}\,. \quad (3)$$

Note that models representing flares with very different spectral shapes can result in similar flux enhancements in Eq. 3.

Furthermore, to test the capability of CTA to detect flares of different duration from the ones described above, we compute the minimum flare duration (using as fiducial flux level the one in the 2011 flare) that could be detected by the CTA northern array (for different values of B and Γ_e). For each of those, we performed 5000 observation simulations of the nebula in both steady and flaring state, and applied chi-square tests between the excess distributions as explained above. Instead of the 10h considered above, we used different observation times, ranging from 0.01 h to 500 h (in adaptative bins varying from 0.01 h to 1 h in size), and calculate the minimum time to detect a significant variation with respect to the steady state. To consider the varying observation time properly, we used the IRFs optimized for an exposure time of 50 h, 5 h, and 0.5 h and re-scaled the total energy in electrons above 1 TeV (W_e) from the one obtained in 10 h.

Finally, we have not considered in our simulations the effect of the systematic errors, which should be in principle the main limitation to measure variability over the nebula baseline flux. The many uncertainties on the CTA final systematics prevent us from estimating its quantitative effect on the simulations. Therefore, the results of this work should be considered as an optimistic case.

3 RESULTS

3.1 Application to the Crab 2011 gamma-ray flare

The general effect of the magnetic field and Γ_e on the expected γ-ray spectra of the flares is summarised in Fig. 3 (for the synchrotron part), and in Fig. 4 (for the IC one). The first figure focuses on the sub-100 GeV region. The synchrotron spectrum in the GeV regime does not depend significantly on the magnetic field, due to the fitting of the synchrotron emission to the LAT data, which constrains strongly the synchrotron flux level above hundreds of MeV. We show (see Table 1 and Fig. 3) that CTA should be able to detect a flare with similar flux to the one observed in 2011 in all cases tested. In fact, our simulations prove that the detection should be possible in less than one hour for $\Gamma_\mathrm{e} > 1.0$ below 200 GeV, representing a variation of integral flux in the GeV regime stronger than 20 per cent of the nebula steady flux. The detection was achieved for stepper spectra ($\Gamma_\mathrm{e} > 2.0$) in less than an hour, even at higher energies (up to 300 GeV). This is possible due to the large flux expected on the GeV regime when the threshold is low enough. For instance, the predicted excess (in counts) for the steady nebula (with 10 h of CTA northern array) from 20 GeV to 120 GeV, is ~ 2 times the excess predicted from 1.25 TeV to 50 TeV. To emphasize the effect of detectability of the synchrotron part, given the high flux expected as the energy threshold decreases, we also showed in Fig. 3 the sensitivity of CTA using only 4 Large Size Telescopes (LSTs) in the North site, and the one of the MAGIC telescopes (Aleksić et al. 2016). For bright flares, the large CTA-LST sub-array should be sufficient to impose strong constrain on the synchrotron tail. Even for current instruments like MAGIC (see Fig. 3, magenta dot-dashed line), prospects are optimistic, allowing a good determination of the particle spectrum if the right observation conditions are met, i.e., for a flux level similar to the one observed in the April 2011 flare, observations at low zenith angle (E < 300 GeV) may have resulted in a detectable enhancement of flux for a soft particle index ($\Gamma > 2$).

Table 1. Observation time (in hours) necessary to detect different models of flares (fitted to the 2011 April flare spectrum) at energies from 20 GeV to 120 GeV with the chi-square test applied to the excess distributions (at 99% CL). Note that we assume that Crab is in flaring state during the entire time of observation.

Γ_e	1.0	1.5	2.0	2.5
Time [h]	0.35	0.14	0.02	<< 1

On the contrary, the magnetic field has a strong effect on the TeV IC component (see Table 2 and Fig. 4), and strongly suppresses the flare contribution for very large intensities. Opposite to the sub-100 GeV regime, soft electron spectra favour the production of GeV-TeV photons, by promoting lower energy electrons which provide a larger SSC photon target field. From the simulations, we derived that only certain combinations of parameters characterising the flare emission result on a detectable variability over the total flux. If the power-law index of emitting particles is hard, $\Gamma_\mathrm{e} < 2.2$, then the IC emission from this population is detectable only for very weak magnetic fields, $\lesssim 50$ μG. For softer electron distributions, i.e. $\Gamma_\mathrm{e} > 2.5$, realizations with magnetic fields as large as 1 mG result in detectable levels of flux.

The observation times listed on Tables 1 and 2 are obtained by evaluating the excess observed over the contribution of the nebula (see Section 2.4). We attempted to reconstruct the spectral shape of the flare contribution, but only in a handful of cases a clear deviation with respect to the nebula steady spectrum was measured. For example, for $\Gamma_\mathrm{e} = 2.5$ and B = 100 μG, a significant difference of spectral indices of 0.66 ± 0.03 was measured below 300 GeV, with respect to the index measured in steady state for the GeV regime (2.33 ± 0.03), and with the break located at an energy of ~ 300 GeV. This effect is also present in the TeV regime (at a 3σ level), for which a significant variation in the spectral index (0.46 ± 0.03, with respect to 2.75 ± 0.03) is observed. Figure 5 shows the enhancement factor as defined in Eq. 3, applied to the flux of the flaring state and steady one above 1 TeV.

It is also interesting to note that none of the performed simulations results on a flux level above the nebula at energies below 1 MeV. Thus, low spatial resolution (> arcmin scale) instruments at lower energies cannot resolve the morphology of the nebula (see Fig. 1), preventing the detection of counterparts. However, this may not be the case if a power-law spectral shape cannot characterize the particle spectrum.

However, the numbers above do not consider the limitations regarding the total energy available in the system (limited to $\sim 5 \times 10^{43}$ erg, see Section 2.1). If no re-acceleration is taken into account (or any other way to provide a larger

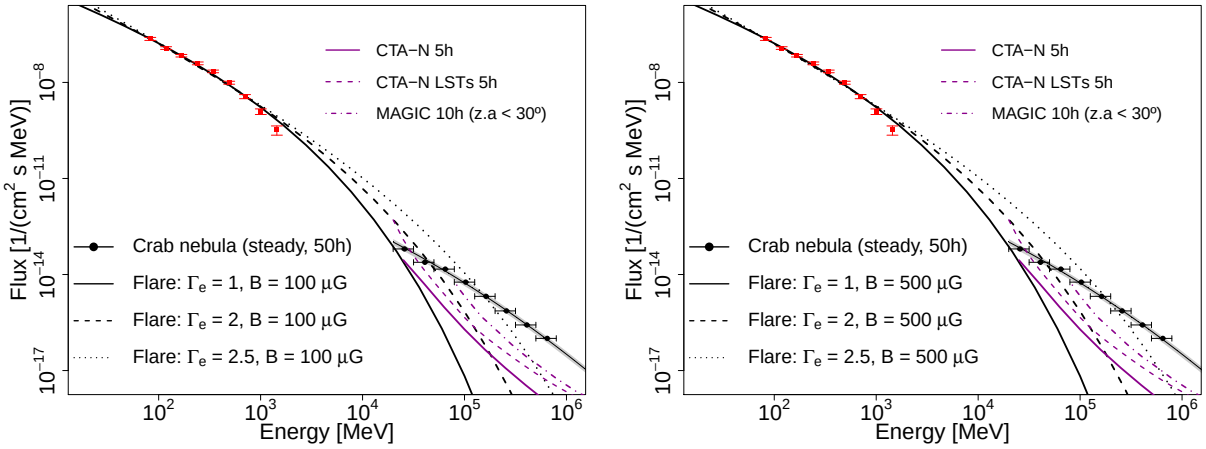

Figure 3. The synchrotron emission for flares (fitted to the 2011 April flare spectrum) of different indices ($\Gamma_e = 1, 2, 2.5$) and magnetic fields ($B = 100$ μG in the left panel, and 500 μG in the right one) together with the simulations of the Crab nebula steady spectrum (in black line with dots), with the 3σ region noted (black shaded area, with only statistical errors). The data recorded by *Fermi* of the 2011 flare is plotted in red squares. The magenta solid and dashed lines correspond to the sensitivities of the CTA northern array and if considering only its four Large Size Telescopes (for 5 h of observation time), respectively (see the instrument response functions[1]). The magenta dot-dashed line corresponds to the sensitivity of MAGIC stereo system at low zenith angle ($< 30°$) (see Tables A.5 and A.6 in Aleksić et al. 2016).

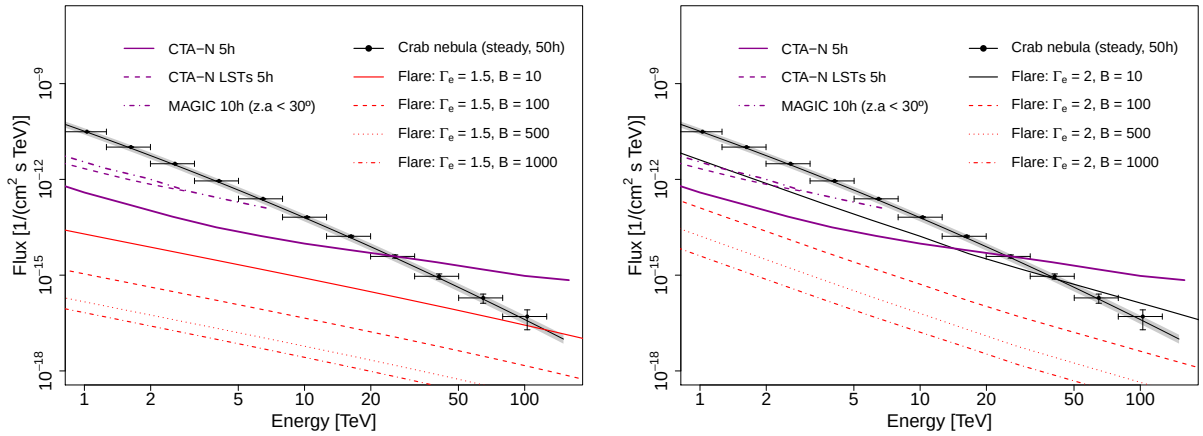

Figure 4. IC emission for different models of flares (fitted to the 2011 April flare spectrum, in black line if the flare is detected in the TeV regime, and in red line otherwise) with $\Gamma_e = 1.5$ (left) and $\Gamma_e = 2$ (right) on top of the simulations of the Crab nebula steady spectrum (in black line with dots), with the 3σ region noted (black shaded area, with only statistical errors). The SSC emission in a region of 2.8×10^{-4} pc in size is taken into account. The sensitivity curves (in magenta) are defined in Figure 3.

Table 2. Observation time (in hours) necessary to detect different models of flares (fitted to the 2011 April flare spectrum) at energies from 1.25 TeV to 50 TeV, obtained as Table 1. We assume that Crab is in flaring state during the entire time of observation. The models indicated with asterisks imply $W_e > 5 \times 10^{43}$ erg, if the duration of the flare is the one indicated. The Crab steady nebula was detected in 3.2 h at 5σ ($\sim 9\sigma$ in 10 h).

B[μG] \ Γ_e	1.5	1.8	2.1	2.5
1000	> 500	> 500	> 500	8.0
500	> 500	> 500	> 500	0.8
100	> 500	> 500	160*	0.02
50	> 500	> 500	40*	$<< 1$
10	> 500	93*	0.3*	$<< 1$

energy budget), only some combinations of magnetic field and spectral indices are therefore possible. For $\Gamma_e > 2.2$, the models with magnetic field below B ~ 500 μG are ruled out ($W_e > 5 \times 10^{43}$ erg). This value has to be increased to 1 mG when considering softer indices, $\Gamma_e > 2.5$. For spectral indices of the order of $\Gamma_e > 1$, only magnetic fields stronger than ~ 150 μG keep the total energy below the limit. This can be seen in Fig. 6, in which the shaded area mark the, in principle, forbidden values of B and Γ_e.

3.2 Application to the Crab 2013 gamma-ray flare

We applied the simulation scheme in Sections 2.3 and 2.4 to fit the *Fermi* data of the 2013 flare from 80 MeV to 1 GeV.

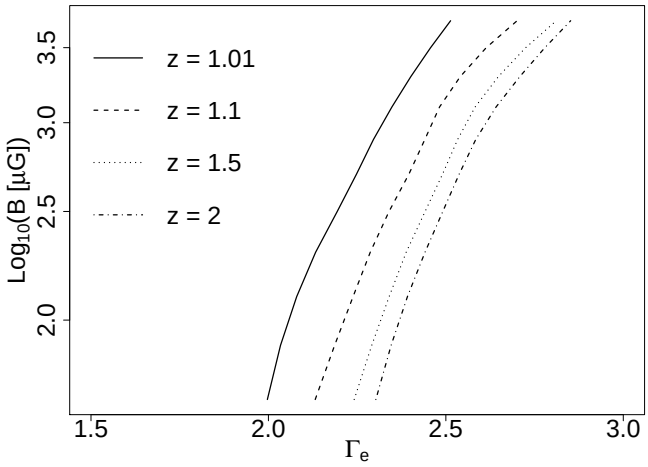

Figure 5. The enhancement of integral flux above 1 TeV (in Eq. 3) for the different models of flare (fitted to the 2011 April flare spectrum), taking into account the SSC.

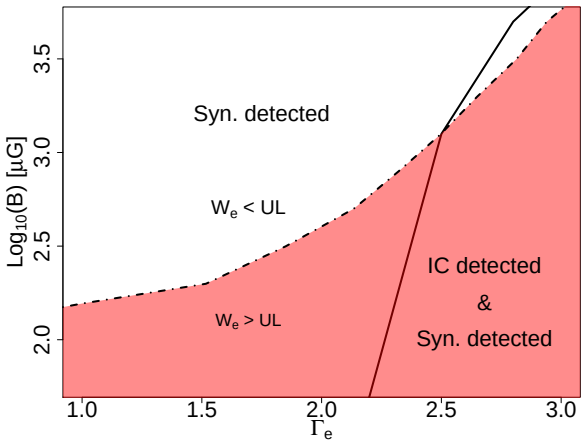

Figure 6. Results of the observation simulations of the flaring nebula, for the different models of flares, fitted to the *Fermi* data of the April 2011 flare. The models located below the solid line would be detected both in the TeV and GeV regimes (i.e., from 1.25 TeV to 50 TeV of energy, and below 200 MeV), if CTA would have observed, while the models above the solid line are detected only in the GeV regime. However, the models below the dash-dotted line (red shaded area) require an energy in electrons $W_e > 5 \times 10^{43}$ erg.

We considered the same parameters space as before, with the magnetic field strength in the range of 10 μG to 5 mG and Γ_e ranging from 1 to 3. For each model of flare simulated we computed the integral flux above 1 TeV, fitting the total IC (with the CMB, NIR and FIR photon fields) and taking into account the SSC in a region of 1.7×10^{-4} pc in size, and compared it to the integral flux of the simulations of the steady nebula. Then, the flux enhancement (see Eq. 3) for the different models of flares was compared to an upper limit similar to ones reported by H.E.S.S. and VERITAS, constraining the accelerating magnetic field and the particle index of the electron population.

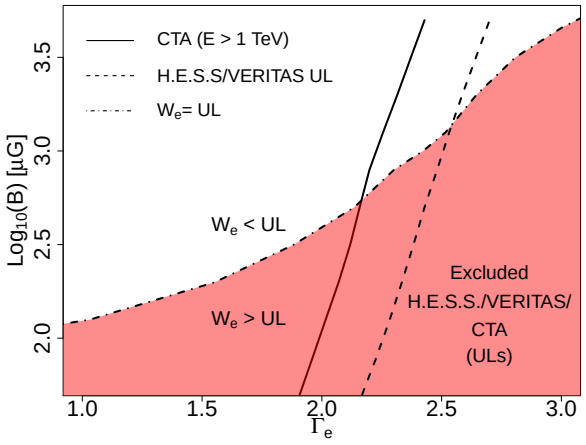

Figure 7. Results of the observation simulations of the flaring nebula, for the different models of flares fitted to the *Fermi* data of the March 2013 flare, compared to the upper limits established by H.E.S.S. and VERITAS observations. The models below the dashed line correspond to an enhancement of integral flux above 1 TeV larger than a 60% (i.e Z > 1.6 in equation 3). Therefore, these models violate the upper limits established by the H.E.S.S. and VERITAS observations of the 2013 flare. The exclusion region (for the integral flux upper limit above 1 TeV) extends up to the solid line (Z > 1.01, with only statistical errors) supposing the flare is not detected with 50 h of CTA northern array. The models below the dashed-dotted line (red shaded area) violate the upper limit estimated for the total energy in electrons.

The flares are detected in the GeV regime for $\Gamma_e > 1.4$, in 10 h of observation time, implying an enhancement of flux (and counts, in the GeV regime) above a 4 per cent with respect to the steady nebula. The results in the TeV regime are summarised in Fig. 7. The shaded area shows the exclusion region as on Fig. 6, due to the nebula energy budget. The CTA exclusion region (solid line) improves with respect to the one constrained by the H.E.S.S. and VERITAS observations (dashed line). It is interesting to note, that if the energy available is the one provided by Eq. 1, only a few combination of B and Γ_e results on a detectable flux, being this restriction more constraining than the one imposed by observations with CTA or the upper limits from the H.E.S.S. and VERITAS telescopes.

3.3 A power-law synchrotron spectrum in the GeV regime

In some theoretical approaches, the resulting emission beyond the maximum of the radiation might follow a power-law extending to high energies, instead of the standard exponential cutoff (as expected in turbulent magnetic field, see, e.g., Fleishman 2006; Kelner et al. 2013). To evaluate this possibility, we fit the *Fermi* data above 400 MeV of the April 2011 flare with a power-law photon spectrum and investigate the detectability in the GeV/TeV regime using the same approach described in Section 2.4. The fit to the LAT data results on a spectral photon index of 3.14 ± 0.13 (at 1σ) and a flux at 850 MeV of $(1.33 \pm 0.07) \times 10^{-9}$ cm^{-2} s^{-1} MeV^{-1} (with a reduced $\chi^2 = 1.4$ for two degrees of freedom). Note that the photon spectrum of the flare in the GeV regime is not

derived, in this case, from fitting the spectrum of an electron particle population.

The simulations of the flare fitted to the data with $\Gamma_{\rm Jit} = 3$ showed that the flare is always detected below 500 GeV (in 10 h), with the chi-square tests applied to the excess distribution. This model corresponded to an increase of integral flux of about $\sim 70\%$ in the GeV regime. We also tested a softer model with $\Gamma_{\rm Jit} = 3.5$, which produces also a detectable emission (in the same time) below 200 GeV of energy, with an increase of integral flux (and excess counts) of $\sim 9\%$ in the GeV regime. For harder spectrum the scenario is optimal. Using a $\Gamma_{\rm Jit} = 2.5$, the flare emission above the nebula can be observed up to TeV energies in 10 h. The integral flux is up to ~ 6 (~ 2) times larger than in steady state, in the GeV (TeV) regime. The enhancement of integral flux above 1 TeV, in this case, is therefore above the upper limit established by H.E.S.S and VERITAS (see Section 2.2).

Note that the simulations of the IC flares depend on the synchrotron emission of a fitted particle population (characterized by an exponential cutoff power-law spectrum, see Section 2.3), which would not reproduce in any case a power-law spectrum emission above 400 MeV as described above. Therefore, the simulations do not allow us to compute the IC emission or the particle spectrum in this scenario, and as a result, the energy in electrons (W_e) either.

4 DISCUSSION

The rapid MeV-GeV flares cannot be easily explained using the standard approach of PWN theory. In such, below few tens of GeV, the emission is believed to be dominated by the high-energy tail of the synchrotron emission produced by leptons in the shocked pulsar wind. This emission is limited, in an ideal MHD outflow, by the synchrotron burn-off limit, which in the plasma co-moving frame the peak of spectral energy distribution is below $\hbar\omega_{\rm MAX} < 200$ MeV (assuming that the acceleration and radiation sites are co-located, see, e.g., Guilbert et al. 1983). The steady spectrum measured in the Crab nebula seems to agree with this limit. To explain the variable emission that peaks above this limiting energy, a second component has to be invoked, that emerges at a few 100 MeV with a flux exceeding the nebula one. The origin of this second component however is unclear, and furthermore, the gamma-ray emission seems to be inconsistent with traditional synchrotron or IC mechanisms: while the fast variability timescale robustly rules the IC scenario out, the large peaking energy excludes the synchrotron scenario in the ideal MHD setup.

Since the discovery of the first flare (Tavani et al. 2011), several interpretations have been put forward to explain the Crab flares. Within the limits of an ideal MHD outflow, a relativistic-moving acceleration site (see, e.g., Bednarek & Idec 2011; Lyubarsky 2012; Lyutikov et al. 2018) and/or a radiation mechanism other than synchrotron (i.e., Jitter radiation as in Teraki & Takahara 2013) could in principle account for the observed emission. Alternatively, if the MHD assumptions are violated in some region, for example, due to reconnection of the magnetic field, an electric field component parallel to the magnetic field can be generated, resulting on a beam of high energy particles that will move along the unscreened electric field. These accelerated particles eventually escape from the region of acceleration and can be deflected by the average magnetic field. If the particles have supercritical energy, they should emit a substantial part of their energy over a time short compared to the girorotation (see, e.g., Cerutti et al. 2012). A somewhat similar situation can be realized if a beam of particles is accelerated in a low pair loading wind (Kirk & Giacinti 2017).

In the following, we discuss the constraints derived from our simulations to the different approaches, when possible, and offer different possiblities and prospects for CTA.

4.1 Relativistically Moving MHD Outflow

In the first class of scenarios (i.e. those that invoke relativistic MHD outflows), the emission site can be described as a region of size R', moving with a significant bulk Lorentz factor Γ, such that the Doppler boosting factor is $\delta_{10} \sim 1$ (here $\delta_{10} = 0.1/(\Gamma(1-\beta\cos\theta))$). In such a case, the strength of the comoving magnetic field B' should be high enough to satisfy the Hillas criteron:

$$R' > 3\times10^{15} E'_{\rm PeV} B'^{-1}_{\rm mG}\ {\rm cm} \tag{4}$$

where $E'_{\rm PeV}$ is the maximum comoving electron energy (in PeVs). Thus, the following condition must be satisfied:

$$E_{peak} = 600 E'^{2}_{\rm PeV} B'_{\rm mG}\ \delta_{10}\ {\rm MeV} \tag{5}$$

Also, if the synchrotron cooling time is responsible for the variability:

$$t_{syn} = 4\times10^{4} E'^{-1}_{\rm PeV} B'^{-2}_{\rm mG}\ \delta_{10}^{-1}\ {\rm s} \tag{6}$$

Combining the expressions above we obtain:

$$E'_{\rm PeV} > \left(\frac{E_{peak}}{600\,{\rm MeV}}\right)^{2/3} \left(\frac{t_{\rm var}}{4\times10^4\,{\rm s}}\right)^{1/3} \delta_{10}^{-1/3} \tag{7}$$

and

$$B'_{\rm mG} < \left(\frac{E_{peak}}{600\,{\rm MeV}}\right)^{-1/3} \left(\frac{t_{\rm var}}{4\times10^4\,{\rm s}}\right)^{-2/3} \delta_{10}^{-1/3} \tag{8}$$

In the expression above E_{peak} refers to the peak photon energy in the observer frame and $t_{\rm var}$ to the flare variability time, with $t_{\rm var} > t_{\rm syn}$.

Using Eqs. (7) and (8) in Eq. (4), one can retrieve the blob size in terms of the peak energy E_{peak} and variability time t_{var}:

$$R' > 3\times10^{15} \left(\frac{E_{peak}}{600\,{\rm MeV}}\right) \left(\frac{t_{\rm var}}{4\times10^4\,{\rm s}}\right)\ {\rm cm} \tag{9}$$

The size of the nebula limits physically the maximum of the blob size to $\sim 3.4\times10^{18}$ cm.

Using the approximations above, we can estimate the minimum and maximum values of the Doopler boosting factor (δ_{10}), by comparing with our simulations. For the different values of magnetic field sampled, we obtain δ_{10max} using Eq. 8. We derive then from our simulations $E'_{\rm PeV}$ in the comoving frame of reference, and obtain the size of the blob using Eq. 4. To check if this approximation is consistent with our data, the parameters resulting from the simulations ($E'_{\rm PeV}$ and R') are compared with the ones obtained with Eq. 7 and 9, respectively.

We conclude that $E'_{\rm PeV}$ is consistent with the relativistic moving outflow scenario if $\Gamma_e > 1.5$ (within a 10% of error),

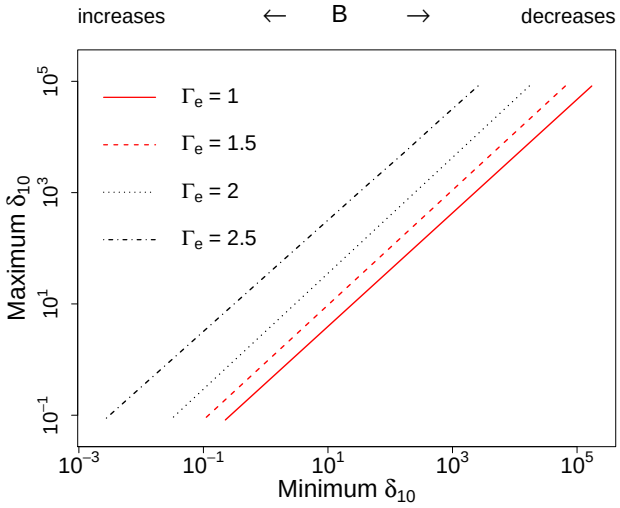

Figure 8. Doppler factor lower and upper limits from Eq. 7 and 8. The simulations plotted in red are not consistent with the relativistic moving outflow scenario for any Doppler factor, since the cutoff energy of the particle spectrum (E'_{PeV}) fitted in these cases is too small for the Doppler boosting factor upper limit derived with Eq. 8.

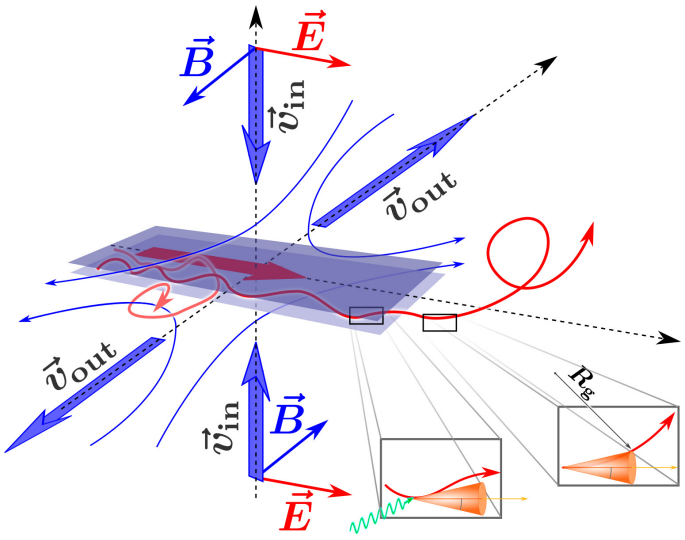

Figure 9. Sketch of Parker-type reconnection region. Two magnetized flows with oppositely directed magnetic field B converge with velocity V_{in} into the reconnection region schematically shown with blue planes. The electric field E, which is co-directed in the converging flow, appears unscreened (shown with thick red arrow) in the reconnection region. Particles propagating in the reconnection region (shown with red lines) can be accelerated to high energies before their escape (plasma escaping from the reconnection region is shown with v_{out}. Accelerated particles can produce IC emission or synchrotron emission in the magnetic field outside the reconnection region (radiation processes are illustrated in in-figure boxes).

allowing a certain range of δ_{10}. The upper and lower limit of δ_{10} must satisfy in each case the inequalities in Eq. 7 and 8. Figure 8 shows the limits on the Doppler boosting factor derived from the comparison with the simulations. A detection on the TeV regime would then constrain the Doppler factor to a very limited range. For instance, models detectable in the TeV regime, with mG magnetic fields (and $W_e < 5 \times 10^{43}$ erg, see Figure 6), are only feasible for Doppler factors ranging from 0.026 to 51.9.

Similarly, the minimum size of the blob computed from simulations is consistent with Eq. 9 ($R' > 4.5 \times 10^{14}$ cm), for $\Gamma_e > 1.5$, resulting at most 1.8×10^{15} cm for $\Gamma_e = 3$, still ~ 2000 times smaller than the size of the nebula.

4.2 Non-synchrotron scenarios

Alternatively to the relativistic motion case, the flare emission can be also generated in an ideal MHD outflow if the radiation mechanism is not synchrotron. Jitter radiation, i.e., a modification of the classical synchrotron radiation for the case turbulent magnetic field (see Kelner et al. 2013, and references therein), was suggested as a possible channel for the flares (Bykov et al. 2012; Teraki & Takahara 2013). The jitter mechanism is characterized by the same cooling time as the synchrotron one (for the same mean magnetic field strength) but the peak energy is increased by a factor $R_g/(\gamma\lambda_{turb})$, where R_g, γ, and λ_{turb} are giro-radius for the mean magnetic field strength, particle Lorentz factor, and turbulent field correlation length.

If the correlation length is small enough (i.e smaller than photon formation length), one would expect a shift on the total spectral energy distribution towards higher energies, facilitating the detection of the flare at the lower energies of CTA. In this case, the resulting spectrum can differ strongly from synchrotron: not only the maximum of the spectrum will be shifted to larger energies, but also the shape of the spectrum above the peak would follow a power-law distribution (Fleishman 2006; Kelner et al. 2013), being the emerging index related to that of the spectrum of the particle distribution and the magnetic turbulence. A power-law high-energy tail is also expected if the correlation length of the magnetic field is comparable to the giro-radius (however in this case the peak maximum would remain unchanged, see Kelner et al. 2013).

We tested this scenario by fitting the flare spectrum above 400 MeV observed in the 2011 flare, with a power-law function (see Section 3.3). The spectrum is well-described with a photon index of $\Gamma_{Jit} \sim 3$. Our simulations show that such spectral shape would result on a clear detection with CTA, with a substantial increase of the integral flux in the sub-100 GeV regime (up to $\sim$70%), if the power-law function continues with such index to high energies. Softer indices up to 3.5 would also result on a sizeable excess above the nebula emission below 200 GeV in 10 h, while a harder index ($\Gamma_{Jit} \sim 2.5$) could be observed at TeVs with an enhancement of flux similar to or larger than the upper limit set by H.E.S.S. and VERITAS to the 2013 flare.

If the jitter mechanism is therefore behind the origin of the Crab flares, the large excess expected below a few hundreds of GeV would result in a clear detection with CTA, of bright, but also moderated, flares, possible to achieve even in early stages of the construction phase.

4.3 Non-MHD scenarios

The third possibility discussed in the literature refers to an alternative mechanism, in which in certain regions of the neb-

ula, magnetic field lines of different orientation draw near each other and create a reconnection layer (see Fig. 9).

There is a number of processes that are activated by magnetic reconnection. First of all, the flow configuration is such that the initially highly magnetized flow that enter the reconnection layer (this motion is vertical in Fig. 9) gets ejected from the reconnection layer. The outlet MHD flow has a high internal energy and might propagate with large bulk Lorentz factors (see for example in the case of Petchek-type relativistic reconnection, Zenitani et al. 2009). Non-thermal processes operating in such outflow operate in the same way as discussed in Sec. 4.1. If the guiding magnetic field is small, then the magnetization of the flow should be small favoring higher IC fluxes. This, however, requires an almost perfect alignment of reconnecting magnetic field, which seems to be a significantly less probable realization than one with not a strictly anti-parallel magnetic field. In this case the guiding magnetic field is comparable to the reconnecting field and the flow remains highly magnetized. In this case, the IC emission is significantly suppressed. Typically, one adopts mG magnetic field in reconnection scenarios (see, e.g., Cerutti et al. 2012), which makes very hard detection of the counterpart IC emission.

If particles are directly accelerated by magnetic field in the reconnection layer (along the thick red arrow in Fig. 9), then during the acceleration process they effectively reside in a region with weaker magnetic field, which suppresses the synchrotron cooling, but the particles still produce some IC emission. The acceleration time in the reconnection layer, $t_{\rm rl,acc} \simeq E_e/ev_{\rm in}B$, is longer by a factor of approximately $c/v_{\rm in}$ than the synchrotron cooling time in magnetic field of B (which, given the location of the synchrotron peak at a few hundreds of MeV, should be about $t_{\rm syn} \simeq E/eBc$). Thus, if the reconnection operates in a non-relativistic regime, $v_{\rm in} \ll c$, then the emission from the reconnection layer may provide the dominant IC contribution. As in this case the particles produce IC and synchrotron emission at very different parts of their trajectories, these two components may have quite different beaming patterns. It is interesting to note, that in principle one could expect *orphan* flares in the TeV regime. That opens exciting prospects when observing bright PWNe in which the spectrum can be measured with good statistics.

The many uncertainties on these models, however, prevent us to make quantitative estimation of the expected radiation based on our simulations.

5 CONCLUSIONS

The simulations performed open exciting prospects for CTA, in particular for the LSTs, that sample with best sensitivity the GeV energy range. We showed that the detection of flares in the Crab nebula at tens of GeV with CTA, can be achieved in the case of synchrotron radiation with hard particle indices ($\Gamma_e = 1.5 - 2.0$) and magnetic fields similar to or stronger than the estimated average magnetic field in the nebula ($B \gtrsim 150\mu$G, implying an energy in TeV electrons for the parent particle population smaller than 5×10^{43} erg, see Figure 3). It should be noted, that the formulation of the synchrotron radiation used in NAIMA is somehow conservative. Several works (Derishev & Aharonian 2019; Khangulyan et al. 2020a) have demonstrated that the spectrum of synchrotron radiation can significantly deviate from the one obtained in random magnetic fields (Aharonian et al. 2010), and extend into the very high energy regime. Observation with Cherenkov telescopes of Crab flares, ensuring an optimal energy threshold, provide a unique opportunity to investigate the magnetic structure in astrophysical environments with great detail. Furthermore, we compared the expected emission from the synchrotron tail with the sensitivity curves for 4 CTA-LSTs and the MAGIC experiment (which can observe the Crab Nebula with low energy threshold). We show that observations of bright flares, similar to the one in 2011, could already provide strong constrains, even in the most pessimistic synchrotron approach considered here.

The IC component faces, in general, more complications: in one hand the variability has to be observed over the overwhelming nebular background, on the other, low magnetic fields should be involved to boost the IC emission. The latest, even if theoretically possible, seems unlikely when considering the fast variations observed in the Crab Nebula light curve during the flares. We found additionally an important drawback: to achieve a detectable TeV flux level in most of the cases explored, the total energy required should exceed the one contained in TeV emitting electrons in the nebula (see Eq. 1). However, several models with soft particle spectra ($\Gamma_e > 2.5$) and mG magnetic fields, show that the detection of flares at TeV energies can be achieved (Fig. 5). In fact, if the energy in electrons available is boosted above the upper limit established (due to re-acceleration of particles processes), the prospects for the detection of flares in the TeV regime with the CTA medium and small size telescopes (MSTs and SSTs, with best sensitivity at TeV energies) can significantly improve.

Observations with CTA will allow us to constrain many physical parameters in the acceleration and emission regions. We show that beside strong constraints on the particle spectrum and magnetic field, different hypothesis can be tested: A jitter mechanism could be easily proven if at work, whereas the dynamic of relativistic blobs can be derived if a MHD outflow is considered. For completeness, we discussed a third scenario, based on a non-MHD approach, that should be further theoretically investigated to infer more accurate predictions that can be compared with observations.

We conclude that even if the detection of the Crab Nebula flares in the TeV regime seems difficult to achieve, prospects to detect them in the sub-100 GeV regime are bright, and feasible in early stages of the CTA operation.

6 DATA AVAILABILITY

The data compilation for the Crab nebula was taken from Meyer et al. 2010 and Buehler et al. 2012. The CTA IRFs are public and available in `https://www.cta-observatory.org/science/cta-performance/`

7 ACKNOWLEDGEMENTS

E. M. and D. F. T. acknowledge the support of the grants AYA2017-92402- EXP, PGC2018-095512-B-I00, iLink 2017-1238 (Ministerio de Economía y Competitividad) and

SGR2017-1383 (Generalitat de Catalunya). We acknowledge the support of the PHAROS COST Action (CA16214). E. de O. W. ackowledges the Alexander von Humboldt Foundation for finantial support. D. K. is supported by JSPS KAKENHI Grant Numbers JP18H03722, JP24105007, and JP16H02170. We made use of the Cherenkov Telescope Array instrument response functions provided by the CTA Consortium and Observatory, see http://www.cta-observatory.org/science/cta-performance/ (version prod3b-v1) for more details. This paper has gone through an internal review by the CTA Consortium. This work was conducted in the context of the CTA Analysis and Simulation Working Group (ASWG). We made use R Project for Statistical Computing (R Core Team 2013). Also, this research made use of ASTROPY, a community-developed core PYTHON package for Astronomy (ASTROPY Collaboration, 2018).

References

Abdalla H., et al., 2019, Nature, 575, 464
Abdo A. A., et al., 2011, Science, 331, 739
Abeysekara A. U., et al., 2019, ApJ, 881, 134
Acharya B. S., et al., 2013, Astroparticle Physics, 43, 3
Aharonian F. A., Atoyan A. M., Kifune T., 1997, MNRAS, 291, 162
Aharonian F. A., et al., 2000, ApJ, 539, 317
Aharonian F. A., Kelner S. R., Prosekin A. Y., 2010, Phys. Rev. D, 82, 043002
Aleksić J., et al., 2015, Journal of High Energy Astrophysics, 5, 30
Aleksić J., et al., 2016, Astroparticle Physics, 72, 76
Aliu E., et al., 2014, ApJ, 781, L11
Amenomori M., et al., 2019, Phys. Rev. Lett., 123, 051101
Arakawa M., Hayashida M., Khangulyan D., Uchiyama Y., 2020a, arXiv e-prints, p. arXiv:2005.07958
Arakawa M., Hayashida M., Khangulyan D., Uchiyama Y., 2020b, arXiv e-prints, p. arXiv:2005.07958
Atoyan A. M., Aharonian F. A., 1996, MNRAS, 278, 525
Balbo M., Walter R., Ferrigno C., Bordas P., 2011, Astronomy & Astrophysics, 527, L4
Bartoli B., et al., 2015, ApJ, 798, 119
Bednarek W., Idec W., 2011, MNRAS, 414, 2229
Buehler R., D'Ammando F., Cannon A., 2011, The Astronomer's Telegram, 3276, 1
Buehler R., et al., 2012, ApJ, 749, 26
Bühler R., Blandford R., 2014, Reports on Progress in Physics, 77, 066901
Bykov A. M., Pavlov G. G., Artemyev A. V., Uvarov Y. A., 2012, MNRAS, 421, L67
Cash W., 1979, ApJ, 228, 939
Cerutti B., Werner G. R., Uzdensky D. A., Begelman M. C., 2012, ApJ, 754, L33
Deil C., et al., 2017, International Cosmic Ray Conference, 35, 766
Derishev E., Aharonian F., 2019, ApJ, 887, 181
Fleishman G. D., 2006, ApJ, 638, 348
Guilbert P. W., Fabian A. C., Rees M. J., 1983, Mon. Not. R. Astron. Soc., 205, 593
H. E. S. S. Collaboration et al., 2014, A&A, 562, L4
Hassan T., et al., 2015, PoS ICRC2015
Hillas A. M., et al., 1998, ApJ, 503, 744
Holler M., et al., 2015, PoS ICRC2015, p. arXiv:1509.02902
Horns D., Aharonian F. A., 2004, in Schoenfelder V., Lichti G., Winkler C., eds, ESA Special Publication Vol. 552, 5th INTEGRAL Workshop on the INTEGRAL Universe. p. 439 (arXiv:astro-ph/0407119)
Kelner S. R., Aharonian F. A., Khangulyan D., 2013, ApJ, 774, 61
Kennel C. F., Coroniti F. V., 1984, ApJ, 283, 710
Khangulyan D., Aharonian F. A., Kelner S. R., 2014, ApJ, 783, 100
Khangulyan D., Aharonian F., Romoli C., Taylor A., 2020a, arXiv e-prints, p. arXiv:2003.00927
Khangulyan D., Arakawa M., Aharonian F., 2020b, MNRAS, 491, 3217
Kirk J. G., Giacinti G., 2017, Phys. Rev. Lett., 119, 211101
Lagarias J., A. Reeds J., H. Wright M., Wright P., 1998, SIAM Journal on Optimization, 9, 112
Longair M. S., 1981, High energy astrophysics: an informal introduction for students of physics and astrophysics. Cambridge Univ. Press, Cambridge, https://cds.cern.ch/record/100003
Lyubarsky Y. E., 2012, MNRAS, 427, 1497
Lyutikov M., Komissarov S., Sironi L., Porth O., 2018, Journal of Plasma Physics, 84, 635840201
MAGIC Collaboration et al., 2019, Nature, 575, 455
Martín J., Torres D. F., Rea N., 2012, MNRAS, 427, 415
Mayer M., Buehler R., Hays E., Cheung C. C., Dutka M. S., Grove J. E., Kerr M., Ojha R., 2013, ApJ, 775, L37
Meagher K., VERITAS Collaboration 2015, in 34th International Cosmic Ray Conference (ICRC2015). p. 792 (arXiv:1508.06442)
Mestre E., de Oña Wilhelmi E., Zanin R., Torres D. F., Tibaldo L., 2020, MNRAS, 492, 708
Meyer M., Horns D., Zechlin H.-S., 2010, A&A, 523, A2
Ojha R., Hays R., Buehler E., Dutka M., 2013, The Astronomer's Telegram, 4855
Piron F., et al., 2001, Astronomy and Astrophysics, 374, 895
Porth O., Komissarov S. S., Keppens R., 2014, in International Journal of Modern Physics Conference Series. p. 1460168, doi:10.1142/S2010194514601689
R Core Team 2013, R: A Language and Environment for Statistical Computing. R Foundation for Statistical Computing, Vienna, Austria, http://www.R-project.org/
Rudak B., Dyks J., 1998, MNRAS, 295, 337
Striani E., et al., 2011, ApJ, 741, L5
Striani E., et al., 2013, ApJ, 765, 52
Tavani M., et al., 2011, Science, 331, 736
Teraki Y., Takahara F., 2013, ApJ, 763, 131
Weisskopf M. C., et al., 2013, ApJ, 765, 56
Wright M., 1996, Direct search methods: Once scorned, now respectable. Addison-Wesley, pp 191–208
Zabalza V., 2015, Proc. of International Cosmic Ray Conference 2015, p. 922
Zenitani S., Hesse M., Klimas A., 2009, ApJ, 696, 1385

MNRAS **000**, 1–11 (2020) Preprint 14 August 2020 Compiled using MNRAS LATEX style file v3.0

SNR G39.2–0.3, an hadronic cosmic rays accelerator

Emma de Oña Wilhelmi[1,2,3]★, Iurii Sushch[3,4,5]†, Robert Brose[3,6], Enrique Mestre[1,2], Yang Su[7] and Roberta Zanin[8]

[1] *Institute of Space Sciences (ICE/CSIC), Campus UAB, Carrer de Can Magrans s/n, 08193 Barcelona, Spain*
[2] *Institut d'Estudis Espacials de Catalunya (IEEC), 08034 Barcelona, Spain*
[3] *Deutsches Elektronen Synchrotron DESY, 15738 Zeuthen, Germany*
[4] *Centre for Space Research, North-West University, 2520 Potchefstroom, South Africa*
[5] *Astronomical Observatory of Ivan Franko National University of Lviv, Kyryla i Methodia 8, 79005 Lviv, Ukraine*
[6] *Institute of Physics and Astronomy, University of Potsdam, 14476 Potsdam, Germany*
[7] *Purple Mountain Observatory and Key Laboratory of Radio Astronomy, Chinese Academy of Sciences, Nanjing 210034, China*
[8] *CTA Observatory GmbH, Via Piero Gobetti 93, I-40129 Bologna, Italy*

Accepted XXX. Received YYY; in original form ZZZ

ABSTRACT

Recent results obtained with gamma-ray satellites have established supernova remnants as accelerators of GeV hadronic cosmic rays. In such processes, CRs accelerated in SNR shocks interact with particles from gas clouds in their surrounding. In particular, the rich medium in which core-collapse SNRs explode provides a large target density to boost hadronic gamma-rays. SNR G39.2–0.3 is one of the brightest SNR in infrared wavelengths, and its broad multiwavelength coverage allows a detailed modelling of its radiation from radio to high energies. We reanalysed the *Fermi*-LAT data on this region and compare it with new radio observations from the MWISP survey. The modelling of the spectral energy distribution from radio to GeV energies favours a hadronic origin of the gamma-ray emission and constrains the SNR magnetic field to be at least ~ 100 μG. Despite the large magnetic field, the present acceleration of protons seems to be limited to ~ 10 GeV, which points to a drastic slow down of the shock velocity due to the dense wall traced by the CO observations, surrounding the remnant. Further investigation of the gamma-ray spectral shape points to a dynamically old remnant subjected to severe escape of CRs and a decrease of acceleration efficiency. The low-energy peak of the gamma-ray spectrum also suggests that that the composition of accelerated particles might be enriched by heavy nuclei which is certainly expected for a core-collapse SNR. Alternatively, the contribution of the compressed pre-existing Galactic cosmic rays is discussed, which is, however, found to not likely be the dominant process for gamma-ray production.

Key words: ISM: individual objects: G39.2–0.3, ISM: supernova remnants, gamma-rays: ISM, clouds: ISM

1 INTRODUCTION

The deep survey performed by the *Fermi* LAT telescope has revealed a large population of gamma-ray bright SNRs (Acero et al. 2016). From these gamma-ray observations, two trends on the SNR population were established, based on their gamma-ray spectra and physical characteristics of the remnant: a population of young, hard-spectrum SNRs, and a second population of older and brighter, often interacting with dense molecular clouds (MC), ones. These evolved SNRs have lost much of their energy budget, but the dense surrounding media enhance the gamma-ray emission via proton-proton interaction. The spectral energy distribution (SED) from this emission process is characterized by a sharp rise in the ~70–200 MeV range (resulting from the neutral pion energy threshold production), followed by a hard emission up to the maximum energy, which is determined by either the maximum energy to which the CRs are accelerated or by the escape of high energy protons into the interstellar medium. The detailed spectral investigation of a handful of those SNR-MC systems have resulted on the detection of such feature, strongly favouring hadronic processes as the origin of the gamma-ray emission observed (Ackermann et al. 2013; Giuliani & AGILE Team 2011; Jogler & Funk 2016; Ambrogi et al. 2019). A second

★ E-mail: emma.de.ona.wilhelmi@desy.de
† E-mail: iurii.sushch@desy.de

possibility to explain the observed gamma-ray spectrum is via bremsstrahlung radiation, in which electrons instead of protons interact with the surrounding media. However, to explain the sharp drop observed, an artificial lower cut-off in the spectrum of electrons has to be invoked (Ambrogi et al. 2019). The emission mechanisms that dominate SNRs depend on many different aspects such as the shock evolution and the circumstellar medium. The fast shock velocity promotes in principle the acceleration of CRs, both of hadronic or leptonic nature. Whether the gamma-ray emission is originated by proton-proton interactions or by electrons off-scattering soft photon fields by inverse Compton mechanisms, or via bremsstrahlung, is still subject of discussion for the brightest sources observed. In general, the global spectral shape found in bright and young SNRs seems to favour a leptonic origin. Still, a hadronic interpretation cannot be completely ruled out under certain conditions (Abdo et al. 2011; Celli et al. 2019a). The spectra of other young but much fainter remnants, such as Cassiopeia A or Tycho, seem to be better explained by hadronic interaction (Ahnen et al. 2017; Archambault et al. 2017; Zirakashvili et al. 2014; Morlino & Caprioli 2012).

SNR G39.2–0.3 belongs to a group of core-collapse SNRs, classified as Type IIL/b SNe (Lee et al. 2009). Type IIL/b SNe go through a phase of red supergiant (RSG), creating a rich and highly in-homogeneous medium in which the remnant expands. Together with SNR G11.2–0.2, RCW 103, W44 and W49B, this SNR shows a bright NIR H_2 emission, evidencing the presence of shocked molecular gas (Lee et al. 2009; Su et al. 2011; Patnaik et al. 1990; Anderson & Rudnick 1993). Based on X-ray and radio mm observations, the age of SNR was estimated to be in the 3 to 7 kyr old range (Su et al. 2011). There is a large uncertainty about its distance, which was estimated using different X-ray and radio observations (Caswell et al. 1975; Olbert et al. 2003; Becker & Kundu 1975; Green et al. 1997). We adopted thus a reference distance of 6.2 kpc.

The large and extensive bibliography on SNR G39.2–0.3 [1] provides a broad range of information. It is an asymmetric composite SNR with its central part dominated by non-thermal emission from the likely associated pulsar wind nebula (Olbert et al. 2003; Sezer et al. 2020). The western shell is brighter in radio and X-ray, suggesting a molecular cloud interaction, whereas it shows a faint tail on the eastern side. The remnant has been largely observed using molecular tracers. Lee et al. 2009 remarked a cavity-like structure at V_{LSR} ~69 km s^{-1} surrounding the remnant. The location of the cavity suggests an associated multishell structure produced by the interactions of the SNR shocks with the RSG wind material. This interpretation was refuted by Su et al. 2011, who proposed a different association with a region located at V_{LSR} ~88 km s^{-1}. At this somehow larger distance, the western boundary seems to be confined by a molecular wall, whereas the fading material to the east matches the X-ray and radio image. Harrus & Slane 1999 estimated a supernova explosion energy of $E \sim 3.5 \times 10^{50}$ ergs, for a filling factor of 1 ($E \sim 7 \times 10^{50}$ ergs for the filling factor of 0.25 expected for Sedov-Taylor solutions), and equipartition magnetic field of $B \sim 100$ μG ($B \sim 140$ μG for the filling factor of 0.25), based on the study of the observed X-ray thermal emission. These estimates are however very uncertain as they rely on the assumption of the pure Sedov-Taylor solution and uniform density. Interaction with a massive molecular cloud would certainly increase the estimates of the explosion energy and equipartition magnetic field by increasing the density of the medium and thus decreasing the filling factor of the X-ray emitting plasma inside the remnant. Cruciani et al. (2016) studied the microwave emission from the remnant and described the spectral energy distribution with a two components, a Synchrotron spectrum with index $\alpha = 0.36$ (compatible with previous radio measurements) and a thermal blackbody component for dust temperature of 25 K and optical depth at 100μm of $3{\cdot}10^{-4}$. The bright emission from SNR G39.2–0.3 is also listed in the Spitzer survey of SNRs in our Galaxy (Reach et al. 2006) and results on a FIR density of u_{FIR} of ~2.4 eV/cm^3.

In the high energy regime, the *Fermi* 4FGL catalogue listed a source located within 0.1° of the SNR, 4FGL J1903.8+0531. The gamma-ray spectrum is represented with a *LogParabola* function (The Fermi-LAT collaboration 2019) and it appears as likely associated with SNR G39.2–0.3. No detection has been claimed at higher energies in the TeV regime (H. E. S. S. Collaboration et al. 2018), where an upper limit of $6{\cdot}10^{-13}$ erg/cm^{2}s was derived from H.E.S.S. observations of the Galactic plane. Recently, Sezer et al. 2020 reanalysed the region, obtaining similar spectral parameters to the one listed in the 4FGL catalogue.

In the following we explore the association between the high-energy source and SNR G39.2–0.3 and investigate the physics mechanisms powering the gamma-rays observed.

2 DATA ANALYSIS AND RESULTS

2.1 High energy emission

We analyzed ~11 yr of data spanning from 2008 August 4 2008 to 2019 June 19 with energies between 100 MeV and 100 GeV. The dataset was analysed using Fermipy[2] v0.17.3: a set of python programmed tools that automatize the PASS8 analysis with the Fermi Science Tools[3]. FRONT+BACK events class was used to increase the statistics. We used P8R3_SOURCE_V2 instrument response function. We applied the energy dispersion to all sources in our model expect for the isotropic (extragalactic) diffuse model. To study the morphology, we selected events with energy above 3 GeV to optimize the instrument angular resolution[4]. Once the best-fitting position and extension is determined, we selected a larger energy range, from 100 MeV to 100 GeV to obtain the spectrum. The latest was derived by performing a maximum likelihood analysis in a circular region (15°) around the best-fitting position. The emission model for our radius of interest includes the LAT sources listed in the fourth LAT catalogue (4FGL, The Fermi-LAT collaboration 2019) within a region of 30° radius around SNR G39.2–0.3

[1] http://www.mrao.cam.ac.uk/surveys/snrs/snrs.G39.2-0.3.html

[2] http://fermipy.readthedocs.io/en/latest/

[3] https://fermi.gsfc.nasa.gov/ssc/data/analysis/documentation/

[4] https://www.slac.stanford.edu/exp/glast/groups/canda/lat_Performance.htr

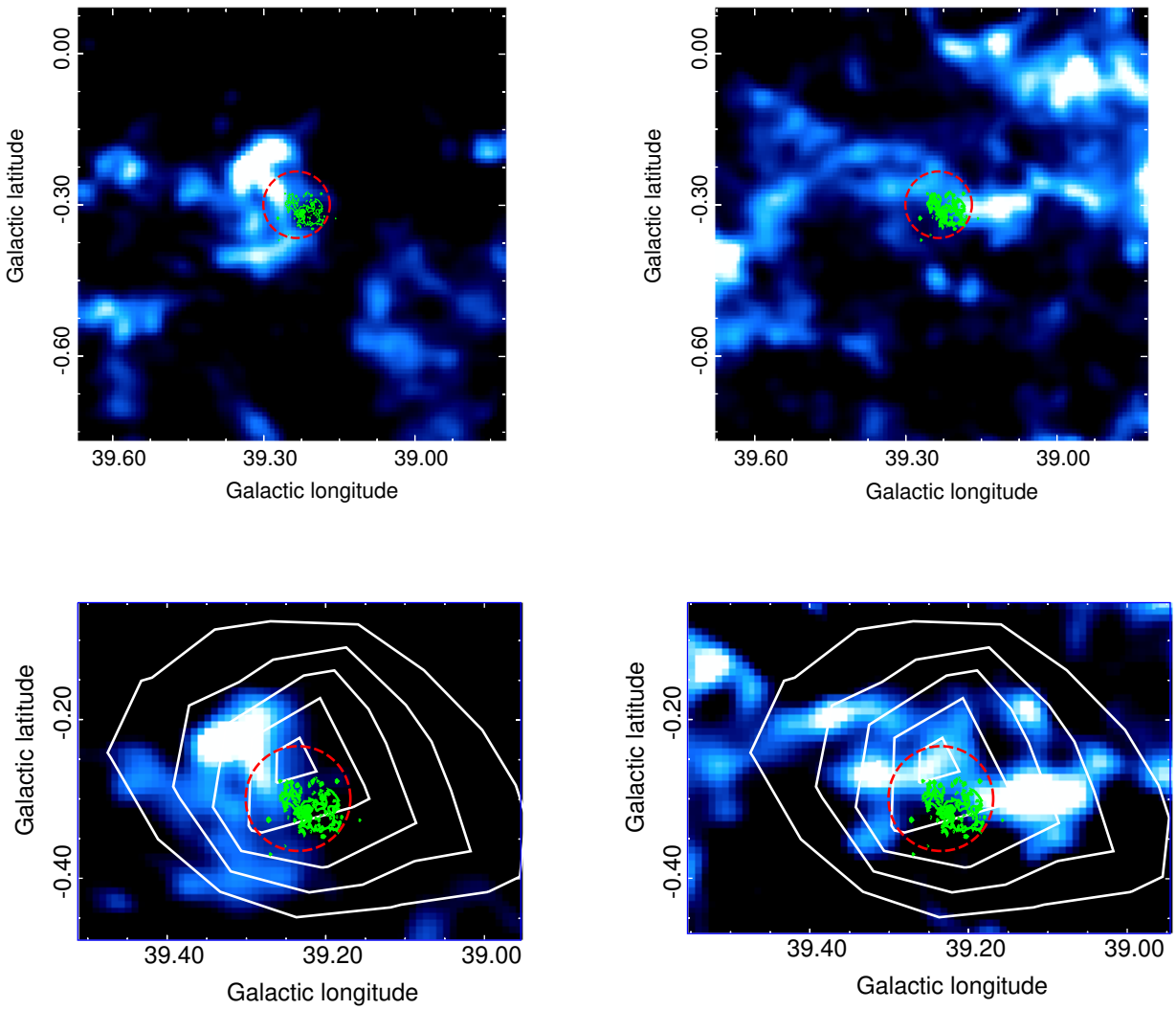

Figure 1. On the top left (a) ^{13}CO large-scale intensity map integrated between 67 km s^{-1} and 74 km s^{-1} obtained from the MWISP survey. On the top right (b) the intensity map integrated between 80 and 88 km s^{-1}. The red dashed-line circle marks the 99 per cent localization error of the reanalysis of 4FGL J1903.8+0531. The green contours correspond to the radio shell, as derived from the image compiled by Ferrand & Safi-Harb 2012. On the bottom we showed the ^{12}CO channel (MWISP survey), centred on the position of SNR G39.2–0.3. The left one (c) for the 69 km s^{-1} map and the right one (d) for the 88 km s^{-1} one. White contours are obtained from LAT significance map above 3 GeV, starting on TS=25 (or $\sim 5\sigma$ in steps of 10).

and the diffuse γ-ray background models; the Galactic diffuse emission modelled by *gll_iem_v07.fits* and the isotropic component by *iso_P8R3_SOURCE_V2_v1.txt*, including the instrumental background and the extragalactic radiation.

We used the tools *localize* and *extension*, which perform a scan of the likelihood surface around the nominal position and compute the likelihood ratio test with respect to the no-extension (point-source) hypothesis, respectively. To obtain the spectral energy distribution, we split the total energy range into 14 logarithmically spaced bins. We required that each spectral point has at least a Test Statistics TS = 4, otherwise a 95 per cent confidence level (CL) upper limit was computed.

The study of the location and extension results on a point-like source, centred at $\mathrm{RA_{J2000}} = (286.01 \pm 0.02)^{\mathrm{o}}$ and $\mathrm{Dec_{J1000}} = (5.47 \pm 0.02)^{\mathrm{o}}$ with an error in the localization at 99 per cent of 0.066 (see red dashed line in Fig. 1). The 99 per cent confidence circle contains the SNR G39.2–0.3 strongly suggesting a physical association between the SNR and the gamma-ray source.

Fig. 2 shows the spectral energy distribution obtained with the likelihood method and using the above-described morphology as extraction regions. The differential energy

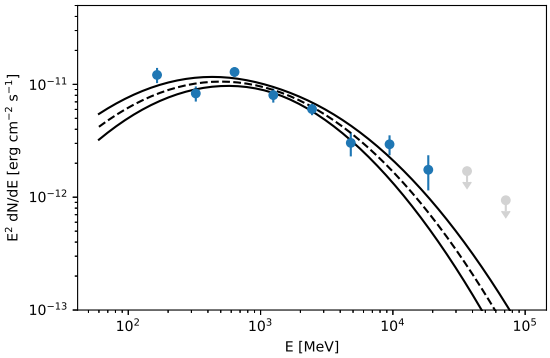

Figure 2. Spectral energy distribution of 4FGL J1903.8+0531, associated to SNR G39.2–0.3. The best-fitting shape and the 1σ error derived for the energy range between 100 MeV and 100 GeV is represented by black lines.

spectrum is well represented by a LogParabola function such $dN/dE = N_o(E/E_{break})^{-(\alpha+\beta\log(E/E_{break})}$, where the best-fitting values are: $N_o = (8.0 \pm 0.7) \cdot 10^{-13}$ MeV^{-1}/cm^{2}s, $\alpha = 2.6 \pm 0.1$ and $\beta = 0.20 \pm 0.03$, for a break energy value of $E_{break} = 2.3$ GeV. The source is detected with a TS of 363 above 100 MeV. The fit values are in good agreements with the ones found by Sezer et al. 2020 and the ones obtained from the 4FLG catalogue (The Fermi-LAT collaboration 2019).

2.2 CO observations

The large-scale CO map is obtained from the MWISP survey (see details in Su et al. 2019). The ^{12}CO(J=1–0), ^{13}CO(J=1–0), and C18O (J=1–0) lines were simultaneously observed using the 13.7 m telescope. The covered region is towards the northern Galactic plane with $|b| < 5^o$. The half-power beam width (HPBW) is ∼50 arcsec at the frequency of ∼ 110 – 115 GHz. The rms noise is ∼ 0.5 K for ^{12}CO and ∼0.3 K for ^{13}CO and C18O, at a velocity resolution of ∼0.2 km s^{-1} with a uniform grid spacing of 30 arcsec.

To evaluate the dense medium in which the SNR is located, we derived the skymap around its position integrating the 3D cube in the two velocity ranges previously proposed: between 67 and 74 km s^{-1} (as discussed in Lee et al. 2009), and between 80 and 88 km s^{-1} (as proposed by Su et al. 2011). To obtain the mass density from the two intensity maps, we use the standard assumption of a linear relationship between the velocity-integrated CO intensity, W_{CO}, and the column density of molecular hydrogen, N(H2), adopting for the conversion factor $X_{CO} = 2.0 \cdot 10^{20}$ cm^2 (K km s^{-1}) (Dame et al. 2001; Bolatto et al. 2013). Given the uncertainties in the distance, we used a fiducial value of 6.2 kpc for both velocity ranges, which translates on a physical size of ∼16 pc (for a 0.15^o source). The integrated mass density of the two velocity ranges is similar, with 440 cm^{-3} and 326 cm^{-3} for the 69 km s^{-1} and 88 km s^{-1} range, respectively.

To understand the giant molecular cloud (GMC) structure around the SNR and the high-energy source, we used the ^{13}CO(J=1–0) channel. Given the complicated velocity field in the Galactic plane, the optical thin channel is thus a better tracer of the different molecular clouds with different velocities (that is, different kinematic distance) at large scales. The two large-scale intensity maps for the 69 km s^{-1} and 88 km s^{-1} velocity ranges are showed in Fig. 1(a) and (b) respectively. The two GMC proposed are clearly visible in the two maps, being the first one (a) slightly offset (∼ 0.15^o) to the North with respect to the position of the *Fermi* source and SNR G39.2–0.3. For a detailed view of the SNR surroundings, we used the ^{12}CO(J=1–0) channel, that traces the denser region (Fig 1 (c) and (d), for the 69 km s^{-1} and 88 km s^{-1} velocity ranges respectively). The gas distribution seems to be more scattered along 4FGL J1903.8+0531 favouring an association with this second region, based on the gas and gamma-ray similar distribution.

3 SPECTRAL MODELLING

The optimal agreement between the gamma-ray source and SNR G39.2–0.3 points to a clear association of the two sources. Moreover, the dense region in which the SNR is embedded, suggests a scenario in which the SNR is accelerating CRs, electrons or hadrons, that interact with the rich medium around the remnant. The high energy spectrum is characterised with a quite narrow photon distribution (see Fig. 2 and Fig. 3, peaking at a few hundreds of MeV. To investigate the nature of the parent particles, we fit the obtained gamma-ray spectral energy distribution of the SNR by both hadronic- and leptonic-induced gamma-ray spectrum. We use the *Naima* package (version v0.8.3, Zabalza 2017) to compute the non-thermal spectral distribution from radio to TeV energies. The X-ray non-thermal emission detected by Chandra is not shown, since it is likely correlated to the associated PWN and not with the shell SNR. The spectral shape of the LAT source makes very unlikely a PWN origin, under the assumption of a Synchrotron/inverse Compton model (see green dashed line in Fig. 3 for the inverse Compton contribution). An unrealistic (few hundreds of eV/cm^3 instead of the ∼2 eV/cm^3 measured) photon field density in the FIR region should be up-scattered to boost the inverse Compton flux to the level of the gamma-ray flux observed. The shape of the low-energy part of the electron spectrum is actually well determined by the fit to the radio data, obtained from the shell region. We used a power-law function with spectral index fixed to 1.8 (corresponding to a Synchrotron spectrum of 0.4) and an exponential cut-off to account for the maximum energy of the accelerated particles within the shell. The corresponding bremsstrahlung emission cannot reproduce the LAT spectrum at high energies, but the latter constrains the amplitude of the electron population to $< 3 \cdot 10^{34}$ eV^{-1} for a density of ∼400 cm^{-3} (obtained from the CO observations) in the cloud, witch is believed to be interacting with the remnant. The combined radio and GeV fit also limits the magnetic field in the SNR to at least $B \geq 150 \mu G$ to reach the level of Synchrotron emission observed for the population of electrons. Even if assuming a 50 per cent error in the estimation of the molecular content, a large magnetic field above $100 \mu G$ is still required to reach the radio emission level. This value is comparable with the one estimated by equipartition arguments (Harrus & Slane 1999) assuming a constant in time density of the ambient medium of 0.5 cm^{-3} extracted from observations of thermal X-rays. This value of magnetic field is larger than what one would expect for an evolved SNR, but still not that surpris-

ing for an SNR interacting with a dense cloud. ?still within the values expected for SNRs of a few thousands years old in a dense region

The magnetic field strengths inside molecular clouds deduced from Zeeman observations by Crutcher et al. (2010) indicates roughly constant magnetic fields of $B_0 = 10\,\mu$G in clouds with densities of $n_0 \lesssim 300\,\mathrm{cm}^{-3}$ (similar to the density of the cloud interacting with SNR G39.2–0.3). This field can be further compressed by a factor of a few by the interaction with the SNR shock. If the shock is already radiative, a dense shell will form in the downstream of the shock, where the field can be further compressed. Assuming a turbulent field in the cloud yields $B_\mathrm{d} = B_0\sqrt{\frac{2\xi^2+1}{3}}$, where ξ is the density-compression ratio between the cloud and the radiative shell. For the not unreasonable case of $\xi = 15$, one can reach the field strengths of $\approx 150\,\mu$G needed to explain the Synchrotron emission. Another possible explanation for a high magnetic field strength is the amplification of a turbulent field by MHD instabilities in the downstream of the shock propagating in an inhomogeneous medium (Fraschetti 2014; Giacalone & Jokipii 2007; Celli et al. 2019a). However, the fields provided by these processes should only convert a fraction of the kinetic (and thermal) energy density of the downstream flow into magnetic fields. In general one expects

$$B_\mathrm{d} \approx \sqrt{\frac{4\pi n m_p \sigma}{\xi}} v_\mathrm{shock}, \quad (1)$$

where σ is the conversion efficiency. A shock velocity of $\approx 150\,\mathrm{km\ s}^{-1}$ and a conversion efficiency of σ=5 per cent yields $B_\mathrm{d} \approx 150\,\mu$G for $\xi = 4$ and $B_\mathrm{d} \approx 80\,\mu$G for $\xi = 15$. It is not clear if the compression of the cloud's field or the amplification of the field by MHD-instabilities will dominate the contribution to the magnetic field. However, the combination of both processes ensures a reasonably high magnetic field to explain the observed Synchrotron emission.

Similarly, the combination of the radio and GeV data constrains the maximum electron energy to $E_\mathrm{cut} \leq 100\,\mathrm{GeV}$ (assuming the electron spectrum follows a power law with an exponential cut-off). Such a high magnetic field would imply severe Synchrotron losses which should modify the electron spectrum introducing a break, but the anticipated break energy would be roughly similar to the maximum energy constrained above and hence taking Synchrotron losses into account would not radically change the picture.

Contrary to the leptonic models, we obtain a satisfactory fit of the high energy data when using hadronic-originated ones. The best fit obtained is plot in Fig. 3 in blue dotted line. For the injected population of protons, we use a broken power law. Such a spectral shape would be naturally expected as a result of a superposition of different cut-off energies during the SNR evolution and subsequent particle escape at later times, or by intrinsic properties of the CR acceleration in the shock (i.e. finite size of the emission region or evolution of the shock in partially ionized medium) (Celli et al. 2019b; Ohira et al. 2011; Aharonian & Atoyan 1996; Zeng et al. 2019; Brose et al. 2020; Malkov et al. 2011). The total energy, normalised to a distance of 6.2 kpc, stored in protons (for $\mathrm{E}_p > 100\,\mathrm{MeV}$) results on $\mathrm{W_p} = 3.2^{+1.1}_{-0.8}10^{49}$ erg, which represents only a few percent of the total energy of the SNR explosion. The best-fit for the two spectral indices are $s_1 = 2.0 \pm 1.5$ and $s_2 = 2.78 \pm 0.06$, for a break energy at $\mathrm{E_b} = 220 \pm 70\,\mathrm{MeV}$. The low break energy results on a large uncertainty on s_1, which is poorly constraint. For simplicity, we also fit the LAT spectrum with a power-law function, resulting on an equally good fit with a spectra index of $s = 2.75^{+0.04}_{-0.06}$ and similar particle energy above 100 MeV as the broken power-law case. This arises as a consequence of the low-energy cut-off in the gamma-ray spectrum from pion decays, which makes s_1, the spectral index obtained in particle acceleration process, irrelevant for the mathematical fit.

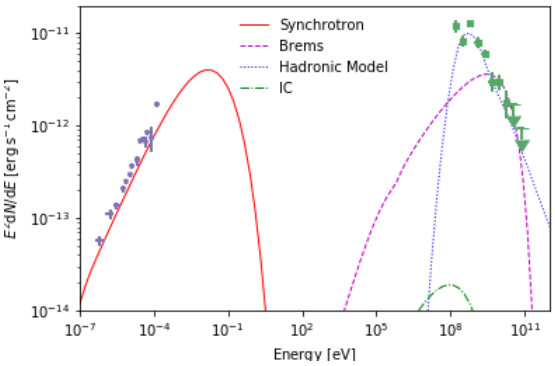

Figure 3. Multiwavelength spectral energy distribution of the SNR G39.2–0.3. The lines indicate the best-fitting models for both leptonic and hadronic interpretation of the high energy emission.

The acceleration of protons and electrons should occur in a similar way, implying a similar spectral shape (at least at lower energies at which electrons are not affected by Synchrotron cooling). This also implies that the spectral break derived for the proton spectrum should also be reflected in the electron spectrum at similar energies. The observed radio spectrum shows a featureless power-law spectrum up to 33 GHz (Cruciani et al. 2016) constraining the energy of a possible break in the electron spectrum. The characteristic energy of the emitted Synchrotron photon is

$$\nu_\mathrm{ch} \simeq 0.8 \left(\frac{E}{1\,\mathrm{GeV}}\right)^2 \left(\frac{B}{150\,\mu\mathrm{G}}\right)\ \mathrm{GHz}, \quad (2)$$

implying that the spectral break cannot occur below $\sim 6\left(\frac{B}{150\,\mu\mathrm{G}}\right)^{-1/2}$ GeV. Hence, to secure a break at a sub-GeV or even a few GeV level one would need to dramatically increase the magnetic field. The plausibility of such a break in the particle spectrum is further discussed in the next section in more detail.

4 DISCUSSION

Given the large magnetic field derived from the comparison between the radio and high energy emission, the low energy cut-off measured makes, in principle, SNR G39.2–0.3 an extremely inefficient in accelerating particles into very-high energies. For a type II SNR of 3 to 7 kyr, exploding in a circumstellar wind of density $n(R) \propto R^{-2}$, shock velocities of the order of 10^3 km s^{-1} could still be expected (see i.e. Gabici et al. 2016 and references therein). This large shock velocity together with the amplified magnetic field should be

enough to accelerate protons to energies of more than TeV. On the contrary, the low cut-off measured suggests either a slow shock, or a large escape rate of TeV protons in the surrounding. This effect could be due to the evolution of the SNR in the dense media of its progenitor. Indeed, the comparison between the gamma-ray emission and the intensity maps obtained in CO (in Fig. 1) revealed a clear enhancement of molecular material on the position of the gamma-ray source. The point-like morphology of the gamma-ray emission, centred on the SNR, instead on the peak of the radio intensity observed on the 67 to 74 km s^{-1} map (Fig. 1 (a) and (c)), suggests an association with the second velocity range proposed (between 80 and 88 km s^{-1}, Fig. 1 (b) and (d)) corresponding to a distance of 6.2 kpc. The multi-wavelength investigation carried on by Su et al. 2011 revealed a thick molecular wall at this velocity, coincident with the bright X-ray, IR and radio emission from the west part of the remnant. Such thick wall could naturally explain a hampering of the SNR expansion, which would limit its acceleration power to very high energies and also the large magnetic field needed to account for the radio emission.

In the following, we compare our results with different scenarios that account for the spectral shape of the derived hadronic component.

4.1 Old dynamical age scenario

The shape of the observed gamma-ray spectrum with a turn-over at low energies ($E_{\rm break}$ = 2.3 GeV in the LogParabola fit) suggests a high dynamical age of the remnant, i.e. the SNR is on the post-adiabatic stage of its evolution featuring a low shock velocity and substantial escape of CRs. Indeed, the slow shock results in a low maximum energy of freshly accelerated protons, while high-energy particles which are already in the system escape to far upstream of the shock. Recent detailed modeling of the time evolution of the CR spectrum in SNRs in post-adiabatic phase which benefited from a self-consistent treatment of the diffusion coefficient by solving the transport equation for magnetic turbulence induced by Alfvenic waves (Brose et al. 2020), showed that inefficient confinement of high-energy particles at late stages of evolution leads to the rapid decrease of the maximum energy reachable in the shock acceleration and hence to the formation of a spectral break at 10 – 100 GeV. Above the break the spectrum softens and can be adequately approximated by a power law with a spectral index of about 2.7. The break energy corresponds to the maximum energy of particles reachable in the acceleration process at the current stage. This spectral structure is similar to the one observed for SNR G39.2–0.3, where the observed gamma-ray spectrum can be explained by hadronic emission from a particle spectrum with the spectral index of $s_2 = 2.78 \pm 0.06$ above the break. The fit of the data, however, suggests an extremely low break energy of $E_{\rm b} = 220 \pm 70$ MeV, implying that particles are no longer being effectively accelerated. This estimate of the break energy is rather uncertain given that the gamma-ray spectrum can be equally well fitted with a simple power-law particle spectrum with the spectral index $s = 2.75^{+0.04}_{-0.06}$.

To examine this farther, we use the post-processing radiation routine of the RATPaC code (Telezhinsky et al. 2012, 2013; Brose et al. 2016; Sushch et al. 2018) designed for numerical simulations of particle acceleration in SNRs. The module to calculate gamma-ray radiation from pion decays relies on Monte Carlo event generators, namely DPMJET-III (Roesler et al. 2001) and UrQMD (Bass et al. 1998; Bleicher et al. 1999), for the calculation of inelastic cross sections and differential production rates of secondary particles produced in nuclei collisions (Bhatt et al. 2020). We use this module to calculate the expected gamma-ray emission from a toy proton spectrum which follows a broken power law in momentum,

$$\frac{dN}{dp} = \begin{cases} N_0 p^{-s_1}, & \text{if } p < p_{\rm b} \\ N_0 p_{\rm b}^{-s_1+s_2} p^{-s_2}, & \text{otherwise,} \end{cases} \quad (3)$$

where $p_{\rm b}$ is the the break momentum of a particle with the kinetic energy $E_{\rm b}$.

First, to study the impact of the break energy $E_{\rm b}$ on the resulting gamma-ray spectrum, we fix spectral indices to $s_1 = 2.0$ (motivated by diffusive shock acceleration, DSA) and $s_2 = 2.75$ (motivated by observations and close to the value predicted by numerical simulations, Brose et al. 2020) and vary the break energy from 1 to 10 GeV. In Fig. 4 we illustrate how the shape of the expected gamma-ray spectrum changes depending on the value of the break energy. For each line N_0 is chosen in a way to obtain the same energy flux of gamma-rays of 0.9×10^{-11} erg cm^{-2} s^{-1} at 1 GeV. Modelled spectra clearly indicate that for $E_{\rm b} \gtrsim 3$ GeV the expected turn-over shifts to higher energies significantly deviating from observations. In other words, if the particle acceleration at the shock produces a typical −2-power-law spectrum the current maximum energy to which particles can be accelerated cannot be larger than 3 GeV to reproduce the observed gamma-ray spectrum. This implies that the dynamical age of the remnant is very old and that it is far into post-adiabatic phase. The interaction with the dense material might enhance the escape of CRs further, besides the increase of the dynamical age. Neutral-charged collisions in the only partially ionized cloud might lead to an evanescence of the Alfvén waves that confine the CRs (Kulsrud & Cesarsky 1971), lower the current maximum energy and modify the CR-spectrum (Malkov et al. 2013). This low break energy is also only marginally compatible with the lower limit implied from the observed radio spectrum (see Section 3) requiring a significantly higher magnetic field.

However, for old remnants the spectrum of accelerated particles may very well deviate from the featureless power-law with the spectral index $s = 2$ obtained in DSA. It can become softer simply because the shock decelerates and becomes weaker resulting in a lower compression ratio. It can be also further modified as a result of substantial pressure of CRs which may provide feedback on the hydrodynamic evolution and modify the structure of the shock. In this case, the particle spectrum would have a concave shape with $s < 2$ below a few GeV and $s > 2$ above that (Blasi 2002; Malkov et al. 2002; Berezhko & Ellison 1999). The soft spectrum of freshly accelerated particles might be another reason of such a low energy of the peak in the gamma-ray spectrum. In Fig. 5 we show how the shape of the gamma-ray spectrum changes for different values of s_1 spanning from 2.0 to 2.75. The break energy here is fixed at $E_{\rm b} = 10$ GeV. Each spectrum is normalized in the same way as in Fig. 4. Indeed, it can be seen that if the particle spectrum is soft enough the

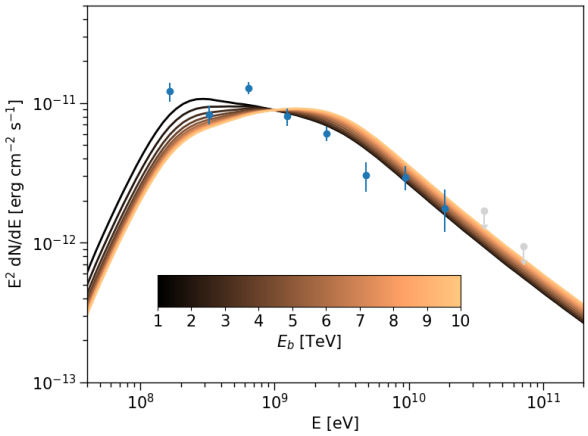

Figure 4. Spectral energy distribution of the modelled hadronic gamma-ray emission generated by a proton population described by a broken power-law spectrum in momentum with spectral indices $s_1 = 2.0$ and $s_2 = 2.75$. Different colours of lines denote different assumed values of the break energy from 1 GeV to 10 GeV. Blue points represent *Fermi*-LAT data analysed in this paper. All the lines are normalized in way to obtain the same energy flux of 0.9×10^{-11} erg cm^{-2} s^{-1} at 1 GeV. This is done only for comparison purposes and for all the cases the required energy in protons represent a small fraction of the explosion energy.

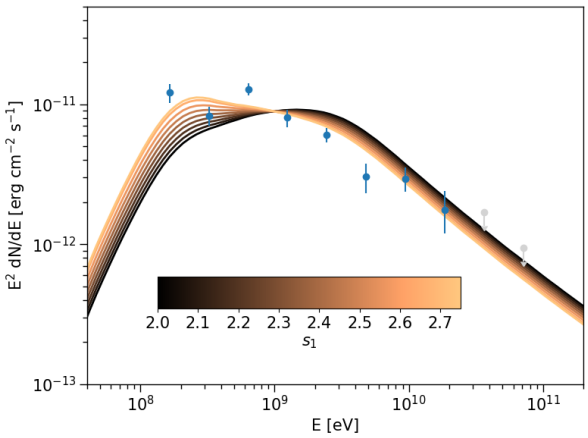

Figure 5. Same as Fig. 4 but with fixed break energy at 10 GeV and varying s_1 from 2.0 to 2.75.

value of the break energy becomes less important. In fact, the observed gamma-ray spectrum can be relatively well explained with a single power-law with the spectral index of 2.75. Soft spectrum, however, disagrees with radio observations which clearly imply a featureless power-law electron spectrum with $s = 1.8$. There is no obvious reason, why would the spectral shape of accelerated protons differ from the spectral shape of accelerated electrons, hence the proton spectrum in place is rather harder than $s = 2.0$ than softer, implying an even lower break energy.

4.2 Heavy composition

Above, we showed that both low break energy and soft spectrum of freshly accelerated particles can explain the shape

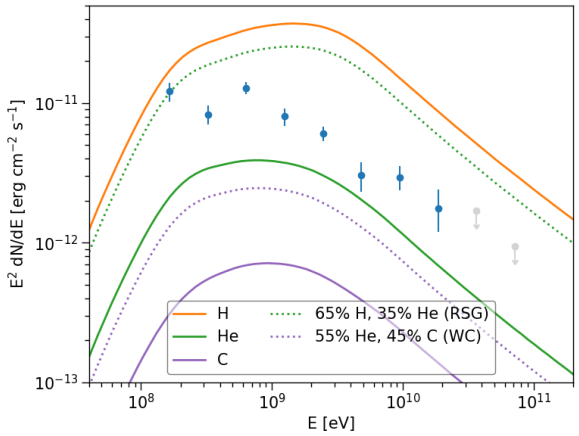

Figure 6. Same as Figs. 4 and 5 but for different composition of accelerated particles for hadronic interactions. The solid lines show mono-elemental compositions for hydrogen (orange), helium (green) and carbon (purple) nuclei. Dotted lines represent mixed compositions (mass fractions) which reflect RSG and WC winds. The spectra are normalized to the same mass density of CRs (and hence the same injection efficiency) to demonstrate the difference in flux normalization when moving to heavier nuclei. The CR spectrum is assumed to follow a broken power-law in momentum with $s_1 = 2.0$, $s_2 = 2.75$ with a break at Zp_b, where p_b defines the break momentum for the hydrogen spectrum corresponding the break energy of 10 GeV. The target material is assumed to be of typical ISM composition with density of 400 cm^{-3}.

of the observed gamma-ray spectrum with the characteristic turn-over at low energies. Both effects strongly suggest an old dynamical age of the remnant which is also in agreement with estimates of the density of the ambient medium which appears to be very high (see Sec. 2.2). Nevertheless, the required break energy ($E_b \lesssim 3$ GeV) is rather hard to get in time evolution models which predict a break energy around 10 – 100 GeV and is only very marginally compatible with the featureless radio synchrotron spectrum up to 33 GHz, while the soft spectral index disagrees with the observed radio spectrum which implies a much harder particle spectral index.

To reconcile these discrepancies one might need to examine and take into account the elemental composition of the ambient medium in which the SNR is evolving. Indeed, heavy elements, both as CRs and as target material, result in a shift of the peak in the gamma-ray spectrum to lower energies (Bhatt et al. 2020; Banik & Bhadra 2017). At the same time, heavy composition is expected for core-collapse SNRs which expand into the stellar wind of their progenitor stars, mostly red supergiants or Wolf-Rayet stars. Given that G39.2–0.3 is a core-collapse remnant of likely Type IIL/b with a RSG progenitor (see Section 1), one can expect a fair fraction of heavy elements which can be accelerated at the shock and/or act as target material for hadronic interactions. In the following, we consider heavy nuclei only for CRs accelerated at the shock, keeping the target material of typical ISM composition with H to He ratio of 10:1. This is motivated by the idea that CRs residing in the SNR were accelerated at earlier stages of evolution while the SNR was still evolving inside the stellar wind bubble, while at this moment of time they are interacting with the dense cloud ma-

terial of the ISM composition, which also suppresses farther particle acceleration due to a severe decrease of the shock velocity. We, however, note that abundance of the heavy elements in the target material would lead to the same effect boosting the modification of the gamma-ray spectrum.

To examine this we construct a momentum spectrum of accelerated particles in the form of:

$$\frac{dN_i}{dp} = \begin{cases} N_{0,i} p^{-s_1}, & \text{if } p < Z p_\mathrm{b} \\ N_{0,i} (Z p_\mathrm{b})^{-s_1+s_2} p^{-s_2}, & \text{otherwise.} \end{cases} \quad (4)$$

where i denotes the type of the particle and Z is the charge number and p_b is the break momentum for hydrogen nuclei. The choice of a break momentum is based on the idea that it should reflect the maximum momentum to which particles can be accelerated at this moment of time (Brose et al. 2020) and hence should scale with rigidity. We assume $s_1 = 2.0$, $s_2 = 2.75$ and p_b corresponds to the break kinetic energy of $E_\mathrm{b} = 10$ GeV for hydrogen nuclei. For helium this would correspond to the break at the kinetic energy of 18 GeV and for carbon at 55 GeV.

In Fig. 6 we show the resulting gamma-ray spectra for CRs consisting of only H (orange solid line), only He (green solid line), and only C (purple solid line), as well as for two mixed compositions which roughly correspond to the RSG (Dessart et al. 2017) and Wolf-Rayet (Sander et al. 2019, and references therein) stellar winds. To calculate the expected gamma-ray spectrum we use the "pion decay" subroutine of the RATPAC code. In these calculations we assume that G39.2−0.3 is located at the distance of 6.2 kpc and has a radius of 7 pc which corresponds to its mean angular radio diameter of 7.8′ (Patnaik et al. 1990). For all the cases we assume the density of the target material to be 400 cm^{-3} (as estimated for the molecular cloud) and keep the mass density of the CRs the same. The latter is done to illustrate how the normalization of the spectrum changes depending on the composition. The parameter space has, however, enough room to adjust the normalization of each model to correspond to the observed flux. The fraction of thermal particles injected into the acceleration process (above 10 MeV) adopted in the models shown in Fig. 6 is

$$\eta = 4 \times 10^{-7} \frac{M_\mathrm{SWB}}{30\, M_\odot}, \quad (5)$$

where M_SWB is the total mass of the material in the wind bubble of the progenitor star. This corresponds to the injection parameter $\chi = 4.0$, which is defined as the multiple of the momentum at the peak of the thermal particle distribution, $p_\mathrm{th} = \sqrt{2 m k_\mathrm{B} T}$, and determines the injection momentum of particles, $p_\mathrm{inj} = \chi p_\mathrm{th}$. This parameter can be as low as 3.5 (Blasi et al. 2005) boosting the injection efficiency by two orders of magnitude, hence any of the illustrated models can effectively match the observations. The total energy in particles for the hydrogen alone case calculated above 10 MeV is 1.1×10^{49} ergs and below that for other cases (4.4×10^{48} ergs for helium and 2.6×10^{48} ergs for carbon), which leaves some room for maneuver also in terms of the energy budget.

It can be seen that for heavy CRs the peak in the gamma-ray spectrum shifts to lower energies while the normalization decreases. Peak energies for hydrogen, helium and carbon are 1.5 GeV, 0.7 GeV, and 0.9 GeV, respectively. The RSG wind (green dotted lines in Fig. 6), which is still dominated by hydrogen, results in a similar spectrum to purely hydrogen CRs, with the peak energy staying essentially the same. On contrary, the carbon-loaded Wolf-Rayet wind (WC, purple dotted lines in Fig. 6)) significantly modifies the expected gamma-ray spectrum shifting the peak energy to 0.8 GeV and much better reproducing the shape of the observed one. It should be noted here, that the total mass in the stellar wind bubble is dominated by the main-sequence stellar wind which has a usual ISM composition. This is, however, not necessarily a problem for this model, since the main-sequence wind should be crushed by the RSG and WR winds, pushing it to the edge of the bubble, and particles injected at the shock would originate from a heavier composition. Likewise the injection efficiency of particles can be increased not violating any physical constraints.

Finally, the gamma-ray spectrum can be also boosted and modified by accounting for the particle acceleration at the reverse shock propagating into the heavy SNR ejecta. The contribution from the reverse shock is, however, expected to be negligible for the remnant of this size and age, because the density of the ejecta is expected to be rather low.

Taking into account the considerations above, a low-energy turn-over of the gamma-ray spectrum, which is observed in G39.2−0.3 and also in a few others SNRs, might be a tentative evidence that observed gamma-rays are produced in interactions of heavy nuclei. Moreover, precise measurements of gamma-ray spectra might in future serve to probe the composition of the media surrounding SNRs and even constrain the nature of their progenitor stars.

4.3 Compression of Galactic CRs

Another mechanism which might be responsible for the gamma-ray emission from SNRs interacting with dense clouds and is widely discussed in the literature in the context of the established hadronic emitters such as W 44 and IC 443 is compression and re-acceleration of Galactic CRs (Uchiyama et al. 2010; Lee et al. 2015; Cardillo et al. 2016; Tang & Chevalier 2014, 2015; Tang 2019). The basic idea is that the interaction of the SNR shock with the dense cloud results in the formation of the radiative shell behind the shock front. The material behind the shock is adiabatically compressed to very high densities potentially boosting for pion-decay generated gamma-ray emission. The adiabatic compression of the pre-existing ambient Galactic CRs in the radiative shell enhances the CR spectrum both energizing particles and increasing the normalization of the spectrum. The compressed CR spectrum can be expressed then as (Uchiyama et al. 2010)

$$n_\mathrm{comp}(p) = \xi^{2/3} n_\mathrm{GCR}(\xi^{-1/3} p) \quad (6)$$

where $n_\mathrm{GCR}(p)$ is the density of Galactic CRs as a function of momentum and $\xi \equiv n_\mathrm{shell}/(r n_0)$ is the adiabatic compression ratio, with n_shell the density of the cooled gas in the shell, n_0 the density of the ambient medium (cloud), and r the shock compression ratio. Additionally the pre-exisiting CRs can be further re-accelerated at the shock. This strong boost of the CR spectrum in combination with high gas density in the shell can result in substantial gamma-ray emission potentially explaining observed gamma-ray fluxes from aged SNRs interacting with dense clouds without necessity of direct particle acceleration at the shock.

In the following we evaluate the feasibility of this scenario for the case of SNR G39.2–0.3. For simplicity we ignore re-acceleration of Galactic CRs taking into account only adiabatic compression, and also define the adiabatic compression ratio as the total compression between the radiative shell and the cloud, i.e. $\xi = n_{\rm shell}/n_0$. Then, assuming that the compression is limited by the magnetic pressure, with the magnetic field in the shell given by $B_{\rm shell} = \sqrt{2/3}\xi B_0$ (where B_0 is the magnetic field in the cloud) the compression ratio can be expressed as:

$$\xi \simeq 94 \left[\frac{n_0}{1\,{\rm cm}^{-3}}\right]^{1/2} \left[\frac{B_0}{1\,\mu{\rm G}}\right]^{-1} \left[\frac{v_{\rm sh}}{10^7\,{\rm cm/s}}\right] \quad (7)$$

For the proton CR spectrum we adopt the approximation of the observed proton flux proposed by Bisschoff & Potgieter (2016) imposed with a spectral hardening at higher energies (Adriani et al. 2011; Aguilar et al. 2015) as in Cardillo et al. 2016[5]:

$$J_{\rm GCR}(E) = 3719 \frac{E^{1.03}}{\beta^2} \left(\frac{E^{1.21} + 0.77^{1.21}}{1 + 0.77^{1.21}}\right)^{-3.18} \times \left[1 + \left(\frac{E}{335}\right)^{\frac{0.119}{0.024}}\right]^{0.024} \quad (8)$$

where E is the kinetic energy of proton and β is the proton velocity in c. The number density of CRs as a function of momentum is given then by

$$n_{\rm GCR}(p) = \beta c\, n_{\rm GCR}(E) = 4\pi J_{\rm GCR}(E) \quad (9)$$

and the compressed spectrum can be found using Eq. 6.

In Fig. 7 we show the computed gamma-ray emission from the compressed Galactic CRs for different values of ξ and compare it to the observed spectrum. Simulated spectra are fit to the observational data by adjusting the volume filling factor f. The density in the cloud is assumed to be $n_0 \sim 400$ cm^{-3} and the distance to the SNR and its radius are assumed to be 6.2 kpc and 7 pc respectively (same as in the previous section). It can be seen from the figure that for large ξ, the simulated gamma-ray spectra do not provide good fits for the data, peaking at larger energy ($\gtrsim 1$ GeV) than the observed spectrum. On the other hand, for lower ξ we found that the filling factor needed to reach the level of the observed emission, is unrealistically high. Indeed, for $f = 0.18$ and $\xi = 10$ the total mass in the radiative shell is $\sim 4 \times 10^4\,M_\odot$. The total cloud mass that can possibly be accumulated within the volume of the SNR, $V_{\rm SNR}$, can be calculated as $V_{\rm SNR} n_0 \mu_{\rm H} = 2 \times 10^4\,M_\odot$ ($\mu_{\rm H}$ is the mass per hydrogen for a typical ISM composition), which is half of the required mass for this scenario to work. A larger distance (and hence larger physical radius of the SNR) could partially alleviate these constraints, but in general this scenario seems rather unlikely to explain the emission observed from SNR G39.2–0.3.

Additionally, the above argument also applies for W 44. Uchiyama et al. 2010 and Cardillo et al. 2016 deducted a filling factor of 0.20 and 0.15 respectively, using a constant density of [5-10]$\times 10^3$ cm^{-3} behind the shock. For the assumed radius of the remnant of 12.5 pc, this corresponds to $\sim (2.5 - 4) \times 10^5\,M_\odot$ which is almost an order of magnitude higher than the total cloud mass ($5.6 \times 10^4\,M_\odot$) for a cloud density of 200 cm^{-3}, applied in both studies. These simple consideration suggests that even if adiabatic compression of Galactic CRs might significantly contribute to the gamma-ray emission, it most probably cannot alone explain the observed flux of W 44.

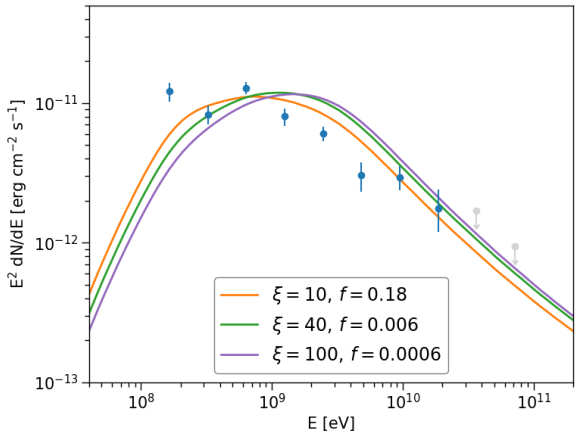

Figure 7. Spectral energy distribution of the modelled hadronic gamma-ray emission generated by compressed Galactic CRs in the radiative shell for different values of the compression ratio. Simulated spectra are fit to the data by adjusting the filling factor f which defines how much of the SNR volume is filled by the radiative shell. Blue points represent *Fermi*-LAT data as in previous figures.

5 CONCLUSIONS

We have identified SNR G39.2–0.3 as a hadronic accelerator through its multi-wavelength properties. The combination of the radio and GeV data together with non-detection of non-thermal X-rays from the remnant clearly indicate that neither inverse Compton (due to a low amount of electrons) nor bremsstrahlung (due to the spectral shape) can be responsible for the observed GeV emission. On contrary, the hadronic scenario provides a relatively good fit to the data for a soft spectrum of protons with the spectral index of ~ 2.75. Such a soft spectrum above some break energy which reflects the current maximum energy of accelerated protons is expected for dynamically old SNRs due to the escape of CRs and decrease of the acceleration efficiency. The total energy stored in CRs reaches $\sim 10^{49}$ erg, which reflects a few percent efficiency of converting kinetic energy into CRs, similarly to what has been observed in other SNR interacting with dense gas in large molecular clouds (Acero et al. 2016). SNR G39.2–0.3 seems in general fainter than the typical interacting SNRs listed in the last *Fermi* LAT SNR catalogue, when comparing with the radio emission (see Fig. 12 in Acero et al. 2016), but still within the main distribution.

The dense medium in which this SNR is evolving implies strong bremsstrahlung emission which in combination with observed GeV emission sets a lower limit on magnetic field of around $\sim 100\mu$G. Such a strong magnetic field is not typ-

[5] Note that in Cardillo et al. (2016) some of the parameters for the proton and helium spectra adopted from Bisschoff & Potgieter (2016) are mistakenly swapped, which however does not change their results considerably.

ical for evolved SNRs but expected for remnants interacting with molecular clouds as the thick medium compresses the shock region, resulting in an amplification of the magnetic field. High magnetic field in principle favours the acceleration of protons to high energies. However, the dense matter also slows down the shock, preventing the acceleration to go beyond a few tens of GeV. Even considering this effect, the low break energy required in SNR G39.2–0.3 seems too low, when considering evolution models of SNRs and the featureless radio Synchrotron spectrum. We investigate further how to reproduce the observed spectral shape by considering several hypothesis. To explain the low-energy peak in the gamma-ray spectrum, the CR spectrum requires a very low break energy, i.e. current maximum energy of protons, of $E_{\rm b} \lesssim 3$ GeV and/or a softer than typical DSA spectrum of protons from the acceleration process, $s_1 \gtrsim 2.3$. Both requirements point to the old dynamical age of the remnant, which means that it is already at the late stages of its evolution. This is not surprising given the interaction with the molecular cloud which drastically increases the density of the ambient medium. However, both of these requirements are not trivial to fulfill even for a dynamically old SNR.

On the other hand, the core-collapse nature of the SNR implies that heavier composition of the surrounding medium may be reflected in the resulting cosmic-ray and gamma-ray spectra. Hadronic interactions involving heavy nuclei result in a peak of the gamma-ray emission at significantly lower energies then proton-proton interactions. We show that accounting for the heavy composition of the circumstellar medium which is translated into the heavy composition of accelerated particles may help to explain the observed gamma-ray spectrum without need for unusually soft spectrum or low break energy, but requiring that the progenitor was a Wolf-Rayet star rather than a red supergiant. This result implies that precise measurements of gamma-ray emission from evolved core-collapse SNRs might potentially probe the composition of the surrounding environment and even the nature of the progenitor star.

We also investigated a scenario in which pre-existing Galactic CRs are compressed within the radiative shell and emit gamma-rays through hadronic interactions. We found that an unrealistically large size of the shell is required to explain the observed gamma-ray emission, which imposes substantial difficulties of this model.

SNR G39.2–0.3 is one of the few (18) SNR detected using the GLIMPSE Legacy science program on the Spitzer Space Telescope (Reach et al. 2006), and therefore one of the brightest SNR in infrared wavelengths. The observed infrared radiation reveals a mixture of molecular and ionic shocks, which indicate a clear production of CRs in this type of SNRs. Indeed, the majority of the infrared-bright SNRs have a counterpart on the *Fermi* LAT catalogue. Comparing the proton spectrum of this population of SNRs would help to understand CRs production in Type II SNRs.

DATA AVAILABILITY

The *Fermi* data underlying this article are available at https://fermi.gsfc.nasa.gov/ssc/data/access/lat/. The CO data were accessed from the MWISP survey and can be shared on reasonable request to the corresponding author.

ACKNOWLEDGEMENTS

This research was supported by the Alexander von Humboldt Foundation. The authors would like to thank J. Li for useful discussions and to the anonymous referee for constructive comments.

REFERENCES

Abdo A. A., et al., 2011, ApJ, 734, 28
Acero F., et al., 2016, ApJS, 224, 8
Ackermann M., et al., 2013, Science, 339, 807
Adriani O., et al., 2011, Science, 332, 69
Aguilar M., et al., 2015, Phys. Rev. Lett., 114, 171103
Aharonian F. A., Atoyan A. M., 1996, A&A, 309, 917
Ahnen M. L., et al., 2017, MNRAS, 472, 2956
Ambrogi L., Zanin R., Casanova S., De Oña Wilhelmi E., Peron G., Aharonian F., 2019, A&A, 623, A86
Anderson M. C., Rudnick L., 1993, ApJ, 408, 514
Archambault S., et al., 2017, ApJ, 836, 23
Banik P., Bhadra A., 2017, Phys. Rev. D, 95, 123014
Bass S. A., et al., 1998, Progress in Particle and Nuclear Physics, 41, 255
Becker R. H., Kundu M. R., 1975, AJ, 80, 679
Berezhko E. G., Ellison D. C., 1999, ApJ, 526, 385
Bhatt M., Sushch I., Pohl M., Fedynitch A., Das S., Brose R., Plotko P., Meyer D. M. A., 2020, Astroparticle Physics, 123, 102490
Bisschoff D., Potgieter M. S., 2016, Ap&SS, 361, 48
Blasi P., 2002, Astroparticle Physics, 16, 429
Blasi P., Gabici S., Vannoni G., 2005, MNRAS, 361, 907
Bleicher M., et al., 1999, Journal of Physics G: Nuclear and Particle Physics, 25, 1859
Bolatto A. D., Wolfire M., Leroy A. K., 2013, ARA&A, 51, 207
Brose R., Telezhinsky I., Pohl M., 2016, A&A, 593, A20
Brose R., Pohl M., Sushch I., Petruk O., Kuzyo T., 2020, A&A, 634, A59
Cardillo M., Amato E., Blasi P., 2016, A&A, 595, A58
Caswell J. L., Murray J. D., Roger R. S., Cole D. J., Cooke D. J., 1975, A&A, 45, 239
Celli S., Morlino G., Gabici S., Aharonian F. A., 2019a, MNRAS, 487, 3199
Celli S., Morlino G., Gabici S., Aharonian F. A., 2019b, MNRAS, 490, 4317
Cruciani A., et al., 2016, MNRAS, 459, 4224
Crutcher R. M., Wandelt B., Heiles C., Falgarone E., Troland T. H., 2010, ApJ, 725, 466
Dame T. M., Hartmann D., Thaddeus P., 2001, ApJ, 547, 792
Dessart L., John Hillier D., Audit E., 2017, A&A, 605, A83
Ferrand G., Safi-Harb S., 2012, Advances in Space Research, 49, 1313
Fraschetti F., 2014, Nuclear Instruments and Methods in Physics Research A, 742, 169
Gabici S., Gaggero D., Zandanel F., 2016, arXiv e-prints, p. arXiv:1610.07638
Giacalone J., Jokipii J. R., 2007, ApJ, 663, L41
Giuliani G., AGILE Team 2011, Mem. Soc. Astron. Italiana, 82, 747
Green A. J., Frail D. A., Goss W. M., Otrupcek R., 1997, AJ, 114, 2058
H. E. S. S. Collaboration et al., 2018, A&A, 612, A3
Harrus I. M., Slane P. O., 1999, ApJ, 516, 811
Jogler T., Funk S., 2016, ApJ, 816, 100
Kulsrud R. M., Cesarsky C. J., 1971, aplett, 8, 189
Lee H.-G., Moon D.-S., Koo B.-C., Lee J.-J., Matthews K., 2009, ApJ, 691, 1042

Lee S.-H., Patnaude D. J., Raymond J. C., Nagataki S., Slane P. O., Ellison D. C., 2015, ApJ, 806, 71
Malkov M. A., Diamond P. H., Jones T. W., 2002, ApJ, 571, 856
Malkov M. A., Diamond P. H., Sagdeev R. Z., 2011, Nature Communications, 2, 194
Malkov M. A., Diamond P. H., Sagdeev R. Z., Aharonian F. A., Moskalenko I. V., 2013, apj, 768, 73
Morlino G., Caprioli D., 2012, A&A, 538, A81
Ohira Y., Murase K., Yamazaki R., 2011, MNRAS, 410, 1577
Olbert C. M., Keohane J. W., Arnaud K. A., Dyer K. K., Reynolds S. P., Safi-Harb S., 2003, ApJ, 592, L45
Patnaik A. R., Hunt G. C., Salter C. J., Shaver P. A., Velusamy T., 1990, A&A, 232, 467
Reach W. T., et al., 2006, AJ, 131, 1479
Roesler S., Engel R., Ranft J., 2001, in , Advanced Monte Carlo for radiation physics, particle transport simulation and applications. Springer, pp 1033–1038
Sander A. A. C., Hamann W. R., Todt H., Hainich R., Shenar T., Ramachandran V., Oskinova L. M., 2019, A&A, 621, A92
Sezer A., Ergin T., Cesur N., Tanaka S. J., Kisaka S., Ohira Y., Yamazaki R., 2020, MNRAS, 492, 1484
Su Y., Chen Y., Yang J., Koo B.-C., Zhou X., Lu D.-R., Jeong I.-G., DeLaney T., 2011, ApJ, 727, 43
Su Y., et al., 2019, ApJS, 240, 9
Sushch I., Brose R., Pohl M., 2018, A&A, 618, A155
Tang X., 2019, MNRAS, 482, 3843
Tang X., Chevalier R. A., 2014, ApJ, 784, L35
Tang X., Chevalier R. A., 2015, ApJ, 800, 103
Telezhinsky I., Dwarkadas V. V., Pohl M., 2012, Astroparticle Physics, 35, 300
Telezhinsky I., Dwarkadas V. V., Pohl M., 2013, A&A, 552, A102
The Fermi-LAT collaboration 2019, arXiv e-prints, p. arXiv:1902.10045
Uchiyama Y., Blandford R. D., Funk S., Tajima H., Tanaka T., 2010, ApJ, 723, L122
Zabalza V., 2017, Naima: Derivation of non-thermal particle distributions through MCMC spectral fitting (ascl:1708.022)
Zeng H., Xin Y., Liu S., 2019, ApJ, 874, 50
Zirakashvili V. N., Aharonian F. A., Yang R., Oña-Wilhelmi E., Tuffs R. J., 2014, ApJ, 785, 130

This paper has been typeset from a TEX/LATEX file prepared by the author.

MNRAS **000**, 1–9 (2015) Preprint 28 April 2021 Compiled using MNRAS LATEX style file v3.0

Probing the hadronic nature of the gamma-ray emission associated with Westerlund 2

Enrique Mestre[1,2], Emma de Oña Wilhelmi[1,2,3]⋆, Diego F. Torres[4,1,2], Tim Lukas Holch[5], Ullrich Schwanke[5], Felix Aharonian[6,7,8], Pablo Saz Parkinson[9,10], Ruizhi Yang[11,12,13], Roberta Zanin[14]

[1]*Institute of Space Sciences (ICE/CSIC), Campus UAB, Carrer de Can Magrans s/n, 08193 Barcelona, Spain*
[2]*Institut d'Estudis Espacials de Catalunya (IEEC), 08034 Barcelona, Spain*
[3]*Deutsches Elektronen Synchrotron DESY, 15738 Zeuthen, Germany*
[4]*Institució Catalana de Recerca i Estudis Avançats (ICREA), E-08010 Barcelona, Spain*
[5]*Humboldt University of Berlin, Newtonstr. 15, 12489 Berlin, Germany*
[6]*Dublin Institute for Advanced Studies, 31 Fitzwilliam Place, Dublin 2, Ireland*
[7]*Max-Planck-Institut für Kernphysik, P.O. Box 103980, D 69029 Heidelberg, Germany*
[8]*Gran Sasso Science Institute, 7 viale Francesco Crispi, 67100 L'Aquila, Italy*
[9]*Department of Physics and Laboratory for Space Research, The University of Hong Kong, Pokfulam Road, Hong Kong*
[10]*Santa Cruz Institute for Particle Physics, University of California, Santa Cruz, CA, 95064, USA*
[11]*Department of Astronomy, School of Physical Sciences, University of Science and Technology of China, Hefei, Anhui 230026, China*
[12] *CAS Key Labrotory for Research in Galaxies and Cosmology, University of Science and Technology of China, Hefei, Anhui 230026, China*
[13]*School of Astronomy and Space Science, University of Science and Technology of China, Hefei, Anhui 230026, China*
[14]*CTA Observatory GmbH, Via Piero Gobetti 93, I-40129 Bologna, Italy*

Accepted XXX. Received YYY; in original form ZZZ

ABSTRACT

Star-forming regions have been proposed as potential Galactic cosmic ray accelerators for decades. Cosmic ray acceleration can be probed through observations of gamma-rays produced in inelastic proton-proton collisions, at GeV and TeV energies. In this paper, we analyze more than 11 years of *Fermi*-LAT data from the direction of Westerlund 2, one of the most massive and best-studied star-forming regions in our Galaxy. In particular, we investigate the characteristics of the bright pulsar PSR J1023–5746 that dominates the gamma-ray emission below a few GeV at the position of Westerlund 2, and the underlying extended source FGES J1023.3–5747. The analysis results in a clear identification of FGES J1023.3–5747 as the GeV counterpart of the TeV source HESS J1023-575, through its morphological and spectral properties. This identification provides new clues about the origin of the HESS J1023-575 gamma-ray emission, favouring a hadronic origin of the emission, powered by Westerlund 2, rather than a leptonic origin related to either the pulsar wind nebula associated with PSR J1023–5746 or the cluster itself. This result indirectly supports the hypothesis that star-forming regions can contribute to the cosmic-ray sea observed in our Galaxy.

Key words: Stars: winds, outflows – ISM: cosmic rays – Galaxy: open clusters and association: indivual: Westerlund 2 – gamma-rays: stars

1 INTRODUCTION

The potential of massive star clusters to accelerate Galactic cosmic rays (GCRs) to very-high energies (VHE, E > 100 GeV) has been recognized since the 1980s (Cesarsky & Montmerle 1983; Bykov et al. 2020; Binns et al. 2005). Several hypotheses have been proposed for acceleration sites to very high energies in star-forming regions (SFRs), either in the vicinity of OB and WR stars, or at the interaction of their fast winds with supernova (SN) shocks, or in so-called super-bubbles (see e.g. Bykov et al. 2020; Gabici et al. 2019 and references therein). The presence of cosmic rays (CRs) can be inferred by means of gamma-ray observations (above a few hundreds of MeV), by looking at the by-product of inelastic proton-proton collisions. The spectral energy distribution (SED) from hadronic-originated gamma-ray sources is characterized by a sharp rise in the ∼70–200 MeV range (resulting from the neutral pion threshold production energy), followed by a hard emission up to the maximum energy. Competing gamma-ray processes related to leptonic emission should have different imprints on the spectral shape, showing a (in many occasions broad) peak in the hundreds of

⋆ E-mail: Emma.de.ona.wilhelmi@desy.de

GeV range. Therefore, sampling the spectrum from a few hundreds of MeV to tens of TeV should result in a strong indication of the origin of the observed radiation. Several SFRs have been identified as likely GCR accelerators in the GeV and TeV regime (Ackermann et al. 2011a; H. E. S. S. Collaboration et al. 2011; Abramowski et al. 2012; H. E. S. S. Collaboration et al. 2015; Yang et al. 2018; Aharonian et al. 2019; Saha et al. 2020; Yang & Wang 2020; Sun et al. 2020). However, a firm identification remains elusive, given the large extension of the sources and/or the presence of some other efficient accelerators in the region, such as pulsars and pulsar wind nebulae (PWNe).

One of the most massive and well-studied SFRs in our Galaxy is Westerlund 2. The cluster itself presents a $\sim 0.2^{o}$ wind-blown bubble observed in infrared (IR) by *Spitzer* and in radio continuum by ATCA (Whiteoak & Uchida 1997; Whitney et al. 2004). This bubble is coincident with a prominent feature at radio wavelengths, known as the *blister*, and with an extended TeV source ($\sim 0.2^{o}$) known as HESS J1023-575 (Aharonian et al. 2007; H. E. S. S. Collaboration et al. 2011). In the GeV regime, the young and energetic pulsar PSR J1023–5746 lies 8 arcmin away from the cluster, and its PWN was initially suggested as possible counterpart of the TeV source (Saz Parkinson et al. 2010; Ackermann et al. 2011b) (see Table 2 for the physical parameters of the pulsar, obtained from Saz Parkinson et al. 2010). Besides the PWN scenario, several accelerators have been proposed to power the TeV emission: Westerlund 2 contains an extraordinary ensemble of hot and massive OB stars (Rauw et al. 2004), for which a total energy release for the collective winds was estimated to be $\sim 5.7 \times 10^{37}$ erg s^{-1}. Westerlund 2 also hosts one of the most massive binary systems, composed of two WN6ha stars (Rauw et al. 2004), dubbed WR 20a. Their orbital period is ~ 3.6 days (Bonanos et al. 2004; Rauw et al. 2004) and the estimated kinetic energy loss rate is $\sim 10^{37}$ erg s^{-1}. Several massive molecular clouds were found within the surrounding of Westerlund 2, overlapping with the GeV and TeV gamma-ray sources (see Fig. 5 in H. E. S. S. Collaboration et al. 2011).

Since the discovery of the Westerlund 2 cluster, there have been several attempts to determine accurately its distance, estimated between 2 kpc and 8 kpc (Salpeter 1955; Moffat et al. 1991; Piatti et al. 1997; Carraro & Munari 2004; Uzpen et al. 2005; Rauw et al. 2005; Dame 2007; Tsujimoto et al. 2007; Rauw et al. 2007; Ascenso et al. 2007; Furukawa et al. 2009; Vargas Álvarez et al. 2013). In the following we adopt a value of 5 kpc, roughly in the mid-range of the recent optical photometric work (Vargas Álvarez et al. 2013; Drew et al. 2018) and at the bottom end of the interstellar medium (ISM) estimates (Dame 2007; Furukawa et al. 2014).

The Large Area Telescope (LAT, Atwood et al. 2009) onboard the *Fermi Gamma-ray Space Telescope*, launched in June 2008, surveys the gamma-ray sky in the 20 MeV to greater than 300 GeV energy range. The LAT data recorded during the last decade has resulted in different catalogues of gamma-ray sources (Ballet et al. 2020). For instance, the 4FGL catalogue (Abdollahi et al. 2020) covers the data recorded during the first 8 years of observations. On the other hand, the extended sources are listed in the *Fermi* Galactic Extended Source (FGES) Catalog (Ackermann et al. 2017a). In this paper, we analyzed the gamma-ray emission towards FGES J1023.3–5747 (Ackermann et al. 2017b) and the pulsar PSR J1023–5746 taking advantage of more than 11 years of *Fermi*-LAT data and the most recent gamma-ray source catalogue released by the *Fermi*-LAT collaboration. The paper is structured as follows. In Sections 2 and 3 we describe the collected data and present the results of the analysis. In Section 4 we discuss the possible leptonic (4.1) or hadronic (4.2) origin of the FGES J1023.3–5747 gamma-ray extended emission. Finally, in Section 5 we summarize the conclusions reached.

2 DATA ANALYSIS

To investigate the characteristics of the gamma-ray emission from FGES J1023.3–5747 and PSR J1023–5746, we used *Fermi*-LAT (P8R3, Atwood et al. 2013; Bruel et al. 2018) data spanning from 2008 August 4 to 2019 April 24 (or 239557417 - 577782027 seconds in *Fermi* Mission Elapsed Time), in the energy range from 200 MeV to 500 GeV. We retrieved the data from a region of interest (ROI) defined by a radius of 20° around the position of PSR J1023–5746 (RA= 155.76°, DEC = −57.77°, Kerr et al. 2015). We analyzed only the dubbed SOURCE class events with a maximum zenith angle of 90° to eliminate Earth limb events. The events were selected with a minimum energy of 200 MeV, to avoid events poorly reconstructed due to the large angular resolution and the large crowding of sources in the region. The analysis of the source spectrum below 200 MeV is crucial to characterize hadronic-originated gamma-rays sources, since neutral pion decay spectrum rises steeply below this energy, a feature often referred to as the pion-decay bump. However, this particular source is not a promising candidate for this analysis: the moderate flux of the source and hard spectrum limits the number of photons in the very low energy regime; the extended morphology complicates the analysis with respect to the point-like case; the presence of several sources in the region may contaminate further the spectrum especially at low energies, preventing an accurate characterization (i.e., overlapping with the PSR J1023–5746 emission). In this work, we focus on studying the general GeV to TeV spectral shape.

To obtain the spectrum and morphology of FGES J1023.3–5747, we first had to disentangle its diffuse gamma-ray emission from the radiation coming from the pulsar PSR J1023–5746 and other nearby sources. For that purpose, we need to derive first the spectral energy distribution of all the sources in the field of view. Therefore, a comprehensive model describing the gamma-ray sources in the ROI is needed. In order to build this model, we included all the LAT sources listed in the *Fermi*-LAT Fourth Source Catalog (4FGL, Abdollahi et al. 2020) in a radius of 20° around the position of FGES J1023.3–5747. On the other hand, the LAT data contain a significant contribution from Galactic and extra-galactic diffuse gamma-rays, which is described with the latest version available of the Galactic (gll_iem_v07) and isotropic (iso_P8R3_SOURCE_V2_v1) diffuse emission models. The model's free parameters correspond to the ones of the sources within 3° around the position of PSR J1023–5746. Beyond this radius, the normalization of all the sources with test statistic greater than ten (TS > 10) is also free. The Test Statistic is defined as TS = $2\log(L/L_0)$, where L is the maximum value of the likelihood function over the ROI including the source in the model and L_0 is the same without the source (Mattox et al. 1996). Hence, the detection significance of a source is usually approximated by the square root of the TS.

The analysis of the LAT data described above was performed by means of the FERMIPY PYTHON package (version 0.18.0), based on the FERMI SCIENCE TOOLS (Wood et al. 2017). The data were binned in 8 energy bins per decade and spatial bins of 0.1° size to perform the analysis. The response of the LAT instrument is evaluated with the Instrument Response Functions (IRF, version P8R3_SOURCE_V2). The energy dispersion correction was ap-

plied to the sources in our model, except for the isotropic diffuse emission model.

The current version of LAT data (i.e PASS 8) classifies the events into quartiles based on the varying quality of the direction reconstruction (PSF events types). In our analysis, we took into account the four Point Spread Function (PSF) event types available (dubbed PSF0, PSF1, PSF2, and PSF3), and applied the appropriate IRF and isotropic background models according to the quality of the reconstructed event directions. Doing so, we are preventing the loss of possibly useful information in the analysis by means of the separate treatment of high-quality events and poorly localized ones. The analysis is performed by means of a joint likelihood fitting process.

In order to discriminate the diffuse gamma-ray emission of FGES J1023.3–5747 from the emission of the nearby pulsar, we first performed a timing analysis on the PSR J1023–5746 data to gate the pulsed emission, by means of the pulsar analysis package TEMPO2 (Hobbs et al. 2006). To obtain the phase curve of PSR J1023–5746, we assigned the corresponding phases to the gamma-ray events localized in a region of 0.6° of radius around the pulsar position (RA = 155.76°, DEC = -57.77°). Then, we computed the phases of the events using the updated ephemeris of PSR J1023–5746 at epoch 55635 MJD. The new ephemeris that allows us to enlarge the data set to more than 11 years was provided by the *Fermi*-LAT collaboration. Finally, we applied the Bayesian Blocks method (Scargle et al. 2013) to the PSR J1023–5746 light curve, and obtained different components, defined as ON, OFF, and *Bridge* emission. We computed the contribution to the phase curve of each of the sources in the model with the *Fermi* tool *gtsrcprob*, which assigns to every event the probability of belonging to each source of the model.

The spectral energy distributions of the sources were obtained for 12 energy bins (spanning from 200 MeV to 500 GeV) using the whole ROI, with the FGES J1023.3–5747 and PSR J1023–5746 spectra characterized by power-law and exponential cutoff power-law models respectively. The sources SEDs are computed for the different components of the phase curve, cutting the events in phase. We tested the spectral analysis consistency studying the systematic uncertainties on the SEDs, mainly due to the LAT effective area (A_{eff}) and the Galactic diffuse emission model. The systematic uncertainties due to the LAT effective area are computed with the bracketing A_{eff} method[1], and the ones due to the diffuse Galactic model were tested by artificially changing the normalization of the same by ±6 per cent with respect to the best-fitted value (Ajello et al. 2011; Li et al. 2018).

On the other hand, the size of FGES J1023.3–5747 was analyzed with the FERMIPY extension method, based on a likelihood ratio test with respect to the point-source hypothesis. We tested both 2D symmetric Gaussian and 2D radial disk models for the morphology of FGES J1023.3–5747. The best-fit extension in each case is computed performing a likelihood profile scan over the source width (68 per cent containment) and maximizing the model likelihood.

Finally, we imposed different additional cuts of energy on the data described above (at 700 MeV, 3 GeV, 10 GeV, 40 GeV, 70 GeV and 135 GeV), and studied the morphological characteristics of FGES J1023.3–5747 re-analysing the data in differential energy bins (see Figure A1).

[1] https://fermi.gsfc.nasa.gov/ssc/data/analysis/scitools/Aeff_Systematics.html

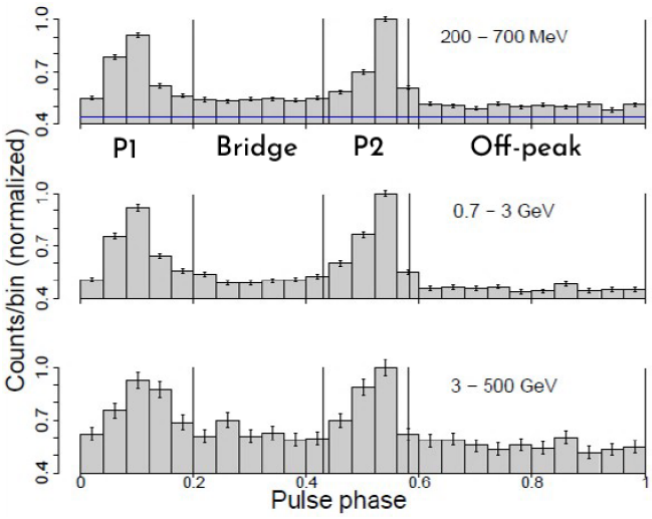

Figure 1. Phase curve of PSR J1023.1-5745 obtained at different energies in a region of 0.6° around the pulsar position (normalized by the height of P2) with the different components of the phase curve noted. The horizontal blue line corresponds to the expected contribution in the phase curve of background sources (i.e., all the sources in the field of view except for FGES J1023.3–5747 and PSR J1023–5746).

3 RESULTS

The analysis of the pulsed emission from PSR J1023–5746 with the Bayesian Blocks method showed two peaks, spanning from 0 to 0.2, and from 0.43 to 0.58 in phase, with a *Bridge* emission in between. The peaks are centered at ≈ 0.09 and ≈ 0.54 in phase respectively and present a similar width ($\sigma \approx 0.02$ in phase if fitted with a Gaussian profile). The pulsed emission was analyzed in three intervals of energy: from 200 MeV to 700 MeV, from 700 MeV to 3 GeV, and above 3 GeV. No significant shift was observed between the peaks at different energies. Also, the relation between the height of the peaks, and between the number of events in each peak (P1/P2 ≈ 0.8), does not differ significantly for the different energy bins. The second peak is the dominant one in the three intervals of energy. The number of events in the *Bridge* component (for the energy bins mentioned) is ∼ 10 per cent larger than the one expected from the off-peak statistics. The three pulse profiles in the different energy bins are shown in Fig. 1 (counts per bin, for each phase). The Galactic diffuse emission is dominant both in the *Bridge* and off-peak regions. Hence, a similar level (in counts per bin) is observed in Fig. 1 for both components. The same contribution from FGES J1023.3–5747 is expected in each bin of the phase curve (for a given energy interval), since the extended source emission should not vary in synchrony with the pulsed one.

PSR J1023–5746 (described as a point-like source with an exponential cutoff power-law spectrum) is located at RA = 155.772° ± 0.005° and DEC = −57.764° ± 0.005° (see Table A1). The source is well-detected in the on-peak and *Bridge* regions with $\sqrt{TS} \gtrsim 80$ in both intervals. The results of the spectral analysis of PSR J1023–5746, performed both in the on-peak and *Bridge* intervals are summarized in Table 1 (see Figure 2 left panel). Note that the spectral energy distribution is characterized by an exponential cutoff located at an energy of ∼ 3 GeV. Also, the cutoff energy obtained in the on-peak region is in agreement with the best fitted one for the *Bridge* component, while the spectral indices in both analyses are compatible within the uncertainties (at 95% CL). In addition, the positions

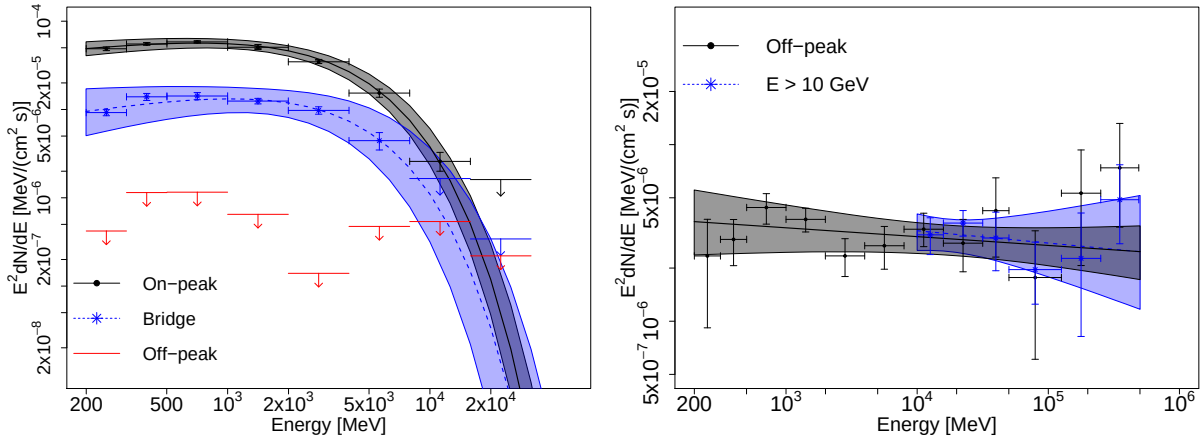

Figure 2. On the left a) Spectral energy distribution (with only statistical errors) of PSR J1023–5746 derived from the on-peak (in black, with dot markers), the *Bridge* (in blue, with star markers), and off-peak-region (red upper limits). On the right b) Spectral energy distribution (with only statistical errors) derived from FGES J1023.3–5747 after gating the pulsar emission (in black) and analysing only the gamma-ray emission above 10 GeV (without cutting in phase, in blue). The shaded area marks the 1σ error on the fitted spectral model.

fitted for PSR J1023–5746, both in the on-peak and *Bridge* regions, are in agreement at 95% CL. The point-like source, however, is not detected if selecting only off-peak events. In this region, only upper limits for the flux of PSR J1023–5746 can be derived (see the red arrows in Figure 2 left panel). This argues in favor of a reduced contribution of the pulsar emission in the defined 'OFF' region in comparison to the 'Bridge'. Admittedly, however, a close flux level between both such regions complicates this distinction.

To investigate the emission associated with the extended source FGES J1023.3–5747, we analyze the off-peak interval (from 0.58 to 1 in phase) to minimize the contamination from PSR J1023–5746. The analysis results in a significant detection of FGES J1023.3–5747 ($\sqrt{TS} \approx 14$), with the source located at RA = 155.93° ± 0.03° and DEC = −57.79° ± 0.03° (see Table A1). The parameters of the best-fitting power-law spectrum for FGES J1023.3–5747 are summarized in Table 1 (see Figure 2 right panel). The source spatial component is best described by a symmetric 2D Gaussian model, and the fit of the extension resulted in a 68 per cent containment radius of $r_{68} = 0.24° \pm 0.03°$ (i.e., an intrinsic size of $\sigma = 0.16 \pm 0.02$, see Lande et al. 2012), with a 0.29° upper limit for the 95 per cent containment radius. We also tested a symmetric 2D disk model, which, however, does not improve the log-likelihood with respect to the best-fit Gaussian model, obtaining a 68 per cent containment radius compatible with the extension above (i.e., 0.25° ± 0.02°). Also, the log-likelihood of the best-fit Gaussian model with an extension fixed to the value measured by H.E.S.S. ($\sigma = 0.18°$, H. E. S. S. Collaboration et al. 2011) is not significantly smaller than the one corresponding to the best-fit extension described above ($\Delta TS \approx 1.6$, as expected, given the similar extension of the GeV and TeV excesses). The extension and position of FGES J1023.3–5747 were also computed for the on-peak and *Bridge* components, where an extended source model was fitted simultaneously to the PSR J1023–5746 emission. No significant difference with respect to the results in the off-peak region was observed. The 'OFF' region of PSR J1023–5746 has been analyzed with LAT data in previous works. In the second catalogue of LAT gamma-ray pulsars (2PC, see Abdo et al. 2013), an unidentified source was reported in the off-pulse region, defined from 0.76 to 0.02 in phase. The analysis of this source showed some indication of spatial extension ($TS_{\rm ext} = 30$). Interestingly, the integrated flux for such source, computed from 100 MeV to 316 GeV of energy, i.e., 1.79×10^{-8} cm^{-2}s^{-1} (with large uncertainty) is compatible with the one derived (in this work) for FGES J1023.3–5747 in the same regime (of energy), i.e., $(1.97 \pm 0, 49) \times 10^{-8}$ cm^{-2}s^{-1} (with only statistical errors). Similarly, the off-peak region was analyzed in Ackermann et al. 2011b, with 16 months of LAT data. In this case, the off-peak emission was detected only at energies above 10 GeV. Despite the off-pulse region (from 0.85 to 1.13 in phase, in the cited paper) differs significantly from the definition in this work, and the small amount of data used compared to the reanalysis we present, the integral flux of the source reported (from 10 GeV to 100 GeV of energy), i.e., $(4.6 \pm 2.2) \times 10^{-10}$ cm^{-2}s^{-1} is also in well agreement with the flux derived for FGES J1023.3–5747 in the same interval $(2.62 \pm 0.37) \times 10^{-10}$ cm^{-2}s^{-1}. A more recent reanalysis of the detected off-pulse emission with 45 months of LAT data (see Acero et al. 2013) reported a similar integrated flux above 10 GeV of energy.

The position of the sources, fitted for the different components of the phase curve, implies a separation between PSR J1023–5746 and the centroid of FGES J1023.3–5747 of 5.3 ± 1.1 arcmin, with the pulsar position well within the extended source (given the size measured for the same, see Fig. 3). In addition, the best-fitted position of FGES J1023.3–5747 (in the off-peak region) is in good agreement with the one estimated by H.E.S.S for HESS J1023-575 (i.e., RA = 155.85° and DEC = −57.79° , H. E. S. S. Collaboration et al. 2011), with a separation between the centroids of the sources of 3.3 ± 1.4 arcmin (account statistical errors only).

To further investigate the spectrum and morphology of the high energy part of FGES J1023.3–5747 we analyzed the data set above 10 GeV (see Table 1 and Figure 2 right panel), where additional cuts in phase are not necessary due to the exponential decrease of the pulsed emission above ∼ 3 GeV (of energy). We included the emission of PSR J1023–5746 (modeled as a point-like source with the spectrum shown in Table 1) in this analysis, detected with low significance at energies above 10 GeV ($\sqrt{TS} \approx 3$). The extension fitted in this case for FGES J1023.3–5747 was $r_{68} = 0.23° +0.03° - 0.02°$ (for a 2D Gaussian model). Note that both the position of the extended source and the best-fitting power-law spectral model are in good agreement with the ones obtained in the off-peak region (at 95% CL, see Figure 2 right panel and Table A1). Also, the spectral index, obtained both in the off-peak region and at energies above

10 GeV, is compatible with $\Gamma = 2$, within the uncertainties (at 95% CL).

To conclude, we studied the morphology of FGES J1023.3–5747 (in the off-peak component) in six energy bins (with break-points in 200 MeV, 700 MeV, 3 GeV, 10 GeV, 40 GeV, 70 GeV, and 500 GeV). For this purpose, we fitted the extension of FGES J1023.3–5747 (measured for a Gaussian profile, i.e 68 per cent containment radius) as a function of the energy (see Figure A1). Then, we tested an energy-dependent shrinking model of the form $\sigma \propto E^{-\alpha}$, but no significant variation of FGES J1023.3–5747 extension was observed. The flux fitted for FGES J1023.3–5747 in each bin of energy is compatible with the one expected from the spectrum fitted in the full range of energy (from 200 MeV to 500 GeV), and the spectral index of the best-fitting model is compatible with $\Gamma = 2$ (at 3σ), for each bin of energy. However, the angular resolution of *Fermi*-LAT ($\sim 0.8^\circ$ at 1 GeV, see Abdollahi et al. 2020) limits the fit of the FGES J1023.3–5747 extension for energies below few GeV's. Note that, since the *Fermi*-LAT PSF is $\sim 0.2^\circ$ at 3 GeV (68 per cent containment radius), an imperfect diffuse modeling can bias the extension measured at lower energies. The large scale diffuse emission, dominant at low energies ($\sim$ 500 MeV), limits the extension measurements performed in this regime, as seen in Figure A1 (note the upper limit in the lowest energy bin). The contamination from the same, however, is decreasingly relevant at higher energies.

4 DISCUSSION

The gamma-ray emission from the bright GeV pulsar PSR J1023–5746 dominates the emission below a few GeV. Within the current statistics, the light curve remains similar in different energy ranges, contrary to other pulsars such as Crab or Vela. It is well described by two narrow peaks and a *Bridge* region between them. The spectrum obtained from this region is very similar to the one from the peaks, with an exponential cut-off at ~3 GeV, indicating a common location of the radiation zone, most likely within the pulsar magnetosphere or its vicinity.

The analysis of the gamma-ray emission, gating off the On- and *Bridge*-regions, combined with the large dataset, allow the detailed investigation of the spectral shape and morphology of the extended underlying source FGES J1023.3–5747. The measured size of the GeV source is in good agreement with the one measured by H.E.S.S. for HESS J1023-575 (see Fig. 3). The spectrum obtained from the ~0.2°region is hard (Γ=2) and connects smoothly the emission observed with LAT with the one in the TeV regime (see Fig. 4), indicating a clear identification of FGES J1023.3–5747 as the GeV counterpart of HESS J1023-575. The spectral results agree with the ones reported in Ackermann et al. 2017b, but are in tension with the ones obtained by Yang et al. 2018. For the latter, the ephemeris used was valid only for a reduced period in comparison to the temporal span of the data analyzed, resulting most likely in a contamination from the pulsar that affected the spectrum of the extended source. For this work, in turn, we have used the most updated ephemeris for the pulsar, valid for the entire data set analyzed.

The new characterization of the emission, thanks to the larger data set and better source discrimination, provides new clues to establish the origin of the gamma-ray emission. Different scenarios are discussed in the following, in the context of the new morphology and spectral features found.

4.1 PWN scenario

The discovery of the energetic pulsar PSR J1023–5746 (with spin down energy $\dot{E} = 10^{37}$ erg s^{-1}), together with the proven efficiency of PWNe to produce TeV gamma-rays (H. E. S. S. Collaboration et al. 2018) triggered the interpretation of HESS J1023-575 as a PWN energised by PSR J1023–5746. The association of the stellar cluster with the birth site of PSR J1023–5746 (τ_c=4.6 ky, Saz Parkinson et al. 2010) is not straight-forward, implying an unrealistic transverse velocity of the pulsar (Ackermann et al. 2011b) if the same is located at the distance the cluster is believed to be ~6 kpc (Dame 2007). Several time-dependent modelings of a Pulsar/PWN scenario have been proposed to connect HESS J1023-575 with PSR J1023–5746 (Ackermann et al. 2011b; H. E. S. S. Collaboration et al. 2018). In the reanalysis presented here, we found a noticeable morphological (see Fig. 3) and spectral (see Fig. 4) overlap between the extended GeV source FGES J1023.3–5747 and the TeV source HESS J1023-575, which provides strong constraints on the PWN interpretation. In the same, the gamma-ray spectrum is expected to show a peak at energies just below the cut-off energy in the electron spectrum, in the TeV regime. The GeV gamma-ray spectrum due to the interactions of electrons with magnetic and radiation fields is effectively uncooled, up to the cut-off energy, since IC and synchrotron loss times are much longer in a typical PWN environment. The IC cooling time corresponding to the photon fields in the region where the pulsar is located (dust IR photons, stellar photons and CMB, see Table 2 where the density of the dust/stellar, $\omega_{\rm FIR/*}$ at temperature $T_{\rm FIR/*}$ is given) is $> 10^4$ yr, whereas a magnetic field of $> 400\ \mu$G should be considered to cool efficiently a few GeV electrons ($\tau_{\rm syn,yr} \simeq 1.3 \times 10^7 B_{\mu\rm G}^{-2} E_{\rm e,TeV}^{-1}$). The uncooled $\Gamma_\gamma \sim 2$ spectrum extends from ~ 200 MeV to a few hundred GeV, where it meets the one measured by H.E.S.S. (see Figure 4). This photon spectrum would correspond to an electron spectrum of index $\alpha \approx 2\Gamma_\gamma - 1 = 3$ (in the Thompson regime, Blumenthal & Gould 1970). Such a spectral index is difficult to reconcile with acceleration theories and typical injection spectra in PWNe. To further investigate this, we model the data using a PWN radiative scenario, in which the particle evolution and radiation are evolving in time according to the approach taken in Torres et al. 2014. The time-dependent gamma-ray spectrum is obtained using the GAMERA software (Hahn 2015). Likewise, we used a broken power-law injection spectrum with similar shape to those found for young PWNe (see Table 2 for details and Table 2 in Torres et al. 2014). The time-dependent modeling used does not account for morphological changes (i.e., assumes energy-independent morphology). The best model representing the data is shown in Fig. 4, integrating in time up to the estimated pulsar age (τ_c ~4.6 kyr). The upper limit on the X-ray emission was obtained by Fujita et al. 2009 using *Suzaku* observations (in a $17'.8 \times 17'.8$ field). The disagreement between the LAT data and the model is evident, especially at the lower energies, and one should then consider a more complex modeling, with more than one electron population, to obtain a good representation of the data. A second possibility to flatten the spectrum involves the contribution of different stellar photon fields, which would be indeed expected from a region like Westerlund 2 (Vargas Álvarez et al. 2013; Guarnieri et al. 1995). However, the morphology of such a source, peaking at the regions of high stellar radiation density, would differ from the one observed, rendering this possibility unlikely. Additionally, the similar extension between the LAT and the H.E.S.S. measurements disfavors further the PWN scenario, where usually a larger GeV nebula, due to cooling or/and

Table 1. Best-fitting models for PSR J1023–5746 and FGES J1023.3–5747. The units of N_0 are $cm^{-2}s^{-1}MeV^{-1}$ for PSR J1023–5746 and $cm^{-2}s^{-1}MeV^{-1}sr^{-1}$ in the case of FGES J1023.3–5747.

Parameter	PSR J1023–5746 (On-peak)	PSR J1023–5746 (*Bridge*)	FGES J1023.3–5747 (Off-peak)
N_0	$(2.51 \pm 0.18_{stat} \pm 0.24_{sys}) \times 10^{-11}$	$(6.57 \pm 1.22_{stat} \pm 2.44_{sys}) \times 10^{-12}$	$(1.02 \pm 0.14_{stat} \pm 0.16_{sys}) \times 10^{-14}$
Γ	$1.74 \pm 0.05_{stat} \pm 0.16_{sys}$	$1.61 \pm 0.17_{stat} \pm 0.56_{sys}$	$2.05 \pm 0.06_{stat} \pm 0.33_{sys}$
E_0 [GeV]	1.95	1.95	17
$E_{\rm cutoff}$ [GeV]	$2.74 \pm 0.24_{stat} \pm 0.39_{sys}$	$2.7 \pm 0.57_{stat} \pm 1.2_{sys}$	-
σ [deg]	-	-	0.16 ± 0.02

Parameter	FGES J1023.3–5747 ($E > 10$ GeV)	FGES J1023.3–5747 (On-peak)	FGES J1023.3–5747 (*Bridge*)
N_0	$(1.09 \pm 0.16_{stat} \pm 0.04_{sys}) \times 10^{-14}$	$(1.03 \pm 0.21_{stat} \pm 0.10_{sys}) \times 10^{-14}$	$(9.83 \pm 2.0_{stat} \pm 0.5_{sys}) \times 10^{-15}$
Γ	$2.07 \pm 0.15_{stat} \pm 0.02_{sys}$	$(2.01 \pm 0.16_{stat} \pm 0.26_{sys})$	$(2.11 \pm 0.14_{stat} \pm 0.22_{sys})$
E_0 [GeV]	17	19.6	19.6
$E_{\rm cutoff}$ [GeV]	-	-	-
σ [deg]	0.15 ± 0.02	0.16 ± 0.04	0.16 ± 0.03

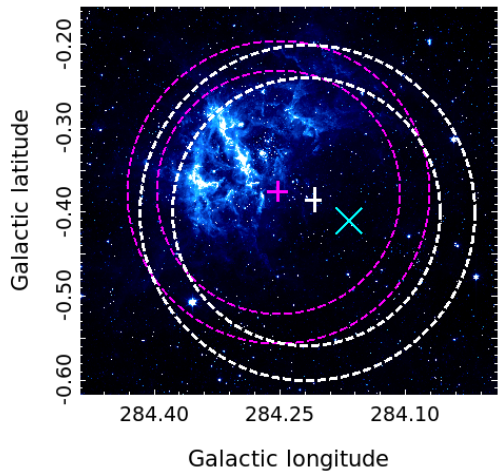

Figure 3. *Spitzer*/IRAC GLIMPSE Mosaic obtained from the GLIMPSE survey archival data. The magenta dashed lines correspond to the 1σ interval for the best-fit extension of FGES J1023.3–5747, with the central cross marking the best-fit position (with the 1σ error). The white dashed lines and cross correspond, similarly, to the morphological characteristics of the H.E.S.S. source HESS J1023-575, as described in H. E. S. S. Collaboration et al. 2011. The cyan cross corresponds to the position of PSR J1023–5746.

Table 2. Physical parameters of PSR J1023–5746 and its putative PWN. The pulsar rotation parameters f and $\dot{f}$ are obtained from ATNF catalogue. The braking index n and ejecta mass M_{ej} are fixed, following the results from Torres et al. 2014. The broken power-law spectral shape of electrons (defined with the indices $\alpha_{1,2}$ and breaking energy γ_b), and magnetic field in the region (B), that best represent the data, are listed in the third section of the table.

Pulsar & Ejecta	
f (Hz)	8.97
$\dot{f}$ (-10^{-12} Hz s^{-1})	30.88
τ_c (kyr)	4.6
$L(t_{age})$ (erg/s)	1.1×10^{37}
n	2.509
D (kpc)	5
M_{ej} ($M_\odot$)	10
Environment	
T_{FIR} (K)	30
w_{FIR} (eV/cm^3)	1
T_* (K)	2500
w_* (eV/cm^3)	2
n_H	1.0
Particles and field	
γ_b	5×10^5
α_1	1.5
α_2	3.0
$B(t_{age})$ (μG)	7

energy-dependent diffusive transport, is observed (Principe et al. 2020; H. E. S. S. Collaboration et al. 2019, 2012).

4.2 Scenarios related to Westerlund 2 massive stars

Electrons can also be efficiently accelerated in open clusters via shocks in e.g. massive stars (Bednarek et al. 2014), generating gamma-rays via IC or Bremsstrahlung radiation. However it is expected that the resulting gamma-rays should correlate with the region of high photon density. The gamma-ray emission extends up to $\sim 25_{d_{5kpc}}$ pc, in contrast with the $\sim 4_{d_{5kpc}}$ pc core radius of the cluster, disfavoring a leptonic origin of the GeV and TeV emission observed. Likewise, the source size remains constant, within the errors, for different energy bands, which indicates a stable dependency of the cooling time with energy, contrary to what is expected in a leptonic scenario.

In contrast, an hadronic interpretation fits naturally the hard spectrum found from ~200 MeV up to a few tens of GeV, where it connects smoothly with the H.E.S.S. spectrum, and continues up to a few TeVs before showing a drop of the flux. Next, we constrain the proton population that powers the gamma-ray source by modeling the 200 MeV to 20 TeV emission using the NAIMA package (version 0.8.4, Zabalza 2015). To calculate the SED, we used a distance of 5 kpc. The molecular content in the region has been deeply investigated by several authors (Dame 2007; Furukawa et al. 2014) using millimeter wave CO spectroscopy. Several massive molecular clouds were found within the surrounding of Westerlund 2. The total mass is estimated to be between $(1.7 - 7.5) \times 10^5 M_\odot$. We used a particle distribution described by a particle index s and an amplitude N_p, up to an energy cut-off $E_{\rm cutoff}$. The corresponding gamma-

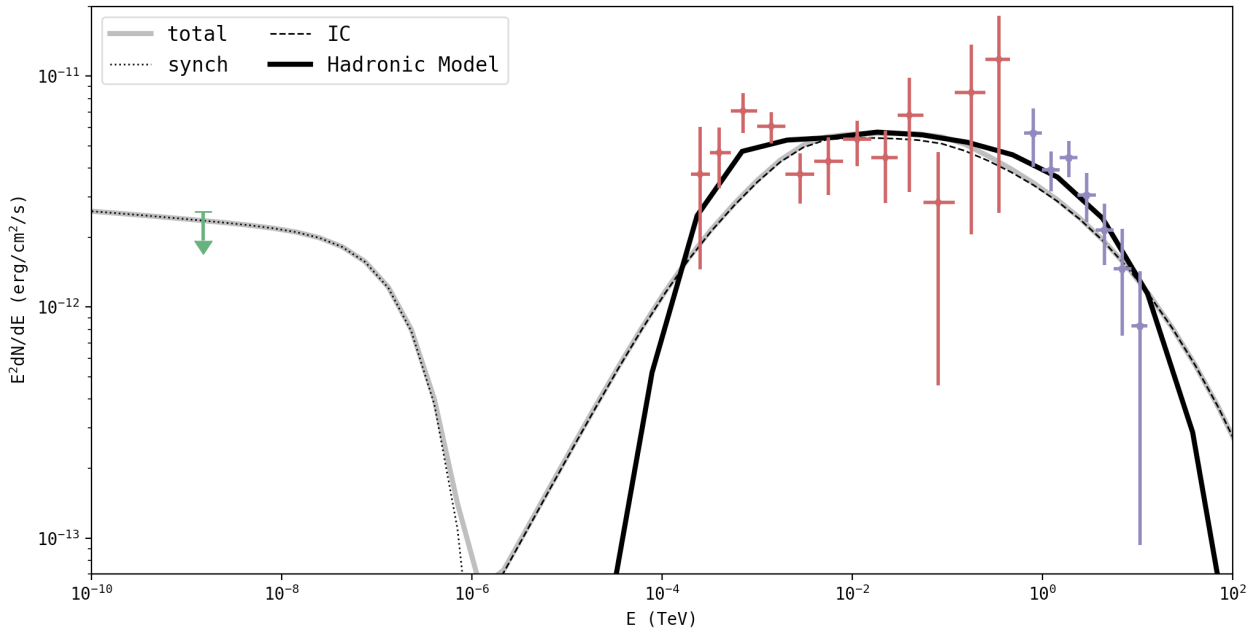

Figure 4. Best-fitting models for FGES J1023.3–5747 spectrum in the pion decay (solid line) and PWN (dashed line) hypotheses. The red points correspond to the *Fermi*-LAT data analysis (with only statistical errors), and the purple ones to H.E.S.S. (H. E. S. S. Collaboration et al. 2011). The upper limit in the X-ray domain is obtained from Fujita et al. 2009.

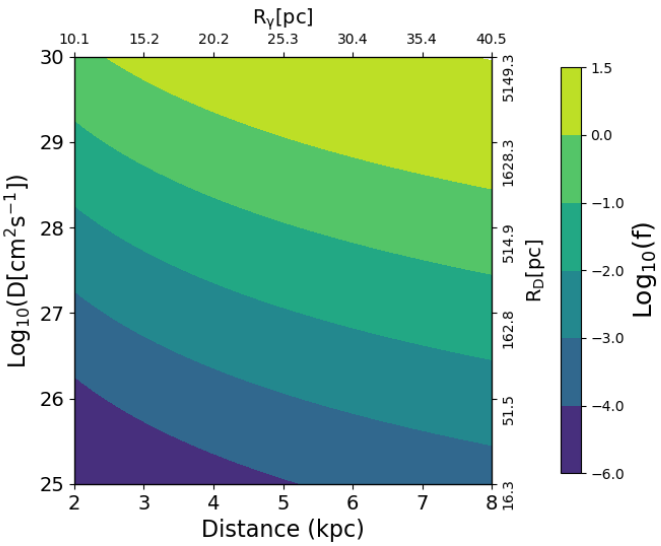

Figure 5. Acceleration efficiency (f) obtained with respect to the distance and diffusion coefficient (D) assumed (for a fiducial target mass in molecular clouds of 4.5×10^5 $M_\odot$). The upper and right axes correspond to the estimated gamma-ray source and CRs diffusion radius, respectively.

ray emission due to pion decay radiation is calculated using the parametrization in Kafexhiu et al. 2014 implemented in NAIMA, and compared to the experimental data. The best-fitting model for the joint *Fermi*-LAT and H.E.S.S. data corresponds to an exponential cut-off power-law proton spectrum with cut-off energy E_{cutoff} = 93 ± 8 TeV, and a particle index of s = 2.09 ± 0.01, referenced to 1 TeV, see Fig. 4). The fit to the data is done by means of a Log-Likelihood approach. For a distance of 5 kpc, the total energy in protons estimated above 1.22 GeV (the threshold kinetic energy for pion production in pp interactions) is $W_p = (1.3 - 5.9) \times 10^{48}$ erg, for densities of n = (7.5 - 1.7)×10^5 $M_\odot/V_{24pc}$, as derived by Furukawa et al. 2014 and Dame 2007, respectively. We estimated a lower limit for the cut-off energy on the proton spectrum of ≈ 37 TeV (at 95% CL), by comparing the maximum likelihoods of the data obtained for the exponential cutoff power-law and power-law models with the likelihood-ratio test.

The total energy in protons (above 1.22 GeV) can be compared with the total mechanical power of the stellar winds in the Westerlund 2 cluster: $W_{tot} = f L_0 T_0$, which results in a modest acceleration efficiency of $f = 10^{-4}$ (10^{-6} / 5×10^{-3}), for the well known age ($T_0 = 2 \times 10^6$ yr), a distance of 5 kpc (2 kpc / 8 kpc) and the available energy budget in the form of kinetic energy of stellar winds ($L_0 = 2 \times 10^{38}$ erg s^{-1}).

If we consider the total volume defined by the size of the GeV source (∼ 24 pc, i.e., V_{24pc} of volume for a spherical source), the energy density of protons in the region is ω_p = (1.3-5.9)×10^{48} erg/V_{24pc} ≃ (0.5 – 2.2) eV/cm^3 (or 0.1-5.6 eV/cm^3 if considering the uncertainty due to the distance to the source), which is comparable to the density of protons found in others massive clusters (Aharonian et al. 2019). The maximum energy of this proton population is constrained by the best fit, described above, to be ∼90 TeV, with a lower limit of 37 TeV on the energy cut-off. It would be possible however that a significant part of these CRs has already escaped from the gamma-ray emission region, where the molecular content is enhanced, and therefore also the gamma-ray radiation. Under the assumption of a continuous injection of protons and spherical expansion (Aharonian & Atoyan 1996), the relation

between the observed energy emitted by protons (W_{em}) and the total energy (in protons) available (W_{tot}) is:

$$W_{em}/W_{tot} = (R_\gamma/R_D)^2 \quad (1)$$

where R_γ and R_D are the gamma-ray source and diffusion radii, respectively. Then, using a diffusion coefficient as in the ISM, i.e., D $\sim 10^{28}$cm^{2}s^{-1} and $R_D = 2\sqrt{T_0 D} = 515$ pc, we obtain that the total energy released in the form of CRs could reach $W_{tot} \sim 5 \times 10^{50}$erg (for a distance of 5 kpc), which is still a few percent of the total available energy in the kinetic winds ($L_0 T_0 \sim 10^{52}$ erg). Note that this number is affected by the uncertainties in the distance: for instance, the efficiency obtained is larger than 10% for a distance of 8 kpc with the quoted diffusion coefficient of the ISM. Likewise, formally, the value of the diffusion coefficient could be larger, and correspondingly, the CR halo could reach up to 5 kpc (for $D \sim 10^{30}$cm^{2}s^{-1}). These uncertainties have an effect on the total efficiency, reaching in some extreme cases an unrealistically large fraction of the total energy to be transferred to CRs.

If the region is, instead, affected by large turbulence, expected in the surrounding of an accelerator, the CRs diffusion could be much slower (Malkov et al. 2013; Schroer et al. 2020). If the size observed at GeV and TeV energies ($R_\gamma \sim 24\,(d/5\mathrm{kpc})$ pc) reflects the propagation depth of CRs, the diffusion coefficient would be much lower than in the ISM $D \sim 3 \times 10^{25}$cm^{2}s^{-1} (or (0.4 - 6)$\times 10^{25}$cm^{2}s^{-1} for 2 and 8 kpc respectively), which is in tension with the value of the diffusion coefficient at these energies in the Bohm regime (Aharonian et al. 2019). That points to a certain CR halo around Westerlund 2, beyond the size traced by LAT and H.E.S.S., that could, in principle, extend up to a few tens of parsecs. The discussion above is roughly summarized in Fig. 5. More precise estimations of the distance to the cluster, foreseen with *Gaia* DR3 (Zeidler et al. 2018) (and therefore of the real gamma-ray size), would provide constraining limits on the diffusion of CRs around the source, for a range of acceleration efficiency f.

Another possibility to explain the gamma-ray emission involves energetic SNR explosions within the cluster, injecting CRs in the surrounding Townsley et al. (2019). The lack of shell-like structure and the high efficiency required in the case of diffusive CRs (50%E_{SN}, for a standard $E_{SN} = 10^{51}$erg) render this hypothesis less attractive, at least for a single SNR event, than the one that attributes the origin of CRs to the stellar winds.

5 CONCLUSIONS

The reanalysis of the large LAT dataset presented here results in a clear identification of the extended source FGES J1023.3–5747 with the TeV source HESS J1023-575. The matching spectral and morphological agreement, with no signs of cooling features in the size of the source, points to a common origin of the radiation. The combination of the two results obtained, that is, the extended source beyond the cluster size and in a good agreement with the TeV radiation, and the hard spectrum that continues towards low energies, constitutes evidence of the hadronic nature of the gamma-ray emission detected using *Fermi*-LAT and H.E.S.S. data. Here we evaluate the different scenarios proposed to explain HESS J1023-575, in light of the new information provided by the LAT spectrum and concluded that the gamma-ray source is compatible with being of hadronic origin, and related to the Westerlund 2 stellar cluster, rather than to leptonic emission from either the PWN associated with PSR J1023–5746, or the cluster itself. However, the PWN scenario, even if unlikely, can not be conclusively ruled out when considering the uncertainties in the data points. Moreover, the reasonable uncertainties of both models as well as the possible existence of a multi-component photon energy density introduce further ambiguity.

The results presented, pointing to the Westerlund 2 cluster as a hadronic accelerator with a hard ~ 2 spectral index, indirectly support the hypothesis of stellar clusters as significant contributors to the GCR sea. In particular, these CRs steaming from Westerlund 2 might also extend to a very large halo (~200 pc radius) around the cluster, as proposed in Yang et al. 2018. The total energy in protons we derive ($\sim 5 \times 10^{50}$erg) can easily account for the total luminosity observed, requiring an acceleration efficiency in the cluster of $f = 0.04$, which is still moderate for acceleration theories in wind shocks. The spectrum at TeV energies seems to change the hard 2 index trend found in the LAT data, softening towards higher energies. This spectral shape would imply a low energy cut-off, disfavoring Westerlund 2 as a PeVatron accelerator. Deeper observations with H.E.S.S. or with sensitive TeV instruments in the South such as CTA (Cherenkov Telescope Array Consortium et al. 2019) in the future should provide a definitive answer to the PeVatron nature of HESS J1023-575.

DATA AVAILABILITY

The *Fermi*-LAT data underlying this article are available at https://fermi.gsfc.nasa.gov/ssc/data/access/lat/. The GLIMPSE survey archival data underlying Figure 3 are available in https://irsa.ipac.caltech.edu/data/SPITZER/GLIMPSE/.

ACKNOWLEDGEMENTS

This research was supported by the Alexander von Humboldt Foundation (EdOW). E. M. & D. F. T. acknowledge the support of the grants AYA2017-92402- EXP, PGC2018-095512-B-I00 (Ministerio de Economía y Competitividad) and SGR2017-1383 (Generalitat de Catalunya). We acknowledge the support of the PHAROS COST Action (CA16214). We made use of R Project for Statistical Computing (R Core Team 2013). The *Fermi*-LAT Collaboration acknowledges generous ongoing support from a number of agencies and institutes that have supported both the development and the operation of the LAT as well as scientific data analysis. These include the National Aeronautics and Space Administration and the Department of Energy in the United States, the Commissariat a' l'Energie Atomique and the Centre National de la Recherche Scientifique / Institut National de Physique Nucléaire et de Physique des Particules in France, the Agenzia Spaziale Italiana and the Istituto Nazionale di Fisica Nucleare in Italy, the Ministry of Education, Culture, Sports, Science and Technology (MEXT), High Energy Accelerator Research Organization (KEK) and Japan Aerospace Exploration Agency (JAXA) in Japan, and the K. A. Wallenberg Foundation, the Swedish Research Council and the Swedish National Space Board in Sweden. This work performed in part under DOE Contract DE-AC02-76SF00515.

REFERENCES

Abdo A. A., et al., 2013, ApJS, 208, 17
Abdollahi S., et al., 2020, The Astrophysical Journal Supplement Series, 247, 33

Abramowski A., et al., 2012, A&A, 537, A114
Acero F., et al., 2013, Astrophys. J., 773, 77
Ackermann M., et al., 2011a, Science, 334, 1103
Ackermann M., et al., 2011b, ApJ, 726, 35
Ackermann M., et al., 2017a, ApJ, 843, 139
Ackermann M., et al., 2017b, ApJ, 843, 139
Aharonian F. A., Atoyan A. M., 1996, A&A, 309, 917
Aharonian F., et al., 2007, A&A, 467, 1075
Aharonian F., Yang R., de Oña Wilhelmi E., 2019, Nature Astronomy, 3, 561
Ajello M., et al., 2011, The Astrophysical Journal, 744, 80
Ascenso J., Alves J., Beletsky Y., Lago M. T. V. T., 2007, A&A, 466, 137
Atwood W. B., et al., 2009, ApJ, 697, 1071
Atwood W., et al., 2013. (arXiv:1303.3514)
Ballet J., Burnett T. H., Digel S. W., Lott B., 2020, arXiv e-prints, p. arXiv:2005.11208
Bednarek W., Pabich J., Sobczak T., 2014, Phys. Rev. D, 90, 103008
Binns W. R., et al., 2005, ApJ, 634, 351
Blumenthal G. R., Gould R. J., 1970, Reviews of Modern Physics, 42, 237
Bonanos A. Z., et al., 2004, ApJ, 611, L33
Bruel P., Burnett T. H., Digel S. W., Johannesson G., Omodei N., Wood M., 2018, Fermi-LAT improved Pass 8 event selection (arXiv:1810.11394)
Bykov A. M., Marcowith A., Amato E., Kalyashova M. E., Kruijssen J. M. D., Waxman E., 2020, Space Sci. Rev., 216, 42
Carraro G., Munari U., 2004, MNRAS, 347, 625
Cesarsky C. J., Montmerle T., 1983, Space Sci. Rev., 36, 173
Cherenkov Telescope Array Consortium et al., 2019, Science with the Cherenkov Telescope Array, doi:10.1142/10986.
Dame T. M., 2007, ApJ, 665, L163
Drew J. E., Herrero A., Mohr-Smith M., Monguió M., Wright N. J., Kupfer T., Napiwotzki R., 2018, MNRAS, 480, 2109
Fujita Y., Hayashida K., Takahashi H., Takahara F., 2009, PASJ, 61, 1229
Furukawa N., Dawson J. R., Ohama A., Kawamura A., Mizuno N., Onishi T., Fukui Y., 2009, ApJ, 696, L115
Furukawa N., et al., 2014, ApJ, 781, 70
Gabici S., Evoli C., Gaggero D., Lipari P., Mertsch P., Orlando E., Strong A., Vittino A., 2019, International Journal of Modern Physics D, 28, 1930022
Guarnieri M. D., Lattanzi M. G., Massone G., Munari U., Moneti A., 1995, in The Formation of the Milky Way. pp 183–184
H. E. S. S. Collaboration et al., 2011, A&A, 525, A46
H. E. S. S. Collaboration et al., 2012, A&A, 548, A46
H. E. S. S. Collaboration et al., 2015, Science, 347, 406
H. E. S. S. Collaboration et al., 2018, A&A, 612, A2
H. E. S. S. Collaboration et al., 2019, A&A, 621, A116
Hahn J., 2015, in 34th International Cosmic Ray Conference (ICRC2015). p. 917
Hobbs G. B., Edwards R. T., Manchester R. N., 2006, MNRAS, 369, 655
Kafexhiu E., Aharonian F., Taylor A. M., Vila G. S., 2014, Phys. Rev. D, 90, 123014
Kerr M., Ray P. S., Johnston S., Shannon R. M., Camilo F., 2015, ApJ, 814, 128
Lande J., et al., 2012, ApJ, 756, 5
Li J., Torres D. F., Lin T. T., Grondin M.-H., Kerr M., Lemoine-Goumard M., de Oña Wilhelmi E., 2018, ApJ, 858, 84
Malkov M. A., Diamond P. H., Sagdeev R. Z., Aharonian F. A., Moskalenko I. V., 2013, ApJ, 768, 73
Mattox J. R., et al., 1996, ApJ, 461, 396
Moffat A. F. J., Shara M. M., Potter M., 1991, AJ, 102, 642
Piatti A. E., Bica E., Claria J. J., 1997, VizieR Online Data Catalog, pp J/A+AS/127/423
Principe G., Mitchell A. M. W., Caroff S., Hinton J. A., Parsons R. D., Funk S., 2020, A&A, 640, A76
R Core Team 2013, R: A Language and Environment for Statistical Computing. R Foundation for Statistical Computing, Vienna, Austria, http://www.R-project.org/
Rauw G., et al., 2004, A&A, 420, L9
Rauw G., et al., 2005, A&A, 432, 985
Rauw G., Manfroid J., Gosset E., Nazé Y., Sana H., De Becker M., Foellmi C., Moffat A. F. J., 2007, A&A, 463, 981
Saha L., Domínguez A., Tibaldo L., Marchesi S., Ajello M., Lemoine-Goumard M., López M., 2020, ApJ, 897, 131
Salpeter E. E., 1955, ApJ, 121, 161
Saz Parkinson P. M., et al., 2010, ApJ, 725, 571
Scargle J. D., Norris J. P., Jackson B., Chiang J., 2013, ApJ, 764, 167
Schroer B., Pezzi O., Caprioli D., Haggerty C., Blasi P., 2020, arXiv e-prints, p. arXiv:2011.02238
Sun X.-N., Yang R.-Z., Wang X.-Y., 2020, MNRAS, 494, 3405
Torres D. F., Cillis A., Martín J., de Oña Wilhelmi E., 2014, Journal of High Energy Astrophysics, 1, 31
Townsley L. K., Broos P. S., Garmire G. P., Povich M. S., 2019, ApJS, 244, 28
Tsujimoto M., et al., 2007, ApJ, 665, 719
Uzpen B., et al., 2005, ApJ, 629, 512
Vargas Álvarez C. A., Kobulnicky H. A., Bradley D. R., Kannappan S. J., Norris M. A., Cool R. J., Miller B. P., 2013, AJ, 145, 125
Vargas Álvarez C. A., Kobulnicky H. A., Bradley D. R., Kannappan S. J., Norris M. A., Cool R. J., Miller B. P., 2013, The Astronomical Journal, 145, 125
Whiteoak J. B. Z., Uchida K. I., 1997, A&A, 317, 563
Whitney B. A., et al., 2004, ApJS, 154, 315
Wood M., Caputo R., Charles E., Di Mauro M., Magill J., Perkins J. S., Fermi-LAT Collaboration 2017, in 35th International Cosmic Ray Conference (ICRC2017). p. 824 (arXiv:1707.09551)
Yang R.-Z., Wang Y., 2020, A&A, 640, A60
Yang R.-z., de Oña Wilhelmi E., Aharonian F., 2018, A&A, 611, A77
Zabalza V., 2015, Proc. of International Cosmic Ray Conference 2015, p. 922
Zeidler P., et al., 2018, AJ, 156, 211

APPENDIX A: ANALYSIS DETAILS

This paper has been typeset from a TEX/LATEX file prepared by the author.

Table A1. Best-fitted position (in equatorial and Galactic coordinates) for PSR J1023–5746 and FGES J1023.3–5747 (in degrees, with only statistical errors).

Parameter	PSR J1023–5746 (On-peak)	PSR J1023–5746 (*Bridge*)	FGES J1023.3–5747 (Off-peak)	FGES J1023.3–5747 ($E > 10$ GeV)
RA	155.772 ± 0.005	155.79 ± 0.01	155.93 ± 0.03	155.93 ± 0.02
DEC	-57.764 ± 0.005	-57.77 ± 0.01	-57.79 ± 0.03	-57.76 ± 0.02
l	284.168 ± 0.005	284.18 ± 0.01	284.25 ± 0.02	284.24 ± 0.02
b	-0.401 ± 0.005	-0.40 ± 0.01	-0.38 ± 0.03	-0.35 ± 0.02

Parameter	FGES J1023.3–5747 (On-peak)	FGES J1023.3–5747 (*Bridge*)
RA	155.98 ± 0.04	155.83 ± 0.03
DEC	-57.77 ± 0.03	-57.81 ± 0.03
l	284.27 ± 0.05	284.22 ± 0.03
b	-0.35 ± 0.03	-0.43 ± 0.03

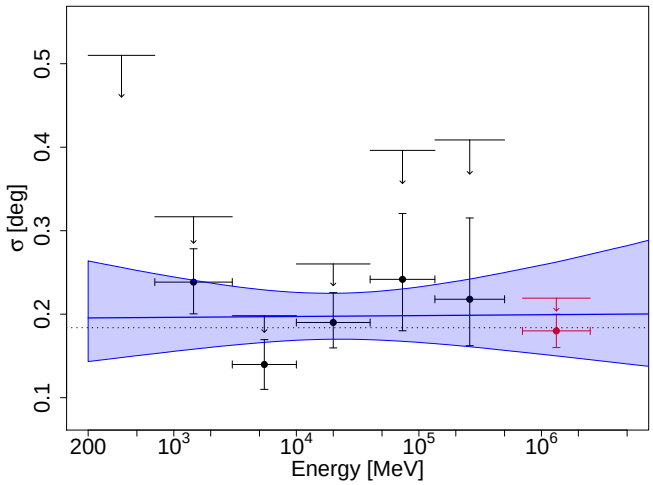

Figure A1. Extension of FGES J1023.3–5747 (i.e., intrinsic width for a Gaussian fit) measured for different energy bins (in black points for LAT data, with only statistical errors). The red point corresponds to the intrinsic extension measured by H.E.S.S. from 0.7 TeV to 2.5 TeV of energy (H. E. S. S. Collaboration et al. 2011). The best-fitted power-law model (for the joint LAT and H.E.S.S. data) is plotted in blue line with the 1σ region noted (the blue shaded area), together with the weighted mean size (black dashed line). The arrows correspond to an upper limit for the extension (i.e., σ, at 95% CL), except for the one in the first energy bin corresponding with the upper limit for the 95% containment radius (r_{95}).